Giorgio Bertotti
Isaak Mayergoyz
Claudio Serpico

NONLINEAR MAGNETIZATION DYNAMICS IN NANOSYSTEMS

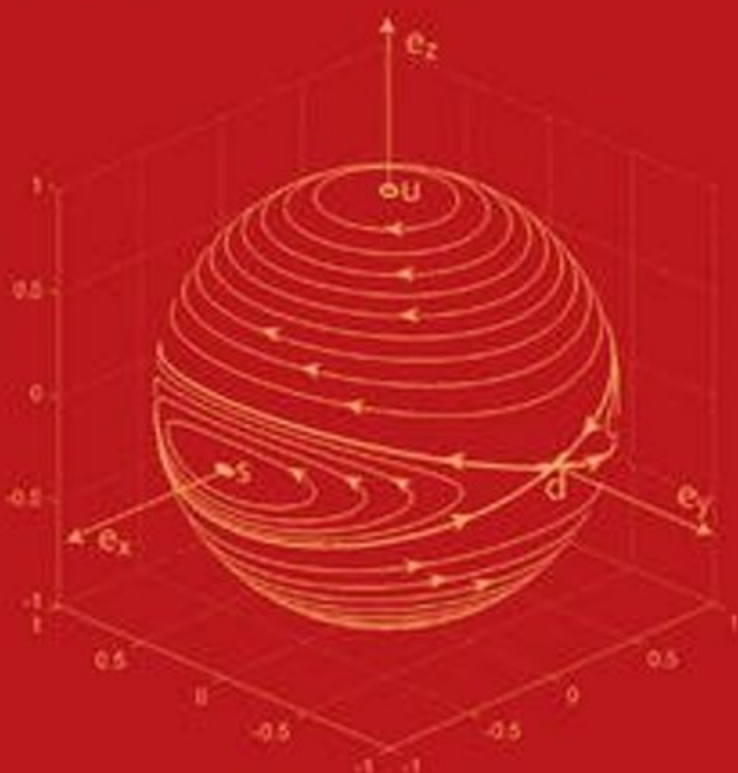

A Volume in the Elsevier Series in Electromagnetism

Elsevier
Linacre House, Jordan Hill, Oxford OX2 8DP, UK
Radarweg 29, PO Box 211, 1000 AE Amsterdam, The Netherlands

First published 2009

British Library Cataloguing in Publication Data
Mayergoyz, I. D.
Nonlinear magnetization dynamics in nanosystems. -
(Elsevier series in electromagnetism)
1. Magnetization 2. Nanoelectromechanical systems
3. Nonlinear systems
I. Title II. Bertotti, Giorgio III. Serpico, Claudio 621.3'4

Library of Congress Cataloguing in Publication Data
Library of Congress Control Number: 2008936730

ISBN: 978-0-0804-4316-4

Printed and bound in MPG, UK

09 10 11 12 13 10 9 8 7 6 5 4 3 2 1

Preface

This book deals with the analytical study of nonlinear magnetization dynamics in nanomagnetic devices and structures. This dynamics is governed by the Landau–Lifshitz equation and its generalizations to the case of spin-polarized current injection. The book is concerned with large magnetization motions when the nonlinear nature of the Landau-Lifshitz equation is strongly pronounced. For this reason, the book is distinctly unique as far as its emphasis, style of exposition, scope and conceptual depth are concerned. It is believed that the topics discussed in the book are of interest to the broad audience of electrical engineers, material scientists, physicists, applied mathematicians and numerical analysts involved in the development of novel magnetic storage technology and novel nanomagnetic devices.

In the book, no attempt is made to refer to all relevant publications, although many of them appear in the reference list. The presentation of the material in the book is largely based on the publications of the authors that have appeared over the last ten years. This book and the research on which it is based are the outcome of truly collective efforts of the three authors. The names of the authors on the cover page are in alphabetic order. This order has no other connotation, and it is invariant with respect to circular permutations as far as the matter of merit is concerned.

We wish to express our gratitude to our former graduate students R. Bonin, M. d'Aquino, and M. Dimian, who assisted us in our research on nonlinear magnetization dynamics. We are also grateful to P. McAvoy for his help in the preparation of the manuscript.

G. Bertotti, I. D. Mayergoyz, C. Serpico
October 2008

CHAPTER 1

Introduction

The analytical study of magnetization dynamics governed by the Landau–Lifshitz equation has been the focus of considerable research for many years. Traditionally, this study has been driven by ferromagnetic resonance problems. In these problems, the main part of magnetization is pinned down by a strong constant in time (dc) magnetic field, while only a small component of magnetization executes resonance motions caused by radio-frequency (rf) fields. These small magnetization motions have been studied by linearizing the Landau–Lifshitz equation around the equilibrium state, i.e., the state corresponding to the applied dc magnetic field. For this reason, the literature on magnetization dynamics has been mostly concerned with the analytical solution of the linearized Landau–Lifshitz equation. However, this linearization approach is rather limited in scope and has little relevance to magnetic data storage technology, where the magnetic writing process results in large magnetization motions. In addition, new directions of research have recently emerged that deal with large magnetization motions and that require the analysis of the nonlinear Landau–Lifshitz equation. These new areas of research are the fast precessional switching of magnetization in thin films and the magnetization dynamics induced by spin-polarized current injection in "nano-pillar" or "nano-contact" devices. Finally, the comprehensive qualitative and quantitative understanding of nonlinear magnetization dynamics is of interest in its own right, because it may reveal new physics and, in this way, it may eventually lead to new technological applications.

In spite of significant theoretical and practical interests, very few books exist that cover nonlinear magnetization dynamics in sufficient depth and breadth. It is hoped that this book will help to bridge this gap.

The book has the following salient and novel features:

- Extensive use of techniques of nonlinear dynamical system theory for the qualitative understanding of nonlinear magnetization dynamics;
- Analytical solutions (in terms of elliptical functions) for large motions of precessional magnetization dynamics and precessional switching;

- Emphasis on the two-time-scale nature of magnetization dynamics and the development of the averaging technique for the analysis of damping switching;
- Exact analytical solutions for damped magnetization dynamics driven by circularly polarized rf fields in the case of uniaxial symmetry;
- Analysis of spin-wave instabilities for large magnetization motions;
- Analytical study of large magnetization motions (including self-oscillations) driven by spin-polarized current injection;
- Extensive analysis of randomly perturbed magnetization dynamics and its power spectral density by using the theory of stochastic processes on graphs;
- Extensive use of perturbation techniques around large magnetization motions for the analytical study of nonlinear magnetization dynamics;
- Development of novel discretization techniques for the numerical integration of the Landau–Lifshitz equation, their extensive testing and their use for the analysis of chaotic magnetization dynamics.

The book contains 11 chapters. The detailed review of the book content is given below, chapter by chapter. This review is presented in purely descriptive terms, i.e., without invoking any mathematical formulas, but rather emphasizing the physical aspects of the matter.

Chapter 2 deals with the discussion of the origin of the Landau–Lifshitz equation. Here, micromagnetics is briefly reviewed and the Landau–Lifshitz (LL) equation is introduced as a dynamic constitutive relation that is compatible with micromagnetic constraints. These constraints are the conservation in time of magnetization magnitude and the alignment of magnetization with the effective magnetic field at equilibria. The Landau–Lifshitz–Gilbert (LLG) equation is then introduced and it is demonstrated that the latter equation is mathematically equivalent to the classical Landau–Lifshitz equation. It is pointed out that the interactions with the thermal bath, which result in the physical phenomena of damping, are accounted for in the LL and LLG equations by introducing different damping terms and by slightly modifying the gyromagnetic constant γ in the precessional terms. It is then shown that, by using the appropriate linear combination of the Landau–Lifshitz and Gilbert damping terms, the LL and LLG equations can be written in the mathematically equivalent form where the precessional term is the same as in the absence of the thermal bath. Equations for the free energy balance are derived from the LL and LLG equation, and it is shown that the free energy is always a decreasing function of time when the external field is constant in time. The nonlinear Bloch equation for the magnetization dynamics is then introduced and

discussed. This Bloch equation may serve as an alternative to the LL and LLG equations in situations when the driving actions of applied magnetic fields are so strong that the magnetization magnitude is no longer preserved, at least during short transients before usual micromagnetic states have emerged. The chapter is concluded with the discussion of the normalized forms of the LL and LLG equations. These forms clearly reveal that these equations have two distinct (fast and slow) time scales associated with precession and damping, respectively.

Chapter 3 deals with spatially uniform magnetization dynamics. This dynamics is of importance for several reasons. First, the spatially uniform magnetization dynamics is often a preferable and desired mode of operation in many nano-devices and structures. Second, exchange forces strongly penalize spatial magnetization nonuniformities on the nano-scale and favor the realization of spatially uniform magnetization dynamics. Third, spatially nonuniform magnetization dynamics may appear in nano-particles and nano-devices as a result of inherent instabilities of spatially uniform magnetization dynamics. For this reason, this spatially nonuniform magnetization dynamics can be studied by means of perturbations of the spatially uniform magnetization dynamics. Finally, the spatially uniform magnetization dynamics deserves special attention because it is the simplest albeit nontrivial case of nonlinear magnetization dynamics. The comprehensive study of this case may help to distinguish the physical effects that can be ascribed to the presence of spatial nonuniformities from those which can be still explained in the framework of nonlinear spatially uniform magnetization dynamics.

It is stressed at the beginning of Chapter 3 that magnetization dynamics is mathematically described by the LLG (or LL) equation that is coupled through the effective field with the magnetostatic Maxwell equations. These LLG–Maxwell equations are nonlinear partial differential equations that can be exactly reduced to nonlinear ordinary differential equations under the conditions of spatial uniformity of (1) the applied field, (2) initial conditions for magnetization, (3) anisotropy properties of ellipsoidal particles, as well as the absence of surface anisotropy. Under these conditions, the particle magnetization is spatially uniform and the solution of the magnetostatic Maxwell equations is given in terms of the demagnetizing factors. As a result, the effective magnetic field can be expressed as a vectorial algebraic function of the spatially uniform magnetization and the entire system of LLG–Maxwell equations is exactly transformed into a single nonlinear LLG (or LL) equation. The vectorial forms of the LLG and LL equations are instrumental in the discussion of theoretical issues; however, representations of these equations in various coordinate systems may be convenient in

applications. For this reason, the representations of the LLG equation in spherical and stereographic coordinates are presented and discussed. The spherical and stereographic coordinates explicitly account for the fact that the magnetization dynamics occurs on the unit sphere. This leads to the reduction of the number of state variables to two.

The structural aspects of the nonlinear magnetization dynamics described by the LL equation are then studied. Basic qualitative features of the dynamics under applied dc magnetic field directly follow from the confinement of this dynamics to the unit sphere. These features are (1) the existence of equilibrium states; (2) the number of these states is at least two and it is always even; (3) chaos is precluded as a consequence of the two-dimensional nature of the phase space; (4) distinct equilibrium states are nodes, foci and saddles. It is demonstrated that for applied dc magnetic fields the magnetic free energy is continuously decreased in time as a result of magnetization dynamics. This implies that the LL equation has a Lyapunov structure with the free energy being a global Lyapunov function. This also implies that magnetization relaxations lead toward equilibria where the magnetic free energy reaches minimum values. The monotonic decrease in the magnetic free energy reveals that no self-oscillations (limit cycles) are possible.

It is then discussed how the LLG and LL equations can be generalized to situations when the magnetization dynamics is driven not only by the applied magnetic field, but by some other forces such as, for instance, spin-polarized current injection. In these situations, the critical points of magnetization dynamics are distinct from micromagnetic equilibrium states and the only constraint which remains is the confinement of the magnetization dynamics to the unit sphere. It turns out that the most general and natural way to account for this constraint is to use the Helmholtz decomposition for vector fields defined on the unit sphere. This decomposition reveals that the dynamics on the unit sphere is driven by the gradients of two potentials. One of these potentials can be identified with the magnetic free energy, while the mathematical expressions for the other potential depend on the physical origin of driving forces distinct from the applied magnetic field. In the particular case when the magnetization dynamics is driven by spin-polarized current injection in the presence (or absence) of applied magnetic fields, the explicit expression for the second potential is given. This expression results in the dynamic equation which has been suggested by J.C. Slonczewski.

Chapter 3 is concluded with the detailed discussion of equilibrium states for the case when the component of the applied magnetic field along one of the principal anisotropy axes is equal to zero. This case is important in the applications related to thin film devices. It is demonstrated that

in this case, the analytical theory for the characterization of equilibrium states can be completely worked out and translated into geometric terms. This theory can be regarded as the far-reaching generalization of the Stoner–Wohlfarth theory for particles with uniaxial anisotropy.

Chapter 4 deals with the analytical study of large magnetization motions of precessional dynamics. In the case of dc applied magnetic fields, this dynamics is conservative in the sense that the magnetic free energy is conserved. The study of the precessional dynamics is important at least for two reasons. First, since the damping constant α is usually quite small, the actual magnetization dynamics on a relatively short time scale is very close to the undamped precessional dynamics. This suggests that the actual dissipative dynamics can be treated as a perturbation of conservative (precessional) dynamics. This perturbation approach is extensively used throughout the book. Second, the study of the precessional magnetization dynamics is also of importance in its own right, because this study lays the foundation for the analysis of the precessional switching of magnetization which is extensively discussed in Chapter 6.

The chapter begins with the analysis of geometric aspects of the conservative precessional dynamics revealed by its phase portrait. The phase portrait of the precessional dynamics is completely characterized by the energy extremal points, i.e., maxima, minima and saddles as well as by the trajectories passing through saddles. These trajectories are called separatrices because they create a natural partition of the phase portrait into different so-called "central regions", which may enclose energy minima (low-energy regions), energy maxima (high-energy regions), or separatrices (intermediate energy regions). A natural way to describe the topological properties of the phase portrait for the precessional dynamics is by introducing an associated graph, with graph edges representing central regions and graph nodes representing saddle equilibrium with associated separatrices. Then, the "unit-disk" representation of the phase portrait of the precessional dynamics is introduced. In this representation, cartesian axes coincide with the principal anisotropy axes, and it is assumed that at least one cartesian component (for instance, h_{az}) of the applied dc magnetic field is equal to zero. Under these conditions, magnetization trajectories of the precessional dynamics on the unit sphere are projected on the $(\mathrm{m}_x, \mathrm{m}_y)$-plane as the family of self-similar elliptic curves confined to the unit disk. These elliptic curves completely represent the phase portrait of the magnetization dynamics on the unit sphere. Elliptic curves tangent to the unit circle are of particular importance because they represent the separatrices of the magnetization dynamics, with the tangency points corresponding to saddle points of the dynamics.

By using the unit-disk representation, shorthand symbolic ("string") notations that completely characterize the phase portraits on the unit sphere are established. The elliptic nature of the projections of precessional trajectories on the unit disk is utilized for the proper parametrization of these trajectories. This parametrization, in turn, serves as the foundation for the derivation of analytical formulas for precessional dynamics in terms of Jacobi elliptical functions. The mathematical machinery of these functions is extensively used to derive the analytical expressions for magnetization components in high, low, and intermediate energy regions for three distinct cases: (1) zero applied magnetic field, (2) applied magnetic field perpendicular to the easy anisotropy axis, (3) applied magnetic field directed along the easy axis. The period of precessional dynamics along a specific trajectory is determined by the value of the magnetic free energy along this trajectory. The analytical expressions for these periods as functions of energy are given in terms of the complete elliptical integrals. The chapter is concluded with the discussion of the Hamiltonian structure of the undamped Landau–Lifshitz equation that describes the precessional dynamics. It is immediately apparent that the precessional Landau–Lifshitz equation written in cartesian coordinate form does not have the canonical Hamiltonian structure because the number of state variables is odd. However, it is demonstrated that by using the special (so-called "rigid-body") Poisson bracket, the precessional Landau–Lifshitz equation can be written in non-canonical Hamiltonian form. It is further pointed out that the classical canonical form of the precessional Landau–Lifshitz equation can be achieved by using spherical coordinates with ϕ and $\cos\ \theta$ being generalized momentum and coordinate, respectively.

Chapter 5 deals with dissipative (damping) magnetization dynamics. This dynamics has two distinct time scales: the fast time scale of the precessional dynamics and the relatively slow time scale of relaxational dynamics controlled by the small damping constant α. The LL and LLG equations are written in terms of magnetization components that generally vary on the fast time scale. In this sense, the slow-time-scale dynamics is hidden and obscured by the "magnetization form" of the LL and LLG equations. One notable exception when the fast and slow time scales of magnetization dynamics are completely decoupled is the damping switching of uniaxial particles or uniaxial media. This type of switching is also of considerable technological interest due to the advent of the perpendicular mode of recording, where the damping mode of switching of uniaxial media is utilized in the writing process. This switching has been extensively studied in the past. The approach presented in the book takes full advantage of the rotational symmetry

of the problem and clearly separates the fast and slow time scales of magnetization dynamics. Namely, it is demonstrated that the dynamics of the magnetization component m_z along the symmetry (anisotropy) axis z is completely decoupled from the fast dynamics of the two other components and entirely controlled by the damping constant α. Simple analytical expressions are derived for the dynamics of m_z and the critical switching field. After computing $m_z(t)$, the fast dynamics of $m_x(t)$ and $m_y(t)$ can be studied. It is noted that the geometry of switching trajectories on the unit sphere is universal in the sense that it does not depend on the applied dc magnetic field. This geometry is controlled only by the damping constant α and by the initial orientation of the magnetization. In other words, the applied magnetic field controls only the time parametrization of the universal damping-switching trajectories.

The slow and fast time scales of magnetization dynamics are mathematically decoupled in the problem of damping switching of uniaxial particles due to the unique symmetry properties of that problem. In general, the slow-time-scale magnetization dynamics is concealed and obscured because all three magnetization components vary on the fast time scale. This is rather unsatisfactory because the slow-time-scale dynamics reveals the actual rate of relaxation to equilibrium and, consequently, the actual switching time. It is clear on physical grounds that the magnetic free energy varies on the slow time scale. In other words, the magnetic free energy is a "slow" variable whose time evolution is not essentially affected by the fast precessional dynamics. For this reason, it is desirable to derive dynamic equations containing the magnetic free energy as a state variable. It is demonstrated that this can be accomplished by using two different techniques. The first technique is based on the two-time-scale reformulation of the LL equation, in which the coupled dynamic equations are derived for the magnetic free energy and two magnetization components. In this two-time-scale formulation, the slow and fast magnetization dynamics are coupled. They can be completely decoupled by using the averaging technique. In the averaging technique, the first-order differential equation for the magnetic free energy is derived through the averaging of certain terms over precession cycles. This time averaging can be carried out analytically by using the formulas derived in Chapter 4 for the precessional dynamics. The averaging technique is used for the analytical study of magnetization relaxations under zero applied magnetic field. Such relaxations are usually referred to as "ringing" phenomena that typically occur during the final stages of magnetization switching after the external magnetic field has been switched off. The averaging technique is also used for the analytical study of magnetization relaxations under applied magnetic fields, and

the problem of damping switching of longitudinal media is discussed in detail. Here, the expression for the critical field of such switching is given and the relaxations are described in terms of Jacobi elliptic functions.

The chapter is concluded with the discussion of the Poincaré–Melnikov theory, which is conceptually similar to the averaging technique. This theory is instrumental for the identification of self-oscillations (limit cycles) of magnetization dynamics when it is driven not only by applied dc magnetic fields but by other stationary forces as well (for instance, by spin-polarized current injection). If these forces are of the same order of smallness as the damping, then along some precessional trajectories the losses of energy due to the damping can be fully balanced out by the influx of energy provided by these forces. This energy balance, which occurs not locally in time but over a period of precessional motion, is the physical mechanism for the formation of limit cycles which lie on the unit sphere in close proximity to the above-mentioned precessional trajectories. To identify these precessional trajectories, the Melnikov function is introduced through the averaging of specific terms of the LL equation over precessional trajectories. Since each precessional trajectory corresponds to the specific value of the magnetic free energy, the Melnikov function is a function of energy. The central result of the Poincaré–Melnikov theory is that the zeros of the Melnikov function are the values of the energy which correspond to the precessional trajectories that can be identified as limit cycles, i.e., as trajectories corresponding to self-oscillations of magnetization. The Poincaré–Melnikov theory is extensively used in Chapters 7 and 9 of the book in the study of quasi-periodic magnetization motions under rotating external field and magnetization self-oscillations caused by spin-polarized current injection.

Chapter 6 is concerned with the analytical study of precessional switching of magnetization in thin films. The physics of this switching is quite different from the conventional damping switching. In the case of damping switching, magnetization reversals are produced by applying magnetic fields opposite to the initial magnetization orientations. This makes initial magnetization states energetically unfavorable and causes magnetization relaxations towards desired equilibrium states. These relaxations are realized through numerous precessional cycles and, for this reason, they are relatively slow. Recently, a new mode of magnetization switching has emerged. This mode exploits fast precessional magnetization dynamics and it is termed “precessional switching”. Precessional switching is usually realized in magnetic nano-films through the following steps. The magnetization is initially along the film easy axis and a magnetic field is applied in the film plane almost

orthogonal to the magnetization. This field produces a torque which tilts the magnetization out of the film plane. This, in turn, results in a strong vertical demagnetizing field, which yields an additional torque that forces the magnetization to precess in the plane of the thin film away from its initial position. The desired magnetization reversal is realized by switching the applied magnetic field off when the magnetization is close to its reversed orientation. After the field is switched off, the magnetization relaxes to its reversed equilibrium state.

The chapter begins with the qualitative analysis of precessional switching and the very notion of precessional switching is defined in precise terms based on the properties of phase portraits of nonlinear magnetization dynamics. Namely, it is demonstrated that the application of an external magnetic field results in the modification of the original phase portrait when heteroclinic trajectories are broken into homoclinic trajectories. More importantly, new precessional magnetization trajectories appear which connect the vicinities of the two energy minima. It is along these trajectories that the precessional switching occurs. However, the switching is realized only if the field pulse duration is properly controlled such that the magnetic field is switched off when the magnetization is close to its reversed orientation. If the magnetic field is switched off when the magnetization is in the high energy regions of the original (unmodified) phase portrait, the eventual result of subsequent relaxations to equilibrium is practically uncertain. This is because the high-energy regions of the phase portraits are very fine mixtures of two basins of attraction, and the smaller the damping constant α, the more intricate and finer the entanglement of the two basins of attraction in the high-energy regions. This fine entanglement leads to the seemingly stochastic nature of precessional switching if the applied field is switched off when the magnetization is still in the high-energy regions. This seemingly stochastic nature of switching has been experimentally observed.

After the qualitative (phase portrait) analysis of precessional switching, the analytical study of the critical fields for precessional switching is presented. This study is based on the unit-disk representation of precessional dynamics and it reveals that the critical fields depend on the orientation of the applied field with respect to the easy axis. These critical fields are appreciably lower than for the traditional damping switching. It is noted that the presented analysis of the critical fields is also valid for the precessional switching of perpendicular media. The precessional switching of perpendicular media may be very appealing from the technological point of view because it can be accomplished by using the same heads as in longitudinal recording, i.e., without

"probe" heads and soft magnetic underlayers for recording media. The central issue for the realization of precessional switching is the proper pulse duration. This issue is discussed for the precessional switching of longitudinal and perpendicular media and analytical formulas are derived for the bounds of pulse durations that guarantee the switching. Then, the comparative analysis of precessional and damping switching is presented. The described analysis of critical switching fields and pulse durations that guarantee the precessional switching is carried out for rectangular pulses of applied magnetic fields, which is a clear limitation. To remove this limitation, the chapter is concluded with the discussion of the "inverse-problem" approach that leads to explicit analytical expressions for nonrectangular magnetic field pulses that result in the precessional switching. In this approach, a desired precessional switching dynamics is first chosen and the magnetic field pulse that guarantees the chosen switching dynamics is then determined. A specific version of the inverse-problem approach that is purely algebraic in nature is fully developed and illustrated. As a byproduct, this approach leads to analytical solutions for precessional nonconservative magnetization dynamics.

Chapter 7 deals with the analytical study of magnetization dynamics under dc bias and rf applied magnetic fields. In contrast with the classical ferromagnetic resonance problems, the main focus of the chapter is to find analytical solutions to the LLG equation for large magnetization motions when the nonlinear nature of the LLG equation is strongly pronounced. This is accomplished for spheroidal particles subject to dc magnetic fields applied along the symmetry axis and circularly polarized rf magnetic fields applied in the plane perpendicular to the symmetry axis. These problems exhibit rotational symmetry that can be fully exploited by using the rotating reference frame in which the external rf field is stationary. The transformation to the rotating reference frame results in the autonomous form of the magnetization dynamics on the unit sphere. Some general properties of such autonomous dynamics are readily available in mathematical literature. Namely, such dynamics has critical (fixed) points which correspond to the uniformly rotating magnetization dynamics in the laboratory reference frame. These periodic rotating solutions to the LLG equation are termed **P**-modes. It is remarkable that these periodic solutions are time-harmonic (i.e., without generation of higher-order harmonics) despite the strongly nonlinear nature of the LLG equation. The number of **P**-modes is predicted by the Poincaré index theorem. This theorem asserts that the number of nodes or foci minus the number of saddles for any autonomous dynamics on the sphere must be equal to two. Therefore, the number of **P**-mode solutions is at least two

and it is even under all circumstances. Furthermore, chaos is precluded, because the phase space of autonomous magnetization dynamics is two-dimensional. This means that the onset of chaotic dynamics is not compatible with the simultaneous constraints of rotational symmetry and spatial uniformity of the magnetization. Only if one or both of these constraints are relaxed may chaotic phenomena appear. Finally, the autonomous magnetization dynamics in the rotating frame may have limit cycles which manifest themselves in the laboratory frame as quasiperiodic solutions termed **Q**-modes.

The extensive analytical study of periodic and quasi-periodic solutions is presented. The periodic time-harmonic solutions (**P**-modes) correspond to the critical points of the autonomous dynamics in the rotating reference frame and, in the case of constant damping α, these critical points and **P**-modes can be found by solving a specific quartic equation. This suggests that there are two or four **P**-mode solutions. For these solutions to be physically realizable and experimentally observable, the corresponding critical points must be stable. The detailed analysis of stability of the critical points with respect to the spatially uniform perturbations is given and the appropriate stability diagram is constructed. It is noted that quasi-periodic solutions (**Q**-modes) appear because periodic motion along limit cycles has to be combined with the periodic motion of the rotating reference frame and their periods are not commensurate. The mathematical machinery of the Poincaré–Melnikov theory is used to analyze the limit cycles of autonomous dynamics in the rotating frame and examples of quasi-periodic solutions are given. The classification of phase portraits of the autonomous dynamics in the rotating frame is introduced and the detailed analysis of bifurcations (i.e., abrupt structural changes of phase portraits) is presented. The saddle-node bifurcation, Andronov–Hopf bifurcation, homoclinic-saddle-connection bifurcation and semi-stable-limit-cycle bifurcation are discussed and the mathematical conditions for these bifurcations are stated. The principles of the construction of bifurcation diagrams are outlined and examples of bifurcation diagrams are given.

The bifurcation analysis is applied to the study of nonlinear ferromagnetic resonance phenomena with the special emphasis on its two manifestations: foldover and rotating magnetic field induced switching. It is demonstrated that the critical rf field for the onset of the foldover phenomena can be exactly and analytically computed. In the typical case when the product of the damping coefficient and radio frequency is quite small, the approximate formula of P. Anderson and H. Suhl for the critical foldover field is recovered. It is also demonstrated that the theory of

the rotating magnetic field induced switching has strong similarities to the Stoner–Wohlfarth theory of dc field induced switching of spheroidal particles. Switching events are treated as bifurcations and the dynamic analog and generalization of the Stoner–Wohlfarth astroid is introduced.

The chapter is concluded with the analysis of magnetization dynamics in the case of deviations from rotational symmetry. Such deviations are treated as perturbations. This perturbation approach leads to linearized equations for magnetization perturbations. The perturbation technique is developed in the rotating reference frame because this results in linear ODEs with constant (in time) coefficients. In contrast with the traditional approach, when the perturbation technique is used to obtain small motion solutions around dc saturation states, the emphasis is on the derivation of analytical formulas for the large motion solutions. These solutions are obtained as perturbations around exact **P**-mode solutions. The accuracy of the perturbation technique has been extensively tested through the comparison with the numerical techniques and several examples of this testing are presented.

Chapter 8 deals with spin-waves and parametric instabilities for large magnetization motions. Previously, spin-wave instabilities were extensively studied for spatially uniform small motions. It was realized that, at some rf input powers, these motions could get strongly coupled to certain thermally generated spin-wave perturbations, forcing them to grow up to nonthermal amplitudes through the so-called Suhl instabilities. The analytical expression for large magnetization motions (**P**-modes) in particles with uniaxial symmetry opens the possibility to carry out the analysis of spin-wave perturbations and spin-wave instabilities for spatially uniform large magnetization motions. This analysis reveals the remarkable result that the rf input powers capable of inducing spin-wave instabilities are bounded from below as well as from above. This implies that sufficiently large spatially uniform magnetization motions are always stable. Furthermore, it turns out that the stability of large magnetization motions may depend on the history of their excitation.

The discussion in the chapter starts with the linearization of the coupled Landau–Lifshitz–Gilbert and Maxwell equations around **P**-mode solutions. To explicitly account for the conservation of magnetization magnitude, the time-dependent basis in the plane normal to the rotating magnetization of the **P**-mode is used for the representation of magnetization perturbations. In this basis, the linearized LLG–Maxwell equations form a set of two coupled integro-partial differential equations with time-dependent integral operators that represent perturbations of magnetostatic field components. By using these linearized equations, the far-from-equilibrium generalizations of magnetostatic modes (Walker

modes) are first studied. These magnetostatic modes naturally appear when exchange forces can be neglected and magnetostatic boundary conditions are dominant. The partial differential equation for the magnetostatic potential inside the particle is derived. In comparison with the Walker equation, the derived equation contains one additional term which accounts for large motions of the unperturbed **P**-mode. Then, the detailed analysis of far-from-equilibrium spin-wave perturbations is presented. In contrast with the discussion of magnetostatic modes, the exchange forces are fully taken into account in this analysis, while the boundary conditions are treated at best approximately. In fact, spin-wave perturbations are plane-wave perturbations that cannot satisfy exactly the interface boundary conditions. The advantage of spin-wave perturbation analysis is the essential mathematical simplification of linearized equations. Indeed, it is demonstrated that for the plane-wave perturbations, the linearized integro-partial differential equations are reduced to two coupled ordinary differential equations with time-periodic coefficients. The Floquet theory for this type of equation is briefly reviewed and its implications to the analysis of spin-wave perturbations are discussed. Some approximate analytical results for spin-wave perturbations in the case of the special orientation of the wave-vector of spin waves or the smallness of the **P**-mode motions are presented.

Next, the detailed analysis of instabilities of the plane-wave perturbations of **P**-modes is carried out. It is stressed that these instabilities are of parametric resonance nature and the mathematical machinery of the one-period map and its eigenvalues (characteristic multipliers) is extensively used in the analysis. The one-period map and its eigenvalues can be computed numerically and an example of such analysis is given. In this example, the stability diagram is constructed, which reveals the pattern typical for parametric resonance phenomena when instability is concentrated along so-called Arnold tongues. The numerical analysis is complemented by the analytical perturbative computations of the one-period map and simple analytical formulas for the characteristic multipliers are obtained and used in the stability analysis. The construction of the combined stability diagram, where the results obtained for spatially uniform perturbations are presented along with the results for spin-wave perturbations, is discussed. A special emphasis is placed on the analysis of instabilities under conditions when the ferromagnetic resonance phenomena occur. Various unique physical features of the spin-wave instabilities of large **P**-mode motions are uncovered. As particular cases of this study, all Suhl instabilities of small magnetization motions are found and discussed. The chapter is concluded with the analysis of spin-wave perturbations in ultra-thin films.

This is a special case where the magnetic charges induced by spin-wave perturbations on the film surfaces must be properly accounted for. It is demonstrated how this can be accomplished and shown that the final equations for spin-wave perturbations are structurally similar to those derived for bulk particles. For this reason, the mathematical techniques developed in the chapter can be immediately used for the analysis of spin-wave instabilities in ultra-thin films.

Chapter 9 deals with the analytical study of dynamics driven by the joint action of applied magnetic fields and spin-polarized current injection. This is a very active area of research with promising applications to current-controlled magnetic random access memories and microwave oscillators. Most experimental work and theoretical analysis in this area are concerned with three-layer structures consisting of a "pinned" magnetic layer with a fixed magnetization, a nonmagnetic spacer, and a "free" magnetic layer. This trilayer structure is traversed by spin-polarized electric current flowing in the direction normal to the plane of the layers and profoundly affecting magnetization dynamics in the free layer. This is the so-called "current-perpendicular-to-plane" configuration. Nanopatterning has been extensively used to produce a "nanopillar" version of the trilayer devices with a noncircular cross-section of layers. This leads to in-plane shape anisotropy which results in a better control of magnetization orientation in the fixed layer and in relatively stable single-domain magnetization configurations in the free layer.

The chapter begins with the discussion of the generalization of the LLG equation to the case of spin-polarized current injection. Following the work of J.C. Slonczewski (based on the semiclassical approach), an additional spin-torque term is introduced in the LLG equation and various mathematically equivalent forms of the resulting equation are discussed. It is stressed that the addition of the spin-transfer term does not affect the conservation of the magnetization magnitude and the normalized LLC–Slonczewski equation describes the magnetization dynamics on the unit sphere. In contrast with the precessional torque term, the spin-transfer term is inherently nonconservative and cannot be described in terms of the gradient of the free energy. For this reason, the LLG–Slonczewski equation describes novel physical effects which are not observable in the classical LLG dynamics. Before discussing these novel effects, the study of the stationary states of the LLG–Slonczewski dynamics is presented. It is pointed out that in the case of dc spin-polarized current injection, the phenomenon of chaos is precluded due to dimensionality considerations, and the only possible stationary states are static solutions, which are critical (fixed) points of the magnetization dynamics, and self-oscillations (limit cycles). The static solutions (critical

points) are then analyzed in the case when the direction of the applied magnetic field and the spin-polarization of the injected current coincide with the easy anisotropy axis. The analysis is performed along the same line of reasoning as the analysis of equilibrium points in Chapter 3. It is demonstrated that small spin-polarized currents do not change the number of critical points which can be equal to six, four, or two (depending on the value of the applied field). However, the spin-polarized current injection does affect the stability of the critical points.

The phenomenon of self-oscillations (limit cycles) is then studied. This is a novel physical effect which is attributed to spin-polarized current injections. The physical origin of self-oscillations is the balancing out of the energy dissipation due to the damping by the energy influx due to the spin-polarized current injection. This balancing occurs not locally in time, but rather over one precessional period. To identify the precessional trajectories over which this balancing occurs, the appropriate Melnikov function is introduced and the analytical expressions for this Melnikov function are derived in terms of elliptical integrals for various (central) regions of the phase portrait of precessional magnetization dynamics. The limit cycles (self-oscillations) are then found by using zeros of the Melnikov function. The central result of the chapter is the construction of the stability diagrams through the study of various bifurcation mechanisms. It is demonstrated that pitchfork bifurcations, Hopf bifurcations, saddle-connection bifurcations, and semi-stable limit cycle bifurcations may appear as a result of the variations of the controlled parameters such as applied magnetic field and spin-polarized current density. The calculation of bifurcation lines in the plane of the controlled parameters is discussed and the example of a stability diagram is presented for trilayer nanopillar devices. This stability diagram reveals many interesting physical effects such as, for instance, hysteretic transitions between self-oscillations and stationary states.

The chapter is concluded with the discussion of axially symmetric nanopillar devices when the directions of the applied dc magnetic field and the easy axes of the free and pinned layers are normal to the plane of the layers. This case is quite interesting because the LLG–Slonczewski equation is appreciably simplified due to the rotational symmetry. As a result, the limit cycles of the autonomous magnetization dynamics can be fully analyzed without resorting to the perturbative Poincaré–Melnikov theory. Finally, phase locking between spin-polarized current-induced self-oscillations and the action of applied circularly polarized rf fields can be fully understood and the explicit conditions for this locking are identified.

Chapter 10 deals with the extensive study of randomly perturbed magnetization dynamics. Random perturbations are caused by thermal fluctuations which become increasingly pronounced in nano-scale devices. Indeed, these thermal fluctuations may induce transitions between various states of magnetization and increase the noise level of output signals. The randomly perturbed magnetization dynamics is a Markovian stochastic process with continuous samples on the unit sphere. As such, it can be studied on two equivalent levels: on the level of random magnetization trajectories which are described by stochastic differential equations, and on the level of transition probability density which is described by the Fokker–Planck–Kolmogorov equation.

The chapter starts with the discussion of randomly perturbed magnetization dynamics described by stochastic differential equations. It is pointed out that thermal fluctuations are traditionally accounted for by introducing an additional stochastic term into the LL and LLG equations. This term is a random precessional torque caused by a vectorial Gaussian white-noise process. This process is treated as a random component of the effective magnetic field. The LL (or LLG) equation with the additional random term is a stochastic differential equation (SDE). It is stressed that there are two interpretations of solutions to such SDEs which belong to Itô and Stratonovich, respectively. It turns out that these mathematical interpretations are closely related to the physical constraint of conservation of magnetization magnitude. It is shown that if the solution of the randomly perturbed LL (or LLG) equation is understood in Stratonovich's sense then the magnetization magnitude is conserved. On the other hand, when the solution is understood in Itô's sense, the magnetization magnitude is conserved only if an additional deterministic (drift) term proportional to magnetization is introduced in the randomly perturbed LL (or LLG) equation. The discussion is then extended to the case of randomly perturbed magnetization dynamics driven by spin-polarized current injection.

Next, the discussion of the Fokker–Planck–Kolmogorov (FPK) equation for the transition probability density of stochastic processes generated by randomly perturbed magnetization dynamic equations is presented. The FPK equation is written in terms of probability current density and explicit expressions for this current are given for different cases of randomly perturbed magnetization dynamics. The analytical solution of the FPK equation for the stationary probability density is then attempted. It is demonstrated that the explicit formula for this stationary density can be found in the case when the probability current density can be expressed in terms of the magnetic free energy and its derivatives. In the case of thermal equilibrium, this stationary density coincides with

the Boltzmann distribution. This fact is used for the derivation of the "fluctuation-dissipation" relation between the damping constant and the noise strength.

The most original part of the chapter is the analysis of randomly perturbed magnetization dynamics by using stochastic processes on graphs. This analysis takes advantage of the fact that the randomly perturbed magnetization dynamics has two distinct time scales: the fast time scale of precessional dynamics and the slow time scale of magnetization dynamics caused by damping, thermal fluctuations, and spin-polarized current injection. Randomly perturbed magnetization dynamic equations are written in terms of magnetization components which are "fast" variables. For this reason, the slow-time-scale stochastic magnetization dynamics is concealed and obscured by the fast time dynamics. It is demonstrated that the slow-time-scale stochastic magnetization dynamics can be revealed by transforming the randomly perturbed magnetization dynamic equations into a stochastic differential equation (and Fokker–Planck–Kolmogorov equation) for energy. It turns out that these equations for energy are defined on graphs which reflect the structure of phase portraits of fast time precessional dynamics. It is demonstrated that, by using the machinery of stochastic processes on graphs, explicit formulas for the stationary probability density for energy can be derived in the case of randomly perturbed spin-polarized current-driven dynamics. Another useful application of stochastic dynamics on graphs is the calculation of autocovariance and spectral density. The classical result for linear time-invariant systems is that the spectral density of the output signal is related to the spectral density of the input signal through the square of the magnitude of the transfer function. This general result is of little value for strongly nonlinear randomly perturbed magnetization dynamics. For such random dynamics, the calculation of autocovariance and spectral density must be based on the FPK equation. The novel algorithm for the calculation of power spectral density based on the FPK equation is presented. The central element of this algorithm is the introduction of auxiliary "effective" probability density by integrating over all degrees of freedom related to "backward" coordinates in the transitional probability density. Calculations are further simplified by employing stochastic dynamics on graphs, and they are finally reduced to the solution of the specific boundary value problem for ordinary differential equations defined on graphs.

The chapter is concluded with the discussion of stochastic dynamics in nonuniformly magnetized objects. The discussion is centered around two topics: discretization of the randomly perturbed dynamic problems for continuous media and the calculation of the stationary probability

density for the properly discretized randomly perturbed magnetization dynamics. The explicit analytical expression for this density is derived and compared with the Boltzmann distribution. On the basis of this comparison, fluctuation-dissipation relations are obtained and used for the identification of noise strength in spatially discretized randomly perturbed magnetization dynamic equations.

Chapter 11 is concerned with the novel techniques for numerical integration of LLG and LL equations. The main emphasis in this chapter is on the derivation of finite difference schemes that preserve the qualitative features of time-continuous magnetization dynamics. The chapter starts with the discussion of the "midpoint" finite difference scheme, which preserves the magnetization magnitude throughout the numerical integration. The midpoint finite difference scheme is of second-order accuracy in time, and it is suggested to use this scheme in combination with the second-order extrapolation formula for so-called generalized effective field. This midpoint finite difference scheme is very convenient for the numerical analysis of spatially nonuniform magnetization dynamics, where it leads to complete spatial decoupling in computations. The midpoint scheme has been extensively tested by comparing the numerical results obtained by using this scheme with analytical results for **P**-mode solutions derived in Chapter 7 for the magnetization dynamics driven by circularly polarized rf fields in uniaxially symmetric particles. The results of this comparison demonstrate high accuracy and numerical stability of the midpoint finite difference scheme. It is important to point out that the midpoint finite difference scheme is consistent with the Stratonovich interpretation of the solution to stochastic differential equations that describe randomly perturbed magnetization dynamics. For this reason, the midpoint finite difference scheme is very instrumental in Monte Carlo-type analysis of stochastic magnetization dynamics. Next, the discussion of another and more sophisticated finite difference scheme for LLG and LL equations is presented. This finite difference scheme is designed in such a way that it replicates (up to the second order of accuracy) the dynamics of magnetic free energy. In particular, this scheme is exact for the precessional magnetization dynamics in the sense that it preserves two integrals of the precessional dynamics: magnetization magnitude and energy. As a result, this finite difference scheme is expected to be very accurate for slightly dissipative magnetization dynamics, which is a generic case in most engineering applications.

The chapter contains many examples of numerical modeling of magnetization dynamics problems. One such problem is of special theoretical interest. This problem is related to the rotationally invariant

magnetization dynamics in uniaxial particles studied in Chapter 7. It is pointed out in that chapter that under a circularly polarized rf magnetic field, the phenomenon of chaos is precluded due to the dimensionality considerations related to rotational symmetry. This prompted the numerical study of the possibility of chaotic dynamics in uniaxial particles under elliptically polarized applied fields when the rotational symmetry is broken. In this study, the elliptical polarization is characterized by the Stokes parameters, which specify a polarization point on the Poincaré sphere. It has been found that only in very close proximity to the equator of the Poincaré sphere (i.e., when the polarization of the rf field is practically linear) chaotic dynamics may appear. The reported numerical simulations suggest that it is reasonable to conjecture that as the elliptical polarization approaches linear, the transition to chaos occurs through the so-called chaotic transient. Indeed, it has been found that the time of chaotic transient (i.e., transient preceding the advent of the periodic solution) progressively increases as the polarization point on the Poincaré sphere approaches its equator. The performed simulations also suggest that as far as the route to chaos through the change of polarization is concerned, the chaotic phenomenon is quite rare and occurs only near the Poincaré sphere equator.

CHAPTER 2

Basic Equations for Magnetization Dynamics

2.1 LANDAU–LIFSHITZ EQUATION

The Landau–Lifshitz equation for magnetization dynamics in ferromagnets can be construed as a dynamic constitutive relation that is compatible with micromagnetic constraints. To better understand the origin and nature of this equation, it is appropriate to start with a brief discussion of the micromagnetic description of ferromagnets subject to classical electromagnetic fields [10,79].

Micromagnetics is a continuum theory, which is highly nonlinear in nature and includes effects on rather different spatial scales such as short-range exchange forces and long-range magnetostatic effects. In micromagnetics, the state of the ferromagnet is described by the differentiable vector field $\mathbf{M}(\mathbf{r}, t)$ representing the local magnetization at every point inside the ferromagnet. When the temperature is well below the Curie temperature of the ferromagnet, the strong exchange interaction prevails over all other forces at the smallest spatial scale compatible with the continuum hypothesis. This fact is taken into account by imposing the following fundamental constraint:

$$|\mathbf{M}(\mathbf{r}, t)| = \mathrm{M}_s, \tag{2.1}$$

which means that the magnitude of the local magnetization vector at each point inside the ferromagnet is equal to the spontaneous magnetization M_s at the given temperature T. The direction of $\mathbf{M}(\mathbf{r}, t)$ is in general nonuniform, i.e., it varies from point to point. At equilibria, the spatial distribution of $\mathbf{M}(\mathbf{r}, t)$ results in extrema of an appropriate Gibbs–Landau free energy $G_L(\mathbf{M}(.); \mathbf{H}_a)$. This free energy depends on the applied magnetic field $\mathbf{H}_a$ and the temperature T. We omit the dependence of G_L and M_s on T, since in the subsequent discussion the temperature will always be assumed to be uniform in space and constant in time.

The micromagnetic free energy G_L for a ferromagnet occupying the region Ω is expressed as the following volume integral:

$$G_L(\mathbf{M}(.);\mathbf{H}_a) = \int_\Omega \left[\frac{A}{\mathrm{M}_s^2}((\nabla \mathrm{M}_x)^2 + (\nabla \mathrm{M}_y)^2 + (\nabla \mathrm{M}_z)^2) + f_{AN}(\mathbf{M}) - \frac{\mu_0}{2}\mathbf{M}\cdot\mathbf{H}_M - \mu_0 \mathbf{M}\cdot\mathbf{H}_a \right] \mathrm{d}V. \quad (2.2)$$

The first term inside the integral represents the exchange energy, which penalizes nonuniformities in the magnetization orientation. The constant A is the so-called exchange stiffness constant; its value in ferromagnets is usually of the order of 10^{-11} J m^{-1}. The second term $f_{AN}(\mathbf{M})$ describes crystal anisotropy effects, while the two last terms represent magnetostatic energy and energy of interaction with the external magnetic field. The magnetostatic contribution is governed by the field $\mathbf{H}_M$. This field is determined by solving the following magnetostatic Maxwell equations:

$$\nabla \times \mathbf{H}_M = 0, \qquad \nabla \cdot \mathbf{H}_M = -\nabla \cdot \mathbf{M}, \quad (2.3)$$

subject to the appropriate interface conditions at the ferromagnet surface. The applied field $\mathbf{H}_a$ is produced by external sources and, in subsequent discussion, it will be considered as a given vector function of space and time. The micromagnetic free energy may contain additional terms describing other energy contributions, for example magnetoelastic effects. These additional terms are beyond the scope of our discussion.

To find equilibrium magnetization states under given applied field $\mathbf{H}_a$, the free energy variation δG_L with respect to arbitrary variations of the vector field $\mathbf{M}(\mathbf{r})$ subject to the constraint (2.1) must first be determined. By using standard variational calculus, one obtains that δG_L corresponding to magnetization variation $\delta\mathbf{M}(\mathbf{r})$ is given by the expression:

$$\delta G_L = -\mu_0 \left[\int_\Omega \mathbf{H}_{\text{eff}} \cdot \delta\mathbf{M}\, \mathrm{d}V - \frac{2A}{\mu_0 \mathrm{M}_s^2} \oint_\Sigma \frac{\partial \mathbf{M}}{\partial n} \cdot \delta\mathbf{M}\, \mathrm{d}S \right], \quad (2.4)$$

where the second integral is over the surface Σ of the ferromagnet, while $\partial/\partial n$ represents the derivative with respect to the outward normal to Σ. The effective field $\mathbf{H}_{\text{eff}}$ is defined as:

$$\mathbf{H}_{\text{eff}} = \mathbf{H}_a + \mathbf{H}_M + \mathbf{H}_{AN} + \mathbf{H}_{EX}, \quad (2.5)$$

where $\mathbf{H}_{AN}$ and $\mathbf{H}_{EX}$ are the anisotropy field and the exchange field, respectively:

$$\mathbf{H}_{AN} = -\frac{1}{\mu_0}\frac{\partial f_{AN}}{\partial \mathbf{M}}, \qquad \mathbf{H}_{EX} = \frac{2A}{\mu_0 \mathrm{M}_s^2}\nabla^2 \mathbf{M}. \tag{2.6}$$

At equilibrium, $\delta G_L = 0$ for any arbitrary variation $\delta\mathbf{M}$ consistent with the constraint (2.1). Such a variation of $\mathbf{M}$ will be of the form:

$$\delta\mathbf{M} = \mathbf{M} \times \delta\mathbf{v}, \tag{2.7}$$

where $\delta\mathbf{v}$ is a small but otherwise arbitrary space-dependent vector. By substituting Eq. (2.7) into Eq. (2.4) and by taking into account that $\delta G_L = 0$ for any arbitrary space-dependent variation $\delta\mathbf{v}$, one finds that at each point in Ω the following equation is valid:

$$\mathbf{M} \times \mathbf{H}_{\text{eff}} = 0, \tag{2.8}$$

whereas at each point on Σ:

$$\mathbf{M} \times \frac{\partial \mathbf{M}}{\partial n} = 0 \quad \text{i.e.} \; \frac{\partial \mathbf{M}}{\partial n} = 0. \tag{2.9}$$

The above two forms of the boundary condition are equivalent because $\partial\mathbf{M}/\partial n$ is perpendicular to $\mathbf{M}$ as a consequence of (2.1). Equation (2.8) is known as Brown's equation; it expresses the fact that the local torque exerted on the magnetization by the effective field must be zero at equilibrium [133,134]. The boundary condition given by Eq. (2.9) is valid when no surface anisotropy is present. Surface anisotropy may give rise to pinning effects that substantially alter the response of the ferromagnet to external magnetic fields. In particular, spatially nonuniform magnetization modes may appear under spatially uniform driving fields in ellipsoidal ferromagnetic particles.

It is important to stress that Brown's equation determines all possible magnetization equilibria regardless of their stability. However, according to the thermodynamic principle of free energy minimization, only G_L minima will correspond to stable equilibria and, thus, will be in principle physically observable. The information on the nature of equilibria can be obtained by computing the second variation of G_L and determining if it is positive under arbitrary variations of the vector field $\mathbf{M}(\mathbf{r})$, subject to the constraint (2.1).

When $\mathbf{M} \times \mathbf{H}_{\text{eff}} \neq 0$, the system is not at equilibrium and will evolve in time according to some appropriate dynamic equation. The equation originally proposed by Landau and Lifshitz [429] is mostly used for the description of magnetization dynamics. This equation is based on the idea that in a ferromagnetic body the effective field $\mathbf{H}_{\text{eff}}$ will induce a precession of local magnetization $\mathbf{M}(\mathbf{r}, t)$ of the form:

$$\frac{\partial \mathbf{M}}{\partial t} = -\gamma \mathbf{M} \times \mathbf{H}_{\text{eff}}, \tag{2.10}$$

where $\gamma > 0$ determines the precession rate. In the following, for simplicity we shall identify γ with the gyromagnetic ratio associated with the electron spin, which yields $\gamma = 2.2 \cdot 10^5 \ \text{A}^{-1} \ \text{ms}^{-1}$. The dynamics described by Eq. (2.10) is such that the magnitude (length) of magnetization $|\mathbf{M}|$ is conserved. Indeed, $\mathbf{M} \cdot \partial \mathbf{M}/\partial t = 0$ is an immediate consequence of Eq. (2.10). Thus, Eq. (2.10) is consistent with the fundamental micromagnetic constraint (2.1). However, this equation cannot describe any approach to equilibrium resulting in energy decrease due to interaction with a thermal bath. Indeed, by using Eqs (2.4) and (2.9) it can be shown that under constant-in-time external field:

$$\frac{\mathrm{d}G_L}{\mathrm{d}t} = -\mu_0 \int_\Omega \mathbf{H}_{\text{eff}} \cdot \frac{\partial \mathbf{M}}{\partial t} \, \mathrm{d}V = 0, \tag{2.11}$$

which means that the dynamics is nondissipative.

Energy relaxation mechanisms can be taken into account by introducing an additional phenomenological term chosen through heuristic considerations. In their original paper, Landau and Lifshitz described damping by a term proportional to the component of $\mathbf{H}_{\text{eff}}$ that is perpendicular to the magnetization:

$$\frac{\partial \mathbf{M}}{\partial t} = -\gamma_L \mathbf{M} \times \mathbf{H}_{\text{eff}} + \alpha \gamma_L \mathrm{M}_s \left(\mathbf{H}_{\text{eff}} - \mathbf{M} \frac{\mathbf{M} \cdot \mathbf{H}_{\text{eff}}}{\mathrm{M}_s^2} \right). \tag{2.12}$$

Here, γ_L is a gyromagnetic-type constant which may be different from γ in Eq. (2.10), while α is a damping constant. The rationale behind Eq. (2.12) can be explained as follows. The effective field $\mathbf{H}_{\text{eff}}$ identifies in $\mathbf{M}$-space the direction of steepest energy decrease, so it would be the natural direction for magnetization relaxation. However, the magnetization magnitude must be preserved as well. This suggests that only the $\mathbf{H}_{\text{eff}}$ component perpendicular to $\mathbf{M}$ may contribute to $\partial \mathbf{M}/\partial t$. It is apparent that this component coincides with the vector

$-\mathbf{M} \times (\mathbf{M} \times \mathbf{H}_{\text{eff}})/\mathrm{M}_s^2$. Consequently, Eq. (2.12) can be written in the equivalent form:

$$\frac{\partial \mathbf{M}}{\partial t} = -\gamma_L \mathbf{M} \times \mathbf{H}_{\text{eff}} - \frac{\alpha \gamma_L}{\mathrm{M}_s} \mathbf{M} \times (\mathbf{M} \times \mathbf{H}_{\text{eff}}) \,. \tag{2.13}$$

This is the form in which the Landau–Lifshitz equation is mostly used in the literature. The normalization used in Eq. (2.13) is such that the damping constant α is dimensionless. Its value is quite small, of the order of 10^{-4}–10^{-3} in garnets and of the order of 10^{-2} in cobalt or permalloy.

One can compute the rate of energy change by starting from the general relation:

$$\frac{\mathrm{d}G_L}{\mathrm{d}t} = -\mu_0 \int_\Omega \mathbf{H}_{\text{eff}} \cdot \frac{\partial \mathbf{M}}{\partial t} \, \mathrm{d}V - \mu_0 \int_\Omega \mathbf{M} \cdot \frac{\partial \mathbf{H}_a}{\partial t} \, \mathrm{d}V, \tag{2.14}$$

which is valid assuming that homogeneous boundary conditions (2.9) are valid during the dynamics. By substituting Eq. (2.13) for $\partial \mathbf{M}/\partial t$ in the last equation, one obtains:

$$\frac{\mathrm{d}G_L}{\mathrm{d}t} = -\frac{\alpha \mu_0 \gamma_L}{\mathrm{M}_s} \int_\Omega |\mathbf{M} \times \mathbf{H}_{\text{eff}}|^2 \, \mathrm{d}V - \mu_0 \int_\Omega \mathbf{M} \cdot \frac{\partial \mathbf{H}_a}{\partial t} \, \mathrm{d}V, \tag{2.15}$$

which shows that the energy is always a decreasing function of time when $\partial \mathbf{H}_a/\partial t = 0$.

The Landau–Lifshitz equation can be justified on the basis of a different line of reasoning, which reveals its universal nature [147]. To this end, let us look for a dynamic equation consistent with the fundamental micromagnetic constraints, namely, the preservation of the magnetization magnitude and the validity of Brown's equation at equilibria. We restrict our choice to first-order dynamic equations:

$$\frac{\partial \mathbf{M}}{\partial t} = \mathbf{V}(\mathbf{M}, \mathbf{r}, t) \,, \tag{2.16}$$

where the vector field $\mathbf{V}$ may depend on the effective field $\mathbf{H}_{\text{eff}}$ or on other quantities characterizing the magnetization dynamics. The vector-function $\mathbf{V}$ can always be decomposed at any instant of time along three mutually orthogonal directions. As the direction of $\mathbf{M}$ plays a particular role in our problem (no magnetization change can occur along $\mathbf{M}$ itself), we choose $\mathbf{M}$, $\mathbf{M} \times \mathbf{a}$, and $\mathbf{M} \times (\mathbf{M} \times \mathbf{a})$ as basis vectors, where $\mathbf{a}$ is

an unknown vector to be determined. Then, Eq. (2.16) can be written as follows:

$$\frac{\partial \mathbf{M}}{\partial t} = c_1 \mathbf{M} + c_2 \mathbf{M} \times \mathbf{a} + c_3 \mathbf{M} \times (\mathbf{M} \times \mathbf{a}) . \tag{2.17}$$

Let us discuss how the micromagnetic constraints affect the form of Eq. (2.17). By taking the dot product of both sides of the equation with $\mathbf{M}$, we find that $\partial |\mathbf{M}|^2 / \partial t = 2c_1 |\mathbf{M}|^2$. Since the magnetization magnitude must be preserved, it can be concluded that $c_1 \equiv 0$. From the last fact and Eq. (2.17), we find that at equilibrium the magnetization $\mathbf{M}$ satisfies the following equation:

$$c_2 \mathbf{M} \times \mathbf{a} + c_3 \mathbf{M} \times (\mathbf{M} \times \mathbf{a}) = 0. \tag{2.18}$$

Since the two terms on the left-hand side of Eq. (2.18) are mutually orthogonal, their sum can be equal to zero only if $\mathbf{M} \times \mathbf{a} = 0$. This equilibrium condition is compatible with Brown's equation (2.8) if $\mathbf{a} \equiv \mathbf{H}_{\text{eff}}$. Thus, Eq. (2.17) is reduced to the Landau–Lifshitz equation (2.13) with the notations $c_2 = -\gamma_L$ and $c_3 = -\alpha\gamma_L / \mathrm{M}_s$.

The previous reasoning suggests that *any* dynamic equation of the form (2.16) is reducible to the Landau–Lifshitz equation (2.13) provided the dynamic equation preserves $|\mathbf{M}|$ and is consistent with static micromagnetics. This implies that different forms of dynamic equation are equivalent to the Landau–Lifshitz equation up to appropriate renormalization of the coefficients γ_L and α. In this sense, the Landau–Lifshitz equation is universal in nature. On the other hand, there is no a priori reason for assuming that the coefficients γ_L and α should be constant. In general they can be functions of the state of the system. It is only for the sake of simplicity that these quantities are assumed to be constant parameters in most studies of magnetization dynamics.

The fact that the effective field $\mathbf{H}_{\text{eff}}$ in Eqs (2.10)–(2.13) is the same as in static Brown's equation is the consequence of specific assumptions. Indeed, the use of magnetostatic equations (2.3) implies that propagation effects are neglected, which means that the electromagnetic wavelength must be much larger than the linear dimensions of the ferromagnet under study. It is also worth remarking that no contributions to $\mathbf{H}_{\text{eff}}$ from eddy currents are included. Strictly speaking, this is true for nonconducting materials only. The presence of eddy currents may be roughly taken into account by renormalizing the damping constant in the LL or LLG dynamics. However, magnetization dynamics in metallic systems will not be discussed in detail.

2.2 LANDAU–LIFSHITZ–GILBERT EQUATION

Another equation for the description of magnetization dynamics in ferromagnets has been proposed by Gilbert [284,285]. This equation has the form:

$$\frac{\partial \mathbf{M}}{\partial t} = -\gamma_G \mathbf{M} \times \mathbf{H}_{\text{eff}} + \frac{\alpha}{\mathrm{M}_s} \mathbf{M} \times \frac{\partial \mathbf{M}}{\partial t}. \tag{2.19}$$

Equation (2.19) deserves special attention, because it can be derived from a suitable Lagrangian formulation of magnetization dynamics and a Rayleigh dissipation function [269]. By writing Eq. (2.19) in the form:

$$\frac{\partial \mathbf{M}}{\partial t} = -\gamma_G \mathbf{M} \times \left(\mathbf{H}_{\text{eff}} - \frac{\alpha}{\gamma_G \mathrm{M}_s} \frac{\partial \mathbf{M}}{\partial t} \right), \tag{2.20}$$

we observe that, in the Gilbert equation, relaxation to equilibrium is accounted for by subtracting from the effective field a viscous-type term proportional to the time derivative of magnetization. This is reflected also in the equation for the energy balance. Instead of Eq. (2.15), one obtains:

$$\frac{\mathrm{d}G_L}{\mathrm{d}t} = -\frac{\alpha \mu_0}{\gamma_G \mathrm{M}_s} \int_\Omega \left| \frac{\partial \mathbf{M}}{\partial t} \right|^2 \mathrm{d}V - \mu_0 \int_\Omega \mathbf{M} \cdot \frac{\partial \mathbf{H}_a}{\partial t} \, \mathrm{d}V. \tag{2.21}$$

Equation (2.19) is mathematically equivalent to Eq. (2.13). The equivalence is readily proven by applying the vector product operation "$\mathbf{M} \times \ldots$" to both sides of Eq. (2.13) and by using the identity: $\mathbf{M} \times (\mathbf{M} \times (\mathbf{M} \times \mathbf{H}_{\text{eff}})) = -\mathrm{M}_s^2 (\mathbf{M} \times \mathbf{H}_{\text{eff}})$. This leads to the formula:

$$\gamma_L \mathbf{M} \times (\mathbf{M} \times \mathbf{H}_{\text{eff}}) = -\mathbf{M} \times \frac{\partial \mathbf{M}}{\partial t} + \alpha \gamma_L \mathrm{M}_s \left(\mathbf{M} \times \mathbf{H}_{\text{eff}} \right). \tag{2.22}$$

By substituting the last formula back into Eq. (2.13), we obtain:

$$\frac{\partial \mathbf{M}}{\partial t} = -\gamma_L \left(1 + \alpha^2 \right) \mathbf{M} \times \mathbf{H}_{\text{eff}} + \frac{\alpha}{\mathrm{M}_s} \mathbf{M} \times \frac{\partial \mathbf{M}}{\partial t}. \tag{2.23}$$

The last equation coincides with the Gilbert equation (2.19) provided that:

$$\frac{\gamma_G}{\gamma_L} = 1 + \alpha^2. \tag{2.24}$$

The mathematical equivalence of Eqs (2.13) and (2.19) is expected, because Eq. (2.19) is consistent with the micromagnetic constraints $|\mathbf{M}(t)| = \mathrm{M}_s$ and $\mathbf{M} \times \mathbf{H}_{\text{eff}} = 0$ at equilibrium. As we have already demonstrated, this type of magnetization dynamics can always be described by Eq. (2.13). However, Eqs (2.13) and (2.19) may not be regarded as physically equivalent, as far as the interpretation of precessional and damping terms is concerned. This raises an interesting question of how to separate in general precessional and relaxational dynamics. It is clear from the previous discussion that the interaction with the thermal bath that leads to damping is accounted for by introducing $\mathbf{M} \times (\mathbf{M} \times \mathbf{H}_{\text{eff}})$ or $\mathbf{M} \times \partial\mathbf{M}/\partial t$ terms and by slightly modifying the precessional term, i.e., by slightly changing γ. In this sense, one might say that the true damping is represented by a certain linear combination of terms $\mathbf{M} \times \mathbf{H}_{\text{eff}}$ and $\mathbf{M} \times (\mathbf{M} \times \mathbf{H}_{\text{eff}})$ or terms $\mathbf{M} \times \mathbf{H}_{\text{eff}}$ and $\mathbf{M} \times \partial\mathbf{M}/\partial t$. According to Eq. (2.22), $\mathbf{M} \times \mathbf{H}_{\text{eff}}$ can be expressed in terms of $\mathbf{M} \times \partial\mathbf{M}/\partial t$ and $\mathbf{M} \times (\mathbf{M} \times \mathbf{H}_{\text{eff}})$. This suggests that the magnetization dynamic equation can always be written in the form:

$$\frac{\partial \mathbf{M}}{\partial t} = -\gamma \mathbf{M} \times \mathbf{H}_{\text{eff}} + \frac{\alpha_1}{\mathrm{M}_s} \mathbf{M} \times \frac{\partial \mathbf{M}}{\partial t} - \frac{\alpha_2 \gamma}{\mathrm{M}_s} \mathbf{M} \times (\mathbf{M} \times \mathbf{H}_{\text{eff}}), \quad (2.25)$$

where the last two terms completely account for damping. It may be interesting to point out that according to Eq. (2.22) the precessional term can be always expressed as a linear combination of Landau–Lifshitz and Gilbert damping terms. For this reason, the Landau–Lifshitz and Gilbert equations can be written in the following equivalent mathematical form that does not contain explicitly any precession-type term:

$$\frac{\partial \mathbf{M}}{\partial t} = c_1 \mathbf{M} \times (\mathbf{M} \times \mathbf{H}_{\text{eff}}) + c_2 \mathbf{M} \times \frac{\partial \mathbf{M}}{\partial t}. \quad (2.26)$$

The discussed issue is part of the general problem of the limits under which the phenomenological introduction of damping is acceptable and is in agreement with microscopic models of spin dynamics [147,648].

The mathematical form of the damping term in the Landau–Lifshitz–Gilbert equation can be introduced by using the Rayleigh dissipation function approach, as originally shown by Gilbert himself. According to this approach, the effect of the thermal bath on magnetization dynamics is accounted for by introducing an additional dissipation (damping) field $\mathbf{H}_{\text{dis}}$ that depends on $\partial\mathbf{M}/\partial t$:

$$\frac{\partial \mathbf{M}}{\partial t} = -\gamma_G \mathbf{M} \times (\mathbf{H}_{\text{eff}} + \mathbf{H}_{\text{dis}}). \quad (2.27)$$

This dissipation field is defined in terms of the Rayleigh function defined as a quadratic form in $\dot{\mathbf{M}} = \partial\mathbf{M}/\partial t$:

$$\mathcal{R} = \frac{1}{2}\dot{\mathbf{M}} \cdot A \cdot \dot{\mathbf{M}}, \tag{2.28}$$

where A is a symmetric positive-definite matrix that does not depend on $\dot{\mathbf{M}}$. The dissipation field is related to the Rayleigh function by the formula:

$$\mathbf{H}_{\text{dis}} = -\frac{\partial \mathcal{R}}{\partial \dot{\mathbf{M}}}. \tag{2.29}$$

By using Eqs (2.28) and (2.29), Eq. (2.27) can be transformed as follows:

$$\frac{\partial \mathbf{M}}{\partial t} = -\gamma_G \mathbf{M} \times \left(\mathbf{H}_{\text{eff}} - A \cdot \dot{\mathbf{M}}\right). \tag{2.30}$$

In the simplest case when:

$$\mathcal{R} = \frac{\alpha |\dot{\mathbf{M}}|^2}{2\gamma_G \mathrm{M}_s}, \tag{2.31}$$

we find that A is proportional to the identity matrix I:

$$A = \frac{\alpha}{\gamma_G \mathrm{M}_s} I, \tag{2.32}$$

and the dynamics equation (2.30) is reduced to the Landau–Lifshitz–Gilbert equation (2.20).

2.3 OTHER EQUATIONS FOR THE DESCRIPTION OF MAGNETIZATION DYNAMICS

The magnetization dynamics equation which is most widely used in the case of nonferromagnetic media is the Bloch equation. In this equation, the conservation of the magnetization magnitude is no longer a constraint. Furthermore, two independent relaxation mechanisms are introduced for the magnetization components parallel and perpendicular to the dc external field. These relaxation mechanisms are controlled by two different time constants, τ_{ss} and τ_{sl}. The relaxation of the magnetization component perpendicular to the applied dc field is attributed to the

progressive disappearance of the phase coherence in the precession of the individual spins and is therefore referred to as "spin–spin relaxation". On the other hand, the magnetization component along the external dc field is assumed to relax to the equilibrium "saturation" magnetization $\mathbf{M}_0$ as a consequence of thermal fluctuations. This process is termed "spin–lattice relaxation".

In the presence of a dc magnetic field $\mathbf{H}_0$ and a time-harmonic (rf) field $\mathbf{H}_1$, the Bloch equation can be written as follows:

$$\frac{\partial \mathbf{M}}{\partial t} = -\gamma \mathbf{M} \times (\mathbf{H}_0 + \mathbf{H}_1) + \frac{\mathbf{e}_0 \times (\mathbf{e}_0 \times \mathbf{M})}{\tau_{ss}} + \mathbf{e}_0 \frac{M_0 - \mathbf{M} \cdot \mathbf{e}_0}{\tau_{sl}}, \quad (2.33)$$

where $\mathbf{e}_0$ is the unit vector along the applied dc field $\mathbf{H}_0$. This form of the Bloch equation is used in the description of nuclear magnetic resonance phenomena and in magnetic resonance imaging.

In the Bloch equation, the direction of the applied dc field is assumed to be dominant, as is expected to be the case in nonferromagnetic, weakly interacting systems where no important contributions to the effective field arise from internal coupling mechanisms. However, one may wonder if a similar equation could be useful in the description of ferromagnetic systems as well, under conditions where the driving action of the field is so strong that the magnetization magnitude is no longer preserved, at least during some short transients before usual micromagnetic states are formed. Such an equation can be written down by using the decomposition along three mutually orthogonal directions, as previously discussed. If the effective field $\mathbf{H}_{\text{eff}}$ is a dominating quantity, one may expect that a useful choice for the orthogonal basis may be represented by the vectors: $\mathbf{H}_{\text{eff}}, \mathbf{H}_{\text{eff}} \times \mathbf{M}, \mathbf{H}_{\text{eff}} \times (\mathbf{H}_{\text{eff}} \times \mathbf{M})$. The magnetization vector $\mathbf{M}$ is used because we want our dynamical equation to be eventually consistent with Brown's equation (2.8), which means that the combination $\mathbf{H}_{\text{eff}} \times \mathbf{M}$ must appear in the formulation. By using this basis, one arrives at the equation of the form:

$$\frac{\partial \mathbf{M}}{\partial t} = c_1 \mathbf{H}_{\text{eff}} + c_2 \mathbf{H}_{\text{eff}} \times \mathbf{M} + c_3 \mathbf{H}_{\text{eff}} \times (\mathbf{H}_{\text{eff}} \times \mathbf{M}) \,. \quad (2.34)$$

Equation (2.33) takes this form if one replaces the direction of the applied dc field $\mathbf{e}_0$ by the direction $\mathbf{e}_{\text{eff}}$ of the effective field. The result is the nonlinear Bloch equation:

$$\frac{\partial \mathbf{M}}{\partial t} = -\gamma \mathbf{M} \times \mathbf{H}_{\text{eff}} + \frac{\mathbf{e}_{\text{eff}} \times (\mathbf{e}_{\text{eff}} \times \mathbf{M})}{\tau_{ss}} + \mathbf{e}_{\text{eff}} \frac{\mathrm{M}_s - \mathbf{M} \cdot \mathbf{e}_{\text{eff}}}{\tau_{sl}}. \quad (2.35)$$

This equation has a number of interesting properties. First, it is consistent with micromagnetics. Indeed, by imposing $\partial \mathbf{M}/\partial t = 0$, one finds that each of the three orthogonal vectors in the right-hand side of Eq. (2.35) must be zero. This yields: $\mathbf{M} \times \mathbf{H}_{\text{eff}} = 0$ and $\mathbf{M} \cdot \mathbf{e}_{\text{eff}} = \mathrm{M}_s$. Thus, at equilibria $\mathbf{M}$ is aligned along $\mathbf{H}_{\text{eff}}$ due to the former equation and $|\mathbf{M}| = \mathrm{M}_s$ due to the latter. These are precisely the micromagnetic constraints previously discussed. By using Eqs (2.4) and (2.9), it can be shown that the volume integral of the dot product $-\mu_0 \mathbf{H}_{\text{eff}} \cdot \partial \mathbf{M}/\partial t$ gives the time derivative $\mathrm{d}G_L/\mathrm{d}t$ of the system free energy under the assumption that the external field is constant in time. From Eq. (2.35) one finds that the energy will certainly decrease, as required on thermodynamic grounds, provided that $\mathbf{M} \cdot \mathbf{e}_{\text{eff}} \leq \mathrm{M}_s$.

2.4 LANDAU–LIFSHITZ–GILBERT EQUATION IN NORMALIZED FORM

It is useful and insightful to rewrite the micromagnetic free energy, the effective field, and magnetization dynamics equations in normalized form, where magnetization and fields are measured in units of M_s, while energies are measured in units of $\mu_0 \mathrm{M}_s^2 V$, where V is the volume of the ferromagnet. Then, magnetization states are described by the unit vector:

$$\mathbf{m}(\mathbf{r}, t) = \frac{\mathbf{M}(\mathbf{r}, t)}{\mathrm{M}_s}, \tag{2.36}$$

and the fundamental micromagnetic constraint (2.1) assumes the form:

$$|\mathbf{m}(\mathbf{r}, t)| = 1. \tag{2.37}$$

The normalized free energy g_L associated with the vector field $\mathbf{m}$ is the sum of normalized exchange, anisotropy, magnetostatic, and Zeeman energies, respectively:

$$\begin{aligned} g_L(\mathbf{m}(.); \mathbf{h}_a) &= \frac{G_L(\mathbf{M}; \mathbf{H}_a)}{\mu_0 \mathrm{M}_s^2 V} \\ &= \frac{1}{V} \int_\Omega \left[\frac{l_{EX}^2}{2} |\nabla \mathbf{m}|^2 + \varphi_{AN}(\mathbf{m}) - \frac{1}{2} \mathbf{h}_M \cdot \mathbf{m} - \mathbf{h}_{\mathrm{a}} \cdot \mathbf{m} \right] \mathrm{d}V, \end{aligned} \tag{2.38}$$

where:

$$l_{EX} = \sqrt{\frac{2A}{\mu_0 \mathrm{M}_s^2}} \tag{2.39}$$

is the so-called exchange length;

$$\varphi_{AN}(\mathbf{m}) = \frac{f_{AN}(\mathrm{M}_s \mathbf{m})}{\mu_0 \mathrm{M}_s^2} \tag{2.40}$$

is the normalized anisotropy energy; and

$$\mathbf{h}_a = \frac{\mathbf{H}_a}{\mathrm{M}_s}, \qquad \mathbf{h}_M = \frac{\mathbf{H}_M}{\mathrm{M}_s}, \tag{2.41}$$

are the normalized applied and magnetostatic fields. The latter is the solution of the following magnetostatic Maxwell equations:

$$\nabla \cdot \mathbf{h}_M = -\nabla \cdot \mathbf{m}, \qquad \nabla \times \mathbf{h}_M = \mathbf{0}, \tag{2.42}$$

subject to the appropriate interface conditions at the ferromagnet surface. It is useful to express also lengths in normalized form, that is, in units of the exchange length l_{EX}. This normalization does not modify the form of Eq. (2.42), while it transforms Eq. (2.38) as follows:

$$g_L(\mathbf{m}(.); \mathbf{h}_a) = \frac{1}{V} \int_\Omega \left[\frac{1}{2} |\nabla \mathbf{m}|^2 + \varphi_{AN}(\mathbf{m}) - \frac{1}{2} \mathbf{h}_M \cdot \mathbf{m} - \mathbf{h}_\mathrm{a} \cdot \mathbf{m} \right] \mathrm{d}V, \tag{2.43}$$

where ∇ now represents the gradient with respect to the normalized position $\mathbf{r}/l_{EX}$.

The first variation of g_L with respect to an arbitrary variation $\delta\mathbf{m}$ of $\mathbf{m}$ is given by:

$$\delta g_L = -\frac{1}{V} \int_\Omega \mathbf{h}_\mathrm{eff} \cdot \delta\mathbf{m} \, \mathrm{d}V + \frac{l_{EX}}{V} \oiint_\Sigma \frac{\partial \mathbf{m}}{\partial n} \cdot \delta\mathbf{m} \, \mathrm{d}S, \tag{2.44}$$

where:

$$\mathbf{h}_\mathrm{eff} = \frac{\mathbf{H}_\mathrm{eff}}{\mathrm{M}_s} = \mathbf{h}_a + \mathbf{h}_M + \mathbf{h}_{AN} + \nabla^2 \mathbf{m}, \tag{2.45}$$

while:

$$\mathbf{h}_{AN} = -\frac{\partial \varphi_{AN}}{\partial \mathbf{m}} = \frac{\mathbf{H}_{AN}}{\mathrm{M}_s} \tag{2.46}$$

is the normalized anisotropy field. An important case of anisotropy, which will be extensively discussed in the sequel, is that of uniaxial anisotropy. In this case, the anisotropy energy has the following form:

$$\varphi_{AN}(\mathbf{m}) = \frac{\kappa}{2}\left[1 - (\mathbf{m}\cdot\mathbf{e}_{AN})^2\right], \tag{2.47}$$

where $\kappa = 2K_1/\mu_0\mathrm{M}_s^2$ is the normalized anisotropy constant, K_1 is the physical anisotropy constant, $\mathbf{e}_{AN}$ is the easy axis unit vector. The anisotropy field is then given by:

$$\mathbf{h}_{AN}(\mathbf{m}) = \kappa \mathbf{e}_{AN}(\mathbf{e}_{AN}\cdot\mathbf{m}). \tag{2.48}$$

Magnetization equilibrium states can be found by imposing $\delta g_L = 0$ for variation of $\mathbf{m}$ consistent with the constraint (2.37), and this leads to the normalized Brown's equation:

$$\mathbf{m}\times\mathbf{h}_{\text{eff}} = 0, \tag{2.49}$$

with the boundary condition:

$$\frac{\partial \mathbf{m}}{\partial n} = 0. \tag{2.50}$$

As previously mentioned in connection with Eq. (2.9), this boundary condition corresponds to the absence of surface anisotropy.

The dynamics of the magnetization vector field $\mathbf{m}$ under nonequilibrium conditions is governed by the normalized version of the LL equation (2.13) or LLG equation (2.19). The dimensionless equation is obtained after a proper renormalization of time. It is convenient to choose the time unit in such a way that the coefficient in front of the dimensionless precessional term is reduced to unity. Thus, by measuring time in units of $(\gamma_L \mathrm{M}_s)^{-1}$, from Eq. (2.13) one obtains the normalized LL equation:

$$\frac{\partial \mathbf{m}}{\partial t} = -\mathbf{m}\times\mathbf{h}_{\text{eff}} - \alpha\mathbf{m}\times(\mathbf{m}\times\mathbf{h}_{\text{eff}}), \tag{2.51}$$

and the associated energy balance equation (see Eq. (2.15)):

$$\frac{\mathrm{d}g_L}{\mathrm{d}t} = -\frac{\alpha}{V}\int_\Omega |\mathbf{m}\times\mathbf{h}_{\text{eff}}|^2 \,\mathrm{d}V - \frac{1}{V}\int_\Omega \mathbf{m}\cdot\frac{\partial \mathbf{h}_a}{\partial t}\,\mathrm{d}V. \tag{2.52}$$

Similarly, by measuring time in units of $(\gamma_G \mathrm{M}_s)^{-1}$, from Eq. (2.13) one obtains the normalized LLG equation:

$$\frac{\partial \mathbf{m}}{\partial t} - \alpha\mathbf{m}\times\frac{\partial \mathbf{m}}{\partial t} = -\mathbf{m}\times\mathbf{h}_{\text{eff}}, \tag{2.53}$$

and the energy balance equation (see Eq. (2.21)):

$$\frac{\mathrm{d}g_L}{\mathrm{d}t} = -\frac{\alpha}{V}\int_\Omega \left|\frac{\partial \mathbf{m}}{\partial t}\right|^2 \mathrm{d}V - \frac{1}{V}\int_\Omega \mathbf{m}\cdot\frac{\partial \mathbf{h}_a}{\partial t}\,\mathrm{d}V. \tag{2.54}$$

Both time units $(\gamma_L \mathrm{M}_s)^{-1}$ and $(\gamma_G \mathrm{M}_s)^{-1}$ are expected to be of the order of $(\gamma \mathrm{M}_s)^{-1}$. In permalloy, with $\gamma = 2.2{\cdot}10^5\ \mathrm{A^{-1}\,ms^{-1}}$ and $\mathrm{M}_s = 8{\cdot}10^5\ \mathrm{A\,m^{-1}}$, one finds $\gamma \mathrm{M}_s = 176$ GHz, that is, $(\gamma \mathrm{M}_s)^{-1} \simeq 6$ ps. The steps made in the derivation of the normalized form of magnetization dynamics reveal that there are three natural scales in the dynamics: the field and magnetization scale is given by M_s, the space scale by l_{EX}, and the time scale by $(\gamma \mathrm{M}_s)^{-1}$. The qualitative properties of the dynamics are controlled by α and by the parameters entering the dimensionless effective field $\mathbf{h}_{\text{eff}}$.

In subsequent chapters, magnetization dynamics will be studied by using either the LL or the LLG form of the equations, i.e., Eq. (2.51) or Eq. (2.53), as convenient. It is worth recalling that these two equations have been obtained by introducing different normalizations for the time scale. Therefore, these different normalizations will have to be taken in due account whenever the equations are transformed from one form to another.

CHAPTER 3

Spatially Uniform Magnetization Dynamics

3.1 SPATIALLY UNIFORM SOLUTIONS OF LLG–MAXWELL EQUATIONS

Magnetization dynamics in ferromagnets is described by the LL equation (2.51) or the LLG equation (2.53), coupled through the effective field (2.45) with magnetostatic Maxwell equations (2.42). In the case where the Gilbert form of the dynamics is used, the problem is described by the following set of coupled equations:

$$\frac{\partial \mathbf{m}}{\partial t} - \alpha \mathbf{m} \times \frac{\partial \mathbf{m}}{\partial t} = -\mathbf{m} \times \mathbf{h}_{\text{eff}}, \tag{3.1}$$

$$\mathbf{h}_{\text{eff}} = \mathbf{h}_a + \mathbf{h}_M + \mathbf{h}_{AN} + \nabla^2 \mathbf{m}, \tag{3.2}$$

$$\nabla \cdot \mathbf{h}_M = -\nabla \cdot \mathbf{m}, \qquad \nabla \times \mathbf{h}_M = \mathbf{0}, \tag{3.3}$$

subject to the boundary conditions:

$$\frac{\partial \mathbf{m}}{\partial \mathbf{n}} = 0, \tag{3.4}$$

$$\mathbf{n} \times (\mathbf{h}_M^- - \mathbf{h}_M^+) = 0, \qquad \mathbf{n} \cdot (\mathbf{h}_M^- - \mathbf{h}_M^+) = \mathbf{n} \cdot \mathbf{m}, \tag{3.5}$$

and the initial condition:

$$\mathbf{m}(\mathbf{r}, t = 0) = \mathbf{m}_0(\mathbf{r}), \tag{3.6}$$

where superscripts "$+$" and "$-$" denote the physical quantities inside and outside the ferromagnet, respectively, while $\mathbf{n}$ is the unit vector directed along the outward normal to the ferromagnet surface.

Equations (3.1)–(3.6) describe a highly nonlinear and spatially distributed dynamical system that may exhibit very complex features such as nonlinear resonances, quasi-periodicity, chaos, turbulence-like

dynamics, nonlinear wave propagations. It is quite remarkable that such a complicated set of equations may admit exact spatially uniform solutions under certain conditions on geometrical and physical properties of the system.

These spatially uniform solutions are of importance for several reasons. First, magnetic storage technologies and spintronics are moving toward the design of increasingly smaller devices with dimensions in the nanometer range. On this spatial scale, exchange forces strongly penalize magnetization nonuniformities and therefore spatially uniform magnetization processes are expected to be the main and desirable modes of operation. Second, the uniform mode theory provides a basis for the study of more complex situations where magnetization dynamics is not spatially uniform. In fact, nonuniform magnetization configurations typically arise in small systems from uniform magnetization states through inherent instabilities. These spatially nonuniform configurations can be analyzed by using perturbation theory around spatially uniform solutions. Finally, spatially uniform magnetization dynamics deserves special attention because it is the simplest albeit nontrivial case of nonlinear magnetization dynamics. This case should be the starting point for the study of spatially nonuniform dynamics, because it may help to discriminate phenomena which can be ascribed to the presence of magnetization nonuniformities from those which can still be explained by nonlinear spatially uniform magnetization dynamics.

It is demonstrated below that spatially uniform solutions of the LLG–Maxwell equations exist under the following conditions:

1. the ferromagnet is of ellipsoidal shape (see Fig. 3.1);
2. no surface anisotropy is present, that is the boundary condition (3.4) is valid at the ferromagnet surface;
3. the parameters (e.g., anisotropy constants, anisotropy axis direction) which characterize the local anisotropy field $\mathbf{h}_{AN}$ are spatially uniform;
4. the applied field $\mathbf{h}_a$ is spatially uniform;
5. the initial distribution of magnetization is spatially uniform.

Under these conditions, the demagnetizing field $\mathbf{h}_M$ will be spatially uniform inside the particle if so is the magnetization. Indeed, the solution of magnetostatic Maxwell equations (3.3) and (3.5) inside uniformly magnetized ellipsoidal objects is spatially uniform and can be expressed in terms of the demagnetizing tensor. By choosing a system of unit vectors $(\mathbf{e}_x, \mathbf{e}_y, \mathbf{e}_z)$ along the principal axes of the ellipsoid (see Fig. 3.1), one obtains:

$$\mathbf{h}_M(\mathbf{m}) = -N_x \mathrm{m}_x \mathbf{e}_x - N_y \mathrm{m}_y \mathbf{e}_y - N_z \mathrm{m}_z \mathbf{e}_z, \tag{3.7}$$

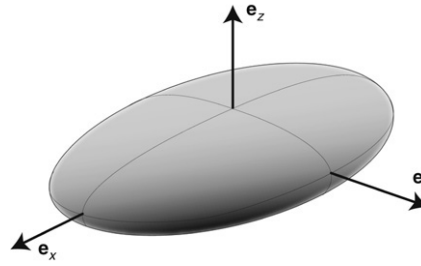

FIGURE 3.1 Ellipsoidal ferromagnet and cartesian reference frame.

where N_x, N_y, N_z are the demagnetizing factors and $N_x + N_y + N_z = 1$. Moreover, uniform magnetization is consistent with the boundary condition (3.4) and the exchange field (the last term in Eq. (3.2)) is equal to zero.

The third condition guarantees that the anisotropy field $\mathbf{h}_{AN}$ is spatially uniform when $\mathbf{m}$ is spatially uniform. We shall limit our discussion to the case of uniaxial anisotropy, where:

$$\mathbf{h}_{AN}(\mathbf{m}) = \kappa(\mathbf{e}_{AN} \cdot \mathbf{m})\mathbf{e}_{AN}. \tag{3.8}$$

In this equation, κ is the normalized anisotropy constant, while $\mathbf{e}_{AN}$ is the unit vector along the easy axis direction.

Thus, under the stated conditions, the effective magnetic field associated with a spatially uniform magnetization state is spatially uniform. This suggests that Eqs (3.1)–(3.6) can be reduced to the solution of the initial-value problem for the LLG ordinary differential equation:

$$\frac{\mathrm{d}\mathbf{m}}{\mathrm{d}t} - \alpha\mathbf{m} \times \frac{\mathrm{d}\mathbf{m}}{\mathrm{d}t} = -\mathbf{m} \times \mathbf{h}_{\text{eff}}(\mathbf{m}, t), \tag{3.9}$$

where:

$$\begin{aligned}\mathbf{h}_{\text{eff}}(\mathbf{m}, t) = \mathbf{h}_a(t) &+ \kappa(\mathbf{e}_{AN} \cdot \mathbf{m})\mathbf{e}_{AN} \\ &- N_x\mathrm{m}_x\mathbf{e}_x - N_y\mathrm{m}_y\mathbf{e}_y - N_z\mathrm{m}_z\mathbf{e}_z,\end{aligned} \tag{3.10}$$

and the initial condition is:

$$\mathbf{m}(\mathbf{r}, t = 0) = \mathbf{m}_0. \tag{3.11}$$

It is apparent that the solution of the initial value problem (3.9)–(3.11) is fully consistent with LLG–Maxwell equations (3.1)–(3.6). In the case when the LL form of the dynamics is used, the initial-value problem must be solved for the equation:

$$\frac{\mathrm{d}\mathbf{m}}{\mathrm{d}t} = -\mathbf{m} \times \mathbf{h}_{\text{eff}}(\mathbf{m}, t) - \alpha \mathbf{m} \times (\mathbf{m} \times \mathbf{h}_{\text{eff}}(\mathbf{m}, t)) , \tag{3.12}$$

where $\mathbf{h}_{\text{eff}}(\mathbf{m}, t)$ is still given by formula (3.10).

It is worth remarking that the sum of the fields $\mathbf{h}_M(\mathbf{m})$ and $\mathbf{h}_{AN}(\mathbf{m})$, corresponding to the last four terms in formula (3.10), is a linear function of $\mathbf{m}$ and thus it can be expressed as follows:

$$\mathbf{h}_M(\mathbf{m}) + \mathbf{h}_{AN}(\mathbf{m}) = -D \cdot \mathbf{m}, \tag{3.13}$$

where D is a symmetric matrix. This matrix D can be diagonalized by using the cartesian reference frame associated with its eigenvectors $\mathbf{e}'_x$, $\mathbf{e}'_y$, $\mathbf{e}'_z$. In this reference frame,

$$\mathbf{h}_{\text{eff}} = \left(\mathrm{h}'_{ax} - D'_x \mathrm{m}'_x\right) \mathbf{e}'_x + \left(\mathrm{h}'_{ay} - D'_y \mathrm{m}'_y\right) \mathbf{e}'_y + \left(\mathrm{h}'_{az} - D'_z \mathrm{m}'_z\right) \mathbf{e}'_z, \tag{3.14}$$

where $\mathrm{h}'_{ax}, \mathrm{h}'_{ay}, \mathrm{h}'_{az}$ are the components of $\mathbf{h}_a$ along $\mathbf{e}'_x$, $\mathbf{e}'_y$, $\mathbf{e}'_z$, and D'_x, D'_y, D'_z are the eigenvalues of D. In the sequel, the less general case will be discussed where the easy axis direction $\mathbf{e}_{AN}$ is aligned with one of the principal axes of the ellipsoid, i.e., with one of the unit vectors $\mathbf{e}_x$, $\mathbf{e}_y$, $\mathbf{e}_z$. In this case:

$$\mathbf{h}_{\text{eff}} = \left(\mathrm{h}_{ax} - D_x \mathrm{m}_x\right) \mathbf{e}_x + \left(\mathrm{h}_{ay} - D_y \mathrm{m}_y\right) \mathbf{e}_y + \left(\mathrm{h}_{az} - D_z \mathrm{m}_z\right) \mathbf{e}_z, \tag{3.15}$$

where the parameters D_x, D_y, D_z account for both demagnetizing and crystal anisotropy effects. Under these conditions, the free energy density is expressed in normalized form as follows:

$$\begin{aligned} g_L(\mathbf{m}; \mathbf{h}_a) = \frac{1}{2} \left(D_x \mathrm{m}_x^2 + D_y \mathrm{m}_y^2 + D_z \mathrm{m}_z^2\right) \\ - \mathrm{h}_{ax} \mathrm{m}_x - \mathrm{h}_{ay} \mathrm{m}_y - \mathrm{h}_{az} \mathrm{m}_z. \end{aligned} \tag{3.16}$$

The effective field (3.15) is related to the free energy by the expression:

$$\mathbf{h}_{\text{eff}} = -\frac{\partial}{\partial \mathbf{m}} g_L(\mathbf{m}; \mathbf{h}_a). \tag{3.17}$$

The LL and LLG equations (3.12) and (3.9) are written without any reference to a specific coordinate system. In this sense, their forms are coordinate-invariant. However, in applications, representations of these equations in various coordinate systems can be often very convenient. In particular, the representation in terms of spherical coordinates is quite natural, since the magnitude of magnetization is preserved ($|\mathbf{m}| = 1$) during the magnetization dynamics, i.e., this dynamics occurs on the unit sphere.

We limit the discussion to the LLG equation (3.9). In terms of spherical coordinates (see Fig. 3.2), the unit vector $\mathbf{m}$ is uniquely defined by the two spherical angles θ and ϕ through the formulas:

$$\mathrm{m}_x = \sin\theta\cos\phi, \qquad \mathrm{m}_y = \sin\theta\sin\phi, \qquad \mathrm{m}_z = \cos\theta. \tag{3.18}$$

By projecting Eq. (3.9) along the constant-ϕ and constant-θ directions, one arrives at the following spherical coordinate form of the equation:

$$\frac{\mathrm{d}\theta}{\mathrm{d}t} + \alpha\sin\theta\frac{\mathrm{d}\phi}{\mathrm{d}t} = -\frac{1}{\sin\theta}\frac{\partial g_L}{\partial\phi}, \tag{3.19}$$

$$-\alpha\frac{\mathrm{d}\theta}{\mathrm{d}t} + \sin\theta\frac{\mathrm{d}\phi}{\mathrm{d}t} = \frac{\partial g_L}{\partial\theta}. \tag{3.20}$$

Equations (3.19) and (3.20) can be written in matrix form as follows:

$$\begin{pmatrix} 1 & \alpha \\ -\alpha & 1 \end{pmatrix}\begin{pmatrix} \mathrm{d}\theta/\mathrm{d}t \\ \sin\theta\mathrm{d}\phi/\mathrm{d}t \end{pmatrix} = \begin{pmatrix} -(1/\sin\theta)\partial g_L/\partial\phi \\ \partial g_L/\partial\theta \end{pmatrix}. \tag{3.21}$$

By inverting the matrix in the left-hand side of Eq. (3.21), one obtains:

$$\begin{pmatrix} \mathrm{d}\theta/\mathrm{d}t \\ \sin\theta\mathrm{d}\phi/\mathrm{d}t \end{pmatrix} = \frac{1}{1+\alpha^2}\begin{pmatrix} 1 & -\alpha \\ \alpha & 1 \end{pmatrix}\begin{pmatrix} -(1/\sin\theta)\partial g_L/\partial\phi \\ \partial g_L/\partial\theta \end{pmatrix}. \tag{3.22}$$

Equation (3.22) coincides, apart from the $1/(1+\alpha^2)$ factor, with the LL equation (3.12). In this sense, the matrix inversion leading from Eq. (3.21) to Eq. (3.22) provides an alternative straightforward proof of the mathematical equivalence of the LL and LLG forms of the dynamics.

The spherical coordinate representation of the LLG equation explicitly accounts for the conservation law $|\mathbf{m}| = 1$ and, in this way, reduces the number of state variables from the three cartesian components of $\mathbf{m}$ to the two angles θ and ϕ. However, differential equations (3.19) and (3.20) have

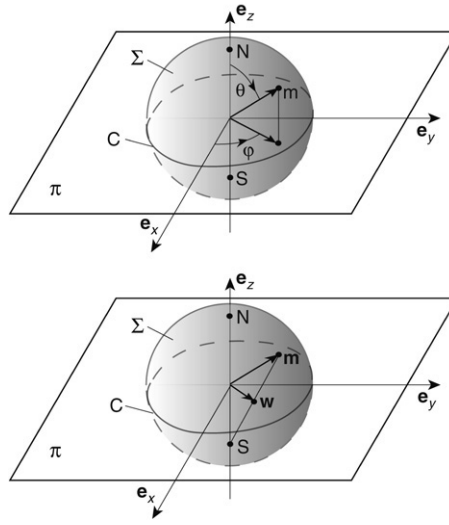

FIGURE 3.2 Spherical and stereographic representation of magnetization state. Σ is the unit sphere, π is the (x, y)-plane and C is the unit circle on π. Top: In the spherical coordinate representation, the point $\mathbf{m}$ on Σ is identified by the angles θ (angle between $\mathbf{m}$ and $\mathbf{e}_z$) and ϕ (angle between the projection of $\mathbf{m}$ on the plane π and $\mathbf{e}_x$). Bottom: In the stereographic representation, the point $\mathbf{m}$ on Σ is projected into the point $\mathbf{w}$ of the plane π by finding the intersection between π and the line connecting $\mathbf{m}$ to the south pole S of the unit sphere Σ.

singularities at the sphere poles. The use of stereographic coordinates may have some advantage in this respect. The stereographic coordinates w_x and w_y (see Fig. 3.2) are related to the cartesian coordinates by the formulas:

$$\mathrm{w}_x = \frac{\mathrm{m}_x}{1 + \mathrm{m}_z}, \qquad \mathrm{w}_y = \frac{\mathrm{m}_y}{1 + \mathrm{m}_z}. \tag{3.23}$$

The last formulas can be easily inverted to yield the expressions:

$$\mathrm{m}_x = \frac{2\mathrm{w}_x}{1 + w^2}, \qquad \mathrm{m}_y = \frac{2\mathrm{w}_y}{1 + w^2}, \qquad \mathrm{m}_z = \frac{1 - w^2}{1 + w^2}, \tag{3.24}$$

where $w^2 = \mathrm{w}_x^2 + \mathrm{w}_y^2$. By substituting the expressions (3.18) into formulas (3.23), we obtain the following relations between stereographic

and spherical coordinates:

$$\mathrm{w}_x = \frac{\sin\theta\cos\phi}{1+\cos\theta}, \qquad \mathrm{w}_y = \frac{\sin\theta\sin\phi}{1+\cos\theta}. \tag{3.25}$$

In terms of w_x and w_y, the LLG equation (3.9) is expressed in matrix form as:

$$\begin{pmatrix} 1 & \alpha \\ -\alpha & 1 \end{pmatrix} \begin{pmatrix} \mathrm{d}\mathrm{w}_x/\mathrm{d}t \\ \mathrm{d}\mathrm{w}_y/\mathrm{d}t \end{pmatrix} = \left(\frac{1+w^2}{2}\right)^2 \begin{pmatrix} -\partial g_L/\partial \mathrm{w}_y \\ \partial g_L/\partial \mathrm{w}_x \end{pmatrix}. \tag{3.26}$$

The expressions for $g_L(\mathrm{w}_x, \mathrm{w}_y)$, $\partial g_L/\partial \mathrm{w}_x$ and $\partial g_L/\partial \mathrm{w}_y$ can be derived by substituting formulas (3.24) into expression (3.16) and performing appropriate differentiations.

3.2 STRUCTURAL ASPECTS OF SPATIALLY UNIFORM MAGNETIZATION DYNAMICS

The magnetization dynamics described by Eq. (3.12) or Eq. (3.9) has structural qualitative properties which are the direct consequence of two key aspects: the fact that the magnetization magnitude $|\mathbf{m}|$ is preserved by the dynamics; and the fact that there exists a balance equation for the system free energy g_L.

The physical consequences of the conservation law $|\mathbf{m}|^2 = 1$ are best revealed by the LL form (3.12) of the magnetization dynamics. Equation (3.12) can be expressed as:

$$\frac{\mathrm{d}\mathbf{m}}{\mathrm{d}t} = \mathbf{v}(\mathbf{m}, t), \tag{3.27}$$

where:

$$\mathbf{v} = -\mathbf{m} \times \mathbf{h}_{\text{eff}} - \alpha \mathbf{m} \times (\mathbf{m} \times \mathbf{h}_{\text{eff}}). \tag{3.28}$$

The vector field $\mathbf{v}(\mathbf{m}, t)$ explicitly depends on time whenever the applied field $\mathbf{h}_a$ is time-dependent. The fact that the magnetization dynamics preserves the magnitude of $\mathbf{m}$ implies that the dynamical system (3.27) evolves on the surface of the unit sphere $|\mathbf{m}|^2 = 1$ and that the vector field $\mathbf{v}(\mathbf{m}, t)$ is tangential to this sphere at every point.

Remarkably, a number of results concerning the magnetization dynamics derive from the very form of Eq. (3.27), as the direct

consequence of the constraints imposed on the dynamics by the unit sphere topology. We shall first discuss the particular case when the dynamics is autonomous, i.e., the vector field $\mathbf{v}$ does not explicitly depend on time ($\mathbf{v} = \mathbf{v}(\mathbf{m})$). Physically, this means that the applied magnetic field is kept constant in time. Autonomous dynamical systems on the unit sphere are characterized by the following properties:

- There always exist equilibrium states for the system, namely points where $\mathbf{v} = 0$. Indeed, a stationary vector field on the sphere necessarily has singular points [529]. In general, these singular points can be either zeros or poles where the magnitude of the vector field tends to infinity. For magnetization dynamics, the vector field $\mathbf{v}$ is expected to be continuous for physical reasons, which precludes the existence of poles.
- The number of equilibria is at least two and it is always even. This conclusion is derived from Poincaré index theorem [529], which asserts that the number of nodes, foci and centers minus the number of saddles of any autonomous dynamics on the sphere is equal to two. The distinctive phase portraits of saddles, nodes, foci, and centers are shown in Fig. 3.3(a)–(d) (see Refs. [529,741,358] for more details on the classifications of equilibria in nonlinear dynamical systems).
- Chaos is precluded, because the phase space is two-dimensional [741,358]. This is the consequence of the generalized version of the Poincaré–Bendixson theorem, which states that on two-dimensional manifolds the only possible steady states are either stationary states associated with equilibria or self-oscillations associated with limit cycles of the dynamics. The phase portrait of limit cycles is shown in Fig. 3.4.

It turns out that for the LL magnetization dynamics the only admissible steady states under constant applied field are stationary states associated with equilibria. No steady self-oscillations are possible. This important conclusion is obtained from the energy balance equation (2.52), which takes the following form for a uniformly magnetized particle:

$$\frac{\mathrm{d}g_L}{\mathrm{d}t} = -\alpha \left|\mathbf{m} \times \mathbf{h}_{\text{eff}}\right|^2 - \mathbf{m} \cdot \frac{\mathrm{d}\mathbf{h}_a}{\mathrm{d}t}. \tag{3.29}$$

Under constant applied field this equation is reduced to:

$$\frac{\mathrm{d}g_L}{\mathrm{d}t} = -\alpha \left|\mathbf{m} \times \mathbf{h}_{\text{eff}}\right|^2. \tag{3.30}$$

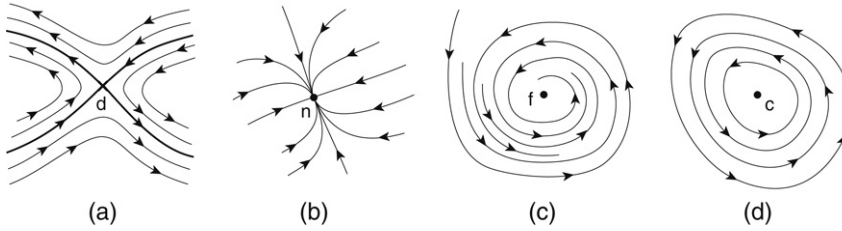

FIGURE 3.3 Qualitative sketches of magnetization dynamics on small portions of the unit sphere in the neighborhoods of equilibrium points of different nature. (a) Saddle equilibrium; (b) stable node (the sketch for the unstable node can be obtained by reversing the arrows); (c) stable focus (the sketch for the unstable focus can be obtained by reversing the arrows); (d) center (this kind of equilibrium is generally present only in conservative (undamped) systems).

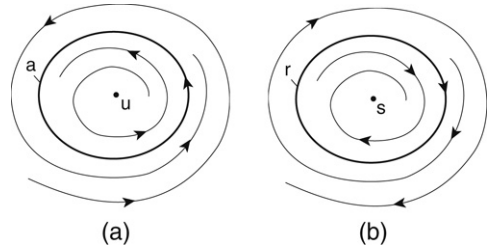

FIGURE 3.4 Schematic representation of limit cycles. (a) Stable limit cycle (a, i.e., attractive) surrounding unstable focus; (b) unstable limit cycle (r, i.e., repulsive) surrounding stable focus.

Equation (3.30) permits one to reach the following conclusions concerning the magnetization dynamics under constant applied field:

- The magnetization dynamics is such that the free energy g_L is always a decreasing function of time, as a consequence of energy dissipation due to the interaction with the thermal bath.
- The time derivative $\mathrm{d}g_L/\mathrm{d}t$ is zero only when $\mathbf{m} \times \mathbf{h}_{\text{eff}} = 0$, i.e., when an equilibrium is reached. Since g_L is always a decreasing function of time, the dynamics always brings the system to one of g_L-minima, and these energy minima are stable equilibria of the dynamics.
- The emergence of magnetization self-oscillations is not possible. Indeed, the necessary condition for the existence of self-oscillations is that g_L is a periodic nonmonotone function of time. This requirement

is in contradiction with the monotone time decrease in the free energy under constant field.
- Since the damping constant α is usually small, $\mathrm{d}g_L/\mathrm{d}t$ also tends to be small. In other words, g_L is a slow variable which evolves on slow time scales in comparison with the magnetization $\mathbf{m}$. This fact will be instrumental in the development of the averaging technique for the magnetization dynamics discussed in Chapter 5.

These conclusions are no longer valid under time-varying applied fields, where more complicated dynamical behavior can be achieved, with the appearance of periodic, quasi-periodic, and chaotic magnetization motions [740].

3.3 GENERALIZED MAGNETIZATION DYNAMICS

The LLG and LL equations (3.9) and (3.12) for the magnetization dynamics are consistent with the two basic micromagnetics constraints:

$$|\mathbf{m}|^2 = 1, \qquad \mathbf{m} \times \mathbf{h}_{\text{eff}} = 0. \tag{3.31}$$

The constraint $\mathbf{m} \times \mathbf{h}_{\text{eff}} = 0$ corresponds to the equilibrium points of magnetization dynamics when it is driven by a constant applied magnetic field. This means that under a constant field, equilibrium states always coincide with certain micromagnetic solutions of Brown equation. However, in situations when the applied field is not constant or when the micromagnetic effective field $\mathbf{h}_{\text{eff}}$ is not the only cause of magnetization dynamics, the system can be brought to nonequilibrium steady-state conditions for which the equation $\mathbf{m} \times \mathbf{h}_{\text{eff}} = 0$ may no longer represent the critical points of the dynamics. This is the case, for instance, when the magnetization dynamics is driven by spin-polarized electric currents giving rise to spin-transfer effects (see Chapter 9). This suggests that a general approach to magnetization dynamics is to assume only that the magnetization magnitude $|\mathbf{m}|^2 = 1$ is preserved, and then to investigate the physical properties of the dynamics which are consistent with this assumption.

Consider again the general magnetization dynamics equation:

$$\frac{\mathrm{d}\mathbf{m}}{\mathrm{d}t} = \mathbf{v}(\mathbf{m}, t), \tag{3.32}$$

under the sole assumption that the vector field $\mathbf{v}(\mathbf{m}, t)$ is tangential to the unit sphere $|\mathbf{m}|^2 = 1$ at every point $\mathbf{m}$. This guarantees that the magnitude

of $\mathbf{m}$ is preserved and implies that the dynamical system (3.32) evolves on the surface of the $\mathbf{m}$ sphere. The results discussed in the previous section, concerning the number of equilibria and the absence of chaos, do not depend on the specific nature of the vector field $\mathbf{v}$ and, thus, they remain valid. Furthermore, intrinsic properties of the dynamics (3.32) are revealed by expressing the vector field $\mathbf{v}(\mathbf{m}, t)$ in a form that follows from the Helmholtz decomposition theorem for vector fields defined on the sphere. According to this theorem, $\mathbf{v}(\mathbf{m}, t)$ can be always uniquely decomposed into the sum of a divergence-free and a curl-free vector field, i.e.:

$$\mathbf{v}(\mathbf{m}, t) = \mathbf{m} \times \nabla_\Sigma \Gamma - \nabla_\Sigma \Omega, \tag{3.33}$$

where Γ and Ω are arbitrary twice differentiable functions, and the subscript Σ indicates that the gradient operator ∇ is applied to a scalar field defined on the unit sphere Σ. In terms of spherical coordinates, the two terms in the right-hand side of Eq. (3.33) can be written as follows:

$$\mathbf{m} \times \nabla_\Sigma \Gamma = -\frac{1}{\sin\theta}\frac{\partial \Gamma}{\partial \phi}\mathbf{e}_\theta + \frac{\partial \Gamma}{\partial \theta}\mathbf{e}_\phi, \tag{3.34}$$

$$\nabla_\Sigma \Omega = \frac{\partial \Omega}{\partial \theta}\mathbf{e}_\theta + \frac{1}{\sin\theta}\frac{\partial \Omega}{\partial \phi}\mathbf{e}_\phi, \tag{3.35}$$

where $(\mathbf{e}_\theta, \mathbf{e}_\phi, \mathbf{m})$ is the right-handed triple of orthogonal unit vectors directed along the constant-ϕ, constant-θ, and normal-to-Σ directions, respectively. The divergence and curl properties of these two terms can be verified by using the expressions for the operators div_Σ and curl_Σ in spherical coordinates. Namely, for any generic vector $\mathbf{a} = a_\theta \mathbf{e}_\theta + a_\phi \mathbf{e}_\phi$, tangential to Σ, we have:

$$\mathrm{div}_\Sigma \mathbf{a} = \frac{1}{\sin\theta}\frac{\partial}{\partial \theta}(a_\theta \sin\theta) + \frac{1}{\sin\theta}\frac{\partial a_\phi}{\partial \phi}, \tag{3.36}$$

$$\mathrm{curl}_\Sigma \mathbf{a} = \left(\frac{\partial a_\theta}{\partial \phi} - \frac{\partial a_\phi}{\partial \theta}\right)\mathbf{m}. \tag{3.37}$$

By using these expressions, it is easy to verify that the two terms in the right-hand side of formula (3.33) represent divergence-free and curl-free vector fields, respectively:

$$\mathrm{div}_\Sigma\,(\mathbf{m} \times \nabla_\Sigma \Gamma) = 0, \tag{3.38}$$

$$\mathrm{curl}_\Sigma\,(\nabla_\Sigma \Omega) = 0. \tag{3.39}$$

By taking the divergence and the curl of Eq. (3.33), one finds that Γ and Ω satisfy the following Poisson equations on the unit sphere:

$$\Delta_\Sigma \Gamma = \mathbf{m} \cdot \mathrm{curl}_\Sigma \mathbf{v}, \tag{3.40}$$

$$\Delta_\Sigma \Omega = -\mathrm{div}_\Sigma \mathbf{v}, \tag{3.41}$$

where $\Delta_\Sigma = \mathrm{div}_\Sigma \nabla_\Sigma$ denotes the Laplace operator on Σ. On this basis, it can be demonstrated that the Helmholtz decomposition (3.33) is unique. In fact, let Γ_1 and Γ_2 be two solutions of Eq. (3.40). Then their difference $\tilde{\Gamma} = \Gamma_1 - \Gamma_2$ satisfies the Laplace equation:

$$\Delta_\Sigma \tilde{\Gamma} = 0. \tag{3.42}$$

By invoking the Green identity:

$$\oiint_\Sigma \tilde{\Gamma} \Delta_\Sigma \tilde{\Gamma} \mathrm{d}S = \oiint_\Sigma |\nabla_\Sigma \tilde{\Gamma}|^2 \mathrm{d}S, \tag{3.43}$$

and using Eq. (3.42) one finds that $\nabla_\Sigma \tilde{\Gamma} = 0$, i.e., $\tilde{\Gamma} = \mathrm{const}$. Similarly, it can also be concluded that Ω is defined by Eq. (3.41) up to a constant.

The performed analysis reveals that the most general form of magnetization dynamics consistent with the constraint $|\mathbf{m}|^2 = 1$ is:

$$\frac{\mathrm{d}\mathbf{m}}{\mathrm{d}t} = \mathbf{m} \times \nabla_\Sigma \Gamma - \nabla_\Sigma \Omega. \tag{3.44}$$

Thus, the dynamics is fully determined by the two scalar potentials Γ and Ω. The divergence-free term (dependent on Γ) may be referred to as the precessional part of the dynamics. This is because, if only this term were present, then the magnetization vector would precess along closed trajectories corresponding to constant values of Γ. In contrast, the curl-free term (dependent on Ω) may be referred to as the relaxational part of the dynamics, because if this were the only term, then the magnetization vector would steadily proceed from the maxima to the minima of the potential Ω. This clear-cut separation between precessional and relaxational effects in principle makes the above two potentials directly accessible to experiments [733].

The generalized dynamic equation (3.44) admits a balance equation for the potential Γ. This balance equation is similar to the energy balance equation (3.29) for ordinary LL dynamics. However, its structure is richer, which may result in the appearance of new types of dynamical

phenomena. This balance equation is derived by dot-multiplying both sides of Eq. (3.44) by $\nabla_\Sigma \Gamma$. By taking into account that:

$$\frac{\mathrm{d}\Gamma}{\mathrm{d}t} = \nabla_\Sigma \Gamma \cdot \frac{\mathrm{d}\mathbf{m}}{\mathrm{d}t} + \frac{\partial \Gamma}{\partial t}, \tag{3.45}$$

one obtains:

$$\frac{\mathrm{d}\Gamma}{\mathrm{d}t} = -\nabla_\Sigma \Gamma \cdot \nabla_\Sigma \Omega + \frac{\partial \Gamma}{\partial t}. \tag{3.46}$$

The key issue now is the physical interpretation of the potentials Γ and Ω. In the following, we shall use heuristic reasoning to identify these potentials. To keep the discussion simple, we shall limit our considerations to autonomous systems, i.e., when the potentials Γ and Ω depend on time only through $\mathbf{m}$, while the various control parameters of the problem are kept constant. We anticipate that the reached conclusions can be extended to nonautonomous conditions as well.

As previously mentioned, the important structural property of Eq. (3.44) is the fact that, when the potential Ω is constant, the dynamics proceeds along closed trajectories corresponding to constant values of the potential Γ. It is natural to identify the conserved quantity Γ with the energy of the system, up to some scaling factor which can be always absorbed by an appropriate renormalization of the time scale. However, the typical situation of interest is a system in contact with the thermal bath and subject to some external action, for example to an applied magnetic field. This suggests that the potential Γ should be identified with the free energy, which is minimized at equilibrium. This free energy is the micromagnetic free energy g_L introduced in Chapter 2. Therefore, we can write Eq. (3.44) as:

$$\frac{\mathrm{d}\mathbf{m}}{\mathrm{d}t} = \mathbf{m} \times \nabla_\Sigma g_L - \nabla_\Sigma \Omega. \tag{3.47}$$

The potential Ω should describe the mechanism that brings the free energy to its minimum. This interpretation is strongly supported by the fact that there exists a general balance equation for the potential Γ, i.e., Eq. (3.46). When $\Gamma \equiv g_L$, this equation yields:

$$\frac{\mathrm{d}g_L}{\mathrm{d}t} = -\nabla_\Sigma g_L \cdot \nabla_\Sigma \Omega + \frac{\partial g_L}{\partial t}. \tag{3.48}$$

This balance equation suggests that under autonomous conditions (i.e., when $\partial g_L/\partial t = 0$), g_L decreases if the dot product on the right-hand side of Eq. (3.48) is positive for any $\mathbf{m}$. The following reasoning helps to identify the appropriate potential Ω consistent with this requirement. Imagine that the interaction with the thermal bath responsible for the relaxation to equilibrium has been switched off. In this case, the system precesses along one of the closed trajectories of constant energy g_L. Let $T(g)$ be the period of this precessional motion. Now, assume that the interaction with the thermal bath is switched on and that this interaction is so small that the precessional motion is not substantially perturbed on the time scale $T(g)$. We shall see in subsequent chapters that this assumption is satisfied in most cases of physical interest. Thus, on the time scale $T(g)$ the system approximately moves along one of the closed trajectories of the precessional dynamics. The presence of relaxation interactions may result in some small increase of $T(g)$, which, however, has no appreciable consequence and basically can be absorbed in the proportionality constant between Γ and g_L, i.e., in the renormalization of the time scale. To quantify the relaxational effect along the precessional trajectory, we note that the curl-free nature of the relaxation term in Eq. (3.47) guarantees that its line integral along the precessional trajectory is zero. In other terms, the relaxational part of the dynamics cannot alter the average velocity at which the system moves along the precessional trajectory. On the other hand, the relaxation effects are due to numerous microscopic interactions with the thermal bath which are not correlated to the large-scale precessional motion and, thus, cannot give rise to large-scale distortions of the precessional velocity. This suggests that the relaxational part of the dynamics must be orthogonal to the precessional trajectories at every point, i.e.:

$$\nabla_\Sigma \Omega = \alpha \nabla_\Sigma g_L. \tag{3.49}$$

By using this equation in Eq. (3.48), one obtains:

$$\frac{\mathrm{d}g_L}{\mathrm{d}t} = -\alpha \left|\nabla_\Sigma g_L\right|^2 + \frac{\partial g_L}{\partial t}, \tag{3.50}$$

which implies that $\alpha > 0$ to ensure relaxation to equilibrium under autonomous conditions. It will be shown in Chapter 10 that the assumption (3.49) is also consistent with statistical mechanics. Indeed, it guarantees that the stochastic magnetization dynamics obtained by introducing appropriate thermal noise terms in Eq. (3.47) asymptotically approaches the equilibrium Boltzmann distribution for $\mathbf{m}$.

It is worth remarking that the precessional and relaxational parts of the dynamics (3.47) are always orthogonal in the integral sense. Indeed, by using the divergence theorem on the unit sphere and by taking into account that $\mathrm{div}_\Sigma\,(\mathbf{m}\times\nabla_\Sigma g_L)=0$ (see Eq. (3.38)), one finds:

$$\oiint_\Sigma (\mathbf{m}\times\nabla_\Sigma g_L)\cdot\nabla_\Sigma\Omega\,\mathrm{d}S=-\oiint_\Sigma \Omega\,\mathrm{div}_\Sigma\,(\mathbf{m}\times\nabla_\Sigma g_L)\,\mathrm{d}S=0. \tag{3.51}$$

Equation (3.49) naturally satisfies this orthogonality relation, because of the local orthogonality of precessional and relaxation terms.

The discussion presented so far can be viewed as another justification for the LL dynamics. Indeed, under the assumption (3.49), Eq. (3.47) can be written in the form:

$$\frac{\mathrm{d}\mathbf{m}}{\mathrm{d}t}=\mathbf{m}\times\nabla_\Sigma g_L-\alpha\nabla_\Sigma g_L. \tag{3.52}$$

This equation is identical to the LL equation (3.12), because:

$$\mathbf{m}\times\nabla_\Sigma f=\mathbf{m}\times\frac{\partial f}{\partial\mathbf{m}},\qquad \nabla_\Sigma f=-\mathbf{m}\times\left(\mathbf{m}\times\frac{\partial f}{\partial\mathbf{m}}\right), \tag{3.53}$$

for any differentiable function $f(\mathbf{m})$, and $\partial g_L/\partial\mathbf{m}=-\mathbf{h}_{\mathrm{eff}}$. However, the importance of Eq. (3.47) is fully revealed by the fact that it provides a general framework for the description of physical situations that go beyond ordinary LL dynamics. This occurs when the system is open and subject to nonequilibrium flows that may drive it to out-of-equilibrium steady-state conditions. As a result, the magnetization dynamics deviates from the purely LL dynamics with the thermal relaxation law (3.49), and an additional term appears in the curl-free part of the dynamics:

$$\nabla_\Sigma\Omega=\alpha\nabla_\Sigma g_L+\nabla_\Sigma\Psi. \tag{3.54}$$

As a consequence, the equation of motion (3.47) and the energy balance equation (3.48) are respectively modified as follows:

$$\frac{\mathrm{d}\mathbf{m}}{\mathrm{d}t}=\mathbf{m}\times\nabla_\Sigma g_L-\alpha\nabla_\Sigma g_L-\nabla_\Sigma\Psi, \tag{3.55}$$

$$\frac{\mathrm{d}g_L}{\mathrm{d}t}=-\alpha\left|\nabla_\Sigma g_L\right|^2-\nabla_\Sigma g_L\cdot\nabla_\Sigma\Psi+\frac{\partial g_L}{\partial t}. \tag{3.56}$$

This generalized balance equation suggests that, even when the free energy g_L does not explicitly depend on time (i.e., $\partial g_L/\partial t = 0$), it may still increase or decrease during the magnetization dynamics, due to the competition between the energy loss caused by thermal relaxation and the energy injection due to the physical processes described by the potential Ψ. In particular, one may encounter situations where these competing trends result in zero net balance on the average, that is, over some characteristic time interval. When this is the case, self-oscillations of magnetization (limit cycles) may occur. We know that this possibility is ruled out for the conventional LL dynamics. A particularly interesting example of generalized dynamics with these properties is the magnetization dynamics driven by injected spin-polarized currents (see Chapter 9).

Zero average energy change is possible when the two terms on the right-hand side of Eq. (3.54) are of the same order of magnitude with respect to α. In such situations, it is useful to introduce the potential Φ defined as:

$$\nabla_\Sigma \Phi = \nabla_\Sigma g_L + \frac{1}{\alpha}\nabla_\Sigma \Psi, \tag{3.57}$$

which (when α is constant) is equivalent to:

$$\Phi = g_L + \frac{1}{\alpha}\Psi + \text{const}. \tag{3.58}$$

In terms of Φ, the equation for the magnetization dynamics (3.47) and the energy balance equation (3.48) are respectively expressed as:

$$\frac{\mathrm{d}\mathbf{m}}{\mathrm{d}t} = \mathbf{m} \times \nabla_\Sigma g_L - \alpha \nabla_\Sigma \Phi, \tag{3.59}$$

$$\frac{\mathrm{d}g_L}{\mathrm{d}t} = -\alpha \nabla_\Sigma g_L \cdot \nabla_\Sigma \Phi + \frac{\partial g_L}{\partial t}. \tag{3.60}$$

These are the basic equations that will be further investigated and used in subsequent chapters. By taking into account the relations (3.53), these equations can be also expressed in the form:

$$\frac{\mathrm{d}\mathbf{m}}{\mathrm{d}t} = \mathbf{m} \times \frac{\partial g_L}{\partial \mathbf{m}} + \alpha \mathbf{m} \times \left(\mathbf{m} \times \frac{\partial \Phi}{\partial \mathbf{m}} \right), \tag{3.61}$$

$$\frac{\mathrm{d}g_L}{\mathrm{d}t} = -\alpha \left(\mathbf{m} \times \frac{\partial g_L}{\partial \mathbf{m}} \right) \cdot \left(\mathbf{m} \times \frac{\partial \Phi}{\partial \mathbf{m}} \right) + \frac{\partial g_L}{\partial t}. \tag{3.62}$$

By using Eq. (3.61) to express $\mathbf{m} \times \partial g_L / \partial \mathbf{m}$, Eq. (3.62) can be also written as follows:

$$\frac{\mathrm{d}g_L}{\mathrm{d}t} = -\alpha \left(\mathbf{m} \times \frac{\partial \Phi}{\partial \mathbf{m}} \right) \cdot \frac{\mathrm{d}\mathbf{m}}{\mathrm{d}t} + \frac{\partial g_L}{\partial t}. \tag{3.63}$$

As previously mentioned, the analysis we have proposed to justify the physical interpretation of the potentials in the generalized magnetization dynamics is valid for autonomous systems. It is natural to extend these results to nonautonomous conditions as well. In this respect, a peculiar situation will be encountered in Chapter 7, where the magnetization dynamics under time-harmonic applied fields will be studied. When the ferromagnet has uniaxial symmetry and the time-varying applied field is circularly polarized in the plane perpendicular to the symmetry axis of the problem, the dynamics can be reduced to autonomous form in the rotating reference frame where the circularly polarized field is stationary [81]. In this frame, the LL equation takes the generalized form discussed in this section.

3.4 ANALYSIS OF EQUILIBRIUM POINTS OF MAGNETIZATION DYNAMICS

An essential step in the analysis of magnetization dynamics is the determination of equilibrium points and the study of their stability. In the case of LL and LLG dynamics and under the assumption (relevant to switching and relaxation problems) that the applied field is constant in time, these equilibrium points are found by solving the micromagnetic Brown equation $\mathbf{m} \times \mathbf{h}_{\text{eff}} = 0$. This vector equilibrium condition can be rewritten in spherical coordinates as two scalar equations:

$$\frac{\partial g_L}{\partial \theta} = 0, \qquad \frac{\partial g_L}{\partial \phi} = 0. \tag{3.64}$$

As previously mentioned, this means that magnetization equilibria are always critical points of the free energy $g_L(\mathbf{m})$ defined on the unit sphere. Thus, these equilibria can be classified as energy maxima, energy minima and energy saddles. If the geometrical shape of the ferromagnet and its crystal anisotropy are invariant with respect to the angle ϕ, then g_L does not depend on ϕ and the second equation in (3.64) can be ignored. This is the case analyzed in the Stoner–Wohlfarth model [639], which permits one to give a complete description of the equilibria in the case of magnetic systems with uniaxial symmetry. For more general cases,

some appropriate extension of the Stoner–Wohlfarth theory is needed. One rather general possibility is to study the system of equations:

$$\mathbf{h}_{\text{eff}}(\mathbf{m}) = \lambda \mathbf{m}, \qquad |\mathbf{m}|^2 = 1, \tag{3.65}$$

which is equivalent to the equation $\mathbf{m} \times \mathbf{h}_{\text{eff}} = 0$. Equations (3.65) are four scalar equations for four unknowns, which are λ and the three components of $\mathbf{m}$. This approach, which has been proposed in Ref. [228], leads to the identification of 2, 4, or 6 equilibrium points for the dynamics, depending on the value and the orientation of the applied field.

Below, a different approach for the determination of equilibria is presented under the assumption that one of the components of the applied field $\mathbf{h}_a$ is zero, which means that $\mathbf{h}_a$ lies in one of the symmetry planes of the ferromagnet. Although it is less general than the method based on Eq. (3.65), this approach has the advantage that the solution can be worked out analytically and can be translated into geometrical terms, which generalize the Stoner–Wohlfarth model. We shall assume that $\mathrm{h}_{az} = 0$ and that the anisotropy parameters D_x, D_y, D_z appearing in the effective field (3.15) are ordered as follows:

$$D_x \leq D_y \leq D_z. \tag{3.66}$$

This means that the axis $\mathbf{e}_x$ is the easy axis of the particle and that the applied field has zero component along the hard axis $\mathbf{e}_z$. The method can be extended to other combinations of anisotropy and applied field relative orientation. These extensions will not be discussed here.

In the case when $\mathrm{h}_{az} = 0$, by using the fact that $\mathrm{m}_z^2 = 1 - \mathrm{m}_x^2 - \mathrm{m}_y^2$, m_z can be eliminated from the expression of the free energy (see Eq. (3.16)). This leads to the following formula:

$$g_L(\mathbf{m}; \mathbf{h}_a) = -\frac{D_z - D_x}{2}\left[(\mathrm{m}_x - a_x)^2 + k^2 (\mathrm{m}_y - a_y)^2 - p_0^2\right], \tag{3.67}$$

where:

$$a_x = -\frac{\mathrm{h}_{ax}}{D_z - D_x}, \qquad a_y = -\frac{\mathrm{h}_{ay}}{D_z - D_y}, \qquad k^2 = \frac{D_z - D_y}{D_z - D_x}, \tag{3.68}$$

$$p_0^2 = a_x^2 + a_y^2 + \frac{D_z}{D_z - D_x}. \tag{3.69}$$

Equation (3.67) is written in the form that accounts for the constraint $|\mathbf{m}|^2 = 1$. In addition, as it will be clear from the subsequent discussion,

this form permits one to readily recognize the nature of equilibria, namely whether they are energy maxima, minima or saddles.

In order to determine equilibria, we compute $\mathbf{h}_{\text{eff}} = -\partial g_L/\partial \mathbf{m}$ from Eq. (3.67) and we substitute it into the Brown equation: $\mathbf{m} \times \mathbf{h}_{\text{eff}} = 0$. In cartesian coordinates, one obtains the following set of coupled equations:

$$(D_z - D_y)\,\mathrm{m}_z\,(\mathrm{m}_y - a_y) = 0, \tag{3.70}$$

$$-(D_z - D_x)\,\mathrm{m}_z\,(\mathrm{m}_x - a_x) = 0, \tag{3.71}$$

$$(D_z - D_x)\,\mathrm{m}_y\,(\mathrm{m}_x - a_x) - (D_z - D_y)\,\mathrm{m}_x\,(\mathrm{m}_y - a_y) = 0. \tag{3.72}$$

Due to the nature of Eqs (3.70)–(3.72), it is apparent that there are two cases of equilibria: equilibria with $\mathrm{m}_z \neq 0$ and equilibria with $\mathrm{m}_z = 0$.

- Equilibrium points with $\mathrm{m}_z \neq 0$.
  In this case Eqs (3.70)–(3.72) immediately suggest that $\mathrm{m}_x = a_x$ and $\mathrm{m}_y = a_y$. The value of m_z can be then determined from the constraint $|\mathbf{m}| = 1$. This leads to two equilibrium points:

  $$\mathrm{m}_x = a_x, \qquad \mathrm{m}_y = a_y, \qquad \mathrm{m}_z = \pm\sqrt{1 - a_x^2 - a_y^2}, \tag{3.73}$$

  which are symmetric with respect to the $(\mathrm{m}_x, \mathrm{m}_y)$-plane. It is clear that this kind of equilibria is possible only when the applied magnetic field is inside the region confined by the curve:

  $$a_x^2 + a_y^2 = 1, \tag{3.74}$$

  which is the ellipse:

  $$\frac{\mathrm{h}_{ax}^2}{(D_z - D_x)^2} + \frac{\mathrm{h}_{ay}^2}{(D_z - D_y)^2} = 1. \tag{3.75}$$

  Equations (3.66) and (3.67) suggest that these equilibria are always energy maxima.
- Equilibrium points with $\mathrm{m}_z = 0$.
  This class of equilibria is characterized by the condition $\mathrm{m}_x^2 + \mathrm{m}_y^2 = 1$. Thus, their positions on the unit circle in the $(\mathrm{m}_x, \mathrm{m}_y)$-plane can be described by the angle ϕ_0 : $\mathrm{m}_x = \cos\phi_0$, $\mathrm{m}_y = \sin\phi_0$. The angle ϕ_0 associated with the equilibrium points is obtained by solving equation (3.72) rewritten in the form:

  $$(D_y - D_x)\sin\phi_0\cos\phi_0 + \mathrm{h}_{ax}\sin\phi_0 - \mathrm{h}_{ay}\cos\phi_0 = 0. \tag{3.76}$$

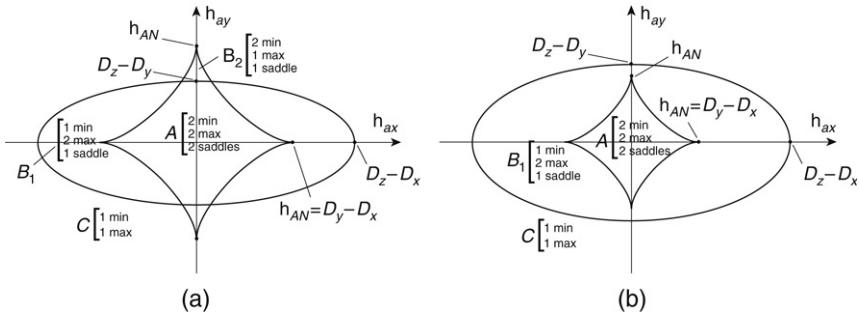

FIGURE 3.5 Bifurcation lines in the $(\mathrm{h}_{ax}, \mathrm{h}_{ay})$ control plane. (a) $D_z - D_y < D_y - D_x$; (b) $D_z - D_y > D_y - D_x$.

In order to grasp the meaning of Eq. (3.76), it is useful to express the system free energy $g_L(\mathbf{m}; \mathbf{h}_a)$ (see Eq. (3.16)) in terms of the angle ϕ_0 for the case $m_z = 0$:

$$g_L\left(\mathrm{m}_z = 0, \phi_0; \mathbf{h}_a\right) = \frac{1}{2} D_x + \frac{1}{2}\left(D_y - D_x\right) \sin^2 \phi_0 - \mathrm{h}_{ax} \cos \phi_0 - \mathrm{h}_{ay} \sin \phi_0. \tag{3.77}$$

This energy expression is identical to the one considered in the Stoner–Wohlfarth model [639] with

$$\mathrm{h}_{AN} = D_y - D_x \tag{3.78}$$

playing the role of anisotropy field. Equation (3.76) coincides with the equation $\partial g_L / \partial \phi_0 = 0$. It can be inferred from this fact that all the results known for the Stoner–Wohlfarth model are applicable to the equilibrium points characterized by the condition $\mathrm{m}_z = 0$. In particular, one immediately concludes that there will be either four equilibrium points, two of which will be energy minima, or two equilibrium points, one of which will be an energy minimum. The bifurcation line where the number of energy minima changes from one to two or vice versa is given by the astroid curve in the $(\mathrm{h}_{ax}, \mathrm{h}_{ay})$ control plane (see Fig. 3.5):

$$\mathrm{h}_{ax}^{2/3} + \mathrm{h}_{ay}^{2/3} = \mathrm{h}_{AN}^{2/3}. \tag{3.79}$$

In conclusion, there are (at most) four distinct cases, separated by the two bifurcation lines given by Eqs (3.75) and (3.79) (see Fig. 3.5).

- Region A, 6 equilibrium points: 2 minima, 2 maxima, 2 saddles.
- Region B_1, 4 equilibrium points: 1 minimum, 2 maxima, 1 saddle.
- Region B_2, 4 equilibrium points: 2 minima, 1 maximum, 1 saddle.
- Region C, 2 equilibrium points: 1 minimum, 1 maximum.

In this classification, the number of saddles has been indirectly determined on the basis of the Poincaré index theorem. It can be noted that for certain values of the parameters D_x, D_y and D_z the region B_2 may not exist. The condition for the existence of region B_2 is that $\mathrm{h}_{AN} = D_y - D_x > D_z - D_y$.

The classification of equilibria in terms of the free energy is also instrumental for the understanding of their stability properties under constant field. According to Eq. (3.30), if the system is not at equilibrium, magnetization motion is such that the free energy decreases in time for $\alpha > 0$ and remains constant for $\alpha = 0$. Thus, for $\alpha > 0$, the dynamics will always bring magnetization away from energy maxima and toward energy minima. On the other hand, for $\alpha = 0$ the magnetization will keep on precessing around an energy minimum or maximum if it is initially close to it. We conclude that for $\alpha > 0$ energy maxima are unstable nodes or foci, and energy minima are stable nodes or foci of the dynamics. Conversely, for $\alpha = 0$ energy maxima and minima are all centers of the dynamics.

These results are related to an interesting geometric relation between precessional $(\alpha = 0)$ and dissipative $(\alpha > 0)$ dynamics. This relation can be established by introducing in Eq. (3.22) the angle ψ defined by:

$$\tan\psi = \alpha. \tag{3.80}$$

One obtains:

$$\begin{pmatrix} \mathrm{d}\theta/\mathrm{d}t \\ \sin\theta \mathrm{d}\phi/\mathrm{d}t \end{pmatrix} = \frac{1}{\sqrt{1+\alpha^2}} \begin{pmatrix} \cos\psi & -\sin\psi \\ \sin\psi & \cos\psi \end{pmatrix} \begin{pmatrix} -(1/\sin\theta)\partial g_L/\partial\phi \\ \partial g_L/\partial\theta \end{pmatrix}. \tag{3.81}$$

On the other hand, when $\alpha = 0$, Eq. (3.22) can be written as:

$$\begin{pmatrix} d\theta/\mathrm{d}t \\ \sin\theta \mathrm{d}\phi/\mathrm{d}t \end{pmatrix} = \begin{pmatrix} -(1/\sin\theta)\partial g_L/\partial\phi \\ \partial g_L/\partial\theta \end{pmatrix}. \tag{3.82}$$

By comparing Eqs (3.81) and (3.82), it can be concluded that the vector field on the unit sphere that governs the dissipative dynamics is

obtained from the vector field that governs the precessional dynamics by a counterclockwise rotation through the angle $\psi = \tan^{-1}\alpha$ and a subsequent rescaling by the factor $(1+\alpha^2)^{-1/2}$.

In the limiting case of slightly dissipative (i.e. small α) magnetization dynamics, the effect of damping is a small rotation through the angle $\psi \simeq \alpha$ of the undamped vector field. This fact has direct consequences on the nature of equilibrium points. When $\alpha = 0$, the system is conservative and for this reason it can only have two types of equilibria: saddles and centers. It can be verified that a small counterclockwise rotation of the vector field transforms centers into foci, while saddle equilibria still remain. This is expressed in bifurcation theory by saying that saddle equilibria are structurally stable with respect to generic perturbations of the differential equation. On the other hand, in the case of strongly dissipative (i.e. large α) dynamics, the rotation angle ψ is almost $\pi/2$, which means that the magnetization evolves along the lines of steepest energy descent toward energy minima. Equilibria are generally either nodes or saddles.

CHAPTER 4

Precessional Magnetization Dynamics

4.1 GEOMETRIC ASPECTS OF PRECESSIONAL DYNAMICS

Exact analytical solutions to LL or LLG equation exist for very few special cases. However, in many problems related to magnetic storage, spintronics, and other applications, the damping constant α is quite small. This means that, on a relatively short time scale, the magnetization dynamics is expected to be very close to the undamped precessional dynamics. This suggests that a first fundamental step is to analyze the conservative precessional magnetization dynamics. This dynamics can be analytically studied by using the techniques developed in this chapter. Due to the smallness of α, the actual dissipative dynamics can be then treated as a perturbation of the conservative dynamics. This perturbation approach will be extensively used throughout the book.

The starting point for the analysis of the conservative dynamics in uniformly magnetized particles is the zero-damping ($\alpha = 0$) equation:

$$\frac{\mathrm{d}\mathbf{m}}{\mathrm{d}t} = -\mathbf{m} \times \mathbf{h}_{\text{eff}} = \mathbf{m} \times \frac{\partial g_L}{\partial \mathbf{m}}. \tag{4.1}$$

As discussed in Chapter 3, this equation admits two integrals of motion, namely, $|\mathbf{m}(t)|^2 = 1$ and $g_L(\mathbf{m}; \mathbf{h}_a) = g_0$, where g_0 is a constant and $g_L(\mathbf{m}; \mathbf{h}_a)$ is given by Eq. (3.16). Thus, magnetization trajectories of precessional dynamics must fulfill the two constraints:

$$\mathrm{m}_x^2 + \mathrm{m}_y^2 + \mathrm{m}_z^2 = 1, \tag{4.2}$$

$$\frac{1}{2}\left(D_x \mathrm{m}_x^2 + D_y \mathrm{m}_y^2 + D_z \mathrm{m}_z^2\right) - \mathrm{h}_{ax}\mathrm{m}_x - \mathrm{h}_{ay}\mathrm{m}_y - \mathrm{h}_{az}\mathrm{m}_z = g_0, \tag{4.3}$$

where g_0 is the free energy of the initial state of magnetization. This means that magnetization trajectories can be viewed as intersections of the unit sphere described by Eq. (4.2) with the quadric surface described by

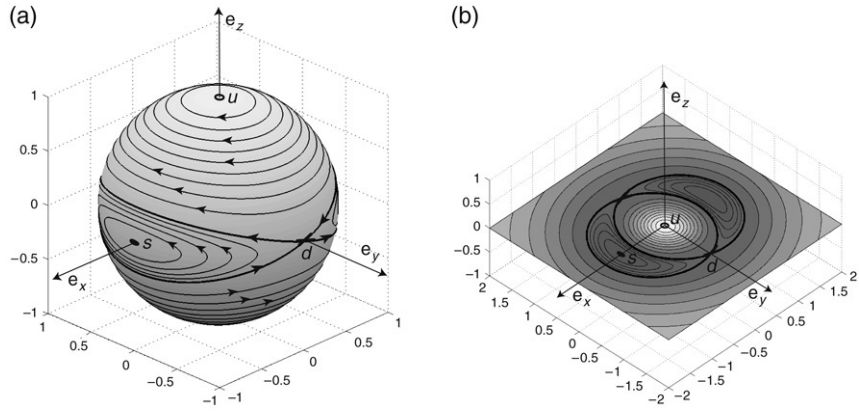

FIGURE 4.1 Precessional magnetization trajectories for $\mathbf{h}_a = 0$. s: energy minima; u: energy maxima; d: energy saddles. (a) Trajectories on the unit sphere; (b) stereographic projection.

Eq. (4.3). An illustrative example of such trajectories is shown in Fig. 4.1(a) for the case $\mathbf{h}_a = 0$. In Fig. 4.1(b), the same trajectories are represented on the stereographic plane (stereographic coordinates have been introduced and discussed in Section 3.1).

The phase portrait of the precessional dynamics is completely characterized by the energy critical points, i.e., maxima, minima and saddles, as well as by the trajectories passing through saddles: either homoclinic trajectories starting and ending at an individual saddle, or heteroclinic trajectories starting at one saddle and ending at a different one. These trajectories are called separatrices because they create a natural partition of the phase portrait into different so-called "central regions". In order to clarify this notion, let us consider the stereographic phase portrait shown in Fig. 4.2. This portrait corresponds to the case when the anisotropy coefficients in Eq. (4.3) satisfy the ordering $D_x < D_y < D_z$ (the x axis and the z axis are the easy and hard magnetization axes, respectively) and the external field is applied along the intermediate y axis. Inspection of this figure reveals that the phase portrait is divided into five regions separated by the saddle trajectories Γ_1 and Γ_2: two regions associated with the two energy minima s_1 and s_2; two regions associated with the two energy maxima u_1 and u_2; one region (indicated with I) between the two homoclinic trajectories Γ_1 and Γ_2, which contains no equilibrium points. Such regions are central regions in the sense that they

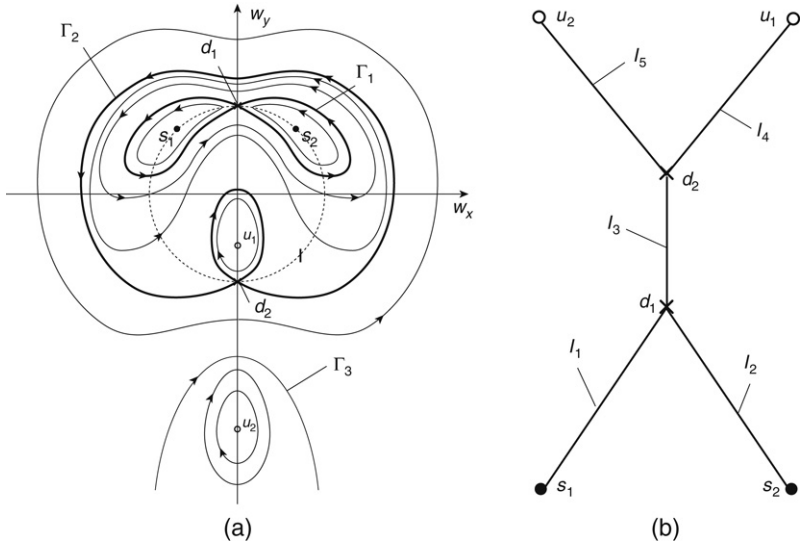

FIGURE 4.2 (a) Stereographic-plane representation of precessional dynamics phase portrait. The following notation is adopted: s for energy minima; u for energy maxima; d for energy saddles. Bold lines Γ_1 and Γ_2 denote separatrices. The dashed line is the unit circle. The symbol I labels the region between the two homoclinic trajectories Γ_1 and Γ_2. The line Γ_3 starts and ends at infinity, and it separates trajectories traversed counterclockwise around the homoclinic trajectory Γ_2 from those traversed clockwise around u_2. This special property of Γ_3 is an artifact of the stereographic projection and it is connected to the singularity of this projection at $\mathrm{m}_z = -1$. On the unit sphere, the trajectory Γ_3 is similar to all other trajectories encircling u_2. (b) Graph representation of the phase portrait.

are filled by a continuum of closed trajectories and in this respect they resemble the behavior of a dynamical system around center equilibria.

The qualitative features of the precessional magnetization dynamics are defined, once a list of the central regions and of the energy critical points is specified. To this end, the following notation proves useful: energy maxima are denoted as u, energy minima as s, and saddles as d. Each central region will be indicated by the symbol ( ). If a central region contains an energy minimum or maximum, then the notation (s) or (u) will be used, respectively. In addition, since in generic situations (i.e., situations with no particular symmetries or fulfillment of bifurcation conditions), a saddle point is always associated with two homoclinic trajectories, we will use the notation $d(\ )(\ )$ to indicate the saddle and the two central regions associated with its homoclinic trajectories. It is

remarkable that, by using these notations, all the fundamental properties of the precessional magnetization dynamics can be specified in terms of short strings of the introduced symbols. For example, the phase portrait shown in Fig. 4.2 corresponds to the string $\{d_1(s_1)(s_2), d_2(u_1)(u_2), (\,)\}$. The empty parentheses $(\,)$ correspond to the central region I which does not contain equilibria. These notations can be further extended to indicate the presence of particular symmetries in the phase portrait. In particular, the exponent 2, i.e., $(\,)^2$, can be used for pairs of central regions $(\,)$ exhibiting mirror symmetry with respect to the plane $(\mathrm{m}_x, \mathrm{m}_y)$.

A natural way to describe the topological properties of the conservative phase portrait for the precessional magnetization dynamics is by introducing an associated graph $\mathcal{G}$ defined as follows: each edge I_k of the graph represents a central region, while each node corresponds to a saddle equilibrium with the associated separatrices. Accordingly, the nodes can be labeled with the same symbol used for saddles, i.e., $d_1, d_2, \ldots$. As an example, the graph for the phase portrait presented in Fig. 4.2(a) is shown in Fig. 4.2(b). This graph representation will prove particularly useful in the discussion of slow-time-scale energy dynamics in slightly dissipative systems (Chapter 5), as well as in the analysis of stochastic magnetization dynamics (Chapter 10). In general, the precessional trajectory on the unit sphere inside the central region (graph edge) I_k will be denoted as $C_k(g)$, and the corresponding period as $T_k(g)$, where $g = g_L(\mathbf{m}; \mathrm{h}_a)$ is the constant energy value along the trajectory.

We shall next analyze the geometrical aspects of the precessional magnetization dynamics in some more detail. As in Section 3.4, it will be assumed that one of the cartesian components of $\mathbf{h}_a$ is equal to zero, namely $\mathrm{h}_{az} = 0$, and that the anisotropy parameters D_x, D_y, D_z satisfy the ordering: $D_x \leq D_y \leq D_z$. In this case, Eq. (4.1) can be written in cartesian coordinates as follows:

$$\frac{\mathrm{d}\mathrm{m}_x}{\mathrm{d}t} = (D_z - D_y)\,\mathrm{m}_z\,(\mathrm{m}_y - a_y)\,, \tag{4.4}$$

$$\frac{\mathrm{d}\mathrm{m}_y}{\mathrm{d}t} = -\,(D_z - D_x)\,\mathrm{m}_z\,(\mathrm{m}_x - a_x)\,, \tag{4.5}$$

$$\frac{\mathrm{d}\mathrm{m}_z}{\mathrm{d}t} = (D_z - D_x)\,\mathrm{m}_y\,(\mathrm{m}_x - a_x) - (D_z - D_y)\,\mathrm{m}_x\,(\mathrm{m}_y - a_y)\,, \tag{4.6}$$

where:

$$a_x = -\frac{\mathrm{h}_{ax}}{D_z - D_x}, \qquad a_y = -\frac{\mathrm{h}_{ay}}{D_z - D_y}. \tag{4.7}$$

When $\mathrm{h}_{az} = 0$, m_z appears in Eq. (4.3) only as a square and thus it can be eliminated by using Eq. (4.2). This leads to the following formula:

$$(\mathrm{m}_x - a_x)^2 + k^2 (\mathrm{m}_y - a_y)^2 = p^2, \tag{4.8}$$

where:

$$p^2 = a_x^2 + k^2 a_y^2 + \frac{D_z - 2g_0}{D_z - D_x}, \tag{4.9}$$

$$k^2 = \frac{D_z - D_y}{D_z - D_x}. \tag{4.10}$$

Equation (4.8) shows that the projections of magnetization trajectories on the $(\mathrm{m}_x, \mathrm{m}_y)$-plane are the family of self-similar elliptic curves with aspect ratio k. All these ellipses are centered at the point (a_x, a_y). The above family of ellipses is generated by varying the free energy value g_0 within an appropriate range. Indeed, for a given value of $\mathbf{h}_a$, the constant g_0 controls the size of the ellipses through Eqs (4.8)–(4.10). It must be pointed out that only those portions of the ellipses which lie inside the circle $\mathrm{m}_x^2 + \mathrm{m}_y^2 \leq 1$ are accessible to the magnetization dynamics. On the other hand, m_z does not appear explicitly in Eq. (4.8), which means that there exist motions with opposite values of m_z resulting in identical projections on the $(\mathrm{m}_x, \mathrm{m}_y)$-plane. By analyzing Eqs (4.4)–(4.6), one finds that for any point $(\mathrm{m}_x, \mathrm{m}_y)$ a change in the sign of m_z produces a change of the sign of $\mathrm{d}\mathrm{m}_x/\mathrm{d}t$ and $\mathrm{d}\mathrm{m}_y/\mathrm{d}t$. This means that the mirror transformation $(\mathrm{m}_x, \mathrm{m}_y, \mathrm{m}_z) \to (\mathrm{m}_x, \mathrm{m}_y, -\mathrm{m}_z)$ results in the transformation $\mathrm{d}\mathrm{m}_x/\mathrm{d}t \to -\mathrm{d}\mathrm{m}_x/\mathrm{d}t$, $\mathrm{d}\mathrm{m}_y/\mathrm{d}t \to -\mathrm{d}\mathrm{m}_y/\mathrm{d}t$, $\mathrm{d}\mathrm{m}_z/\mathrm{d}t \to \mathrm{d}\mathrm{m}_z/\mathrm{d}t$. It can be inferred from this symmetry property that when the curve described by Eq. (4.8) contains no point on the unit-disk boundary $\mathrm{m}_x^2 + \mathrm{m}_y^2 = 1$, then Eq. (4.8) corresponds to two distinct trajectories; in the opposite case, Eq. (4.8) represents two mirror parts of the same trajectory with positive and negative m_z traversed in succession during the magnetization motion.

Based on these observations, a useful "unit-disk" representation of the phase portrait of the precessional dynamics can be introduced. Although this representation involves only two components of magnetization, information on the third component m_z can be immediately obtained via the relation $\mathrm{m}_z^2 = 1 - (\mathrm{m}_x^2 + \mathrm{m}_y^2)$. For example, $\mathrm{m}_z = \pm 1$ when $(\mathrm{m}_x, \mathrm{m}_y) = (0, 0)$; $\mathrm{m}_z = 0$ when $(\mathrm{m}_x, \mathrm{m}_y)$ lies on the unit circle. Information about the sign of m_z can then be obtained by analyzing the unit-disk representation in the light of the mirror symmetry property discussed above.

Two examples of unit-disk representations are shown in Fig. 4.3. In order to clarify the interpretation of this representation, it is useful to

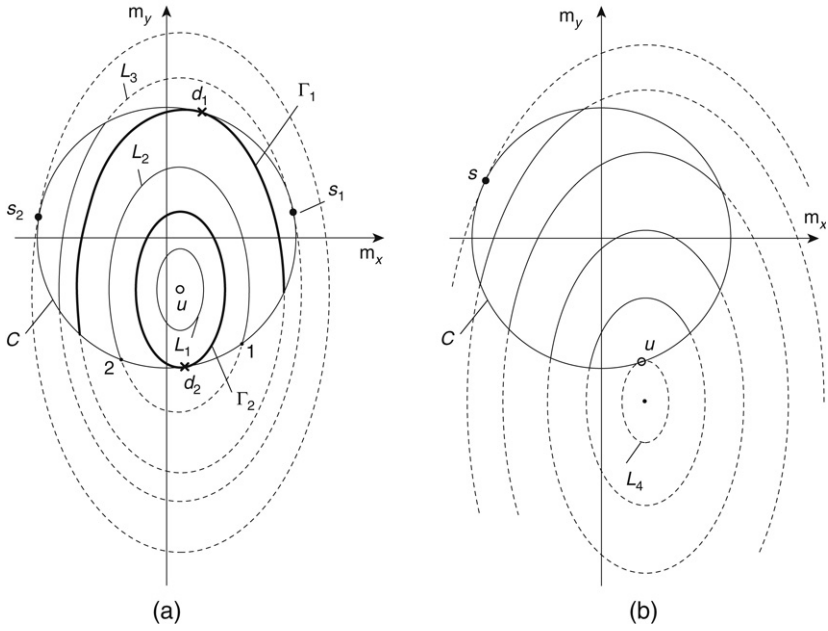

FIGURE 4.3 Sketches of the unit-disk representation for two different values of $\mathbf{h}_a$. Magnetization trajectories correspond to those portions of the ellipses given by Eq. (4.8) that are enclosed by the unit circle $\mathrm{m}_x^2 + \mathrm{m}_y^2 = 1$. The dashed portions of the ellipses are irrelevant to the actual trajectories. The following notation is adopted to indicate equilibrium points: s denotes energy minima, u denotes energy maxima, and d denotes energy saddles. Bold lines Γ_1 and Γ_2 correspond to the projections of separatrices.

discuss this figure in some detail. The ellipses that do not intersect the unit circle (see trajectory L_1 in Fig. 4.3(a)) represent two distinct trajectories on opposite hemispheres, which have exactly the same projection on the $(\mathrm{m}_x, \mathrm{m}_y)$-plane but opposite directions of motion. These types of trajectory exist only in the case when $a_x^2 + a_y^2 < 1$, and they always encircle an energy maximum located at $\mathrm{m}_x = a_x, \mathrm{m}_y = a_y$. Next, let us discuss how to interpret the unit-disk representation in the case of ellipses that intersect with the unit circle. Consider the ellipse L_2 shown in Fig. 4.3(a). Suppose that the sign of m_z is such that the motion along the ellipse L_2 is from point 1 toward point 2. When point 2 is reached, m_z achieves zero value and subsequently changes its sign. This means that the magnetization motion continues on the opposite hemisphere and the

projection of the magnetization trajectory on the $(\mathrm{m}_x, \mathrm{m}_y)$-plane retraces the curve L_2 in the opposite direction, that is, from 2 to 1.

The critical curves separating the above two classes of ellipses are those tangent to the unit circle. At the point of tangency, the normal to the constant-energy surface described by Eq. (4.3) is parallel to the normal to the unit sphere. Since the former coincides with the direction of the effective field $\mathbf{h}_{\text{eff}}$ and the latter with the direction of $\mathbf{m}$, one concludes that the tangency point is an equilibrium, because $\mathbf{h}_{\text{eff}}$ is aligned with $\mathbf{m}$. There are three different cases of tangency: tangency from inside (curves Γ_1, Γ_2 in Fig. 4.3(a)); tangency from outside with inward convexity (curve L_3 in Fig. 4.3(a)); tangency from outside with outward convexity (curve L_4 in Fig. 4.3(b)). By taking into account that according to Eqs (4.8)–(4.10) an increase in energy g_0 results in a decrease in the ellipse size, one concludes that tangency from inside corresponds to saddle points, tangency from outside with inward convexity corresponds to energy minima, and tangency from outside with outward convexity corresponds to energy maxima.

Ellipses tangent from inside play a particularly significant role. Since a tangency point from inside is a saddle, the corresponding tangent ellipse represents a separatrix. As previously discussed, separatrices identify central energy regions and thus define the essential aspects of the phase portrait. This simple geometrical interpretation of separatrices makes the unit-disk representation very useful for the classification of precessional phase portraits, especially when it is used in conjunction with the previously introduced string notations for phase portraits. As an example, Fig. 4.4(a)–(d), depict unit-disk representations corresponding to the four regions A, B_1, B_2, C defined in Fig. 3.5 from Chapter 3. Figure 4.5 presents the highly symmetric case where the field is aligned along the x-axis (easy axis). This case is interesting because it exhibits the presence of heteroclinic trajectories. We shall use the special notation $d^2(\ )^2(\ )(\ )$, without commas, to indicate the two saddles connected by heteroclinic trajectories and the four associated central energy regions.

4.2 ANALYTICAL STUDY OF PRECESSIONAL DYNAMICS

The starting point for the derivation of analytical solutions for precessional magnetization dynamics is Eq. (4.8), which reveals that the projection of the magnetization trajectory onto the $(\mathrm{m}_x, \mathrm{m}_y)$-plane is an elliptical curve. Therefore, the trajectory can be expressed in the parametric form:

$$\mathrm{m}_x = a_x - p\cos u, \qquad \mathrm{m}_y = a_y + \frac{p}{k}\sin u, \tag{4.11}$$

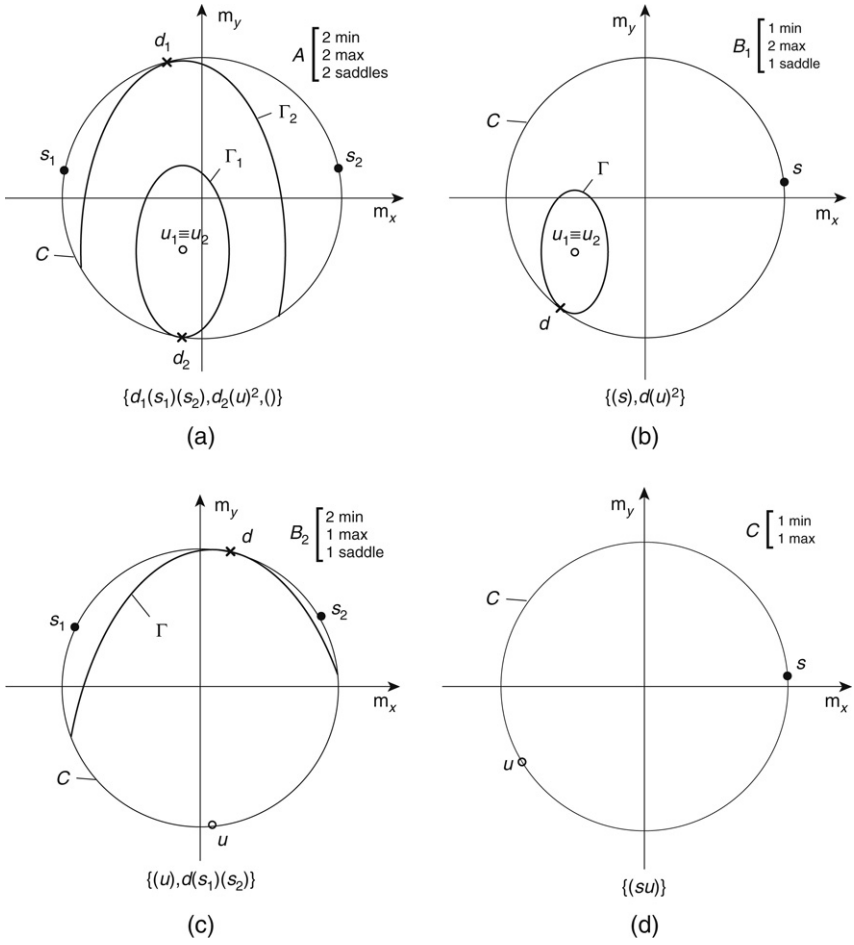

FIGURE 4.4 Classification of phase portraits by means of unit-disk representation for different regions in the control plane $(\mathrm{h}_{ax}, \mathrm{h}_{ay})$. In particular, unit-disk representations are shown for applied fields in regions A (a), B_1 (b), B_2 (c), C (d), defined in Fig. 3.5.

where the connection between the parametric variable u and time is to be determined. Equation (4.11) implies that the remaining magnetization component m_z is given by:

$$\mathrm{m}_z = \pm\sqrt{1-(a_x - p\cos u)^2 - (a_y + (p/k)\sin u)^2}. \tag{4.12}$$

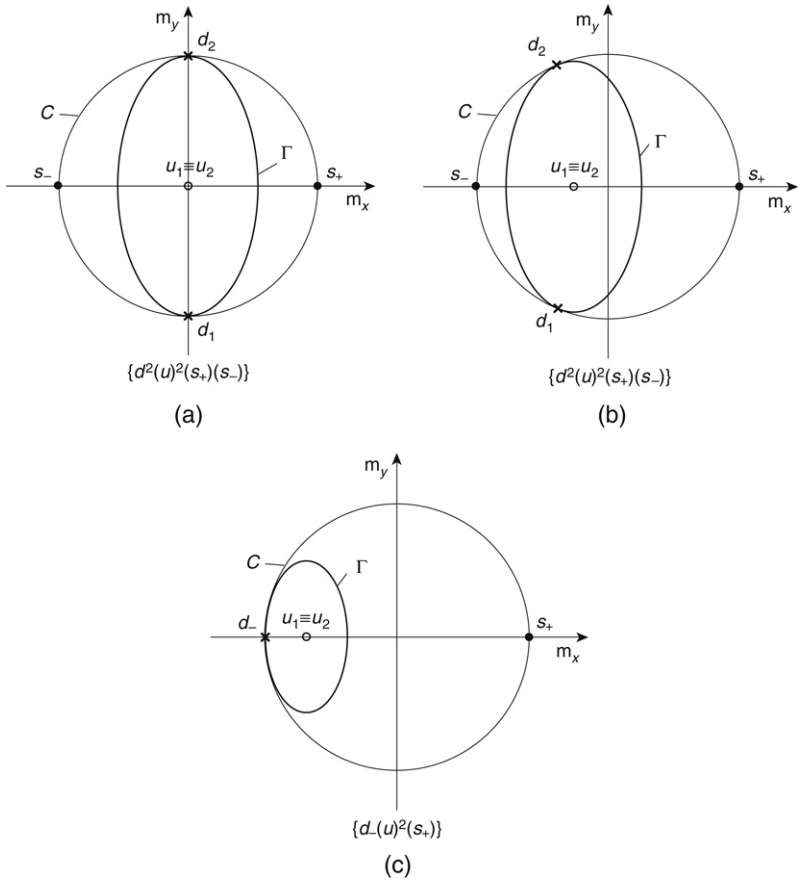

FIGURE 4.5 Unit-disk representation and corresponding string description of phase portraits under x-directed field. (a) Zero-field case characterized by the existence of symmetric heteroclinic trajectories; (b) portrait under nonzero field when heteroclinic trajectories are still present; (c) portrait under larger field when heteroclinic trajectories have been transformed into homoclinic ones.

By inserting Eq. (4.11) into Eq. (4.5) one finds:

$$\frac{\mathrm{d}u}{\mathrm{d}t} = k\,(D_z - D_x)\,\mathrm{m}_z, \tag{4.13}$$

which yields the desired equation for $u(t)$, since m_z depends on u only. By using the method of separation of variables, one obtains:

$$\frac{\mathrm{d}u}{\sqrt{1-(a_x-p\cos u)^2-(a_y+(p/k)\sin u)^2}}=k\,(D_z-D_x)\,\mathrm{d}t, \quad (4.14)$$

where the "±" signs are omitted because the last equation is to be construed as an equation for a multi-branch function.

Equation (4.14) is solvable in terms of elliptic integrals and elliptic functions. This can be shown by carrying out the substitution:

$$w=\tan(u/2), \quad (4.15)$$

which transforms Eq. (4.14) into the equation:

$$\frac{\mathrm{d}w}{\sqrt{P_4(w)}}=\frac{k}{2}\,(D_z-D_x)\,\mathrm{d}t, \quad (4.16)$$

where $P_4(w)$ represents the fourth-order polynomial:

$$\begin{aligned}P_4(w)=&\left(1+w^2\right)^2-\left[a_x(1+w^2)-p(1-w^2)\right]^2\\&-\left[a_y(1+w^2)+(2p/k)w\right]^2.\end{aligned} \quad (4.17)$$

By integrating Eq. (4.16), we obtain:

$$\int_0^w\frac{\mathrm{d}w'}{\sqrt{P_4(w')}}=\frac{k}{2}\,(D_z-D_x)\,t. \quad (4.18)$$

The integral in the left-hand side of Eq. (4.18) belongs to the class of incomplete elliptic integrals. The equation can be inverted, i.e., it can be solved for w as a function of t. This inversion leads to the expression for w in terms of elliptic functions. To ascertain the nature of these elliptic functions, detailed information is needed on the roots of the polynomial $P_4(w)$. This is not an easy task, because these roots are given by rather complicated formulas. For this reason, before attempting the study of Eq. (4.14) in all its complexity, it is useful to get some insight into the properties of precessional magnetization dynamics by considering the particular case of zero applied field. This case is simple enough to be solved without complicated technical discussions. The phase portrait corresponding to this case is shown in Fig. 4.1. Under zero field, $a_x = a_y = 0$ (see Eq. (4.7)). Hence, the magnetization components (Eqs (4.11)

and (4.12)) can be expressed as functions of:

$$w = \sin u. \tag{4.19}$$

Indeed, one finds:

$$\mathrm{m}_x = \mp p\sqrt{1-w^2}, \qquad \mathrm{m}_y = \frac{p}{k}w, \qquad \mathrm{m}_z = \pm\frac{k'p}{k}\sqrt{w_0^2 - w^2}, \tag{4.20}$$

where:

$$w_0 = \frac{k}{k'p}\sqrt{1-p^2}, \tag{4.21}$$

$k'^2 = 1 - k^2$, and p^2 is linearly related to the system energy through Eq. (4.9), which for zero field is reduced to:

$$p^2 = \frac{D_z - 2g_0}{D_z - D_x}. \tag{4.22}$$

By making the change of variable (4.19) in Eq. (4.14), one obtains the following equation:

$$\frac{\mathrm{d}w}{\sqrt{(1-w^2)\,(1-k_H^2 w^2)}} = \Omega_H \mathrm{d}t, \tag{4.23}$$

where:

$$k_H = \frac{1}{w_0} = \frac{k'p}{k}\frac{1}{\sqrt{1-p^2}}, \tag{4.24}$$

$$\Omega_H = k\sqrt{1-p^2}\,(D_z - D_x)\,. \tag{4.25}$$

By integrating Eq. (4.23), one finds:

$$\int_0^w \frac{\mathrm{d}w'}{\sqrt{(1-w'^2)\,(1-k_H^2 w'^2)}} = \Omega_H t. \tag{4.26}$$

The left-hand side of this formula is the incomplete elliptic integral of the first kind $\boldsymbol{F}(w, k_H)$. By inverting this integral, i.e., by solving Eq. (4.26) with respect to w as a function of t, one arrives at the expression for w in

terms of the $\mathrm{sn}(x,k)$ Jacobi elliptic function [321]:

$$w = \mathrm{sn}\left(\Omega_H t, k_H\right). \tag{4.27}$$

The function $\mathrm{sn}(x,k)$ can be regarded as a generalization of the trigonometric "sin" function, as implied by its notation. For real x and $0 \leq k^2 < 1$, $\mathrm{sn}(x,k)$ is periodic in x with period $4\boldsymbol{K}(k)$, where $\boldsymbol{K}(k)$ is the complete elliptic integral of the first kind:

$$\boldsymbol{K}(k) = \int_0^1 \frac{\mathrm{d}x}{\sqrt{(1-x^2)\left(1-k^2x^2\right)}}. \tag{4.28}$$

The connection with trigonometric functions is revealed by the fact that $\mathrm{sn}(x,0) \equiv \sin x$, $\mathrm{sn}(0,k) = 0$. In addition to $\mathrm{sn}(x,k)$, there exist two other Jacobi elliptic functions $\mathrm{cn}(x,k)$ and $\mathrm{dn}(x,k)$, related to $\mathrm{sn}(x,k)$ through the formulas:

$$\mathrm{sn}^2(x,k) + \mathrm{cn}^2(x,k) = 1, \tag{4.29}$$

$$k^2\mathrm{sn}^2(x,k) + \mathrm{dn}^2(x,k) = 1. \tag{4.30}$$

The period of $\mathrm{cn}(x,k)$ and $\mathrm{dn}(x,k)$ is $4\boldsymbol{K}(k)$ and $2\boldsymbol{K}(k)$, respectively. Furthermore, $\mathrm{cn}(x,0) \equiv \cos x$, $\mathrm{cn}(0,k) = 1$, $\mathrm{dn}(x,0) \equiv 1$, $\mathrm{dn}(0,k) = 1$.

By inserting Eq. (4.27) into Eq. (4.20) and by taking into account relations (4.29)–(4.30), one obtains the following expressions for the magnetization components:

$$\mathrm{m}_x = \mp p\,\mathrm{cn}\left(\Omega_H t, k_H\right), \tag{4.31}$$

$$\mathrm{m}_y = \frac{p}{k}\,\mathrm{sn}\left(\Omega_H t, k_H\right), \tag{4.32}$$

$$\mathrm{m}_z = \pm\sqrt{1-p^2}\,\mathrm{dn}\left(\Omega_H t, k_H\right). \tag{4.33}$$

One finds two sets of solutions, depending on the choice made for the sign of m_z. The appropriate sign of m_x is determined by using Eq. (4.4).

Magnetization components m_x, m_y, and m_z given by Eqs (4.31)–(4.33) depend on the energy g_0 of the precessional dynamics through the parameter p defined by Eq. (4.22). This parameter has clear geometrical meaning. It is evident from Eq. (4.8) that p measures the size of the ellipse that corresponds to the magnetization dynamics in the unit-disk representation. According to Eq. (4.3), in the case of zero applied field the

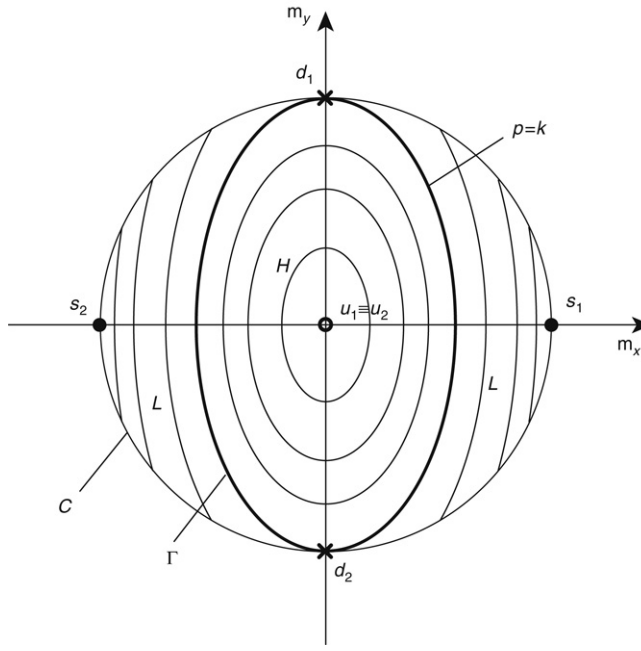

FIGURE 4.6 Unit-disk representation of phase portrait under zero field. The following notation is used: s for energy minima; u for energy maxima; d for energy saddles. Labels H and L denote high-energy and low-energy regions, respectively. They are separated by doubly-connected separatrices Γ.

energy values are in the range:

$$\frac{D_x}{2} \leq g_0 \leq \frac{D_z}{2}. \tag{4.34}$$

By using this result in Eq. (4.22), one finds that the corresponding range for p is $0 \leq p^2 \leq 1$. When the energy is varied in this interval, Eqs (4.31)–(4.33) generate the unit-disk phase portrait shown in Fig. 4.6. The energy maxima correspond to $p = 0$. In this case, the constant-energy ellipse (see Eq. (4.8)) is reduced to the point (a_x, a_y). On the other hand, when $p = 1$ the energy minima are achieved and the corresponding ellipse is tangent to the unit circle from outside. The heteroclinic separatrix trajectories (bold lines in Fig. 4.6) divide the unit-disk portrait into the high-energy (H) and low-energy (L) regions.

- Region H
  This region consists of two separate subregions, which are mirror images with respect to the $(\mathrm{m}_x, \mathrm{m}_y)$-plane. In this region, the system energy varies in the interval $D_y/2 \leq g_0 \leq D_z/2$, that is:

$$0 \leq p^2 \leq k^2. \tag{4.35}$$

  According to Eq. (4.24), $0 \leq k_H \leq 1$ in this region. This implies that the magnetization dynamics is a precessional motion around the hard z axis. The precession period is given by the expression:

$$T(g_0) = \frac{4\boldsymbol{K}(k_H)}{\Omega_H}, \tag{4.36}$$

  where $\boldsymbol{K}(k_H)$ (see Eq. (4.28)) represents the complete elliptic integral of the first kind.
- Region L
  This region consists of two separate subregions, which are mirror images with respect to the $(\mathrm{m}_y, \mathrm{m}_z)$-plane. In this region, the energy varies in the interval $D_x/2 \leq g_0 \leq D_y/2$. Therefore:

$$k^2 \leq p^2 \leq 1, \tag{4.37}$$

  which implies that $1 \leq k_H \leq \infty$. The nature of the corresponding magnetization dynamics becomes clear once we observe that the $\mathrm{cn}(x,k)$ and $\mathrm{dn}(x,k)$ Jacobi functions are transformed into one another when $k > 1$. By using known transformation rules for Jacobi functions, one can write Eqs (4.31)–(4.33) as follows:

$$\mathrm{m}_x = \mp p\,\mathrm{dn}\left(\Omega_L t, k_L\right), \tag{4.38}$$

$$\mathrm{m}_y = \frac{1}{k'}\sqrt{1-p^2}\,\mathrm{sn}\left(\Omega_L t, k_L\right), \tag{4.39}$$

$$\mathrm{m}_z = \pm\sqrt{1-p^2}\,\mathrm{cn}\left(\Omega_L t, k_L\right), \tag{4.40}$$

  where:

$$\Omega_L = k_H \Omega_H = k' p\left(D_z - D_x\right), \tag{4.41}$$

$$k_L = \frac{1}{k_H} = \frac{k}{k' p}\sqrt{1-p^2}. \tag{4.42}$$

It can be verified that $0 \leq k_L \leq 1$. This implies that Eqs (4.38)–(4.40) describe a precessional dynamics around the x axis. The precession period is:

$$T(g_0) = \frac{4\boldsymbol{K}(k_L)}{\Omega_L}. \tag{4.43}$$

In the following two sections, we discuss in some detail the solution of Eq. (4.14) under nonzero field in the cases of particular physical interest when the applied magnetic field is aligned along one of the anisotropy axes.

4.3 PRECESSIONAL DYNAMICS UNDER TRANSVERSE MAGNETIC FIELD

In this section, we shall discuss the case of transverse field, when $\mathrm{h}_{ax} = \mathrm{h}_{az} = 0$, while $\mathrm{h}_{ay} \neq 0$. This case is of particular importance in the analysis of the precessional switching phenomena discussed in Chapter 6. The phase portrait for this case and the corresponding energy graph are shown in Fig. 4.7. The same phase portrait was also previously presented as an example in Fig. 4.2 in stereographic projection form. To avoid ambiguities, we shall assume $\mathrm{h}_{ay} > 0$, i.e., $a_y < 0$ (see Eq. (4.7)). We shall next use the change of variables given by Eq. (4.19). In terms of w, the magnetization components (Eqs (4.11) and (4.12)) are expressed as follows:

$$\begin{aligned} \mathrm{m}_x &= \mp p\sqrt{1-w^2}, \qquad \mathrm{m}_y = a_y + \frac{p}{k}w, \\ \mathrm{m}_z &= \pm\frac{k'p}{k}\sqrt{(w-w_-)(w_+-w)}, \end{aligned} \tag{4.44}$$

where:

$$w_\pm = -\frac{ka_y}{pk'^2} \pm \frac{k}{k'p}\sqrt{1-p^2+\frac{k^2a_y^2}{k'^2}}. \tag{4.45}$$

By making the same change of variables in Eq. (4.14), one obtains:

$$\frac{\mathrm{d}w}{\sqrt{(1-w^2)\,(w-w_-)\,(w_+-w)}} = k'p\,(D_z - D_x)\,\mathrm{d}t. \tag{4.46}$$

The integration and inversion of Eq. (4.46) in order to obtain w as a function of time depend on how the four roots of the integrand

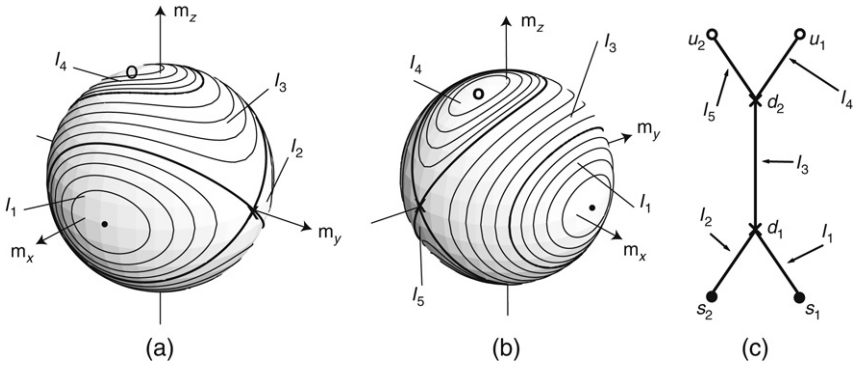

FIGURE 4.7 (a), (b) Phase portrait of the precessional magnetization dynamics on the unit sphere when the applied field is directed along the positive y axis. Full dot: energy minimum; open dot: energy maximum; cross: energy saddle; bold lines: separatrices. (c) Corresponding graph. s_1, s_2: minima; d_1, d_2: saddles; u_1, u_2: maxima. I_1, I_2, I_3, I_4, I_5: central energy regions.

denominator are ordered for various energy ranges. To understand this root ordering, we shall consider the unit-disk representation of the phase portrait of the magnetization dynamics shown in Fig. 4.8 for the case $a_x = 0$, $a_y < 0$, and $|a_y| < 1$. It is apparent from Eq. (4.44) that w is a linear function of m_y and that the equalities $w = w_\pm$ are equivalent to $\mathrm{m}_z = 0$, which means that the corresponding points are on the boundary of the unit disk. The presence of the field breaks the heteroclinic connections shown in Fig. 4.6 into two pairs of homoclinic trajectories represented by the bold lines in Fig. 4.8. These trajectories divide the phase portrait into high-energy (H), intermediate-energy (I), and low-energy (L) regions.

- Region H
  The region H exists only if $|a_y| < 1$. It consists of two separate subregions which are symmetric with respect to the $(\mathrm{m}_x, \mathrm{m}_y)$-plane. In this region, the parameter p varies in the interval:

$$0 \le p^2 \le k^2 \left(1 - |a_y|\right)^2 , \tag{4.47}$$

  and the root ordering is: $w_- < -1 < 1 < w_+$. The variable w varies in the interval $(-1, 1)$ during the magnetization dynamics. When $p = 0$ (energy maxima), $w_- \to -\infty$, $w_+ \to +\infty$. Conversely, $w_- = -1, w_+ > 1$ when $p = k(1 - |a_y|)$.
- Region I

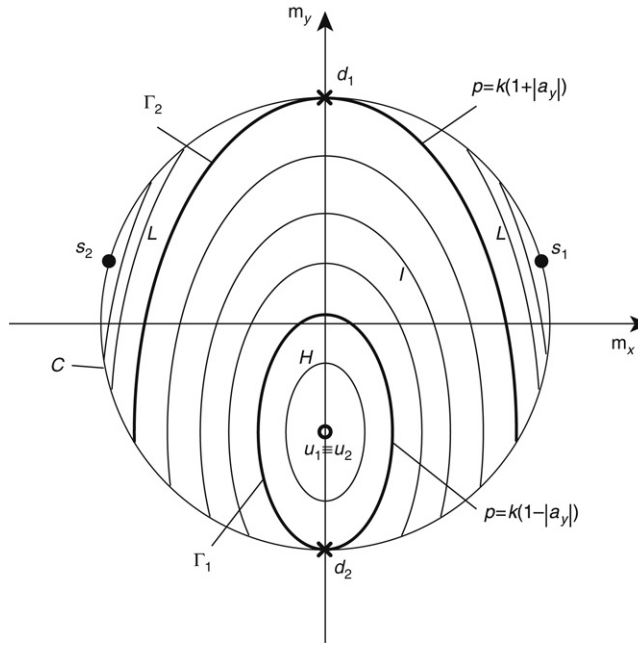

FIGURE 4.8 Unit-disk representation of phase portrait when field is applied along the positive y axis. Adopted notation is as follows. s: energy minima; u: energy maxima; d: energy saddles. Labels H, I and L denote high-energy, intermediate-energy, and low-energy regions, respectively. Lines Γ_1 and Γ_2 correspond to separatrices.

The region I is symmetric with respect to the $(\mathrm{m}_x, \mathrm{m}_y)$- and $(\mathrm{m}_y, \mathrm{m}_z)$-planes. In this region, the parameter p varies in the interval:

$$k^2 \left(1 - |a_y|\right)^2 \leq p^2 \leq k^2 \left(1 + |a_y|\right)^2, \tag{4.48}$$

and the root ordering is: $-1 < w_- < 1 < w_+$. The variable w varies in the interval $(w_-, 1)$ during the magnetization dynamics.

- Region L
  The region L exists only if $|a_y| < k'^2/k^2$. It consists of two subregions which are symmetric with respect to the $(\mathrm{m}_y, \mathrm{m}_z)$-plane. In this region, the parameter p varies in the interval:

$$k^2 \left(1 + |a_y|\right)^2 \leq p^2 \leq 1 + \frac{k^2 a_y^2}{k'^2}, \tag{4.49}$$

and the root ordering is: $-1 < w_- < w_+ < 1$. The variable w varies in the interval (w_-, w_+) during the magnetization dynamics. When $p^2 = k^2\left(1 + |a_y|\right)^2$, then $w_- > -1$ and $w_+ = 1$, whereas $-1 < w_- = w_+ < 1$ when $p^2 = 1 + k^2 a_y^2/k'^2$.

We shall first discuss regions H and L. Region I will require a slightly different treatment.

Solution for region H

In order to integrate Eq. (4.46), it is useful to carry out a transformation leaving the ± 1 roots of the denominator unchanged, while transforming the roots w_+ and w_- into roots with opposite values. This can be achieved by using the following Möbius transformation [588]:

$$\xi = \frac{w - q}{1 - qw}, \qquad w = \frac{\xi + q}{1 + q\xi}. \tag{4.50}$$

This transformation maps $w = \pm 1$ into $\xi = \pm 1$, respectively. The parameter q has to be chosen in such a way that $\xi_+ + \xi_- = 0$, where $\xi_\pm = (w_\pm - q)/(1 - qw_\pm)$. This leads to the equation:

$$q^2 - 2sq + 1 = 0, \tag{4.51}$$

where:

$$s = \frac{1 + w_+ w_-}{w_+ + w_-}. \tag{4.52}$$

The solutions $q = s \pm \sqrt{s^2 - 1}$ of Eq. (4.51) are real only when $s^2 - 1 \geq 0$. It can be verified that $s^2 - 1 = (w_+^2 - 1)(w_-^2 - 1)/(w_+ + w_-)^2$. Thus, $s^2 - 1 \geq 0$ when the $w_\pm$ roots are both outside or both inside the interval $(-1, 1)$. This is precisely the root ordering associated with regions H and L, respectively. The Möbius transformation given by Eq. (4.50) has the determinant equal to $1 - q^2$. Therefore, of the two acceptable values of q, it is convenient to use the one for which $1 - q^2 > 0$. Indeed, this is because this choice of q preserves the order of the polynomial roots when making the change of variable from w to ξ. Thus, we choose:

$$q = s\left(1 - \sqrt{1 - \frac{1}{s^2}}\right). \tag{4.53}$$

By applying the change of variables (4.50) in Eq. (4.46) and integrating, after straightforward but somewhat lengthy transformations one finds that:

$$\int_0^{\xi} \frac{\mathrm{d}\xi'}{\sqrt{(1-\xi'^2)\,(1-k_H^2\xi'^2)}} = \Omega_H t, \tag{4.54}$$

where:

$$k_H^2 = \left(\frac{1-qw_+}{w_+-q}\right)^2 = \left(\frac{1-qw_-}{w_--q}\right)^2, \tag{4.55}$$

$$\Omega_H = k'p\sqrt{\frac{1-q^2}{k_H^2-q^2}}\,(D_z-D_x)\,. \tag{4.56}$$

It must be noted that the function under the square root in Eq. (4.56) is positive. Indeed, it can be verified that $(1-q^2)/(k_H^2-q^2) = (q-w_-)(w_+-q)/(1-q^2)$. The latter quantity is positive because $w_- < q < w_+$. This is the consequence of the order-preserving property of the $w \to \xi$ transformation and of the fact that $w = q$ is transformed into $\xi = 0$ by Eq. (4.50).

By inverting Eq. (4.54), one obtains a solution for ξ in terms of Jacobi elliptic functions:

$$\xi = \mathrm{sn}\,(\Omega_H t, k_H)\,. \tag{4.57}$$

By using Eqs (4.50) and (4.57) in Eq. (4.44) one obtains the expressions for the magnetization components in region H:

$$\mathrm{m}_x = \mp p\sqrt{1-q^2}\,\frac{\mathrm{cn}_H}{1+q\mathrm{sn}_H}, \tag{4.58}$$

$$\mathrm{m}_y = a_y + \frac{p}{k}\,\frac{q+\mathrm{sn}_H}{1+q\mathrm{sn}_H}, \tag{4.59}$$

$$\mathrm{m}_z = \pm\frac{k'p\sqrt{1-q^2}}{k}\sqrt{\frac{1-q^2}{k_H^2-q^2}}\,\frac{\mathrm{dn}_H}{1+q\mathrm{sn}_H}, \tag{4.60}$$

where sn_H, cn_H, and dn_H denote the corresponding Jacobi elliptic functions of argument $(\Omega_H t, k_H)$. According to Eq. (4.55), $0 < k_H^2 < 1$, because $w_+ > 1$ for region H. The $\pm$ signs in Eqs (4.58) and (4.60) reflect the fact that region H consists of two subregions which are symmetric

with respect to the $(\mathrm{m}_x, \mathrm{m}_y)$-plane (see Fig. 4.8), and cover the same energy range. From Eqs (4.58)–(4.60), one finds that the precession period is:

$$T(g_0) = \frac{4\boldsymbol{K}(k_H)}{\Omega_H}. \tag{4.61}$$

Solution for region L

Equations (4.58)–(4.60) are valid for region L too. The only essential difference is that $k_H^2 > 1$. This can be inferred from Eq. (4.55) and the inequality $-1 < w_+ < 1$, which is valid in region L. The solution can be reduced to elliptic functions with modulus smaller than 1 by using Jacobi function identities [321,625]. The final result is:

$$\mathrm{m}_x = \mp p\sqrt{1-q^2}\,\frac{\mathrm{dn}_L}{1+qk_L\mathrm{sn}_L}, \tag{4.62}$$

$$\mathrm{m}_y = a_y + \frac{p}{k}\,\frac{q+k_L\mathrm{sn}_L}{1+qk_L\mathrm{sn}_L}, \tag{4.63}$$

$$\mathrm{m}_z = \pm\frac{k'p\sqrt{1-q^2}}{k}\sqrt{\frac{1-q^2}{1-q^2k_L^2}}\,\frac{k_L\mathrm{cn}_L}{1+qk_L\mathrm{sn}_L}, \tag{4.64}$$

where $k_L^2 = 1/k_H^2$. The symbols sn_L, cn_L, and dn_L are the notations for the corresponding elliptic functions of argument $(\Omega_L t, k_L)$, where $\Omega_L = k_H\Omega_H$. The precession period is:

$$T(g_0) = \frac{4\boldsymbol{K}(k_L)}{\Omega_L}. \tag{4.65}$$

Solution for region I

In this case, it is convenient to apply two sequential transformations of Eq. (4.46). First, the ordering $-1 < w_- < 1 < w_+$ is transformed into $w_-^* < -1 < 1 < w_+^*$ by an intermediate transformation leaving 1 unchanged and transforming w_- into -1. This transformation is given by the formula:

$$w^* = 1 - 2\frac{1-w}{1-w_-}, \qquad w = 1 + \frac{1}{2}\,(1-w_-)\,(w^*-1)\,. \tag{4.66}$$

In terms of the new variable w^*, Eq. (4.46) can be written as follows:

$$\frac{\mathrm{d}w^*}{\sqrt{\left(1-w^{*2}\right)\left(w^*-w_-^*\right)\left(w_+^*-w^*\right)}} = ck'p\left(D_z-D_x\right)\mathrm{d}t, \tag{4.67}$$

where:

$$c = \frac{1-w_-}{2}, \tag{4.68}$$

$$w_-^* = 1-\frac{4}{1-w_-}, \qquad w_+^* = 1-2\frac{1-w_+}{1-w_-}, \tag{4.69}$$

and $w_-^* < -1 < 1 < w_+^*$. Given this inequality, Eq. (4.67) can be integrated and inverted by the method previously used for region H. By introducing the notations:

$$s^* = \frac{1+w_+^*w_-^*}{w_+^*+w_-^*}, \tag{4.70}$$

$$q^* = s^*\left(1-\sqrt{1-\frac{1}{s^{*2}}}\right), \tag{4.71}$$

one arrives at the following equation, analogous to Eq. (4.54):

$$\int_0^{\xi^*}\frac{\mathrm{d}\xi'}{\sqrt{\left(1-\xi'^2\right)\left(1-k_I^2\xi'^2\right)}} = \Omega_I t, \tag{4.72}$$

where:

$$k_I^2 = \left(\frac{1-q^*w_+^*}{w_+^*-q^*}\right)^2 = \left(\frac{1-q^*w_-^*}{w_-^*-q^*}\right)^2, \tag{4.73}$$

$$\Omega_I = ck'p\sqrt{\frac{1-q^{*2}}{k_I^2-q^{*2}}}\left(D_z-D_x\right). \tag{4.74}$$

By inverting Eq. (4.72), one finds the solution for ξ^* in terms of Jacobi elliptic functions:

$$\xi^* = \mathrm{sn}\left(\Omega_I t, k_I\right). \tag{4.75}$$

The connection between ξ^* and the magnetization components is more complicated than before, because of the intermediate transformation from w to w^*. After algebraic manipulations analogous to those carried out for region H and an appropriate change of the time origin, the following analytical expressions are obtained:

$$\mathrm{m}_x = cp\,(1-q^*)\sqrt{\frac{1+q^*}{k_I-q^*}} \times \frac{\sqrt{(\mathrm{dn}_I - k_I\mathrm{cn}_I)\,(1+\mathrm{dn}_I)}}{\mathrm{dn}_I - q^*\mathrm{cn}_I}\mathrm{cn}\,(\Omega_I t/2, k_I)\,, \tag{4.76}$$

$$\mathrm{m}_y = a_y + \frac{p}{k} - \frac{cp\,(1-q^*)}{k}\frac{\mathrm{dn}_I + \mathrm{cn}_I}{\mathrm{dn}_I - q^*\mathrm{cn}_I}, \tag{4.77}$$

$$\mathrm{m}_z = -\frac{cpk'\,(1+q^*)}{k}\sqrt{\frac{1-q^*}{k_I+q^*}} \times \frac{\sqrt{(\mathrm{dn}_I + k_I\mathrm{cn}_I)\,(1+\mathrm{dn}_I)}}{\mathrm{dn}_I - q^*\mathrm{cn}_I}\frac{k_I'\mathrm{sn}\,(\Omega_I t/2, k_I)}{\mathrm{dn}\,(\Omega_I t/2, k_I)}, \tag{4.78}$$

where $k_I'^2 = 1 - k_I^2$. The symbols sn_I, cn_I, and dn_I denote the corresponding elliptic functions of argument $(\Omega_I t, k_I)$.

4.4 PRECESSIONAL DYNAMICS UNDER LONGITUDINAL MAGNETIC FIELD

This is the case when $\mathrm{h}_{ax} \neq 0$, while $\mathrm{h}_{ay} = \mathrm{h}_{az} = 0$. This case will be instrumental in the analysis of magnetization relaxation discussed in Chapter 6 and in the treatment of spin-transfer-driven dynamics presented in Chapter 9. The phase portrait for this case and the corresponding energy graph are shown in Fig. 4.9. To avoid ambiguities, we shall assume that $\mathrm{h}_{ax} > 0$, i.e., $a_x < 0$ (see Eq. (4.7)). We shall next introduce the variable:

$$w = -\cos u. \tag{4.79}$$

In terms of w, the magnetization components (Eqs (4.11) and (4.12)) are expressed as follows:

$$\begin{aligned} &\mathrm{m}_x = a_x + pw, \qquad \mathrm{m}_y = \pm\frac{p}{k}\sqrt{1-w^2}, \\ &\mathrm{m}_z = \pm\frac{k'p}{k}\sqrt{(w-w_-)(w-w_+)}, \end{aligned} \tag{4.80}$$

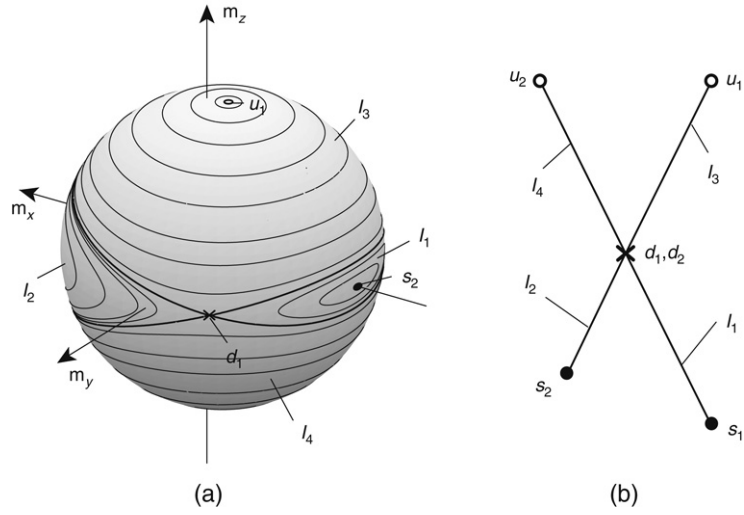

FIGURE 4.9 (a) Phase portrait of the precessional magnetization dynamics on the unit sphere when the applied field is directed along the positive x axis. Full dot: energy minimum; open dot: energy maximum; cross: energy saddle; bold lines: separatrices. (b) Corresponding graph. s_1, s_2: minima; d_1, d_2: saddles; u_1, u_2: maxima. I_1, I_2, I_3, I_4: central energy regions.

where:

$$w_{\pm} = \frac{k^2 a_x}{k'^2 p} \pm \frac{1}{k'p}\sqrt{p^2 - k^2\left(1 - \frac{a_x^2}{k'^2}\right)}. \tag{4.81}$$

We shall see that the expression under the square root may become negative under certain conditions, i.e., $w_{\pm}$ can be complex conjugate. By using the transformation (4.79) in Eq. (4.14), one obtains:

$$\frac{\mathrm{d}w}{\sqrt{(1-w^2)\,(w-w_-)\,(w-w_+)}} = k'p\,(D_z - D_x)\,\mathrm{d}t. \tag{4.82}$$

The integration and inversion of Eq. (4.82) in order to obtain w as a function of time depend on the nature of the roots $w_{\pm}$, which may be real or complex conjugate. When the roots are real, the nature of their ordering affects the inversion as well. The unit-disk representation of the phase portrait of the magnetization dynamics is shown in Fig. 4.10. It is

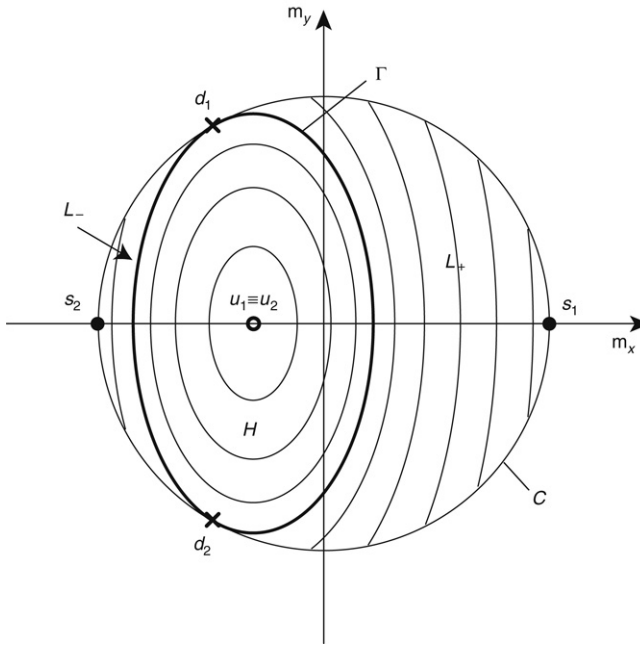

FIGURE 4.10 Unit-disk representation of the phase portrait when the magnetic field is applied along positive x axis. Adopted notation is as follows. s: energy minima; u: energy maxima; d: energy saddles. Labels H and $L_{\pm}$ denote high-energy and low-energy regions, respectively. They are separated by doubly-connected separatrices Γ.

apparent from this figure that the presence of the applied magnetic field does not break the heteroclinic connections originally present in Fig. 4.6, but rather shifts them. As a result, the portrait is divided into high-energy (H) and low-energy (L) regions as in the case of zero field.

- Region H
  This region exists only if $|a_x| < 1$. It consists of two separate subregions which are symmetric with respect to the $(\mathrm{m}_x, \mathrm{m}_y)$-plane. The range of variation of the parameter p depends on whether region L_- exists or not, namely:

$$\begin{aligned} &0 \leq p^2 \leq k^2 \left(1 - \frac{a_x^2}{k'^2}\right) \quad \text{if } |a_x| \leq k'^2, \\ &0 \leq p^2 \leq \left(1 - |a_x|\right)^2 \quad \text{if } |a_x| \geq k'^2. \end{aligned} \tag{4.83}$$

The roots $w_{\pm}$ are complex conjugate if $p^2 < k^2\left(1 - a_x^2/k'^2\right)$ (see Eq. (4.81)), otherwise they are real and follow the ordering: $w_- < w_+ < -1 < 1$. The variable w varies in the interval $(-1, 1)$ during the magnetization dynamics.

- Region L_+
  This is the low-energy region around the energy minimum at $\mathrm{m}_x = 1$. Under positive field (i.e., $a_x < 0$), this region is always present. The range of variation of the parameter p depends on whether region L_- exists or not, namely:

$$\begin{aligned} &k^2\left(1 - \frac{a_x^2}{k'^2}\right) \leq p^2 \leq (1 + |a_x|)^2 \quad \text{if } |a_x| \leq k'^2, \\ &(1 - |a_x|)^2 \leq p^2 \leq (1 + |a_x|)^2 \quad \text{if } |a_x| \geq k'^2. \end{aligned} \tag{4.84}$$

  The corresponding root ordering is: $-1 < w_- < w_+ < 1$ if $p^2 < (1 - |a_x|)^2$; otherwise: $w_- < -1 < w_+ < 1$. The variable w varies in the interval $(w_+, 1)$ during the magnetization dynamics.
- Region L_-
  This is the low-energy region around the energy minimum at $\mathrm{m}_x = -1$. Under positive field (i.e., $a_x < 0$), this region exists only if $|a_x| \leq k'^2$. The parameter p varies within the range:

$$k^2\left(1 - \frac{a_x^2}{k'^2}\right) \leq p^2 \leq (1 - |a_x|)^2, \tag{4.85}$$

  and the corresponding root ordering is: $-1 < w_- < w_+ < 1$. The variable w varies in the interval $(-1, w_-)$ during the magnetization dynamics.

The analytical formulas for the magnetization dynamics in the different energy regions can be obtained by applying the same line of reasoning as in the previous section. For this reason, we shall refer to that section for the definition of the various parameters that will be used in the subsequent discussion. Depending on the properties of the roots $w_{\pm}$, one can conveniently identify two cases which are solved through different variable transformations.

Case 1

This is the case when the roots $w_{\pm}$: (i) are real and follow the ordering $-1 < w_- < w_+ < 1$ (region L_-; region L_+ for $p^2 < (1 - |a_x|)^2$); or (ii) are complex conjugate (region H for $p^2 < k^2\left(1 - a_x^2/k'^2\right)$). The derivation

proceeds by applying the Möbius transformation (4.50) already used in the previous section. This leads to the equation:

$$\int_1^{\xi} \frac{\mathrm{d}\xi'}{\sqrt{(1-\xi'^2)\,(\xi'^2-k_L'^2)}} = \mp\Omega_L t, \tag{4.86}$$

where the $\mp$ sign refers to regions L_+ and L_-, respectively, while:

$$k_L'^2 = \left(\frac{w_+ - q}{1 - q w_+}\right)^2 = \left(\frac{w_- - q}{1 - q w_-}\right)^2, \tag{4.87}$$

$$\Omega_L = k' p \sqrt{\frac{1-q^2}{1-q^2 k_L'^2}}\,(D_z - D_x)\,, \tag{4.88}$$

and q is defined by Eqs (4.53), (4.52) and (4.81). The elliptic integral in Eq. (4.86) can be inverted by using the Jacobi elliptic function "dn":

$$\xi = \pm \mathrm{dn}\,(\Omega_L t, k_L)\,, \tag{4.89}$$

where $k_L^2 = 1 - k_L'^2$.

- Regions L_+ and L_-
  By using Eqs (4.89), (4.50) and (4.80), one obtains the following analytical expressions for the magnetization components:

$$\mathrm{m}_x = a_x + p\frac{q \pm \mathrm{dn}_L}{1 \pm q\mathrm{dn}_L}, \tag{4.90}$$

$$\mathrm{m}_y = -\frac{p}{k}\sqrt{1-q^2}\,\frac{k_L \mathrm{sn}_L}{1 \pm q\mathrm{dn}_L}, \tag{4.91}$$

$$\mathrm{m}_z = \pm\frac{k' p\sqrt{1-q^2}}{k}\sqrt{\frac{1-q^2}{1-q^2k_L'^2}}\,\frac{k_L \mathrm{cn}_L}{1 \pm q\mathrm{dn}_L}, \tag{4.92}$$

  where the $\pm$ signs refer to region L_+ and region L_-, respectively, whereas sn_L, cn_L, and dn_L are the notations for the corresponding elliptic functions of argument $(\Omega_L t, k_L)$. The precession period is:

$$T(g_0) = \frac{4\boldsymbol{K}(k_L)}{\Omega_L}. \tag{4.93}$$

- Region H
  Formulas (4.90)–(4.92) are also valid for region H. However, in this case the roots $w_\pm$ are complex conjugate and, according to Eq. (4.87), $k_L'^2 < 0$ and $k_L^2 > 1$. The transformation rules for the Jacobi elliptic functions [321,625] can be used to represent Eqs (4.90)–(4.92) in terms of Jacobi elliptic functions with a modulus smaller than 1. After taking proper account of sign consistencies, one obtains the following result:

$$\mathrm{m}_x = a_x + p\frac{q + \mathrm{cn}_H}{1 + q\mathrm{cn}_H}, \tag{4.94}$$

$$\mathrm{m}_y = \pm\frac{p}{k}\sqrt{1-q^2}\,\frac{\mathrm{sn}_H}{1 + q\mathrm{cn}_H}, \tag{4.95}$$

$$\mathrm{m}_z = \mp\frac{k'p\sqrt{1-q^2}}{k}\sqrt{\frac{1-q^2}{k_H^2 + q^2k_H'^2}}\,\frac{\mathrm{dn}_H}{1 + q\mathrm{cn}_H}, \tag{4.96}$$

  where $k_H^2 = 1/k_L^2$, $k_H'^2 = 1 - k_H^2$, and the two signs refer to the two subregions with opposite values of m_z that form region H. The symbols sn_H, cn_H, and dn_H are notations for the corresponding elliptic functions of argument $(\Omega_H t, k_H)$, where $\Omega_H = k_L\Omega_L$. As before, the precession period is:

$$T(g_0) = \frac{4\boldsymbol{K}(k_H)}{\Omega_H}. \tag{4.97}$$

Case 2

This is the case when the roots $w_\pm$: (i) follow the ordering $w_- < -1 < w_+ < 1$ (region L_+ for $p^2 > (1 - |a_x|)^2$); or (ii) follow the ordering $w_- < w_+ < -1 < 1$ (region H for $p^2 > k^2\left(1 - a_x^2/k'^2\right)$). The derivation proceeds by applying the same sequence of transformations already used in the previous section when region I was discussed. By first applying the intermediate transformation given by Eq. (4.66) one obtains:

$$\frac{\mathrm{d}w^*}{\sqrt{\left(1 - w^{*2}\right)\left(w^* - w_-^*\right)\left(w^* - w_+^*\right)}} = ck'p\left(D_z - D_x\right)\mathrm{d}t, \tag{4.98}$$

where $-1 < w_-^* < w_+^* < 1$ for region L_+ and $-1 < w_+^* < w_-^* < 1$ for region H. Equation (4.98) can be integrated and inverted by the method used for case 1. Due to the different ordering of w_-^* and w_+^* in region L_+ and region H, different formulas are obtained for the magnetization components:

- Region L_+

$$\mathrm{m}_x = a_x + p - cp(1-q^*)\frac{1-\mathrm{dn}^*}{1+q^*\mathrm{dn}^*}, \tag{4.99}$$

$$\mathrm{m}_y = -\frac{cp\,(1-q^*)}{k}\sqrt{\frac{1+q^*}{1-q^*k^{*\prime}}}\sqrt{\frac{\mathrm{dn}^*+k^{*\prime}}{1+\mathrm{dn}^*}}\frac{k^*\mathrm{sn}^*}{1+q^*\mathrm{dn}^*}, \tag{4.100}$$

$$\mathrm{m}_z = \frac{ck'p\,(1+q^*)}{k}\sqrt{\frac{1-q^*}{1+q^*k^{*\prime}}}\sqrt{\frac{1+\mathrm{dn}^*}{\mathrm{dn}^*+k^{*\prime}}}\frac{k^*\mathrm{cn}^*}{1+q^*\mathrm{dn}^*}. \tag{4.101}$$

- Region H

$$\mathrm{m}_x = a_x + p - cp(1-q^*)\frac{1-\mathrm{dn}^*}{1+q^*\mathrm{dn}^*}, \tag{4.102}$$

$$\mathrm{m}_y = \pm\frac{cp\,(1-q^*)}{k}\sqrt{\frac{1+q^*}{1+q^*k^{*\prime}}} \times \frac{1}{\sqrt{(\mathrm{dn}^*+k^{*\prime})\,(1+\mathrm{dn}^*)}}\frac{k^{*2}\mathrm{sn}^*\mathrm{cn}^*}{1+q^*\mathrm{dn}^*}, \tag{4.103}$$

$$\mathrm{m}_z = \mp\frac{ck'p\,(1+q^*)}{k}\sqrt{\frac{1-q^*}{1-q^*k^{*\prime}}} \times \sqrt{(\mathrm{dn}^*+k^{*\prime})\,(1+\mathrm{dn}^*)}\frac{1}{1+q^*\mathrm{dn}^*}. \tag{4.104}$$

The two signs correspond to the two subregions with opposite m_z that form region H.

In the previous expressions, q^* is defined by Eqs (4.69)–(4.71) and (4.81), while:

$$k^{*\prime 2} = \left(\frac{w_+^*-q^*}{1-q^*w_+^*}\right)^2 = \left(\frac{w_-^*-q^*}{1-q^*w_-^*}\right)^2, \tag{4.105}$$

and $k^{*2} = 1 - k^{*\prime 2}$. The symbols sn^*, cn^*, and dn^* are the notations for the corresponding elliptic functions of argument $(\Omega^* t, k^*)$, where:

$$\Omega^* = k'p\sqrt{\frac{1-q^{*2}}{1-q^{*2}k^{*\prime 2}}}\,(D_z - D_x)\,. \tag{4.106}$$

The product $\mathrm{sn}^*\mathrm{cn}^*$ in Eq. (4.103) has the same period as dn^*. This means that the period of the precessional dynamics in Region H is:

$$T(g_0) = \frac{2\boldsymbol{K}(k^*)}{\Omega^*}. \tag{4.107}$$

4.5 HAMILTONIAN STRUCTURE OF PRECESSIONAL DYNAMICS

It is known that conservative mechanical systems can be described by the canonical Hamiltonian equations:

$$\frac{\mathrm{d}\mathbf{p}}{\mathrm{d}t} = -\frac{\partial \mathcal{H}}{\partial \mathbf{q}}, \tag{4.108}$$

$$\frac{\mathrm{d}\mathbf{q}}{\mathrm{d}t} = \frac{\partial \mathcal{H}}{\partial \mathbf{p}}, \tag{4.109}$$

where the state variables $\mathbf{p}$ and $\mathbf{q}$ are "generalized" momenta and coordinates, respectively, while the function $\mathcal{H}(\mathbf{q}(t), \mathbf{p}(t))$, called Hamiltonian, has the physical meaning of energy.

The Hamiltonian system (4.108)–(4.109) can also be written in the matrix form:

$$\begin{pmatrix} \mathrm{d}\mathbf{p}/\mathrm{d}t \\ \mathrm{d}\mathbf{q}/\mathrm{d}t \end{pmatrix} = S \cdot \begin{pmatrix} \partial\mathcal{H}/\partial\mathbf{q} \\ \partial\mathcal{H}/\partial\mathbf{p} \end{pmatrix}, \tag{4.110}$$

where S is the antisymmetric matrix:

$$S = \begin{pmatrix} 0 & -I \\ I & 0 \end{pmatrix}, \tag{4.111}$$

with I representing the identity matrix.

Hamiltonian equations play a central role in modern physics because they reveal that the underlying dynamics is controlled by energy. This fundamental physical feature is replicated in the structure of quantum mechanics. The Hamiltonian equations (4.108)–(4.109) are highly symmetric, an aspect widely exploited in the development of the extensive mathematical theory of Hamiltonian systems. The most salient results of this theory are the conservation of phase volumes, the conservation of "symplectic areas", and the existence of the Poincaré–Cartan integral invariant.

Due to the importance of Hamiltonian systems, it is interesting to examine if the structure of the precessional Landau–Lifshitz equation:

$$\frac{\mathrm{d}\mathbf{m}}{\mathrm{d}t} = \mathbf{m} \times \frac{\partial g_L}{\partial \mathbf{m}} \tag{4.112}$$

is Hamiltonian. One important distinction between canonical Hamiltonian equations like (4.108)–(4.109) and magnetization dynamic equation (4.112) is immediately apparent: the number of state variables in Eq. (4.112) is odd, while the number of state variables in canonical Hamiltonian systems is always even. However, there is some similarity as well. In fact, Eq. (4.112) can be written in the matrix form:

$$\frac{\mathrm{d}\mathbf{m}}{\mathrm{d}t} = \Lambda \cdot \frac{\partial g_L}{\partial \mathbf{m}}, \tag{4.113}$$

where Λ is the antisymmetric matrix:

$$\Lambda = \begin{pmatrix} 0 & -\mathrm{m}_z & \mathrm{m}_y \\ \mathrm{m}_z & 0 & -\mathrm{m}_x \\ -\mathrm{m}_y & \mathrm{m}_x & 0 \end{pmatrix}. \tag{4.114}$$

This form of Eq. (4.112) resembles Eq. (4.110) of Hamiltonian dynamics.

To further reveal the Hamiltonian structure of Eq. (4.112), it is appropriate to mention that canonical Hamiltonian equations like (4.108)–(4.109) can be written in terms of Poisson brackets. The classical (canonical) Poisson bracket for two differentiable functions f and h of $\mathbf{p}(t)$ and $\mathbf{q}(t)$ is defined by the formula:

$$\{f, h\} = \sum_k \left(\frac{\partial f}{\partial p_k} \frac{\partial h}{\partial q_k} - \frac{\partial f}{\partial q_k} \frac{\partial h}{\partial p_k} \right), \tag{4.115}$$

where p_k and q_k are the components of $\mathbf{p}$ and $\mathbf{q}$, respectively.

By using formula (4.115), Hamiltonian equations (4.108)–(4.109) can be represented in the form:

$$\frac{\mathrm{d}p_k}{\mathrm{d}t} = \{\mathcal{H}, p_k\}, \qquad \frac{\mathrm{d}q_k}{\mathrm{d}t} = \{\mathcal{H}, q_k\}. \tag{4.116}$$

It turns out that Eq. (4.112) for precessional dynamics can also be written in the form (4.116), if we use the so-called "rigid-body" Poisson bracket

defined as:

$$\{f, h\} = \mathbf{m} \cdot \left(\frac{\partial f}{\partial \mathbf{m}} \times \frac{\partial h}{\partial \mathbf{m}} \right). \tag{4.117}$$

It can be shown that the bracket defined by Eq. (4.117) has the same four fundamental properties as the classical Poisson bracket: (i) bilinearity; (ii) antisymmetry; (iii) Leibnitz relation; (iv) Jacobi identity.

The Poisson bracket (4.117) can also be written as follows:

$$\{f, h\} = \frac{\partial h}{\partial \mathbf{m}} \cdot \left(\mathbf{m} \times \frac{\partial f}{\partial \mathbf{m}} \right). \tag{4.118}$$

By choosing:

$$h = \mathrm{m}_x, \qquad f = g_L, \tag{4.119}$$

we obtain:

$$\{g_L, \mathrm{m}_x\} = \mathbf{e}_x \cdot \left(\mathbf{m} \times \frac{\partial g_L}{\partial \mathbf{m}} \right) = \frac{\mathrm{d}\mathrm{m}_x}{\mathrm{d}t}. \tag{4.120}$$

Now, it is apparent that Eq. (4.112) for the precessional magnetization dynamics can be written in the form:

$$\frac{\mathrm{d}\mathrm{m}_x}{\mathrm{d}t} = \{g_L, \mathrm{m}_x\}, \qquad \frac{\mathrm{d}\mathrm{m}_y}{\mathrm{d}t} = \{g_L, \mathrm{m}_y\}, \qquad \frac{\mathrm{d}\mathrm{m}_z}{\mathrm{d}t} = \{g_L, \mathrm{m}_z\}, \tag{4.121}$$

which is similar to the form (4.116) of canonical Hamiltonian equations. Thus, it can be concluded that precessional magnetization dynamics has noncanonical Hamiltonian structure that can be represented in terms of "rigid-body" Poisson bracket (4.117) in the same mathematical form as canonical Hamiltonian equations written in terms of classical Poisson bracket (4.115).

Next, we consider the condition for the function $h(\mathbf{m}(t))$ being an integral of motion for the precessional dynamics. One has:

$$\frac{\mathrm{d}h}{\mathrm{d}t} = \frac{\partial h}{\partial \mathbf{m}} \cdot \frac{\mathrm{d}\mathbf{m}}{\mathrm{d}t} = \frac{\partial h}{\partial \mathbf{m}} \cdot \left(\mathbf{m} \times \frac{\partial g_L}{\partial \mathbf{m}} \right). \tag{4.122}$$

By using Eq. (4.118) in the last equation, we obtain:

$$\frac{\mathrm{d}h}{\mathrm{d}t} = \{g_L, h\}. \tag{4.123}$$

Thus, the conservation of $h(\mathbf{m}(t))$ can be written in the familiar form:

$$\{g_L, h\} = 0. \tag{4.124}$$

Casimir integrals of motion are integrals of motion that satisfy the equality:

$$\{f, \mathcal{C}(\mathbf{m})\} = 0 \tag{4.125}$$

for any differentiable function f. The function:

$$\mathcal{C}(\mathbf{m}(t)) = |\mathbf{m}(t)|^2 \tag{4.126}$$

is a Casimir integral of motion for the precessional dynamics. Indeed, according to Eqs (4.118) and (4.126):

$$\{f, \mathcal{C}(\mathbf{m})\} = 2\mathbf{m} \cdot \left(\mathbf{m} \times \frac{\partial f}{\partial \mathbf{m}}\right) = 0. \tag{4.127}$$

It is interesting to point out that the canonical Hamiltonian structure for precessional magnetization dynamics can be achieved by representing this dynamics in spherical coordinates. Indeed, according to Eqs (3.19) and (3.20) from Chapter 3, the precessional (i.e., with $\alpha = 0$) magnetization dynamics is described in spherical coordinates by the following equations:

$$\frac{\mathrm{d}\phi}{\mathrm{d}t} = \frac{1}{\sin\theta}\frac{\partial g_L}{\partial \theta}, \tag{4.128}$$

$$-\sin\theta \frac{\mathrm{d}\theta}{\mathrm{d}t} = \frac{\partial g_L}{\partial \phi}. \tag{4.129}$$

The last two equations can be reduced to the canonical Hamiltonian form:

$$\frac{\mathrm{d}\phi}{\mathrm{d}t} = -\frac{\partial g_L}{\partial \cos\theta}, \tag{4.130}$$

$$\frac{\mathrm{d}\cos\theta}{\mathrm{d}t} = \frac{\partial g_L}{\partial \phi}, \tag{4.131}$$

with ϕ and $\cos\theta$ as generalized momentum and coordinate, respectively. It is worthwhile noting that the magnetization magnitude conservation is automatically accounted for by Eqs (4.130)–(4.131), due to the very nature of spherical coordinates.

CHAPTER 5

Dissipative Magnetization Dynamics

5.1 DAMPING SWITCHING IN UNIAXIAL MEDIA

Landau–Lifshitz magnetization dynamics contains two distinct time scales: the fast time scale of precessional dynamics and the relatively slow time scale of the relaxational dynamics controlled by the small damping constant α. The Landau–Lifshitz and Landau–Lifshitz–Gilbert equations are written in terms of magnetization components that generally vary on the fast time scale, and for this reason the underlying slow-time-scale dynamics is not immediately revealed. However, there is one notable exception where fast and slow time scales of magnetization dynamics can be completely separated. This exception is the "damping" switching of uniaxial media. This type of switching is of significant technological interest due to the advent of perpendicular magnetic recording, where the damping switching of uniaxial media is instrumental to the writing process.

To start the discussion, consider a spatially uniform pulsed magnetic field applied along the easy anisotropy axis of uniaxial (perpendicular) media (see Fig. 5.1). The analytical study of the magnetization dynamics caused by this applied field will be carried out by using the LL equation in the dimensionless form (2.51):

$$\frac{\mathrm{d}\mathbf{m}}{\mathrm{d}t} = -\mathbf{m} \times \mathbf{h}_{\text{eff}} - \alpha \mathbf{m} \times (\mathbf{m} \times \mathbf{h}_{\text{eff}}). \tag{5.1}$$

Under the assumption that the anisotropy axis of the medium and the applied field are both parallel to the z coordinate axis, the effective field $\mathbf{h}_{\text{eff}}$ is expressed as (see Eq. (3.15)):

$$\mathbf{h}_{\text{eff}} = \mathrm{h}_{az}\mathbf{e}_z - D_\perp(\mathrm{m}_x\mathbf{e}_x + \mathrm{m}_y\mathbf{e}_y) - D_z\mathrm{m}_z\mathbf{e}_z, \tag{5.2}$$

where $D_\perp = D_x = D_y$ and $D_z < D_\perp$, while the normalized applied field h_{az} is assumed to be constant during the pulse duration. The last

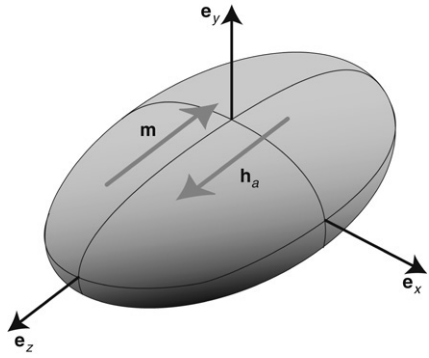

FIGURE 5.1 Damping-switching mechanism in uniaxial particle with easy axis along the $\mathbf{e}_z$ direction. The applied field is opposite to the initial magnetization.

expression for the effective field can be mathematically transformed as follows:

$$\mathbf{h}_{\text{eff}} = \mathrm{h}_{az}\mathbf{e}_z + (D_\perp - D_z)\,\mathrm{m}_z\mathbf{e}_z - D_\perp\mathbf{m}. \tag{5.3}$$

It is clear from the mathematical form of LL equation (5.1) that there exists an equivalence class of effective magnetic fields which all result in the same magnetization dynamics. This class is described by the formula:

$$\mathbf{h}_{\text{eff}}^{(eq)} = \mathbf{h}_{\text{eff}} + \chi\mathbf{m}, \tag{5.4}$$

where $\mathbf{h}_{\text{eff}}$ is a generic element of this class, while χ is an arbitrary scalar function of $\mathbf{m}$. By using the last observation, Eq. (5.3) for the effective field can be simplified as follows:

$$\mathbf{h}_{\text{eff}} = (\mathrm{h}_{az} + \kappa_{\text{eff}}\mathrm{m}_z)\,\mathbf{e}_z, \tag{5.5}$$

where we have introduced the effective anisotropy constant:

$$\kappa_{\text{eff}} = D_\perp - D_z > 0, \tag{5.6}$$

which accounts for both demagnetizing fields and crystal anisotropy. The magnetic free energy which corresponds to the effective field (5.5) is given

by the formula:

$$g_L = -\frac{\kappa_{\text{eff}}}{2}\mathrm{m}_z^2 - \mathrm{h}_{az}\mathrm{m}_z. \tag{5.7}$$

It is worthwhile pointing out that Kikuchi [394] considered a similar problem for an isotropic ferromagnetic sphere, where the effective field is defined by the expression:

$$\mathbf{h}_{\text{eff}} = -\frac{1}{3}\mathbf{m} + \mathrm{h}_{az}\mathbf{e}_z. \tag{5.8}$$

The difference in the mathematical forms of Eqs (5.5) and (5.8) results in a profound difference in magnetization switching. In the case of the effective field (5.8), there exists an infinite set of equilibrium states for $\mathrm{h}_{az} = 0$ and no critical field is required to switch from one equilibrium state to another. In contrast, in the case of the effective field (5.5), there are only two equilibrium states for $\mathrm{h}_{az} = 0$ with $\mathbf{m} = -\mathbf{e}_z$ and $\mathbf{m} = \mathbf{e}_z$, respectively, and the switching from one equilibrium state to the other is only possible if the applied field h_{az} exceeds some critical value.

Mallinson studied in [459] the damping switching with the effective field given by Eq. (5.5). His analysis is based on the solution of the LLG equation in spherical coordinates. The approach presented below is simpler because it takes explicit advantage of the rotational symmetry of the problem and clearly separates fast and slow time scales of magnetization dynamics.

The mathematical forms of Eqs (5.1) and (5.5) are invariant with respect to rotations of coordinate axes x and y around the z axis. In other words, the mathematical forms of Eqs (5.1) and (5.5) are the same for any choice of directions of axes x and y in the plane perpendicular to the z axis. As a result of this rotational symmetry, it is expected that $\mathrm{d}\mathrm{m}_z/\mathrm{d}t$ depends only on the z component of $\mathbf{m}$. Indeed, by using simple algebra, one finds from Eq. (5.5) that:

$$\left(\mathbf{m} \times \mathbf{h}_{\text{eff}}\right)_z = 0, \tag{5.9}$$

$$\left(\mathbf{m} \times \left(\mathbf{m} \times \mathbf{h}_{\text{eff}}\right)\right)_z = -\left(\mathrm{h}_{az} + \kappa_{\text{eff}}\mathrm{m}_z\right)\left(1 - \mathrm{m}_z^2\right). \tag{5.10}$$

By using Eqs (5.9) and (5.10) in Eq. (5.1), we arrive at the equation:

$$\frac{\mathrm{d}\mathrm{m}_z}{\mathrm{d}t} = \alpha\left(\mathrm{h}_{az} + \kappa_{\text{eff}}\mathrm{m}_z\right)\left(1 - \mathrm{m}_z^2\right). \tag{5.11}$$

It is clear from the last equation that the magnetization switching from the state $\mathbf{m} = -\mathbf{e}_z$ to the state $\mathbf{m} = \mathbf{e}_z$ (or vice versa) is driven exclusively by damping. In this sense, this switching can be termed as "damping" switching. The dynamics of m_z occurs on the slow time scale. This slow relaxational dynamics is completely decoupled from the fast precessional dynamics of m_x and m_y.

Equation (5.11) shows that no switching is possible if the magnetization is initially in the equilibrium state $\mathbf{m} = -\mathbf{e}_z$. However, due to thermal effects, the magnetization slightly fluctuates around the aforementioned equilibrium state. As a result, the value of m_z at the instant when the applied field is turned on may be slightly different from -1 and the switching process is initiated. This argument justifies the solution of Eq. (5.11) with the initial condition:

$$\mathrm{m}_z|_{t=0} = \mathrm{m}_{z0}, \tag{5.12}$$

where m_{z0} is close to -1. It is apparent from Eq. (5.11) that:

$$\frac{\mathrm{d}\mathrm{m}_z}{\mathrm{d}t} > 0 \quad \text{if } \mathrm{h}_{az} > \kappa_{\text{eff}}, \tag{5.13}$$

and switching to the equilibrium state $\mathbf{m} = \mathbf{e}_z$ will proceed for any $\mathrm{m}_{z0} > -1$. On the other hand, for m_z sufficiently close to -1 we have:

$$\frac{\mathrm{d}\mathrm{m}_z}{\mathrm{d}t} < 0 \quad \text{if } \mathrm{h}_{az} < \kappa_{\text{eff}}, \tag{5.14}$$

and no switching is possible. The above argument clearly reveals that:

$$h_{\text{crit}} = \kappa_{\text{eff}} \tag{5.15}$$

plays the role of critical field for switching. In the sequel, it is assumed that $\mathrm{h}_{az} > h_{\text{crit}}$.

By separating variables in Eq. (5.11), we obtain:

$$\int_{\mathrm{m}_{z0}}^{\mathrm{m}_z} \frac{\mathrm{d}\mathrm{m}_z}{(1-\mathrm{m}_z^2)(\mathrm{h}_{az} + \kappa_{\text{eff}}\mathrm{m}_z)} = \alpha t. \tag{5.16}$$

By performing the integration, we arrive at:

$$\alpha t = \frac{1}{2(\mathrm{h}_{az} - \kappa_{\text{eff}})} \ln \frac{1+\mathrm{m}_z}{1+\mathrm{m}_{z0}} - \frac{1}{2(\mathrm{h}_{az} + \kappa_{\text{eff}})} \ln \frac{1-\mathrm{m}_z}{1-\mathrm{m}_{z0}} - \frac{\kappa_{\text{eff}}}{\mathrm{h}_{az}^2 - \kappa_{\text{eff}}^2} \ln \frac{\mathrm{h}_{az} + \kappa_{\text{eff}}\mathrm{m}_z}{\mathrm{h}_{az} + \kappa_{\text{eff}}\mathrm{m}_{z0}}. \quad (5.17)$$

By using the last equation, the minimal pulse time needed for switching can be evaluated. Indeed, if the duration of the field pulse is such that a positive value of m_z is reached, then the magnetization will be in the basin of attraction of the reversed state $\mathbf{m} = \mathbf{e}_z$, and the switching will be achieved. Thus, the minimal pulse duration τ can be found by substituting $\mathrm{m}_z = 0$ in Eq. (5.17). We derive the following expression for τ:

$$\tau = \frac{1}{\alpha} \left[\frac{\ln(1+\cos\theta_0)}{2(\mathrm{h}_{az} + h_{\text{crit}})} - \frac{\ln(1-\cos\theta_0)}{2(\mathrm{h}_{az} - h_{\text{crit}})} - \frac{h_{\text{crit}}}{\mathrm{h}_{az}^2 - h_{\text{crit}}^2} \ln \frac{\mathrm{h}_{az}}{\mathrm{h}_{az} - h_{\text{crit}} \cos\theta_0} \right], \quad (5.18)$$

where:

$$h_{\text{crit}} = \kappa_{\text{eff}}, \quad (5.19)$$

$$\mathrm{m}_{z0} = -\cos\theta_0, \quad (5.20)$$

i.e., θ_0 is the angle formed by the initial magnetization with the negative z axis.

It is interesting to point out that for the typical case of small angle θ_0, the minimal pulse time τ is very close to the actual switching time at which m_z reaches a value almost equal to 1. This is because for sufficiently small m_z (large angles θ), m_z increases much faster (see Eq. (5.11)) than when m_z is close to equilibrium values. The last observation is supported by the calculations performed by using the analytical formula (5.17) and shown in Fig. 5.2. It is clear from this figure that the initial dynamics of m_z near equilibrium is very slow and takes most of the time, while magnetization dynamics away from equilibrium is significantly faster. Thus, the switching time is close to the minimal pulse time τ calculated above.

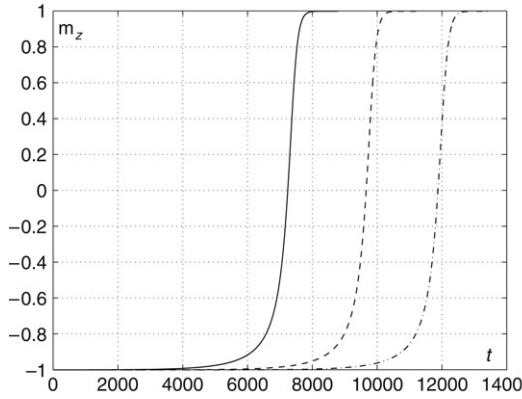

FIGURE 5.2 Evolution of m_z with time calculated from Eq. (5.17), with $m_{z0} = -\cos\theta_0$. Continuous line: $\theta_0 = 1^\circ$; dashed line: $\theta_0 = 0.3^\circ$; dash-dotted line: $\theta_0 = 0.1^\circ$. Parameter values: $\alpha = 0.01$, $\kappa_{\text{eff}} = 0.25$, $h_{az} = 1.2\kappa_{\text{eff}}$. Time is in units of $(\gamma M_s)^{-1}$.

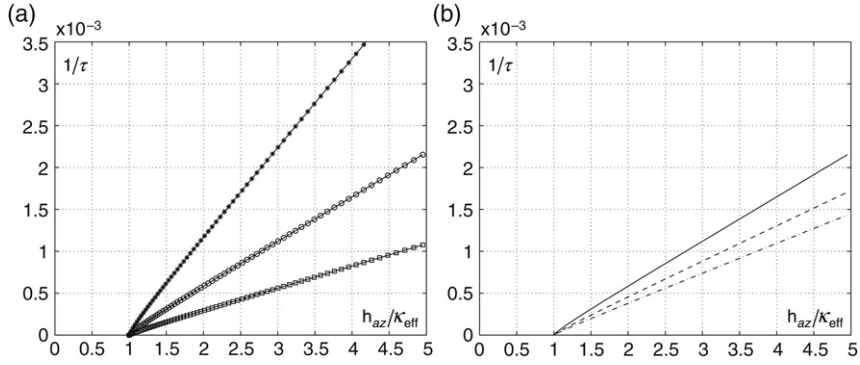

FIGURE 5.3 Inverse of minimum pulse duration $1/\tau$ versus ratio between applied field and critical switching field $h_{\text{crit}} = \kappa_{\text{eff}}$, calculated from Eq. (5.18) for damping switching. (a) $\theta_0 = 1^\circ$; □: $\kappa_{\text{eff}} = 0.125$; ○: $\kappa_{\text{eff}} = 0.25$; ∗: $\kappa_{\text{eff}} = 0.5$. (b) $\kappa_{\text{eff}} = 0.25$; continuous line: $\theta_0 = 1^\circ$; dashed line: $\theta_0 = 0.3^\circ$; dash-dotted line: $\theta_0 = 0.1^\circ$. Damping constant is $\alpha = 0.01$. Duration τ is measured in units of $(\gamma M_s)^{-1}$.

Figure 5.3 presents the dependence of $1/\tau$ on the applied field calculated by using Eq. (5.18). This dependence is almost linear, except for field values very close to the critical field h_{crit}. Indeed, for small values

of the initial angle θ_0, the second term in the right-hand side of Eq. (5.18) is dominant. By neglecting the two other terms and by using standard trigonometric formulas, one arrives at the following expression:

$$\frac{1}{\tau} \simeq -\alpha \ln(\theta_0/\sqrt{2})\,(h_{az} - h_{\text{crit}})\,. \tag{5.21}$$

According to the last formula, in the limit of short pulse durations the value of the applied field needed for switching is inversely proportional to the pulse duration τ. For this reason, one may say that dynamic (short time) coercivity appreciably exceeds the static coercivity h_{crit}. This fact has been observed in numerous experiments [669,229,564], from which the following expression has been deduced:

$$\frac{1}{\tau} = \frac{1}{S}(\mathrm{h}_{az} - h_{\text{crit}}). \tag{5.22}$$

Expressions (5.21) and (5.22) become identical if:

$$S = -\frac{1}{\alpha \ln(\theta_0/\sqrt{2})}. \tag{5.23}$$

Up to this point, our discussion has been concerned with the slow-time-scale dynamics of $\mathrm{m}_z(t)$. Next, we shall discuss the fast-time-scale dynamics of $\mathrm{m}_x(t)$ and $\mathrm{m}_y(t)$. This dynamics can be analyzed by using cylindrical coordinates:

$$\phi(t) = \arctan \frac{\mathrm{m}_y(t)}{\mathrm{m}_x(t)}, \tag{5.24}$$

$$\rho(t) = \sqrt{\mathrm{m}_x^2(t) + \mathrm{m}_y^2(t)}, \tag{5.25}$$

and by deriving the differential equation for $\phi(t)$ in terms of $\mathrm{m}_z(t)$. To this end, we shall first differentiate Eq. (5.24):

$$\frac{\mathrm{d}\phi}{\mathrm{d}t} = \frac{1}{\mathrm{m}_x^2 + \mathrm{m}_y^2}\left(\mathrm{m}_x \frac{\mathrm{d}\mathrm{m}_y}{\mathrm{d}t} - \mathrm{m}_y \frac{\mathrm{d}\mathrm{m}_x}{\mathrm{d}t}\right). \tag{5.26}$$

By using Eq. (5.1), it can be shown that:

$$\frac{\mathrm{d}\mathrm{m}_x}{\mathrm{d}t} = -\mathrm{m}_y h_{\text{eff}} - \alpha \mathrm{m}_x \mathrm{m}_z h_{\text{eff}}, \tag{5.27}$$

$$\frac{\mathrm{d}\mathrm{m}_y}{\mathrm{d}t} = \mathrm{m}_x h_{\mathrm{eff}} - \alpha \mathrm{m}_y \mathrm{m}_z h_{\mathrm{eff}}, \tag{5.28}$$

where:

$$h_{\mathrm{eff}} = \mathrm{h}_{az} + \kappa_{\mathrm{eff}} \mathrm{m}_z. \tag{5.29}$$

By substituting Eqs (5.27) and (5.28) into Eq. (5.26), we obtain:

$$\frac{\mathrm{d}\phi}{\mathrm{d}t} = h_{\mathrm{eff}}. \tag{5.30}$$

By using Eqs (5.11) and (5.29), we arrive at the following equation:

$$\frac{\mathrm{d}\phi}{\mathrm{d}t} = \frac{1}{\alpha(1-\mathrm{m}_z^2)} \frac{\mathrm{d}\mathrm{m}_z}{\mathrm{d}t}. \tag{5.31}$$

The fact that the small damping constant α appears in the denominator of the right-hand side of Eq. (5.31) reveals that magnetization precession takes place on the fast time scale. By performing the integration in Eq. (5.31), we derive:

$$\phi(t) = \frac{1}{2\alpha} \ln \frac{1+\mathrm{m}_z(t)}{1-\mathrm{m}_z(t)} + 2C, \tag{5.32}$$

where:

$$C = \frac{\phi_0}{2} - \frac{1}{4\alpha} \ln \frac{1+\mathrm{m}_{z0}}{1-\mathrm{m}_{z0}}, \tag{5.33}$$

$$\phi_0 = \arctan \frac{\mathrm{m}_{y0}}{\mathrm{m}_{x0}}. \tag{5.34}$$

By inverting Eq. (5.32), we can express m_z in terms of ϕ. Then, by using Eq. (5.25), ρ can also be expressed in terms of ϕ. In this way, we arrive at the following cylindrical coordinate equations for the trajectory of damping switching:

$$\mathrm{m}_z(t) = \tanh(\alpha\phi(t) - C), \tag{5.35}$$

$$\rho(t) = \mathrm{sech}(\alpha\phi(t) - C). \tag{5.36}$$

It is remarkable that the applied magnetic field h_{az} does not appear in these equations. This means that the magnetization trajectory of damping

switching is independent of the applied magnetic field. The shape of the trajectory is determined only by the damping constant α and by the initial orientation of the magnetization. For different applied magnetic fields, the same trajectory will be traversed with different speeds. In other words, the applied magnetic field determines the time parametrization of the universal damping-switching trajectory. The number N of precessional cycles during the switching time τ can be evaluated by using Eqs (5.32) and (5.33), and by taking into account that $\mathrm{m}_z(\tau) = 0$ according to the definition of τ. The final formula is as follows:

$$N = \left[\frac{\phi(\tau) - \phi_0}{2\pi}\right]_{\text{int}} = \left[\frac{1}{4\pi\alpha} \ln \frac{1 + \mathrm{m}_{z0}}{1 - \mathrm{m}_{z0}}\right]_{\text{int}}, \tag{5.37}$$

where $[\lambda]_{\text{int}}$ stands for the integer part of λ.

Finally, it is worthwhile pointing out that the exact differential equation for the time evolution of the system free energy g_L can be derived in the case of the damping switching of uniaxial media. The starting point of this derivation is the equation:

$$\frac{\mathrm{d}g_L}{\mathrm{d}t} = \frac{\partial g_L}{\partial \mathbf{m}} \cdot \frac{\mathrm{d}\mathbf{m}}{\mathrm{d}t} = -\mathbf{h}_{\text{eff}} \cdot \frac{\mathrm{d}\mathbf{m}}{\mathrm{d}t}. \tag{5.38}$$

By using Eqs (5.7) and (5.11), we obtain:

$$\frac{\mathrm{d}g_L}{\mathrm{d}t} = -\alpha(\mathrm{h}_{az} + \kappa_{\text{eff}}\mathrm{m}_z)^2(1 - \mathrm{m}_z^2). \tag{5.39}$$

Equation (5.7) can be treated as a quadratic equation with respect to m_z, which, once account is taken of the fact that $\mathrm{h}_{az} > \kappa_{\text{eff}}$, leads to:

$$\mathrm{m}_z = \frac{-\mathrm{h}_{az} + \mathrm{sign}(g_L)\sqrt{\mathrm{h}_{az}^2 - 2\kappa_{\text{eff}} g_L}}{\kappa_{\text{eff}}}. \tag{5.40}$$

By substituting Eq. (5.40) into Eq. (5.39), we obtain the differential equation for the free energy:

$$\frac{\mathrm{d}g_L}{\mathrm{d}t} = -\alpha f(g_L, \mathrm{h}_{az}, \kappa_{\text{eff}}), \tag{5.41}$$

where the expression for $f(g_L, \mathrm{h}_{az}, \kappa_{\text{eff}})$ is as follows:

$$f(g_L, \mathrm{h}_{az}, \kappa_{\text{eff}}) = (\mathrm{h}_{az}^2 - 2\kappa_{\text{eff}} g_L) \times \left[1 - \frac{\left(-\mathrm{h}_{az} + \text{sign}(g_L)\sqrt{\mathrm{h}_{az}^2 - 2\kappa_{\text{eff}} g_L} \right)^2}{\kappa_{\text{eff}}^2} \right]. \tag{5.42}$$

This idea of using the differential equation for the free energy to study the slow time scale of magnetization dynamics will be extensively used in this chapter and throughout this book.

5.2 TWO-TIME-SCALE FORMULATION OF LLG DYNAMICS AND AVERAGING TECHNIQUE

It has been demonstrated in the previous section that fast and slow time scales of magnetization dynamics can be separated and mathematically decoupled in the problem of damping switching of uniaxial media. This has been achieved due to the unique symmetry properties of that problem. In the general case, the slow-time-scale magnetization dynamics is concealed and obscured by the "magnetization form" of LL and LLG equations, because all three magnetization components usually vary on the fast time scale. This is rather unsatisfactory because the slow-time-scale dynamics reveals the actual rate of relaxation to equilibrium. It is clear on physical grounds that the magnetic free energy g_L varies on the slow time scale. In other words, the magnetic free energy is a "slow" variable whose time evolution is not essentially affected by the fast precessional dynamics. For this reason, it is desirable to derive dynamic equations containing the magnetic free energy as one of the state variables. These equations will represent the two-time-scale formulation of magnetization dynamics.

To start the derivation, consider a thin uniformly magnetized film subject to a spatially uniform magnetic field, held constant in time. The magnetization dynamics is described by the LL equation (5.1), where the magnetic free energy and the effective magnetic field are given by Eqs (3.15) and (3.16), namely:

$$\mathbf{h}_{\text{eff}} = -D_x \mathrm{m}_x \mathbf{e}_x - D_y \mathrm{m}_y \mathbf{e}_y - D_z \mathrm{m}_z \mathbf{e}_z + \mathbf{h}_a, \tag{5.43}$$

$$g_L(\mathbf{m}; \mathbf{h}_a) = \frac{1}{2} D_x \mathrm{m}_x^2 + \frac{1}{2} D_y \mathrm{m}_y^2 + \frac{1}{2} D_z \mathrm{m}_z^2 - \mathbf{h}_a \cdot \mathbf{m}. \tag{5.44}$$

Here, as before, D_x, D_y, and D_z are the anisotropy constants along the principal directions, while $\mathbf{h}_a$ is the applied magnetic field, expressed in units of M_s.

In the presence of the applied field, at least one of its components must be nonzero. Let us designate h_{ay} as this component. Furthermore, we shall recall that the magnetization magnitude is conserved. Thus:

$$\mathrm{m}_x^2 + \mathrm{m}_y^2 + \mathrm{m}_z^2 = 1. \tag{5.45}$$

By using formulas (5.44) and (5.45), the following expression for m_y can be derived:

$$\begin{aligned}\mathrm{m}_y = {} & \frac{D_x - D_y}{2\mathrm{h}_{ay}}\mathrm{m}_x^2 + \frac{D_z - D_y}{2\mathrm{h}_{ay}}\mathrm{m}_z^2 \\ & - \frac{\mathrm{h}_{ax}}{\mathrm{h}_{ay}}\mathrm{m}_x - \frac{\mathrm{h}_{az}}{\mathrm{h}_{ay}}\mathrm{m}_z - \frac{g_L}{\mathrm{h}_{ay}} + \frac{D_y}{2\mathrm{h}_{ay}}.\end{aligned} \tag{5.46}$$

This expression suggests using m_x, m_z, and g_L as the state variables for the description of magnetization dynamics. This dynamics occurs not on the surface of the unit sphere (Eq. (5.45)), but rather on the manifold described by the following equation:

$$\begin{aligned}\left(\frac{D_x - D_y}{2\mathrm{h}_{ay}}\mathrm{m}_x^2 + \frac{D_z - D_y}{2\mathrm{h}_{ay}}\mathrm{m}_z^2 - \frac{\mathrm{h}_{ax}}{\mathrm{h}_{ay}}\mathrm{m}_x - \frac{\mathrm{h}_{az}}{\mathrm{h}_{ay}}\mathrm{m}_z - \frac{g_L}{\mathrm{h}_{ay}} + \frac{D_y}{2\mathrm{h}_{ay}}\right)^2 \\ + \mathrm{m}_x^2 + \mathrm{m}_z^2 = 1,\end{aligned} \tag{5.47}$$

which is obtained by substituting Eq. (5.46) into Eq. (5.45). Next, we shall derive the equations for the magnetization dynamics in terms of the variables m_x, m_z, and g_L. The first step in this direction is to consider the balance equation (3.30) for g_L:

$$\frac{\mathrm{d}g_L}{\mathrm{d}t} = -\alpha \left|\mathbf{m} \times \mathbf{h}_{\mathrm{eff}}\right|^2. \tag{5.48}$$

Now, we shall combine the LL dynamic equations for m_x and m_z from Eq. (5.1) with the dynamic equation (5.48) for the energy g_L and express the right-hand sides of these equations in terms of m_x, m_z, and g_L:

$$\frac{\mathrm{d}\mathrm{m}_x}{\mathrm{d}t} = -Q_0\left(\mathrm{m}_x, \mathrm{m}_z, g_L\right) - \alpha Q_1\left(\mathrm{m}_x, \mathrm{m}_z, g_L\right), \tag{5.49}$$

$$\frac{\mathrm{d}\mathrm{m}_z}{\mathrm{d}t} = -P_0\left(\mathrm{m}_x, \mathrm{m}_z, g_L\right) - \alpha P_1\left(\mathrm{m}_x, \mathrm{m}_z, g_L\right), \tag{5.50}$$

$$\frac{\mathrm{d}g_L}{\mathrm{d}t} = -\alpha R\left(\mathrm{m}_x, \mathrm{m}_z, g_L\right). \tag{5.51}$$

The expressions for Q_0, P_0, and R are as follows:

$$Q_0\left(\mathrm{m}_x, \mathrm{m}_z, g_L\right) = -\mathrm{h}_{ay}\mathrm{m}_z - \left[\left(D_z - D_y\right)\mathrm{m}_z - \mathrm{h}_{az}\right]\mathrm{m}_y, \tag{5.52}$$

$$P_0\left(\mathrm{m}_x, \mathrm{m}_z, g_L\right) = \mathrm{h}_{ay}\mathrm{m}_x + \left[\left(D_x - D_y\right)\mathrm{m}_x - \mathrm{h}_{ax}\right]\mathrm{m}_y, \tag{5.53}$$

$$R\left(\mathrm{m}_x, \mathrm{m}_z, g_L\right) = \left|\mathbf{m} \times \mathbf{h}_{\text{eff}}\right|^2. \tag{5.54}$$

The above functions are polynomial functions of m_x, m_z, and g_L under the condition that Eq. (5.46) is substituted for m_y.

Polynomial functions for Q_1 and P_1 can be explicitly written as follows:

$$\begin{aligned} Q_1\left(\mathrm{m}_x, \mathrm{m}_z, g_L\right) = &-\mathrm{h}_{ax} + \left(D_x - \frac{D_y}{2}\right)\mathrm{m}_x \\ &- \frac{D_x - D_y}{2}\mathrm{m}_x^3 - \frac{D_z - D_y}{2}\mathrm{m}_x\mathrm{m}_z^2 - \mathrm{m}_x g_L, \end{aligned} \tag{5.55}$$

$$\begin{aligned} P_1\left(\mathrm{m}_x, \mathrm{m}_z, g_L\right) = &-\mathrm{h}_{ax} + \left(D_z - \frac{D_y}{2}\right)\mathrm{m}_z \\ &- \frac{D_z - D_y}{2}\mathrm{m}_z^3 - \frac{D_x - D_y}{2}\mathrm{m}_z\mathrm{m}_x^2 - \mathrm{m}_z g_L. \end{aligned} \tag{5.56}$$

Equations (5.49)–(5.51) represent the two-time-scale formulation of magnetization dynamics in terms of the fast variables m_x and m_z and of the slow variable g_L. This formulation is mathematically equivalent to the LL dynamics described by Eq. (5.1). One of the immediate applications of this two-time-scale formulation is the development of the perturbation technique with respect to the small damping parameter α. In this perturbation approach, it is assumed that $\alpha \ll 1$, and the following perturbation expansions are used:

$$\mathbf{m}(t) = \mathbf{m}_0(t) + \alpha\mathbf{m}_1(t) + \ldots, \tag{5.57}$$

$$g_L(t) = g_0(t) + \alpha g_1(t) + \ldots. \tag{5.58}$$

By substituting Eqs (5.57) and (5.58) into Eqs (5.49)–(5.51) and by equating the terms of zero order with respect to α, we obtain:

$$\frac{\mathrm{d}g_0}{\mathrm{d}t} = 0, \qquad g_0(t) = \text{const}, \tag{5.59}$$

$$\frac{\mathrm{d}\mathbf{m}_0}{\mathrm{d}t} = -\mathbf{m}_0(t) \times \mathbf{h}_{\text{eff}}\left(\mathbf{m}_0(t)\right). \tag{5.60}$$

In the derivation of the last equation, the equivalence of Eqs (5.49)–(5.51) and Eq. (5.1) has been used. Equation (5.60) describes the conservative magnetization dynamics that has been extensively studied in the previous chapter. The results from that chapter can be used for the computation of $\mathbf{m}_0(t)$.

By substituting the expansions (5.57) and (5.58) into Eq. (5.51) and by equating the terms of first order with respect to α, we obtain:

$$\frac{\mathrm{d}g_1}{\mathrm{d}t} = -\left|\mathbf{m}_0(t) \times \mathbf{h}_{\text{eff}}\left(\mathbf{m}_0(t)\right)\right|^2. \tag{5.61}$$

Hence:

$$g_L(t) = g_0 - \alpha \int_0^t \left|\mathbf{m}_0(t') \times \mathbf{h}_{\text{eff}}\left(\mathbf{m}_0(t')\right)\right|^2 \mathrm{d}t'. \tag{5.62}$$

Thus, by using the zero order (i.e., conservative) approximation for the fast variables, we can derive the explicit expression (5.62) for the first-order approximation for the slow variable g_L.

The two-time-scale formulation (5.49)–(5.51) of magnetization dynamics has two substantial shortcomings. On the one hand, while the approximation (5.62) is quite accurate for short times, its accuracy deteriorates for longer times. On the other hand, the slow-time-scale magnetization dynamics described by Eq. (5.51) is mathematically coupled with the fast-time-scale dynamics described by Eqs (5.49)–(5.50), which prevents one from obtaining separate information about the slow-time-scale dynamics. However, there exists a powerful (albeit approximate) method to decouple the slow-time-scale dynamics from the fast one. This method is the so-called averaging technique, which we shall discuss next.

The starting point for the exposition of the averaging technique is the equation:

$$\frac{\mathrm{d}g_L}{\mathrm{d}t} = -\alpha \left|\frac{\mathrm{d}\mathbf{m}}{\mathrm{d}t}\right|^2, \tag{5.63}$$

derived in Chapter 3 for the case of a uniformly magnetized ferromagnet subject to a constant-in-time applied magnetic field. The development of the averaging technique is based on the following reasoning. For small α, the magnetization dynamics during one precession cycle closely mimics

the undamped conservative dynamics. Thus, it can be assumed with high accuracy that during one precession cycle the energy is constant and therefore:

$$\mathbf{m}(t) \simeq \mathbf{m}_c(t; g), \tag{5.64}$$

where $\mathbf{m}_c(t; g)$ represents the conservative trajectory with energy g in some central energy region. By substituting Eq. (5.64) into Eq. (5.63) and by averaging the resulting equation over one period of the precessional conservative dynamics, we obtain:

$$\frac{\mathrm{d}\bar{g}}{\mathrm{d}t} = -\frac{\alpha}{T(\bar{g})} \int_0^{T(\bar{g})} \left| \frac{\mathrm{d}\mathbf{m}_c(t; \bar{g})}{\mathrm{d}t} \right|^2 \mathrm{d}t, \tag{5.65}$$

where $\bar{g}$ stands for the value of the free energy averaged over one precession period, $T(\bar{g})$ is the period of the precessional dynamics along the trajectory corresponding to the free energy value $\bar{g}$ and $\mathbf{m}_c(t; \bar{g})$ is the magnetization for the conservative motion along the previously mentioned trajectory. Equation (5.65) can be written in the form:

$$\frac{\mathrm{d}\bar{g}}{\mathrm{d}t} = -\alpha f(\bar{g}), \tag{5.66}$$

where:

$$f(\bar{g}) = \frac{1}{T(\bar{g})} \int_0^{T(\bar{g})} \left| \frac{\mathrm{d}\mathbf{m}_c(t; \bar{g})}{\mathrm{d}t} \right|^2 \mathrm{d}t \tag{5.67}$$

is some function of $\bar{g}$ which can be computed from the analysis of conservative precessional dynamics carried out in Chapter 4. Equation (5.66) can be integrated by using the separation of variables:

$$\mathcal{F}(\bar{g}) - \mathcal{F}(\bar{g}_0) = \int_{\bar{g}_0}^{\bar{g}} \frac{\mathrm{d}\bar{g}'}{f(\bar{g}')} = -\alpha(t - t_0). \tag{5.68}$$

It is worthwhile pointing out the distinction between Eqs (5.51) and (5.66). In Eq. (5.51) the time dynamics of energy depends on the details of the fast-time-scale dynamics of magnetization, while this fast-time-scale dynamics does not appear in Eq. (5.66) because it has been eliminated through the averaging process. In this sense, in Eq. (5.66) the slow-time-scale dynamics of energy is completely decoupled from the fast-time-scale

dynamics of the magnetization components. After the slow dynamics of the free energy is found through the solution of Eq. (5.66), Eq. (5.47) can be used to find the expression for m_z in terms of m_x and $\bar{g}(t)$. This expression for m_z can then be substituted into Eq. (5.49) to arrive at the differential equation for $\mathrm{m}_x(t)$ only. By solving the latter equation, the fast-time-scale dynamics of magnetization components can be fully recovered.

In the case of the damping switching of uniaxial media previously discussed, an equation identical in form to Eq. (5.66), i.e., Eq. (5.41) holds for the energy. This equation was derived without resorting to any averaging, by taking advantage of the rotational invariance in the problem. Thus, in uniaxial systems the decoupling of the slow-time-scale relaxation of the system free energy from the fast-time-scale dynamics of the magnetization is an inherent property of the dynamics which is always valid and requires no approximations. In particular, it does not require any assumption concerning the smallness of the damping constant α. This suggests that the averaging technique may be accurate even in cases when α is not particularly small.

The averaging technique reveals a direct connection between the slow-time-scale dynamics of the energy and the phase portrait of the undamped precessional dynamics, discussed in Chapter 4. In particular, there exists one function $f(\bar{g})$ (see Eq. (5.67)) for each central energy region of the phase portrait. This means that the time evolution of the energy occurs on the graph introduced in Chapter 4, whose edges and nodes represent central energy regions and separatrices, respectively [103]. This graph representation of the energy dynamics will prove particularly useful in the investigation of stochastic magnetization dynamics in Chapter 10.

5.3 MAGNETIZATION RELAXATION UNDER ZERO APPLIED MAGNETIC FIELD

In this section, we shall apply the averaging technique to the analysis of magnetization relaxation to equilibrium when no external magnetic field is applied. Such relaxations are usually termed "ringing" phenomena. They typically occur during the final stages of magnetization precessional switching (see Chapter 6), after the external magnetic field has been switched off [38,39,587,377]. During ringing, the magnetization is in the energy well around the desired equilibrium state and it relaxes to this state (see Fig. 6.8).

To be specific, consider a thin, uniformly magnetized film characterized by anisotropy constants D_x, D_y, and D_z, with $D_x < D_y < D_z$ (i.e., the x axis is the easy axis). We assume that the value g_0 of the magnetic

free energy immediately after the switching-off of the external magnetic field is known. This value will be used as the initial condition for the differential equation (5.66):

$$\bar{g}(0) = g_0. \tag{5.69}$$

To utilize Eq. (5.66), we have to find the expression for $f(\bar{g})$ in terms of $\bar{g}$. This can be accomplished by using Eq. (5.67) and taking into account that $\mathbf{m}_c(t;\bar{g})$ in this formula corresponds to the precessional dynamics under zero applied field. This dynamics has been extensively discussed in Chapter 4.

To start the derivation of the expression for $f(\bar{g})$, we shall first use the formula:

$$\left|\frac{\mathrm{d}\mathbf{m}_c(t;\bar{g})}{\mathrm{d}t}\right|^2 = \left|\frac{\mathrm{d}\mathbf{m}_c(t;\bar{g})}{\mathrm{d}w}\right|^2 \left|\frac{\mathrm{d}w}{\mathrm{d}t}\right|^2, \tag{5.70}$$

where the variable w is related to the components of $\mathbf{m}_c(t;\bar{g})$ through Eq. (4.20), namely:

$$\mathrm{m}_x = \mp p\sqrt{1-w^2}, \qquad \mathrm{m}_y = \frac{p}{k}w, \qquad \mathrm{m}_z = \pm\frac{k'p}{k}\sqrt{w_0^2 - w^2}, \tag{5.71}$$

where:

$$p^2 = \frac{D_z - 2\bar{g}}{D_z - D_x}, \qquad w_0 = \frac{k}{k'p}\sqrt{1-p^2}, \qquad k'^2 = 1 - k^2. \tag{5.72}$$

By using Eqs (5.70) and (5.71), one finds:

$$\left|\frac{\mathrm{d}\mathbf{m}_c(t;\bar{g})}{\mathrm{d}w}\right|^2 = \frac{p^2}{1-w^2} + \frac{k'^2}{k^2}\frac{w_0^2 p^2}{w_0^2 - w^2}. \tag{5.73}$$

On the other hand, one has (see Eqs (4.23)–(4.25) from Chapter 4):

$$\frac{\mathrm{d}w}{\mathrm{d}t} = k'p\,(D_z - D_x)\sqrt{(1-w^2)\,(w_0^2 - w^2)}. \tag{5.74}$$

By substituting Eqs (5.73) and (5.74) into Eq. (5.70), after simple transformations we obtain:

$$\left|\frac{\mathrm{d}\mathbf{m}_c(t;\bar{g})}{\mathrm{d}t}\right|^2 \mathrm{d}t = k' p^3 w_0 \left(D_z - D_x\right) \left(\sqrt{\frac{1-w^2/w_0^2}{1-w^2}} + \frac{k'^2}{k^2}\sqrt{\frac{1-w^2}{1-w^2/w_0^2}}\right) \mathrm{d}w. \quad (5.75)$$

By inserting this expression into Eq. (5.67), one obtains an integral which can be reduced to canonical elliptic integrals of the first and second kind. Moreover, the variable of integration w spans four times the interval of integration $(0, w_0)$ during one precession period. By taking this fact into account as well as Eq. (4.43) for $T(\bar{g})$, the following differential equation is derived for $\bar{g}$:

$$\frac{\mathrm{d}\bar{g}}{\mathrm{d}t} = -\alpha\left(D_z - 2\bar{g}\right)\left[2\bar{g} + \left(D_y - D_x\right)\frac{\boldsymbol{E}(k_L(\bar{g}))}{\boldsymbol{K}(k_L(\bar{g}))} - D_y\right], \quad (5.76)$$

where $\boldsymbol{K}$ and $\boldsymbol{E}$ represent the complete elliptic integrals of the first and second kind, respectively, while:

$$k_L^2 = w_0^2 = \frac{D_z - D_y}{D_y - D_x}\frac{2\bar{g} - D_x}{D_z - 2\bar{g}}. \quad (5.77)$$

Equation (5.76) is a first-order differential equation that can be integrated by the method of separation of variables. Explicit analytical solutions to Eq. (5.76) can be obtained when the magnetization is sufficiently close to the equilibrium state, that is, when:

$$\bar{g} \simeq \frac{D_x}{2}. \quad (5.78)$$

Under such condition, according to Eq. (5.77), we have that $k_L^2 \ll 1$, so the following asymptotic approximations can be used for the elliptic integrals $\boldsymbol{K}$ and $\boldsymbol{E}$:

$$\boldsymbol{K}(k_L) \simeq \frac{\pi}{2}\left(1 + \frac{k_L^2}{4}\right), \quad (5.79)$$

$$\boldsymbol{E}(k_L) \simeq \frac{\pi}{2}\left(1 - \frac{k_L^2}{4}\right). \quad (5.80)$$

By substituting these asymptotic expansions into Eq. (5.76), we derive the following differential equation for $\bar{g}$:

$$\frac{\mathrm{d}\bar{g}}{\mathrm{d}t} = -\alpha\left(2\bar{g} - D_x\right)\left(D_{yz} - 2\bar{g}\right), \tag{5.81}$$

where:

$$D_{yz} = \frac{D_y + D_z}{2}. \tag{5.82}$$

Equation (5.81) can be integrated by the method of separation of variables. The final result is:

$$\bar{g}(t) = \frac{D_x}{2} + \frac{\left(D_{yz} - D_x\right)\left(g_0 - D_x/2\right)}{\left(2g_0 - D_x\right) + \left(D_{yz} - 2g_0\right)\exp\left[2\alpha\left(D_{yz} - D_x\right)t\right]}. \tag{5.83}$$

The accuracy of the averaging technique has been tested by first numerically integrating the LLG equation for a thin magnetic film with anisotropy constants: $D_x = -0.05$, $D_y = 0$, $D_z = 1$, and initial energy $g_0 = -0.005$. The results of the numerical integration are shown in Figs 5.4 and 5.5. By using the results of the numerical integration in the expression for the energy (see Eq. (5.44)):

$$g_L(t) = -0.025\mathrm{m}_x^2(t) + 0.5\mathrm{m}_z^2(t), \tag{5.84}$$

the time evolution of the energy $g_L(t)$ was computed. The result is shown by the continuous line in Fig. 5.5. The dashed line on the same figure represents the time variation of the energy $\bar{g}(t)$ computed through integration of Eq. (5.76). Finally, the dotted line represents the time evolution of $\bar{g}(t)$ computed by using the analytical expression (5.83). It is clear from the figure that the averaging technique leads to quite accurate results. The approximate analytical formula (5.83) is also quite satisfactory, especially if one takes into account that the initial state is far from equilibrium and corresponds to $k_L \simeq 0.89$.

5.4 MAGNETIZATION RELAXATION UNDER APPLIED MAGNETIC FIELDS

In this section, we shall apply the averaging technique to the analysis of magnetization relaxation to equilibrium caused by applied magnetic

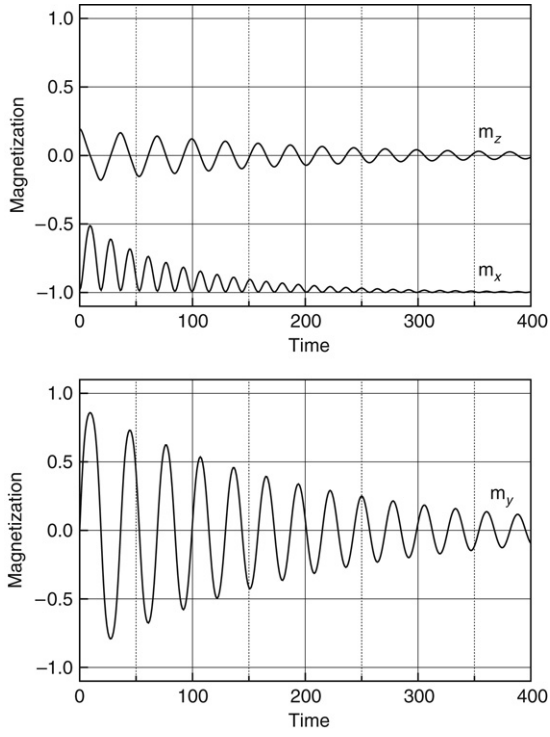

FIGURE 5.4 Magnetization components versus time obtained by numerical integration of LLG equation. Parameters: $\alpha = 0.01$, $D_x = -0.05$, $D_y = 0$, $D_z = 1$, $g_0 = -0.005$. Time is measured in units of $(\gamma \mathrm{M}_s)^{-1}$.

fields. As before, we consider the case of uniformly magnetized thin-film media characterized by anisotropy constants D_x, D_y, D_z, with $D_x < D_y < D_z$. To be specific, it will be assumed that the medium is initially magnetized along the $-\mathbf{e}_x$ direction and that a rectangular pulse of magnetic field is applied opposite to the magnetization, that is in the $\mathbf{e}_x$ direction, with the purpose of switching the magnetization to the $\mathbf{m} = \mathbf{e}_x$ equilibrium state. This is actually the problem of damping switching of longitudinal media, and it is of technological interest in longitudinal recording. For switching to be initiated, the equilibrium state corresponding to the initial condition $\mathbf{m} = -\mathbf{e}_x$ must become unstable as a result of the action of the applied field. According to the analysis presented in Chapter 3, this will occur if the applied field exceeds the value $D_y - D_x$. In this sense, the following expression for the critical field

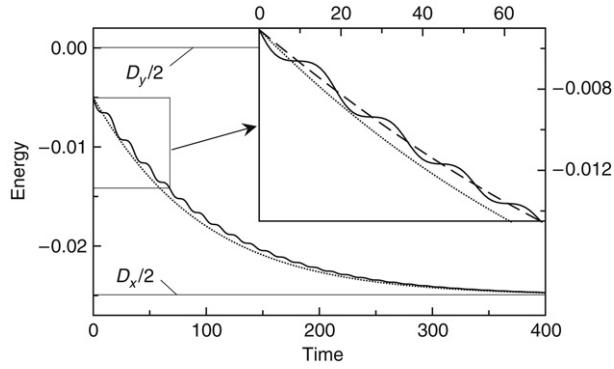

FIGURE 5.5 Comparison between numerically and analytically computed energy relaxation to equilibrium. Continuous line: numerical integration of LLG equation; dashed line (omitted in the main diagram for the sake of clarity but shown in the inset): numerical integration of Eq. (5.76); dotted line: Eq. (5.83). Parameters: $\alpha = 0.01$, $D_x = -0.05$, $D_y = 0$, $D_z = 1$, $g_0 = -0.005$. Time is measured in units of $(\gamma \mathrm{M}_s)^{-1}$.

h_{crit} of damping switching of longitudinal media is valid:

$$h_{\mathrm{crit}} = D_y - D_x. \tag{5.85}$$

In the sequel, we consider the case when the applied field h_{ax} satisfies the inequalities:

$$D_y - D_x < \mathrm{h}_{ax} < D_z - D_x. \tag{5.86}$$

As discussed in Chapter 4, there are four critical points under the condition (5.86). They are: the energy minimum $\mathrm{m}_x = 1$; the saddle point $\mathrm{m}_x = -1$; the two energy maxima $\mathrm{m}_x = a_x$, $\mathrm{m}_y = 0$, $\mathrm{m}_z = \pm\sqrt{1 - a_x^2}$, where $a_x = -\mathrm{h}_{ax}/(D_z - D_x)$ (see Eq. (4.7)). This situation is illustrated by the unit-disk representation (see Chapter 4 for the meaning of this representation) shown in Fig. 5.6. In this figure, the gray region L represents the magnetization states with energy below the energy of the saddle point. Magnetization relaxation towards the minimum energy state $\mathrm{m}_x = 1$ proceeds through this gray region L. Thermal perturbations move the magnetization away from the saddle point and result in nonzero initial torque that drives thermal relaxation. Since magnetization states in region L have lower free energy than the energy of the saddle point state,

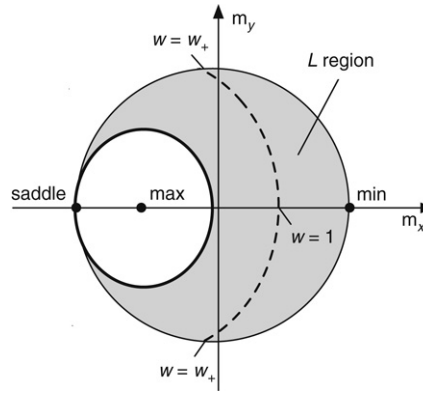

FIGURE 5.6 Unit-disk representation with indication of the critical points of the dynamics present when $\mathrm{h}_{ax} > D_y - D_x$ (min: energy minimum, max: energy maximum, saddle). Heavy line trajectory passing through the saddle divides phase space into energy regions containing the non-saddle fixed points. Grayed region: L region containing energy minimum. Broken line: example of trajectory belonging to L region with indication of corresponding interval of variation of w.

initially thermal perturbations most likely drive magnetization to one of the gray region states. This justifies the following condition for the initial free energy g_0:

$$g_0 < \frac{D_x}{2} + \mathrm{h}_{ax}. \tag{5.87}$$

Next, we shall use Eq. (5.66) to analyze the time evolution of $\bar{g}(t)$. The first and most important step in this direction is to find the expression for $f(\bar{g})$ by using Eq. (5.67). We recall that $\mathbf{m}_c(t;\bar{g})$ in this formula corresponds to the precessional dynamics under magnetic field applied along the easy axis. This dynamics has been extensively discussed in Chapter 4 and we shall use the basic formulas derived in that chapter in the expressions relevant to our considerations. It is shown in Chapter 4 that the unit-disk projection of a precessional trajectory of magnetization is an elliptical curve (see the dashed line in Fig. 5.6), described by the equation:

$$(\mathrm{m}_x - a_x)^2 + k^2 \mathrm{m}_y{}^2 = p^2, \tag{5.88}$$

where a_x is given by Eq. (4.7), while p and k are defined as follows:

$$p^2 = a_x^2 + \frac{D_z - 2\bar{g}}{D_z - D_x}, \qquad k^2 = \frac{D_z - D_y}{D_z - D_x}. \tag{5.89}$$

Equation (5.88) can be written in parametric form in terms of w as a parameter:

$$\mathrm{m}_x = a_x + pw, \tag{5.90}$$

$$\mathrm{m}_y = \pm\frac{p}{k}\sqrt{1 - w^2}, \tag{5.91}$$

$$\mathrm{m}_z = \pm\frac{k'p}{k}\sqrt{(w - w_+)(w - w_-)}, \tag{5.92}$$

where $k'^2 = 1 - k^2$, while:

$$w_+ = b + r, \qquad w_- = b - r, \tag{5.93}$$

$$b = \frac{k^2 a_x}{k'^2 p}, \qquad r^2 = \frac{1}{k'^2 p^2}\left[p^2 - k^2\left(1 - \frac{a_x^2}{k'^2}\right)\right]. \tag{5.94}$$

As shown in Chapter 4, the dynamic equation for $\mathbf{m}_c(t;\bar{g})$ can be written in parametric form as follows:

$$\frac{\mathrm{d}w}{\sqrt{(1 - w^2)(w - w_-)(w - w_+)}} = \pm k' p\,(D_z - D_x)\,\mathrm{d}t. \tag{5.95}$$

To evaluate $|\mathrm{d}\mathbf{m}_c(t;\bar{g})/\mathrm{d}t|^2$ in Eq. (5.67), we shall use Eq. (5.70) along with the parametric equations (5.90)–(5.92). This leads to the following result:

$$\begin{aligned}\left|\frac{\mathrm{d}\mathbf{m}_c(t;\bar{g})}{\mathrm{d}t}\right|^2 \mathrm{d}t = \frac{k'p^3}{k^2}\,(D_z - D_x) \\ \times\left[\sqrt{\frac{(w - w_-)(w - w_+)}{1 - w^2}}\right. \\ \left. + k'^2 r^2\sqrt{\frac{1 - w^2}{(w - w_-)(w - w_+)}}\right]\mathrm{d}w.\end{aligned} \tag{5.96}$$

By substituting the last expression into Eq. (5.67) and by taking into account that the variable of integration spans four times the interval

of integration $(w_+, 1)$ during one precessional period, the following expression is derived after lengthy but simple transformations:

$$\frac{\mathrm{d}\bar{g}}{\mathrm{d}t} = -\frac{4\alpha k' p^3}{T(\bar{g})k^2}\left(D_z - D_x\right)\left[I_1\left(w_-, w_+\right) + k'^2 r^2 I_2\left(w_-, w_+\right)\right], \quad (5.97)$$

where the following notations have been introduced:

$$I_1 = \int_{w_+}^{1} \sqrt{\frac{(w-w_-)(w-w_+)}{1-w^2}}\mathrm{d}w, \quad (5.98)$$

$$I_2 = \int_{w_+}^{1} \sqrt{\frac{1-w^2}{(w-w_-)(w-w_+)}}\mathrm{d}w. \quad (5.99)$$

We recall that $T(\bar{g})$ in Eq. (5.97) is the precessional period, which is completely described by the following relations:

$$T(\bar{g}) = \frac{4\boldsymbol{K}(k^*)}{\Omega^*}, \quad (5.100)$$

$$\Omega^* = k' p\left(D_z - D_x\right)\sqrt{1 - b^* q^*}, \quad (5.101)$$

$$k^{*2} = \frac{b^* q^{*-1} - b^* q^*}{1 - b^* q^*}, \quad (5.102)$$

$$q^* = \frac{1}{2b^*}\left[1 + w_1^* w_2^* - \sqrt{\left(1 - w_1^{*2}\right)\left(1 - w_2^{*2}\right)}\right], \quad (5.103)$$

$$b^* = \frac{2(r-1)}{1-b+r}, \qquad w_1^* = 1 - \frac{4}{1-w_-}, \qquad w_2^* = 1 - \frac{2(1-w_+)}{1-w_-}. \quad (5.104)$$

Equation (5.97) is a differential equation of the type (5.66), because the right-hand side of this equation depends on energy $\bar{g}$ and the applied field h_{ax} through the parameters p, $T(\bar{g})$, r^2, w_-, and w_+. This equation can be integrated to find the time evolution of $\bar{g}(t)$ during the relaxation to equilibrium. In the example presented in Fig. 5.7, $\bar{g}(t)$ was computed by using Eq. (5.97) with the initial condition $g_0 = D_x/2 + 0.98\mathrm{h}_{ax}$, that is, close to the saddle point.

It has been emphasized before that when $\alpha \ll 1$ the damped magnetization motion at time t is very close to the precessional motion corresponding to the energy $\bar{g}(t)$. For this reason, it can be expected that a fairly accurate description of damped magnetization dynamics can be

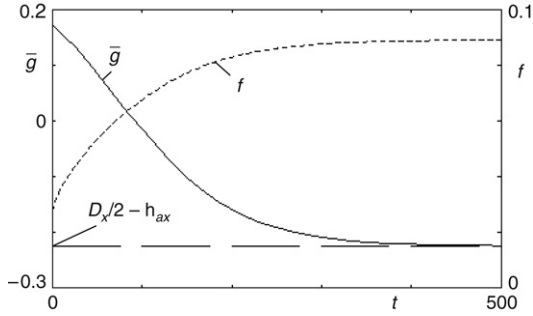

FIGURE 5.7 Time evolution of mean energy $\bar{g}$ obtained from Eq. (5.97) and corresponding evolution of precessional frequency $f = \Omega^*/4\boldsymbol{K}(k^*)$. Parameters: $D_x = -0.05$, $D_y = 0$, $D_z = 1$, $\alpha = 0.01$, $\mathrm{h}_{ax} = 4\,(D_y - D_x)$. Initial energy of the motion is $g_0 = (D_x/2 + \mathrm{h}_{ax}) - 0.02\mathrm{h}_{ax}$. Time is expressed in units of $(\gamma \mathrm{M}_s)^{-1}$, frequency in units of $\gamma \mathrm{M}_s$, energy density in units of $\mu_0 \mathrm{M}_s^2$.

obtained by substituting the solution of Eq. (5.97) into the solution of the precessional dynamics, that is (see Chapter 4):

$$\mathrm{m}_x \simeq a_x - (c-1)p + cp\frac{q^* + \mathrm{dn}^*}{1 + q^*\mathrm{dn}^*}, \tag{5.105}$$

$$\mathrm{m}_y \simeq -\frac{cp(1-q^*)}{k}\sqrt{\frac{(1+q^*)(\mathrm{dn}^* + k^{*\prime})}{(1-q^*k^{*\prime})(1+\mathrm{dn}^*)}}\frac{k^*\mathrm{sn}^*}{1+q^*\mathrm{dn}^*}, \tag{5.106}$$

where dn^* and sn^* denote the corresponding Jacobi elliptic functions of argument $(\Omega^* t, k^*)$, while:

$$c = \frac{1 - w_-}{2}, \qquad k^{*\prime 2} = 1 - k^{*2}. \tag{5.107}$$

Figure 5.8 presents the results of such calculations for the case where $\bar{g}(t)$ varies as shown in Fig. 5.7. It is evident from Fig. 5.8 that the fast-time-scale magnetization dynamics exhibits some nontrivial features. Namely, the amplitude of m_y does not decay monotonically with time. In addition, the nonlinear nature of the relaxation process manifests itself in a continuous change of the precessional frequency during the relaxation process. It is apparent that the fast-time-scale magnetization dynamics shown in Fig. 5.8 can be quite accurate for fairly small values of α, that is,

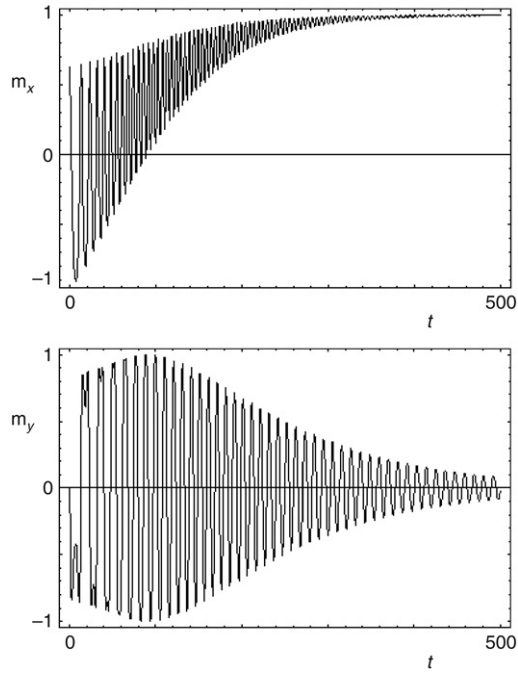

FIGURE 5.8 Time evolution of normalized magnetization components m_x and m_y calculated from Eqs (5.105) and (5.106), when the energy relaxes as shown in Fig. 5.7. Parameters and time normalization are the same as for Fig. 5.7.

when the magnetization undergoes many precessional oscillations before reaching equilibrium.

5.5 SELF-OSCILLATIONS AND POINCARÉ–MELNIKOV THEORY

A technique conceptually similar to the averaging technique can be used in the study of self-oscillations in magnetization dynamics. These oscillations may occur in the case of the generalized magnetization dynamics introduced in Section 3.3 for situations where other forces in addition to the micromagnetic effective field $\mathbf{h}_{\text{eff}}$ drive the magnetization dynamics. It was demonstrated there that the general equation for the magnetization motion is Eq. (3.61):

$$\frac{\mathrm{d}\mathbf{m}}{\mathrm{d}t} = \mathbf{m} \times \frac{\partial g_L}{\partial \mathbf{m}} + \alpha \mathbf{m} \times \left(\mathbf{m} \times \frac{\partial \Phi}{\partial \mathbf{m}} \right), \tag{5.108}$$

where:

$$\Phi = g_L + \frac{1}{\alpha}\Psi. \tag{5.109}$$

The potential Φ contains two terms: g_L, which is associated with thermal relaxation processes; and Ψ/α, which describes additional driving actions of nonconservative nature. The energy balance equation for this type of dynamics is given by Eqs (3.62) or (3.63). When the potentials g_L and Ψ do not explicitly depend on time, this balance equation takes the simple form:

$$\frac{\mathrm{d}g_L}{\mathrm{d}t} = -\alpha\mathcal{P}(\mathbf{m}(t),\zeta), \tag{5.110}$$

where:

$$\mathcal{P}(\mathbf{m},\zeta) = \left(\mathbf{m}\times\frac{\partial g_L}{\partial \mathbf{m}}\right)\cdot\left(\mathbf{m}\times\frac{\partial \Phi}{\partial \mathbf{m}}\right) = \left(\mathbf{m}\times\frac{\partial \Phi}{\partial \mathbf{m}}\right)\cdot\frac{\mathrm{d}\mathbf{m}}{\mathrm{d}t}, \tag{5.111}$$

while ζ generically denotes the control parameters associated with the additional non-conservative driving actions. The function $\mathcal{P}(\mathbf{m},\zeta)$ is proportional to the rate at which energy is lost ($\mathcal{P}(\mathbf{m},\zeta) > 0$) or gained ($\mathcal{P}(\mathbf{m},\zeta) < 0$) by the system during the magnetization dynamics. For this reason, it will be called the power function of the magnetization dynamics. The function $\mathcal{P}(\mathbf{m},\zeta)$ plays a particularly important physical role, because, as mentioned in Section 3.3, $\mathcal{P}(\mathbf{m},\zeta)$ may have either sign. This implies the possibility that periodic magnetization motions, or limit cycles, may exist. Indeed, periodic solutions $\mathbf{m}_p(t)$ may occur for trajectories along which an average balance of energy takes place, i.e.:

$$g_L(T_p) - g_L(0) = -\alpha\int_0^{T_p}\mathcal{P}(\mathbf{m}_p(t),\zeta)\mathrm{d}t = 0, \tag{5.112}$$

where T_p is the period of the periodic motion. In other words, Eq. (5.112) represents a necessary condition for the existence of periodic solutions $\mathbf{m}_p(t)$.

The study of these periodic magnetization motions is particularly challenging. In fact, there are no general mathematical techniques for the prediction of the number, the position, and the period of limit cycles for nonlinear dynamical systems. This is true even in the simplest case when the dynamics occurs on a two-dimensional planar or spherical

surface. Nevertheless, there exists a case for which significant albeit approximate analytical results can be worked out. This is when the magnetization dynamics can be viewed as a small perturbation of the precessional dynamics $\mathrm{d}\mathbf{m}/\mathrm{d}t = -\mathbf{m} \times \mathbf{h}_{\text{eff}}$. In terms of Eqs (5.108) and (5.109), this occurs when the damping constant α and the potential Ψ are both small quantities, $\alpha \ll 1$ and $\Psi \ll 1$. These conditions are not unrealistic. In fact, it is well known that the condition $\alpha \ll 1$ is typically satisfied in magnetic materials. Moreover, there are physical phenomena where also the condition $\Psi \ll 1$ is satisfied. An important example is the magnetization dynamics under the action of spin-polarized electric currents (see Chapter 9).

Assuming that α and Ψ are of the same order of magnitude, i.e., $\alpha \ll 1$, $\Psi \ll 1$, $\Psi/\alpha \sim 1$, predictions on periodic magnetization motions can be obtained by invoking a powerful perturbation technique known as the Poincaré–Melnikov method. This method is applicable to the study of the existence, the position, the stability, and the bifurcations of limit cycles for two-dimensional autonomous dynamical systems. This class of systems includes dynamical systems on the plane and on regular two-dimensional manifolds (e.g., sphere, torus, etc.). In this section, we shall apply the method to the generalized magnetization dynamics on the unit sphere, under the assumption that the free energy g_L and the potential Ψ do not explicitly depend on time. The general and rigorous mathematical discussion of the method can be found in Refs. [528,529].

For the application of the Poincaré–Melnikov method, it is convenient to introduce a system of curvilinear coordinates (x_1, x_2) for $\mathbf{m}$, which map a certain region of the unit sphere onto the plane. The nature and the properties of this region will become clear as the analysis proceeds. We shall assume that the mapping is invertible in this region. We shall use the vector notation:

$$\mathbf{x} = \begin{pmatrix} x_1 \\ x_2 \end{pmatrix}, \tag{5.113}$$

and we shall write all equations for $\mathbf{x}$ in vector form. In particular, once expressed in terms of $\mathbf{x}$, the equation for the magnetization dynamics (5.108) becomes:

$$\frac{\mathrm{d}\mathbf{x}}{\mathrm{d}t} = \mathbf{f}_0(\mathbf{x}) + \alpha \mathbf{f}_1(\mathbf{x}, \zeta), \tag{5.114}$$

where the vector functions $\mathbf{f}_0(\mathbf{x})$ and $\mathbf{f}_1(\mathbf{x}, \zeta)$ correspond to the precessional and relaxational part of the dynamics, respectively, while α

is the perturbation parameter. The unperturbed equation:

$$\frac{\mathrm{d}\mathbf{x}}{\mathrm{d}t} = \mathbf{f}_0(\mathbf{x}) \tag{5.115}$$

corresponds to the precessional dynamics $\mathrm{d}\mathbf{m}/\mathrm{d}t = -\mathbf{m} \times \mathbf{h}_{\text{eff}}$. This implies that the general form of the function $\mathbf{f}_0(\mathbf{x})$ must be:

$$\mathbf{f}_0(\mathbf{x}) = \lambda(\mathbf{x}) \begin{pmatrix} \partial g_L/\partial x_2 \\ -\partial g_L/\partial x_1 \end{pmatrix}, \tag{5.116}$$

where $g_L(\mathbf{x})$ is the free energy $g_L(\mathbf{m})$ expressed in terms of $\mathbf{x}$, while $\lambda(\mathbf{x})$ is a scalar function dependent on the choice of curvilinear coordinates. Indeed, the form (5.116) guarantees that the free energy $g_L(\mathbf{x})$ is an integral of motion of the unperturbed dynamics (5.115). This is verified by computing $\mathrm{d}g_L/\mathrm{d}t$ along the trajectories of the unperturbed dynamics. By using Eqs (5.115) and (5.116), one obtains:

$$\frac{\mathrm{d}g_L}{\mathrm{d}t} = \frac{\partial g_L}{\partial \mathbf{x}} \cdot \frac{\mathrm{d}\mathbf{x}}{\mathrm{d}t} = \frac{\partial g_L}{\partial \mathbf{x}} \cdot \mathbf{f}_0(\mathbf{x}) = 0, \tag{5.117}$$

where the dot notation represents the usual dot product of vectors, while:

$$\frac{\partial g_L}{\partial \mathbf{x}} = \begin{pmatrix} \partial g_L/\partial x_1 \\ \partial g_L/\partial x_2 \end{pmatrix} \tag{5.118}$$

is the vector of partial derivatives of g_L with respect to (x_1, x_2). If the $\mathbf{x}$ coordinates are chosen in such a way that $\lambda(\mathbf{x}) = 1$, then the unperturbed dynamics (5.115) acquires Hamiltonian form with g_L, x_1, and x_2 being the Hamiltonian, the canonical coordinate, and the canonical momentum, respectively. The Hamiltonian nature of Eq. (5.115) results in the following property:

$$\nabla \cdot \mathbf{f}_0 = 0, \tag{5.119}$$

where:

$$\nabla \cdot \mathbf{f}_0 = \frac{\partial \mathrm{f}_{0,1}}{\partial x_1} + \frac{\partial \mathrm{f}_{0,2}}{\partial x_2}. \tag{5.120}$$

The existence of the integral of motion $g_L(\mathbf{x})$ implies that the trajectories of the unperturbed dynamics are given by the curves $C(g_0)$

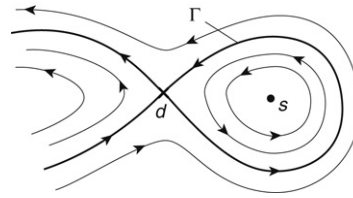

FIGURE 5.9 Portion of the phase portrait of the unperturbed dynamics with a central region enclosed by the homoclinic trajectory Γ starting and ending on the saddle equilibrium d. The trajectories correspond to different values of the integral of motion $g_L(\mathbf{x})$. Point s is a local energy minimum.

defined implicitly by the equation $g_L(\mathbf{x}) = g_0$. These trajectories have been extensively discussed in Chapter 4. It has been shown there that in general the phase portrait of the precessional dynamics consists of several central regions separated by homoclinic or heteroclinic trajectories. Each central region is filled with the family of closed constant-energy trajectories (see Fig. 5.9 for an example). The coordinates (x_1, x_2) map one of these central energy regions onto the plane. In the sequel, we will denote by $\mathbf{x}_c(t; g_0)$ the solution of the unperturbed dynamics with energy g_0 and by $T(g_0)$ the corresponding period.

The solutions of the perturbed dynamics (5.114) slightly deviate from the constant-energy trajectories of the unperturbed dynamics. To study these deviations, the "Poincaré map" is used. To obtain this map, we first have to choose a Poincaré section, namely a curve in the plane with the property of being transversal (nontangent) to the trajectories of the dynamical system (5.114) in the central region of interest. In Fig. 5.10, this Poincaré section is denoted by L. The situation shown in Fig. 5.10 is when the central region is around a center equilibrium. However, the discussion can be readily extended to any other type of central region. Since the form of the Poincaré section does not affect the results of the method, in the following we consider a transversal line L normal everywhere to the unperturbed vector field $\mathbf{f}_0(\mathbf{x})$.

Let us consider the state $\mathbf{x}_a$ on the Poincaré section (see Fig. 5.10). The Poincaré map is defined as the map:

$$\mathbf{x}_b = M_P(\mathbf{x}_a, \zeta, \alpha), \tag{5.121}$$

where $\mathbf{x}_b$ is the first state on the Poincaré section reached by the trajectory that originates from $\mathbf{x}_a$. In principle, the limit cycles of the perturbed dynamics could be found by determining the fixed points of the Poincaré

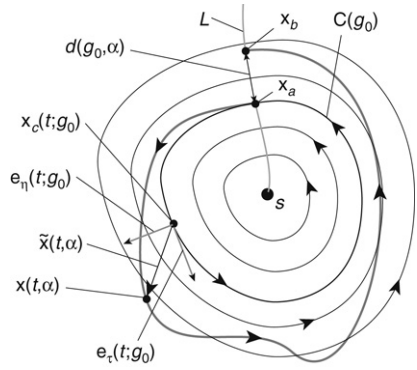

FIGURE 5.10 Graphical representation of Poincaré section with definition of the various quantities involved in the Poincaré–Melnikov method.

map, Eq. (5.121). However, explicit formulas for the Poincaré map are generally not available, for two reasons. First, the analytical solution to the nonlinear differential equation (5.114) is in general not known; and, second, the time necessary for a trajectory to come back to a point of the Poincaré section is not a priori known. These difficulties can be circumvented in the limit of small α by using perturbation methods to derive a suitable expression for the displacement $d(g_0, \alpha)$ between the points $\mathbf{x}_b$ and $\mathbf{x}_a$ [528,529]:

$$d^2(g_0, \alpha) = (x_{b,1} - x_{a,1})^2 + (x_{b,2} - x_{a,2})^2 . \tag{5.122}$$

To this end, one first considers the quantity:

$$\tilde{\mathbf{x}}(t, \alpha) = \mathbf{x}(t, \alpha) - \mathbf{x}_c(t; g_0), \tag{5.123}$$

which represents the deviation of the trajectory $\mathbf{x}(t, \alpha)$ of the perturbed dynamics starting from $\mathbf{x}_a$ from the trajectory $\mathbf{x}_c(t; g_0)$ of the unperturbed dynamics starting from the same point. Then, one assumes that $\tilde{\mathbf{x}}(t, \alpha)$ admits the following perturbation expansion:

$$\tilde{\mathbf{x}}(t, \alpha) = \alpha \Delta \mathbf{x}(t) + \mathcal{O}(\alpha^2). \tag{5.124}$$

By substituting Eq. (5.124) into Eq. (5.114) and by keeping only first-order terms in α, one ends up with the equation:

$$\frac{\mathrm{d}}{\mathrm{d}t}\Delta\mathbf{x} = \frac{\partial \mathbf{f}_0}{\partial \mathbf{x}}(\mathbf{x}_c(t;g_0)) \cdot \Delta\mathbf{x} + \mathbf{f}_1(\mathbf{x}_c(t;g_0),\zeta). \tag{5.125}$$

Equation (5.125) is a linear differential equation with periodic coefficients, because the Jacobian $\partial\mathbf{f}_0/\partial\mathbf{x}$ is computed along the periodic unperturbed trajectory $\mathbf{x}_c(t;g_0)$ of period $T(g_0)$. No general analytical method is known for the solution of this type of equation. However, this difficulty can be partially circumvented by introducing a vector basis for $\Delta\mathbf{x}(t)$ that takes into account the periodicity of the problem. Namely, let us introduce the pair of time-dependent orthogonal unit vectors:

$$\mathbf{e}_\tau(t;g_0) = \frac{\mathbf{f}_0(\mathbf{x}_c(t;g_0))}{|\mathbf{f}_0(\mathbf{x}_c(t;g_0))|}, \qquad \mathbf{e}_\eta(t;g_0) = \begin{pmatrix} e_{\tau,2}(t;g_0) \\ -e_{\tau,1}(t;g_0) \end{pmatrix}, \tag{5.126}$$

which are respectively tangent and perpendicular to the trajectory $C(g_0)$ at the point $\mathbf{x}_c(t;g_0)$ (see Fig. 5.10). The perturbation $\Delta\mathbf{x}(t)$ can be expressed in terms of $\mathbf{e}_\tau(t;g_0)$ and $\mathbf{e}_\eta(t;g_0)$ as follows:

$$\Delta\mathbf{x}(t) = \Delta x_\tau(t)\mathbf{e}_\tau(t;g_0) + \Delta x_\eta(t)\mathbf{e}_\eta(t;g_0). \tag{5.127}$$

By substituting Eq. (5.127) into Eq. (5.125) one finds that the displacement $d(g_0,\alpha)$ (see Eq. (5.122) and Fig. 5.10) is related only to the component $\Delta x_\eta(t)$:

$$d(g_0,\alpha) = \alpha\Delta x_\eta(T(g_0)) + \mathcal{O}(\alpha^2). \tag{5.128}$$

At the same time, it turns out that the equation for $\Delta x_\eta(t)$ is independent of $\Delta x_\tau(t)$. More precisely, we define the quantity:

$$\rho(t) = \Delta x_\eta(t)|\mathbf{f}_0(\mathbf{x}_c(t;g_0))| = \Delta\mathbf{x}(t) \wedge \mathbf{f}_0(\mathbf{x}_c(t;g_0)), \tag{5.129}$$

where the symbol $\mathbf{v}\wedge\mathbf{w}$ represents the so-called wedge product of the two generic vectors $\mathbf{v} = (v_1, v_2)$ and $\mathbf{w} = (w_1, w_2)$:

$$\mathbf{v} \wedge \mathbf{w} = v_1 w_2 - w_2 v_1. \tag{5.130}$$

By using the above expressions, one finds that the evolution of $\rho(t)$ is governed by the following differential equation:

$$\frac{\mathrm{d}\rho}{\mathrm{d}t} = [\nabla \cdot \mathbf{f}_0(\mathbf{x}_c(t;g_0))]\,\rho - \mathbf{f}_0(\mathbf{x}_c(t;g_0)) \wedge \mathbf{f}_1(\mathbf{x}_c(t;g_0),\zeta). \tag{5.131}$$

This equation can be solved by the method of separation of variables. One obtains:

$$\rho(t) = -\exp\left[\int_0^t \nabla\cdot\mathbf{f}_0(\mathbf{x}_c(t';g_0))\mathrm{d}t'\right]\int_0^t \mathbf{f}_0(\mathbf{x}_c(t';g_0))\wedge\mathbf{f}_1(\mathbf{x}_c(t';g_0),\zeta) \times \exp\left[-\int_0^{t'}\nabla\cdot\mathbf{f}_0(\mathbf{x}_c(t'';g_0))\mathrm{d}t''\right]\mathrm{d}t'. \tag{5.132}$$

By using Eqs (5.128) and (5.129), one can express the displacement $d(g_0,\alpha)$ as:

$$d(g_0,\alpha) = \alpha\frac{\rho(T(g_0))}{|\mathbf{f}_0(\mathbf{x}_a)|} + \mathcal{O}(\alpha^2), \tag{5.133}$$

where $\rho(T(g_0))$ is computed from Eq. (5.132).

As previously mentioned, limit cycles are periodic orbits corresponding to fixed points of the Poincaré map, that is, to states $\mathbf{x}_a$ for which $d(g_0,\alpha) = 0$. Since $|\mathbf{f}_0(\mathbf{x}_a)| \neq 0$, one can infer from Eq. (5.133) that, for sufficiently small α, the zeros of $d(g_0,\alpha)$ can be computed from the zeros of the function $M(g_0,\zeta) = \rho(T(g_0))$, known as the Melnikov function:

$$M(g_0,\zeta) = -\exp\left[\int_0^{T(g_0)}\nabla\cdot\mathbf{f}_0(\mathbf{x}_c(t;g_0))\mathrm{d}t\right] \times\int_0^{T(g_0)}\mathbf{f}_0(\mathbf{x}_c(t;g_0))\wedge\mathbf{f}_1(\mathbf{x}_c(t;g_0),\zeta) \times\exp\left[-\int_0^t\nabla\cdot\mathbf{f}_0(\mathbf{x}_c(t';g_0))\mathrm{d}t'\right]\mathrm{d}t. \tag{5.134}$$

The simplest form for $M(g_0,\zeta)$ is obtained when the (x_1,x_2) representation of the unperturbed dynamics has Hamiltonian form, i.e., $\nabla\cdot\mathbf{f}_0 = 0$. Then one has:

$$M(g_0,\zeta) = \int_0^{T(g_0)}\mathbf{f}_1(\mathbf{x}_c(t;g_0),\zeta)\wedge\mathbf{f}_0(\mathbf{x}_c(t;g_0))\mathrm{d}t. \tag{5.135}$$

By taking into account that Eq. (5.115) holds along the precessional trajectory $\mathbf{x}_c(t;g_0)$, the last expression can be transformed into the

following line integral along the precessional trajectory $C(g_0)$:

$$M(g_0,\zeta)=\oint_{C(g_0)}\mathbf{f}_1(\mathbf{x},\zeta)\wedge \mathrm{d}\mathbf{x}. \tag{5.136}$$

This equation shows that the Melnikov function does not really depend on the details of the time evolution of $\mathbf{x}_c(t;g_0)$, but only on the geometrical shape of the precessional trajectory of energy g_0.

The Melnikov function for the generalized magnetization dynamics (5.108) can be computed from Eq. (5.135), once the (x_1,x_2) representation has been chosen in such a way that the precessional part of the dynamics has Hamiltonian form. As discussed in Chapter 4, a choice satisfying this requirement is:

$$x_1=\cos\theta, \qquad x_2=\phi, \tag{5.137}$$

where θ and ϕ are the usual spherical coordinates on the unit sphere. In this coordinate system, Eq. (5.108) is written as:

$$\frac{\mathrm{d}\cos\theta}{\mathrm{d}t}=\frac{\partial g_L}{\partial\phi}-\alpha\sin^2\theta\frac{\partial\Phi}{\partial\cos\theta}, \tag{5.138}$$

$$\frac{\mathrm{d}\phi}{\mathrm{d}t}=-\frac{\partial g_L}{\partial\cos\theta}-\frac{\alpha}{\sin^2\theta}\frac{\partial\Phi}{\partial\phi}. \tag{5.139}$$

By comparing Eqs (5.138) and (5.139) with Eq. (5.114), one finds that:

$$\mathbf{f}_0(\cos\theta,\phi)=\begin{pmatrix}\partial g_L/\partial\phi\\ -\partial g_L/\partial\cos\theta\end{pmatrix}, \tag{5.140}$$

$$\mathbf{f}_1(\cos\theta,\phi,\zeta)=\begin{pmatrix}-\sin^2\theta\,\partial\Phi/\partial\cos\theta\\ -(1/\sin^2\theta)\partial\Phi/\partial\phi\end{pmatrix}. \tag{5.141}$$

The unperturbed motion is indeed Hamiltonian as anticipated, i.e., $\nabla\cdot\mathbf{f}_0=0$. By substituting Eqs (5.140) and (5.141) into Eq. (5.135), one obtains:

$$M(g_0,\zeta)=\int_0^{T(g_0)}\left[\frac{\partial g_L}{\partial\theta}\frac{\partial\Phi}{\partial\theta}+\frac{1}{\sin^2\theta}\frac{\partial g_L}{\partial\phi}\frac{\partial\Phi}{\partial\phi}\right]_{\mathbf{m}_c(t;g_0)}\mathrm{d}t, \tag{5.142}$$

where the subscript $\mathbf{m}_c(t;g_0)$ indicates that the integrand is to be computed along the precessional magnetization trajectory $\mathbf{m}_c(t;g_0)$ with energy g_0. By using the expression for the gradient operator ∇_Σ on the

sphere:

$$\nabla_\Sigma = \mathbf{e}_\theta \frac{\partial}{\partial \theta} + \mathbf{e}_\phi \frac{1}{\sin\theta} \frac{\partial}{\partial \phi}, \tag{5.143}$$

formula (5.142) can be written in the following coordinate-invariant form:

$$M(g_0, \zeta) = \int_0^{T(g_0)} \left[\nabla_\Sigma g_L \cdot \nabla_\Sigma \Phi\right]_{\mathbf{m}_c(t;g_0)} \mathrm{d}t. \tag{5.144}$$

This expression reveals the intimate connection existing between the Melnikov function and the power function (5.111). Indeed, by using the vector identity:

$$\nabla_\Sigma g_L \cdot \nabla_\Sigma \Phi = \left(\mathbf{m} \times \frac{\partial g_L}{\partial \mathbf{m}}\right) \cdot \left(\mathbf{m} \times \frac{\partial \Phi}{\partial \mathbf{m}}\right), \tag{5.145}$$

and by taking into account the expression (5.111) for $\mathcal{P}(\mathbf{m}, \zeta)$, one obtains:

$$M(g_0, \zeta) = \int_0^{T(g_0)} \mathcal{P}(\mathbf{m}_c(t; g_0), \zeta) \mathrm{d}t. \tag{5.146}$$

Thus, the quantity $\alpha M(g_0, \zeta)$ represents the total energy loss (if $M(g_0, \zeta) > 0$) or gain (if $M(g_0, \zeta) < 0$) over one period of motion of the system along the precessional trajectory $\mathbf{m}_c(t; g_0)$. The actual magnetization motion does not occur precisely on this unperturbed trajectory. However, as previously discussed, it remains very close to it during the time interval $T(g_0)$, due to the smallness of α. To the first order in α, the quantity $\alpha M(g_0, \zeta)$ gives the energy gain or loss along the actual trajectory and $M(g_0, \zeta) = 0$ provides the condition for the existence of a limit cycle. In fact, by using the Poincaré–Melnikov method it can be proven that the necessary condition (5.112) for the existence of a periodic motion is the sufficient condition as well [528].

It was mentioned above that the Melnikov function eventually depends only on the geometrical shape of the precessional trajectory, rather than the time evolution of the magnetization along it. In the case of Eq. (5.146), this property is the straightforward consequence of the second expression for $\mathcal{P}(\mathbf{m}, \zeta)$ in Eq. (5.111). By using this formula in Eq. (5.146), one expresses the Melnikov function as the following line integral along

the precessional trajectory $C(g_0)$:

$$M(g_0, \zeta) = \oint_{C(g_0)} \left(\mathbf{m} \times \frac{\partial \Phi}{\partial \mathbf{m}} \right) \cdot \mathrm{d}\mathbf{m}. \tag{5.147}$$

The perturbation analysis presented in this section applies to each central energy region of the phase portrait of the precessional dynamics. Therefore, there will exist one Melnikov function for each central region. In this sense, the Melnikov function is defined on the graph $\mathcal{G}$ introduced in Chapter 4 to describe the energy landscape and the connection between central energy regions. According to the notation introduced in that chapter, each central region corresponds to one of the graph edges, denoted as I_k. The trajectory of energy g inside the central region I_k has been denoted as $C_k(g)$ and the corresponding period as $T_k(g)$. It is only natural that the Melnikov function for the same central region will be denoted as $M_k(g, \zeta)$.

Although the Melnikov function has been introduced here for the study of limit cycles and self-oscillations, the fact that it represents the energy loss or gain in the system during one precessional period makes it intimately related to the averaging technique previously discussed in Section 5.2. Indeed, the time integral in Eq. (5.65) is nothing else but the Melnikov function for ordinary LLG magnetization dynamics. It is easy to see that the averaging technique can be applied with little change to the generalized magnetization dynamics discussed in this section. Whenever the relaxational part of the dynamics is small, the energy is a slow variable, the system executes many precessional oscillations before the energy is appreciably changed, and one can average the energy balance equation (5.110) over one period of constant-energy precessional motion with no appreciable error. Since the time integral of the power function $\mathcal{P}(\mathbf{m}, \zeta)$ over one precessional period is precisely the Melnikov function (see Eq. (5.146)), one immediately concludes that the averaged energy inside the central energy region I_k follows the equation:

$$\frac{\mathrm{d}\bar{g}}{\mathrm{d}t} = -\alpha \frac{M_k(\bar{g}, \zeta)}{T_k(\bar{g})}. \tag{5.148}$$

Equation (5.148) can be rewritten in the form:

$$\frac{\mathrm{d}\bar{g}}{\mathrm{d}t} = -\alpha \frac{\partial U_k}{\partial \bar{g}}, \tag{5.149}$$

where the effective potential $U_k(\bar{g})$ is defined, up to a constant, as:

$$U_k(g) = \int_{g_k^-}^{g} \frac{M_k(u,\zeta)}{T_k(u)} \mathrm{d}u, \tag{5.150}$$

where g_k^- is the minimum energy value in the central region I_k. Equation (5.149) shows that, to the first order in α, the energy follows a viscous-like dynamics governed by the effective potential $U_k(g,\zeta)$. The smaller the value of α, the more accurate this description. Finally, we note that the critical points of U_k defined by $\partial U_k/\partial g = 0$ correspond to fixed points and limit cycles of the magnetization dynamics. More specifically, since $\partial U_k^2/\partial g^2 = (\partial M_k/\partial g)/T_k(g)$ when $\partial U_k/\partial g = 0$, minima and maxima of U_k correspond to stable and unstable steady states, respectively, since $\partial M_k/\partial g$ is positive or negative for these states, respectively.

CHAPTER 6

Magnetization Switching

6.1 PHYSICAL MECHANISMS OF PRECESSIONAL SWITCHING

In the previous chapter, the detailed analysis of damping switching of magnetization has been carried out. In this type of switching, magnetization reversal is produced by applying magnetic fields oriented almost antiparallel to the initial magnetization direction. This makes the initial magnetization state energetically unfavorable and causes magnetization relaxation toward the desired final equilibrium state. This relaxation is realized through numerous precessional oscillations and, as a result, it is relatively slow. Recently, a new mode of magnetization switching has emerged [587]. This mode exploits fast precessional magnetization dynamics and, for this reason, it has been termed "precessional switching". This mode of switching has been mostly studied experimentally and through numerical solution of LLG equation. It has been found that this type of switching is very sensitive to the duration of the magnetic field pulse inducing the switching. At the same time, the seemingly stochastic nature of precessional switching has been observed for some ranges of pulse durations. Limited analytical and qualitative study of precessional switching has been performed and the very notion of precessional switching has not been defined in precise terms based on the properties of phase portraits of nonlinear magnetization dynamics.

In this section, we present a complete qualitative analysis of precessional switching by using phase portraits of magnetization dynamics. Precessional switching is usually realized in nano-scale thin magnetic films [54] through the following steps (see Fig. 6.1). The magnetization is initially along the film easy axis and a magnetic field is applied approximately orthogonal to the easy axis in the film plane. This field produces a torque which tilts the magnetization out of the film plane. This results in a strong vertical demagnetizing field which yields an additional torque that forces the magnetization to precess in the plane of the film away from its initial position. Magnetization reversal is realized by switching off the applied magnetic field when the magnetization is close to its reversed orientation. After the field is switched off, the magnetization relaxes to the reversed equilibrium state.

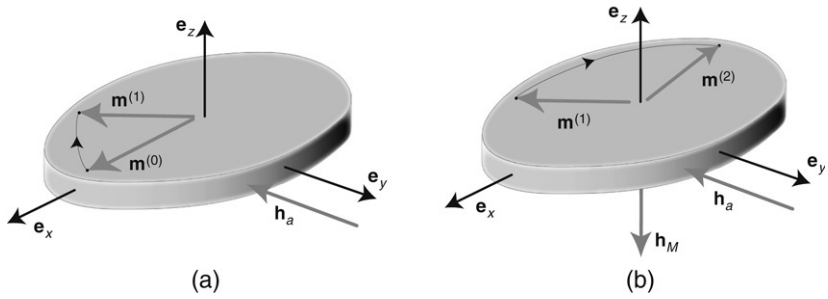

FIGURE 6.1 Different stages of precessional switching. (a) The torque exerted by the applied field tilts the magnetization from the position $\mathbf{m}^{(0)}$ to the out-of-plane position $\mathbf{m}^{(1)}$. (b) The resulting vertical demagnetizing field $\mathbf{h}_M$ produces an additional torque which drives the magnetization from the position $\mathbf{m}^{(1)}$ to the position $\mathbf{m}^{(2)}$ toward the reversed state $-\mathbf{e}_x$.

It is apparent that, in contrast with damping switching, precessional switching is accomplished by controlling the magnetization precession within a time interval so short that the role of dissipation is usually negligible. This type of switching can be considerably faster and it may require lower applied fields in comparison with traditional switching. However, the switching is realized only if the field pulse duration is accurately controlled in such a way that the magnetic field is switched off when the magnetization is close to its reversed orientation.

The basic properties of the precessional switching are revealed by the examination of the phase portrait of conservative magnetization dynamics. The phase portrait on the stereographic plane for the case when no field is applied is illustrated by Fig. 6.2(a). This phase portrait is characterized by six equilibrium points: s_1, s_2 (energy minima); u_1, $u_2 = +\infty$ (energy maxima); d_1, d_2 (saddles). Heteroclinic trajectories connect one saddle point to another. All trajectories, except the heteroclinic ones, enclose one equilibrium point. The shaded regions indicate the low-energy regions (potential wells) around the energy minima $\mathbf{m} = \mathbf{e}_x$ and $\mathbf{m} = -\mathbf{e}_x$. The remaining white regions are the high-energy regions around the energy maxima u_1 and u_2. These shaded and white regions will be superimposed on subsequent diagrams in order to give an idea of the expected dynamics after the field is switched off. According to Fig. 6.2(a), no magnetization switching is possible under zero field, because there is no trajectory connecting the state $\mathbf{m} = \mathbf{e}_x$ to the shaded region around $\mathbf{m} = -\mathbf{e}_x$.

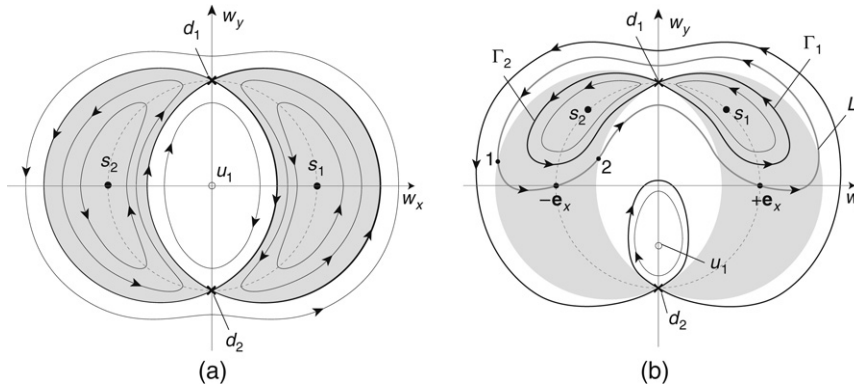

FIGURE 6.2 Stereographic-plane representation of phase portraits for conservative LLG dynamics. The dashed line represents the unit circle. (a) $\mathbf{h}_a = 0$; (b) $\mathbf{h}_a = \mathrm{h}_{ay}\mathbf{e}_y$ ($\mathrm{h}_{ay} > 0$).

The phase-portrait modifications brought about by the application of the field along the positive y direction are shown in Fig. 6.2(b). The equilibrium points are shifted to new positions and, more importantly, the heteroclinic trajectories are broken into homoclinic trajectories, that is, closed trajectories starting from a saddle and coming back to the same saddle. The so-called homoclinic structure consisting of a pair of homoclinic trajectories is formed for each saddle. For example, the homoclinic trajectories Γ_1 and Γ_2 form the homoclinic structure associated with d_1. The key point is that a new type of magnetization trajectories appears in the phase portrait, namely, trajectories that enclose the homoclinic structures (e.g., curve L in Fig. 6.2(b)). It is along this type of trajectory that magnetization dynamics may occur from one shaded region to another and, in this way, magnetization switching may be realized from one well to another. Indeed, if $\mathbf{m}$ is initially in the position $\mathbf{m} = \mathbf{e}_x$ in Fig. 6.2(b), the switching is realized if the magnetic field is switched off in the time interval during which magnetization is between points 1 and 2 on the trajectory L. When the field is switched off, the magnetization remains trapped in the potential well around the reversed state $\mathbf{m} = -\mathbf{e}_x$ (see Fig. 6.2(a)). Subsequent relaxation due to the dissipative nature of the magnetization dynamics will bring the magnetization to the final equilibrium state $\mathbf{m} = -\mathbf{e}_x$. It is evident from the above discussion that switching becomes possible only when the applied field is large enough that the homoclinic trajectory Γ_1 does not enclose the initial state $\mathbf{m} = \mathbf{e}_x$. It will be shown below that the critical

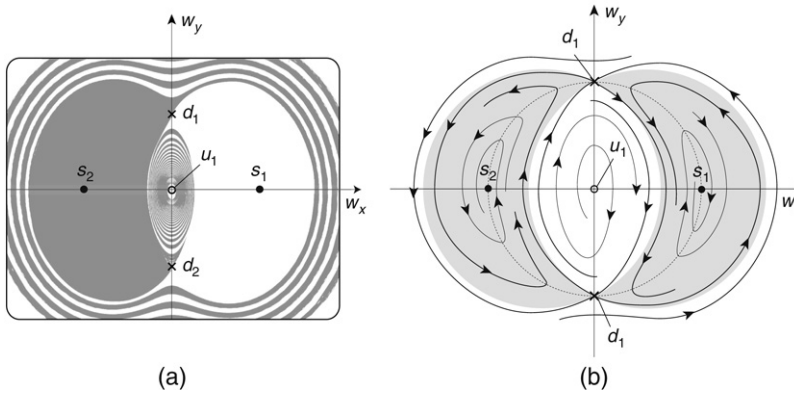

FIGURE 6.3 Stereographic-plane representation of phase portraits of dissipative LLG dynamics for $\mathbf{h}_a = 0$. (a) Numerically computed basins of attraction of stable focus s_1 (white region) and stable focus s_2 (shaded region); (b) qualitative sketch of dissipative dynamics (shaded regions represent the energy wells of the corresponding conservative dynamics (see Fig. 6.2)).

field at which Γ_1 passes through the point $\mathbf{m} = \mathbf{e}_x$ is:

$$h_{\text{crit}} = \frac{D_y - D_x}{2}. \tag{6.1}$$

A field pulse of amplitude exceeding this threshold will guarantee switching, provided the field pulse duration is properly tuned.

If the magnetic field is switched off when the magnetization is not between points 1 and 2 but in the high-energy regions of the phase portrait, the result of the subsequent relaxation to equilibrium is practically uncertain. This is due to the very convoluted and closely entangled nature exhibited in these regions by the trajectories of the dissipative dynamics leading to different final equilibrium states s_1 or s_2 (see Fig. 6.3). Indeed, it is clear that there exist two basins of attraction in the magnetization dynamics: the basin of initial states for which the magnetization will end up in s_1 and the basin of initial states for which the magnetization will end up in s_2. The high-energy regions of the phase portrait are very fine mixtures of these two basins of attraction, and the smaller the damping constant α, the more intricate and finer the entanglement of the two basins of attraction in the high-energy regions. This fine entanglement may lead to a seemingly stochastic nature of precessional switching if the field is switched off when magnetization

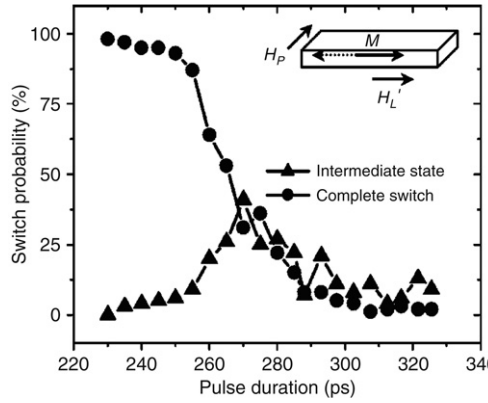

FIGURE 6.4 Probability of switching versus duration of applied field pulse. Dots indicate probability of complete switching (which is the case considered in this chapter); triangles indicate probability of final intermediate state. Inset: Field pulse H_p is along the hard axis while H_L' is a bias field applied along the easy-axis direction. M indicates the initial free layer magnetization direction. Reprinted with permission from S. Kaka and S.E. Russek, *Applied Physics Letters*, 80, 2958 (2002).

is in the high-energy regions, because in that case the final equilibrium that will be reached is strongly dependent on the exact magnetization conditions immediately after the magnetic field is switched off. This seemingly stochastic nature of precessional switching could explain various experimental results presented in the literature. In Fig. 6.4, the experimental results presented in Ref. [377] are shown. The outcome of the experiment is characterized in this reference statistically by representing the "probability" of switching versus the applied field pulse duration.

6.2 CRITICAL FIELDS FOR PRECESSIONAL SWITCHING

We shall next proceed to the detailed analytical treatment of precessional switching. We shall consider the case where the field pulse is applied along some direction in the (x, y)-plane, as shown in Fig. 6.5. We shall assume that the pulse is of rectangular shape and we shall study the magnetization dynamics in the time interval during which the field is on. This time interval is usually very short, so the effect of damping can be neglected as a first approximation. For this reason, we will use the

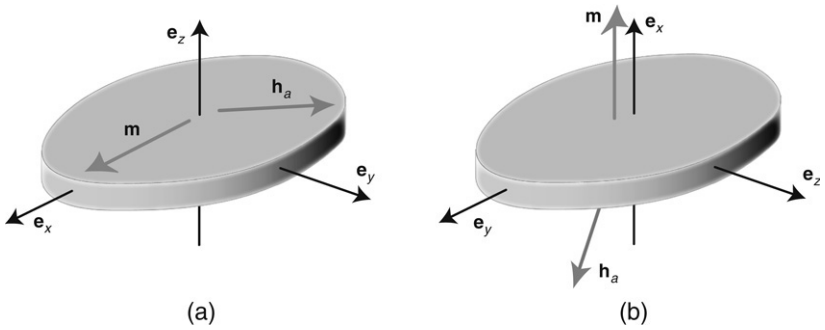

FIGURE 6.5 Schematic representation of precessional switching. (a) Longitudinal media with in-plane anisotropy. (b) Perpendicular media with easy axis perpendicular to the film plane and uniaxial symmetry around it. In both cases, the $\mathbf{e}_x$ direction is along the easy axis and the applied field $\mathbf{h}_a$ lies in the (x, y)-plane.

conservative LLG equation to describe the magnetization dynamics:

$$\frac{\mathrm{d}\mathbf{m}}{\mathrm{d}t} = -\mathbf{m} \times \mathbf{h}_{\text{eff}}(\mathbf{m}). \tag{6.2}$$

After the field has been switched off, the relaxation dynamics is governed by damping and, therefore, dissipation has to be taken into account. This case has been treated in detail in the previous chapter.

Since the applied field is in the film plane ($\mathrm{h}_{az} = 0$), the analysis of magnetization dynamics can be carried out by using the unit-disk representation introduced in Chapter 4. We recall that in this representation, magnetization trajectories are projected on the $(\mathrm{m}_x, \mathrm{m}_y)$-plane and these projections are ellipsoidal curves (arcs) described by the equation:

$$(\mathrm{m}_x - a_x)^2 + k^2 (\mathrm{m}_y - a_y)^2 = p^2, \tag{6.3}$$

where a_x, a_y, k^2, and p^2 are defined by the following formulas:

$$a_x = -\frac{\mathrm{h}_{ax}}{D_z - D_x}, \qquad a_y = -\frac{\mathrm{h}_{ay}}{D_z - D_y}, \qquad k^2 = \frac{D_z - D_y}{D_z - D_x}, \tag{6.4}$$

$$p^2 = a_x^2 + k^2 a_y^2 + k_g^2, \quad k_g^2 = \frac{D_z - 2g_0}{D_z - D_x}. \tag{6.5}$$

The parameter g_0 represents the free energy of the system during the precessional dynamics. We will assume that the initial magnetization state is $\mathbf{m} = \mathbf{e}_x$, that is, $m_x = 1$, $m_y = m_z = 0$. Hence, the initial energy of the system, immediately after the field has been switched on, is:

$$g_0 = \frac{1}{2} D_x - \mathrm{h}_{ax}, \tag{6.6}$$

which corresponds to:

$$k_g^2 = 1 - 2a_x, \qquad p^2 = (1 - a_x)^2 + k^2 a_y^2. \tag{6.7}$$

The unit-disk representation of the magnetization trajectories starting from the initial state $m_x = 1$ are described by the equation:

$$(\mathrm{m}_x - a_x)^2 + k^2 (\mathrm{m}_y - a_y)^2 = (1 - a_x)^2 + k^2 a_y^2. \tag{6.8}$$

This equation represents a family of ellipses corresponding to different values of h_{ax} and h_{ay}. Various examples of possible elliptic trajectories on the $(\mathrm{m}_x, \mathrm{m}_y)$-plane are shown in Fig. 6.6(a)–(d). In these figures, the shaded regions correspond to the low-energy shaded regions of Fig. 6.2. On the contrary, the two white high-energy regions present in Fig. 6.2 are projected onto a single region in Fig. 6.6(a)–(d), namely, the white central region confined by the ellipse Γ described by the equation:

$$\mathrm{m}_x^2 + k^2 \mathrm{m}_y^2 = k^2. \tag{6.9}$$

This ellipse is the unit-disk representation of the heteroclinic trajectories existing for zero applied field (see Fig. 6.2(a)).

In the unit-disk representation, every elliptic trajectory in the $(\mathrm{m}_x, \mathrm{m}_y)$-plane corresponds to a closed trajectory on the unit sphere, symmetric with respect to the $(\mathrm{m}_x, \mathrm{m}_y)$-plane. As a consequence of this symmetry, the precessional dynamics on the unit sphere is orthogonally projected onto a back-and-forth motion along the corresponding elliptic trajectory in the $(\mathrm{m}_x, \mathrm{m}_y)$-plane. By examining the geometrical properties of these $(\mathrm{m}_x, \mathrm{m}_y)$ trajectories for different values of h_{ax} and h_{ay}, we shall determine the region in the $(\mathrm{h}_{ax}, \mathrm{h}_{ay})$ control plane in which precessional switching is possible, in the sense that the corresponding trajectory connects the initial state $\mathrm{m}_x = 1$ with the low-energy region around the reversed state $\mathrm{m}_x = -1$. A necessary condition for this is that the trajectory must intersect the ellipse Γ. The four different ways in which

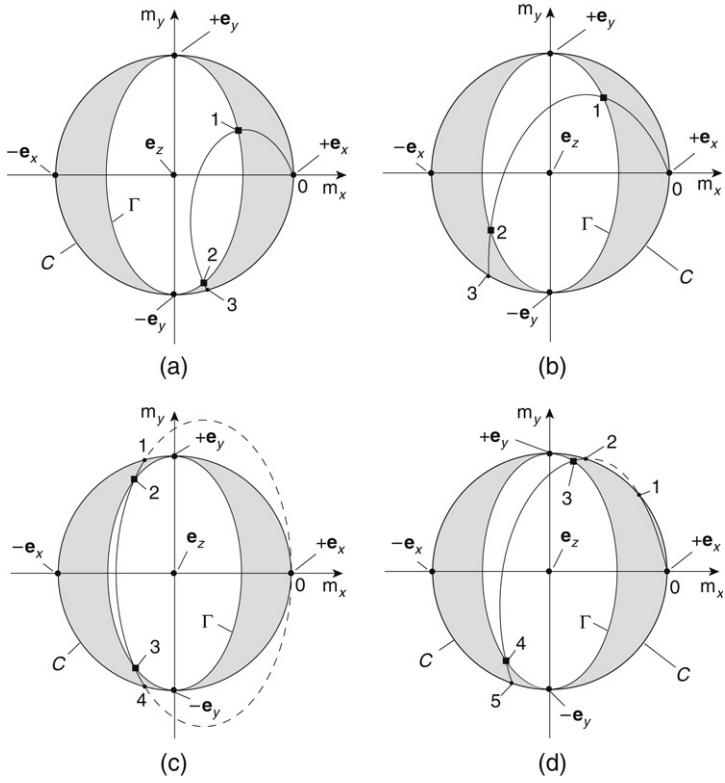

FIGURE 6.6 Unit-disk representation of trajectories starting from initial state $m_x = 1$ for different values of the applied field. The two intersections of the ellipse passing through $m_x = 1$ with the ellipse Γ (see Eq. (6.9)) are indicated with squares. (a) Both intersections occur for $m_x > 0$; (c) both intersections occur for $m_x < 0$; (b), (d) the intersections occur for opposite signs of m_x.

this intersection may occur are shown in Fig. 6.6(a)–(d). It is apparent that only Fig. 6.6(b) corresponds to precessional switching. The switching trajectory shown in this figure is characterized by the following two properties.

- Property A: the trajectory intersects the ellipse Γ at two points with opposite signs of m_x.
- Property B: the initial state $m_x = 1$ and the two points of intersection with Γ belong to the same physical trajectory (Fig. 6.6(b)). This is not the case in Fig. 6.6(d), where $m_x = 1$ and the intersection points belong

to disjoint physical trajectories (0-1 and 2-3-4-5) even though these trajectories are parts of the same ellipse described by Eq. (6.8).

Property A can be expressed in algebraic form by using Eqs (6.8) and (6.9). By combining these equations, one finds:

$$a_x \mathrm{m}_x + k^2 a_y \mathrm{m}_y = a_x - \frac{k'^2}{2}, \tag{6.10}$$

where:

$$k'^2 = 1 - k^2 = \frac{D_y - D_x}{D_z - D_x}. \tag{6.11}$$

By inserting Eq. (6.10) into Eq. (6.9), one obtains the following quadratic equation for m_x:

$$\begin{aligned} &\left(a_x^2 + k^2 a_y^2\right) \mathrm{m}_x^2 - 2a_x \left(a_x - k'^2/2\right) \mathrm{m}_x \\ &\quad + \left[\left(a_x - k'^2/2\right)^2 - k^4 a_y^2\right] = 0. \end{aligned} \tag{6.12}$$

The roots of Eq. (6.12) are certainly real and have opposite signs if:

$$\left[\left(a_x - k'^2/2\right)^2 - k^4 a_y^2\right] < 0. \tag{6.13}$$

This inequality expresses Property A. By using Eqs (6.4) and (6.11), one finds:

$$\left|\mathrm{h}_{ax} + \frac{\mathrm{h}_{AN}}{2}\right| \leq \left|\mathrm{h}_{ay}\right|, \tag{6.14}$$

where:

$$\mathrm{h}_{AN} = D_y - D_x \tag{6.15}$$

is the in-plane anisotropy field. The inequality expressed by Eq. (6.14) is represented by the shaded region in Fig. 6.7(a).

Next, we shall discuss Property B. For each point $(\mathrm{h}_{ax}, \mathrm{h}_{ay})$ inside the shaded region in Fig. 6.7(a) there are two sets of trajectories: the one shown in Fig. 6.6(b) or that shown in Fig. 6.6(d). The latter is not compatible with precessional switching, since the magnetization remains trapped inside

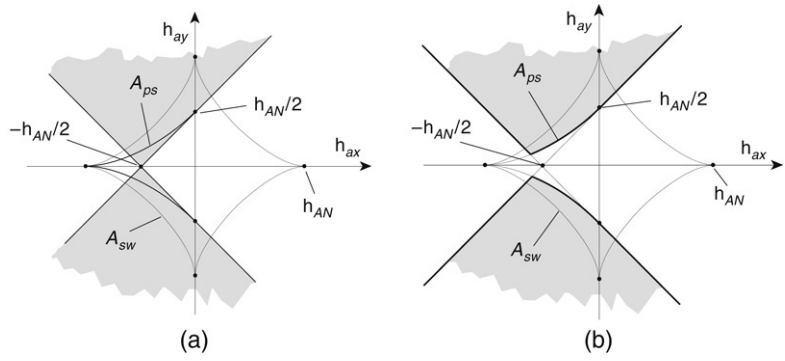

FIGURE 6.7 Regions in the $(\mathrm{h}_{ax}, \mathrm{h}_{ay})$ control plane related to the conditions for precessional switching. The curves labeled by A_{sw} and A_{ps} correspond to the Stoner-Wohlfarth model and to Eq. (6.21), respectively. (a) Comparison between Property A (shaded region defined by Eq. (6.14)) and Property B (Eqs (6.21)); (b) resulting $(\mathrm{h}_{ax}, \mathrm{h}_{ay})$ region (shaded region) where precessional switching can be achieved.

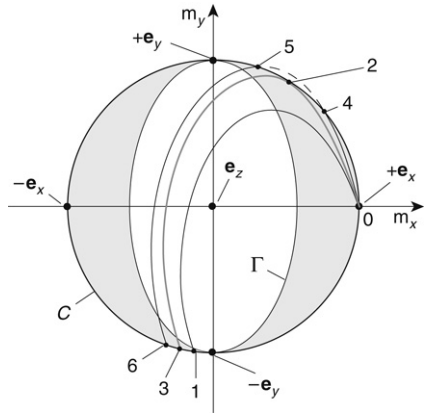

FIGURE 6.8 Unit-disk representation of precessional switching trajectories.

the $\mathrm{m}_x > 0$ hemisphere, between points 0 and 1. The boundary between these two sets is represented by the critical trajectory 0-2-3 shown in Fig. 6.8. This trajectory is tangent to the unit circle:

$$\mathrm{m}_x^2 + \mathrm{m}_y^2 = 1, \tag{6.16}$$

at some point with $\mathrm{m}_x > 0$. By imposing the condition of tangency on the curves described by Eqs (6.8) and (6.16), one derives the equation:

$$\mathrm{h}_{AN}\mathrm{m}_x\mathrm{m}_y + \mathrm{h}_{ax}\mathrm{m}_y - \mathrm{h}_{ay}\mathrm{m}_x = 0, \tag{6.17}$$

where h_{AN} is given by Eq. (6.15). Since the tangency point lies on the unit circle, its coordinates can be expressed in the parametric form:

$$\mathrm{m}_x = \cos\phi_0, \qquad \mathrm{m}_y = \sin\phi_0, \tag{6.18}$$

where $-\pi/2 \leq \phi_0 \leq \pi/2$ as a consequence of the fact that $\mathrm{m}_x \geq 0$. By substituting Eq. (6.18) into Eq. (6.17) as well as by taking into account that the tangency point lies on a trajectory whose energy is given by Eq. (6.6), one arrives at the set of equations:

$$\mathrm{h}_{ay}\cos\phi_0 - \mathrm{h}_{ax}\sin\phi_0 = \mathrm{h}_{AN}\sin\phi_0\cos\phi_0, \tag{6.19}$$

$$\mathrm{h}_{ay}\sin\phi_0 - \mathrm{h}_{ax}\left(1-\cos\phi_0\right) = \frac{\mathrm{h}_{AN}}{2}\sin^2\phi_0. \tag{6.20}$$

These are coupled equations with respect to h_{ax} and h_{ay}, whose solution is given by the formulas:

$$\mathrm{h}_{ax} = -\mathrm{h}_{AN}\cos\phi_0\cos^2\frac{\phi_0}{2}, \qquad \mathrm{h}_{ay} = \mathrm{h}_{AN}\sin\phi_0\sin^2\frac{\phi_0}{2}. \tag{6.21}$$

These formulas coincide with the formulas derived in a different context and by using a different line of reasoning in Ref. [541]. By varying the parameter ϕ_0 in the interval $(-\pi/2, \pi/2)$, one obtains the curve denoted by A_{ps} in Fig. 6.7. One can verify that Property B is satisfied in the regions above A_{ps} for $\mathrm{h}_{ay} > 0$ and below A_{ps} for $\mathrm{h}_{ay} < 0$. Therefore, the field region where precessional switching can be achieved is the shaded region in Fig. 6.7(b). It can be shown that the minimum field amplitude for precessional switching is equal to $0.385\,\mathrm{h}_{AN}$ and it is achieved when the applied field orientation is such that $\mathrm{h}_{ay}/\mathrm{h}_{ax} = -\sqrt{2}$. Indeed, from formulas (6.21) we obtain:

$$\frac{\mathrm{h}_{ay}}{\mathrm{h}_{ax}} = -\tan\phi_0\tan^2\frac{\phi_0}{2}, \tag{6.22}$$

$$\mathrm{h}_{ax}^2 + \mathrm{h}_{ay}^2 = \mathrm{h}_{AN}^2\left[\cos^3\phi_0 + \frac{1}{4}\left(1-\cos\phi_0\right)^2\right]. \tag{6.23}$$

Differentiation of Eq. (6.23) leads to the following extremum condition:

$$3\cos^2\phi_0 + \frac{1}{2}\cos\phi_0 - \frac{1}{2} = 0, \tag{6.24}$$

from which we find:

$$\cos\phi_0 = \frac{1}{3}. \tag{6.25}$$

By substituting Eq. (6.25) into Eqs (6.22) and (6.23), we obtain:

$$\frac{\mathrm{h}_{ay}}{\mathrm{h}_{ax}} = -\sqrt{2}, \tag{6.26}$$

$$h_{\text{crit}} = \frac{2}{3\sqrt{3}}\,\mathrm{h}_{AN} \simeq 0.385\,\mathrm{h}_{AN}. \tag{6.27}$$

A remarkable property of the precessional switching region shown in Fig. 6.7(b) is that it is independent of D_z. Therefore, identical predictions for switching are obtained for problems with any value of D_z, provided that the anisotropy field $\mathrm{h}_{AN} = D_y - D_x$ is the same. In particular, this means that the results obtained above are valid not only for the longitudinal media shown in Fig. 6.5(a), but also for perpendicular media (Fig. 6.5(b)), where the thin-film easy axis $\mathbf{e}_x$ is perpendicular to the film plane and $D_z \simeq D_y \ll 1$. The precessional switching of perpendicular media may be very appealing from the technological point of view, because this type of switching can be accomplished without the use of "probe" heads, but rather by using the same heads as in longitudinal recording. This also means that recording media without soft magnetic underlayers could be utilized.

6.3 FIELD-PULSE DURATION FOR PRECESSIONAL SWITCHING

When the applied field is above the critical field corresponding to the boundary of the shaded regions shown in Fig. 6.7(b), switching can be accomplished under the condition that the field pulse duration is appropriately chosen. According to Fig. 6.6(b), switching is achieved only if the applied field is switched off in the time interval corresponding to the magnetization motion from point 2 to point 3 and back. Let us assume that the applied field is switched on at $t = 0$ and let us denote by (t_{in}, t_{fin}) the time interval in which the field should be switched off. It has been shown

in Chapter 4 that the equation describing the precessional dynamics can be transformed into the form:

$$\frac{\mathrm{d}u}{\sqrt{1-(a_x-p\cos u)^2-(a_y+(p/k)\sin u)^2}} = k\,(D_z-D_x)\,\mathrm{d}t, \quad (6.28)$$

where a_x, a_y, p, and k have been previously defined (see Eqs (4.7)–(4.10)). By integrating this equation, we derive:

$$t_{in} = \frac{1}{k\,(D_z-D_x)} \times \int_{u_0}^{u_2} \frac{\mathrm{d}u}{\sqrt{1-(a_x-p\cos u)^2-(a_y+(p/k)\sin u)^2}}, \quad (6.29)$$

$$t_{fin} = t_{in} + \frac{2}{k\,(D_z-D_x)} \times \int_{u_2}^{u_3} \frac{\mathrm{d}u}{\sqrt{1-(a_x-p\cos u)^2-(a_y+(p/k)\sin u)^2}}, \quad (6.30)$$

where u_0, u_2, and u_3 correspond to points 0, 2, and 3 in Fig. 6.6(b), respectively. These values of u are obtained by calculating m_x corresponding to points 2 and 3 from Eq. (6.12) and then substituting the result in Eq. (4.11) from Chapter 4. As discussed in that chapter, the integrals in Eqs (6.29) and (6.30) can be reduced to elliptic integrals. In general, these derivations can be quite involved. For this reason, direct numerical evaluation of these integrals can be preferable.

In the case of perpendicular media (see Fig. 6.5(b)), the calculation of the field pulse duration becomes simpler. Indeed, the fact that $D_z - D_y = 0$ implies that the ellipse Γ in Figure 6.6(b) is reduced to the line $\mathrm{m}_x = 0$. This means that the low-energy region surrounding the reversed state $\mathrm{m}_x = -1$ coincides with the entire hemisphere $\mathrm{m}_x \leq 0$. On the other hand, in the limit of $D_z - D_y \to 0$, the LLG equation for m_x (see Eq. (6.2)) can be written as follows:

$$\frac{\mathrm{d}\mathrm{m}_x}{\mathrm{d}t} = \mathrm{h}_{ay}\mathrm{m}_z. \quad (6.31)$$

By using the formula for the system free energy and the condition $\mathrm{m}_x^2 + \mathrm{m}_y^2 + \mathrm{m}_z^2 = 1$, one can express m_z^2 as a fourth-order polynomial in m_x. Hence, the bounds for the time interval (t_{in}, t_{fin}) in which the applied field must be switched off are given by the following integrals

with respect to m_x:

$$t_{in} = \int_0^1 \frac{\mathrm{dm}_x}{|\mathrm{h}_{ay}\mathrm{m}_z(\mathrm{m}_x)|}, \tag{6.32}$$

$$t_{fin} = t_{in} - 2\int_0^{m_{x3}} \frac{\mathrm{dm}_x}{|\mathrm{h}_{ay}\mathrm{m}_z(\mathrm{m}_x)|}, \tag{6.33}$$

where m_{x3} is the value of m_x corresponding to point 3 in Fig. 6.7(b).

Next, we consider the particular case where the field is applied along the y direction. Under these conditions, all the details of the magnetization dynamics driven by the field pulse are known from the exact analytical solution obtained in Chapter 4. The time dynamics of the magnetization components is given by Eqs (4.76)–(4.78) from that chapter, provided that the value $g_0 = D_x/2$ (see Eq. (6.6)) is used in all energy-dependent parameters. As a result of symmetry, the trajectory originating from $\mathrm{m}_x = 1$ runs through the reversed state $\mathrm{m}_x = -1$. The state $\mathrm{m}_x = -1$ is reached after the time interval:

$$T_{ps} = \frac{2\boldsymbol{K}(k_I)}{\Omega_I}, \tag{6.34}$$

where $\boldsymbol{K}(k_I)$ represents the complete elliptic integral of the first kind, while k_I and Ω_I are defined by Eqs (4.73) and (4.74) from Chapter 4, respectively. The expressions for these quantities can be simplified in our case where $g_0 = D_x/2$ and $p^2 = 1 + k^2 a_y^2$. The simplified expressions are:

$$k_I^2 = \frac{k'^2}{k^2}\frac{(\nu-1)(\nu+1+2k^2/k'^2)}{4\nu}, \qquad \Omega_I = |\mathrm{h}_{ay}|\sqrt{\nu}, \qquad \nu^2 = 1 + \frac{1}{k^2 a_y^2}. \tag{6.35}$$

A field pulse of duration T_{ps} brings the magnetization exactly to the final reversed state $\mathrm{m}_x = -1$. In this sense, T_{ps} represents the "ideal switching time" for the case of y-directed field. Figure 6.9 shows the field dependence of the inverse switching time $1/T_{ps}$ computed by using Eq. (6.34) for different anisotropy fields. The switching time becomes increasingly longer when the field approaches the critical value $\mathrm{h}_{AN}/2$. For fields much larger than the critical field, the dependence of $1/T_{ps}$ on h_{ay} becomes approximately linear. It is worth recalling that T_{ps} is a dimensionless quantity, expressed in units of $(\gamma \mathrm{M}_s)^{-1}$. As an example,

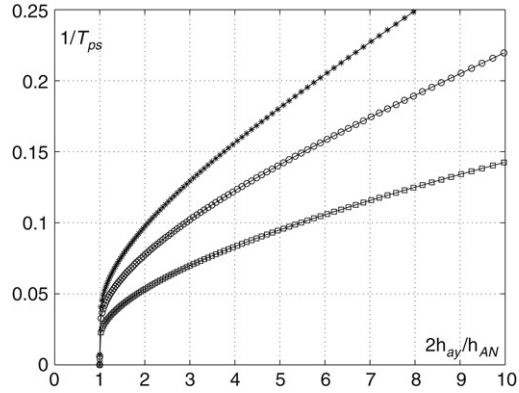

FIGURE 6.9 Inverse switching time $1/T_{ps}$ versus ratio $2\mathrm{h}_{ay}/\mathrm{h}_{AN}$, calculated by using Eqs (6.34) and (6.35) for a thin-film element with $D_y = 0$, $D_z = 1$. "□": $\mathrm{h}_{AN} = 0.05$; "∘": $\mathrm{h}_{AN} = 0.1$; "∗": $\mathrm{h}_{AN} = 0.15$. T_{ps} is measured in units of $(\gamma \mathrm{M}_s)^{-1}$.

$T_{ps} \approx 10$ represents a physical switching time on the order of 100 ps in a material for which $\gamma \mathrm{M}_s \approx 10^{11}\,\mathrm{s}^{-1}$.

Formulas (6.35) can be simplified for perpendicular media. In fact, when $D_z - D_y \to 0$, one has that $k^2 \to 0$, $k'^2 \to 1$, $k^2 a_y^2 \to \infty$, $\nu \to 1$, and $k^4 a_y^2 \to \mathrm{h}_{ay}^2/\mathrm{h}_{AN}^2$. As a result, we obtain:

$$k_I^2 = \frac{(\mathrm{h}_{AN}/2)^2}{\mathrm{h}_{ay}^2}, \qquad \Omega_I = |\mathrm{h}_{ay}|. \tag{6.36}$$

Figure 6.10 presents the field dependence of $1/T_{ps}$ for perpendicular media, computed by using Eqs (6.34) and (6.36). In this case, the linear dependence of $1/T_{ps}$ on h_{ay} is particularly evident. This can be explained by observing that, according to Eq. (6.36), $k_I^2 \ll 1$ when $\mathrm{h}_{ay} \gg \mathrm{h}_{AN}$, so $\boldsymbol{K}(k_I) \simeq \pi/2$ and Eq. (6.34) is reduced to:

$$\frac{1}{T_{ps}} \simeq \frac{|\mathrm{h}_{ay}|}{\pi}. \tag{6.37}$$

In our discussion, energy dissipation has been completely neglected in the analytical treatment of precessional switching. It is therefore instructive to illustrate through an example the accuracy of this approximation. Figure 6.11 presents the comparison between the

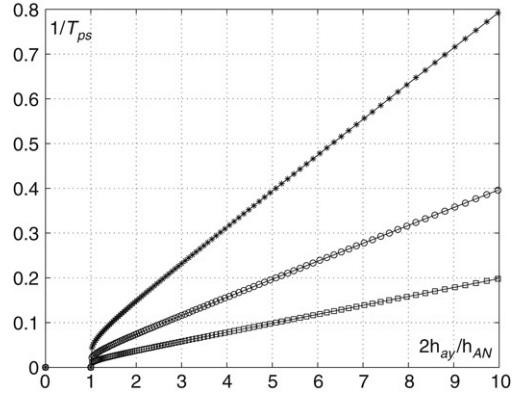

FIGURE 6.10 Inverse switching time $1/T_{ps}$ versus ratio $2\mathrm{h}_{ay}/\mathrm{h}_{AN}$, calculated by using Eqs (6.34) and (6.36) for perpendicular media with $D_y = D_z$. "□": $\mathrm{h}_{AN} = 0.125$; "∘": $\mathrm{h}_{AN} = 0.25$; "∗": $\mathrm{h}_{AN} = 0.5$. T_{ps} is measured in units of $(\gamma \mathrm{M}_s)^{-1}$.

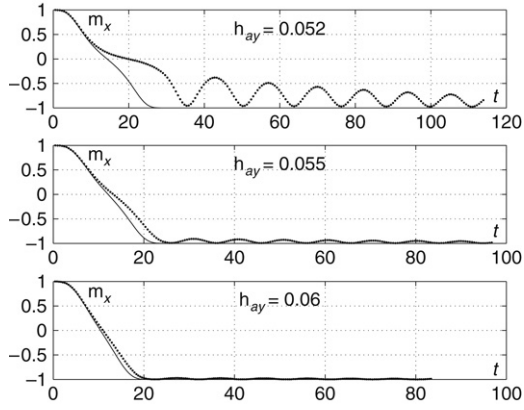

FIGURE 6.11 Plots of m_x versus t during precessional switching induced by a rectangular field pulse of duration T_{ps} for various applied fields h_{ay}. Continuous line: analytical solution of conservative dynamics; dots: numerical integration of LLG equation for $\alpha = 0.01$. Parameter values: $D_x = -0.1$, $D_y = 0$, $D_z = 1$. Critical switching field is $\mathrm{h}_{ay} = \mathrm{h}_{AN}/2 = 0.05$. Time is measured in units of $(\gamma \mathrm{M}_s)^{-1}$.

switching dynamics of m_x predicted analytically under the assumption $\alpha = 0$ and computed by numerical integration of LLG equation for

$\alpha = 0.01$. In this example, the applied field values are fairly close to the critical field $h_{AN}/2 = 0.05$. This has been done deliberately, because under this condition the analytical treatment is expected to be less accurate. It is apparent from the figure that when the field is switched off, the analytical solution for the purely precessional dynamics is at the reversed state $m_x = -1$, as expected by construction. In contrast, the solution for the dissipative dynamics exhibits extra oscillations which are particularly evident for $h_{ay} = 0.052$, i.e., when the field is quite close to the critical value. However, a slight increase in the applied field is sufficient to suppress these oscillations. For $h_{ay} = 0.06$, the nonconservative and conservative dynamics are very close and no substantial error is introduced by neglecting damping.

In conclusion of this section, we shall give a brief comparative analysis of precessional and damping switching of perpendicular media. It was previously emphasized that in the case of precessional switching the field pulse duration must be carefully tuned, that is, complete switching is achieved only if the field is switched off in a certain time-window. No such timing is required for damping switching, because any field pulse of duration exceeding the minimum time T_{ds} will lead to magnetization switching. In this sense, precessional switching is more difficult to realize. On the other hand, it has clear advantages in comparison with damping switching. Namely, the critical field is lower and the switching time is appreciably shorter, as it can be inferred from Fig. 6.10 and Fig. 5.3 from Chapter 5. It is instructive to compare switching times for precessional and damping switching for the same value of the ratio r_c between applied fields and corresponding critical fields. The ratio T_{ps}/T_{ds} can be expressed in the form:

$$\frac{T_{ps}}{T_{ds}} = \frac{\alpha}{1+\alpha^2} F(r_c), \tag{6.38}$$

where the function $F(r_c)$ is obtained from Eqs (6.34), (6.36) and (5.18) from Chapter 5, with the tacit understanding that $T_{ds} \simeq \tau$. The graph of the function $F(r_c)$ is shown in Fig. 6.12 for different values of the angle θ_0 involved in damping switching. It is clear from this figure and Eq. (6.38) that precessional switching is (for $\alpha \ll 1$) approximately $1/\alpha$ times faster than damping switching. For applied fields close to their respective critical fields (i.e., r_c close to 1), this difference is even more pronounced.

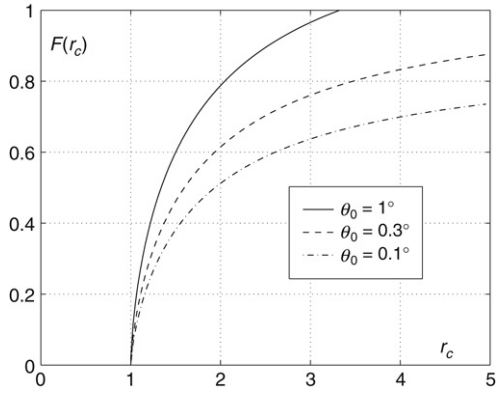

FIGURE 6.12 Comparison between precessional and damping-switching times. Plot of the function $F(r_c) = T_{ps}/T_{ds}$ versus the ratio r_c between applied field and corresponding critical field. The function is plotted for different values of the initial angle θ_0 characterizing damping switching. Continuous line: $\theta_0 = 1^\circ$; dashed line: $\theta_0 = 0.3^\circ$; dash-dotted line: $\theta_0 = 0.1^\circ$.

6.4 SWITCHING UNDER NONRECTANGULAR FIELD PULSES (INVERSE-PROBLEM APPROACH)

One of the central problems in the research on precessional switching is the design of magnetic field pulses that will guarantee the magnetization reversal. In the literature, this problem has been mostly addressed experimentally or numerically by using a trial-and-error approach. In the previous section, the design of magnetic field pulses has been discussed only for the case of rectangular pulses, which is a clear limitation. In this section, the "inverse-problem" approach is developed that leads to explicit expressions for nonrectangular magnetic field pulses that guarantee the precessional switching. The inverse nature of the approach is reflected in the fact that, instead of deriving the magnetization dynamics for an assigned magnetic field time variation, this magnetic field time-variation is determined on the basis of the desired switching dynamics.

We shall develop the inverse-problem approach for the case of a thin film with in-plane anisotropy along the x axis (see Fig. 6.5(a)). The analysis can be extended to more general cases by following a similar line of reasoning. If the film thickness is much smaller than its lateral dimensions, then it can be assumed that $D_x < 0$, $D_y = 0$, $D_z = 1$, and the anisotropy field is $\mathrm{h}_{AN} = -D_x$. We will consider the case where the field is applied along the y axis. Under these circumstances, the effective field can be

written in the form:

$$\mathbf{h}_{\text{eff}} = -D_x \mathrm{m}_x \mathbf{e}_x + \mathrm{h}_{ay}(t)\mathbf{e}_y - \mathrm{m}_z \mathbf{e}_z. \tag{6.39}$$

As in previous sections, it will be assumed that the switching dynamics is so fast that dissipative effects can be neglected and the switching process can be studied by using the conservative LLG equation (6.2). Our purpose is to find such a field pulse $\mathrm{h}_{ay}(t)$ that will guarantee the desired precessional switching of the magnetization from its initial equilibrium state $\mathbf{m} = -\mathbf{e}_x$ to the final reversed state $\mathbf{m} = \mathbf{e}_x$. This implies that the desired monotonic dynamics of $\mathrm{m}_x(t)$ between the equilibrium points $\mathrm{m}_x = -1$ and $\mathrm{m}_x = 1$ can be chosen and then the dynamic equation (6.2) must be used to find the appropriate $\mathrm{h}_{ay}(t)$. This can be accomplished as follows. Equation (6.2) is first written for the cartesian components of magnetization and the integral of motion $|\mathbf{m}|^2 = 1$ is then used instead of the equation for $\mathrm{d}\mathrm{m}_z/\mathrm{d}t$. This leads to the following coupled equations:

$$\frac{\mathrm{d}\mathrm{m}_x}{\mathrm{d}t} = (\mathrm{m}_y + \mathrm{h}_{ay})\mathrm{m}_z, \tag{6.40}$$

$$\frac{\mathrm{d}\mathrm{m}_y}{\mathrm{d}t} = -(1 - D_x)\mathrm{m}_x \mathrm{m}_z, \tag{6.41}$$

$$\mathrm{m}_x^2 + \mathrm{m}_y^2 + \mathrm{m}_z^2 = 1. \tag{6.42}$$

From Eqs (6.41) and (6.42) we derive:

$$\frac{\mathrm{d}\mathrm{m}_y}{\mathrm{d}t} = -(1 - D_x)\mathrm{m}_x(t)\sqrt{1 - \mathrm{m}_x^2(t) - \mathrm{m}_y^2(t)}, \tag{6.43}$$

where the positive sign of the square root (i.e., of m_z) is chosen. As soon as the desired dynamics of $\mathrm{m}_x(t)$ which leads to the precessional switching of magnetization is chosen, Eq. (6.43) can be treated as a differential equation with respect to $\mathrm{m}_y(t)$. By solving this equation with zero initial condition, $\mathrm{m}_y(t)$ can be found. Then, from Eq. (6.40) we can recover the pulsed magnetic field:

$$\mathrm{h}_{ay}(t) = \frac{1}{\sqrt{1 - \mathrm{m}_x^2(t) - \mathrm{m}_y^2(t)}} \frac{\mathrm{d}\mathrm{m}_x}{\mathrm{d}t} - \mathrm{m}_y(t). \tag{6.44}$$

This pulse will guarantee the desired precessional switching. The described approach is straightforward because it is always easy to choose such a function $\mathrm{m}_x(t)$ that guarantees the precessional switching.

However, this approach requires numerical integration of Eq. (6.43) and does not lead to the explicit analytical expressions for $\mathrm{h}_{ay}(t)$. It turns out that there exists an alternative approach that exploits the fact that the applied field appears only in Eq. (6.40). This approach is purely algebraic in nature and can be preferable as far as explicit expressions for $\mathrm{h}_{ay}(t)$ are concerned. The essence of this approach can be explained as follows. The dynamics of $\mathrm{m}_y(t)$ which leads to the precessional switching must be first chosen. Then, by using Eqs (6.41) and (6.42), $\mathrm{m}_x(t)$ and $\mathrm{m}_z(t)$ are computed. Afterwards, the pulsed magnetic field $\mathrm{h}_{ay}(t)$ is found from Eq. (6.40). The main difficulty with this approach is the choice of the appropriate $\mathrm{m}_y(t)$ that guarantees the precessional switching. Next, it is discussed how this difficulty can be circumvented.

By assuming that $\mathrm{m}_y(t)$ is known, Eqs (6.41) and (6.42) can be treated as algebraic equations with respect to $\mathrm{m}_x(t)$ and $\mathrm{m}_z(t)$. By eliminating $\mathrm{m}_z(t)$ from Eqs (6.41) and (6.42), we arrive at the following equation for $\mathrm{m}_x(t)$:

$$\mathrm{m}_x^4 - (1 - \mathrm{m}_y^2)\mathrm{m}_x^2 + \frac{1}{(1 - D_x)^2}\left(\frac{\mathrm{d}\mathrm{m}_y}{\mathrm{d}t}\right)^2 = 0. \tag{6.45}$$

Equations (6.41) and (6.42) are symmetric with respect to $\mathrm{m}_x(t)$ and $\mathrm{m}_z(t)$. This implies that Eq. (6.45) is valid for $\mathrm{m}_z(t)$ as well. Therefore, we find:

$$\mathrm{m}_{x,z}^2 = \frac{1}{2}\left(1 - \mathrm{m}_y^2 \pm \sqrt{\left(1 - \mathrm{m}_y^2\right)^2 - \frac{4}{(1 - D_x)^2}\left(\frac{\mathrm{d}\mathrm{m}_y}{\mathrm{d}t}\right)^2}\right). \tag{6.46}$$

Thus, there are "positive" and "negative" solutions (branches) of Eq. (6.45) that correspond to the $\pm$ signs in Eq. (6.46), respectively. It is apparent that different branches in Eq. (6.46) should be identified with $\mathrm{m}_x(t)$ and $\mathrm{m}_z(t)$. At the beginning of precessional switching, this identification is performed on the basis of the initial conditions:

$$\mathrm{m}_x(-T/2) = -1, \qquad \mathrm{m}_z(-T/2) = 0, \tag{6.47}$$

where it is assumed that the precessional switching is accomplished during the time interval $[-T/2, T/2]$. From Eqs (6.41) and (6.47) it follows that:

$$\frac{\mathrm{d}\mathrm{m}_y}{\mathrm{d}t}(-T/2) = 0. \tag{6.48}$$

It is clear from Eqs (6.47) and (6.48) that at the beginning of the precessional switching $\mathrm{m}_x(t)$ must be identified with the positive branch of Eq. (6.46), while the negative branch corresponds to $\mathrm{m}_z(t)$. Now, we shall discuss the conditions on $\mathrm{m}_y(t)$ that guarantee the precessional switching. To this end, we consider the discriminant:

$$\Delta(t) = \left[1 - \mathrm{m}_y^2(t)\right]^2 - \frac{4}{(1 - D_x)^2}\left(\frac{\mathrm{dm}_y}{\mathrm{d}t}\right)^2. \tag{6.49}$$

Equations (6.46) and (6.49) show that those $\mathrm{m}_y(t)$ for which $\Delta(t) < 0$ at some instant of time are not physically realizable. It is also apparent that those $\mathrm{m}_y(t)$ for which $\Delta(t)$ is strictly positive do not correspond to the precessional switching. Indeed, if $\Delta(t) > 0$ then the positive and negative branches in Eq. (6.46) are separated. Since $\mathrm{m}_x(t)$ is a continuous function of t and it is identified with the positive branch of Eq. (6.46) at the beginning of magnetization dynamics, it must be identified with this branch at all instants of time. Then, according to Eq. (6.46), $\mathrm{m}_x^2(t)$ is strictly positive and cannot reach zero and, consequently, no precessional switching may occur. Next, we state the following criterion for precessional switching.

- If $\mathrm{m}_y(t)$ is such that $\Delta(t) \geq 0$ and the equation $\Delta(t) = 0$ has an odd number of solutions before the negative branch of Eq. (6.46) reaches zero, the precessional switching will occur.

We shall provide the demonstration for the simplest case of "symmetric" switching where $\mathrm{h}_{ay}(t)$ and $\mathrm{m}_y(t)$ are even functions of time in $[-T/2, T/2]$, and the equation $\Delta(t) = 0$ has one solution t_0 in $[-T/2, 0]$ (see Fig. 6.13). According to Eqs (6.46) and (6.49), at time t_0 the positive and negative branches are not continuously differentiable. Indeed, by differentiating Eq. (6.46) and taking into account Eq. (6.49), we derive:

$$\mathrm{m}_{x,z}(t)\frac{\mathrm{dm}_{x,z}}{\mathrm{d}t}(t) = \frac{1}{4}p'(t) \pm \frac{1}{8}\frac{\Delta'(t)}{\sqrt{\Delta(t)}}, \tag{6.50}$$

where $p(t) = 1 - \mathrm{m}_y^2(t)$. By using Taylor expansions for $\Delta(t)$ and $\Delta'(t)$ around t_0, we find:

$$\Delta(t) \simeq \Delta(t_0) + \Delta'(t_0)(t - t_0) + \frac{\Delta''(t_0)}{2}(t - t_0)^2, \tag{6.51}$$

$$\Delta'(t) \simeq \Delta'(t_0) + \Delta''(t_0)(t - t_0). \tag{6.52}$$

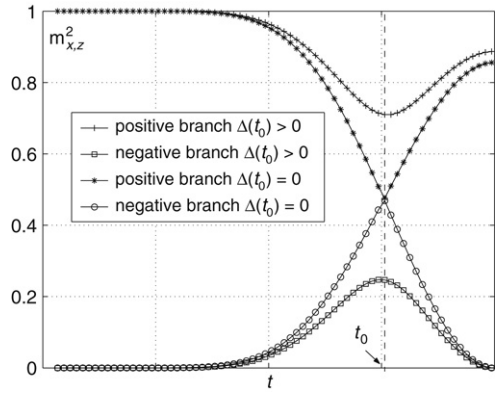

FIGURE 6.13 Positive and negative branches of Eq. (6.46). Two cases are represented which correspond to two different choices of $m_y(t)$. In the first case $\Delta(t) > 0$ (symbols "+" and "□" for the positive and negative branches, respectively); in the second case $\Delta(t) \geq 0$ and zero is attained at $t = t_0$ (symbols "$*$" and "$\circ$" for the positive and negative branches, respectively).

Since $\Delta(t)$ is nonnegative and reaches zero at $t = t_0$, this means that:

$$\Delta(t_0) = 0, \qquad \Delta'(t_0) = 0, \tag{6.53}$$

and:

$$\Delta(t) \simeq \frac{\Delta''(t_0)}{2}(t - t_0)^2, \tag{6.54}$$

$$\Delta'(t) \simeq \Delta''(t_0)(t - t_0). \tag{6.55}$$

From Eqs (6.54) and (6.55), we conclude that:

$$\lim_{t \to t_0^-} \frac{\Delta'(t)}{\sqrt{\Delta(t)}} = -\sqrt{2\Delta''(t_0)}, \tag{6.56}$$

while:

$$\lim_{t \to t_0^+} \frac{\Delta'(t)}{\sqrt{\Delta(t)}} = \sqrt{2\Delta''(t_0)}. \tag{6.57}$$

From formulas (6.50), (6.56) and (6.57), we obtain:

$$\mathrm{m}_{x,z}(t_0)\frac{\mathrm{dm}_{x,z}}{\mathrm{d}t}(t_0^-) = \frac{1}{4}p'(t_0) \pm \left(-\frac{1}{4}\sqrt{\frac{\Delta''(t_0)}{2}}\right), \tag{6.58}$$

$$\mathrm{m}_{x,z}(t_0)\frac{\mathrm{dm}_{x,z}}{\mathrm{d}t}(t_0^+) = \frac{1}{4}p'(t_0) \pm \left(+\frac{1}{4}\sqrt{\frac{\Delta''(t_0)}{2}}\right), \tag{6.59}$$

where $\mathrm{dm}_{x,z}/\mathrm{d}t(t_0^-)$ and $\mathrm{dm}_{x,z}/\mathrm{d}t(t_0^+)$ are the limits from "below" and "above" t_0, respectively.

Equations (6.58) and (6.59) show that positive and negative branches of Eq. (6.46) are not continuously differentiable at $t = t_0$ (see Fig. 6.13), and consequently these branches cannot be identified with $\mathrm{m}_x(t)$ and $\mathrm{m}_z(t)$ on the entire time interval $[-T/2, 0]$. It is also clear from Eqs (6.58) and (6.59) that the negative branch for $t > t_0$ is a continuously differentiable extension of the positive branch for $t < t_0$ and vice versa (Fig. 6.13). Thus, $\mathrm{m}_x(t)$ can be identified with the positive branch for $-T/2 \le t \le t_0$ and with the negative branch for $t_0 < t < 0$. Since $\mathrm{m}_y(t)$ is a continuously differentiable even function, $\mathrm{dm}_y/\mathrm{d}t(0) = 0$. Hence, according to Eq. (6.46), the negative branch as well as $\mathrm{m}_x(t)$ reach zero at $t = 0$. For the time interval $[0, T/2]$, $\mathrm{m}_x(t)$ is the odd function extension of $\mathrm{m}_x(t)$ in the time interval $[-T/2, 0]$, and this is tantamount to the precessional switching. In the previous reasoning, it was tacitly assumed that $\Delta''(t) \neq 0$. However, the reasoning can be easily modified for the case $\Delta''(t) = 0$, because the first nonzero derivative of $\Delta(t)$ at $t = t_0$ is of even order. The latter is the consequence of the fact that $\Delta(t)$ is nonnegative and assumes its minimum zero value at $t = t_0$.

Thus, we have found the conditions on $\mathrm{m}_y(t)$ in terms of $\Delta(t)$ that result in the precessional switching. From Eqs (6.40) and (6.46), the applied magnetic field corresponding to this switching is given by:

$$\begin{aligned}\mathrm{h}_{ay}(t) = &-\frac{D_x + 1}{2}\mathrm{m}_y \\ &\pm \frac{1 - D_x}{2\sqrt{\Delta(t)}}\left[(1 - \mathrm{m}_y^2)\mathrm{m}_y + \frac{2}{(1 - D_x)^2}\frac{\mathrm{d}^2\mathrm{m}_y}{\mathrm{d}t^2}\right],\end{aligned} \tag{6.60}$$

where $\Delta(t)$ is given by Eq. (6.49), the sign "+" must be taken in the intervals $-T/2 < t < -|t_0|$ and $|t_0| < t < T/2$, while the sign "−" must be taken in the interval $-|t_0| < t < +|t_0|$. We observe that this inverse-problem approach generates exact analytical solutions to the

Landau–Lifshitz equation for various magnetic field pulses; this fact is of interest in its own right.

Next, we present a technique that helps to choose $\mathrm{m}_y(t)$ in such a way that the conditions for precessional switching are satisfied. To this end, consider the set of functions:

$$\mathrm{m}_y(t) = bf(t), \tag{6.61}$$

depending on the parameter $b \in [0, 1]$. It is assumed that $f(t)$ is even on $[-T/2, T/2]$, and $f(0) = 1$. From the initial conditions (6.47), it follows that $f(-T/2) = 0$. It turns out that there exists only one value of b such that $\Delta(t) \geq 0$ on $[-T/2, 0]$ and one zero is attained in this interval. The proof proceeds as follows. By using Eq. (6.49), we find that the inequality $\Delta(t) \geq 0$ is equivalent to:

$$1 - \mathrm{m}_y^2(t) \geq \frac{2}{1 - D_x} \left| \frac{\mathrm{d}\mathrm{m}_y(t)}{\mathrm{d}t} \right|, \tag{6.62}$$

which can then be written as follows:

$$\mathrm{m}_y^2(t) + \frac{2}{1 - D_x} \left| \frac{\mathrm{d}\mathrm{m}_y(t)}{\mathrm{d}t} \right| - 1 \leq 0. \tag{6.63}$$

According to Eqs (6.49) and (6.61), the previous assertion is equivalent to the existence of a unique solution for the following equation:

$$F(b) = \max_{t \in [-T/2, 0]} \left\{ b^2 f^2(t) + \frac{2b}{1 - D_x} |f'(t)| - 1 \right\} = 0. \tag{6.64}$$

The function $F(b)$ is a continuous and monotonically increasing function of b and, due to the definition of $f(t)$, we have:

$$F(b) > b^2 + \frac{2b}{1 - D_x} |f'(0)| - 1. \tag{6.65}$$

This implies that:

$$\lim_{b \to 0} F(b) = -1, \qquad \lim_{b \to 1} F(b) \geq 0. \tag{6.66}$$

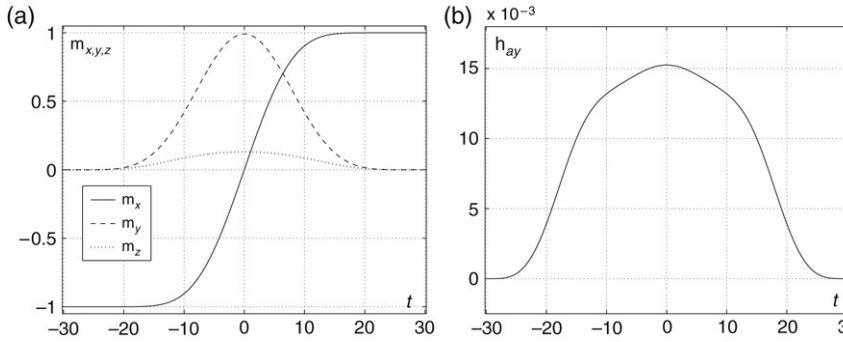

FIGURE 6.14 Plots of magnetization and applied field computed by the inverse approach. (a) Chosen time variation of $\mathrm{m}_y(t)$ (dashed line) and corresponding time variations of $\mathrm{m}_x(t)$ (solid line) and $\mathrm{m}_z(t)$(dotted line), computed by using Eq. (6.46). (b) Applied field pulse computed by means of Eq. (6.60). The function $\mathrm{m}_y(t)$ has the form specified in Eq. (6.68), with $\delta = 3$, $T = 58.03$, and $b = 1.239{,}2179 \cdot 10^{-1}$. The value of b was obtained by finding the zero of Eq. (6.64) by bisection method. Anisotropy field is $\mathrm{h}_{AN} = 0.008$ ($D_x = -0.008$). Time is measured in units of $(\gamma \mathrm{M}_s)^{-1}$.

Thus, there is only one solution for Eq. (6.64) and, consequently, there is only one b that satisfies our assertion. This b can be found by solving the one-dimensional nonlinear equation (6.64).

It is instructive to give an example of pulse design by using the inverse-problem approach. Consider a magnetic thin film with $\mathrm{h}_{AN} = 0.008$. The function $f(t)$ is chosen as follows:

$$f(t) = \frac{1}{2^\delta}(1 + \cos(2\pi t/T))^\delta. \tag{6.67}$$

It is apparent that $f(t)$ is even and $f(0) = 1$, as well as $f(-T/2) = 0$ and $f'(-T/2) = 0$ for $\delta > 1$. According to Eq. (6.61), we have:

$$\mathrm{m}_y(t) = \frac{b}{2^\delta}(1 + \cos(2\pi t/T))^\delta. \tag{6.68}$$

Here δ and T are parameters that can be used to control the pulse shape. In the present example, they have been chosen as follows: $\delta = 3$ and $T = 58.03$, which corresponds to a pulse duration of $300\,\mathrm{ps}$ in a permalloy-type material with $\mu_0 \mathrm{M}_s = 1.1\ \mathrm{T}$. The parameter b is then determined by solving Eq. (6.64). Figure 6.14(a) shows the time dynamics of the three

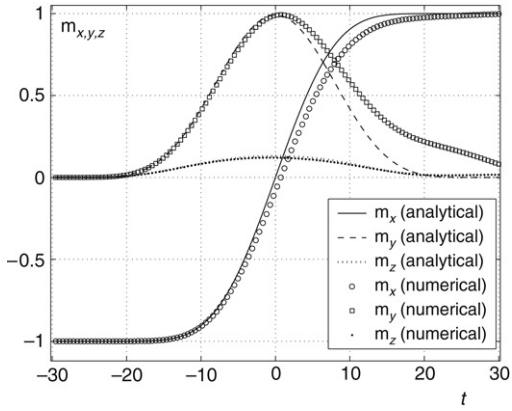

FIGURE 6.15 Comparison between analytically and numerically computed precessional switching under nonrectangular field pulse. The analytical conservative solutions (solid, dashed and dotted lines) are the same as in Fig. 6.14(a). The numerical solutions (symbols) were computed by using the field pulse shape shown in Fig. 6.14(b) and $\alpha = 0.01$. All the other parameters are the same as in Fig. 6.14.

components of $\mathbf{m}$ computed by the inverse approach. The corresponding time variation of the applied field $\mathrm{h}_{ay}(t)$ computed by using Eq. (6.60) is shown in Fig. 6.14(b). In order to check the accuracy of the inverse-problem approach, we have computed the numerical solutions to the LLG equation for the found field $\mathrm{h}_{ay}(t)$ and $\alpha = 0.01$. Figure 6.15 presents the comparison between the analytically computed conservative dynamics and the numerically computed dissipative dynamics. These results confirm that dissipative effects can be neglected for the design of the magnetic field pulses leading to precessional switching.

CHAPTER 7

Magnetization Dynamics under Time-Harmonic Excitation

7.1 LLG DYNAMICS IN THE PRESENCE OF ROTATIONAL INVARIANCE

This chapter deals with the analytical study of magnetization dynamics driven by time-harmonic magnetic fields. Traditionally, this study has been concerned with ferromagnetic resonance problems, when the main part of magnetization is pinned by a strong dc field while only a small transverse component of magnetization executes resonance motions caused by ac magnetic fields. These small magnetization motions are studied by linearizing the LLG equation. For this reason, the literature on analytical studies of magnetization dynamics is mostly concerned with the linearized LLG equation. In contrast, the main focus of this chapter is to find analytical solutions to the LLG equation for large magnetization motions. This is accomplished by exploiting the rotational symmetry of certain classes of magnetization dynamics problems.

To start the discussion, consider a spheroidal particle with spatially uniform magnetization $\mathbf{m}(t)$. The symmetry axis of the particle will be assumed to coincide with the z axis. As discussed in Chapter 3, the magnetostatic (demagnetizing) field $\mathbf{h}_M$ is spatially uniform inside the spheroidal particle when the magnetization is spatially uniform. This field can be expressed as follows:

$$\mathbf{h}_M = -N_z \mathbf{m}_z - N_\perp \mathbf{m}_\perp, \tag{7.1}$$

where $\mathbf{m}_z$ and $\mathbf{m}_\perp$ are the magnetization components along the z axis and in the plane perpendicular to it, respectively. The demagnetizing factors N_z and $N_\perp$ satisfy the relation:

$$N_z + 2N_\perp = 1. \tag{7.2}$$

We shall further assume that all particle properties are invariant with respect to rotations around the z axis. This means that the damping parameter α is a state function which is invariant with respect to rotations around the z axis, whereas crystal anisotropy is uniaxial, with the anisotropy axis along the z direction. We shall measure crystal anisotropy by the dimensionless parameter $\kappa = 2K_1/\mu_0 \mathrm{M}_s^2$, where K_1 is the physical anisotropy constant. Therefore, the anisotropy field is equal to (compare with Eq. (3.8)):

$$\mathbf{h}_{AN} = \kappa \mathrm{m}_z \mathbf{e}_z. \tag{7.3}$$

Finally, we assume that the external magnetic field consists of two distinct components: the dc magnetic field $\mathrm{h}_{az}\mathbf{e}_z$ directed along the symmetry axis and the circularly polarized radio-frequency magnetic field $\mathbf{h}_{a\perp}(t)$ in the plane perpendicular to the symmetry axis, that is:

$$\mathbf{h}_a(t) = \mathbf{h}_{a\perp}(t) + \mathrm{h}_{az}\mathbf{e}_z, \tag{7.4}$$

where:

$$\mathbf{h}_{a\perp}(t) = \mathrm{h}_{a\perp}\left(\mathbf{e}_x \cos\omega t + \mathbf{e}_y \sin\omega t\right), \tag{7.5}$$

and $(\mathbf{e}_x, \mathbf{e}_y)$ are mutually orthogonal unit vectors in the $\perp$-plane. Under these conditions, the effective field can be written as follows:

$$\mathbf{h}_{\text{eff}} = \mathbf{h}_{a\perp} + \left(\mathrm{h}_{az} + \kappa_{\text{eff}}\mathrm{m}_z\right)\mathbf{e}_z - N_\perp \mathbf{m}, \tag{7.6}$$

where:

$$\kappa_{\text{eff}} = \kappa + N_\perp - N_z. \tag{7.7}$$

The free energy $g_L\left(\mathbf{m};\mathbf{h}_a\right)$ corresponding to the effective field (7.6) is:

$$g_L\left(\mathbf{m};\mathbf{h}_a\right) = \frac{1}{2}\left(N_z \mathrm{m}_z^2 + N_\perp \mathrm{m}_\perp^2\right) - \frac{1}{2}\kappa \mathrm{m}_z^2 - \mathbf{h}_a \cdot \mathbf{m}. \tag{7.8}$$

As before, the energy $g_L\left(\mathbf{m};\mathbf{h}_a\right)$ is expressed in units of $\mu_0 \mathrm{M}_s^2 V$, where V is the volume of the particle.

The magnetization dynamics will be studied by using the LLG equation (3.9):

$$\frac{\mathrm{d}\mathbf{m}}{\mathrm{d}t} - \alpha\mathbf{m} \times \frac{\mathrm{d}\mathbf{m}}{\mathrm{d}t} = -\mathbf{m} \times \mathbf{h}_{\text{eff}}, \tag{7.9}$$

where $\mathbf{h}_{\text{eff}}$ is given by Eq. (7.6). The magnetic system under study is characterized by the parameters $(\alpha, \kappa_{\text{eff}})$, while the excitation conditions are described by the control parameters $(\omega, \mathrm{h}_{az}, \mathrm{h}_{a\perp})$.

The dynamics on the unit sphere described by Eq. (7.9) is not autonomous, because $\mathbf{h}_{\text{eff}}$ explicitly depends on time through the external field $\mathbf{h}_{a\perp}(t)$. However, the complications due to the nonautonomous nature of the dynamics can be circumvented by taking advantage of the rotational symmetry of the problem. This becomes evident when one considers the form of Eq. (7.9) in the rotating frame of reference in which the external field is stationary. In the frame which is rotated at the angular frequency ω around the $\mathbf{e}_z$ axis, the magnetization derivative is transformed as follows:

$$\left[\frac{\mathrm{d}\mathbf{m}}{\mathrm{d}t}\right]_{\text{lab.frame}} = \left[\frac{\mathrm{d}\mathbf{m}}{\mathrm{d}t}\right]_{\text{rot.frame}} - \omega\mathbf{m} \times \mathbf{e}_z. \tag{7.10}$$

Therefore, in this rotating frame Eq. (7.9) takes the form:

$$\frac{\mathrm{d}\mathbf{m}}{\mathrm{d}t} - \alpha\mathbf{m} \times \frac{\mathrm{d}\mathbf{m}}{\mathrm{d}t} = -\mathbf{m} \times \left(\mathbf{h}_{\text{eff}} - \omega\mathbf{e}_z + \alpha\omega\mathbf{m} \times \mathbf{e}_z\right). \tag{7.11}$$

The field $\mathbf{h}_{\text{eff}}$ is still given by Eq. (7.6); however $\mathbf{h}_{a\perp}$ is now time-independent because it moves in synchronism with the rotating frame. On the other hand, no new time dependence appears as a result of the transformation to the rotating frame, as all the parameters of the problem are invariant with respect to rotations around the symmetry axis. Thus, no explicit time dependence is present anymore in the right-hand side of Eq. (7.11). In other words, the transformation to the rotating frame results in the fact that the magnetization dynamics in this frame is autonomous.

Next, we shall discuss important topological aspects of magnetization dynamics in the rotating frame, described by Eq. (7.11). This equation corresponds to an autonomous dynamical system evolving on the surface of the unit sphere $|\mathbf{m}|^2 = 1$. The autonomous character of the dynamics permits one to study its properties in geometric terms, through the phase portrait [741,358,529,319] of the equation (see Fig. 7.1 for an example). The notions of phase portrait, saddle, focus, node, etc. are extensively discussed in Chapter 3. In that Chapter, it has also been discussed which general aspects of the magnetization dynamics immediately follow from the constraints that the state space (unit sphere) imposes on the phase

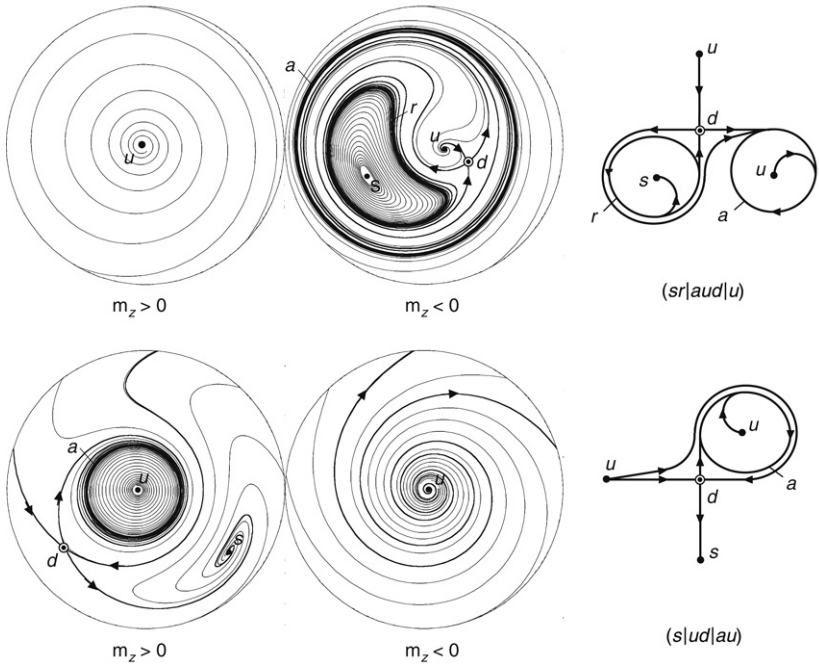

FIGURE 7.1 Examples of phase portraits of LLG dynamics in the rotating frame of reference. Each phase portrait is represented in terms of joint stereographic projections onto the unit disk of the two hemispheres corresponding to $\mathrm{m}_z > 0$ and $\mathrm{m}_z < 0$. The point of contact of the two disks corresponds to $m_{\perp a} = 1$, i.e., magnetization fully aligned along the rf field $\mathbf{h}_{a\perp}$. The following notation is adopted. s: stable node; u: unstable node; d: saddle; a: stable limit cycle; r: unstable limit cycle. System parameters: $\alpha = 0.1$, $\kappa_{\text{eff}} = -1$. Field frequency: $\omega = 0.5$. The upper phase portrait corresponds to $\mathrm{h}_{az} = -0.2, \mathrm{h}_{a\perp} = 0.08$; this phase portrait is of $(sr|aud|u)$ type according to the classification discussed in Section 7.4. The lower phase portrait corresponds to $\mathrm{h}_{az} = 0.8, \mathrm{h}_{a\perp} = 0.08$; this phase portrait is of $(s|ud|au)$ type according to the classification discussed in the same section. The simplified graphical representation of phase portraits is given on the right.

portrait. These constraints apply also to the rotating-frame dynamics of interest here.

- Existence of fixed points
  Any phase portrait on the sphere must necessarily contain a nonzero number of fixed points for which $\mathrm{d}\mathbf{m}/\mathrm{d}t = 0$ [529]. These fixed points occur in the rotating frame of reference. In the laboratory frame, each

of these fixed points corresponds to a magnetization mode in which the magnetization precesses about the symmetry axis z in synchronism with the external field. In other words, these fixed points correspond to periodic time-harmonic solutions of the LLG equation in the laboratory frame. These rotating modes will be termed **P**-modes. Therefore, one reaches the remarkable conclusion that a certain number of **P**-modes must exist *for any value* of the control parameters $(\omega, \mathrm{h}_{az}, \mathrm{h}_{a\perp})$. Interestingly, in the case of a **P**-mode the system response to a time-harmonic excitation (see Eq. (7.5)) is itself time-harmonic, with no generation of higher-order harmonics, despite the inherent strongly nonlinear character of the magnetization dynamics.

- Number of fixed points
  The number of **P**-modes can be predicted by using Poincaré index theorem [529]. This theorem asserts that the number of nodes or foci minus the number of saddles of any autonomous dynamics on the sphere must be equal to two. Therefore, the number of **P**-modes is at least two and it is even under all circumstances. Following this result, one can classify LLG phase portraits for rotationally invariant systems according to the number and nature of their fixed points as follows:
  – phase portraits with 2 fixed points: 2 nodes or foci;
  – phase portraits with 4 fixed points: 3 nodes or foci + 1 saddle;
  – and so on.
  The nature of a fixed point (node, focus, or saddle) can be determined through the analysis of its stability, as discussed in subsequent sections.
- Non-existence of chaos
  Chaos is precluded, because the phase space is two-dimensional [741]. The onset of chaotic phenomena is not compatible with the simultaneous existence of rotational symmetry and uniform magnetization. Only when one or both of these requirements are relaxed, chaotic phenomena may appear [740,250].

7.2 PERIODIC MAGNETIZATION MODES

The study of periodic solutions to the magnetization dynamics (**P**-modes) can be conveniently carried out in the rotating frame by introducing the spherical-angle state variables (θ, ϕ), representing the tilt angle of $\mathbf{m}$ with respect to $\mathbf{e}_z$ $(0 \leq \theta \leq \pi)$ and the lag angle of $\mathbf{m}_\perp$ with respect to $\mathbf{h}_{a\perp}$ $(-\pi \leq \phi \leq \pi)$, respectively. In other words, we express the magnetization as follows:

$$\begin{aligned} \mathbf{m} &= m_{\perp a}\mathbf{e}_a + m_{\perp b}\mathbf{e}_b + \mathrm{m}_z\mathbf{e}_z \\ &= \mathbf{e}_a \sin\theta\cos\phi - \mathbf{e}_b \sin\theta\sin\phi + \mathbf{e}_z\cos\theta, \end{aligned} \tag{7.12}$$

where $(\mathbf{e}_a, \mathbf{e}_b, \mathbf{e}_z)$ is a right-handed cartesian set of unit vectors for the rotating frame, with $\mathbf{e}_a$ directed along $\mathbf{h}_{a\perp}$. The minus sign in the expression for $m_{\perp b}$ reflects the fact that ϕ represents the angle by which the rotating component of magnetization *lags* behind the rotating magnetic field. After substitution of Eqs (7.12) and (7.6) into Eq. (7.11) one finds:

$$\frac{\mathrm{d}\theta}{\mathrm{d}t} - \alpha \sin\theta \frac{\mathrm{d}\phi}{\mathrm{d}t} = \mathrm{h}_{a\perp} \sin\phi - \alpha\omega \sin\theta, \tag{7.13}$$

$$\alpha \frac{\mathrm{d}\theta}{\mathrm{d}t} + \sin\theta \frac{\mathrm{d}\phi}{\mathrm{d}t} = \mathrm{h}_{a\perp} \cos\phi \cos\theta - (\mathrm{h}_{az} - \omega + \kappa_{\text{eff}} \cos\theta) \sin\theta. \tag{7.14}$$

By setting $\mathrm{d}\theta/\mathrm{d}t = \mathrm{d}\phi/\mathrm{d}t = 0$ one obtains the equations for the fixed (critical) points of the dynamics in the rotating frame:

$$\mathrm{h}_{a\perp} \sin\phi_0 - \alpha\omega \sin\theta_0 = 0, \tag{7.15}$$

$$\mathrm{h}_{a\perp} \cos\phi_0 \cos\theta_0 - (\mathrm{h}_{az} - \omega + \kappa_{\text{eff}} \cos\theta_0) \sin\theta_0 = 0. \tag{7.16}$$

It is convenient to rewrite these equations in the form:

$$\nu_0 = \frac{\mathrm{h}_{az} - \omega}{\cos\theta_0} + \kappa_{\text{eff}}, \tag{7.17}$$

$$\nu_0^2 = \frac{\mathrm{h}_{a\perp}^2}{\sin^2\theta_0} - \alpha^2\omega^2, \tag{7.18}$$

where:

$$\nu_0 = \alpha\omega \cot\phi_0. \tag{7.19}$$

The angle ϕ_0 is always in one-to-one correspondence with ν_0 because $0 \le \phi_0 \le \pi$. In fact, according to Eq. (7.15), $\sin\phi_0 \ge 0$ for all **P**-modes, because $\mathrm{h}_{a\perp}$, α, ω, and $\sin\theta_0$ are all positive by definition. In other words, in the case of a **P**-mode the magnetization always lags behind the field. The plane $(\cos\theta_0, \nu_0)$ is the natural plane for the representation of **P**-modes. A generic **P**-mode will be located in the region $-1 \le \cos\theta_0 \le 1$, $-\infty < \nu_0 < \infty$, i.e., $0 \le \theta_0 \le \pi$, $0 \le \phi_0 \le \pi$.

By solving Eqs (7.17) and (7.18), one obtains the values of $(\cos\theta_0, \nu_0)$ for the **P**-modes existing under given excitation conditions $\left(\omega, h_{a\parallel}, \mathrm{h}_{a\perp}\right)$. Conversely, Eqs (7.17) and (7.18) can be written in the form:

$$\mathrm{h}_{az} = (\nu_0 - \kappa_{\text{eff}}) \cos\theta_0 + \omega, \tag{7.20}$$

$$\mathrm{h}_{a\perp} = \sqrt{(1-\cos^2\theta_0)\,(\nu_0^2+\alpha^2\omega^2)}, \tag{7.21}$$

whereby one can compute the field conditions that will produce a **P**-mode with desired values of $(\cos\theta_0, \nu_0)$. For a particular **P**-mode solution of Eqs (7.17) and (7.18), the corresponding magnetization components in the rotating frame can be expressed in terms of $\cos\theta_0$ only, as follows:

$$m_{\perp a} = \left(\frac{\mathrm{h}_{az}-\omega}{\cos\theta_0} + \kappa_{\text{eff}}\right)\frac{\sin^2\theta_0}{\mathrm{h}_{a\perp}}, \tag{7.22}$$

$$m_{\perp b} = -\frac{\alpha\omega\sin^2\theta_0}{\mathrm{h}_{a\perp}}, \tag{7.23}$$

$$\mathrm{m}_z = \cos\theta_0. \tag{7.24}$$

In the derivation of Eqs (7.22)–(7.24), Eq. (7.12) has been used and the ϕ_0 variable has been eliminated by making use of Eqs (7.15) and (7.16). In the sequel, the notation $\mathbf{m}_0$ will be used for **P**-modes.

Since the **P**-mode is a fixed point of the dynamics in the rotating frame, we derive from Eq. (7.11) that $\mathbf{m}_0$ satisfies the relation:

$$\mathbf{m}_0 \times \left(\mathbf{h}_{\text{eff}}^{(0)} - \omega\mathbf{e}_z + \alpha\omega\mathbf{m}_0\times\mathbf{e}_z\right) = 0, \tag{7.25}$$

where $\mathbf{h}_{\text{eff}}^{(0)}$ is the effective field corresponding to $\mathbf{m}_0$. Equation (7.25) implies that:

$$\mathbf{h}_{\text{eff}}^{(0)} - \omega\mathbf{e}_z + \alpha\omega\mathbf{m}_0\times\mathbf{e}_z = \lambda_0\mathbf{m}_0, \tag{7.26}$$

where λ_0 is a constant depending on $(\cos\theta_0, \nu_0)$. By expressing $\mathbf{m}_0$ through Eqs (7.22)–(7.24), we derive:

$$\lambda_0 = \nu_0 - N_\perp. \tag{7.27}$$

This equation will be useful in the discussion of **P**-mode stability.

In the laboratory frame, the **P**-mode represents a spatially uniform time-harmonic solution. We have that (compare with Eq. (7.5)):

$$\mathbf{m}_0(t) = \mathbf{e}_x\sin\theta_0\cos(\omega t-\phi_0) + \mathbf{e}_y\sin\theta_0\sin(\omega t-\phi_0) + \mathbf{e}_z\cos\theta_0. \tag{7.28}$$

The **P**-mode dynamics in the laboratory frame is described by the equation:

$$\frac{\mathrm{d}\mathbf{m}_0}{\mathrm{d}t} = -\omega \mathbf{m}_0 \times \mathbf{m}_0 \mathbf{e}_z, \tag{7.29}$$

i.e., $\mathbf{m}_0(t)$ is a unit vector which uniformly rotates around the z axis at the angular frequency ω.

Up to this point, it has not been assumed in our discussion that the damping parameter α is a constant. However, if α is constant, then Eqs (7.17) and (7.18) can be reduced to a fourth-order polynomial equation with respect to $\mathrm{m}_z = \cos\theta_0$. In fact, by eliminating ν_0 from Eqs (7.17) and (7.18) one arrives at the equation:

$$\frac{\mathrm{h}_{a\perp}^2}{\sin^2\theta_0} - \left(\frac{\mathrm{h}_{az} - \omega}{\cos\theta_0} + \kappa_{\text{eff}}\right)^2 = \alpha^2\omega^2. \tag{7.30}$$

This equation can be transformed as follows:

$$\begin{aligned}&(1+\Omega^2)\cos^4\theta_0 + 2b_z\cos^3\theta_0 \\ &\quad + [b_\perp^2 + b_z^2 - (1+\Omega^2)]\cos^2\theta_0 - 2b_z\cos\theta_0 - b_z^2 = 0,\end{aligned} \tag{7.31}$$

where:

$$\Omega = \frac{\alpha\omega}{\kappa_{\text{eff}}}, \qquad b_z = \frac{\mathrm{h}_{az} - \omega}{\kappa_{\text{eff}}}, \qquad b_\perp = \frac{\mathrm{h}_{a\perp}}{\kappa_{\text{eff}}}. \tag{7.32}$$

Equation (7.31) may have up to four real roots. However, by invoking the Poincaré index theorem, one concludes that only two possibilities exist under constant α:

- Equation (7.31) has two real solutions: the phase portrait contains two **P**-modes;
- Equation (7.31) has four real solutions: the phase portrait contains four **P**-modes.

The dynamics under constant α leads to a specific mapping between the **P**-mode plane $(\cos\theta_0, \nu_0)$ and the field control plane $(\mathrm{h}_{az}, \mathrm{h}_{a\perp})$. The starting point is the fact that, for given system parameters $(\alpha, \kappa_{\text{eff}})$, given frequency ω, and variable $\cos\theta_0$, Eq. (7.30) defines a one-parameter family of hyperbolic lines in the $(\mathrm{h}_{az}, \mathrm{h}_{a\perp})$ plane. These lines identify the field conditions that will produce a **P**-mode with the desired value of $\cos\theta_0$

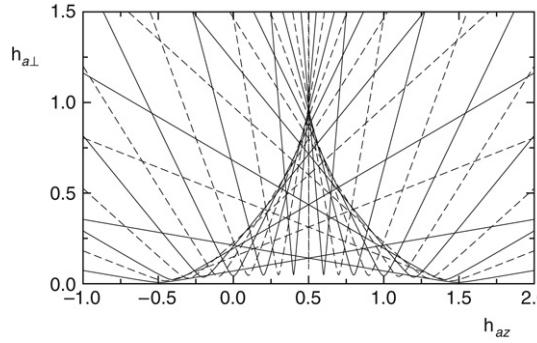

FIGURE 7.2 Hyperbolic lines in $(\mathrm{h}_{az}, \mathrm{h}_{a\perp})$-plane (Eq. (7.30)) identifying field conditions that will produce **P**-modes with the desired value of $\cos\theta_0$. System parameters: $\alpha = 0.1$, $\kappa_{\text{eff}} = -1$. Field frequency: $\omega = 0.5$. Alternate continuous and broken lines are used to facilitate the visualization.

(see Fig. 7.2). It is apparent from Fig. 7.2 that, for a given point in the field plane, two or four hyperbolic lines will pass through that point. In other words, there will be two or four **P**-modes associated with given field conditions, in agreement with the Poincaré index theorem. According to Eq. (7.30), the vertex of each hyperbolic line is located at:

$$\mathrm{h}_{az} = \omega - \kappa_{\text{eff}} \cos\theta_0, \tag{7.33}$$

$$\mathrm{h}_{a\perp} = \alpha\omega \sin\theta_0. \tag{7.34}$$

This is the point where the desired value of $\cos\theta_0$ is realized by using the rotating field of minimum amplitude. According to Eq. (7.17), this condition corresponds to $\nu_0 = 0$, i.e., $\phi_0 = \pi/2$. The parameter ν_0 increases along the hyperbolic line when one moves to the right or to the left according to whether $\cos\theta_0$ is positive or negative, respectively.

Next, we shall discuss the question whether a given **P**-mode may or may not be physically realizable. Indeed, only the modes that are dynamically stable will survive for long times and will be experimentally observable. Dynamical stability can be studied by perturbing the **P**-mode solution and by analyzing the ensuing time-behavior of the perturbation. To be completely general, this analysis should be carried out for arbitrary space and time-dependent perturbations compatible with the boundary conditions of the problem. In the present section, however, this analysis will be limited only to spatially uniform perturbations. Physically, this means that we consider magnetic particles so small that exchange

forces rule out the appearance of spatial nonuniformities however small. Stability with respect to generic spatially nonuniform perturbations will be treated in Chapter 8.

Under the assumption of spatial uniformity, a given **P**-mode will be dynamically stable if the corresponding fixed point of the magnetization dynamics in the rotating frame is stable. Stability is studied by standard methods [358,428], by linearizing Eq. (7.11) around the **P**-mode fixed point. Let us denote the **P**-mode magnetization (which is constant in the rotating frame) by $\mathbf{m}_0$ and let us consider a perturbed mode: $\mathbf{m}(t) = \mathbf{m}_0 + \delta\mathbf{m}(t)$, where $|\delta\mathbf{m}(t)| \ll 1$. The perturbation must preserve the magnetization amplitude $|\mathbf{m}|^2 = 1$. Therefore, $\delta\mathbf{m}(t)$ must be perpendicular to $\mathbf{m}_0$ at all times:

$$\delta\mathbf{m}(t) \cdot \mathbf{m}_0 = 0. \tag{7.35}$$

A convenient basis for the representation of $\delta\mathbf{m}$ in the plane perpendicular to $\mathbf{m}_0$ is given by the unit vectors:

$$\mathbf{e}_1 = \frac{(\mathbf{e}_z \times \mathbf{m}_0) \times \mathbf{m}_0}{|(\mathbf{e}_z \times \mathbf{m}_0) \times \mathbf{m}_0|}, \tag{7.36}$$

$$\mathbf{e}_2 = \frac{\mathbf{e}_z \times \mathbf{m}_0}{|\mathbf{e}_z \times \mathbf{m}_0|}. \tag{7.37}$$

Let us express $\delta\mathbf{m}$ as $\delta\mathbf{m}(t) = \delta m_1(t)\mathbf{e}_1 + \delta m_2(t)\mathbf{e}_2$. After substituting $\mathbf{m}_0 + \delta\mathbf{m}(t)$ into Eq. (7.11), linearizing the latter equation with respect to $\delta\mathbf{m}$ and using Eqs (7.17) and (7.18) for $\mathbf{m}_0$, one arrives at the equation:

$$\frac{\mathrm{d}}{\mathrm{d}t}\begin{pmatrix}\delta m_1 \\ \delta m_2\end{pmatrix} = A_0 \begin{pmatrix}\delta m_1 \\ \delta m_2\end{pmatrix}, \tag{7.38}$$

where:

$$A_0 = \frac{1}{1+\alpha^2}\begin{pmatrix}1 & -\alpha \\ \alpha & 1\end{pmatrix}\begin{pmatrix}-\alpha\omega\cos\theta_0 & -\nu_0 \\ \nu_0 - \kappa_{\text{eff}}\sin^2\theta_0 & -\alpha\omega\cos\theta_0\end{pmatrix}, \tag{7.39}$$

and the pair $(\cos\theta_0, \nu_0)$ identifies the particular **P**-mode being considered. Stability is controlled by the eigenvalues of the matrix A_0, which can be expressed in terms of its determinant and its trace. The determinant of A_0 is given by the expression:

$$\det A_0 = \frac{1}{1+\alpha^2}\left(\nu_0^2 - \kappa_{\text{eff}}\sin^2\theta_0\nu_0 + \alpha^2\omega^2\cos^2\theta_0\right), \tag{7.40}$$

and its trace by the expression:

$$\mathrm{tr}\ A_0 = -\frac{2\alpha}{1+\alpha^2}\left(\nu_0 - \frac{\kappa_{\mathrm{eff}}\sin^2\theta_0}{2} + \omega\cos\theta_0\right). \tag{7.41}$$

The characteristic frequency $\omega_0^2 = \det A_0 - (\mathrm{tr}\ A_0)^2/4$ is then equal to:

$$\omega_0^2 = \frac{1}{(1+\alpha^2)^2}\left[\left(\nu_0 - \frac{\kappa_{\mathrm{eff}}\sin^2\theta_0}{2} - \alpha^2\omega\cos\theta_0\right)^2 - \left(1+\alpha^2\right)\frac{\kappa_{\mathrm{eff}}^2\sin^4\theta_0}{4}\right]. \tag{7.42}$$

Now, **P**-mode stability can be classified as follows [358]:

- $\det A_0 < 0$. Saddle-type fixed point.
- $\det A_0 > 0$ and $\omega_0^2 < 0$. Node-type fixed point:
  - $\mathrm{tr}\ A_0 < 0$: stable node;
  - $\mathrm{tr}\ A_0 > 0$: unstable node.
- $\det A_0 > 0$ and $\omega_0^2 > 0$. Focus-type fixed point:
  - $\mathrm{tr}\ A_0 < 0$: stable focus;
  - $\mathrm{tr}\ A_0 > 0$: unstable focus.

The difference between a node and a focus is not relevant to the rest of our analysis: we will use the term node in a generic sense, to denote either of them. The symbols (s), (u), and (d) will be used to denote stable nodes, unstable nodes, and saddles, respectively. A given **P**-mode represents a physically realizable solution only when it is of (s) type, that is, when $\det A_0 > 0$ and $\mathrm{tr}\ A_0 < 0$.

Stability results can be presented in a transparent form on the $(\cos\theta_0, \nu_0)$ **P**-mode plane. Stability is controlled by the equations $\det A_0 = 0$ and $\mathrm{tr}\ A_0 = 0$ when $\det A_0 > 0$. The expressions for $\det A_0$ and $\mathrm{tr}\ A_0$ are given by Eqs (7.40) and (7.41), respectively. These equations can be solved in order to obtain ν_0 as a function of $\cos\theta_0$. The results are as follows:

- $\det A_0 = 0$:

$$\nu_0 = \frac{\kappa_{\mathrm{eff}}\sin^2\theta_0}{2} \pm \sqrt{\frac{\kappa_{\mathrm{eff}}^2\sin^4\theta_0}{4} - \alpha^2\omega^2\cos^2\theta_0}. \tag{7.43}$$

The above two values are real in the interval:

$$\cos^2\theta_0 \leq \left(\sqrt{1+\frac{\alpha^2\omega^2}{\kappa_{\text{eff}}^2}}-\sqrt{\frac{\alpha^2\omega^2}{\kappa_{\text{eff}}^2}}\right)^2. \tag{7.44}$$

- $\text{tr}\ A_0 = 0$ when $\det A_0 \geq 0$:

$$\nu_0 = \frac{\kappa_{\text{eff}}\sin^2\theta_0}{2} - \omega\cos\theta_0. \tag{7.45}$$

By inserting Eq. (7.45) into Eq. (7.40) one finds that $\det A_0 \geq 0$ when:

$$\cos^2\theta_0 \geq \left(\sqrt{1+\frac{(1+\alpha^2)\,\omega^2}{\kappa_{\text{eff}}^2}}-\sqrt{\frac{(1+\alpha^2)\omega^2}{\kappa_{\text{eff}}^2}}\right)^2. \tag{7.46}$$

Figure 7.3 shows the lines $\det A_0 = 0$ and $\text{tr}\ A_0 = 0$ when $\det A_0 \geq 0$ computed by using Eqs (7.43) and (7.45) for a thin film with negligible crystal anisotropy. These lines divide the **P**-mode plane into three regions associated with stable nodes (**S**), unstable nodes (**U**), and saddles (**D**). Physically realizable **P**-modes are only those located in region **S**.

These results are more difficult to represent on the field control plane $(\text{h}_{az}, \text{h}_{a\perp})$. This is because there are two or four **P**-modes associated with any given point on that plane. For this reason, the functions $\det A_0$ and $\text{tr}\ A_0$ will take the form of two-folded or four-folded sheets (Riemann surfaces) when represented on the control plane (see Figs 7.4 and 7.5). According to the Poincaré index theorem, when four **P**-modes are present one of them is necessarily a saddle for which $\det A_0 < 0$. Therefore, the control plane region admitting four **P**-modes coincides with the region where $\det A_0 < 0$ for one of the **P**-modes. By substituting Eq. (7.43) into Eqs (7.20) and (7.21), one obtains a parametric representation of the boundary ($\det A_0 = 0$) between the two and four **P**-mode regions, with $\cos\theta_0$ as the independent variable (see Fig. 7.6 and compare with Fig. 7.2). Similarly, one can determine the line $(\text{tr}\ A_0 = 0, \det A_0 > 0)$ (broken line in Fig. 7.6) by substituting Eq. (7.45) into Eqs (7.20) and (7.21). The region where $\det A_0 < 0$ can be construed as the dynamic generalization of the Stoner–Wohlfarth astroid region [639,79]. Indeed, it can be verified that this region coincides with the usual astroid region in the limit $\omega \to 0$.

Equations (7.17) and (7.18) are invariant under the following transformation: $\cos\theta_0 \to -\cos\theta_0$, $\nu_0 \to -\nu_0$, $\kappa_{\text{eff}} \to -\kappa_{\text{eff}}$. Given a **P**-mode solution of the original equations, this transformation gives a

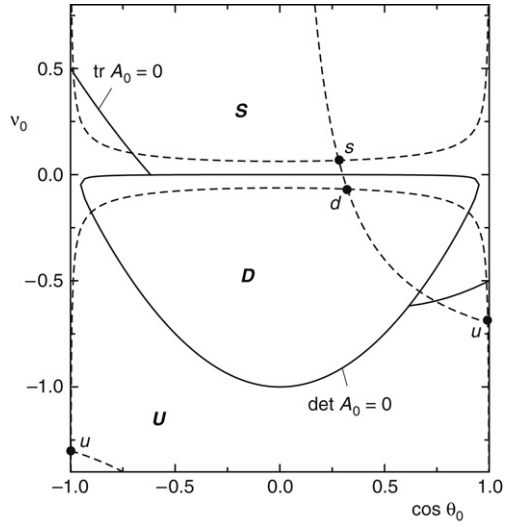

FIGURE 7.3 Classification of **P**-modes on the $(\cos\theta_0, \nu_0)$-plane. Continuous lines represent solutions of equations $\det A_0 = 0$ and $\mathrm{tr}\ A_0 = 0$ when $\det A_0 > 0$. **P**-modes inside region **D** are saddle points of the dynamics in the rotating frame, while those outside **D** are stable nodes (region **S**) or unstable nodes (region **U**). Broken lines represent solutions of Eq. (7.17) for $\mathrm{h}_{az} = 0.8$ and of Eq. (7.18) for $\mathrm{h}_{a\perp} = 0.08$. Solid points are intersection points representing the four **P**-modes associated with $\mathrm{h}_{az} = 0.8$, $\mathrm{h}_{a\perp} = 0.08$ (see bottom phase portrait in Fig. 7.1). System parameters: $\alpha = 0.1$, $\kappa_{\mathrm{eff}} = -1$. Field frequency: $\omega = 0.5$.

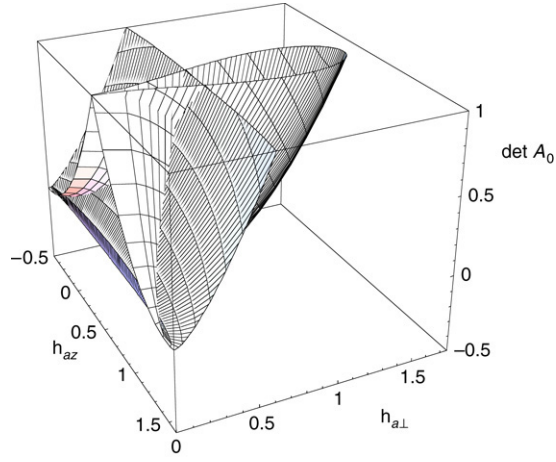

FIGURE 7.4 Example of $\det A_0$ surface defined by Eqs (7.40), (7.20), and (7.21) on $(\mathrm{h}_{az}, \mathrm{h}_{a\perp})$-plane. System parameters: $\alpha = 0.1$, $\kappa_{\mathrm{eff}} = -1$. Field frequency: $\omega = 0.5$.

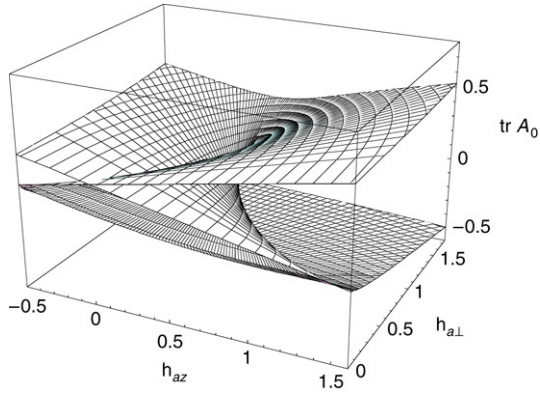

FIGURE 7.5 Example of $\mathrm{tr}\ A_0$ surface defined by Eqs (7.41), (7.20), and (7.21) on $(h_{az}, h_{a\perp})$-plane. System parameters: $\alpha = 0.1$, $\kappa_{\text{eff}} = -1$. Field frequency: $\omega = 0.5$.

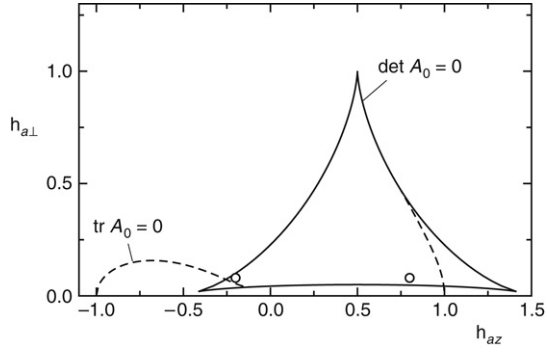

FIGURE 7.6 Representation on $(h_{az}, h_{a\perp})$ control plane of lines where $\det A_0 = 0$ and $\mathrm{tr}\ A_0 = 0$ when $\det A_0 > 0$. System parameters: $\alpha = 0.1$, $\kappa_{\text{eff}} = -1$. Field frequency: $\omega = 0.5$. Small empty circles represent location of the two phase portraits shown in Fig. 7.1.

corresponding **P**-mode solution for the case where the effective anisotropy takes the opposite value. According to Eqs (7.40) and (7.41), $\mathrm{tr}\ A_0 \rightarrow -\mathrm{tr}\ A_0$ and $\det A_0 \rightarrow \det A_0$ as a result of the above transformation. This means that, when the sign of anisotropy is reversed, stable **P**-modes are transformed into unstable ones and vice versa while the $\det A_0 = 0$ and $\mathrm{tr}\ A_0 = 0$ lines remain unaffected. These rules permit one to extend the results of the analysis to magnetic particles with effective anisotropy of opposite sign. Furthermore, Eq. (7.40) indicates that $\det A_0 > 0$ whenever ν_0 and κ_{eff} have opposite signs. Therefore, the saddle point can exist only

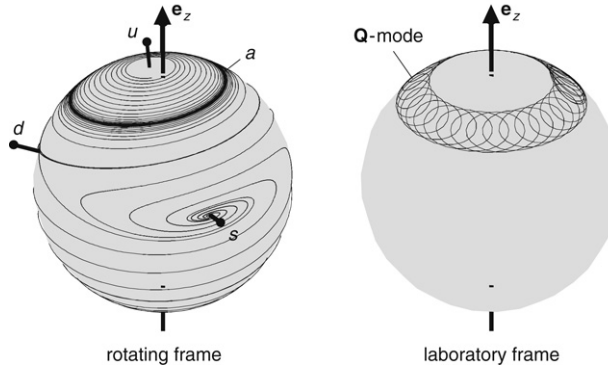

FIGURE 7.7 Representation on the unit sphere of the bottom phase portrait from Fig. 7.1 and corresponding quasi-periodic motion in the laboratory frame (**Q**-mode generated by stable limit cycle a). System parameters: $\alpha = 0.1$, $\kappa_{\text{eff}} = -1$. Field frequency: $\omega = 0.5$. Field amplitude: $\mathrm{h}_{az} = 0.8$, $\mathrm{h}_{a\perp} = 0.08$.

provided ν_0 and κ_{eff} have identical sign. This means that for the saddle points we have $0 \leq \phi_0 < \pi/2$ when $\kappa_{\text{eff}} > 0$ and $\pi/2 < \phi_0 \leq \pi$ when $\kappa_{\text{eff}} < 0$.

It is worth pointing out that the mentioned connection between fixed-point stability and anisotropy sign reflects a more general property of LLG dynamics (see Eqs (7.13) and (7.14)), namely the fact that the reversing of the sign of the effective anisotropy is essentially equivalent to the reversing of the direction of time. Indeed, Eqs (7.13) and (7.14) are invariant under the transformation: $\theta \to \pi - \theta$, $\phi \to \pi - \phi$, $\kappa_{\text{eff}} \to -\kappa_{\text{eff}}$, $t \to -t$, from which the **P**-mode symmetries just discussed can be derived as a particular case.

7.3 QUASI-PERIODIC MAGNETIZATION MODES

In order to be physically realizable, a **P**-mode must be a stable node of the magnetization dynamics in the rotating frame. When no **P**-mode is stable, there will exist (at least) one attracting limit cycle of the above dynamics (Poincaré–Bendixson theorem) [529]. A limit cycle represents a periodic magnetization motion along a closed path on the unit sphere. This conclusion holds in the rotating reference frame. In the laboratory frame, the periodic motion along the limit cycle has to be combined with the rotation of the reference frame and this results in a quasi-periodic magnetization mode (**Q**-mode) (see Fig. 7.7). The quasi-periodicity arises because the external-field and the limit-cycle periods are usually not commensurable.

The following argument proves that **Q**-modes are necessarily present under appropriate conditions. Let us consider the case of small rotating field amplitudes, $\mathrm{h}_{a\perp} \to 0$, for which $\sin\theta_0 \to 0$ and $\cos\theta_0 \to \pm 1$. By using Eqs (7.17)–(7.18), one can write Eqs (7.40) and (7.41) in the approximate form:

$$\det A_0 \simeq \frac{1}{1+\alpha^2}\left(\nu_0^2 + \alpha^2\omega^2\right), \tag{7.47}$$

$$\mathrm{tr}\ A_0 \simeq -\frac{2\alpha}{1+\alpha^2}\left(\kappa_{\mathrm{eff}} \pm h_{az}\right). \tag{7.48}$$

Only two **P**-modes are possible, because $\det A_0 > 0$. Furthermore, the sign of $\mathrm{tr}\ A_0$ is opposite to that of κ_{eff} for both modes in the interval $|h_{az}| < |\kappa_{\mathrm{eff}}|$. Therefore, in this interval both **P**-modes are unstable for any system with negative effective anisotropy and a **Q**-mode will necessarily appear.

This formal result has an intuitive physical interpretation. Let us assume that $\kappa_{\mathrm{eff}} < 0$ and that initially only the constant positive field $h_{az} < |\kappa_{\mathrm{eff}}|$ is applied, i.e., $\mathrm{h}_{a\perp} = 0$. In this case, no time-dependent driving field is present. In the laboratory frame there exists a continuous set of static equilibria characterized by fixed $\cos\theta$ and arbitrary ϕ. In fact, by expressing the energy of the system (Eq. (7.8)) in terms of θ and ϕ one finds:

$$g_L\left(\theta,\phi;\mathrm{h}_{az},\mathrm{h}_{a\perp}\right) = \frac{N_\perp}{2} - \frac{\kappa_{\mathrm{eff}}}{2}\cos^2\theta - \mathrm{h}_{az}\cos\theta - \mathrm{h}_{a\perp}\sin\theta\cos\phi. \tag{7.49}$$

When $\kappa_{\mathrm{eff}} < 0$ and $\mathrm{h}_{a\perp} = 0$, the energy is independent of ϕ and assumes its minimum value for $\cos\theta = \mathrm{h}_{az}/|\kappa_{\mathrm{eff}}|$. In the rotating frame, this continuous set of states results in a limit cycle of period $2\pi/\omega$. When the small rotating field $\mathrm{h}_{a\perp}$ is applied, the set of equivalent static states is changed into a quasi-periodic motion. In fact, the rotating field is not strong enough to force the magnetization into synchronous rotation. The magnetization follows the field only for a small part of each rotation period and then periodically falls off synchronism. The result is a **Q**-mode characterized by a slow average $\mathbf{m}$ precession around the symmetry axis, accompanied by a nutation of frequency ω. Only when $\mathrm{h}_{a\perp}$ exceeds a certain threshold, $\mathbf{m}$ gets locked to the field and the **Q**-mode is destroyed in favor of a stable **P**-mode.

In general, one expects that both stable (i.e., attracting, denoted by (a)) and unstable (i.e., repelling, denoted by (r)) limit cycles may be

present in the dynamics in the rotating frame. The problem of theoretically predicting the number and the location of limit cycles for a given dynamical system is of extraordinary mathematical difficulty. However, the fact that the damping parameter α is small permits one to investigate the problem by the Poincaré–Melnikov method [529,304] discussed in Chapter 5. The starting point is the fact that Eq. (7.11) is an example of generalized magnetization dynamics, of the type discussed in Chapter 3, Section 3.2 and Chapter 5, Section 5.5. As a matter of fact, to apply the Poincaré–Melnikov method it is better to pass to the LL form of the dynamics. By assuming Eq. (3.12) rather than Eq. (3.9) as the starting point and then using Eq. (7.10) to express $\mathrm{d}\mathbf{m}/\mathrm{d}t$ in the rotating frame, one arrives at the rotating-frame equation:

$$\frac{\mathrm{d}\mathbf{m}}{\mathrm{d}t} = \mathbf{m} \times \frac{\partial \tilde{g}_L}{\partial \mathbf{m}} + \alpha \mathbf{m} \times \left(\mathbf{m} \times \frac{\partial g_L}{\partial \mathbf{m}} \right), \tag{7.50}$$

where:

$$\tilde{g}_L \left(\mathbf{m}; \mathbf{h}_a \right) = g_L \left(\mathbf{m}; \mathbf{h}_a \right) + \omega \mathrm{m}_z. \tag{7.51}$$

In Chapter 3 we discussed cases of generalized magnetization dynamics for which additional contributions to the relaxational part of the dynamics appeared as the consequence of additional driving actions on the system. However, the situation described by Eq. (7.50) is different, because here the generalized form of the dynamics appears as a consequence of the non-inertial character of the reference frame transformation. This difference is reflected in the fact that the precessional part of the dynamics rather than the relaxational one is affected by the transformation. The function $\tilde{g}_L$ plays the role of effective energy in the rotating frame: it represents the quantity that is conserved during the magnetization motion when damping can be neglected. Thus, under this approximation the magnetization trajectories in the rotating frame coincide with the closed trajectories $C(\tilde{g}_0)$ corresponding to the constant energy $\tilde{g}_L = \tilde{g}_0$. From Eqs (7.8) and (7.51) one finds that $\tilde{g}_L \left(\mathbf{m}; \mathbf{h}_a \right)$ can be expressed as:

$$\tilde{g}_L \left(\mathbf{m}; \mathbf{h}_a \right) = \frac{1}{2} N_\perp - \frac{1}{2} \kappa_{\text{eff}} \mathrm{m}_z^2 - (\mathrm{h}_{az} - \omega) \mathrm{m}_z - \mathrm{h}_{a\perp} m_{\perp a}. \tag{7.52}$$

Therefore, the line $C\left(\tilde{g}_0\right)$ is described by the equation:

$$\kappa_{\text{eff}} \mathrm{m}_z^2 + 2 \left(\mathrm{h}_{az} - \omega \right) \mathrm{m}_z + 2 \mathrm{h}_{a\perp} m_{\perp a} = N_\perp - 2 \tilde{g}_0. \tag{7.53}$$

When α is small but cannot be neglected, the rate at which the effective energy $\tilde{g}_L$ changes during the magnetization motion is described by the power function $\mathcal{P}(\mathbf{m}, \zeta)$ introduced in Section 5.5. Since in the case of Eq. (7.50) the role of the second potential Φ is played by g_L itself, then the power function (5.111) is equal to:

$$\mathcal{P}(\mathbf{m}, \zeta) = -(\mathbf{m} \times \mathbf{h}_{\text{eff}}) \cdot \frac{\mathrm{d}\mathbf{m}}{\mathrm{d}t}. \tag{7.54}$$

Note that this function would be zero if the magnetization trajectory coincided with constant g_L level curves, but this is not the case even under negligible damping, because $\tilde{g}_L$ rather than g_L is conserved in that limit.

Following the general analysis presented in Section 5.5, we know that limit cycles are related to the zeros of the Melnikov function (5.147), i.e.:

$$M(\tilde{g}_0, \zeta) = -\oint_{C(\tilde{g}_0)} (\mathbf{m} \times \mathbf{h}_{\text{eff}}) \cdot \mathrm{d}\mathbf{m}. \tag{7.55}$$

The equation $M(\tilde{g}_0, \zeta) = 0$ represents, in the limit of small damping, the necessary and sufficient condition for the existence of a limit cycle coinciding with the trajectory $C(\tilde{g}_0)$ of the undamped dynamics in the rotating frame. The limit cycle is stable or unstable depending on whether $\partial M/\partial \tilde{g}_0$ is respectively positive or negative at the energy $\tilde{g}_0$ where $M(\tilde{g}_0, \zeta) = 0$.

The Melnikov function $M(\tilde{g}_0, \zeta)$ can be studied by analytical or numerical methods under quite general conditions because $\mathbf{h}_{\text{eff}}$ (Eq. (7.6)) and $\tilde{g}_L$ (Eq. (7.51)) are all known functions of $\mathbf{m}$. As discussed in Chapter 5 and shown by Eq. (7.55), there is no need to know the precise time parametrization $\mathbf{m}_c(t; \tilde{g}_0)$ for the undamped magnetization dynamics in order to calculate the Melnikov function: it is sufficient to know the geometrical shape of the unperturbed trajectories, i.e., the constant-$\tilde{g}_L$ lines given by Eq. (7.53). Figure 7.8 illustrates the example of application of this method to the thin film with negligible crystal anisotropy considered in Fig. 7.1. The Melnikov function is calculated from Eqs (7.6), (7.51) and (7.55) for all energies in the interval $\tilde{g}_d \leq \tilde{g}_0 \leq \tilde{g}_u$, where $\tilde{g}_d$ and $\tilde{g}_u$ represent the energies of the critical points d and u in the $\mathrm{m}_z > 0$ hemisphere in Fig. 7.8. One finds that: $M(\tilde{g}_d) < 0$; $M(\tilde{g}_u) = 0$, in agreement with the fact that the Melnikov function is zero by definition for every energy extremum; $\partial M/\partial \tilde{g}_0|_{\tilde{g}_0 = \tilde{g}_u} < 0$, which means that the energy maximum is going to be an unstable focus of the dissipative dynamics. The above facts imply that there must exist at least one additional $M(\tilde{g}_0)$ zero inside the interval $\tilde{g}_d < \tilde{g}_0 < \tilde{g}_u$. In fact, one finds just one

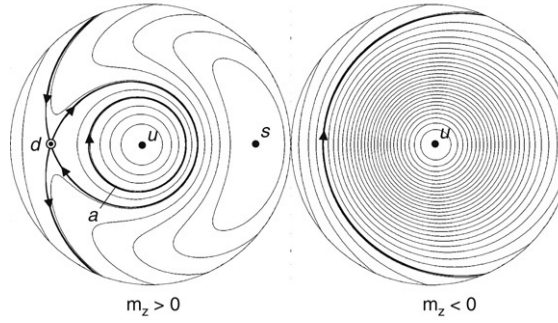

FIGURE 7.8 Phase portrait for nondissipative dynamics. Trajectories coincide with the lines of constant effective energy $\tilde{g}_L(\mathbf{m}; \mathbf{h}_a) = \tilde{g}_0$ (see Eqs (7.8) and (7.51)). The following notation is used. s: $\tilde{g}_L$ minimum; u: $\tilde{g}_L$ maxima; d: $\tilde{g}_L$ saddle. System parameters: $\alpha = 0$, $\kappa_{\text{eff}} = -1$. Field frequency: $\omega = 0.5$. Field amplitude: $\mathrm{h}_{az} = 0.8$, $\mathrm{h}_{a\perp} = 0.08$. Trajectory labeled by a is a stable limit cycle present in the dissipative dynamics in the limit of small damping α, as predicted by the Poincaré–Melnikov method (compare with bottom phase portrait in Fig. 7.1).

additional zero. The corresponding trajectory is labeled by a in Fig. 7.8. This trajectory will be a stable limit cycle of the dissipative dynamics for sufficiently small α. The comparison with Fig. 7.1 shows that this limit cycle is indeed present in the dynamics even when α is as large as 0.1.

7.4 BIFURCATION DIAGRAMS

The autonomous nature of LLG dynamics in the rotating frame permits one to describe this dynamics in geometric terms by using its phase portrait [741,358,529,319]. An example was shown in Fig. 7.1. The basic qualitative aspects of the dynamics are determined by the number of stable (s), unstable (u), and saddle (d) fixed points (**P**-modes), as well as by the number of stable (a) and unstable (r) limit cycles (**Q**-modes). In this section, we discuss the conditions under which qualitatively different phase portraits are to be expected.

It has been demonstrated that when the damping parameter α is constant, the phase portraits of the magnetization dynamics belong to one of two classes, depending on whether they contain two or four fixed points. The simplest representatives of these two classes are shown in Figs 7.9 and 7.10.

- Two **P**-modes: $(s|u)$ portrait (Fig. 7.9)

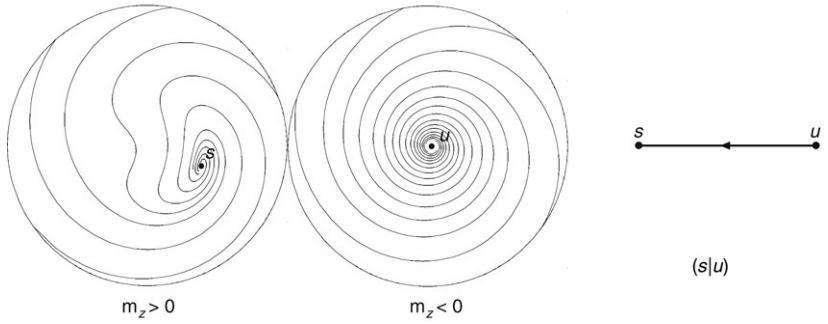

FIGURE 7.9 Example of $(s|u)$ phase portrait. System parameters: $\alpha = 0.1$, $\kappa_{\text{eff}} = -1$. Field frequency: $\omega = 0.5$. Field amplitude: $\mathrm{h}_{az} = 1.3$, $\mathrm{h}_{a\perp} = 0.1$. s: stable node; u: unstable node. Simplified graphical representation of phase portrait is given on the right.

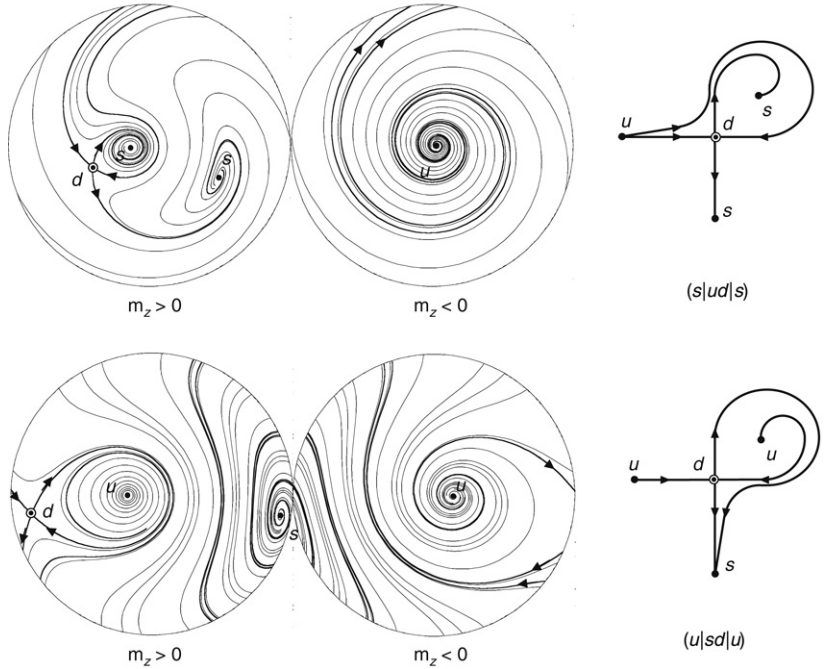

FIGURE 7.10 Examples of $(s|ud|s)$ and $(u|sd|u)$ phase portraits. System parameters: $\alpha = 0.1$, $\kappa_{\text{eff}} = -1$. Field frequency: $\omega = 0.5$. Top: $\mathrm{h}_{az} = 1.1$, $\mathrm{h}_{a\perp} = 0.1$. Bottom: $\mathrm{h}_{az} = 0.6$, $\mathrm{h}_{a\perp} = 0.3$. s: stable node; u: unstable node; d: saddle. Simplified graphical representation of phase portraits is given on the right.

The two fixed points are both nodes (foci) of the dynamics. One of them is stable, (s), while the other is unstable, (u). All magnetization trajectories proceed from u to s. For this class of phase portraits, we shall adopt the notation: $(s|u)$.

- Four **P**-modes: $(u|sd|u)$ or $(s|ud|s)$ portraits (Fig. 7.10)
  In this case, as predicted by Poincaré index theorem, there are three nodes and one saddle. The presence of the saddle governs the structure of the phase portrait. The separatrix trajectories originating from the saddle must be connected to one of the remaining fixed points. Since there are three fixed points and four separatrix lines, one of the nonsaddle fixed points will be connected to the saddle by two separatrix lines. Two situations are possible: (i) the doubly connected fixed point is stable and the remaining two fixed points are unstable; (ii) the doubly connected fixed point is unstable and the remaining two fixed points are stable. These two phase portraits will be denoted as $(u|sd|u)$ and $(s|ud|s)$, respectively. The symbol next to d denotes the fixed point doubly connected to the saddle.

The simplified graphical representation on the right of Figs 7.9 and 7.10 reflects the essential features of the respective phase portrait.

Starting from the two fundamental types of phase portrait shown in Figs 7.9 and 7.10, more complicated phase portraits containing one or more limit cycles can be conceived. In fact, a stable (unstable) fixed point surrounded by an unstable (stable) limit cycle is equivalent to an unstable (stable) fixed point as far as the connectivity to the rest of the phase portrait is concerned. Formally one can use substitution rules of the form $s \rightarrow ua$ or $u \rightarrow sr$ in the phase-portrait notation previously introduced, in order to construct phase portraits of increasing complexity. These rules can be translated into corresponding modifications in the simplified graphical representations introduced in Figs 7.9 and 7.10. For example, given an $(s|u)$ phase portrait, one arrives at new phase portraits of type $(ua|u)$ and $(s|rs)$. Similarly, starting from $(u|sd|u)$ phase portraits, one obtains phase portraits of type $(sr|sd|u)$, $(u|uad|u)$, $(sr|uad|u)$, etc. The simplified graphical representations in Fig. 7.1 illustrate this idea in the case of phase portraits with one or two limit cycles. We shall see that the stable limit cycle in a $(ua|u)$ phase portrait plays a role similar to that of the sd pair in a $(u|sd|u)$ phase portrait. For this reason, the symmetric notation, $(u|a|u)$ or $(s|r|s)$ instead of $(ua|u)$ or $(sr|s)$, will also be used whenever it will be appropriate.

In principle, by using the substitution rules just outlined one can generate phase portraits containing an arbitrary number of limit cycles. However, one does not know if all of these phase portraits can be

admissible phase portraits of the physical LLG dynamics. In fact, determining which phase portraits are admissible and which are not is a problem of remarkable difficulty, for which no general solution is known (see Chapter 5). The direct inspection of the individual phase portraits generated by specific excitation conditions may be often necessary in order to obtain quantitative information about the number of limit cycles actually present in the dynamics.

For a given phase portrait, a slight change in the control parameters will usually lead to slight modifications of the phase portrait, without altering its structure. When this is the case, the phase portrait is said to be structurally stable. Bifurcation phenomena are structural changes in the topology of the phase portrait occurring at some critical value of the control parameters [358,428,304]. One can have local bifurcations, related to changes in the number and/or the nature of fixed points, or global bifurcations, where changes occur in the connectivity of trajectories, even if the number and the nature of the fixed points does not change. Important cases of bifurcations are discussed below.

- Saddle–node bifurcation
  This bifurcation occurs when a saddle–node pair is created or annihilated and the system passes from two to four fixed points or vice versa. The bifurcation condition is expressed by the equation $\det A_0 = 0$ (see Eq. (7.43)).
- Andronov–Hopf bifurcation
  This bifurcation takes place when a nonsaddle fixed point is changed from stable to unstable or vice versa with the simultaneous creation or destruction of a limit cycle around the fixed point. The bifurcation condition is $(\mathrm{tr}\, A_0 = 0, \det A_0 > 0)$ (see Eq. (7.45)). At a Hopf bifurcation point, the eigenvalues of the stability matrix A_0 are purely imaginary, i.e., they are of the form $\pm \mathrm{i}\omega_H$, where $\omega_H = (\det A_0)^{1/2}$. The parameter ω_H represents the angular frequency of the periodic motion along the limit cycle that is created or destroyed by the bifurcation. By calculating the value of $\det A_0$ when $\mathrm{tr}\, A_0 = 0$ by means of Eqs (7.40) and (7.41) one finds:

$$\omega_H = \sqrt{\omega^2 \cos^2 \theta_0 - \frac{\kappa_{\mathrm{eff}}^2 \sin^4 \theta_0}{4\,(1+\alpha^2)}}. \tag{7.56}$$

- Homoclinic-saddle-connection bifurcation
  This bifurcation occurs when a homoclinic saddle connection is formed and the connection between the saddle and the other fixed

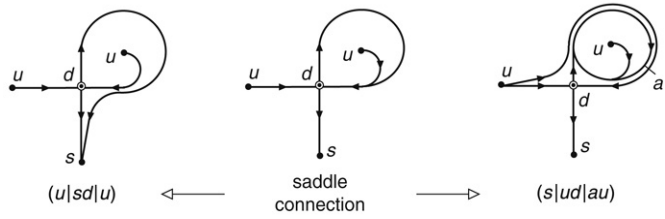

FIGURE 7.11 Simplified graphical representation of homoclinic-saddle-connection bifurcation.

points is changed (see Fig. 7.11 for an example). A limit cycle is created or destroyed when the saddle connection is formed. The bifurcation condition can be expressed in terms of the Melnikov function associated with the energy region bounded by the saddle connection:

$$M\left(\tilde{g}_{sc}, \zeta\right) = 0, \tag{7.57}$$

where $\tilde{g}_{sc}$ is the energy of the undamped saddle-connection trajectory. In fact, this energy must be a zero of the Melnikov function if a limit cycle is to be created or annihilated as a result of the saddle-connection bifurcation.

- Semi-stable-limit-cycle bifurcation
  In this bifurcation a pair of limit cycles with opposite stability is created or annihilated. Also in this case the bifurcation condition can be expressed in terms of the Melnikov function, namely:

$$M\left(\tilde{g}_0, \zeta\right) = 0, \qquad \frac{\partial M\left(\tilde{g}_0, \zeta\right)}{\partial \tilde{g}_0} = 0. \tag{7.58}$$

  The above conditions guarantee that a pair of zeros of the Melnikov function (i.e., a pair of limit cycles) will be simultaneously created or annihilated.

The classification of LLG phase portraits and bifurcations presented above is the starting point for the study of the phase diagram of magnetization dynamics in the $(\mathrm{h}_{az}, \mathrm{h}_{a\perp})$ control plane under constant ω. The diagram can be progressively developed starting from the stability properties of **P**-modes for large and low values of magnetic fields, where particularly simple results are valid.

Let us first consider the case of large field amplitudes. By eliminating $\cos\theta_0$ from Eqs (7.17) and (7.18) one obtains:

$$\frac{\mathrm{h}_{a\perp}^2}{\nu_0^2+\alpha^2\omega^2}+\left(\frac{h_{az}-\omega}{\nu_0-\kappa_{\text{eff}}}\right)^2=1. \tag{7.59}$$

This equation shows that $\mathrm{h}_{a\perp}^2+\left(\mathrm{h}_{az}-\omega\right)^2\simeq\nu_0^2$ for very large ν_0^2. Therefore, the limit $\nu_0^2\to\infty$ represents the limit of large field amplitudes. By letting $\nu_0^2\to\infty$ in Eq. (7.40) and taking into account that $\alpha\ll 1$, one finds that $\det A_0\simeq\nu_0^2/\left(1+\alpha\right)^2$. Only two **P**-modes can be present at large fields, because $\det A_0>0$. In addition, when the applied field is large it dominates the effective field, which means that the Melnikov function (Eq. (7.55)) can be calculated under the approximation: $\mathbf{m}\times\mathbf{h}_{\text{eff}}\simeq\mathbf{m}\times\mathbf{h}_a$ and $\mathrm{d}\mathbf{m}/\mathrm{d}t\simeq-\mathbf{m}\times\mathbf{h}_a$. This shows that $M\left(\tilde{g}_0\right)>0$, so no limit cycles can be present. Therefore, at high fields the phase portrait is always of $(s|u)$ type. On the other hand, at low rotating field amplitudes one can take advantage of the analysis presented in the previous section to infer the existence of **Q**-modes. That analysis indicates that the typical phase portrait at low rotating fields will be either of $(s|r|s)$ or $(u|a|u)$ type.

The complete phase diagram for a given system can be constructed by using these limit cases as a starting point and by incorporating the changes in the phase portrait that occur when bifurcation lines are crossed. The plane $(\mathrm{h}_{az},\mathrm{h}_{a\perp})$ is divided into regions associated with different phase portraits by the lines $\det A_0=0$ and $\mathrm{tr}\,A_0=0$ when $\det A_0>0$. These are the lines along which saddle–node and Hopf bifurcations take place. Additional partitions of the control plane arise because of the presence of homoclinic-saddle-connection or semi-stable-limit-cycle bifurcation lines. These bifurcations can be studied by analyzing the zeros of the Melnikov function (7.55). Some hint to the location of these global bifurcation lines comes from the fact that Hopf, homoclinic-saddle-connection, and semi-stable limit-cycle bifurcations are the only mechanisms creating or destroying limit cycles. Therefore, any region in the control plane associated with a phase portrait containing limit cycles must necessarily be confined by one of these bifurcation lines.

The various phase diagrams associated with different values of the system parameters $(\alpha,\kappa_{\text{eff}})$ and the field frequency ω result in a large number of interesting situations, which cannot be all discussed here. In general, when $|\kappa_{\text{eff}}|\gg\omega$ the situation approaches that of the Stoner–Wohlfarth model [639,79] and the results known for that model become approximately valid. Conversely, a rich variety of new situations is encountered when one departs from that limit. We shall restrict our discussion to a few cases of particular physical interest.

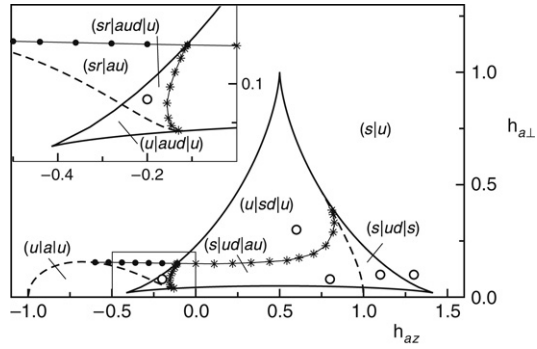

FIGURE 7.12 Phase diagram in $(\mathrm{h}_{az}, \mathrm{h}_{a\perp})$ control plane for a thin-film disk with negligible crystal anisotropy. Bifurcation lines: saddle–node (continuous); Hopf (dashed); homoclinic-saddle-connection (asterisks); semi-stable limit cycles (black circles). Inset: magnified view of framed region. Small empty circles indicate the locations corresponding to the phase portraits shown in Figs 7.1, 7.9 and 7.10. System parameters: $\alpha = 0.1$, $\kappa_{\text{eff}} = -1$. Field frequency: $\omega = 0.5$.

Figure 7.12 shows the complete phase diagram for a soft thin-film disk characterized by $\kappa = 0$ and $N_z = 1$, i.e., $\kappa_{\text{eff}} = -1$. A remarkably rich structure is revealed. Phase portraits with zero, one, or two limit cycles are present, separated by bifurcation lines of the four types previously discussed. As an example of the information that can be obtained from this diagram, let us analyze the behavior of the thin-film disk when the field h_{az} is kept at the constant value $\mathrm{h}_{az} = 0.6$ and the radio-frequency field amplitude $\mathrm{h}_{a\perp}$ is gradually increased. When $\mathrm{h}_{a\perp} = 0$ (i.e., there is no rotating field), the situation is static. According to Eqs (7.15) and (7.16) there exist two fixed points for the magnetization corresponding to $\sin\theta_0 = 0$, i.e., $\theta_0 = 0$ and $\theta_0 = \pi$. It can be verified that both these fixed points are unstable. However, when $\mathrm{h}_{a\perp} = 0$, Eqs (7.13)–(7.14) admit another solution: $\cos\theta = -h_{\text{eff}}/\kappa_{\text{eff}}, \mathrm{d}\phi/\mathrm{d}t = \omega$. This solution represents a limit cycle (**Q**-mode) traversed at the angular frequency $\omega_Q = \omega$. Accordingly, the phase portrait is of $(u|a|u)$ type. In the laboratory frame, this limit cycle results in a continuous set of marginally stable equilibrium states characterized by the same value of θ and arbitrary angle ϕ (see previous section). According to Eq. (7.49), the energy is minimum with respect to θ for all these states. When $\mathrm{h}_{a\perp}$ is increased, the value of $\cos\theta_0$ associated with the two unstable fixed points is reduced: the limit cycle, initially centered about the symmetry axis, becomes increasingly distorted, and the associated angular frequency ω_Q is progressively

reduced. In the laboratory frame, the limit cycle gives rise to a **Q**-mode, i.e., to a quasi-periodic motion where the magnetization precesses about the symmetry axis at the angular frequency $\omega - \omega_Q$ with superimposed nutations at the frequency ω. It looks as if the magnetization follows the rotating field periodically falling off synchronism. When $\mathrm{h}_{a\perp}$ becomes large enough, the critical value is reached (~ 0.15 for the case shown in Fig. 7.12) for which the limit cycle is destroyed by the homoclinic-saddle-connection bifurcation. The system jumps from the **Q**-mode to a stable **P**-mode: the magnetization gets locked to the field and is driven in synchronism with the field at the frequency ω. It is instructive to note that hysteresis will appear in the response under increasing or decreasing rotating field amplitude. In fact, under increasing field there is a jump from the **Q**-mode to the **P**-mode through the homoclinic-saddle-connection bifurcation, whereas under decreasing field there is a jump from the **P**-mode to the **Q**-mode through the saddle–node bifurcation which occurs at a definitely lower value of $\mathrm{h}_{a\perp}$, of the order of 0.05.

The phase diagram for a system with $\kappa_{\text{eff}} = 1$, i.e., a bistable particle with the easy magnetization axis along $\mathbf{e}_z$ and total effective anisotropy equal to 1, can be immediately obtained from that shown in Fig. 7.12 by changing everywhere s into u fixed points and vice versa, as well as a into r limit cycles and vice versa. This rule is derived from the previously discussed fact that changing the sign of the effective anisotropy constant is basically equivalent to reversing the direction of time. Interestingly, $(s|rsd|s)$ phase portraits become possible under positive anisotropy for those field values for which $(u|aud|u)$ portraits are predicted under negative anisotropy (see Fig. 7.12). This means that phase portraits with three stable **P**-modes are made possible by the driving action of the radio-frequency field despite the bistable character of the free energy.

Completely different results are obtained when one considers a sphere with negligible crystal anisotropy, i.e., $\kappa = 0$, $N_z = 1/3$, $\kappa_{\text{eff}} = 0$. In this case, the $\det A_0 \leq 0$ region is reduced to the single point $(\cos\theta_0 = 0, \nu_0 = 0)$, i.e., $(\mathrm{h}_{az} = \omega, \mathrm{h}_{a\perp} = \alpha\omega)$. Therefore, two **P**-modes only will exist for any arbitrary choice of the control parameters. On the other hand, the line $\mathrm{tr}\, A_0 = 0$ is reduced to $\nu_0 + \omega\cos\theta_0 = 0$, which, after substitution into Eqs (7.20) and (7.21), yields:

$$\left[\mathrm{h}_{az} - \frac{\omega\left(1+\alpha^2\right)}{2}\right]^2 + \mathrm{h}_{a\perp}^2 = \frac{\omega^2\left(1+\alpha^2\right)^2}{4}. \tag{7.60}$$

This equation represents a circular arc joining the origin with the point $(\mathrm{h}_{az} = \omega, \mathrm{h}_{a\perp} = \alpha\omega)$, the center of the circle lying on the h_{az} axis (see

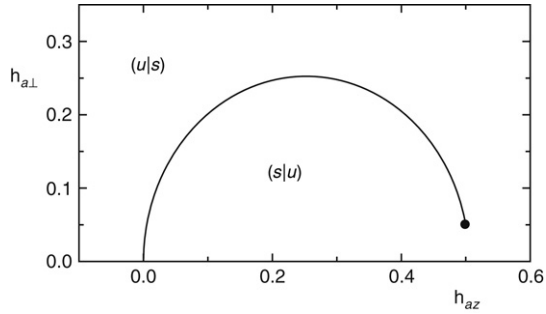

FIGURE 7.13 Phase diagram in $(h_{az}, h_{a\perp})$ control plane for a sphere with negligible crystal anisotropy. Continuous line: highly nongeneric bifurcation line (see Eq. (7.60)) connecting origin with point $(\omega, \alpha\omega)$. System parameters: $\alpha = 0.1$, $\kappa_{\text{eff}} = 0$. Field frequency: $\omega = 0.5$.

Fig. 7.13). This line identifies a highly nongeneric bifurcation condition. The phase portrait is of $(s|u)$ type in the entire control plane. Whenever the bifurcation line is crossed the stability of the two **P**-modes is simultaneously reversed. The entire phase portrait takes the form of concentric, closed trajectories surrounding the fixed points. Accordingly, switching from the unstable to the stable **P**-mode will occur through lengthy transients hardly distinguishable from a quasi-periodic response.

7.5 NONLINEAR FERROMAGNETIC RESONANCE, FOLDOVER, AND SWITCHING PHENOMENA

The field region close to the right-hand corner of the region $\det A_0 < 0$ in Fig. 7.12 is where ferromagnetic resonance phenomena occur [740,306]. In typical ferromagnetic resonance experiments, the large dc field $h_{az} > 0$ is initially applied with $h_{a\perp} = 0$. In this case, the ensuing **P**-mode coincides with the magnetization saturation state along the positive $\mathbf{e}_z$ axis. Then the rf field of amplitude $h_{a\perp}$ and angular frequency ω is switched on. The resonance experiment is carried out by slowly decreasing the field h_{az} while keeping $h_{a\perp}$ and ω constant. Resonance occurs when the Larmor frequency associated with the effective field becomes equal to the rotating field frequency ω. In dimensionless notation, this means that:

$$h_{az} + \kappa_{\text{eff}} \simeq \omega. \tag{7.61}$$

The resonance becomes manifest when one considers the power p absorbed in the **P**-mode regime under fixed $\mathrm{h}_{a\perp}$ and variable h_{az}. By using Eqs (7.23) and (7.18) one obtains:

$$p \equiv \mathbf{h}_{a\perp} \cdot \frac{\mathrm{d}\mathbf{m}_\perp}{\mathrm{d}t} = \alpha\omega^2 \sin^2\theta_0 = \frac{\alpha\omega^2 \mathrm{h}_{a\perp}^2}{\nu_0^2 + \alpha^2\omega^2}. \tag{7.62}$$

When the rf field is small, the angle θ_0 is small as well and one can use Eq. (7.17) with the approximation $\cos\theta_0 \simeq 1$ to express ν_0 in terms of h_{az}. Under this approximation, Eq. (7.62) yields:

$$p = \frac{\alpha\omega^2 \mathrm{h}_{a\perp}^2}{\left(\mathrm{h}_{az} + \kappa_{\mathrm{eff}} - \omega\right)^2 + \alpha^2\omega^2}. \tag{7.63}$$

We obtain the Lorentzian-shape line typical for linear resonance. The absorbed power is maximum for $\mathrm{h}_{az} + \kappa_{\mathrm{eff}} = \omega$, as anticipated, and the line width is $\alpha\omega$.

For larger rf fields, large precessional motions occur and the approximation $\cos\theta_0 \simeq 1$ is no longer acceptable. To deal with this nonlinear regime, we can use Eq. (7.30) to express h_{az} as a function of $\cos\theta_0$ for the **P**-mode under consideration. As a result, one finds:

$$\mathrm{h}_{az} = \omega - \kappa_{\mathrm{eff}} \cos\theta_0 \pm \cos\theta_0 \sqrt{\frac{\mathrm{h}_{a\perp}^2}{\sin^2\theta_0} - \alpha^2\omega^2}. \tag{7.64}$$

Equations (7.62) and (7.64) give the parametric representation for the absorbed power $p(\mathrm{h}_{az})$ under nonlinear conditions. An example is shown in Fig. 7.14 for the case of a thin-film disk with negligible crystal anisotropy ($\kappa_{\mathrm{eff}} = -1$). The initial condition, where $\cos\theta_0 \simeq 1$ and h_{az} is very large and positive corresponds to choosing the branch with the positive sign in Eq. (7.64). This is the correct branch to consider when $\cos\theta_0$ is decreased from $\cos\theta_0 = 1$ down to $\sin^2\theta_0 = \mathrm{h}_{a\perp}^2/\alpha^2\omega^2$, where the square root in Eq. (7.64) vanishes. This is where the absorbed power is maximum. From here, the branch with the negative sign in Eq. (7.64) must be considered for $\cos\theta_0$ increasing from the minimum resonance value back to $\cos\theta_0 = 1$. As shown in Fig. 7.14, the absorbed power profile gets increasingly distorted under increasing rf field amplitude. According to Eq. (7.62), the state of maximum absorbed power always corresponds to $\nu_0 = 0$. From Eqs (7.17) and (7.18) one finds that this condition is described

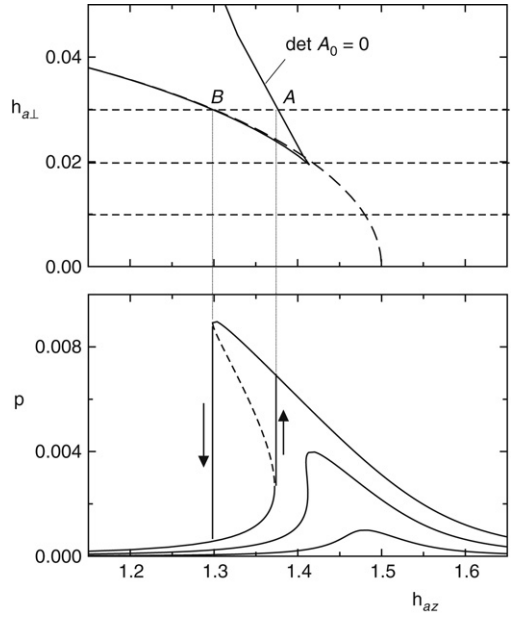

FIGURE 7.14 Top: Magnified view of right-hand corner of $\det A_0 < 0$ region shown in Fig. 7.12 for the case of a soft magnetic thin film. Horizontal dashed lines: h_{az} field variations for resonance experiments with rf field amplitudes $h_{a\perp} = 0.01, 0.02, 0.03$. Curved dashed line: $\nu_0 = 0$ nonlinear resonance condition (Eq. (7.65)). A and B: saddle–node bifurcation points where instability in system response may occur. Bottom: Absorbed power (Eqs (7.62) and (7.64)) for $h_{a\perp} = 0.01, 0.02, 0.03$ with representation of foldover jumps taking place for the highest rf field amplitude at points A and B. System parameters: $\alpha = 0.1$, $\kappa_{\text{eff}} = -1$. Field frequency: $\omega = 0.5$.

by the equation:

$$h_{a\perp} = \frac{\alpha\omega}{|\kappa_{\text{eff}}|}\sqrt{\kappa_{\text{eff}}^2 - (h_{az} - \omega)^2}. \tag{7.65}$$

This is the curved dashed line shown in Fig. 7.14.

When κ_{eff} is negative and large enough, the distortion of the absorbed power profile can become so important that the system becomes unstable and hysteretic jumps appear in the absorbed power. This phenomenon has been observed and is known in the literature as "foldover" [590,254]. Foldover effects are properly understood by using the bifurcation analysis

presented in the previous section. Let us consider the representation of **P**-modes in the $(\mathrm{h}_{az}, \mathrm{h}_{a\perp})$ field control plane. During the resonance experiment, the **P**-mode under study moves from right to left along a horizontal line in the control plane, as shown in Fig. 7.14. If this line crosses the boundary of the $\det A_0 < 0$ region (point A in Fig. 7.14), a saddle–node pair of additional **P**-modes is created. The **P**-mode motion is destroyed at point B in Fig. 7.14 by a second saddle–node bifurcation involving the saddle previously created at point A. Consequently, the system becomes unstable and jumps to a different **P**-mode of definitely smaller amplitude. If the field h_{az} is now increased, the newly attained **P**-mode evolves under the action of the field until it is destroyed by the saddle–node bifurcation at point A in Fig. 7.14 where the system jumps back to the original **P**-mode. It is clear from this analysis that the $\mathrm{h}_{a\perp}$ threshold beyond which foldover becomes possible coincides with the ordinate of the lower right-hand tip of the curve defined by the equation $\det A_0 = 0$. This tip has the largest h_{az} coordinate and the smallest $\mathrm{h}_{a\perp}$ coordinate among all points of the above curve. Consequently, the corresponding value $\cos\theta_F$ of $\cos\theta_0$ can be found as the solution of the equation:

$$\frac{\mathrm{d}\mathrm{h}_{az}}{\mathrm{d}\cos\theta_0} = \frac{\partial \mathrm{h}_{az}}{\partial \cos\theta_0} + \frac{\partial \mathrm{h}_{az}}{\partial \nu_0}\frac{\mathrm{d}\nu_0}{\mathrm{d}\cos\theta_0} = 0. \tag{7.66}$$

By using Eq. (7.20) for h_{az} and by taking into account Eq. (7.43) for the function $\nu_0(\cos\theta_0)$ describing the curve $\det A_0 = 0$, after somewhat lengthy but straightforward calculations, we derive from Eq. (7.66) the following equation for $x = \cos^2\theta_F$:

$$3x^2 - 2(4A - 1)x + 3 = 0, \tag{7.67}$$

where:

$$A = 1 + \frac{2\alpha^2\omega^2}{\kappa_{\mathrm{eff}}^2}. \tag{7.68}$$

By solving Eq. (7.67), one finds:

$$\cos^2\theta_F = 1 + \frac{8}{3}\frac{\alpha^2\omega^2}{\kappa_{\mathrm{eff}}^2} - \sqrt{\left(1 + \frac{8}{3}\frac{\alpha^2\omega^2}{\kappa_{\mathrm{eff}}^2}\right)^2 - 1}. \tag{7.69}$$

By substituting Eq. (7.69) first into Eq. (7.43) and then into Eq. (7.21) for $h_{a\perp}$, we find the exact expression for the critical field for the foldover phenomenon. This expression is quite lengthy; however, in the typical case when $\alpha\omega \ll 1$ it can be simplified and presented in the form:

$$h_{a\perp}^2 \simeq \frac{16\,(\alpha\omega)^3}{3\sqrt{3}|\kappa_{\text{eff}}|}. \tag{7.70}$$

The last formula is consistent with the classical estimate of Anderson and Suhl [22]:

$$h_{a\perp}^2 \simeq 3.08\frac{(\alpha\omega)^3}{|\kappa_{\text{eff}}|}, \tag{7.71}$$

obtained for thin-film geometries through an approximate linear analysis.

Next, we shall discuss magnetization switching under rotating magnetic fields. This type of switching is of significant interest in the area of microwave-assisted magnetic recording [762]. In the classical Stoner–Wohlfarth (SW) theory [639,79], the possible magnetization states of a uniformly magnetized spheroidal particle with uniaxial anisotropy are determined as a function of the field acting on the particle. Let us denote by h_{az} and $h_{a\perp}$ the field components parallel and perpendicular to the anisotropy axis, respectively. Irreversible jumps in the magnetization orientation occur whenever the stability of the state occupied by the system is destroyed by the action of the field. The field conditions which lead to this occurrence are described by the astroid equation:

$$h_{az}^{2/3} + h_{a\perp}^{2/3} = h_{AN}^{2/3}, \tag{7.72}$$

where h_{AN} is the anisotropy field. The system admits four energy extrema inside the astroid: two energy minima, one energy maximum and one saddle. In addition, two extrema exist outside the astroid: one energy minimum and one energy maximum. Energy minima are the stable equilibrium states for the system and switching occurs from one to another at the astroid boundary. The SW model provides a simple framework of fundamental importance for the interpretation of magnetization reversal in fine particles and thin films.

The analysis of **P**-mode properties in uniformly magnetized particles worked out in the previous sections may be construed as a dynamic generalization of the SW model, in which the field component $h_{a\perp}$ is rotated at the frequency ω and the LLG equation is solved in order to

calculate the magnetization dynamics driven by this field [392,453]. The analogy becomes manifest in the rotating frame of reference in which the field is stationary and the dynamics acquire autonomous form. **P**-modes are the dynamic counterparts of the static equilibrium states present in the SW model. In fact, similarly to the SW case, only two types of dynamics are possible, characterized by two or four **P**-modes. The boundary between the field regions where these two situations are realized corresponds to the condition $\det A_0 = 0$. In parametric form it is described by Eqs (7.20)–(7.21), with $\cos\theta_0$ as a parameter (the only parameter after one uses Eq. (7.43) to express ν_0 as a function of $\cos\theta_0$). This boundary is the natural generalization of the astroid (7.72), and indeed it is reduced to it in the limit of $\omega \to 0$.

Magnetization switching under rotating fields can be studied by analyzing **P**-mode stability under constant ω and variable $(\mathrm{h}_{az}, \mathrm{h}_{a\perp})$. Switching events are the physical counterpart of the occurrence of bifurcations in the system dynamics. In the SW model, there is only one possibility, i.e., switching caused by a saddle–node bifurcation at the astroid boundary. In contrast, more complicated switching processes may occur under the rotating field as a consequence of the various bifurcation mechanisms, i.e., Andronov–Hopf, homoclinic saddle connection, semi-stable limit cycle, present in LLG dynamics in addition to saddle–node bifurcations (see the discussion in the previous sections). These additional bifurcation mechanisms play an important role because they involve the creation or destruction of limit cycles (**Q**-modes). As a consequence, switching from **P**-type to **Q**-type response or vice versa becomes possible.

As an example of hysteresis and switching under circularly polarized field, let us consider a particle with $\kappa_{\text{eff}} > 0$ subject to a rotating field of constant amplitude $\mathrm{h}_{a\perp}$ and let us analyze the response of the system when the field h_{az} is slowly cycled between opposite large values. The condition of constant $\mathrm{h}_{a\perp}$ and slowly varying h_{az} is described by a horizontal line in the $(\mathrm{h}_{az}, \mathrm{h}_{a\perp})$-plane (see Fig. 7.15). The points A, B, etc. where this line crosses the various bifurcation lines of the problem are potential switching points where the system may jump from one **P**-mode to another or between **P**-type and **Q**-type responses. The two or four **P**-modes present in the dynamics are characterized by different values of the magnetization component $\mathrm{m}_z \equiv \cos\theta_0$ as a function of h_{az}, obtained by solving Eq. (7.30) (see Fig. 7.16). The field history determines which m_z state is realized under given h_{az}. For monotonically increasing field h_{az}, bifurcations encountered at points A, B, etc. involve states different from the state occupied by the system. Switching occurs only at point E, where the system becomes unstable because of a Hopf bifurcation. Switching

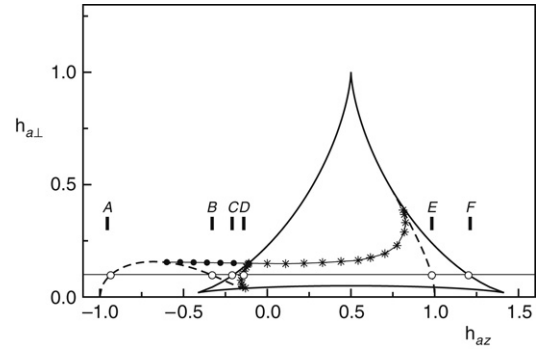

FIGURE 7.15 Control plane $(h_{az}, h_{a\perp})$ with bifurcation lines for a bistable particle with positive effective anisotropy (compare with the system with opposite anisotropy shown in Fig. 7.12). The horizontal continuous line describes field variation in which $h_{a\perp} = 0.1$ and h_{az} is swept between large opposite values. Circles labeled A through E are points where the field crosses bifurcation lines and magnetization switching may occur (see Fig. 7.16). System parameters: $\alpha = 0.1$, $\kappa_{\text{eff}} = 1$. Field frequency: $\omega = 0.5$.

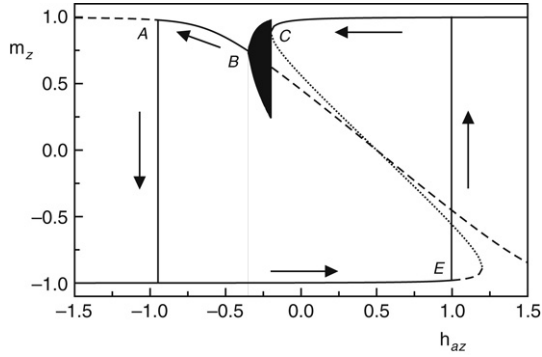

FIGURE 7.16 Representation of $m_z \equiv \cos\theta_0$ versus h_{az} under constant $h_{a\perp} = 0.1$ for different **P**-modes, calculated from Eq. (7.30). Continuous lines: stable states; dashed lines: unstable states; dotted line: saddle state. Letters A, B, C, E refer to bifurcation points indicated in Fig. 7.15. Arrows indicate hysteresis loop traversed when h_{az} is swept between large opposite values. The gray region from C to B represents the region of quasi-periodic response (**Q**-mode) in which m_z oscillates between the lower and upper bounds of the region. System parameters: $\alpha = 0.1$, $\kappa_{\text{eff}} = 1$. Field frequency: $\omega = 0.5$.

results in the sudden m_z jump from negative to positive value shown in Fig. 7.16. Note that, in contrast with what occurs in the SW model,

the saddle–node bifurcation at the astroid boundary F plays no role in this case. For monotonically decreasing field h_{az}, the situation is more complex. A first switching event occurs at point C, where the stable state occupied by the system is destroyed by a saddle–node bifurcation. The system jumps from **P**-type to **Q**-type response, with the appearance of spontaneous magnetization oscillations at a frequency much lower than ω. These oscillations persist in the entire field interval from C to B. At point B, the **Q**-mode is changed into a **P**-mode by a Hopf bifurcation. No magnetization jump occurs at this point. Finally, switching occurs at point A, because of a second Hopf bifurcation in which m_z jumps back from positive to negative values. The increasing-field branch of the loop is fully reversible up to point E, where switching occurs. This is not the case for the decreasing-field branch. In fact, if the field is decreased down to a value in the interval from B to A and then increased again, one obtains a different sequence of states: the quasi-periodic motion survives up to higher values of h_{az}, until it is destroyed by the saddle-connection bifurcation at point D. Finally, it is worth remarking that the upper and lower branches of the hysteresis loop in Fig. 7.16 are no longer symmetric as they would be under quasi-static excitation. This is because the choice of the sense of rotation of the radio-frequency field with respect to the orientation of the dc field h_{az} breaks the usual hysteresis loop symmetry.

7.6 MAGNETIZATION DYNAMICS UNDER DEVIATIONS FROM ROTATIONAL SYMMETRY

The **P**-mode analytical solutions obtained in the previous sections do exist as a consequence of the autonomous character of the magnetization dynamics in the rotating frame of reference, which in turn is the direct consequence of the rotational invariance of the original problem. In this section we discuss how the **P**-mode solutions can be extended to the case when the system is not rotationally invariant. This is accomplished by treating the deviations from uniaxial (rotational) symmetry as perturbations of the symmetric problem [86]. This perturbation approach leads to linearized equations for magnetization perturbations. The perturbation technique is developed in the rotational frame of reference which moves in synchronism with circularly polarized fields. This choice of reference frame leads to a linear equation for perturbation with constant (time-independent) coefficients, which significantly facilitates their analytical solution. It is important to stress that in this section the perturbation technique is applied around the analytical solution of the LLG equation for "large motions". This is in contrast with the

conventional approach where the perturbation technique is used in order to obtain "small motion" solutions of the LLG equation [306].

In order to discuss the deviations from rotational invariance, we shall write the effective field in the form:

$$\mathbf{h}_{\text{eff}} = \mathbf{h}_a(t) + \mathbf{h}_{AN} - N_x \mathrm{m}_x \mathbf{e}_x - N_y \mathrm{m}_y \mathbf{e}_y - N_z \mathrm{m}_z \mathbf{e}_z, \tag{7.73}$$

where $\mathbf{e}_x$, $\mathbf{e}_y$, $\mathbf{e}_z$ are cartesian unit vectors in the laboratory frame, whereas N_x and N_y describe possible deviations from the demagnetizing factor $N_\perp$ of the spheroid. We shall express the applied field $\mathbf{h}_a(t)$ as follows:

$$\mathbf{h}_a(t) = \mathbf{h}_a^{\text{dc}} + \mathbf{h}_a^{\text{rf}}(t), \tag{7.74}$$

where $\mathbf{h}_a^{\text{dc}}$ and $\mathbf{h}_a^{\text{rf}}(t)$ represent the dc and radio-frequency fields, respectively.

In general, deviations from rotational invariance can be caused by perturbations of the terms $\mathbf{h}_a^{\text{dc}}$, $\mathbf{h}_a^{\text{rf}}$, h_{AN}, N_x, N_y, present in Eqs (7.73) and (7.74). One can express the dc magnetic field as follows:

$$\mathbf{h}_a^{\text{dc}} = \mathrm{h}_{az}\mathbf{e}_z + \Delta\mathrm{h}_{a\perp}^{\text{dc}}\mathbf{e}_\perp(\psi_{\text{dc}}), \tag{7.75}$$

where as before the symbol "$\perp$" indicates components normal to the $\mathbf{e}_z$ axis, $\mathbf{e}_\perp(\psi_{\text{dc}})$ indicates the unit vector orthogonal to the $\mathbf{e}_z$ axis and forming the angle ψ_{dc} with the x axis, h_{az} and $\Delta\mathrm{h}_{a\perp}^{\text{dc}}$ are the components of $\mathbf{h}_a^{\text{dc}}$ along the z axis and in the (x, y)-plane, respectively. The second term on the right-hand side of Eq. (7.75) represents the deviation of the dc field from its axial direction. When the rf field $\mathbf{h}_a^{\text{rf}}(t)$ is time harmonic and elliptically polarized, its projection on the (x, y)-plane can be decomposed into the sum of two time-harmonic circularly polarized fields, rotating in opposite directions with the same angular frequency ω. This decomposition leads to the following expression:

$$\begin{aligned}\mathbf{h}_a^{\text{rf}}(t) = {} & \mathrm{h}_{a\perp}\left[\cos(\omega t)\mathbf{e}_x + \sin(\omega t)\mathbf{e}_y\right] \\ & + \Delta\mathrm{h}_{a\perp}^{\text{rf}}\left[\cos(\omega t + \psi_\perp)\mathbf{e}_x - \sin(\omega t + \psi_\perp)\mathbf{e}_y\right] \\ & + \Delta\mathrm{h}_{az}^{\text{rf}}\cos(\omega t + \psi_z)\mathbf{e}_z,\end{aligned} \tag{7.76}$$

where $\Delta\mathrm{h}_{az}^{\text{rf}}$ is the amplitude of the z component of the rf field, while $\mathrm{h}_{a\perp}$ and $\Delta\mathrm{h}_{a\perp}^{\text{rf}}$ are, respectively, the amplitudes of the counterclockwise and clockwise rotating components of the rf field in the plane normal to the $\mathbf{e}_z$

axis, and $\psi_\perp$ and ψ_z are initial phases. If the rf field is circularly polarized in the (x, y)-plane, then $\Delta \mathrm{h}_{a\perp}^{\mathrm{rf}} = \Delta \mathrm{h}_{az}^{\mathrm{rf}} = 0$. The anisotropy field h_{AN} is given by:

$$\mathbf{h}_{AN} = \kappa(\mathbf{m} \cdot \mathbf{e}_{AN})\mathbf{e}_{AN}, \tag{7.77}$$

where κ is the anisotropy constant and $\mathbf{e}_{AN}$ is the unit vector parallel to the easy axis. We shall denote by θ_{AN} the angle that $\mathbf{e}_{AN}$ forms with the $\mathbf{e}_z$ axis and by ψ_{AN} the angle between the component of $\mathbf{e}_{AN}$ normal to the $\mathbf{e}_z$ axis and the x axis. Finally, the (x, y) demagnetizing factors can be written as:

$$N_x = N_\perp + \Delta N_\perp, \qquad N_y = N_\perp - \Delta N_\perp, \tag{7.78}$$

where $N_\perp$ is the spheroid demagnetizing factor and the parameter $\Delta N_\perp$ controls the breaking of the spheroidal symmetry.

Let us apply the perturbation technique to the **P**-mode solutions previously discussed in this chapter, by treating $\Delta \mathrm{h}_{a\perp}^{\mathrm{dc}}$, $\Delta \mathrm{h}_{az}^{\mathrm{rf}}$, $\Delta \mathrm{h}_{a\perp}^{\mathrm{rf}}$, θ_{AN}, $\Delta N_\perp$, as small perturbations. We denote by $\mathbf{m}_0(t)$ a given **P**-mode solution, as it appears in the laboratory frame. The perturbed mode can be expressed as:

$$\mathbf{m}(t) = \mathbf{m}_0(t) + \delta\mathbf{m}(t) + \ldots, \tag{7.79}$$

where $\delta\mathbf{m}(t)$ is the perturbation of magnetization dynamics. The equation governing the evolution of the first-order perturbation term $\delta\mathbf{m}(t)$ can be derived by substituting Eq. (7.79) into Eq. (7.9), by using Eqs (7.73)–(7.78) and by neglecting all second-order terms containing products of small quantities such as $\Delta \mathrm{h}_{a\perp}^{\mathrm{dc}}$, $\Delta \mathrm{h}_{az}^{\mathrm{rf}}$, $\Delta \mathrm{h}_{a\perp}^{\mathrm{rf}}$, θ_{AN}, $\Delta N_\perp$ and the components of the vector $\Delta\mathbf{m}(t)$. This leads to the following equation:

$$\begin{aligned} &\frac{\mathrm{d}\delta\mathbf{m}(t)}{\mathrm{d}t} - \alpha\mathbf{m}_0(t) \times \frac{\mathrm{d}\delta\mathbf{m}(t)}{\mathrm{d}t} \\ &= -\delta\mathbf{m}(t) \times \left(\mathbf{h}_{\mathrm{eff}}^{(0)}(t) - \alpha \frac{\mathrm{d}\mathbf{m}_0(t)}{\mathrm{d}t} \right) - \mathbf{m}_0(t) \times \delta\mathbf{h}_{\mathrm{eff}}, \end{aligned} \tag{7.80}$$

where $\mathbf{h}_{\mathrm{eff}}^{(0)} = \mathbf{h}_{a\perp}(t) - N_\perp \mathbf{m}_{0\perp}(t) + [\mathrm{h}_{az} + (\kappa - N_z) m_{0z}]\, \mathbf{e}_z$, $\mathbf{h}_{a\perp}(t)$ is given by Eq. (7.5), and $\delta\mathbf{h}_{\mathrm{eff}}$ is the perturbation of the effective field. This perturbation can be decomposed into two parts: $\delta'\mathbf{h}_{\mathrm{eff}}$ which depends on $\delta\mathbf{m}(t)$ and $\delta''\mathbf{h}_{\mathrm{eff}}$ which contains $\Delta \mathrm{h}_{a\perp}^{\mathrm{dc}}$, $\Delta \mathrm{h}_{az}^{\mathrm{rf}}$, $\Delta \mathrm{h}_{a\perp}^{\mathrm{rf}}$, θ_{AN}, $\delta N_\perp$. One finds

for the two components of $\delta\mathbf{h}_{\text{eff}}$ the following expressions:

$$\delta'\mathbf{h}_{\text{eff}} = -N_\perp \delta\mathbf{m}_\perp + (\kappa - N_z)\delta m_z, \tag{7.81}$$

$$\begin{aligned}\delta''\mathbf{h}_{\text{eff}} = {} & \Delta\mathrm{h}^{\text{dc}}_{a\perp}\mathbf{e}_\perp(\psi_{\text{dc}}) + \Delta\mathrm{h}^{\text{rf}}_{az}\cos(\omega t + \psi_z)\mathbf{e}_z \\ & + \Delta\mathrm{h}^{\text{rf}}_{a\perp}\left[\cos(\omega t + \psi_\perp)\mathbf{e}_x - \sin(\omega t + \psi_\perp)\mathbf{e}_y\right] \\ & + \Delta\kappa m_{0z}\mathbf{e}_\perp(\psi_{\text{AN}}) + \Delta\kappa m_{0\perp}\cos(\omega t - \phi_0 - \psi_{\text{AN}})\mathbf{e}_z \\ & - \Delta N_\perp m_{0\perp}\left[\cos(\omega t - \phi_0)\mathbf{e}_x + \sin(\omega t - \phi_0)\mathbf{e}_y\right],\end{aligned} \tag{7.82}$$

where $\Delta\kappa = \kappa\theta_{\text{AN}}$ and ϕ_0 is the lag angle between the **P**-mode and $\mathbf{h}_{a\perp}$. It is important to stress that $\mathbf{m}_0(t)$ and $\delta\mathbf{h}_{\text{eff}}$ are known functions of time and, thus, the last term in Eq. (7.80) is the driving term.

The perturbation $\delta\mathbf{m}(t)$ must be such that $\mathbf{m}_0(t)\cdot\delta\mathbf{m}(t) = 0$. This is a consequence of the requirement that the magnetization magnitude must be preserved by the perturbations. Therefore, $\delta\mathbf{m}(t)$ can be expressed in terms of the unit vectors $\mathbf{e}_1$ and $\mathbf{e}_2$ defined by formulas (7.36) and (7.37):

$$\delta\mathbf{m}(t) = \delta m_1(t)\mathbf{e}_1(t) + \delta m_2(t)\mathbf{e}_2(t). \tag{7.83}$$

The vectors $\mathbf{e}_1$ and $\mathbf{e}_2$ are explicitly time-dependent in the laboratory frame. The differential equation for $\delta m_1(t)$ and $\delta m_2(t)$ is obtained by projecting Eq. (7.80) onto the unit vectors $\mathbf{e}_1(t)$ and $\mathbf{e}_2(t)$. After straightforward calculations, one obtains the equation:

$$\frac{\mathrm{d}}{\mathrm{d}t}\begin{pmatrix}\delta m_1 \\ \delta m_2\end{pmatrix} = A_0\begin{pmatrix}\delta m_1 \\ \delta m_2\end{pmatrix} + B_0\begin{pmatrix}\delta'' h_{\text{eff},1}(t) \\ \delta'' h_{\text{eff},2}(t)\end{pmatrix}, \tag{7.84}$$

where:

$$B_0 = \frac{1}{1+\alpha^2}\begin{pmatrix}1 & -\alpha \\ \alpha & 1\end{pmatrix}, \tag{7.85}$$

A_0 is given by Eq. (7.39), whereas $\delta'' h_{\text{eff},1}(t)$ and $\delta'' h_{\text{eff},2}(t)$ are the components of the field $\delta''\mathbf{h}_{\text{eff}}(t)$ along $\mathbf{e}_1(t)$ and $\mathbf{e}_2(t)$, respectively.

It is quite remarkable that, due to the introduction of the basis vectors $\mathbf{e}_1(t)$ and $\mathbf{e}_2(t)$, the nonhomogeneous system of linear ordinary differential equations with time-periodic coefficients given by Eq. (7.80) has been reduced to the nonhomogeneous system of linear ordinary differential equations with constant-in-time coefficients, Eq. (7.84). This system of equations can be solved analytically. In fact, according to Eq. (7.82) and the choice of basis $\mathbf{e}_1(t)$ and $\mathbf{e}_2(t)$, $\delta''\mathbf{h}_{\text{eff}}(t)$ is the sum of time-harmonic terms with frequencies multiples of the frequency ω of the

rf driving field. The periodic steady state solution of Eq. (7.84) can be obtained by separately finding the steady state sinusoidal solutions due to each term in $\delta''\mathbf{h}_{\text{eff}}(t)$ and by using the superposition principle to obtain the complete solution. By using the phasor technique, we express each of the sinusoidal terms contributing to the steady state in the complex form:

$$\delta m_1(t) = \text{Re}\left[\tilde{a}_1 \text{e}^{\text{i}\omega_\text{p} t}\right], \qquad \delta m_2(t) = \text{Re}\left[\tilde{a}_2 \text{e}^{\text{i}\omega_\text{p} t}\right], \tag{7.86}$$

where ω_p is the frequency of the perturbative term and $\tilde{a}_1$, $\tilde{a}_2$ are two unknown complex amplitudes. By substituting Eq. (7.86) into Eq. (7.84) one finds for the unknowns $\tilde{a}_1$, $\tilde{a}_2$:

$$\begin{pmatrix} \tilde{a}_1 \\ \tilde{a}_2 \end{pmatrix} = \left(\text{i}\omega_\text{p} I - A_0\right)^{-1} B_0 \begin{pmatrix} \tilde{b}_1 \\ \tilde{b}_2 \end{pmatrix}, \tag{7.87}$$

where I represents the identity matrix whereas $\tilde{b}_1$ and $\tilde{b}_2$ are the complex amplitudes of the corresponding sinusoidal perturbation term. These complex amplitudes have the following analytical forms for the various perturbation terms.

(a) Perturbation associated with $\Delta\text{h}_{a\perp}^{\text{dc}}$ ($\omega_\text{p} = \omega$):

$$\begin{pmatrix} \tilde{b}_1 \\ \tilde{b}_2 \end{pmatrix} = \Delta\text{h}_{a\perp}^{\text{dc}} \begin{pmatrix} \cos\theta_0 \\ \text{i} \end{pmatrix} \text{e}^{-\text{i}(\phi_0 + \psi_\text{dc})}. \tag{7.88}$$

(b) Perturbation associated with $\Delta\text{h}_{a\perp}^{\text{rf}}$ ($\omega_\text{p} = 2\omega$):

$$\begin{pmatrix} \tilde{b}_1 \\ \tilde{b}_2 \end{pmatrix} = \Delta\text{h}_{a\perp}^{\text{rf}} \begin{pmatrix} \cos\theta_0 \\ \text{i} \end{pmatrix} \text{e}^{\text{i}(\psi_\perp - \phi_0)}. \tag{7.89}$$

(c) Perturbation associated with $\Delta\text{h}_{az}^{\text{rf}}$ ($\omega_\text{p} = \omega$):

$$\begin{pmatrix} \tilde{b}_1 \\ \tilde{b}_2 \end{pmatrix} = \Delta\text{h}_{az}^{\text{rf}} \begin{pmatrix} -\sin\theta_0 \\ 0 \end{pmatrix} \text{e}^{\text{i}\psi_z}. \tag{7.90}$$

(d) Perturbation associated with $\Delta\kappa$ ($\omega_\text{p} = \omega$):

$$\begin{pmatrix} \tilde{b}_1 \\ \tilde{b}_2 \end{pmatrix} = \Delta\kappa \begin{pmatrix} \cos 2\theta_0 \\ \text{i}\cos\theta_0 \end{pmatrix} \text{e}^{-\text{i}(\phi_0 + \psi_\text{AN})}. \tag{7.91}$$

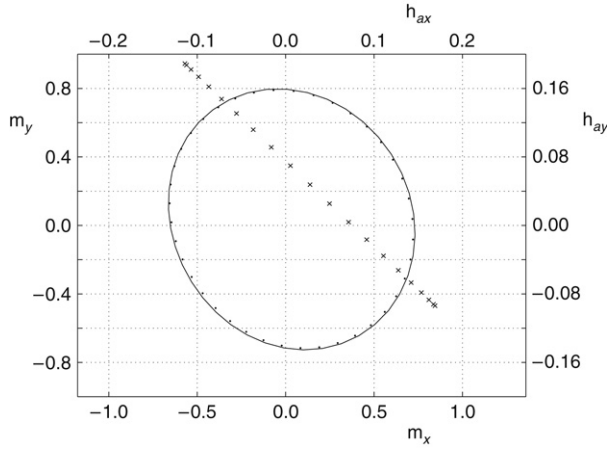

FIGURE 7.17 Comparison of analytically computed (continuous line) and numerically computed (dots) solution of the LLG equation for the case of linearly polarized field. The line marked by "×" is the locus of points described by the applied field. System parameters: $\kappa = 0.1$, $N_\perp = 0.2$, $N_z = 0.6$ (i.e., $\kappa_{\text{eff}} = -0.3$), $\alpha = 0.01$. Excitation conditions: $\omega = 0.8$, $\mathrm{h}_{az} = 1.1$, $\mathrm{h}_{a\perp} = 0.1$. Perturbation parameters: $\Delta\mathrm{h}_{a\perp}^{\mathrm{dc}} = 0.05\mathrm{h}_{az}$, $\Delta\mathrm{h}_{az}^{\mathrm{rf}} = 0.05\mathrm{h}_{a\perp}$, $\Delta\mathrm{h}_{a\perp}^{\mathrm{rf}} = \mathrm{h}_{a\perp}$ (i.e., linearly polarized field), $\theta_{\mathrm{AN}} = 0.2$, $\Delta N_\perp = 0.1$, $\psi_{\mathrm{dc}} = \pi/3$, $\psi_\perp = \pi/2$, $\psi_z = \psi_{\mathrm{AN}} = 0$.

(f) Perturbation associated with $\Delta N_\perp$ ($\omega_{\mathrm{p}} = 2\omega$):

$$\begin{pmatrix} \tilde{b}_1 \\ \tilde{b}_2 \end{pmatrix} = \Delta N_\perp \begin{pmatrix} -\sin\theta_0 \cos\theta_0 \\ -\mathrm{i}\sin\theta_0 \end{pmatrix} \mathrm{e}^{-2\mathrm{i}\phi_0}. \tag{7.92}$$

The inverse of the matrix $(\mathrm{i}\omega_{\mathrm{p}} I - A_0)$ is well defined unless $\mathrm{i}\,\omega_{\mathrm{p}}$ is an eigenvalue of A_0. This is possible only if the trace of A_0 vanishes, which is a non-generic situation associated with a Hopf bifurcation for the **P**-mode. It is also important to observe that each harmonic perturbation $(\delta m_1(t), \delta m_2(t))$ with angular frequency ω_p produces three terms in $\delta\mathbf{m}(t)$ with angular frequencies $\omega_{\mathrm{p}} + \omega$, ω_{p}, and $\omega_{\mathrm{p}} - \omega$.

The accuracy of the perturbation technique can be tested by comparing the value of magnetization $\mathbf{m}_0(t) + \delta\mathbf{m}(t)$ obtained by using the analytical perturbation technique with those obtained by direct numerical integration of Eqs (7.9) and (7.73). Extensive numerical testing carried out for a wide range of values of the perturbation parameters suggests a remarkable accuracy of the perturbation technique. Here we present in detail the comparison results for the rather significant case of linear

polarization of the rf field, i.e., the case when $\Delta h_{a\perp}^{rf} = h_{a\perp}$. This case represents an appreciable deviation from the symmetry of the driving field, nevertheless it can still be treated by the perturbation technique. The results are shown in Fig. 7.17. The values of the parameters were chosen to be fairly close to nonlinear resonance conditions. In this situation, the angle between the magnetization and the symmetry axis is appreciable and the usual "small motion" linearization technique cannot be applied. The comparison of the analytically computed magnetization dynamics with the numerically computed dynamics clearly demonstrates the high accuracy of the perturbation technique even in this extreme case of symmetry breaking.

CHAPTER 8

Spin-Waves and Parametric Instabilities

8.1 LINEARIZED LLG EQUATION

The **P**-mode solutions to the LLG equation discussed in the previous chapter provide important examples of dynamic states analogous to static saturation, i.e., states of spatially uniform magnetization motion. Spatially uniform dynamic states were originally of interest in relation to the ferromagnetic resonance phenomenon. Initially, it was assumed that spatially uniform radio-frequency fields would certainly induce spatially uniform magnetization motions. Later, it became clear that, because of the nonlinear nature of LLG dynamics, at some rf input powers spatially uniform motions could get coupled to certain spin-wave perturbations, forcing them to grow up to nonthermal amplitudes and to give rise to complicated spatially nonuniform magnetization motions through the so-called Suhl's instabilities [645,646,740,306]. The main limitation of those approaches is that they were carried out for excited states close to static saturation. In this respect, the existence of **P**-modes, studied in the previous chapter, suggests that the analysis of spin-wave effects can be carried out (at least for systems with uniaxial symmetry) for fields of *arbitrary amplitude and frequency*. We will show in this chapter that this analysis leads to remarkable results. For instance, it would seem quite natural to suggest that since spatially uniform motions are unstable for relatively weak excitations, they will be even more so under larger excitations. However, this is not the case. The reason is that the nature of the spin-wave perturbations for large magnetization motions is altered by the fact that these perturbations must remain orthogonal to the uniform motions at all times, in order to preserve the magnetization magnitude M_s. This physical constraint affects the parametric resonance conditions governing instabilities and yields the remarkable result that the rf input powers capable of inducing spin-wave instabilities are bounded from *both below and above*. This means that large enough uniform motions are always

stable. In addition, it turns out that the stability of large motions may depend on the history of their excitation.

The spin-wave notion is basic to the description of the spontaneous fluctuations of magnetization at thermal equilibrium as well as to the understanding of the magnetization response to rf external magnetic fields [338,646,740,306]. Spin-waves with wavelength much larger than the atomic spacing can be described by using a classical continuous-medium model with no reference to the details of the atomic structure. In this description, spin-waves appear as plane-wave perturbations of the magnetization $\mathbf{M}$ which are orthogonal to the large-scale magnetization state of the ferromagnet. Spin-wave dynamics is then governed by the LLG equation for $\mathbf{M}(\mathbf{r}, t)$. This approach has been primarily used to describe the spectrum of thermally generated spin-waves when the large-scale magnetization state is the state of equilibrium saturation magnetization. However, the results presented for **P**-modes in the previous chapter suggest a nonequilibrium generalization of the spin-wave picture. In this picture, a specific **P**-mode driven by the radio-frequency magnetic field becomes the reference state analogous to the saturation state for equilibrium spin-waves. Similarly to what occurs for static magnetic saturation, one expects that **P**-modes will be slightly affected by various kinds of perturbations arising from nonuniformities of the medium, thermal agitation, and other causes. These perturbations correspond to slight deviations of the local direction of $\mathbf{M}$ from that of the **P**-mode motion. If some of these perturbations turn out to have an exponentially growing amplitude, then the **P**-mode will be disrupted in favor of some new magnetization configuration. Otherwise, the **P**-mode will be stable and will be physically realizable and observable. By linearizing the Landau–Lifshitz–Gilbert equation around a given **P**-mode, one obtains the equations for generic out-of-equilibrium perturbations, and in particular for spin-wave-type plane-wave perturbations. The crucial difference with respect to the conventional analysis based on linearization around the saturation state is that these perturbations can be no longer considered as low-energy excitations above the thermodynamic equilibrium state of static saturation, but rather as deviations from far-from-equilibrium dynamic states driven by the rf external field. This physical difference results in a basic change in the mathematical structure of the spin-wave equations. In fact, spin-wave perturbations must be orthogonal to the **P**-mode motion at all times in order to preserve the magnetization magnitude. This requirement introduces a nontrivial time-dependent constraint in the spin-wave equations which dominates the problem and substantially alters the nature of spin-waves in the presence of large **P**-mode motions. The main spin-wave properties (e.g., dispersion

relation) are modified and new conclusions are reached about spin-wave stability of far-from-equilibrium driven states. We stress that the linearization approach just outlined is completely different from the one usually introduced in quasi-equilibrium magnetization dynamics studies. In fact, we are not assuming that the magnetization motion is small. On the contrary, we are considering truly nonlinear conditions in which large motions are realized (**P**-modes). It is the existence of explicit formulas for **P**-modes that enables one to linearize the LLG equation around these **P**-mode motions in order to obtain the equations for **P**-mode perturbations.

Consider a specific **P**-mode of magnetization $\mathbf{m}_0(t)$, which is slightly distorted by the perturbation $\delta\mathbf{m}(\mathbf{r},t)$, with $|\delta\mathbf{m}(\mathbf{r},t)| \ll 1$. This means that we are looking for solutions to the LLG equation in the form: $\mathbf{m}(\mathbf{r},t) = \mathbf{m}_0(t) + \delta\mathbf{m}(\mathbf{r},t)$. The magnetostatic field $\mathbf{h}_M$ can be expressed as $\mathbf{h}_M(\mathbf{r},t) = -N_\perp \mathbf{m}_{0\perp}(t) - N_z \mathbf{m}_{0z} + \delta\mathbf{h}_M(\mathbf{r},t)$, where $\mathbf{m}_{0z}$ and $\mathbf{m}_{0\perp}(t)$ are the components of $\mathbf{m}_0(t)$ along $\mathbf{e}_z$ and in the plane perpendicular to it, respectively, whereas $\delta\mathbf{h}_M$ represents the magnetostatic field produced by the perturbation $\delta\mathbf{m}$. The field $\mathbf{h}_M$ is the solution of magnetostatic Maxwell equations: $\nabla\cdot\mathbf{h}_M = -\nabla\cdot\mathbf{m}, \nabla\times\mathbf{h}_M = 0$, with the usual interface conditions at the body surface. By substituting $\mathbf{m} = \mathbf{m}_0 + \delta\mathbf{m}$ and $\mathbf{h}_M = -N_\perp\mathbf{m}_{0\perp} - N_z\mathbf{m}_{0z} + \delta\mathbf{h}_M$ into the LLG equation and by keeping only first-order terms in $\delta\mathbf{m}$, one finds:

$$\frac{\partial\delta\mathbf{m}}{\partial t} - \alpha\mathbf{m}_0\times\frac{\partial\delta\mathbf{m}}{\partial t} = -\delta\mathbf{m}\times\left(\mathbf{h}_{\text{eff}}^{(0)} - \alpha\frac{\mathrm{d}\mathbf{m}_0}{\mathrm{d}t}\right) - \mathbf{m}_0\times\delta\mathbf{h}_{\text{eff}}, \quad (8.1)$$

where:

$$\mathbf{h}_{\text{eff}}^{(0)} = \mathbf{h}_{a\perp}(t) + (\mathrm{h}_{az} + \kappa_{\text{eff}}\mathrm{m}_{0z})\,\mathbf{e}_z - N_\perp\mathbf{m}_0, \quad (8.2)$$

$$\delta\mathbf{h}_{\text{eff}} = \delta\mathbf{h}_M + \kappa\delta\mathrm{m}_z\mathbf{e}_z + \nabla^2\delta\mathbf{m}, \quad (8.3)$$

and $\kappa_{\text{eff}} = \kappa + N_\perp - N_z$. The magnetization magnitude must be preserved, i.e., $|\mathbf{m}|^2 = 1$. Therefore, $\mathbf{m}_0\cdot\delta\mathbf{m} = 0$ at any time. It can be verified that Eq. (8.1) predicts indeed that $\partial\left(\mathbf{m}_0\cdot\delta\mathbf{m}\right)/\partial t \equiv 0$, which means that the condition $\mathbf{m}_0\cdot\delta\mathbf{m} = 0$ is preserved if it is initially fulfilled. Therefore, it is convenient to represent $\delta\mathbf{m}$ in a basis chosen in the plane perpendicular to $\mathbf{m}_0$, because $\delta\mathbf{m}$ is constrained to this plane. One such basis is provided by the time-dependent unit vectors $\mathbf{e}_1(t)$ and $\mathbf{e}_2(t)$ analogous to the ones defined in the previous chapter for spatially uniform perturbations (see Eqs (7.36) and (7.37)):

$$\mathbf{e}_1(t) = \frac{(\mathbf{e}_z\times\mathbf{m}_0(t))\times\mathbf{m}_0(t)}{|(\mathbf{e}_z\times\mathbf{m}_0(t))\times\mathbf{m}_0(t)|}, \quad (8.4)$$

$$\mathbf{e}_2(t) = \frac{\mathbf{e}_z \times \mathbf{m}_0(t)}{|\mathbf{e}_z \times \mathbf{m}_0(t)|}. \tag{8.5}$$

The relationship with the laboratory-frame basis vectors $\mathbf{e}_x$, $\mathbf{e}_y$, and $\mathbf{e}_z$ is given by the expressions:

$$\begin{aligned}\mathbf{e}_1(t) = {} & \mathbf{e}_x \cos\theta_0 \, \cos(\omega t - \phi_0) \\ & + \mathbf{e}_y \cos\theta_0 \, \sin(\omega t - \phi_0) - \mathbf{e}_z \sin\theta_0, \end{aligned} \tag{8.6}$$

$$\mathbf{e}_2(t) = -\mathbf{e}_x \sin(\omega t - \phi_0) + \mathbf{e}_y \cos(\omega t - \phi_0), \tag{8.7}$$

where (θ_0, ϕ_0) are the spherical angles identifying the **P**-mode in the rotating-frame representation introduced in the previous chapter. Namely, θ_0 is the angle between $\mathbf{m}_0(t)$ and $\mathbf{e}_z$, while ϕ_0 is the lag angle between $\mathbf{m}_{0\perp}$ and $\mathbf{h}_{a\perp}$. The magnetization perturbation can be represented as $\delta\mathbf{m}(\mathbf{r}, t) = \delta m_1(\mathbf{r}, t)\mathbf{e}_1(t) + \delta m_2(\mathbf{r}, t)\mathbf{e}_2(t)$. By using Eqs (7.26)–(7.29) from Chapter 7 as well as Eqs (8.6) and (8.7), Eq. (8.1) can be transformed into the following coupled differential equations written in the matrix form:

$$\begin{aligned}&\begin{pmatrix} 1 & \alpha \\ -\alpha & 1 \end{pmatrix} \frac{\partial}{\partial t} \begin{pmatrix} \delta m_1 \\ \delta m_2 \end{pmatrix} = \begin{pmatrix} \delta \mathrm{h}_{M2} \\ -\delta \mathrm{h}_{M1} \end{pmatrix} \\ &+ \begin{pmatrix} -\alpha\omega\cos\theta_0 & -\nu_0 + N_\perp + \nabla^2 \\ \nu_0 - N_\perp - \kappa\sin^2\theta_0 - \nabla^2 & -\alpha\omega\cos\theta_0 \end{pmatrix} \begin{pmatrix} \delta m_1 \\ \delta m_2 \end{pmatrix}, \end{aligned} \tag{8.8}$$

where $\cos\theta_0$ and $\nu_0 = \alpha\omega\cot\phi_0$ identify the **P**-mode, while $\delta\mathrm{h}_{M1} = \delta\mathbf{h}_M \cdot \mathbf{e}_1(t)$ and $\delta\mathrm{h}_{M2} = \delta\mathbf{h}_M \cdot \mathbf{e}_2(t)$. According to the natural boundary conditions $\partial\mathbf{m}/\partial n = 0$, the normal derivatives of δm_1 and δm_2 at the surface of the ferromagnet must be equal to zero.

The introduction of the time-dependent basis vectors $\mathbf{e}_1$ and $\mathbf{e}_2$ proves to be important because Eq. (8.8) explicitly depends on time only through the magnetostatic field components $\delta\mathrm{h}_{M1}$ and $\delta\mathrm{h}_{M2}$. These components can be expressed in the form:

$$\begin{pmatrix} \delta \mathrm{h}_{M1} \\ \delta \mathrm{h}_{M2} \end{pmatrix} = -\begin{pmatrix} \mathbb{N}_{11}(t) & \mathbb{N}_{12}(t) \\ \mathbb{N}_{21}(t) & \mathbb{N}_{22}(t) \end{pmatrix} \begin{pmatrix} \delta m_1 \\ \delta m_2 \end{pmatrix}, \tag{8.9}$$

where:

$$\mathbb{N}_{hk}(t) f = -\frac{1}{4\pi} \mathbf{e}_h(t) \cdot \nabla_{\mathbf{r}} \int_\Omega f(\mathbf{r}') \mathbf{e}_k(t) \cdot \nabla_{\mathbf{r}'} \left(\frac{1}{|\mathbf{r} - \mathbf{r}'|} \right) \mathrm{d}V_{\mathbf{r}'}, \tag{8.10}$$

with $k, h = 1, 2$ and f representing either δm_1 or δm_2. The operators $\mathbb{N}_{hk}(t)$ are periodic in time with period $T = 2\pi/\omega$: $\mathbb{N}_{hk}(t) = \mathbb{N}_{hk}(t + T)$. By substituting Eq. (8.9) into Eq. (8.8), one obtains:

$$\begin{pmatrix} 1 & \alpha \\ -\alpha & 1 \end{pmatrix} \frac{\partial}{\partial t} \begin{pmatrix} \delta m_1 \\ \delta m_2 \end{pmatrix} = - \begin{pmatrix} \mathbb{N}_{21}(t) & \mathbb{N}_{22}(t) \\ -\mathbb{N}_{11}(t) & -\mathbb{N}_{12}(t) \end{pmatrix} \begin{pmatrix} \delta m_1 \\ \delta m_2 \end{pmatrix} + \begin{pmatrix} -\alpha\omega \cos\theta_0 & -\nu_0 + N_\perp + \nabla^2 \\ \nu_0 - N_\perp - \kappa \sin^2\theta_0 - \nabla^2 & -\alpha\omega \cos\theta_0 \end{pmatrix} \begin{pmatrix} \delta m_1 \\ \delta m_2 \end{pmatrix}, \quad (8.11)$$

where the parametric nature of the dynamics becomes apparent.

The fact that explicit time dependencies are present only in the magnetostatic contribution represents an important simplification. Nevertheless, the analytical solution of Eq. (8.11) for a generic perturbation remains out of reach. A simple solution can be only obtained for spatially uniform perturbations, which fulfill the requirement of zero normal derivative at the particle surface by definition. For uniform perturbations, $\delta\mathbf{h}_M = -N_\perp \delta\mathbf{m}_\perp - N_z \delta \mathrm{m}_z \mathbf{e}_z = -N_\perp \delta\mathbf{m} + (N_\perp - N_z)\, \delta \mathrm{m}_z \mathbf{e}_z$. Thus:

$$\begin{pmatrix} \delta \mathrm{h}_{M1} \\ \delta \mathrm{h}_{M2} \end{pmatrix} = - \begin{pmatrix} N_\perp - (N_\perp - N_z) \sin^2\theta_0 & 0 \\ 0 & N_\perp \end{pmatrix} \begin{pmatrix} \delta m_1 \\ \delta m_2 \end{pmatrix}. \quad (8.12)$$

By using these formulas one finds that Eq. (8.8) is simply reduced to Eqs (7.38)–(7.39), discussed in Chapter 7. In fact, for spatially uniform perturbations there is no difference between introducing the local time-dependent vector basis $\mathbf{e}_1$ and $\mathbf{e}_2$ at each point in space, as it has been done in order to obtain Eq. (8.8), or making a global transformation to the rotating reference frame, as it was done in the previous chapter. However, the difference becomes essential when the two methods are applied to the analysis of spatially nonuniform perturbations, because in that case the global passage to the rotating frame of reference would lead to the appearance of additional "convection terms" in the LLG equation, terms that are usually difficult to deal with.

Although the emphasis in this chapter is mostly on spin-wave perturbations, it is useful to provide a brief discussion of a different approximation [90], which leads to modes that are the natural generalization of the magnetostatic modes originally studied by Walker [716,717,306]. By magnetostatic modes we mean the spontaneous long-wavelength deviations from uniform magnetization occurring in ferromagnets whose linear dimensions are large with respect to the exchange length. Under these conditions, exchange forces play a minor

role and can be neglected. The spectrum of magnetostatic modes is instead dominated by magnetostatic boundary conditions at the particle surface. In fact, these boundary conditions become dominant when the mode wavelength is comparable with the linear dimensions of the ferromagnet. The frequency spectrum and the space-time structure of the resulting magnetostatic modes have been extensively studied in [716,717,262].

It is natural to expect that similar magnetostatic deviations from **P**-modes might exist under nonequilibrium conditions as well. These modes are sought as approximate solutions of Eq. (8.1) obtained for perturbations with wavelength of the order of the linear dimensions of the ferromagnet, when these dimensions are much larger than the exchange length. Exchange forces can then be neglected, i.e., the Laplacian term in Eqs (8.3) and (8.8) can be dropped. In addition, despite the fact that the properties of **P**-modes crucially depend on the value of the damping constant α even when $\alpha \ll 1$, **P**-mode perturbations can be safely studied under the approximation $\alpha \simeq 0$, as is usually done for normal modes in linear systems. Finally, we limit our analysis to the particular case of a particle with spherical shape and vanishing crystal anisotropy, i.e., $\kappa = 0$, which, as we shall see, greatly simplifies the treatment of boundary conditions. Consider time-harmonic perturbations of angular frequency ω_M, i.e., $\delta\mathbf{m} = \mathbf{a}_m(\mathbf{r})\exp(\mathrm{i}\omega_M t)$, then $\delta\mathbf{h}_M = \mathbf{a}_h(\mathbf{r})\exp(\mathrm{i}\omega_M t)$. Under the stated approximations, Eq. (8.8) is reduced to the form:

$$\begin{pmatrix} \mathrm{i}\omega_M & \omega_H \\ -\omega_H & \mathrm{i}\omega_M \end{pmatrix} \begin{pmatrix} \delta m_1 \\ \delta m_2 \end{pmatrix} = \begin{pmatrix} \delta \mathrm{h}_{M2} \\ -\delta \mathrm{h}_{M1} \end{pmatrix}, \tag{8.13}$$

where $\omega_H \equiv \nu_0 - N_\perp = (\mathrm{h}_{az} - \omega)/\cos\theta_0 - N_z$. The formal similarity of Eq. (8.13) to the law governing usual Walker modes is striking. However, there is a substantial difference: the relation (8.13) holds now in the time-dependent basis $(\mathbf{e}_1(t), \mathbf{e}_2(t))$ (see Eq. (8.6)–(8.7)). Therefore, it describes an anisotropic constitutive law with time-dependent anisotropy directions controlled by the **P**-mode orientation $\mathbf{m}_0(t)$. The efficient way to solve magnetostatic Maxwell equations for this medium with time-dependent properties is by passing to a new reference frame, rotated with the angular frequency ω around $\mathbf{e}_z$, in which both the **P**-mode direction $\mathbf{m}_0$ and the $(\mathbf{e}_1, \mathbf{e}_2)$ basis become stationary. We take the new rotating cartesian axes along $(\mathbf{e}_{x'}(t), \mathbf{e}_{y'}(t), \mathbf{e}_z)$, where $\mathbf{e}_{y'}(t) \equiv \mathbf{e}_2(t)$ and $\mathbf{e}_{x'}(t) = \mathbf{e}_2(t) \times \mathbf{e}_z$. We will denote by (x', y', z) the cartesian coordinates along the $(\mathbf{e}_{x'}, \mathbf{e}_{y'}, \mathbf{e}_z)$ axes, respectively. In the new reference frame, the anisotropic properties of the medium become time-independent. However, there is a price to pay for this: the original LLG equation has to be modified in order to introduce the appropriate convection terms associated with the change

of reference frame. More precisely, in the rotating frame the simplified equation previously derived from Eq. (8.8), i.e., Eq. (8.13), takes the form:

$$\begin{pmatrix} \mathrm{i}\omega_M & \omega_H \\ -\omega_H & \mathrm{i}\omega_M \end{pmatrix} \begin{pmatrix} \delta m_1 \\ \delta m_2 \end{pmatrix} - \omega \frac{\partial}{\partial \phi'} \begin{pmatrix} \delta m_1 \\ \delta m_2 \end{pmatrix} = \begin{pmatrix} \delta \mathrm{h}_{M2} \\ -\delta \mathrm{h}_{M1} \end{pmatrix}, \tag{8.14}$$

where ϕ' is the azimuthal angle around $\mathbf{e}_z$ measured with respect to $\mathbf{e}_{x'}$. The connection between ϕ' and the azimuthal angle ϕ defined in the laboratory frame with respect to $\mathbf{e}_x$ is $\phi = \phi' + \omega t - \phi_0$. Thus, the study of generalized magnetostatic modes is reduced to the joint solution, in the (x', y', z) frame, of Eq. (8.14) and of the equation for the magnetostatic potential defined for the perturbed magnetostatic field, i.e., $\delta \mathbf{h}_M = -\nabla \psi_M$. The general solution of these equations is by no means straightforward. Here, we shall discuss two particular cases that give a useful illustration of the physical nature of far-from-equilibrium magnetostatic modes.

Let us first consider the case of spatially uniform perturbations. Under these conditions, $\delta \mathbf{h}_M = -N_\perp \delta \mathbf{m}_\perp - N_z \delta \mathrm{m}_z \mathbf{e}_z$ and $\partial \delta \mathbf{m} / \partial \phi' = 0$, so Eq. (8.14) is reduced to an eigenvalue equation for ω_M which can be immediately solved by standard methods. As a matter of fact, this case is part of the general analysis of the stability of **P**-modes with respect to spatially uniform perturbations discussed in the previous chapter. From the physical viewpoint, uniform **P**-mode perturbations are similar to the Kittel modes observed around static saturation [306]. The main difference is that the perturbation motion is now a uniform precession of angular frequency ω_M around the **P**-mode direction $\mathbf{m}_0(t)$, which in turn is rotated at the frequency ω around $\mathbf{e}_z$ by the action of the rotating driving field. Therefore, these generalized Kittel modes will eventually result in quasi-periodic motions of frequency $\omega \pm \omega_M$. These modes will be excited whenever the rotating field $\mathbf{h}_{a\perp}(t)$ deviates from perfect circular polarization in such a way that it contains the mentioned additional frequencies.

As a second example, we shall discuss one particular family of Walker-type nonuniform solutions. The structure of Eq. (8.14) suggests looking for solutions in the form:

$$\delta m_k = a_k(r, \theta) \exp\left(-\mathrm{i}p\phi'\right) \exp\left(\mathrm{i}\omega_M t\right), \quad k = 1, 2, \tag{8.15}$$

where (r, θ, ϕ') are the spherical coordinates associated with (x', y', z) and p is an integer. It is not immediately clear why solutions with this symmetry should exist. Nevertheless, it will be verified below that this

is indeed the case. By substituting formula (8.15) into Eq. (8.14) and by inverting the ensuing matrix relation one finds:

$$\begin{pmatrix} \delta m_1 \\ \delta m_2 \end{pmatrix} = \begin{pmatrix} \chi_H & \mathrm{i}\chi'_M \\ -\mathrm{i}\chi'_M & \chi_H \end{pmatrix} \begin{pmatrix} \delta \mathrm{h}_{M1} \\ \delta \mathrm{h}_{M2} \end{pmatrix}, \tag{8.16}$$

where:

$$\chi_H = \frac{\omega_H}{\omega_H^2 - \omega_M'^2}, \qquad \chi'_M = \frac{\omega'_M}{\omega_H^2 - \omega_M'^2}, \tag{8.17}$$

and $\omega'_M = \omega_M + p\,\omega$. Equation (8.16) describes a vector relation in the $(\mathbf{e}_1, \mathbf{e}_2, \mathbf{m}_0)$ basis. It is written in two-dimensional form thanks to the fact that the $\mathbf{m}_0$ component of $\delta\mathbf{m}$ is zero. Let us transform Eq. (8.16) to the $(\mathbf{e}_{x'}, \mathbf{e}_{y'}, \mathbf{e}_z)$ basis by making use of the known relationship between the bases $(\mathbf{e}_1, \mathbf{e}_2, \mathbf{m}_0)$ and $(\mathbf{e}_{x'}, \mathbf{e}_{y'}, \mathbf{e}_z)$. To first order in θ_0, which is a good approximation whenever the **P**-mode motion is not very large, one obtains:

$$\begin{pmatrix} \delta \mathrm{m}_{x'} \\ \delta \mathrm{m}_{y'} \\ \delta \mathbf{m}_z \end{pmatrix} = \begin{pmatrix} \chi_H & \mathrm{i}\chi'_M & -\chi_H \sin\theta_0 \\ -\mathrm{i}\chi'_M & \chi_H & \mathrm{i}\chi'_M \sin\theta_0 \\ -\chi_H \sin\theta_0 & -\mathrm{i}\chi'_M \sin\theta_0 & 0 \end{pmatrix} \begin{pmatrix} \delta \mathrm{h}_{Mx'} \\ \delta \mathrm{h}_{My'} \\ \delta \mathrm{h}_{Mz} \end{pmatrix}. \tag{8.18}$$

Equation (8.18) provides the desired anisotropic constitutive relation between perturbations, which can be used in magnetostatic Maxwell equations to obtain the equation obeyed by the magnetostatic potential ψ_M. After straightforward calculations, one finds that the potential satisfies the equation:

$$(1 + \chi_H)\left(\frac{\partial^2 \psi_M}{\partial x'^2} + \frac{\partial^2 \psi_M}{\partial y'^2}\right) + \frac{\partial^2 \psi_M}{\partial z^2} - 2\chi_H \sin\theta_0 \frac{\partial^2 \psi_M}{\partial x' \partial z} = 0 \tag{8.19}$$

inside the particle and Laplace equation outside. Equation (8.19) is similar to the equation for ordinary Walker modes [716,717], except for the additional last term. Furthermore, the interface conditions at the particle surface are the same as for ordinary Walker modes, despite the fact that we are solving the problem in the rotating frame $(\mathbf{e}_{x'}, \mathbf{e}_{y'}, \mathbf{e}_z)$. This is due to the spherical shape of the particle. One can verify that a family of solutions to the problem is given by the Walker-type potentials:

$$\psi_M = A_p \left(x' - \mathrm{i}y'\right)^{p+1}, \quad p = 1, 2, \ldots. \tag{8.20}$$

In Walker's notation [716], these would be modes $(m, m, 0)$, with $m \equiv p + 1$. For this family of solutions, one finds:

$$\begin{aligned} \mathrm{h}_{Mx'} &= -(p+1)A_p\,(x' - \mathrm{i}y')^p\,, \\ \mathrm{h}_{My'} &= \mathrm{i}(p+1)A_p\,(x' - \mathrm{i}y')^p\,, \\ \mathrm{h}_{Mz} &= 0. \end{aligned} \tag{8.21}$$

By substituting these expressions into Eq. (8.18), one obtains the corresponding components of $\delta\mathbf{m}$ and eventually $(\delta m_1, \delta m_2)$, by passing to the basis $(\mathbf{e}_1, \mathbf{e}_2, \mathbf{m}_0)$. All magnetization components are proportional to $(x' - \mathrm{i}y')^p = (r\sin\theta)^p \exp(-\mathrm{i}p\phi')$, in agreement with Eq. (8.15). This confirms that we have obtained admissible solutions to the problem.

The eigenfrequencies associated with the modes described by Eq. (8.21) are obtained by observing that $\omega'_M = \omega_M + p\omega$ is the quantity playing the role of the Walker eigenfrequency in Eqs (8.16) and (8.17). Therefore, Walker's results for $(m, m, 0)$ modes [716] directly apply to ω'_M, i.e., $\omega'_M - \omega_H = (p+1)\,/\,[2\,(p+1)+1]$. This is equivalent to:

$$\omega_M = \frac{\mathrm{h}_{az} - \omega}{\cos\theta_0} - N_z - p\omega + \frac{p+1}{2(p+1)+1}. \tag{8.22}$$

It is interesting to see if these generalized magnetostatic modes are indeed reduced to the corresponding ordinary Walker modes in the limit of vanishing **P**-mode motion, i.e., $\cos\theta_0 \to 1$. In this limit, the **P**-mode is reduced to the saturation state. We see from Eq. (8.15) that the mode time dependence in the laboratory frame is of the form $\exp[\mathrm{i}\,(\omega_M + p\omega)\,t]$, because $\phi' = \phi - \omega t + \phi_0$. According to Eq. (8.22), this is the correct Walker-mode frequency apart from a shift by the amount $-\omega$. This shift is due to the fact that the $\delta m_{1,2}$ components are time-dependent in the laboratory frame. In the limit of vanishing **P**-mode motion, the basis $(\mathbf{e}_1, \mathbf{e}_2, \mathbf{m}_0)$ is reduced to a basis which is rotated at the angular frequency ω around the $\mathbf{e}_z$ axis. Therefore, when the perturbation is expressed in terms of its time-independent components $\delta m_{x,y}$ an additional ωt term appears in the phase of the perturbation which cancels out the previously mentioned shift. One can verify that also the space dependence is reduced to that of ordinary Walker modes.

This close connection between ordinary and generalized Walker modes can be visualized as follows. When the **P**-mode motion becomes increasingly large, the spatial pattern of $(m, m, 0)$ Walker modes is little affected. However, the plane in which the mode lives is no longer the $(\mathbf{e}_x, \mathbf{e}_y)$ plane but the time-dependent $(\mathbf{e}_1, \mathbf{e}_2)$ plane, whose normal

$\mathbf{m}_0$ executes a precession of angular frequency ω around $\mathbf{e}_z$ under the driving action of the rotating field. As a consequence, at each point inside the particle there appears a mode component along $\mathbf{e}_z$, oscillating as $\exp(\mathrm{i}\omega'_M t)$. Similarly to ordinary Walker modes, these generalized modes will be excited whenever the rotating field deviates from spatial uniformity and contains components with the same spatial symmetry as the generalized Walker modes.

8.2 SPIN-WAVE PERTURBATIONS

Spin-wave solutions of Eq. (8.8) are obtained by using approximations different from the ones assumed in the previous section for magnetostatic modes. The main difference is that while exchange terms are neglected for magnetostatic modes, they are fully taken into account for spin-waves. However, it is very difficult to deal with boundary conditions in a rigorous way when both exchange and magnetostatic effects are taken into account. Spin-waves are plane-wave perturbations which can only be approximate solutions, because they do not satisfy the boundary condition for the magnetization on the boundary of the ferromagnet and they do not account for the magnetostatic fields due to the magnetic charges produced by the perturbation on the particle boundary. However, these magnetostatic fields are concentrated in a thin boundary layer, whose thickness is of the order of the plane-wave wavelength. Therefore, these fields are customarily neglected and spin-waves are treated with no consideration of boundary conditions whenever the perturbation wavelength is much smaller than the typical linear dimensions of the particle [646]. We shall adopt this approximation in the rest of this section. The role of boundary conditions will be revisited in the last section of the present chapter, where spin-wave instabilities in ultra-thin films will be discussed.

Let us consider a plane-wave perturbation with wave-vector $\mathbf{q}$, expressed in complex form as follows:

$$\delta\mathbf{m}_q(\mathbf{r},t) = \mathbf{c}_q(t)\exp(\mathrm{i}\mathbf{q}\cdot\mathbf{r}), \tag{8.23}$$

where the amplitude $\mathbf{c}_q$ lies in the plane $(\mathbf{e}_1,\mathbf{e}_2)$ defined by Eqs (8.4) and (8.5):

$$\mathbf{c}_q(t) = c_{q1}(t)\mathbf{e}_1(t) + c_{q2}(t)\mathbf{e}_2(t). \tag{8.24}$$

The magnetostatic field associated with this plane-wave perturbation is straightforwardly calculated if boundary conditions are neglected.

One finds:

$$\delta\mathbf{h}_M(\mathbf{r},t) = -\frac{\mathbf{q}}{q^2}\mathbf{q}\cdot\mathbf{c}_q(t)\exp(\mathrm{i}\mathbf{q}\cdot\mathbf{r}). \tag{8.25}$$

We are interested in the components of $\delta\mathbf{h}_M$ along $\mathbf{e}_1$ and $\mathbf{e}_2$: $\delta\mathrm{h}_{M1} = \delta\mathbf{h}_M\cdot\mathbf{e}_1(t)$ and $\delta\mathrm{h}_{M2} = \delta\mathbf{h}_M\cdot\mathbf{e}_2(t)$. They can be expressed as follows:

$$\begin{pmatrix}\delta\mathrm{h}_{M1}\\ \delta\mathrm{h}_{M2}\end{pmatrix} = -\frac{1}{q^2}\begin{pmatrix}q_1^2 & q_1q_2\\ q_1q_2 & q_2^2\end{pmatrix}\begin{pmatrix}\delta m_1\\ \delta m_2\end{pmatrix}, \tag{8.26}$$

where $\delta m_1 = c_{q1}\exp(\mathrm{i}\mathbf{q}\cdot\mathbf{r})$, $\delta m_2 = c_{q2}\exp(\mathrm{i}\mathbf{q}\cdot\mathbf{r})$, and:

$$q_1(t) = \mathbf{q}\cdot\mathbf{e}_1(t) = -q\left(\sin\theta_0\cos\theta_q - \cos\theta_0\sin\theta_q\cos\omega t\right), \tag{8.27}$$

$$q_2(t) = \mathbf{q}\cdot\mathbf{e}_2(t) = -q\sin\theta_q\sin\omega t. \tag{8.28}$$

In these equations, θ_0 is the polar angle identifying the **P**-mode, while θ_q is the angle between $\mathbf{q}$ and $\mathbf{e}_z$. Constant terms as well as terms with angular frequency ω and 2ω appear when q_1^2, q_2^2, and q_1q_2 are computed from Eqs (8.27) and (8.28) and inserted into Eq. (8.26). In particular, the constant terms, which appear only in q_1^2 and q_2^2, act as effective demagnetizing factors for the spin-wave perturbation, similarly to Eq. (8.12) for spatially uniform perturbations. On the other hand, the time-harmonic contributions give rise to parametric effects and related instabilities that will be analyzed in detail in the sequel.

The equation for the amplitudes (c_{q1}, c_{q2}) is derived by substituting Eq. (8.26) into Eq. (8.8), by taking into account that $\delta m_1 = c_{q1}(t)\exp(\mathrm{i}\mathbf{q}\cdot\mathbf{r})$ and $\delta m_2 = c_{q2}(t)\exp(\mathrm{i}\mathbf{q}\cdot\mathbf{r})$, and by using formulas (8.26)–(8.28). As a result, one obtains:

$$\frac{\mathrm{d}}{\mathrm{d}t}\begin{pmatrix}c_{q1}\\ c_{q2}\end{pmatrix} = A_q\begin{pmatrix}c_{q1}\\ c_{q2}\end{pmatrix} + \left[R_1(t) + R_2(t)\right]\begin{pmatrix}c_{q1}\\ c_{q2}\end{pmatrix}, \tag{8.29}$$

where:

$$A_q = \frac{1}{1+\alpha^2}\begin{pmatrix}1 & -\alpha\\ \alpha & 1\end{pmatrix}\begin{pmatrix}-\alpha\omega\cos\theta_0 & -\nu_q\\ \nu_q - \kappa_q\sin^2\theta_0 & -\alpha\omega\cos\theta_0\end{pmatrix}, \tag{8.30}$$

$$R_1(t) = -\frac{\sin 2\theta_q}{2\left(1+\alpha^2\right)}\begin{pmatrix}1 & -\alpha\\ \alpha & 1\end{pmatrix}\begin{pmatrix}\sin\theta_0\sin\omega t & 0\\ \sin 2\theta_0\cos\omega t & -\sin\theta_0\sin\omega t\end{pmatrix}, \tag{8.31}$$

$$R_2(t) = \frac{\sin^2\theta_q}{2\left(1+\alpha^2\right)}\begin{pmatrix}1 & -\alpha\\ \alpha & 1\end{pmatrix}\begin{pmatrix}\cos\theta_0\sin 2\omega t & \cos 2\omega t\\ \cos^2\theta_0\cos 2\omega t & -\cos\theta_0\sin 2\omega t\end{pmatrix}, \tag{8.32}$$

$$\nu_q = \nu_0 - N_\perp + q^2 + \frac{1}{2}\sin^2\theta_q, \tag{8.33}$$

$$\kappa_q = \kappa - 1 + \frac{3}{2}\sin^2\theta_q. \tag{8.34}$$

The matrix A_q is formally identical to the matrix A_0 derived for spatially uniform perturbations in the previous chapter, with ν_q and κ_q in the place of ν_0 and κ_{eff}, respectively.

Equations (8.29)–(8.34) represent the basic set of equations for generalized spin-waves under far-from-equilibrium conditions. The analysis of these equations presents nontrivial difficulties caused by the use of the time-dependent vector basis $(\mathbf{e}_1, \mathbf{e}_2)$ to preserve the magnetization magnitude. The $(\mathbf{e}_1, \mathbf{e}_2)$ basis identifies a moving plane which is always orthogonal to the **P**-mode magnetization. When studied in this plane, magnetization perturbations are described by Eq. (8.8), in which time is explicitly present only through the magnetostatic part, namely h_{M1} and h_{M2}, as shown by Eqs (8.26)–(8.28). This explicit time dependence is the origin of distinctive aspects of **P**-mode perturbations. In particular, this explicit time dependence results in the appearance of the time-dependent matrices $R_1(t)$ and $R_2(t)$ in Eq. (8.29), which act multiplicatively on the spin-wave amplitudes and give rise to parametric resonance phenomena.

In this connection, it is worthwhile mentioning the simplest case of parametric resonance in the parametric harmonic oscillator [33] described by the equation:

$$\frac{\mathrm{d}^2 x}{\mathrm{d}t^2} + \alpha\frac{\mathrm{d}x}{\mathrm{d}t} + \omega_0^2\left(1 + \epsilon\cos\omega t\right)x = 0, \tag{8.35}$$

with $\alpha \ll 1$, $\epsilon \ll 1$. In terms of the variables x and $\dot{x} = \mathrm{d}x/\mathrm{d}t$, Eq. (8.35) can be written as the set of coupled equations:

$$\frac{\mathrm{d}}{\mathrm{d}t}\begin{pmatrix} x \\ \dot{x} \end{pmatrix} = \begin{pmatrix} 0 & 1 \\ -\omega_0^2 & -\alpha \end{pmatrix}\begin{pmatrix} x \\ \dot{x} \end{pmatrix} + \epsilon\begin{pmatrix} 0 & 0 \\ -\omega_0^2\cos\omega t & 0 \end{pmatrix}\begin{pmatrix} x \\ \dot{x} \end{pmatrix}. \tag{8.36}$$

These equations have been widely studied in the literature [33,431], because they clearly reveal that the time-dependent matrix in Eq. (8.36) may render the equilibrium state ($x = \dot{x} = 0$) unstable, despite the fact that this state is stable in the absence of the parametric part. The lowest possible values of ϵ leading to instability are obtained when the intrinsic frequency ω_0 and the frequency ω of the parametric perturbation satisfy

the resonance condition:

$$\omega_0 = n\omega/2, \quad n = 1, 2, \ldots . \tag{8.37}$$

The instability threshold is controlled by damping and increases with the resonance order n as $\epsilon \sim (\alpha\omega)^{1/n}$ [431]. The structure of Eq. (8.29) is similar to that of Eq. (8.36). Thus, parametric effects are expected to play a crucial role in the stability of generalized, out-of-equilibrium spin-waves.

The main difficulty with Eq. (8.29) is the fact that the parametric matrices $R_1(t)$ and $R_2(t)$ contain elements which are not small and cannot be treated by perturbative techniques except for very special cases. Nevertheless, some general results concerning the behavior of the spin-wave amplitude can be obtained by using Floquet's theory for linear differential equations with periodic coefficients [529], of which Eq. (8.29) is an example.

Let us consider the equation obeyed by the principal matrix solution $\Phi_q(t)$ of Eq. (8.29):

$$\frac{\mathrm{d}\Phi_q}{\mathrm{d}t} = A_q\Phi_q + [R_1(t) + R_2(t)]\,\Phi_q, \tag{8.38}$$

with the initial condition $\Phi_q(0) = I$, where I represents the 2×2 identity matrix. In Floquet's theory [529], one proves that the solution of Eq. (8.38) can always be represented in the form:

$$\Phi_q(t) = \Pi_q(t) \exp\left(\Omega_q t\right), \tag{8.39}$$

where $\Pi_q(t)$ is periodic with period $2\pi/\omega$, $\Pi_q(0) = I$, and Ω_q is a constant matrix. Unfortunately, the proof of formula (8.39) is not constructive. This means that in general it is not known how to compute $\Pi_q(t)$ and Ω_q for a given equation. Nevertheless, the very structure of Eq. (8.39) has some direct implications for the properties of spin-wave perturbations. First, the matrix $\Pi_q(t)$ provides the transformation to the basis in which Eq. (8.29) has constant coefficients. Indeed, by using Eq. (8.39) in Eq. (8.38) one finds that $\Pi_q(t)$ satisfies the equation:

$$\frac{\mathrm{d}\Pi_q}{\mathrm{d}t} + \Pi_q\Omega_q = A_q\Pi_q + [R_1(t) + R_2(t)]\,\Pi_q. \tag{8.40}$$

Let us introduce the new amplitudes (z_{q1}, z_{q2}) defined by the formula:

$$\begin{pmatrix} c_{q1} \\ c_{q2} \end{pmatrix} = \Pi_q(t) \begin{pmatrix} z_{q1} \\ z_{q2} \end{pmatrix}. \tag{8.41}$$

By substituting this expression into Eq. (8.29) and by taking account of Eq. (8.40), one finds:

$$\frac{\mathrm{d}}{\mathrm{d}t} \begin{pmatrix} z_{q1} \\ z_{q2} \end{pmatrix} = \Omega_q \begin{pmatrix} z_{q1} \\ z_{q2} \end{pmatrix}, \tag{8.42}$$

where Ω_q is the time-independent matrix from Eq. (8.39). In terms of the discriminant:

$$\omega_q^2 = \det \Omega_q - \frac{(\mathrm{tr}\ \Omega_q)^2}{4}, \tag{8.43}$$

the eigenvalues of Ω_q can be written as follows: $\lambda_q^{\pm} = \mathrm{tr}\ \Omega_q/2 \pm |\omega_q|$ if $\omega_q^2 < 0$, or $\lambda_q^{\pm} = \mathrm{tr}\ \Omega_q/2 \pm \mathrm{i}\omega_q$ if $\omega_q^2 > 0$. Propagating waves occur when $\omega_q^2 > 0$. By calculating the two associated eigenmodes through Eq. (8.42) and by inserting them into Eqs (8.41), (8.23), and (8.24), one obtains modulated plane-wave solutions in the time-dependent basis $(\mathbf{e}_1, \mathbf{e}_2)$. These solutions can be written in the form:

$$\begin{pmatrix} \delta m_{q1}^{\pm}(\mathbf{r}, t) \\ \delta m_{q2}^{\pm}(\mathbf{r}, t) \end{pmatrix} = \exp(-\eta_q t)\, \Pi_q(t) \begin{pmatrix} z_1^{\pm} \\ z_2^{\pm} \end{pmatrix} \exp\left[\mathrm{i}\left(\mathbf{q} \cdot \mathbf{r} \pm \omega_q t\right)\right], \tag{8.44}$$

where $\eta_q = -\mathrm{tr}\ \Omega_q/2$, while $(z_1^{\pm}, z_2^{\pm})$ are the Ω_q eigenmodes in the (z_{q1}, z_{q2}) representation. The complete space-time behavior $\delta\mathbf{m}_q^{\pm}(\mathbf{r}, t)$ of the spin-wave perturbation in the laboratory frame is obtained by recalling that:

$$\delta\mathbf{m}_q^{\pm}(\mathbf{r}, t) = \delta m_{q1}^{\pm}(\mathbf{r}, t)\, \mathbf{e}_1(t) + \delta m_{q2}^{\pm}(\mathbf{r}, t)\, \mathbf{e}_2(t), \tag{8.45}$$

and by substituting in this expression formula (8.44) for $\delta m_{q1,2}^{\pm}(\mathbf{r}, t)$ and formulas (8.6)–(8.7) for $\mathbf{e}_{1,2}(t)$.

Equations (8.42) and (8.44) show that, once the periodic matrix $\Pi_q(t)$ is known, the spin-wave analysis is reduced to the investigation of a simple dynamic equation with constant coefficients, i.e., Eq. (8.42). This equation has an intrinsic physical significance, because the function $\omega_q^2(\mathbf{q})$ defined by Eq. (8.43) can be construed as the generalized dispersion relation for

spin-wave excitations of the given **P**-mode. Unfortunately, no general method is known for the explicit analytical calculation of the matrix Ω_q, on which $\omega_q^2(\mathbf{q})$ depends. In this sense, the statement that Eq. (8.43) provides the intrinsic spin-wave dispersion relation remains a purely theoretical one.

Nevertheless, helpful results can be obtained by the following approximate method. Suppose that the parametric part of Eq. (8.29) is sufficiently small. Then one can identify Ω_q with the matrix A_q in Eq. (8.29). This approximation permits one to obtain immediate information about the spin-wave spectrum, and subsequently study deviations from this behavior by treating the time-dependent part of Eq. (8.29) as a perturbation. Even when the parametric part in Eq. (8.29) is not small, one can often use heuristic or symmetry considerations to pass from the (c_{q1}, c_{q2}) representation to some other representation where parametric effects are significantly reduced. More precisely, let us consider the transformation, similar to Eq. (8.41):

$$\begin{pmatrix} c_{q1} \\ c_{q2} \end{pmatrix} = S_q(t) \begin{pmatrix} c'_{q1} \\ c'_{q2} \end{pmatrix}, \tag{8.46}$$

where $S_q(t)$ is some invertible periodic matrix, with period $2\pi/\omega$. By substituting Eq. (8.46) into Eq. (8.29) one obtains:

$$\begin{aligned} &\frac{\mathrm{d}}{\mathrm{d}t} \begin{pmatrix} c'_{q1} \\ c'_{q2} \end{pmatrix} \\ &\quad = S_q^{-1}(t) \left[A_q + R_1(t) + R_2(t) - \frac{\mathrm{d}S_q}{\mathrm{d}t} S_q^{-1}(t) \right] S_q(t) \begin{pmatrix} c'_{q1} \\ c'_{q2} \end{pmatrix}. \end{aligned} \tag{8.47}$$

This transformed equation is still of the type:

$$\frac{\mathrm{d}}{\mathrm{d}t} \begin{pmatrix} c'_{q1} \\ c'_{q2} \end{pmatrix} = A'_q \begin{pmatrix} c'_{q1} \\ c'_{q2} \end{pmatrix} + R'(t) \begin{pmatrix} c'_{q1} \\ c'_{q2} \end{pmatrix}, \tag{8.48}$$

where A'_q has constant coefficients while $R'(t)$ is periodic with period $2\pi/\omega$. If $S_q(t)$ is appropriately chosen in such a way that $R'(t)$ is sufficiently small, then one can approximate Ω_q by the matrix A'_q and $\Pi_q(t)$ by $S_q(t)$, leaving to subsequent steps the study of the effect of the time-dependent part by perturbation methods. This leads to the following approximate expression for the spin-wave amplitudes, similar to Eq. (8.44):

$$\begin{pmatrix} \delta m_{q1}^{\pm}(\mathbf{r},t) \\ \delta m_{q2}^{\pm}(\mathbf{r},t) \end{pmatrix} \simeq \exp\left(-\eta_q' t\right) S_q(t) \begin{pmatrix} c_1'^{\pm} \\ c_2'^{\pm} \end{pmatrix} \exp\left[\mathrm{i}\left(\mathbf{q}\cdot\mathbf{r} \pm \omega_q' t\right)\right], \quad (8.49)$$

where:

$$\omega_q'^2 = \det A_q' - \frac{\left(\mathrm{tr}\, A_q'\right)^2}{4}, \quad (8.50)$$

$\eta_q' = -\mathrm{tr}\, A_q'/2$, and $(c_1'^{\pm}, c_2'^{\pm})$ are the A_q' eigenmodes in the (c_{q1}', c_{q2}') representation.

There are two cases of physical interest where these approximate methods prove particularly useful:

- Spin-waves with wave-vector nearly aligned along the symmetry axis: $\theta_q \ll 1$
  Equations (8.31) and (8.32) show that in this limit the matrices $R_1(t)$ and $R_2(t)$ are of the order of θ_q and θ_q^2, respectively, and can thus be treated as perturbations. The spin-wave amplitude is obtained by neglecting the time-dependent part of Eq. (8.29), i.e., by assuming that $\Omega_q = A_q$ and $\Pi_q(t) = I$ in Floquet analysis. The spin-wave amplitude can be calculated from Eqs (8.41) and (8.42) by standard methods. By also neglecting damping, one finds that Eq. (8.44) is reduced to:

$$\delta\mathbf{m}_q^{\pm}(\mathbf{r},t) = C_q \left[\sqrt{\nu_q}\, \mathbf{e}_1(t) \mp \mathrm{i}\sqrt{\nu_q - \kappa_q \sin^2\theta_0}\, \mathbf{e}_2(t)\right] \times \exp\left[\mathrm{i}\left(\mathbf{q}\cdot\mathbf{r} \pm \omega_q t\right)\right]. \quad (8.51)$$

  In Eq. (8.51), C_q is a constant whereas ω_q is to be calculated from Eq. (8.43) by assuming $\Omega_q = A_q$. Thus, one obtains:

$$\omega_q^2 = \frac{1}{\left(1+\alpha^2\right)^2}\left[\left(\nu_q - \frac{\kappa_q \sin^2\theta_0}{2} - \alpha^2\omega\cos\theta_0\right)^2 - \left(1+\alpha^2\right)\frac{\kappa_q^2 \sin^4\theta_0}{4}\right]. \quad (8.52)$$

  In the first-order approximation with respect to the damping constant α, Eq. (8.52) is reduced to the simpler form:

$$\omega_q^2 \simeq \nu_q\left(\nu_q - \kappa_q \sin^2\theta_0\right), \quad (8.53)$$

where ν_q and κ_q are given by Eqs (8.33) and (8.34), respectively. Equation (8.52) plays the role of generalized dispersion relation for nonequilibrium spin-waves with wave-vector nearly aligned along the symmetry axis of the problem. This relation is valid for arbitrarily large **P**-mode motions. In addition, it explicitly depends on the **P**-mode angle θ_0, which means that different dispersion relations will coexist under given excitation conditions $(\omega, \mathrm{h}_{az}, \mathrm{h}_{a\perp})$, because different **P**-modes may be realized in general for those conditions. Finally, it must be stressed that although Eq. (8.51) has the typical structure of elliptically polarized spin-waves, its physical interpretation is definitely more complex than for traditional spin-waves. As previously discussed, the behavior described by Eq. (8.51) holds in the time-dependent basis $(\mathbf{e}_1, \mathbf{e}_2)$. When observed in the laboratory frame, the spin-wave oscillations will appear to be quasi-periodic, due to the combination of the spin-wave frequency ω_q with the driving field frequency ω. This effect can be quantified by expressing $\mathbf{e}_1(t)$ and $\mathbf{e}_2(t)$ in the laboratory-frame basis $(\mathbf{e}_x, \mathbf{e}_y, \mathbf{e}_z)$ through Eqs (8.6)–(8.7) (see Eq. (8.45)).

- Spin-waves under small **P**-mode motions: $\theta_0 \ll 1$

  In general, the parametric part of Eq. (8.29) is not small in this limit. However, one can attempt an appropriate transformation of the type described by Eq. (8.46) in order to make the parametric part of Eq. (8.29) as small as possible. This transformation creates a direct bridge between the present theory and conventional spin-wave studies close to equilibrium. Consider the transformation (8.46) and assume that the matrix $S_q(t)$ is equal to:

$$S_q(t) = \frac{1}{1 - \sin^2\theta_0 \cos^2\omega t} \begin{pmatrix} \cos\theta_0 \cos\omega t & \sin\omega t \\ -\sin\omega t & \cos\theta_0 \cos\omega t \end{pmatrix}. \tag{8.54}$$

By using this expression in Eq. (8.47), one obtains the equation:

$$\frac{\mathrm{d}}{\mathrm{d}t} \begin{pmatrix} c'_{q1} \\ c'_{q2} \end{pmatrix} = A'_q \begin{pmatrix} c'_{q1} \\ c'_{q2} \end{pmatrix} + R'(t) \begin{pmatrix} c'_{q1} \\ c'_{q2} \end{pmatrix} + \mathcal{O}\left(\sin^2\theta_0\right), \tag{8.55}$$

where:

$$A'_q = \frac{1}{1+\alpha^2} \begin{pmatrix} 1 & -\alpha \\ \alpha & 1 \end{pmatrix} \times \begin{pmatrix} 0 & -\nu_q - \omega + \sin^2\theta_q/2 \\ \nu_q + \omega + \sin^2\theta_q/2 & 0 \end{pmatrix}, \tag{8.56}$$

$$R'(t) = \frac{\sin\theta_0 \sin\theta_q \cos\theta_q}{1+\alpha^2} \begin{pmatrix} 1 & -\alpha \\ \alpha & 1 \end{pmatrix} \begin{pmatrix} \sin\omega t & 0 \\ -2\cos\omega t & -\sin\omega t \end{pmatrix}. \quad (8.57)$$

In this representation, the parametric part is indeed of the order of θ_0. Therefore, by taking $\Omega_q \simeq A'_q$, $\Pi_q(t) \simeq S_q(t)$ and by additionally neglecting damping, one obtains:

$$\delta\mathbf{m}_q^{\pm}(\mathbf{r},t) \simeq C_q \exp\left[\mathrm{i}\left(\mathbf{q}\cdot\mathbf{r} \pm \omega'_q t\right)\right] \times \left[\sqrt{\nu_q + \omega - \sin^2\theta_q/2}\,\mathbf{e}_x \mp \mathrm{i}\sqrt{\nu_q + \omega + \sin^2\theta_q/2}\,\mathbf{e}_y\right], \quad (8.58)$$

where ω'_q is given by Eq. (8.50) and use has been made of Eqs (8.6) and (8.7). To the first order in α, one finds from Eq. (8.50) that:

$$\omega'^2_q \simeq \left(\nu_q + \omega + \sin^2\theta_q/2\right)\left(\nu_q + \omega - \sin^2\theta_q/2\right). \quad (8.59)$$

By using Eq. (8.33) and the expression Eq. (7.17) for ν_0 from the previous chapter under the approximation $\cos\theta_0 \simeq 1$, Eq. (8.59) can be expressed in the form:

$$\omega'^2_q \simeq \left(\mathrm{h}_{az} - N_z + \kappa + q^2\right)\left(\mathrm{h}_{az} - N_z + \kappa + q^2 + \sin^2\theta_q\right). \quad (8.60)$$

Equations (8.58) and (8.60) coincide with the classical relations describing spin-waves around static magnetic saturation [646,306]. In fact, when the **P**-mode motion is small, the plane $(\mathbf{e}_1, \mathbf{e}_2)$ approaches the $\perp$-plane and the vectors $(\mathbf{e}_1, \mathbf{e}_2)$ are rotated at the angular frequency ω in this plane. At the same time, the transformation $S_q^{-1}(t)$ is reduced to a rotation in the same plane at the angular frequency $-\omega$, because $\cos\theta_0 \simeq 1$. Therefore, the transformed spin-wave amplitudes (c'_{q1}, c'_{q2}) appearing in Eq. (8.46) are reduced to the spin-wave amplitudes in the laboratory frame.

8.3 STABILITY ANALYSIS

Spin-wave perturbations with initial nonzero amplitude, generated by thermal fluctuations or other causes, will evolve in time in accordance with Eqs (8.29)–(8.34). When the solution of these equations results in an exponentially growing spin-wave amplitude, the phenomenon occurs where the energy injected into the system by the action of the rotating

external field is continuously transferred to the spin-wave perturbations resulting in their growth to large, nonthermal amplitudes. This means that the **P**-mode around which the spin-wave perturbation analysis is being carried out is no longer a stable observable large-scale magnetization motion and that magnetization motions with strong spatial nonuniformity occur instead. There are two mechanisms leading to **P**-mode instability: (i) one of the eigenvalues of the matrix A_q in Eq. (8.29) has a positive real part; (ii) parametric instability is caused by the oscillating terms $R_1(t)$ and $R_2(t)$ in Eq. (8.29). In fact, these two mechanisms are not independent, but rather coupled, which leads to an extremely rich and complex spin-wave behavior.

In this respect, a particularly instructive example is represented by the case of spin-waves with wave-vector $\mathbf{q}$ parallel to symmetry axis $\mathbf{e}_z$, i.e., $\theta_q = 0$ [87]. In this case, $R_1(t)$ and $R_2(t)$ in Eq. (8.29) are identically zero. Hence, for any **P**-mode, the corresponding spin-wave behavior is entirely governed by the constant-coefficient matrix A_q (Eq. (8.30)), which coincides with the matrix Ω_q of Floquet's analysis. It can be inferred (see the section on stability analysis in the previous chapter) that **P**-mode instability occurs when $\mathrm{tr}\ A_q > 0$ or when $\det A_q < 0$, where:

$$\mathrm{tr}\ A_q = -\frac{2\alpha}{1+\alpha^2}\left(\nu_q - \frac{\kappa_q \sin^2\theta_0}{2} + \omega\cos\theta_0\right), \tag{8.61}$$

$$\det A_q = \frac{1}{1+\alpha^2}\left(\nu_q^2 - \kappa_q \sin^2\theta_0 \nu_q + \alpha^2\omega^2\cos^2\theta_0\right), \tag{8.62}$$

with $\nu_q = \nu_0 - N_\perp + q^2$ and $\kappa_q = \kappa - 1$ (see Eqs (8.33) and (8.34) for $\theta_q = 0$). The comparison of Eqs (8.61), (8.62) and (8.52) with the corresponding equations for the stability of spatially uniform perturbations from the previous chapter reveals that there is a complete analogy between the stability analysis for spin-waves with $\theta_q = 0$ and the one for uniform perturbations. Instabilities due to spin-waves with $\theta_q = 0$ are governed by the effective anisotropy $\kappa_q = \kappa - 1$, identical to the one controlling uniform perturbations in a thin film. In this sense, a generic spheroidal particle behaves like a thin film as far as spin-waves with $\theta_q = 0$ are concerned. In fact, this result, reached through heuristic arguments, represented one of the starting points for the development of nonlinear ferromagnetic resonance theories [22]. We shall see in the sequel that instabilities due to spin-waves with $\theta_q = 0$ represent the natural extension to large motions of the second-order Suhl's instability observed in ferromagnetic resonance.

The case of spin-waves with $\theta_q = 0$ is quite special, because oscillating parametric terms are completely absent. In general, for spin-waves with

wave-vector not aligned along the symmetry axis of the problem, spin-wave stability is controlled not only by the eigenvalues of the A_q matrix, but also by the possible onset of parametric resonance effects. General conclusions about the importance of parametric effects can be reached through the analysis of the properties of the so-called one-period map [529,319] associated with Eq. (8.29). Consider Eq. (8.38) again. Due to the periodicity of the coefficients involved, it is easy to conclude that if $\Phi_q(t)$ is a solution of Eq. (8.38), then the function $\Phi_q(t+2\pi/\omega)$ is also be a solution of the same equation, and thus is linearly related to the original solution. In matrix form, one can write:

$$\Phi_q(t+2\pi/\omega) = \Phi_q(t) M_q. \tag{8.63}$$

The matrix M_q generates the so-called one-period map associated with Eq. (8.38). By using Eq. (8.39) in this relation and by taking into account the periodicity of $\Pi_q(t)$ one immediately concludes that:

$$M_q = \exp\left(\frac{2\pi}{\omega}\Omega_q\right). \tag{8.64}$$

As a consequence of Eq. (8.63), the principal solution over subsequent periods can be expressed as: $\Phi_q(t+2n\pi/\omega) = \Phi_q(t)(M_q)^n, n = 1, 2, \ldots$. This result shows that the **P**-mode under consideration will be unstable with respect to certain spin-wave perturbations when at least one of M_q eigenvalues exceeds 1 in magnitude. These eigenvalues are called characteristic multipliers of the equation and will be denoted by $\mu_\pm$.

Some immediate conclusion concerning the stability of spin-waves can be obtained from the one-period map via the Liouville theorem [319]. This theorem, when applied to Eq. (8.38), leads to the equation:

$$\begin{aligned} \det M_q &= \exp\left[\int_0^{2\pi/\omega} \mathrm{tr}\ [A_q + R_1(t) + R_2(t)]\,\mathrm{d}t\right] \\ &= \exp\left(\frac{2\pi}{\omega}\mathrm{tr}\ A_q\right). \end{aligned} \tag{8.65}$$

The second equality is the consequence of the fact that A_q is constant whereas R_1 and R_2 have zero average over one period. Since $\det M_q = |\mu_+|\,|\mu_-|$, the **P**-mode will be certainly unstable if $\det M_q > 1$. By using this fact and Eq. (8.65), one concludes that $\mathrm{tr}\ A_q > 0$ is a sufficient condition for instability. The Liouville theorem does not provide any information

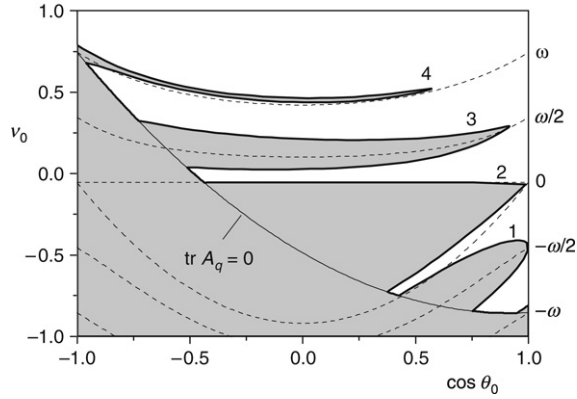

FIGURE 8.1 Gray region: **P**-modes unstable with respect to spin-wave perturbations with $q^2 = 0.01$ and $\sin\theta_q = 0.3$, determined by numerical integration of Eq. (8.38). Dashed lines: $\omega_q = 0$ (i.e., $\nu_q = 0$ and $\nu_q = \kappa_q \sin^2\theta_0$, see Eq. (8.53)), $\omega_q = \pm\omega/2$ (Eq. (8.79)), $\omega_q = \pm\omega$ (Eq. (8.80)). Numbers 1 through 4: parametric resonance order n. System parameters: $N_\perp = 0$, $\kappa = 0$, $\alpha = 0.01$. Field frequency: $\omega = 0.8$.

on stability when $\det M_q < 1$, i.e., $\mathrm{tr}\ A_q < 0$. Detailed numerical and analytical investigation is needed to explore stability in this region.

One can determine the stability of **P**-modes with respect to any particular spin-wave perturbation by numerical integration of Eq. (8.38). In fact, according to the definition of one-period map, if $\Phi_q(0) = I$ then $\Phi_q(2\pi/\omega) = M_q$. Therefore, numerical integration of the equation over one period combined with inspection of the eigenvalues of the resulting matrix solution directly yields the desired stability information. Figure 8.1 shows an example of this numerical study, represented in the **P**-mode plane $(\cos\theta_0, \nu_0)$. The gray region identifies all the **P**-modes that are unstable with respect to spin-wave perturbations with $q^2 = 0.01$ and $\sin\theta_q = 0.3$. All **P**-modes for which $\mathrm{tr}\ A_q > 0$ are unstable, as previously discussed. Conversely, the region $\mathrm{tr}\ A_q < 0$ is characterized by a pattern typical of parametric resonance [33,431], with instability concentrated along so-called Arnold tongues.

The essential features of the remarkably rich structure shown in Fig. 8.1 can be explained through a perturbative approach. To start the discussion, consider a solution to Eq. (8.38) in the form:

$$\Phi_q(t) = \exp(A_q t)\, B_q(t), \tag{8.66}$$

with the initial condition $B_q(0) = I$. The matrix $B_q(t)$ obeys the Volterra integral equation:

$$B_q(t) = I + \int_0^t R\,(t')\,B_q\,(t')\,\mathrm{d}t', \tag{8.67}$$

where:

$$R(t) = \exp\,(-A_q t)\,[R_1(t) + R_2(t)]\exp\,(A_q t)\,. \tag{8.68}$$

Equation (8.67) can be solved by iterations. Taking into account that $M_q = \Phi_q(2\pi/\omega) = \exp(2\pi A_q/\omega)B_q(2\pi/\omega)$, one arrives at the following one-period map series expansion:

$$M_q = \exp\left(\frac{2\pi}{\omega}A_q\right) \times \left[I + \int_0^{2\pi/\omega} R\,(t')\,\mathrm{d}t' + \int_0^{2\pi/\omega}\mathrm{d}t' \int_0^{t'} R\,(t')\,R\,(t'')\,\mathrm{d}t'' + \ldots\right]. \tag{8.69}$$

Let us discuss this result at various orders of approximation.

- Zero-order solution for the one-period map
  Equation (8.69) gives for the zero-order solution $M_q^{(0)}$:

$$M_q^{(0)} = \exp\left(\frac{2\pi}{\omega}A_q\right). \tag{8.70}$$

  The corresponding characteristic multipliers are then equal to:

$$\mu_{\pm}^{(0)} = \left(\cos\frac{2\pi\omega_q}{\omega} \pm \mathrm{i}\sin\frac{2\pi\omega_q}{\omega}\right)\exp\left(\frac{\pi}{\omega}\mathrm{tr}\;A_q\right), \tag{8.71}$$

  where $\mathrm{tr}\;A_q$ is given by Eq. (8.61), while ω_q is given by Eq. (8.52) or Eq. (8.53). Equation (8.71) shows that in the region $\mathrm{tr}\;A_q < 0$ no instability can occur if $\omega_q^2 > 0$, because the characteristic multipliers are then complex conjugate with squared magnitude equal to $\exp\,(2\pi\;\mathrm{tr}\;A_q/\omega) < 1$. Conversely, when $\omega_q^2 < 0$ the characteristic

multipliers are real:

$$\mu_{\pm}^{(0)} = \exp\left[\frac{\pi}{\omega}\left(\mathrm{tr}\ A_q \pm 2|\omega_q|\right)\right]. \tag{8.72}$$

Therefore, one of the multipliers will exceed 1 in magnitude and instability will occur if $\omega_q^2 < -(\mathrm{tr}\ A_q)^2/4$, i.e., $\det A_q < 0$. This result is identical to the one previously discussed for spin-waves with $\theta_q = 0$. In fact, only the constant-coefficient matrix A_q is involved in the zero-order approximation for the one-period map. Since $\mathrm{tr}\ A_q$ is of the order of α and $\alpha \ll 1$, the boundary of the instability region is very close to $\omega_q^2 = 0$. According to Eq. (8.53), the condition $\omega_q^2 = 0$ is satisfied to the first order in α when $\nu_q = 0$ or $\nu_q = \kappa_q \sin^2\theta_0$. These two lines correspond to the two dashed lines indicated by the 0 label in Fig. 8.1.

- First-order solution for the one-period map

  For the first-order solution $M_q^{(1)}$, Eq. (8.69) gives:

$$M_q^{(1)} = \exp\left(\frac{2\pi}{\omega}A_q\right)\left[I + \int_0^{2\pi/\omega} R\left(t'\right)\mathrm{d}t'\right]. \tag{8.73}$$

After lengthy calculations of the matrix elements of $M_q^{(1)}$, one arrives at the following expression for the characteristic multipliers:

$$\mu_{\pm}^{(1)} = \left(\cos\frac{2\pi\omega_q}{\omega} \pm \mathrm{i}\sqrt{1 - Z_q^2}\sin\frac{2\pi\omega_q}{\omega}\right)\exp\left(\frac{\pi}{\omega}\mathrm{tr}\ A_q\right), \tag{8.74}$$

where:

$$Z_q = Z_{q1} - Z_{q2}, \tag{8.75}$$

$$Z_{q1} = \frac{\sin 2\theta_q}{4\left(1+\alpha^2\right)^{3/2}} \times \frac{\sin\theta_0\left[\omega\left(1+\alpha^2\right) - 2\left(\nu_q - \alpha^2\omega\cos\theta_0\right)\cos\theta_0\right]}{\left(\omega/2\right)^2 - \omega_q^2}, \tag{8.76}$$

$$Z_{q2} = \frac{\sin^2\theta_q}{4\left(1+\alpha^2\right)^{3/2}} \times \frac{2\omega\left(1+\alpha^2\right)\cos\theta_0 - \left(\nu_q - \alpha^2\omega\cos\theta_0\right)\left(1+\cos^2\theta_0\right) + \kappa_q\sin^2\theta_0}{\omega^2 - \omega_q^2}. \tag{8.77}$$

The similarity between Eqs (8.71) and (8.74) is striking. For all **P**-modes for which $Z_q^2 < 1$, instability appears only when $\omega_q^2 < 0$ and the characteristic multipliers take the real values:

$$\mu_\pm^{(1)} = \mu_\pm^{(0)} \mp \left(1 - \sqrt{1 - Z_q^2}\right) \frac{\mu_+^{(0)} - \mu_-^{(0)}}{2}, \tag{8.78}$$

where $\mu_\pm^{(0)}$ is the zero-order contribution given by Eq. (8.72). Instability occurs in the region of the $(\cos\theta_0, \nu_0)$ plane where one of these multipliers exceeds 1 in magnitude. This region represents the first-order correction to the zero-order instability region $\det A_q < 0$. However, if $Z_q^2 > 1$ for some **P**-mode, the corresponding characteristic multipliers become real for $\omega_q^2 > 0$, and an additional instability mechanism is possible. This is indeed the case around $\omega_q = \pm\omega/2$ and $\omega_q = \pm\omega$, where respectively Z_{q1} and Z_{q2} tend to infinity. These instability conditions are described by corresponding lines in the $(\cos\theta_0, \nu_0)$-plane, obtained by solving the equations $\omega_q^2 - \omega^2/4 = 0$ and $\omega_q^2 - \omega^2 = 0$. From Eq. (8.53) one finds that to the first order in α the condition $\omega_q = \pm\omega/2$ corresponds to:

$$\nu_q = \frac{\kappa_q \sin^2\theta_0}{2} \pm \sqrt{\frac{\kappa_q^2 \sin^4\theta_0}{4} + (\omega/2)^2}. \tag{8.79}$$

These are the two dashed lines labeled by $\pm\omega/2$ in Fig. 8.1. Similarly, the condition $\omega_q = \pm\omega$ leads to:

$$\nu_q = \frac{\kappa_q \sin^2\theta_0}{2} \pm \sqrt{\frac{\kappa_q^2 \sin^4\theta_0}{4} + \omega^2} \tag{8.80}$$

(dashed lines labeled by $\pm\omega$ in Fig. 8.1). Comparison with the numerical results in Fig. 8.1 shows that indeed Eqs (8.79) and (8.80) correctly identify the regions where **P**-mode instability occurs despite the fact that $\mathrm{tr}\, A_q < 0$.

At the beginning of the previous section, we anticipated the fact that the instabilities we are discussing are parametric in nature and are caused by periodic oscillations in the magnetostatic field. The parametric nature of the phenomenon is best appreciated by considering Eqs (8.55)–(8.57), valid in the limit of small **P**-mode motions. Comparison with Eq. (8.36) shows that spin-wave dynamics exhibits the typical structure

of parametric resonance problems. The frequency ω_q' defined by Eq. (8.59) plays the role of characteristic oscillator frequency, while ω is the frequency of the parametric part. Therefore, one can immediately conclude that spin-wave instabilities are expected around $\omega_q' = n\omega/2, n = 1, 2, \ldots$. This sequence corresponds to the instability sequence $\omega_q = -\omega/2, 0, \omega/2, \omega$ previously derived ($\omega_q = -\omega$ is not a real instability, as shown by Fig. 8.1). This correspondence becomes evident when one considers small **P**-mode motions. In fact, in this limit the vector bases associated with Eqs (8.29) and (8.55) differ by a rotation at the angular frequency ω around $\mathbf{e}_z$ (see the discussion at the end of the previous section), which implies that $\omega_q' \simeq \omega_q + \omega$. In this sense, one can say that the instabilities labeled by $\omega_q = -\omega/2, 0, \omega/2, \omega$ represent the extension to large **P**-mode motions of the small-motion parametric-resonance sequence $\omega_q' = n\omega/2$ for $n = 1, 2, 3, 4$. This is the meaning of the labels $1, 2, 3, 4$ in Fig. 8.1. In principle, also instabilities characterized by $n = 5, 6, \ldots$ are possible. However, they are expected to be much weaker, because they come from higher-order terms of the series expansion (8.69).

8.4 SPIN-WAVE INSTABILITIES AND INSTABILITY DIAGRAMS

The main result of the LLG analysis discussed in the previous chapter is that, given the excitation conditions $(\omega, \mathrm{h}_{az}, \mathrm{h}_{a\perp})$, there exist two or four spatially uniform dynamical modes (**P**-modes), depending on the system parameters $(\alpha, \kappa_{\text{eff}})$. The two central questions of physical interest are: (i) which of these **P**-modes will be experimentally observable; (ii) given an observable **P**-mode, under what conditions the mode will become unstable when we slowly change the amplitude and/or the frequency of the external field. Based on the discussion presented in the previous sections, we can say that the complete answer to these questions should come from the analysis of the full spectrum of solutions of Eq. (8.8) for the **P**-mode of interest. Such complete spectrum is generally not known. However, two types of solutions are expected to play a particularly important role: spatially uniform perturbations, discussed in the previous chapter, and spin-wave perturbations, considered in the previous section. In this section we analyze the scenario obtained when one assumes that instabilities with respect to these two types of perturbations dominate the problem. In particular, we shall discuss the behavior of the system close to ferromagnetic resonance conditions (see the previous chapter), where the resonant behavior of the system at low rf power is gradually distorted when the power is increased, until a number of instabilities, in particular foldover phenomena or Suhl's instabilities appear.

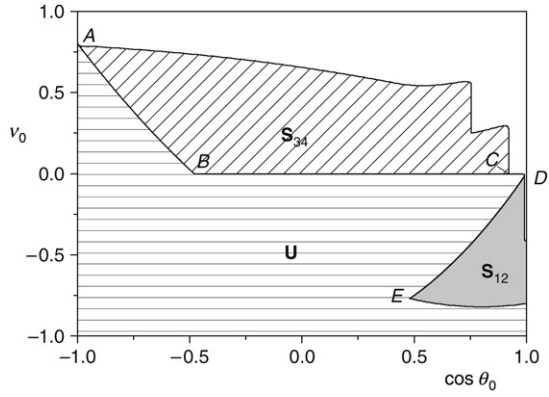

FIGURE 8.2 **P**-mode stability diagram for a thin-film disk with negligible crystal anisotropy. **U**: **P**-modes unstable with respect to uniform perturbations. $\mathbf{S}_{12}$ and $\mathbf{S}_{34}$: **P**-modes unstable because of spin-wave parametric resonance of order $n = 1, 2$ and $n = 3, 4$, respectively. Points A through E are indicated for the sake of comparison with Fig. 8.3. Detailed structure of $\mathbf{S}_{12}$ for $\cos\theta_0 \simeq 1$, not visible in the figure, results in regions **I** and **II** in Fig. 8.3. System parameters: $N_\perp = 0$, $\kappa = 0$, $\alpha = 0.01$. Field frequency: $\omega = 0.8$.

By "instability diagram" we mean a diagram in the **P**-mode plane $(\cos\theta_0, \nu_0)$ indicating which **P**-modes are stable and which are unstable under certain conditions. An example is given by Fig. 8.2. Several regions are shown in this figure, each of which corresponds to **P**-modes that are unstable because of different mechanisms. Let us discuss in more detail how an instability diagram of this type can be constructed.

Region **U** in the diagram corresponds to **P**-modes that are unstable with respect to spatially uniform perturbations. **P**-mode stability with respect to spatially uniform perturbations was discussed in Chapter 7. The main result of that analysis is represented by Fig. 7.3. The **U** and **D** regions in that figure are respectively associated with unstable-node and saddle **P**-modes. The union of those two regions is the region labeled by **U** in Fig. 8.2.

The next step is to discuss if some of the **P**-modes outside this region may be unstable because of spin-wave instabilities. These instability regions are determined by carrying out the analysis discussed in the previous section and illustrated by Fig. 8.1. This analysis must be carried out for all admissible spin-wave modes with $0 \leq \sin^2\theta_q \leq 1$ and $q^2 > 0$. Then, the total resulting instability regions are obtained by taking the union of all the individual instability regions obtained for single values

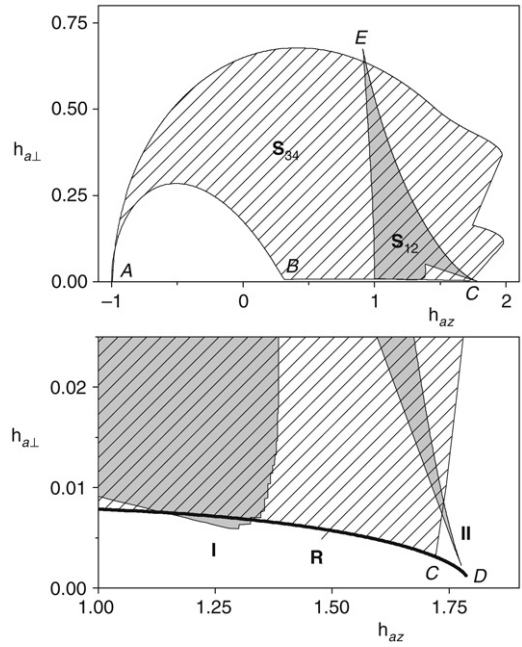

FIGURE 8.3 Regions $\mathbf{S}_{12}$ and $\mathbf{S}_{34}$ of Fig. 8.2, as they appear in $(\mathrm{h}_{az}, \mathrm{h}_{a\perp})$ plane. Bottom: magnified view of ferromagnetic resonance region. **R**: Riemann cut. CD: foldover segment. **I**: first-order Suhl's instability. **II**: second-order Suhl's instability. System parameters: $N_\perp = 0$, $\kappa = 0$, $\alpha = 0.01$. Field frequency: $\omega = 0.8$.

of $\sin^2\theta_q$ and q^2. Remarkably, the only place where q^2 appears in the entire analysis is Eq. (8.33). Therefore, given the instability diagram for a particular value of $\sin^2\theta_q$ and $q^2 \simeq 0$, all the diagrams for the same value of $\sin^2\theta_q$ and larger values of q^2 are immediately obtained by shifting the initial diagram downward in the $(\cos\theta_0, \nu_0)$ plane by the amount q^2. Figure 8.2 shows the constructed diagram for a thin-film disk with negligible crystal anisotropy, obtained by repeating this analysis for all values of $\sin^2\theta_q$ in the interval $0 \leq \sin^2\theta_q \leq 1$. **P**-modes in regions $\mathbf{S}_{12}$ and $\mathbf{S}_{34}$ are made unstable by spin-wave parametric resonance of order $n = 1, 2$ and $n = 3, 4$, respectively (compare with Fig. 8.1).

Figure 8.3 was obtained by transforming Fig. 8.2 from the plane $(\cos\theta_0, \nu_0)$ to the field control plane $(\mathrm{h}_{az}, \mathrm{h}_{a\perp})$, which is of interest in experiments. Regions $\mathbf{S}_{12}$ and $\mathbf{S}_{34}$ fill out only a limited part of the field control plane. This occurs because the system is stable for large positive ν_0 (see Fig. 8.2) as a result of the absence of high-order parametric

instabilities. In thin films, for which $N_\perp = 0$, an approximate ν_0 upper bound for spin-wave instabilities can be obtained from Eqs (8.33) and (8.53) by neglecting terms proportional to α^2. Equation (8.33) yields the inequality $\nu_0 < \nu_q$. At the same time, by applying Eq. (8.53) to the instabilities characterized by $\omega_q^2 = \omega^2$ and by assuming that $\kappa_q < 0$ for these instabilities one finds that $\nu_q \leq \omega_q = \omega$. By combining the two inequalities one concludes that instabilities are limited to the region $\nu_0 < \omega$. By using this result in the equations that connect $(\cos\theta_0, \nu_0)$ with $(\mathrm{h}_{az}, \mathrm{h}_{a\perp})$, one concludes that the system can be unstable only if $\mathrm{h}_{a\perp}^2 < \omega^2 \sin^2\theta_0$ and $(\mathrm{h}_{az} - \omega)/\cos\theta_0 + \kappa_{\text{eff}} < \omega$. Whenever the excitation conditions are outside this range, the system will be stable. It is worth stressing that according to these inequalities, stability can be achieved by applying a sufficiently large rf field. Thus, a sufficiently strong driving action of the field will make the system stable, contrary to what might seem to be suggested by the onset of spin-wave instabilities under increasing rf power.

The transformation from Fig. 8.2 to Fig. 8.3 is not one to one, because there are 2 or 4 **P**-modes associated with each point in the $(\mathrm{h}_{az}, \mathrm{h}_{a\perp})$-plane. Therefore, **P**-mode properties in the $(\mathrm{h}_{az}, \mathrm{h}_{a\perp})$ plane are defined on a Riemann surface with two or four folded sheets. An example is the behavior of the trace and the determinant of the **P**-mode stability matrix shown in Figs 7.4 and 7.5 in the previous chapter. This folded structure has remarkable physical consequences. As an example let us consider the following "thought" experiment. Let us initially apply the large dc field $\mathrm{h}_{az} > 0$ with no rf power (i.e., $\mathrm{h}_{a\perp} = 0$). The system will be in a **P**-mode which coincides with the saturation state along the field direction. At this point let us switch on the rf power and follow the behavior of the **P**-mode when h_{az} is slowly decreased down to the value h_{final} smaller than the resonance field $\omega - \kappa_{\text{eff}}$. By using the construction shown in Fig. 7.3 from the previous chapter to determine the location of the **P**-mode and by comparing Fig. 8.2 with Fig. 8.3 one finds that the **P**-mode will hit region $\mathbf{S}_{34}$ but not region $\mathbf{S}_{12}$ if the **P**-mode remains above the line **R** shown in Fig. 8.3. This line acts as a Riemann cut in the control plane. Region $\mathbf{S}_{12}$ lies on a different sheet of the Riemann surface. This region can be reached by following a different field history, that is, by decreasing the dc field down to $\mathrm{h}_{az} = h_{\text{final}}$ before switching on the rf power. In this way the line **R** is approached from below and one has access to the region where first-order (**I**) and second-order (**II**) Suhl's instabilities may be observed, as discussed below. Therefore, we come to the important conclusion that at large rf power the dynamical behavior of the system, and in particular the excitation of spin-wave instabilities, becomes dependent on the magnetic field history.

Finally, we comment on the foldover effect discussed in the previous chapter. Figure 8.3 shows that foldover can be partly masked by spin-wave instabilities. In fact, foldover is the first instability mechanism encountered by the system under decreasing h_{az} only in the interval CD indicated in the figure. For larger rf field amplitudes, the system encounters the boundary of the $\mathbf{S}_{34}$ spin-wave instability region before reaching the astroid boundary. Under these conditions, the spin-wave instability will set in before foldover can be produced.

Figure 8.3 shows that the instability region $\mathbf{S}_{12}$ is present down to rather small values of $h_{a\perp}$. Thus, one expects that this type of instability should be detected in experiments at relatively low radio-frequency powers. This is in fact the case. What is observed in this case is universally known as Suhl's instabilities [645,646,527,740,306]. We have discussed the fact that the lower boundary of the $\mathbf{S}_{12}$ region is associated with spin-wave modes for which $\omega_q^2 \simeq \omega^2/4$ or $\omega_q^2 \simeq 0$. These two possibilities lead to so-called first-order and second-order Suhl's instabilities. We shall discuss the first-order instability by considering the associated behavior of the one-period-map characteristic multipliers introduced in the previous section. Then, the second-order instability will be discussed by a different approach.

It is possible to derive explicit expressions for the location of the $\omega_q^2 = \omega^2/4$ instability boundary by analyzing the behavior of the characteristic multipliers close to parametric resonance. However, in principle spin-wave perturbations with arbitrary values of θ_q may be involved in the instability. For the modes with large values of θ_q the perturbative approach followed in previous sections would not be accurate, because the parametric terms involved in the spin-wave dynamics are then not small. However, since we are looking for instabilities occurring at relatively low radio-frequency powers, we can take advantage of the fact that the **P**-mode motions excited by such rf fields will not be very large. This means that the parametric terms will be small in the "primed" basis introduced by Eqs (8.46)–(8.57). The correct strategy is therefore to study the one-period-map properties in the "primed" basis. Once the change of basis has been carried out, there is no basic difference in the analysis. Through calculations similar to those discussed in the previous section, one arrives at the following first-order expression for the characteristic multipliers (compare with Eq. (8.74)):

$$\mu_{\pm}^{\prime(1)} = \left(\cos\frac{2\pi\omega_q'}{\omega} \pm \mathrm{i}\sqrt{1 - Z_{q1}'^2}\,\sin\frac{2\pi\omega_q'}{\omega}\right)\exp\left(\frac{\pi}{\omega}\mathrm{tr}\;A_q'\right). \qquad (8.81)$$

The trace $\mathrm{tr}\ A'_q$ calculated from Eqs (8.56) and (8.33) is equal to:

$$\mathrm{tr}\ A'_q = -\frac{2\alpha}{1+\alpha^2}\left(h_q + \frac{\sin^2\theta_q}{2}\right), \tag{8.82}$$

where:

$$h_q = \nu_0 + \omega - N_\perp + q^2. \tag{8.83}$$

The frequency ω'_q is given (to the first order in α) by Eq. (8.59), which in terms of h_q becomes:

$$\omega'^2_q = h_q\left(h_q + \sin^2\theta_q\right). \tag{8.84}$$

Finally, the term Z'_{q1} is similar to Eq. (8.76):

$$Z'_{q1} = \frac{\sin 2\theta_q}{4\left(1+\alpha^2\right)^{3/2}} \frac{\sin\theta_0\left[\omega\left(1+\alpha^2\right)+2h_q\right]}{(\omega/2)^2 - \omega'^2_q}. \tag{8.85}$$

When ω'_q is close to $\omega/2$, the multipliers $\mu'^{(1)}_\pm$ in Eq. (8.81) are both real, because $Z'_{q1} \gg 1$, and close to -1. The threshold for instability is reached when one of the multipliers becomes equal to -1. This yields the equation:

$$-\cos\frac{2\pi\omega'_q}{\omega} + \sqrt{Z'^2_{q1}-1}\sin\frac{2\pi\omega'_q}{\omega} = \exp\left(-\frac{\pi}{\omega}\mathrm{tr}\ A'_q\right). \tag{8.86}$$

The lowest instability threshold occurs when ω'_q is precisely equal to $\omega/2$ and Z'_{q1} diverges. By taking the limit $\omega'_q \to \omega/2$ in Eq. (8.86) and by further approximating both Z'_{q1} and the exponential term to the first order in α, one obtains the threshold condition:

$$\sin\theta_0 = \frac{\alpha\omega}{\sin\theta_q\cos\theta_q}\frac{h_q + \sin^2\theta_q/2}{h_q + \omega/2}. \tag{8.87}$$

Equation (8.87) describes the instability caused by spin-waves with given θ_q. The modes producing instability at the lowest radio-frequency power will be those for which the right-hand side of Eq. (8.87) is minimum. In the minimization, one must take into account that θ_q and h_q are not independent, because $\omega'^2_q = h_q(h_q + \sin^2\theta_q) = \omega^2/4$ (see Eq. (8.84)).

By using this equation to express $\sin\theta_q$ and $\cos\theta_q$ as a function of h_q, one transforms Eq. (8.87) into:

$$\sin\theta_0 = \frac{\alpha\omega\left(h_q^2+\omega^2/4\right)}{2\left(h_q+\omega/2\right)\sqrt{\left(\omega^2/4-h_q^2\right)\left(h_q^2+h_q-\omega^2/4\right)}}. \tag{8.88}$$

The interval in which Eq. (8.88) is applicable is $\left(\sqrt{1+\omega^2}-1\right)/2 < h_q < \omega/2$, corresponding to $1 > \sin\theta_q > 0$. Let us denote by $h_{\rm I}$ the value of h_q for which the right-hand side of Eq. (8.88) is minimum. The quantity $h_{\rm I}$ depends on ω only. For the case shown in Fig. 8.3, where $\omega = 0.8$, one finds $h_{\rm I} \simeq 0.274$. By inserting this value into the equation $h_{\rm I}(h_{\rm I}+\sin^2\theta_q) = \omega^2/4$ (see Eq. (8.84)) one finds that $\sin^2\theta_q \simeq 0.31$, that is, $\theta_q \simeq 34$ degrees, for the spin-waves producing instability. Let us denote by $\sin\theta_{\rm I}$ the value of $\sin\theta_0$ corresponding to $h_q = h_{\rm I}$. By inserting $h_{\rm I} \simeq 0.274$ into Eq. (8.88) one finds: $\sin\theta_{\rm I} \simeq 1.376\alpha\omega$. This condition can be realized by a variety of different experimental arrangements. In fact, by using Eq. (8.83) and Eq. (7.17) from Chapter 7 under the approximation $\cos\theta_0 \simeq 1$ (valid to the first order in α), one finds:

$$h_q = \mathrm{h}_{az} + q^2 + \kappa - N_z. \tag{8.89}$$

Therefore, the minimization procedure determines the sum $\mathrm{h}_{az} + q^2 = h_{\rm I} - \kappa + N_z$, which means that spin-waves with different values of q^2 will be responsible for the instability when the field h_{az} is varied. By inserting $\sin\theta_{\rm I}$ into Eqs (7.17)–(7.18) and by keeping only first-order terms in α, one obtains the following expression for the instability threshold in the $(\mathrm{h}_{az}, \mathrm{h}_{a\perp})$ plane:

$$\mathrm{h}_{a\perp} = -\sin\theta_{\rm I}\left(\mathrm{h}_{az} - \omega + \kappa_{\rm eff}\right), \tag{8.90}$$

valid in the interval $\mathrm{h}_{az} \leq h_{\rm I} - \kappa + N_z$. This prediction corresponds to the straight-line part of the line labeled by **I** in Fig. 8.4. The instability threshold deviates from this straight-line behavior when the field reaches the value $\mathrm{h}_{az} = h_{\rm I} - \kappa + N_z$. This is the field at which the spin-waves involved in the instability are those with $q^2 = 0$. For larger fields, the threshold is given by the expression:

$$\mathrm{h}_{a\perp} = -\sin\theta'_{\rm I}\left(\mathrm{h}_{az} - \omega + \kappa_{\rm eff}\right), \tag{8.91}$$

where $\sin\theta'_{\rm I}$ is obtained by taking $h_q = \mathrm{h}_{az} + \kappa - N_z$ instead of $h_q = h_{\rm I}$ in Eq. (8.88). Equation (8.91) is valid in the interval $h_{\rm I} - \kappa + N_z < \mathrm{h}_{az} <$

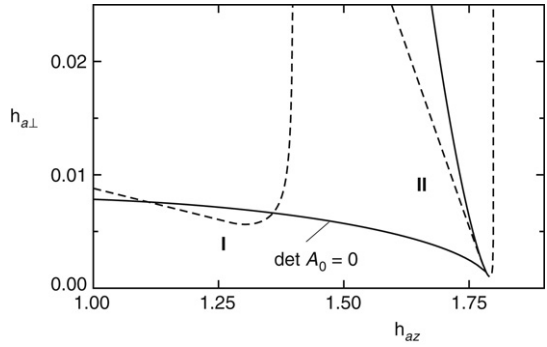

FIGURE 8.4 Suhl's instability thresholds in the (h_{az}, $h_{a\perp}$)-plane. Dashed line **I**: threshold for first-order Suhl's instability calculated analytically through Eqs (8.88), (8.90), and (8.91), as discussed in the text. Dashed line **II**: threshold for second-order Suhl's instability calculated analytically through Eqs (8.95), (8.98), and (8.99), as discussed in the text. Parameters: $\alpha = 0.01$, $\kappa_{\text{eff}} = -1$, $\omega = 0.8$. Continuous line is dynamical astroid boundary where saddle–node bifurcation occurs. Compare with Fig. 8.3.

$\omega/2 - \kappa + N_z$. The threshold diverges when h_{az} approaches the limit value $\omega/2 - \kappa + N_z$ (see Fig. 8.4).

Next, we shall discuss the second-order Suhl's instability, which is due to spin-waves for which $\omega_q^2 \simeq 0$ and $\theta_q \simeq 0$. This means that the parametric terms in Eq. (8.29) are small and one can apply the perturbative analysis presented in previous sections, which does not require moving to a different vector basis, as done for the analysis of the first-order instability. When $\omega_q^2 \simeq 0$, one is far from the parametric resonance conditions where Z_{q1} or Z_{q2} gives an important contribution to Eq. (8.74). Therefore, instability is basically governed by the zeroth-order characteristic multipliers given by Eq. (8.71). Under this approximation, the instability condition where one of the multipliers becomes equal to 1 in magnitude is $\det A_q = 0$, where $\det A_q$ is given by Eq. (8.62). By solving this equation with respect to $\sin\theta_0$, one finds:

$$\sin^2\theta_0 = \frac{\nu_q^2 + \alpha^2\omega^2}{\kappa_q\nu_q + \alpha^2\omega^2}, \tag{8.92}$$

where κ_q is given by Eq. (8.34). By minimizing this threshold with respect to ν_q under fixed θ_q, one finds that the minimum threshold is achieved for:

$$\nu_q = \kappa_q \left(\frac{\alpha^2\omega^2}{\kappa_q^2} + \frac{\alpha\omega}{|\kappa_q|}\sqrt{1 + \frac{\alpha^2\omega^2}{\kappa_q^2}} \right). \tag{8.93}$$

By inserting this result into Eq. (8.92), one finds that (to the first order in α) the minimum threshold corresponds to:

$$\sin^2\theta_0 = \frac{2\alpha\omega}{|\kappa_q|}. \tag{8.94}$$

Equation (8.94) gives the instability threshold due to spin-waves with given θ_q, under the assumption that θ_q is small for all the spin-waves of interest. The value of θ_q for the spin-waves that dominate the instability is obtained by minimizing the right-hand side of Eq. (8.94) with respect to θ_q in the neighborhood of $\theta_q = 0$. Equation (8.34) shows that $|\kappa_q|$ is maximum for $\theta_q = 0$ whenever $\kappa < 1$. Therefore, the minimum threshold occurs precisely for $\theta_q = 0$. This means that the correct expression for the threshold is obtained by taking $\theta_q = 0$ in Eq. (8.92). This yields:

$$\sin^2\theta_0 = \frac{(h_q - \omega)^2 + \alpha^2\omega^2}{(\kappa - 1)(h_q - \omega) + \alpha^2\omega^2}, \tag{8.95}$$

where h_q is given by Eq. (8.83). As a function of h_q, the right-hand side of Eq. (8.95) is minimum when $h_q = h_{\mathrm{II}}$, where:

$$h_{\mathrm{II}} = \omega - \frac{\alpha^2\omega^2}{1-\kappa} - \alpha\omega\sqrt{1 + \frac{\alpha^2\omega^2}{(1-\kappa)^2}}. \tag{8.96}$$

Let us denote by $\sin\theta_{\mathrm{II}}$ the value of $\sin\theta_0$ corresponding to $h_q = h_{\mathrm{II}}$. By inserting Eq. (8.96) into Eq. (8.95) and by keeping only first-order terms in α, one finds that:

$$\sin\theta_{\mathrm{II}} = \sqrt{\frac{2\alpha\omega}{1-\kappa}}. \tag{8.97}$$

Similarly to the first-order instability, this condition can be realized by a variety of different experimental arrangements. In fact, according to Eq. (8.89) the minimization determines the sum $\mathrm{h}_{az} + q^2 = h_{\mathrm{II}} - \kappa + N_z$, which means that spin-waves with different values of q^2 will be responsible for the instability when the field h_{az} is varied. By inserting $\sin\theta_{\mathrm{II}}$ in Eqs (7.17)–(7.18) and by keeping only first-order terms in α, one obtains the

following expression for the instability threshold in the $(\mathrm{h}_{az}, \mathrm{h}_{a\perp})$-plane:

$$\mathrm{h}_{a\perp} = \sin\theta_{\mathrm{II}} \sqrt{\left(\frac{\mathrm{h}_{az} - \omega}{\cos\theta_{\mathrm{II}}} + \kappa_{\mathrm{eff}}\right)^2 + \alpha^2\omega^2}, \tag{8.98}$$

valid in the interval $\mathrm{h}_{az} \leq h_{\mathrm{II}} - \kappa + N_z$. This prediction is shown in Fig. 8.4. The instability threshold deviates from this behavior when the field reaches the value $\mathrm{h}_{az} = h_{\mathrm{II}} - \kappa + N_z$. This is the field at which the spin-waves involved in the instability are those with $q^2 = 0$. For larger fields, the threshold is given by the expression:

$$\mathrm{h}_{a\perp} = \sin\theta'_{\mathrm{II}} \sqrt{\left(\frac{\mathrm{h}_{az} - \omega}{\cos\theta'_{\mathrm{II}}} + \kappa_{\mathrm{eff}}\right)^2 + \alpha^2\omega^2}, \tag{8.99}$$

where θ'_{II} is obtained by taking $h_q = \mathrm{h}_{az} + \kappa - N_z$ instead of $h_q = h_{\mathrm{II}}$ in Eq. (8.95). Equation (8.99) is valid in the interval $h_{\mathrm{II}} - \kappa + N_z < \mathrm{h}_{az} < \omega - \kappa + N_z$. The threshold diverges when h_{az} approaches the limit value $\omega - \kappa + N_z$ (see Fig. 8.4).

This analysis assumes that the second-order Suhl's instability is the only possible instability route for the **P**-mode under consideration. In practice, if other instability mechanisms are present, they need to be included in the analysis. For example, in Fig. 8.4 the large-h_{az} part of the second-order instability is actually not observable (compare with Fig. 8.3) because the **P**-mode is annihilated by the saddle–node bifurcation occurring at the astroid boundary before the spin-wave mechanism has the possibility of becoming active.

8.5 SPIN-WAVE PERTURBATIONS FOR ULTRA-THIN FILMS

The spin-wave analysis discussed in the previous sections cannot be immediately applied to the case of ultra-thin films because the basic simplifying hypothesis that boundary effects can be neglected is grossly inaccurate. In fact, one has to take into account the following two important effects when evaluating the effective field for ultra-thin ferromagnets: first, the contribution to the magnetostatic field due to the surface magnetic charges induced on the film surface; second, the effect of the finiteness of the film volume.

In this section, we discuss how the **P**-mode stability analysis is modified when one passes from an extended spheroidal particle to an ultra-thin disk whose thickness d is comparable with the exchange length.

In this case, it is appropriate to assume that the magnetization vector does not change appreciably across the film thickness. If the z axis is perpendicular to the film plane, then it can be assumed that the generic **P**-mode perturbation depends on x and y only, i.e., $\delta\mathbf{m}(\mathbf{r},t) = \delta\mathbf{m}(x,y,t)$. We shall also assume that the origin of the cartesian reference frame is in the middle plane of the film so that the disk is within the region $-d/2 \le z \le d/2$.

As was discussed at the beginning of this chapter, it is convenient to study the stability of **P**-modes by expressing the linearized equation for the perturbation in the vector basis $\mathbf{e}_1(t)$ and $\mathbf{e}_2(t)$, normal to the magnetization of the **P**-mode. This leads to the following equations:

$$\begin{aligned}\begin{pmatrix} 1 & \alpha \\ -\alpha & 1 \end{pmatrix} \frac{\partial}{\partial t} \begin{pmatrix} \delta m_1 \\ \delta m_2 \end{pmatrix} &= \begin{pmatrix} 0 & 1 \\ -1 & 0 \end{pmatrix} \begin{pmatrix} \delta \mathrm{h}_{M1} \\ \delta \mathrm{h}_{M2} \end{pmatrix} \\ &+ \begin{pmatrix} -\alpha\omega\cos\theta_0 & -\nu_0 + N_\perp + \nabla_\perp^2 \\ \nu_0 - N_\perp - \kappa\sin^2\theta_0 - \nabla_\perp^2 & -\alpha\omega\cos\theta_0 \end{pmatrix} \begin{pmatrix} \delta m_1 \\ \delta m_2 \end{pmatrix},\end{aligned} \tag{8.100}$$

where, as before, $\delta m_1 = \delta\mathbf{m}\cdot\mathbf{e}_1(t)$ and $\delta m_2 = \delta\mathbf{m}\cdot\mathbf{e}_2(t)$, while:

$$\nabla_\perp^2 = \frac{\partial^2}{\partial x^2} + \frac{\partial^2}{\partial y^2}, \tag{8.101}$$

the coordinates x and y being expressed in units of the exchange length l_{EX}. By integrating both sides of Eq. (8.100) with respect to z in the interval $[-d/2, d/2]$ and then dividing by d, one obtains the following equations:

$$\begin{aligned}\begin{pmatrix} 1 & \alpha \\ -\alpha & 1 \end{pmatrix} \frac{\partial}{\partial t} \begin{pmatrix} \delta m_1 \\ \delta m_2 \end{pmatrix} &= \begin{pmatrix} 0 & 1 \\ -1 & 0 \end{pmatrix} \begin{pmatrix} \langle \delta \mathrm{h}_{M1} \rangle \\ \langle \delta \mathrm{h}_{M2} \rangle \end{pmatrix} \\ &+ \begin{pmatrix} -\alpha\omega\cos\theta_0 & -\nu_0 + N_\perp + \nabla_\perp^2 \\ \nu_0 - N_\perp - \kappa\sin^2\theta_0 - \nabla_\perp^2 & -\alpha\omega\cos\theta_0 \end{pmatrix} \begin{pmatrix} \delta m_1 \\ \delta m_2 \end{pmatrix},\end{aligned} \tag{8.102}$$

where:

$$\langle \delta \mathrm{h}_{M\,1,2} \rangle = \frac{1}{d} \int_{-d/2}^{d/2} \delta \mathrm{h}_{M\,1,2}(x,y,z)\, \mathrm{d}z. \tag{8.103}$$

The important difference with respect to the treatment discussed in previous sections is the fact that the magnetostatic field components in

Eq. (8.102) are now averaged over the film thickness. We shall now derive analytical expressions for these components.

Consider as before a plane-wave perturbation:

$$\delta\mathbf{m}(x,y,t) = \mathbf{c}_q(t)\exp(\mathrm{i}\mathbf{q}\cdot\mathbf{r}), \tag{8.104}$$

where the wave-vector $\mathbf{q}$ is now constrained to the (x,y)-plane:

$$\mathbf{q}\cdot\mathbf{e}_z = 0. \tag{8.105}$$

where $\mathbf{e}_z$ is the unit vector along the z axis, which is the symmetry axis of the problem. We shall further assume that the wave-vector $\mathbf{q}$ is directed along $\mathbf{e}_x$: $\mathbf{q} = q\mathbf{e}_x$. This assumption does not limit the generality of the analysis and later it will be removed.

The magnetization perturbation $\delta\mathbf{m}$ results in two contributions to the magnetostatic field:

$$\delta\mathbf{h}_M = \delta\mathbf{h}_M^{\sigma} + \delta\mathbf{h}_M^{\rho}. \tag{8.106}$$

The component $\delta\mathbf{h}_M^{\sigma}$ is due to the magnetic charges at the film surface created by the normal component of magnetization, while $\delta\mathbf{h}_M^{\rho}$ is due to the volume charges created by magnetization nonuniformities inside the film volume. Only the latter was considered in the spin-wave analysis discussed in previous sections. In this section, the effect of surface charges will be taken into account for charges appearing at the top and bottom film surface, but not for those present on the lateral boundary of the disk. In this sense, the analysis is for a film of infinite extension in the (x,y)-plane.

To start the derivation of the expression for $\delta\mathbf{h}_M^{\sigma}$, consider a plane-wave of surface magnetic charges on the plane $z = 0$:

$$\sigma(x) = \sigma_0\exp(\mathrm{i}qx). \tag{8.107}$$

The magnetostatic field created by these charges in free space is given by the following expression:

$$\mathbf{h}_M^{\pm}(x,z) = \frac{\sigma_0}{2}\exp(\mathrm{i}qx - q|z|)\left(-\mathrm{i}\mathbf{e}_x \pm \mathbf{e}_z\right), \tag{8.108}$$

where the $\pm$ sign refers to positive and negative z, respectively.

The perturbation $\mathbf{c}_q(t)\exp(\mathrm{i}\mathbf{q}\cdot\mathbf{r})$ produces two surface charge distributions at the upper and lower film surface: $\sigma(x) = c_{qz}\exp(\mathrm{i}qx)$ at

$z = d/2$ and $\sigma(x) = -c_{qz} \exp(\mathrm{i}qx)$ at $z = -d/2$, where $c_{qz}(t) = \mathbf{e}_z \cdot \mathbf{c}_q(t)$. By using the superposition principle and Eq. (8.108), one arrives at the following expression for the magnetostatic field generated by surface magnetic charges in the region $-d/2 \le z \le d/2$, i.e., inside the film:

$$\delta\mathbf{h}_M^{\sigma}(x,z,t) = -c_{qz}(t) \exp(\mathrm{i}qx - qd/2) \left(\mathrm{i}\mathbf{e}_x \sinh qz + \mathbf{e}_z \cosh qz\right). \tag{8.109}$$

Now, we consider the magnetic field $\delta\mathbf{h}_M^{\rho}$ due to volume charges. The problem can be formulated in terms of a scalar magnetic potential:

$$\delta\mathbf{h}_M^{\rho} = -\nabla\psi_{\text{in}} \quad \text{for } |z| \le d/2, \tag{8.110}$$

$$\delta\mathbf{h}_M^{\rho} = -\nabla\psi_{\text{out}} \quad \text{for } |z| \ge d/2. \tag{8.111}$$

In terms of ψ, we have the following boundary value problem:

$$\nabla^2\psi_{\text{in}} = -\rho_M \quad \text{for } |z| \le d/2, \tag{8.112}$$

$$\nabla^2\psi_{\text{out}} = 0 \quad \text{for } |z| \ge d/2, \tag{8.113}$$

$$\psi_{\text{in}} = \psi_{\text{out}} \quad \text{for } z = \pm d/2, \tag{8.114}$$

$$\frac{\partial\psi_{\text{in}}}{\partial n} = \frac{\partial\psi_{\text{out}}}{\partial n} \quad \text{for } z = \pm d/2, \tag{8.115}$$

where n denotes the direction of the normal to the film surface, which coincides with $\mathbf{e}_z$ at $z = d/2$ and $-\mathbf{e}_z$ at $z = -d/2$, while ρ_M is the volume charge distribution inside the film. One has:

$$\rho_M = -\nabla \cdot [\mathbf{c}_q \exp(\mathrm{i}qx)] = -\mathrm{i}qc_{qx} \exp(\mathrm{i}qx), \tag{8.116}$$

where $c_{qx} = \mathbf{c}_q \cdot \mathbf{e}_x$.

The stated problem can be solved in two steps. First, we find a particular solution $\tilde{\psi}$ which satisfies Eqs (8.112)–(8.114) but has a discontinuity of the normal derivative at $z = \pm d/2$. Then we add to $\tilde{\psi}$ a continuous solution of the Laplace equation in the whole space which has a discontinuity of the normal derivative at $z = \pm d/2$ which exactly cancels out the discontinuity of $\tilde{\psi}$. The particular solution $\tilde{\psi}$ can be written as follows:

$$\tilde{\psi}_{\text{in}} = -\frac{\mathrm{i}}{q} c_{qx} \exp(\mathrm{i}qx) \quad \text{for } |z| \le d/2, \tag{8.117}$$

$$\tilde{\psi}_{\text{out}} = -\frac{\mathrm{i}}{q} c_{qx} \exp(\mathrm{i}qx) \exp\left[-q(|z| - d/2)\right] \quad \text{for } |z| \ge d/2. \tag{8.118}$$

This solution has a discontinuity of normal derivative:

$$\frac{\partial\tilde{\psi}_{\text{in}}}{\partial n} - \frac{\partial\tilde{\psi}_{\text{out}}}{\partial n} = -\mathrm{i}c_{qx}\exp(\mathrm{i}qx) = \tilde{\sigma}, \tag{8.119}$$

both at $z = d/2$ and $z = -d/2$. Thus, to find a solution which fulfills Eqs (8.112)–(8.115), we have to add to $\tilde{\psi}$ a harmonic potential generated by a surface charge opposite to that appearing in Eq. (8.119), i.e., $-\tilde{\sigma} = \mathrm{i}c_{qx}\exp(\mathrm{i}qx)$, distributed over the planes $z = \pm d/2$. By using again formula (8.108) and the superposition principle, we end up with the following expression of the "correction field" inside the film:

$$\delta\mathbf{h}_M^{\tilde{\sigma}} = c_{qx}\exp\left(\mathrm{i}qx - qd/2\right)\left(\mathbf{e}_x\cosh qz - \mathrm{i}\mathbf{e}_z\sinh qz\right). \tag{8.120}$$

The total magnetostatic field due to volume charges is:

$$\delta\mathbf{h}_M^{\rho} = -\nabla\tilde{\psi}_{\text{in}} + \delta\mathbf{h}_M^{\tilde{\sigma}}. \tag{8.121}$$

By using Eqs (8.120) and (8.117), one obtains:

$$\begin{aligned}\delta\mathbf{h}_M^{\rho}(x,z,t) = {} & c_{qx}(t)\exp(\mathrm{i}qx) \\ & \times\left[\left(\exp(-qd/2)\cosh qz - 1\right)\mathbf{e}_x - \mathrm{i}\exp(-qd/2)\sinh qz\,\mathbf{e}_z\right].\end{aligned} \tag{8.122}$$

Equations (8.106), (8.109), and (8.122) provide the desired expressions for the magnetostatic field $\delta\mathbf{h}_M$ caused in the film by the plane-wave perturbation. As previously discussed, we are interested in the average over the film thickness. One obtains:

$$\langle\delta\mathbf{h}_M\rangle = -\exp(\mathrm{i}qx)\left[\mathbf{e}_x c_{qx}(1-s_q) + \mathbf{e}_z c_{qz}s_q\right], \tag{8.123}$$

where:

$$s_q = \frac{1-\exp(-qd)}{qd} \tag{8.124}$$

plays the role of "shape" function for ultra-thin films. In the more general case when $\mathbf{q}$ is directed in an arbitrary direction in the (x,y)-plane,

formula Eq. (8.123) can be expressed as:

$$\langle \delta \mathbf{h}_M \rangle = -\left[\frac{\mathbf{q}}{q^2} \mathbf{q} \cdot \mathbf{c}_q(t)(1 - s_q) + \mathbf{e}_z (\mathbf{e}_z \cdot \mathbf{c}_q(t)) s_q \right] \times \exp(\mathrm{i}\mathbf{q} \cdot \mathbf{r}). \tag{8.125}$$

This expression should be compared with Eq. (8.25), valid for bulk systems. The latter is recovered from Eq. (8.125) in the limit $d \to \infty$, where $s_q \to 0$.

By projecting the averaged magnetostatic field $\langle \delta \mathbf{h}_M \rangle$ (Eq. (8.125)) along the unit vectors $\mathbf{e}_1(t)$ and $\mathbf{e}_2(t)$, one obtains the components $\langle \delta \mathrm{h}_{M1} \rangle$ and $\langle \delta \mathrm{h}_{M2} \rangle$ to be inserted into Eq. (8.102). By making this substitution and by carrying out algebraic transformations similar to the ones previously discussed for spin-waves in bulk systems, one arrives at the following equations for the spin-wave amplitude in ultra-thin films:

$$\frac{\mathrm{d}}{\mathrm{d}t} \begin{pmatrix} c_{q1} \\ c_{q2} \end{pmatrix} = A_q \begin{pmatrix} c_{q1} \\ c_{q2} \end{pmatrix} + R_2(t) \begin{pmatrix} c_{q1} \\ c_{q2} \end{pmatrix}, \tag{8.126}$$

where:

$$A_q = \frac{1}{1 + \alpha^2} \begin{pmatrix} 1 & -\alpha \\ \alpha & 1 \end{pmatrix} \begin{pmatrix} -\alpha\omega \cos\theta_0 & -\nu_q \\ \nu_q - \kappa_q \sin^2\theta_0 & -\alpha\omega \cos\theta_0 \end{pmatrix}, \tag{8.127}$$

$$R_2(t) = \frac{1 - s_q}{2\,(1 + \alpha^2)} \begin{pmatrix} 1 & -\alpha \\ \alpha & 1 \end{pmatrix} \begin{pmatrix} \cos\theta_0 \sin 2\omega t & \cos 2\omega t \\ \cos^2\theta_0 \cos 2\omega t & -\cos\theta_0 \sin 2\omega t \end{pmatrix}. \tag{8.128}$$

$$\nu_q = \nu_0 - N_\perp + q^2 + \frac{1}{2}(1 - s_q), \tag{8.129}$$

$$\kappa_q = \kappa - 1 + \frac{3}{2}(1 - s_q). \tag{8.130}$$

These expressions are structurally very similar to Eqs (8.29)–(8.34), derived for bulk systems. The main difference is that the parametric term proportional to $R_1(t)$ is absent from Eq. (8.126), in agreement with the fact that the angle θ_q between the wave-vector $\mathbf{q}$ and the symmetry axis is now $\theta_q = \pi/2$, i.e., $\sin 2\theta_q = 0$. On the other hand, the expressions (8.32)–(8.34) for $R_2(t)$, ν_q, and κ_q become identical to Eqs (8.128)–(8.130) under the substitution $\sin^2\theta_q \to 1 - s_q$. Due to these similarities, the mathematical techniques developed in the previous sections can be used for the study of spin-wave instabilities in ultra-thin films as well. In particular, perturbation techniques can prove effective since $s_q \to 1$ for $d \to 0$ and therefore the parameter $(1 - s_q)$ as well as the matrix $R_2(t)$ in Eq. (8.126) are all small quantities.

CHAPTER 9

Spin-Transfer-Driven Magnetization Dynamics

9.1 SPIN-TRANSFER MODIFICATION OF THE LLG EQUATION

Electrons exert a torque of quantum-mechanical origin when they flow across a ferromagnetic element. This torque is known as spin-transfer pseudo-torque. There is also the magnetic torque that any electric current traversing a ferromagnetic element generates because of the Oersted field produced by the current. When the current density is sufficiently large (of the order of $10^7 - 10^8 \mathrm{A\ cm^{-2}}$) and the ferromagnetic element is sufficiently small (lateral dimensions of the order of 100 nanometers), the spin transfer torque exceeds the Oersted-field torque and the wealth of spin-transfer-driven effects appears in the magnetization dynamics of the ferromagnetic element. The theoretical basis for the interpretation of these effects was laid down in the 1990's by the work of Berger and Slonczewski [68,622].

Spin-transfer effects are most often investigated in three-layer structures consisting of two ferromagnetic layers separated by a nonmagnetic metallic spacer (see Fig. 9.1). The observation and the interpretation of spin-transfer effects is greatly simplified when the magnetization in one of the magnetic layers is more or less independent of external actions due to large volume, large anisotropy, or pinning by additional underlayers. Then that layer, commonly known as the "fixed" or the "pinned" layer, simply acts as the reference polarizer for the electron spins. The second layer, termed the "free" layer, is the one where various dynamic phenomena occur. The trilayer structure is traversed by an electric current flowing in the direction normal to the plane of the layers. This configuration is called "current-perpendicular-to-plane" (CPP) geometry.

The spin-transfer interaction between the electric current and the magnetization can give rise to two main effects [651,758,635,444,59,101]: current-induced magnetization switching; coherent magnetization oscillations or spin-wave emission at microwave frequencies. These effects have potential applications in magnetic storage technology and spintronics, for

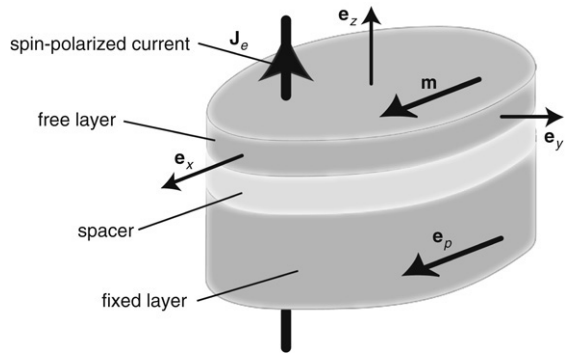

FIGURE 9.1 Schematic representation of the active region of a spin-torque device in the current-perpendicular-to-plane (CPP) configuration. The device consists of a three-layer ferromagnetic conductor-normal conductor-ferromagnetic conductor structure. The thicker layer ("fixed" layer) has a fixed magnetization along the direction $\mathbf{e}_p$. The dynamic phenomena of interest occur in the thinner layer ("free" layer). J_e is the spin-polarised current density.

novel types of current-controlled magnetic random access memory elements or current-controlled microwave oscillators that can be integrated with semiconductor electronics.

Various experimental arrangements have been developed to observe spin transfer effects. Point-contact setups were initially proposed, where a sharp tip is brought into electric contact with a layered structure consisting of a large number of alternating normal metal/ferromagnet sublayers [679–681]. The point-contact method has then evolved into the preparation of nanocontact areas on top of three-layer structures [500,558,378,462]. Finally, nanopatterning has been used to prepare so-called "nanopillar" devices [14,387,501,398,419], in which the device cross-section can be made non-circular in order to introduce in-plane shape anisotropy that leads to a better control of the orientation of the magnetization in the fixed layer and to more stable single-domain magnetization configurations in the free layer.

Current-induced switching of the magnetization has been observed in point-contact configurations [500] and later in nanopillar devices [14,501,297,15,691,418]. More challenging has been the search for current-induced excitation of magnetization oscillations at microwave frequencies. First results obtained for multilayers [680,681] were interpreted in terms of coherent magnon generation. Later studies on patterned nanocontacts [558] gave evidence of excitations whose

frequency could be a decreasing or increasing function of current, depending on field orientation. Similar results were obtained for nanopillar devices [398,399]. Direct monitoring of these excitations in time [419] permitted one to conclude that the excitations are associated with large-amplitude coherent precession of the magnetization in which spatial uniformity is by and large preserved in time. Great interest has been generated by the discovery that spin-transfer-driven magnetization oscillations in closely located nanocontacts may exhibit phase-locking effects, mediated by spin-waves or oscillating fields of magnetostatic origin [378,462,618], with consequent enhancement of the total generated microwave power. The phenomenology becomes even richer when ac currents and fields are applied in addition to dc currents and fields. Alternating currents can induce frequency modulation of the spin-transfer-driven magnetization oscillations [546] as well as resonance effects [688,579].

The magnetic volumes involved in spin-torque experiments are rather small, which means that thermal fluctuations can easily induce transitions from one dynamical regime to another. Such transitions and the associated random-telegraph signals have been experimentally observed [501,691, 418,246]. These effects can be described theoretically by adding (in analogy to what Brown proposed for the study of thermal switching in single-domain particles [135]) a random torque to the equation for the magnetization dynamics [445,448,24,711,103,598]. This leads to a Langevin-type stochastic differential equation for the magnetization and to a related Fokker–Planck equation for the magnetization probability distribution. On this basis, one can develop a thermal-activation-type approach, where the effective potential barrier controlling the transition between different dynamical regimes contains a nonequilibrium current-dependent part which cannot be expressed merely in terms of the system free energy [448,711,598]. These aspects will be discussed in more detail in Chapter 10.

The effect of spin transfer on magnetization dynamics can be studied (quite independently of the details of the microscopic mechanism responsible for it) by adding an appropriate spin-transfer term to the Landau–Lifshitz–Gilbert (LLG) equation for the free-layer magnetization. The first essential step, before proceeding to the detailed micromagnetic simulation of magnetization dynamics in complex spin-transfer devices, is to study the ideal case where the magnetization in the free layer is assumed to be spatially uniform [59,94,101].

In order to introduce a model equation for magnetization dynamics in the presence of spin-polarized currents, Slonczewski [622] considered a five-layer structure consisting of the trilayer structure shown in Fig. 9.1

with two additional paramagnetic conductors as contacts. The magnetic state of the ferromagnetic layers is described by the vectors $\mathbf{S}_1$ and $\mathbf{S}_2$, representing the global spin orientation per unit area in the fixed and free layers, respectively. The relation of these two vectors with the total angular momenta $\mathbf{L}_1$ and $\mathbf{L}_2$ in the two layers is: $\mathbf{L}_1 = \hbar \mathbf{S}_1 A_s$, $\mathbf{L}_2 = \hbar \mathbf{S}_2 A_s$, where $\hbar$ is the Planck constant and A_s is the cross-sectional area of the multilayer structure. By applying a semiclassical approach to the analysis of spin transfer between the two ferromagnetic layers, Slonczewski derived the following generalized LLG equation:

$$\frac{\mathrm{d}\mathbf{S}_2}{\mathrm{d}t} = \mathbf{s}_2 \times \left(\gamma \mathrm{H}_{AN} (\mathbf{e}_x \cdot \mathbf{S}_2) \mathbf{e}_x - \alpha \frac{\mathrm{d}\mathbf{S}_2}{\mathrm{d}t} - \frac{G J_e}{|e|} \mathbf{s}_1 \times \mathbf{s}_2 \right), \tag{9.1}$$

where $\mathbf{s}_1$ and $\mathbf{s}_2$ are the unit vectors respectively along $\mathbf{S}_1$ and $\mathbf{S}_2$, $\gamma = 2.2 \cdot 10^5\,\mathrm{mA^{-1}s^{-1}}$ is the absolute value of the gyromagnetic ratio, H_{AN} is the anisotropy field magnitude, $\mathbf{e}_x$ identifies the direction of in-plane anisotropy in the free layer, α is the Gilbert damping constant, e is the electron charge, and J_e is the electric current density, taken as positive when the electrons flow from the free into the fixed layer. The quantity G is given by the expression:

$$G = \left[-4 + (1+P)^3 \frac{(3 + \mathbf{s}_1 \cdot \mathbf{s}_2)}{4P^{3/2}} \right]^{-1}, \tag{9.2}$$

where P is the spin-polarizing factor of the incident current (see Ref. [622] for details). Typical values in ferromagnetic metals are $P \simeq 0.3 \div 0.4$.

Equation (9.1) refers to a free layer subject to anisotropy effects. The equation can be generalized to the case where the generic effective field $\mathbf{H}_{\text{eff}}$ acts on the system by observing that the anisotropy field involved in Eq. (9.1) is $\mathbf{H}_{AN} = -\mathrm{H}_{AN}(\mathbf{e}_x \cdot \mathbf{s}_2)\mathbf{e}_x$. The minus sign is due to the fact that the spin direction $\mathbf{s}_2$ is opposite to that of the magnetization. Thus, the correct way to generalize Eq. (9.1) is to replace $-\mathrm{H}_{AN}(\mathbf{e}_x \cdot \mathbf{s}_2)\mathbf{e}_x$ with $\mathbf{H}_{\text{eff}} = \mathbf{H}_a + \mathbf{H}_{AN} + \mathbf{H}_M$. This permits one to account for external fields and demagnetizing effects, the latter being particularly important for thin films. Next, Eq. (9.1) can be expressed in terms of the average magnetization $\mathbf{M}$ in the free layer by using the relation between $\mathbf{S}_2$ and $\mathbf{M}$. The total magnetic moment of the free layer is equal to $-\gamma\hbar\mathbf{S}_2 A_s/\mu_0$, whereas its volume is equal to $A_s d$, where d is the free-layer thickness. Therefore: $\mathbf{M} = -\gamma\hbar\mathbf{S}_2/\mu_0 d$. Finally, $\mathbf{s}_2 \equiv -\mathbf{m} = -\mathbf{M}/\mathrm{M}_s$, where $\mathbf{m}$ is the unit vector along $\mathbf{M}$ and M_s is the saturation magnetization. By using

these relations in Eq. (9.1), one arrives at the equation:

$$\frac{\mathrm{d}\mathbf{m}}{\mathrm{d}t} = -\gamma \mathrm{M}_s \mathbf{m} \times \left(\mathbf{h}_{\text{eff}} - \frac{\alpha}{\gamma \mathrm{M}_s} \frac{\mathrm{d}\mathbf{m}}{\mathrm{d}t} - \frac{J_e G}{J_p} \mathbf{e}_p \times \mathbf{m} \right), \tag{9.3}$$

where $\mathbf{h}_{\text{eff}} = \mathbf{H}_{\text{eff}}/\mathrm{M}_s$, $\mathbf{e}_p \equiv -\mathbf{s}_1$ identifies the magnetization direction in the fixed layer, and the current-density parameter J_p is equal to:

$$J_p = \mu_0 \mathrm{M}_s^2 \frac{|e| d}{\hbar}. \tag{9.4}$$

As an example, $J_p \simeq 1.1 \cdot 10^9\ \mathrm{A\ cm^{-2}}$ for a 3 nm thick layer of cobalt, for which $\mathrm{M}_s \simeq 1.4 \cdot 10^6\ \mathrm{A\ m^{-1}}$.

Similarly to what was done in previous chapters, it is natural to express time in units of $(\gamma \mathrm{M}_s)^{-1}$, i.e., $t \to \gamma \mathrm{M}_s t$. In colbalt, where $\mathrm{M}_s \simeq 1.4 \cdot 10^6\ \mathrm{A\ m^{-1}}$, one finds that $\gamma \mathrm{M}_s \simeq 3.1 \cdot 10^{11}\ \mathrm{s^{-1}}$, i.e., $(\gamma \mathrm{M}_s)^{-1} \simeq 3.2\ \mathrm{ps}$. In terms of this normalized time, Eq. (9.3) takes the dimensionless form:

$$\frac{\mathrm{d}\mathbf{m}}{\mathrm{d}t} - \alpha \mathbf{m} \times \frac{\mathrm{d}\mathbf{m}}{\mathrm{d}t} = -\mathbf{m} \times \mathbf{h}_{\text{eff}} + \beta \frac{\mathbf{m} \times (\mathbf{m} \times \mathbf{e}_p)}{1 + c_p \mathbf{m} \cdot \mathbf{e}_p}, \tag{9.5}$$

where Eq. (9.2) has been used to express the spin-torque effect in terms of the parameters:

$$\beta = b_p \frac{J_e}{J_p}, \tag{9.6}$$

$$b_p = \frac{4P^{3/2}}{3\left(1+P\right)^3 - 16P^{3/2}}, \tag{9.7}$$

$$c_p = \frac{\left(1+P\right)^3}{3\left(1+P\right)^3 - 16P^{3/2}}. \tag{9.8}$$

One finds that $1/3 \leq c_p < 1$ and $0 \leq b_p < 0.5$ when P is increased from 0 to 1. As an example, $c_p \simeq 0.55$ and $b_p \simeq 0.17$ for the typical value $P = 0.3$. One concludes from these estimates that in thin Co layers, where $J_p \approx 10^9\ \mathrm{A\ cm^{-2}}$, at most $\beta \approx 10^{-3}$–10^{-2} for the largest current densities $J_e \approx 10^7$–$10^8\ \mathrm{A\ cm^{-2}}$ reported in experiments. In subsequent extensions of the theory, where spin-diffusion effects are taken into account [624], the parameters b_p and c_p are controlled by two parameters instead of P only. In the case of a symmetric three-layer structure with identical ferromagnetic layers, c_p is directly related to the deviation of

the magnetoresistance of the device from a pure $(1+\cos\theta)$ law and may attain positive as well as negative values in the interval $-1 < c_p < 1$.

The effective field $\mathbf{h}_{\text{eff}}$ in Eq. (9.5) is the sum of the applied, demagnetizing, and anisotropy fields. We shall assume that the free layer can be approximately described as a flat ellipsoid, and that crystal anisotropy is uniaxial in character, with the anisotropy axis parallel to one of the principal axes of the ellipsoid. Identical assumptions were made in Chapters 3–5 for the general study of spatially uniform magnetization dynamics. Accordingly, the effective field $\mathbf{h}_{\text{eff}}$ and the normalized free energy g_L of the free layer can be expressed as (see Eqs (3.15) and (3.16)):

$$\begin{aligned}\mathbf{h}_{\text{eff}} &= \mathbf{h}_a - D\cdot\mathbf{m}\\ &= \mathbf{h}_a - D_x\mathrm{m}_x\mathbf{e}_x - D_y\mathrm{m}_y\mathbf{e}_y - D_z\mathrm{m}_z\mathbf{e}_z,\end{aligned} \tag{9.9}$$

$$g_L(\mathbf{m};\mathbf{h}_a) = \frac{1}{2}\left(D_x\mathrm{m}_x^2 + D_y\mathrm{m}_y^2 + D_z\mathrm{m}_z^2\right) - \mathbf{h}_a\cdot\mathbf{m}, \tag{9.10}$$

where D is the diagonal anisotropy tensor and $\mathbf{h}_a$ is the applied field.

Equation (9.5) describes the magnetization dynamics in the free layer under the assumption that this magnetization is spatially uniform. Given the submicrometer lateral dimensions of typical spin-transfer devices, this is a natural and useful starting point. However, nonuniformities might become important under certain conditions, for example in point-contact geometries where the spin-transfer-active region is a small part of a laterally unbounded medium. In such cases, one has to resort to the study of the complete space-dependent form of Eq. (9.5) [623,56, 351]. Appropriate numerical methods have been developed in order to carry out computer simulations of switching processes, magnetization oscillations, and thermal effects in nonuniformly magnetized devices [493, 444,76,77].

In the following sections, two cases of particular physical interest will be considered: (i) the applied field and the spin-polarization are both parallel to the free-layer easy axis, identified with the x axis: $\mathbf{h}_a = \mathrm{h}_{ax}\mathbf{e}_x$, $\mathbf{e}_p \equiv \mathbf{e}_x$, $D_x < D_y < D_z$; (ii) the entire problem exhibits uniaxial symmetry around the z axis: $\mathbf{h}_a = h_{az}\mathbf{e}_z$, $\mathbf{e}_p \equiv \mathbf{e}_z$, $D_x = D_y = D_\perp$. Indeed, these are the situations most often encountered in spin-transfer experiments. The physical reasons for the appearance of stationary and self-oscillation states as well as the associated phase diagrams will be discussed in the next sections for case (i), leaving to a final separate section the analysis of the consequences of symmetry for uniaxial systems.

9.2 STATIONARY STATES

The equation (9.5) governing the dynamics of the free-layer magnetic moment corresponds to a nonlinear dynamical system with state vector $\mathbf{m}(t)$, driven far from equilibrium by the action of the spin-polarized electron flow. We discussed in Chapter 3 that the natural tool for the study of this dynamics is nonlinear dynamical system theory on the unit sphere [529,428,358]. The dynamical-system perspective reveals certain physical aspects of the problem which are general and robust because they are topological in nature. In fact, when the external field $\mathbf{h}_a$ and the electric current, i.e., β, are constant in time, Eq. (9.5) describes an autonomous (i.e., time-invariant) system on the unit sphere. This immediately leads to certain conclusions concerning the admissible dynamical response to the field and current (see Section 3.2):

- chaos is precluded;
- the only possible steady states of magnetization dynamics are:
  - *stationary states* associated with static solutions (fixed points) of Eq. (9.5);
  - *self-oscillations* associated with periodic solutions (limit cycles) of Eq. (9.5).

The existence and stability of the stationary modes associated with the fixed points of the modified LLG equation (9.5) can be analyzed in sufficient detail [101,59]. When the external field and the spin-polarization vector are directed along the easy axis of the free layer (x axis), the fixed-point magnetization $\mathbf{m}_0$ is the solution of the equation obtained by imposing $\mathrm{d}\mathbf{m}/\mathrm{d}t = 0$ in Eq. (9.5). Let us write this equation in the form:

$$\frac{\mathrm{d}\mathbf{m}}{\mathrm{d}t} - \alpha\mathbf{m} \times \frac{\mathrm{d}\mathbf{m}}{\mathrm{d}t} = -\mathbf{m} \times \boldsymbol{\mathcal{H}}_{\text{eff}}, \tag{9.11}$$

where:

$$\boldsymbol{\mathcal{H}}_{\text{eff}} = \mathbf{h}_{\text{eff}} - \beta \frac{\mathbf{m} \times \mathbf{e}_p}{1 + c_p \mathbf{m} \cdot \mathbf{e}_p}. \tag{9.12}$$

Then, the equation for the fixed-point magnetization $\mathbf{m}_0$ is:

$$\boldsymbol{\mathcal{H}}_{\text{eff}} \times \mathbf{m}_0 = 0. \tag{9.13}$$

One can express Eq. (9.13) in the form (compare with Eq. (3.65)):

$$\mathbf{h}_{\text{eff}}\left(\mathbf{m}_0\right) - \beta \frac{\mathbf{m}_0 \times \mathbf{e}_p}{1 + c_p \mathbf{m}_0 \cdot \mathbf{e}_p} = \lambda \mathbf{m}_0, \tag{9.14}$$

where λ is an unknown parameter to be determined. By using Eq. (9.9) and by taking into account that $\mathbf{h}_a = \mathrm{h}_{ax}\mathbf{e}_x$, $\mathbf{e}_p \equiv \mathbf{e}_x$, Eq. (9.14) is reduced to the set of equations:

$$\left(\lambda + D_x\right) m_{0x} = \mathrm{h}_{ax}, \tag{9.15}$$

$$\left(\lambda + D_y\right) m_{0y} + \beta_x m_{0z} = 0, \tag{9.16}$$

$$\beta_x m_{0y} - \left(\lambda + D_z\right) m_{0z} = 0, \tag{9.17}$$

where:

$$\beta_x = \frac{\beta}{1 + c_p m_{0x}}. \tag{9.18}$$

Equations (9.15)–(9.17) consist of an equation for m_{0x} and a set of two coupled equations for (m_{0y}, m_{0z}). Therefore we can classify the fixed points as follows:

- Fixed points with $m_{0y} = m_{0z} = 0$
  There are two such fixed points:

  $$m_{0x} = \pm 1, \qquad m_{0y} = m_{0z} = 0. \tag{9.19}$$

  These two fixed points are always present and never destroyed whatever the field and current conditions. The corresponding values of λ and β_x are:

  $$\lambda = \lambda_{\pm} = -D_x \pm \mathrm{h}_{ax}, \qquad \beta_x = \beta_{\pm} = \frac{\beta}{1 \pm c_p}. \tag{9.20}$$

- Fixed points with $m_{0y} \neq 0$, $m_{0z} \neq 0$
  This solution is possible only if the determinant of Eqs (9.16)–(9.17) is equal to zero:

  $$\left(\lambda + D_y\right)\left(\lambda + D_z\right) + \beta_x^2 = 0. \tag{9.21}$$

This gives two solutions for λ:

$$\lambda = \lambda'_{\pm} = -\frac{D_z + D_y}{2} \pm \sqrt{\frac{(D_z - D_y)^2}{4} - \beta_x^2}. \tag{9.22}$$

Note that $-D_z \leq \lambda'_{\pm} \leq -D_y < -D_x$. The fixed points are obtained by inserting $\lambda'_{\pm}$ into Eq. (9.15):

$$\left(\lambda'_{\pm} + D_x\right) m_{0x} = \mathrm{h}_{ax}. \tag{9.23}$$

This is an equation for m_{0x}, in which $\lambda'_{\pm}$ depends on m_{0x} through β_x. By rearranging terms, squaring, and taking into account that $\lambda'_{\pm} + D_x < 0$, one obtains:

$$\left(\frac{\mathrm{h}_{ax}}{m_{0x}} + D_z - D_x\right)\left(\frac{\mathrm{h}_{ax}}{m_{0x}} + D_y - D_x\right) + \beta_x^2 = 0. \tag{9.24}$$

To the first order in β, this equation can be solved by taking $\beta_x^2 = 0$. This is an acceptable approximation whenever $\beta_x^2 \ll (D_z - D_y)^2/4 - D_x^2$. This requirement is usually satisfied in spin-transfer experiments, where $\beta \ll 1$ (current limit), $D_z \approx 1$ (thin-film geometry), and $c_p \approx 0.5$ (level of spin polarization). Equation (9.24) gives two solutions for m_{0x}. Each of these solutions gives two fixed points with opposite values of m_{0y} and m_{0z}, obtained by imposing $m_{0y}^2 + m_{0z}^2 = 1 - m_{0x}^2$ and by using Eq. (9.16) or Eq. (9.17). The result is the following two pairs of fixed points:

– Fixed points which coincide with g_L maxima when $\beta = 0$.

$$m_{0x} = -\frac{\mathrm{h}_{ax}}{D_z - D_x}, \tag{9.25}$$

$$\lambda = \lambda'_-, \qquad \beta_x = \beta'_- = \frac{\beta}{1 - c_p \mathrm{h}_{ax}/(D_z - D_x)}, \tag{9.26}$$

$$m_{0y} = \mp\beta'_- \sqrt{\frac{1 - m_{0x}^2}{\left(\lambda'_- + D_y\right)^2 + \beta'^2_-}}, \tag{9.27}$$

$$m_{0z} = \pm\left(\lambda'_- + D_y\right) \sqrt{\frac{1 - m_{0x}^2}{\left(\lambda'_- + D_y\right)^2 + \beta'^2_-}}. \tag{9.28}$$

These fixed points exist only in the field interval $|\mathrm{h}_{ax}| \leq (D_z - D_x)$. This condition is found by imposing $m_{0x}^2 \leq 1$ in Eq. (9.25).

– Fixed points which coincide with g_L saddles when $\beta = 0$.

$$m_{0x} = -\frac{\mathrm{h}_{ax}}{D_y - D_x}, \tag{9.29}$$

$$\lambda = \lambda'_+, \qquad \beta_x = \beta'_+ = \frac{\beta}{1 - c_p \mathrm{h}_{ax}/\left(D_y - D_x\right)}, \tag{9.30}$$

$$m_{0y} = \pm\left(\lambda'_+ + D_z\right)\sqrt{\frac{1 - m_{0x}^2}{\left(\lambda'_+ + D_z\right)^2 + \beta'^2_+}}, \tag{9.31}$$

$$m_{0z} = \pm\beta'_+\sqrt{\frac{1 - m_{0x}^2}{\left(\lambda'_+ + D_z\right)^2 + \beta'^2_+}}. \tag{9.32}$$

These fixed points exist only in the field interval $|\mathrm{h}_{ax}| \leq (D_y - D_x)$.

In conclusion, the number of fixed points is as follows:

- 6 fixed points for $|\mathrm{h}_{ax}| < D_y - D_x$;
- 4 fixed points for $D_y - D_x < |\mathrm{h}_{ax}| < D_z - D_x$;
- 2 fixed points for $|\mathrm{h}_{ax}| > D_z - D_x$.

This result coincides with the one previously found for the magnetization dynamics in the absence of spin transfer (see Section 3.4). Thus, to the first order in β the spin-polarized current has no influence on the number of fixed points. However, the current does affect fixed-point stability, as will be discussed in subsequent sections in connection with dynamic stability diagrams.

9.3 SELF-OSCILLATIONS

Periodic solutions of Eq. (9.5) represent limit cycles, i.e., self-oscillations of the magnetization. The study of these self-oscillations can be carried out by the Poincaré–Melnikov method discussed in Section 5.5. Indeed, as previously mentioned, both the damping constant α and the parameter β measuring the intensity of the spin transfer effect are small quantities of the order of 10^{-2} or less, which are precisely the conditions under which the Poincaré–Melnikov method can be applied. The first step in this direction is to bring Eq. (9.5) to the form (5.108). By writing Eq. (9.5) in the form (9.11), then transforming this equation to LL form, and finally keeping only first-order terms in α and β, we obtain:

$$\frac{\mathrm{d}\mathbf{m}}{\mathrm{d}t} = -\mathbf{m} \times \mathbf{h}_{\text{eff}} + \alpha\mathbf{m} \times \left(\mathbf{m} \times \frac{\partial \Phi}{\partial \mathbf{m}}\right), \tag{9.33}$$

where:

$$\Phi = g_L + \frac{\beta}{\alpha}\frac{\ln(1 + c_p \mathbf{m}\cdot\mathbf{e}_p)}{c_p}. \tag{9.34}$$

By comparing this equation with the definition (5.109) for Φ, we see that the potential Ψ describing spin-transfer effects is:

$$\Psi = \beta\frac{\ln(1 + c_p \mathbf{m}\cdot\mathbf{e}_p)}{c_p}. \tag{9.35}$$

The energy balance equation for Eq. (9.33) was derived in Section 3.2 (Eq. (3.62)). In terms of Ψ, we have:

$$\frac{\mathrm{d}g_L}{\mathrm{d}t} = -\alpha\left|\mathbf{m}\times\mathbf{h}_{\text{eff}}\right|^2 - \left(\mathbf{m}\times\frac{\partial\Psi}{\partial\mathbf{m}}\right)\cdot\frac{\mathrm{d}\mathbf{m}}{\mathrm{d}t} + \frac{\partial g_L}{\partial t}. \tag{9.36}$$

In the case where the applied field and the injected current are constant in time, neither g_L nor Ψ are explicitly dependent on time and Eq. (9.36) can be expressed in terms of a power function as in Eq. (5.110):

$$\frac{\mathrm{d}g_L}{\mathrm{d}t} = -\alpha\mathcal{P}(\mathbf{m}, \beta/\alpha), \tag{9.37}$$

where β/α plays the role of control parameter for the spin-transfer effect. By using Eqs (9.35)–(9.36) and also the fact that to the first order in α one can change $|\mathbf{m}\times\mathbf{h}_{\text{eff}}|^2$ into $|\mathrm{d}\mathbf{m}/\mathrm{d}t|^2$, we can write the power function in a form that will prove particularly useful for subsequent developments:

$$\mathcal{P}(\mathbf{m}, \beta/\alpha) = \left|\frac{\mathrm{d}\mathbf{m}}{\mathrm{d}t}\right|^2 + \frac{\beta}{\alpha}\frac{\mathbf{m}\times\mathbf{e}_p}{1 + c_p\mathbf{m}\cdot\mathbf{e}_p}\cdot\frac{\mathrm{d}\mathbf{m}}{\mathrm{d}t}. \tag{9.38}$$

Equations (9.37) and (9.38) show that when the spin-polarized current is injected into the free layer (i.e., $\beta \neq 0$), situations where the energy transferred to the system via spin-transfer counterbalances the energy dissipation via intrinsic damping become possible. When this occurs, the system reaches a periodic steady-state regime resulting in steady-state self-oscillations. As discussed in Chapter 5, predictions about these self-oscillations are obtained from the Melnikov function (5.146), i.e.:

$$M\left(g_0, \beta/\alpha\right) = \int_0^{T(g_0)} \mathcal{P}(\mathbf{m}_c(t; g_0), \beta/\alpha)\mathrm{d}t, \tag{9.39}$$

where $\mathcal{P}(\mathbf{m}, \beta/\alpha)$ is given by Eq. (9.38), while $\mathbf{m}_c(t; g_0)$ represents the solution with energy g_0 of the unperturbed precessional dynamics corresponding to $\alpha = \beta = 0$. As discussed in Chapter 5, the importance of the Melnikov function is in the following fundamental property:

- In the limit $\alpha \ll 1, \beta \ll 1, \beta/\alpha \sim 1$, there exist as many limit cycles in the spin-transfer-driven dynamics as there are energy zeros g_{lc} of the Melnikov function: $M(g_{lc}, \beta/\alpha) = 0$. Then, in the limit $\alpha \to 0$ the limit cycle trajectory corresponding to g_{lc} coincides with the trajectory $\mathbf{m}_c(t; g_{lc})$ of the precessional dynamics. In addition, the limit cycle is stable if $\partial M/\partial g_0|_{g_0=g_{lc}} > 0$ and unstable if $\partial M/\partial g_0|_{g_0=g_{lc}} < 0$.

Each of the stable limit cycles thus predicted represents steady-state self-oscillations of the magnetization, which in principle should be experimentally observable under appropriate conditions.

These results make clear that detailed knowledge of the unperturbed precessional dynamics is necessary in order to make predictions about self-oscillations. Accurate information about this dynamics has been obtained in Chapter 4. In particular, explicit analytical expressions for the magnetization trajectories when the external field is directed along the easy axis of the free layer have been derived in Section 4.4. The corresponding phase portrait is divided by heteroclinic or homoclinic trajectories into several central energy regions (see Figs 4.5 and 4.10), and the solutions $\mathbf{m}_c(t; g_0)$ have different properties depending on the region to which they belong. As discussed in Chapter 5, a different Melnikov function is associated with each of these energy regions, and a careful study of the properties of all these Melnikov function branches is necessary in order to get a comprehensive grasp of the conditions for the appearance of self-oscillations.

We shall now compute these Melnikov function branches in detail. We start from the following expression obtained by substituting Eq. (9.38) into Eq. (9.39):

$$M\left(g_0, \beta/\alpha\right) = \int_0^{T(g_0)} \left[\left| \frac{\mathrm{d}\mathbf{m}}{\mathrm{d}t} \right|^2 + \frac{\beta}{\alpha} \frac{\mathbf{m} \times \mathbf{e}_p}{1 + c_p \mathbf{m} \cdot \mathbf{e}_p} \cdot \frac{\mathrm{d}\mathbf{m}}{\mathrm{d}t} \right]_{\mathbf{m}_c(t; g_0)} \mathrm{d}t, \tag{9.40}$$

where the subscript indicates that the integrand must be evaluated along the precessional trajectory $\mathbf{m}_c(t; g_0)$. The Melnikov function can be computed by reducing it to integrals with respect to the variable w

introduced in Eqs (4.79) and (4.80). Let us first compute the term $|\mathrm{d}\mathbf{m}/\mathrm{d}t|^2$ in Eq. (9.40). By using the identity $|\mathrm{d}\mathbf{m}/\mathrm{d}t|^2 = |\mathrm{d}\mathbf{m}/\mathrm{d}w|^2|\mathrm{d}w/\mathrm{d}t|^2$, we derive from Eq. (4.80):

$$\left|\frac{\mathrm{d}\mathbf{m}}{\mathrm{d}w}\right|^2 = \frac{p^2}{k^2}\left[\frac{1}{1-w^2} + \frac{k'^2 r^2}{(w-w_-)(w-w_+)}\right], \tag{9.41}$$

where $r = (w_+ - w_-)/2$. The term $\mathrm{d}w/\mathrm{d}t$ can be obtained from Eq. (4.82) from Chapter 4:

$$\frac{\mathrm{d}w}{\mathrm{d}t} = \pm k' p\,(D_z - D_x)\sqrt{(1-w^2)(w-w_-)(w-w_+)}. \tag{9.42}$$

Therefore:

$$\left|\frac{\mathrm{d}\mathbf{m}}{\mathrm{d}t}\right|^2 \mathrm{d}t = \frac{k' p^3}{k^2}(D_z - D_x)\left[\sqrt{\frac{(w-w_-)(w-w_+)}{1-w^2}} + k'^2 r^2 \sqrt{\frac{1-w^2}{(w-w_-)(w-w_+)}}\right]\mathrm{d}w. \tag{9.43}$$

For the spin-transfer term, we have:

$$\frac{\mathbf{m}\times\mathbf{e}_p}{1+c_p\mathbf{m}\cdot\mathbf{e}_p}\cdot\frac{\mathrm{d}\mathbf{m}}{\mathrm{d}t} = \frac{1}{1+c_p\mathrm{m}_x}\left(\mathrm{m}_z\frac{\mathrm{d}\mathrm{m}_y}{\mathrm{d}w} - \mathrm{m}_y\frac{\mathrm{d}\mathrm{m}_z}{\mathrm{d}w}\right)\frac{\mathrm{d}w}{\mathrm{d}t}. \tag{9.44}$$

By using Eqs (4.80) and (9.42), we find:

$$\frac{\mathbf{m}\times\mathbf{e}_p}{1+c_p\mathbf{m}\cdot\mathbf{e}_p}\cdot\frac{\mathrm{d}\mathbf{m}}{\mathrm{d}t}\mathrm{d}t = -\frac{k' p^2}{k^2(1+c_p a_x)}\left[\frac{w}{wd+1}\sqrt{\frac{(w-w_-)(w-w_+)}{1-w^2}} + \frac{w-b}{wd+1}\sqrt{\frac{1-w^2}{(w-w_-)(w-w_+)}}\right]\mathrm{d}w, \tag{9.45}$$

where $b = (w_+ + w_-)/2$, $d = c_p\,p/(1+c_p\,a_x)$, and signs have been adjusted by taking into account that $\mathrm{m}_z\mathrm{d}\mathrm{m}_y/\mathrm{d}t \propto -w$ and $\mathrm{m}_y\,\mathrm{d}\mathrm{m}_z/\mathrm{d}t \propto w - b$. By using Eqs (9.43) and (9.45) in Eq. (9.40) one arrives at the following

Melnikov function expression:

$$M(g_0, \beta/\alpha) = \frac{n_w k' p^2}{k^2}\left[p(D_z - D_x)\left(I_1 + k'^2 r^2 I_2\right) - \frac{\beta}{\alpha}\frac{1}{1 + c_p a_x}(J_1 + J_2)\right], \tag{9.46}$$

where n_w is the number of times that w sweeps its interval of variation during one period of the conservative motion, while I_1, I_2, J_1, and J_2 represent the following elliptic-type integrals:

$$I_1 = \int_{w_1}^{w_2} \sqrt{\frac{(w - w_-)(w - w_+)}{1 - w^2}}\, \mathrm{d}w, \tag{9.47}$$

$$I_2 = \int_{w_1}^{w_2} \sqrt{\frac{1 - w^2}{(w - w_-)(w - w_+)}}\, \mathrm{d}w, \tag{9.48}$$

$$J_1 = \int_{w_1}^{w_2} \frac{w}{wd + 1}\sqrt{\frac{(w - w_-)(w - w_+)}{1 - w^2}}\, \mathrm{d}w, \tag{9.49}$$

$$J_2 = \int_{w_1}^{w_2} \frac{w - b}{wd + 1}\sqrt{\frac{1 - w^2}{(w - w_-)(w - w_+)}}\, \mathrm{d}w. \tag{9.50}$$

The limits of integration w_1 and w_2 depend on the energy of the system and the value of the external field. The limits of integration and the values of n_w associated with the various central regions of the phase portrait are specified as follows:

- Region L_- : $w_1 = -1, w_2 = w_-, n_w = 4$.
- Region L_+ : $w_1 = w_+, w_2 = 1, n_w = 4$.
- Region H : $w_1 = -1, w_2 = 1, n_w = 2$.

There will be one Melnikov function for each of these regions, provided the region exists under the field conditions of interest.

9.4 PHASE PORTRAITS AND BIFURCATIONS

Based on the discussion presented in the previous sections, we shall now determine the stable stationary states as well as the steady-state self-oscillations present in a spin-transfer device subject to the external field h_{ax} along the free-layer easy axis and the spin-polarized current density J_e. The parameter β/α will be used to represent the current density.

For each point in the $(\mathrm{h}_{ax}, \beta/\alpha)$ control plane, we shall determine the corresponding phase portrait for the magnetization dynamics and follow the evolution of this portrait as the field or the current is varied. When a small change in the control parameters induces correspondingly small, continuous modifications in the phase portrait, the portrait is said to be structurally stable. However, there exist bifurcation conditions where the control-parameter change leads to qualitative changes in the phase portrait, namely changes in the number and stability of fixed points and limit cycles. These bifurcation conditions result in bifurcation lines in the $(\mathrm{h}_{ax}, \beta/\alpha)$-plane. The knowledge of the location and nature of these lines is essential for the interpretation of spin-transfer experiments. The final result of this study will be the theoretical stability diagram shown in Figs 9.3 and 9.4.

It has been previously mentioned that an essential role in the analysis of spin-transfer-driven magnetization dynamics is played by the fact that α and β are small quantities, of the order of 10^{-2} or less. This fact implies that the phase portraits of the dynamics can be viewed as perturbations of the corresponding conservative phase portraits obtained for the same value of the field and $\alpha = \beta = 0$. Therefore, one expects that the classification of conservative phase portraits discussed in Chapter 4 can be instrumental in the description of spin-transfer effects as well. In order to demonstrate how this can be accomplished, let us first recall that all the essential information about a generic conservative portrait can be coded by listing the number of saddles, central regions, and fixed points present in this portrait. The phase portraits of interest here are those that correspond to the field aligned along the easy axis of the free layer, i.e., the x axis. These portraits have been extensively analyzed in Chapter 4. According to Figs 4.5 and 4.10, there are three distinct phase portraits for this field direction:

- Phase portrait $\{d^2(u)^2(s_-)(s_+)\}$
  This is the portrait existing for $|a_x| \leq k'^2$, i.e., $|\mathrm{h}_{ax}| \leq D_y - D_x$, namely, when both regions L_- and L_+ are present. The symbol d^2 represents the two saddles connected by heteroclinic trajectories; $(u)^2$ represents region H, made up of two symmetric regions containing the two energy maxima u; (s_-) represents region L_- containing the energy minimum at $\mathrm{m}_x = -1$, indicated as s_-; (s_+) represents region L_+ containing the energy minimum at $\mathrm{m}_x = 1$, indicated as s_+.
- Phase portraits $\{d_-(u)^2, (s_+)\}$ for $\mathrm{h}_{ax} > 0$; $\{d_+(u)^2, (s_-)\}$ for $\mathrm{h}_{ax} < 0$
  These are the phase portraits existing for $k'^2 \leq |a_x| \leq 1$, i.e., $D_y - D_x \leq |\mathrm{h}_{ax}| \leq D_z - D_x$. One of the low-energy regions, e.g., region L_- under positive field, has disappeared. The symbol d_- (d_+) expresses the fact that the fixed point $\mathrm{m}_x = -1$ ($\mathrm{m}_x = 1$) is now a saddle.

- Phase portrait $\{(u_- s_+)\}$
  This phase portrait is realized for $|a_x| \geq 1$, i.e., $|\mathrm{h}_{ax}| \geq D_z - D_x$. Region H has also disappeared and only two energy extrema at $\mathrm{m}_x = \pm 1$ are present.

One can create a direct correspondence between these conservative phase portraits and the spin-torque portraits for the same field value and $\alpha \neq 0$, $\beta \neq 0$, by using the following facts:

- The fact that $\alpha \neq 0$, $\beta \neq 0$ has no effect on the number of fixed points, because the equations for the fixed points of the dynamics do not contain α and the number of fixed points is independent of β to the first order in β. In addition, the states $\mathrm{m}_x = \pm 1$ are always fixed points for any field and current conditions, so the "$\pm$" subscripts used in the coding of conservative portraits retain the same meaning for spin-transfer phase portraits as well.
- The fact that $\alpha \neq 0$, $\beta \neq 0$ has a negligible effect on the partition of the phase portraits into energy regions. The effect of α and β is to break the heteroclinic or homoclinic connections present in the conservative dynamics. However, since α and β are small quantities, the ensuing distortions in the phase portrait structure are small as well and do not substantially alter the pattern of energy regions characterizing the conservative dynamics.

Therefore, given a certain zero-current portrait, for instance $\{d_-(u)^2, (s_+)\}$, a string with identical structure, i.e., $\{d_-(\ldots)^2, (\ldots)\}$, will represent the portraits under nonzero spin-polarized current and the same field. The dot placeholders express the fact that, although the spin-polarized current has no effect on the number of fixed points and energy regions, it may affect the stability of the fixed points and lead to the appearance of one or more limit cycles inside some of the energy regions. Thus, the portrait $\{d_-(u)^2, (s_+)\}$ may be transformed by the spin-polarized current into a portrait of the type $\{d_-(u)^2, (ars_+)\}$, or $\{d_-(u)^2, (au_+)\}$, or $\{d_-(au)^2, (rs_+)\}$, and so on, where, as before, we have used the symbols a and r to denote stable (i.e., attractive) and unstable (i.e., repulsive) limit cycles, respectively. These possibilities are illustrated in Fig. 9.2 by using the unit-disk representation.

The notations just introduced are purely formal, in the sense that they give no indications which of the admissible possibilities will be actually realized in a spin-transfer experiment. Some preliminary heuristic considerations may be helpful before addressing this problem in detailed analytical terms. We already know that when no current is injected ($\beta = 0$)

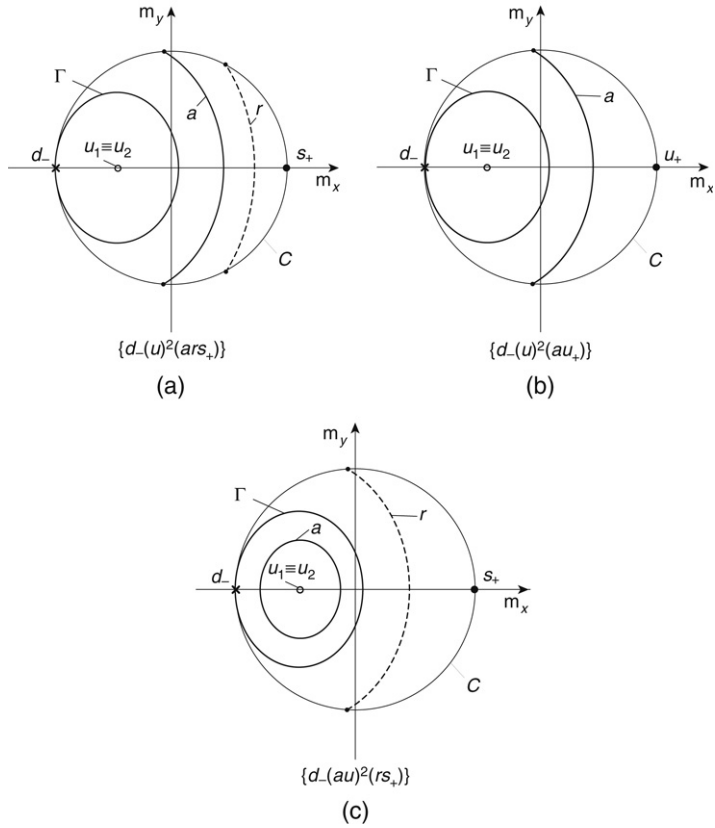

FIGURE 9.2 Unit-disk representation of phase portraits for spin-torque-driven magnetization dynamics, with examples of limit cycles present in one or more energy regions as a result of the injection of the spin-polarized current. (a) $\mathbf{P}/\mathbf{O}_+$-type portrait; (b) $\mathbf{O}_+$-type portrait; (c) $\mathbf{P}/\mathbf{O}^2$-type portrait. The string notation and the bold symbols are defined in the text.

the presence of intrinsic damping ($\alpha \neq 0$) forces the energy to decrease for any magnetization motion. The closed orbits of the conservative dynamics are transformed into closely spiraling trajectories approaching one of the energy minima at $\mathrm{m}_x = 1$ or $\mathrm{m}_x = -1$. These are the only observable magnetization modes under zero current; no self-oscillations are possible. However, the situation is significantly altered when the spin-polarized current is injected ($\beta \neq 0$). Indeed, consider a magnetization motion close to $\mathrm{m}_x = 1$. Due to the smallness of α and β, the motion over time

intervals of the order of one precession period is nearly coincident with one of the constant-energy orbits of the conservative dynamics. Along this orbit $\mathbf{m} \times \mathbf{e}_p$ is approximately opposite to $\mathrm{d}\mathbf{m}/\mathrm{d}t$. By using this fact in Eqs (9.37) and (9.38), one concludes that $\mathrm{d}g_L/\mathrm{d}t \simeq (K\beta - \alpha)|\mathrm{d}\mathbf{m}/\mathrm{d}t|^2$, where K is some positive constant. Thus, $\mathrm{d}g_L/\mathrm{d}t > 0$ when $\beta/\alpha \gtrsim 1/K$, which means that the magnetization will start to move along a trajectory of increasing energy, i.e., away from the energy minimum at $\mathrm{m}_x = 1$. The conclusion of this analysis is that the state $\mathrm{m}_x = 1$ can be made unstable by a sufficiently strong positive current. This instability mechanism is known as a Hopf bifurcation. Hopf bifurcations have the remarkable property that they are always accompanied by the appearance or disappearance of a limit cycle, i.e., of persistent self-oscillations. Thus, magnetization self-oscillations must appear in the free layer if the spin-polarized current is made sufficiently large.

This discussion is suggestive of the astonishingly rich dynamical structure that emerges once the problem is studied by rigorous analytical tools, namely, by investigating the various bifurcation mechanisms [741, 358,428,529] expected in the free-layer magnetization dynamics.

The classification of spin-transfer phase portraits previously introduced is based on the knowledge of the number of fixed points present in the dynamics for any value of the field. According to the analysis carried out in Section 9.2, this number changes from 6 to 4 or vice versa for $|\mathrm{h}_{ax}| = D_y - D_x$, and from 4 to 2 or vice versa for $|\mathrm{h}_{ax}| = D_z - D_x$. The corresponding bifurcations are symmetric saddle–node bifurcations known as pitchfork bifurcations. It has been shown in Section 9.2 that to the first-order in β this conclusion is valid with no modification under the presence of nonzero spin-polarized current. This means that pitchfork bifurcations will be described by vertical lines in the $(\mathrm{h}_{ax}, \beta/\alpha)$ control plane, located at $\mathrm{h}_{ax} = \pm(D_y - D_x)$ and $\mathrm{h}_{ax} = \pm(D_z - D_x)$.

A more complex analysis is needed to study the modifications in the stability of nonsaddle fixed points caused by Hopf bifurcation mechanisms. When $\beta = 0$, g_L minima are stable foci and g_L maxima are unstable foci of the magnetization dynamics. However, as suggested by the previous discussion, this situation can be substantially altered by the spin-polarized current injection, with the appearance of Hopf bifurcations where a focus changes from stable to unstable or vice versa with the simultaneous creation or annihilation of a limit cycle [358]. Hopf bifurcations can be studied by linearizing the LLG equation, Eq. (9.5), around the fixed point of interest and by determining the conditions under which the trace of the stability matrix controlling the dynamics of the linear perturbation is equal to zero. To this end, let us consider one of the fixed-point solutions $\mathbf{m}_0$ of Eq. (9.14), and let us introduce the perturbed

magnetization $\mathbf{m}(t) = \mathbf{m}_0 + \delta\mathbf{m}(t)$. The perturbation must be such that $\mathbf{m}_0 \cdot \delta\mathbf{m} = 0$, because the magnetization magnitude must be preserved. By inserting $\mathbf{m}(t)$ in Eq. (9.5), one obtains the following linearized LLG equation for $\delta\mathbf{m}$:

$$\frac{\mathrm{d}\delta\mathbf{m}}{\mathrm{d}t} - \alpha\mathbf{m}_0 \times \frac{\mathrm{d}\delta\mathbf{m}}{\mathrm{d}t} = \mathbf{m}_0 \times \Bigg[\lambda\delta\mathbf{m} + D \cdot \delta\mathbf{m} + \beta_x \left(\delta\mathbf{m} \times \mathbf{e}_x - c_p \frac{\mathbf{m}_0 \times \mathbf{e}_x}{1 + c_p m_{0x}} \delta\mathbf{m} \cdot \mathbf{e}_x\right)\Bigg], \tag{9.51}$$

where λ and β_x are defined by Eqs (9.14) and (9.18), respectively. The stability analysis is conveniently carried out by introducing the vector basis $(\mathbf{e}_1, \mathbf{e}_2, \mathbf{m}_0)$, where $\mathbf{m}_0$ is the fixed point under consideration whereas $(\mathbf{e}_1, \mathbf{e}_2)$ identify the plane perpendicular to $\mathbf{m}_0$ (see Eqs (7.36) and (7.37)). Indeed, the perturbation $\delta\mathbf{m}$ lies in the plane $(\mathbf{e}_1, \mathbf{e}_2)$ by construction:

$$\delta\mathbf{m} = \delta m_1 \mathbf{e}_1 + \delta m_2 \mathbf{e}_2. \tag{9.52}$$

Accordingly, Eq. (9.51) can be reduced to a two-dimensional equation in this plane:

$$\frac{\mathrm{d}}{\mathrm{d}t}\begin{pmatrix}\delta m_1 \\ \delta m_2\end{pmatrix} = A_0 \begin{pmatrix}\delta m_1 \\ \delta m_2\end{pmatrix}, \tag{9.53}$$

where the matrix A_0 controls the stability of the fixed point. In particular, the equation $\mathrm{tr}\ A_0 = 0$ will describe Hopf bifurcations provided that the fixed point considered is not a saddle. After some algebra, one finds:

$$\mathrm{tr}\ A_0 = -\frac{2\alpha}{1+\alpha^2}\left[\lambda + \frac{D_p}{2} - \frac{\beta}{\alpha}\frac{1}{1 + c_p m_{0x}}\left(m_{0x} + \frac{c_p}{2}\frac{1 - m_{0x}^2}{1 + c_p m_{0x}}\right)\right], \tag{9.54}$$

where:

$$D_p = D_x\left(1 - m_{0x}^2\right) + D_y\left(1 - m_{0y}^2\right) + D_z\left(1 - m_{0z}^2\right). \tag{9.55}$$

This reasoning permits one to determine the location of Hopf bifurcations on the $(\mathrm{h}_{ax}, \beta/\alpha)$-plane, for all the nonsaddle fixed-point solutions:

- Fixed points $m_{0x} = \pm 1$, $m_{0y} = m_{0z} = 0$
  For these fixed points, $\lambda = -D_x \pm \mathrm{h}_{ax}$ and $D_p = D_z + D_y$. By using these relations in Eqs (9.54) and (9.55), one obtains the following bifurcation conditions:
  - $m_{0x} = 1$
    For this fixed point the Hopf bifurcation occurs for $\mathrm{h}_{ax} \leq -(D_z - D_x)$ or $\mathrm{h}_{ax} \geq -(D_y - D_x)$. The fixed point is a saddle of the dynamics when $-(D_z - D_x) \leq \mathrm{h}_{ax} \leq -(D_y - D_x)$. The bifurcation condition is:

$$\frac{\beta}{\alpha} = (1 + c_p)\left[\mathrm{h}_{ax} + \left(\frac{D_z + D_y}{2} - D_x\right)\right]. \tag{9.56}$$

  - $m_{0x} = -1$
    For this fixed point the Hopf bifurcation occurs for $\mathrm{h}_{ax} \leq D_y - D_x$ or $\mathrm{h}_{ax} \geq D_z - D_x$. The fixed point is a saddle of the dynamics when $D_y - D_x \leq \mathrm{h}_{ax} \leq D_z - D_x$. The bifurcation condition is:

$$\frac{\beta}{\alpha} = (1 - c_p)\left[\mathrm{h}_{ax} - \left(\frac{D_z + D_y}{2} - D_x\right)\right]. \tag{9.57}$$

  Equations (9.56) and (9.57) represent straight lines in the field-current plane. Their slope is different because the spin-torque effect has different intensity when the magnetization in the free layer is either parallel or anti-parallel to that of the fixed layer.
- Fixed points which coincide with g_L maxima when $\beta = 0$
  For these fixed points, to the first order in β: $m_{0x} = -\mathrm{h}_{ax}/(D_z - D_x)$, $m_{0y} = 0$, $\lambda = -D_z$, $D_p = D_x + D_y + (D_z - D_x)\, m_{0x}^2$. The corresponding bifurcation line is:

$$\frac{\beta}{\alpha} = -\frac{\left[(D_z - D_y) + (D_z - D_x)\left(1 - m_{0x}^2\right)\right](1 + c_p m_{0x})^2}{2m_{0x} + c_p\left(1 + m_{0x}^2\right)}, \tag{9.58}$$

$$m_{0x} = -\frac{\mathrm{h}_{ax}}{D_z - D_x}.$$

  This line actually represents two bifurcations simultaneously involving the two fixed points present in the two symmetric regions of which region H is made (see Fig. 4.10).

The last class of bifurcation mechanisms of interest is that of saddle-connection and semi-stable-limit-cycle global bifurcations. Both of them can be studied by using the Melnikov-function method discussed in Section 5.5.

In the saddle-connection bifurcation, a limit cycle is created or destroyed at the boundary of one of the energy regions present in the phase portrait of the magnetization dynamics. The bifurcation condition is that the Melnikov function must be equal to zero for the value of energy, $g_0 = g_c$, corresponding to the homoclinic or heteroclinic trajectory representing the boundary of the region of interest:

$$M\left(g_c, \beta/\alpha\right) = 0. \tag{9.59}$$

The energy g_c is known for each energy region of the phase portrait (see Section 4.4). For example, in the case of the $\left\{d^2(u)^2(s_-)(s_+)\right\}$ portrait, region L_+ covers the p^2 interval $k^2\left(1 - a_x^2/k'^2\right) \leq p^2 \leq \left(1 + |a_x|\right)^2$ (Eq. (4.84)). According to Eq. (4.9), the minimum value of p^2 corresponds to the maximum value of energy in the region, i.e., to the energy g_c of the heteroclinic trajectory at the boundary of the region. Thus, one finds:

$$g_c = \frac{D_y}{2} + \frac{1}{2}\frac{\mathrm{h}_{ax}^2}{D_y - D_x}. \tag{9.60}$$

Similar calculations can be carried out for any other region. By using Eq. (9.46), the solution of Eq. (9.59) can be written in the form:

$$\frac{\beta}{\alpha} = p\left(D_z - D_x\right)\left(1 + c_p a_x\right)\frac{I_1 + k'^2 r^2 I_2}{J_1 + J_2}, \tag{9.61}$$

where $g_0 = g_c$ must be used in all the energy-dependent parameters present in the right-hand side of the equation. Equation (9.61) may not have solutions for all the energy regions considered. A careful study of this equation must be carried out separately for each energy region.

Finally, semi-stable-limit-cycle bifurcations are characterized by the fact that a pair of limit cycles of opposite stability is created or annihilated inside one of the energy regions of the phase portrait. The corresponding bifurcation condition is that both the Melnikov function and its derivative

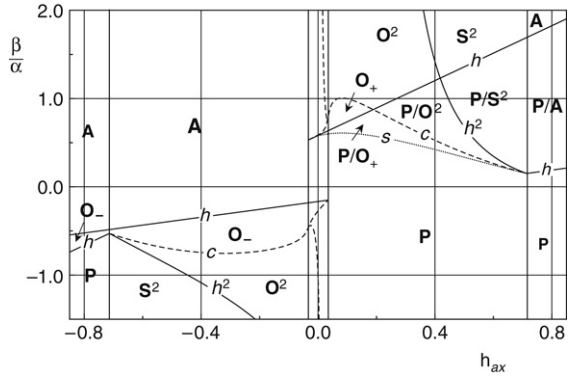

FIGURE 9.3 Dynamic stability diagram in the $(\mathrm{h}_{ax}, \beta/\alpha)$ control plane. Symbols are defined and discussed in the text. The central part of the diagram around $\mathrm{h}_{ax} = 0$ is shown in more detail in Fig. 9.4. System parameters: $D_x = -0.034, D_y = 0, D_z = 0.68$, $P = 0.3$.

with respect to the energy must be zero:

$$\begin{aligned} &M\left(g_0, \beta/\alpha\right) = 0, \\ &\frac{\partial}{\partial g_0} M\left(g_0, \beta/\alpha\right) = 0. \end{aligned} \tag{9.62}$$

This set of coupled equations must be solved with respect to g_0 and β/α for a given field. The investigation of these equations must be carried out separately for each energy region. It may (and actually does) occur that these equations admit no solutions for one or more of the energy regions. This means that no semi-stable-limit-cycle bifurcation will occur in those regions.

9.5 STABILITY DIAGRAMS

By using the results obtained for fixed points and bifurcations, the theoretical dynamic stability diagram for spin-torque-driven magnetization dynamics can be now constructed in the $(\mathrm{h}_{ax}, \beta/\alpha)$ control plane. This diagram provides complete information about the phase portraits existing under given field and current conditions as well as about the bifurcation lines where qualitative changes occur in the dynamic behavior of the free-layer magnetization. We shall discuss in some detail the example shown in Figs 9.3 and 9.4, which was generated for the following parameter values: $D_x = -0.034, D_y = 0, D_z = 0.68$, $P = 0.3$. This choice was

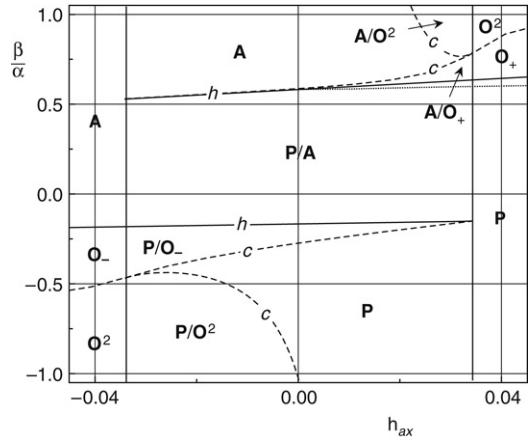

FIGURE 9.4 Magnified view of the central part of the stability diagram shown in Fig. 9.3. Symbols are defined and discussed in the text. System parameters: $D_x = -0.034, D_y = 0, D_z = 0.68, P = 0.3$.

inspired by the experimental work reported in Ref. [398]. A great number of different dynamic regimes are predicted, which differ in the number of stable stationary states and stable limit cycles available to the system. The bold symbols in Figs 9.3 and 9.4 identify the regions of occurrence of these dynamic regimes. Namely, the following notations are adopted:

- **A** and **P** indicate the control-plane regions where the states $\mathrm{m}_x = -1$ and $\mathrm{m}_x = 1$ are stable, respectively;
- $\mathbf{O}_+$ and $\mathbf{O}_-$ indicate the control-plane regions where a stable limit cycle exists in region L_+ and region L_- of the phase portrait, respectively (see Fig. 4.10);
- $\mathbf{O}^2$ indicates the control-plane regions where two symmetric stable limit cycles are present in the two symmetric parts of region H of the phase portrait (see Fig. 4.10);
- $\mathbf{S}^2$ indicates the control-plane regions where two symmetric stable stationary states are present in region H of the phase portrait.

The slash notation (e.g., in $\mathbf{P}/\mathbf{O}_+$) indicates the coexistence of more than one stable state in the phase portrait.

Two features of the diagram deserve special attention. First, the spin-polarized current is accounted for in the diagram only through the ratio β/α. This is the consequence of the fact that the parameters α and β always appear in that combination in the theoretical treatment of fixed

points and self-oscillations. According to Eqs (9.4) and (9.6), the current density corresponding to some critical condition $(\beta/\alpha)_{\text{crit}}$ resulting from the stability diagram is:

$$J_e = \frac{\alpha\mu_0 \mathrm{M}_s^2 |e| d}{\hbar b_p} \left(\frac{\beta}{\alpha}\right)_{\text{crit}}. \tag{9.63}$$

This equation has an important physical implication. Namely, it reveals how the various physical parameters of the problem, such as free-layer thickness, saturation magnetization, and damping constant, jointly determine the conditions leading to specific dynamic regimes.

The dynamic regimes are separated from one another by bifurcation lines of different nature. Local bifurcations are represented in Figs 9.3 and 9.4 by continuous lines, global bifurcations by broken lines. The specification of these lines is as follows:

- Vertical lines: pitchfork bifurcations
  These are the lines where the number of fixed points changes by 2.
- Lines h and h^2: Hopf bifurcations
  The lines labeled by h are computed by using Eqs (9.56) and (9.57). These are the lines where one of the fixed points $\mathrm{m}_x = 1$ or $\mathrm{m}_x = -1$ reverses its stability through the creation or annihilation of a limit cycle. The lines labeled by h^2 are obtained from Eq. (9.58). These are the lines where the two fixed points in the two symmetric parts of region H of the phase portrait simultaneously reverse their stability with the creation or annihilation of two symmetric out-of-plane limit cycles.
- Lines c: saddle-connection bifurcations
  These are the lines where a saddle connection appears at the boundary of one of the central regions of the phase portrait. They were obtained by solving Eq. (9.59) with respect to β/α under a given field. The saddle-connection bifurcation always entails the creation or annihilation of a limit cycle coincident with the homoclinic trajectory that appears at the bifurcation point.
- Line s: semi-stable-limit-cycle bifurcation
  This line represents the condition where a pair of limit cycles with opposite stability and finite size is created or annihilated inside region L_+ of the phase portrait. This line was obtained by solving Eqs (9.62) with respect to g_0 and β/α under a given field. It turns out that for the specific values of the parameters chosen for Fig. 9.3, region L_+ is the only central region where this type of bifurcation occurs.

The notation used in Figs 9.3 and 9.4 is in direct correspondence with experiments, because only stable stationary states and stable limit

cycles (self-oscillations) can be experimentally observed. However, to comprehend the bifurcation mechanisms transforming one dynamic regime into another, the complete structure of the phase portrait must be considered. The number and nature of the stable states is not sufficient to determine this structure in all aspects. Complete information about the phase portrait is conveyed by using the more advanced notation previously discussed. The correspondence between stable states and phase portrait structures is listed below. Bold symbols are used in the phase portrait strings to identify the stable states present in each phase portrait.

- **P**-type portraits:
  - $\{d^2(u)^2(\mathbf{s}_+)(u_-)\}$ for $|\mathrm{h}_{ax}| \le D_y - D_x$;
  - $\{d_-(u)^2, (\mathbf{s}_+)\}$ for $D_y - D_x \le \mathrm{h}_{ax} \le D_z - D_x$;
  - $\{(\mathbf{s}_+ u_-)\}$ for $|\mathrm{h}_{ax}| \ge D_z - D_x$.
- **A**-type portraits:
  - $\{d^2(u)^2(u_+)(\mathbf{s}_-)\}$ for $|\mathrm{h}_{ax}| \le D_y - D_x$;
  - $\{d_+(u)^2, (\mathbf{s}_-)\}$ for $-(D_z - D_x) \le \mathrm{h}_{ax} \le -(D_y - D_x)$;
  - $\{(u_+ \mathbf{s}_-)\}$ for $|\mathrm{h}_{ax}| \ge D_z - D_x$.
- **P**/**A**-type portraits:
  - $\{d^2(u)^2(\mathbf{s}_+)(\mathbf{s}_-)\}$ for $|\mathrm{h}_{ax}| \le D_y - D_x$;
  - $\{(\mathbf{s}_+ r\mathbf{s}_-)\}$ for $\mathrm{h}_{ax} \ge D_z - D_x$.
- **O**$_+$ portrait: $\{d_-(u)^2, (\mathbf{a}u_+)\}$.
- **P**/**O**$_+$ portrait: $\{d_-(u)^2, (\mathbf{a}r\mathbf{s}_+)\}$.
- **A**/**O**$_+$ portrait: $\{d^2(u)^2(\mathbf{a}u_+)(\mathbf{s}_-)\}$.
- **O**$_-$-type portraits:
  - $\{d_+(u)^2, (\mathbf{a}u_-)\}$ for $-(D_z - D_x) \le \mathrm{h}_{ax} \le -(D_y - D_x)$;
  - $\{(u_+ \mathbf{a}u_-)\}$ for $\mathrm{h}_{ax} \le -(D_z - D_x)$.
- **P**/**O**$_-$ portrait: $\{d^2(u)^2(\mathbf{s}_+)(\mathbf{a}u_-)\}$.
- **O**^{2}-type portraits:
  - $\{d_-(\mathbf{a}u)^2, (u_+)\}$ for $\mathrm{h}_{ax} \ge D_y - D_x$;
  - $\{d_+(\mathbf{a}u)^2, (u_-)\}$ for $\mathrm{h}_{ax} \le -(D_y - D_x)$.
- **P**/**O**^{2}-type portraits:
  - $\{d^2(\mathbf{a}u)^2(\mathbf{s}_+)(u_-)\}$ for $|\mathrm{h}_{ax}| \le D_y - D_x$;
  - $\{d_-(\mathbf{a}u)^2, (r\mathbf{s}_+)\}$ for $\mathrm{h}_{ax} \ge D_y - D_x$.
- **A**/**O**^{2} portrait: $\{d^2(\mathbf{a}u)^2(u_+)(\mathbf{s}_-)\}$.
- **S**^{2}-type portraits:
  - $\{d_-(\mathbf{s})^2, (u_+)\}$ for $\mathrm{h}_{ax} \ge D_y - D_x$;
  - $\{d_+(\mathbf{s})^2, (u_-)\}$ for $\mathrm{h}_{ax} \le -(D_y - D_x)$.
- **P**/**S**^{2} portrait: $\{d_-(\mathbf{s})^2, (r\mathbf{s}_+)\}$.

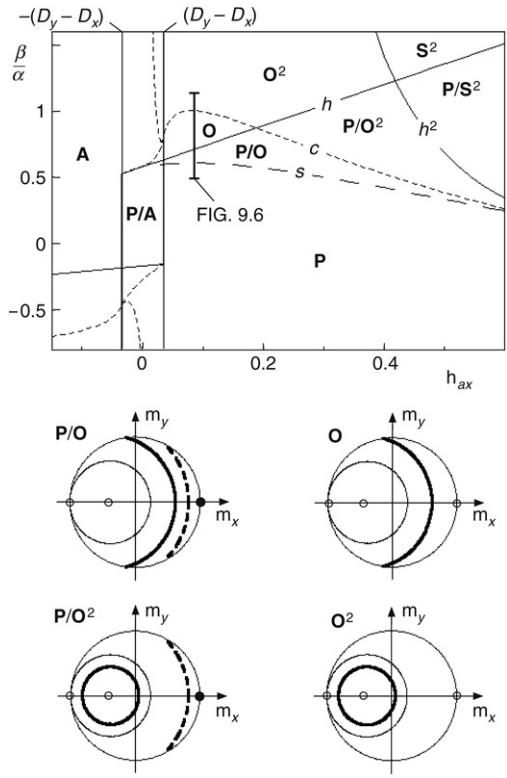

FIGURE 9.5 Top. Simplified view of dynamical stability diagram of Fig. 9.3. System parameters: $D_x = -0.034$, $D_y = 0$, $D_z = 0.68$, $P = 0.3$, $d = 3$ nm, $\mu_0 \mathrm{M}_s = 1.76$ T (these parameters refer to sample 2 of Ref. [398]; in that case, $\beta/\alpha = 1$ for a current of 5.6 mA). Vertical bar: current interval considered in Fig. 9.6. Bottom. Unit-disk representation of current-induced dynamical regimes. Black dots: stable state at $\mathrm{m}_x = 1$; empty dots: unstable states; bold lines: stable limit cycle; bold dashed lines: unstable limit cycle.

A great variety of different physical situations may be encountered, depending on the field and current conditions under which a spin-torque experiment is carried out. We illustrate this richness by considering in some detail a specific condition, namely, the case where the external field is kept fixed at a constant value $\sim$0.1 and the spin-polarized current is increased from zero up to large positive values (see Fig. 9.5). Under zero current, the system magnetization points along the positive x axis, because $\mathrm{m}_x = 1$ is the only stable state available to the system (**P** regime). When

the positive current is injected, the critical condition is reached (line s) where a pair of stable and unstable limit cycles appears inside region L_+ of the phase portrait. However, the appearance of a stable limit cycle does not result in any self-oscillation, because the magnetization remains in the state $\mathrm{m}_x = 1$, which is still stable ($\mathbf{P}/\mathbf{O}_+$ regime, Fig. 9.2(a)). The two limit cycles move apart from each other when the current is further increased. At the critical current where line h is crossed, the unstable limit cycle is reduced to the point $\mathrm{m}_x = 1$, where it gives rise to a Hopf bifurcation which makes the state $\mathrm{m}_x = 1$ unstable. The jump from the state $\mathrm{m}_x = 1$ to the previously formed stable limit cycle ($\mathbf{O}_+$ regime, Fig. 9.2(b)) occurs. Self-oscillations of finite amplitude suddenly appear in the system response. When the current is further increased, this stable limit cycle moves toward and eventually reaches the boundary of region L_+ (line c). Here the limit cycle splits into two symmetric limit cycles which simultaneously appear in the two symmetric parts of region H of the phase portrait ($\mathbf{O}^2$ regime). A spontaneous symmetry breaking occurs in the magnetization response, with the appearance of out-of-plane self-oscillations characterized by a nonzero average value of m_z. When the current is decreased starting from large values, the system response reversibly reproduces previous self-oscillations until it enters the $\mathbf{P}/\mathbf{O}_+$ regime. Here the response is hysteretic, with the self-oscillations persisting down to lower currents when the current is decreased. In other words, for the current interval in between line s and line h, the system is in the stationary state $\mathrm{m}_x = 1$ under increasing current and in the self-oscillation steady state under decreasing current. Under larger fields, e.g., $\mathrm{h}_{ax} = 0.3$, the order in which lines h and c are encountered under increasing current is reversed. This means that the symmetry breaking related to the creation of two limit cycles in region H occurs when the state $\mathrm{m}_x = 1$ is still stable ($\mathbf{P}/\mathbf{O}^2$ regime, Fig. 9.2(c)). In this case, self-oscillations appear only when the system reaches the $\mathbf{O}^2$ regime and are immediately out-of-plane in nature.

The presented method leads not only to the determination of the bifurcation lines where qualitative changes occur in the system response, but also to detailed predictions for the time-dependent magnetization $\mathbf{m}(t)$ associated with self-oscillations. This is obtained by analytically solving the equation $\mathrm{d}\mathbf{m}/\mathrm{d}t = -\mathbf{m} \times \mathbf{h}_{\text{eff}}$ and by using in the resulting solution $\mathbf{m}_c\,(t; g_0)$ the values of g_0 obtained by solving the equation $M\,(g_0, \beta/\alpha) = 0$ [92]. Figure 9.6 shows an example of the predicted magnetization response under varying positive current. For small currents the system is in the $\mathrm{m}_x = 1$ state and the system response is time-independent. The frequency f plotted in Fig. 9.6 for this state is the frequency of small-amplitude Kittel-type oscillations. At

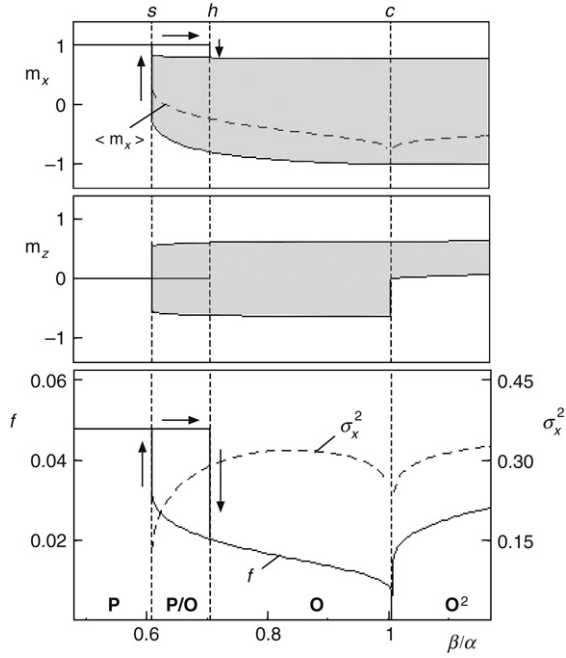

FIGURE 9.6 Magnetization response under varying current and $h_{ax} = 0.08$ for system parameters used in Fig. 9.3. Vertical dashed lines: bifurcation points. Arrows indicate hysteretic response. Top. Gray regions: range of variation of m_x and m_z during self-oscillations; dashed line: time average $\langle m_x \rangle$. Bottom. Continuous line: self-oscillation frequency f in units of γM_s; dashed line: variance $\sigma_x^2 = \langle m_x^2 \rangle - \langle m_x \rangle^2$ for self-oscillations.

the Hopf bifurcation point where the state $m_x = 1$ becomes unstable the system jumps to the stable limit cycle. This results in the sudden appearance of large-amplitude self-oscillations. Figure 9.6 shows that the self-oscillation frequency is a decreasing function of the current up to the saddle-connection bifurcation point. Here, as previously mentioned, the stable limit cycle splits into two symmetric out-of-plane limit cycles. A spontaneous symmetry breaking occurs in the magnetization response, with the appearance of out-of-plane self-oscillations (see plot of m_z in Fig. 9.6). From this point on, the self-oscillation frequency becomes an increasing function of the current. When the current is decreased starting from large values, the system response reversibly reproduces previous self-oscillations until it enters the $\mathbf{P/O}$ regime, where stable stationary states and stable self-oscillation states coexist. Here the response is

hysteretic, with the self-oscillations persisting down to lower currents. The **P**/**O** regime is where thermally induced transitions between coexisting states and the related appearance of random-telegraph signals are expected. These phenomena will be discussed in detail in Chapter 10.

9.6 SYSTEMS WITH UNIAXIAL SYMMETRY

The results discussed in the previous sections are valid when the free-layer easy axis and the fixed-layer magnetization are parallel and lie in the film plane [398,94,598]. In this section we shall consider the case when the entire problem exhibits uniaxial symmetry around the z axis perpendicular to the free-layer plane. It turns out that the complete analytical treatment of this problem can be developed and certain physical aspects of the magnetization dynamics are revealed with particular clarity. On the other hand, systems with this type of symmetry are of strong interest in view of potential data-storage applications [465].

Uniaxial symmetry is realized when: the anisotropy coefficients appearing in Eq. (9.10) are such that $D_x = D_y = D_\perp$; the spin-polarization vector $\mathbf{e}_p$ in Eq. (9.5) is directed along the z axis; and the external field is applied along the z axis as well. Under these conditions, both the system energy g_L (Eq. (9.10)) and the potential Φ (Eq. (9.34)) become functions of m_z only. It is convenient to discuss the problem in terms of spherical coordinates (θ, ϕ). Then, after dropping inessential additive constants, one obtains the following expression for g_L and Φ:

$$g_L = -\frac{\kappa_{\text{eff}}}{2}\cos^2\theta - \mathrm{h}_{az}\cos\theta, \tag{9.64}$$

$$\Phi = -\frac{\kappa_{\text{eff}}}{2}\cos^2\theta - \mathrm{h}_{az}\cos\theta + \frac{\beta}{\alpha}\frac{\ln(1 + c_p\cos\theta)}{c_p}. \tag{9.65}$$

Here, h_{az} is the z component of the external field, which can be positive or negative, whereas:

$$\kappa_{\text{eff}} = D_\perp - D_z \tag{9.66}$$

plays the role of effective anisotropy constant. By using Eqs (9.64) and (9.65) in Eq. (9.33), one obtains the following equations of motion for θ and ϕ:

$$\frac{\mathrm{d}\theta}{\mathrm{d}t} = -\alpha\frac{\partial\Phi}{\partial\theta}, \tag{9.67}$$

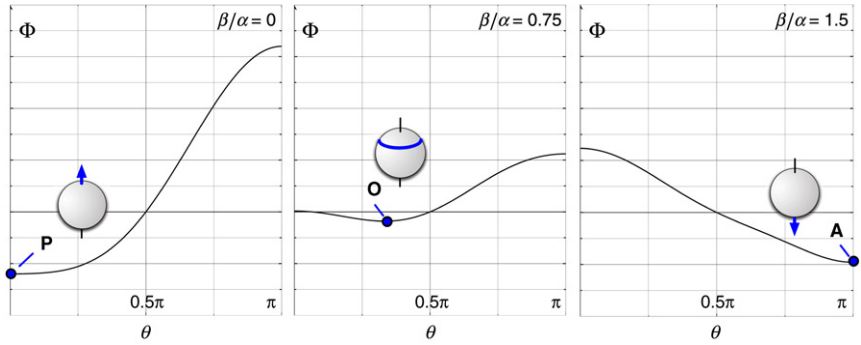

FIGURE 9.7 Potential Φ as a function of θ for different injected currents. Parameters: $\kappa_{\text{eff}} = -1$, $c_p = 0.5$, $\mathrm{h}_{az} = 1.1$. Bold symbols and corresponding pictures of the magnetization sphere indicate the stable states at the different current values: magnetization parallel to the applied field (**P**); magnetization precessing around the field axis (**O**); magnetization anti-parallel to the applied field (**A**).

$$\frac{\mathrm{d}\phi}{\mathrm{d}t} = \frac{1}{\sin\theta}\frac{\partial g_L}{\partial \theta}. \tag{9.68}$$

Equation (9.67) shows that the polar angle θ follows a viscous-type relaxation dynamics in the effective potential Φ. This potential accounts for the effects of the applied magnetic field and the injected spin-polarized current. In particular, steady-state regimes will coincide with the minima of this potential. Figure 9.7 shows an example of the possible responses predicted under these conditions. The figure refers to a soft thin film with $\kappa_{\text{eff}} = -1$ (i.e., easy-plane shape anisotropy), subject to the external field $\mathrm{h}_{az} = 1.1$. Under no current ($\beta/\alpha = 0$), the potential Φ has a minimum at $\theta = 0$, which is in agreement with the fact that the state with magnetization parallel to the field is stable whenever $\mathrm{h}_{az} > |\kappa_{\text{eff}}|$. The existence of such a stable state is indicated by the symbol **P** on the figure. However, the stability of this state can be detroyed by the injected current. The figure shows that when $\beta/\alpha = 0.75$ the previous state of magnetization is no longer stable, since the potential minimum has moved from $\theta = 0$ to $\theta = \theta_0 \simeq 0.4\,\pi$. This corresponds to the appearance of stable steady precession of the magnetization (indicated by **O** on the figure) with constant amplitude θ_0 and a precessional frequency controlled by Eq. (9.68). When the injected current is further increased ($\beta/\alpha = 1.5$), the situation is reached where the state with magnetization antiparallel to the field (state **A**) is stable. Therefore, a state which would be unstable under

the sole presence of the field is made stable by the injection of the spin-polarized current.

These effects can be quantitatively studied by computing the force $\partial\Phi/\partial\theta$. Indeed, Eq. (9.65) yields:

$$\frac{\partial\Phi}{\partial\theta} = \sin\theta\left(\kappa_{\text{eff}}\cos\theta + \mathrm{h}_{az} - \frac{\beta}{\alpha}\frac{1}{1+c_p\cos\theta}\right). \tag{9.69}$$

This equation shows that the two states for which $\sin\theta = 0$, i.e., $\theta = 0$ and $\theta = \pi$, are always equilibrium points for the potential. On the other hand, the expression inside brackets is equal to zero in the case of limit-cycle dynamics, in which the magnetization precesses around the symmetry axis at some constant polar angle θ_0. This angle is a solution to the equation:

$$\frac{\beta}{\alpha} = (\mathrm{h}_{az} + \kappa_{\text{eff}}\cos\theta_0)\,(1 + c_p\cos\theta_0)\,. \tag{9.70}$$

The stability of these critical points and limit cycles is controlled by the curvature of the effective potential Φ. Physically observable regimes will be those corresponding to potential minima, i.e., points for which $\partial^2\Phi/\partial\theta^2 > 0$.

As illustrated by Fig. 9.7, when the external field or the injected current is slowly varied in time, the stability of one or the other of the fixed points at $\theta = 0$ and $\theta = \pi$ may be reversed (from stable to unstable or vice versa) via a Hopf bifurcation entailing the creation or the annihilation of a limit cycle. The conditions under which this will occur around $\theta = 0$ are obtained by setting $\cos\theta = 1$ in Eq. (9.70). One finds:

$$\frac{\beta}{\alpha} = (1 + c_p)(\mathrm{h}_{az} + \kappa_{\text{eff}}). \tag{9.71}$$

Analogously, the condition for the Hopf bifurcation around $\theta = \pi$ is:

$$\frac{\beta}{\alpha} = (1 - c_p)(\mathrm{h}_{az} - \kappa_{\text{eff}}). \tag{9.72}$$

Equations (9.71) and (9.72) represent straight lines in the field-current control plane $(\mathrm{h}_{az}, \beta/\alpha)$. These two lines identify the regions where limit cycles exist. On this basis, one can construct the complete dynamical phase diagram for spin-transfer-driven magnetization dynamics in systems with uniaxial symmetry [59]. Figure 9.8 shows two examples of this phase

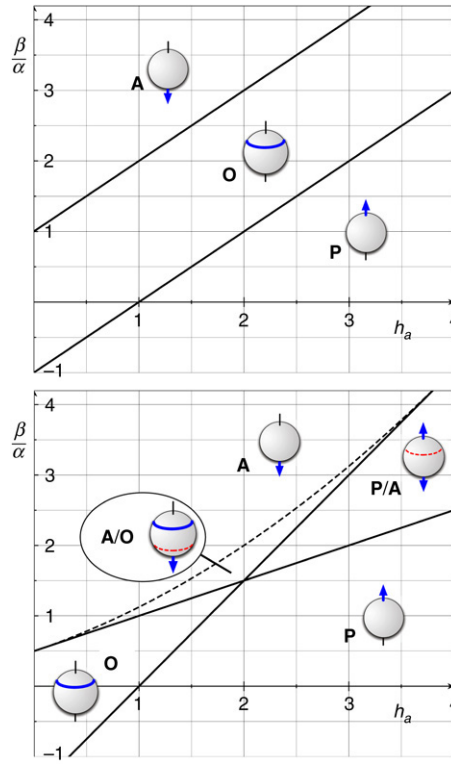

FIGURE 9.8 Phase diagram for spin-transfer-driven magnetization dynamics in a uniaxial system with $\kappa_{\text{eff}} = -1$. Top: $c_p = 0$. Bottom: $c_p = 0.5$. Continuous lines: Hopf bifurcation. Dashed line: semi-stable-limit-cycle bifurcation. Symbols are defined and discussed in the text.

diagram for $c_p = 0$ and $c_p \neq 0$. As for previous diagrams, the symbols **P** and **A** indicate the regions where the states $\theta = 0$ and $\theta = \pi$ are stable, respectively, while the symbol **O** indicates the regions where a stable limit cycle exists. The slash notation (e.g., **P**/**O**) indicates that different stable regimes coexist. The continuous lines represent Hopf bifurcation lines, where the stability of one of the fixed points at $\theta = 0$ or $\theta = \pi$ is reversed. The dashed line instead represents a semi-stable-limit-cycle bifurcation line, where a pair of stable and unstable limit cycles is created or annihilated (compare with line s in Fig. 9.3).

A stable limit cycle will result in steady-state magnetization oscillations. From Eq. (9.68) one obtains the following formula for the

frequency f_0 of these oscillations:

$$f_0 = \frac{1}{2\pi}\frac{1}{\sin\theta_0}\left.\frac{\partial g_L}{\partial\theta}\right|_{\theta_0} = \frac{1}{2\pi}\left(\mathrm{h}_{az} + \kappa_{\text{eff}}\cos\theta_0\right), \tag{9.73}$$

where the energy g_L has been expressed by using Eq. (9.64). Remarkably, this frequency coincides with the Kittel frequency of free precession of a system subject to no damping and no current injection, i.e., $\alpha = \beta = 0$, provided its trajectory coincides with the trajectory of the limit cycle. Thus, spin transfer has no direct influence on the free precession of the system, but rather promotes one of the possible precession trajectories to the status of stable limit cycle of the dissipative dynamics.

In Chapter 7, the presence of uniaxial symmetry made it possible to perform a comprehensive study of magnetization dynamics driven by circularly polarized radio-frequency (rf) fields. Interestingly, the same approach can be extended to spin-transfer devices, when a spin-polarized current and an rf magnetic field are simultaneously applied. Indeed, in uniaxial systems the dynamics under nonzero injected current and nonzero rf field is identical in its mathematical structure to the magnetization dynamics under zero current, provided the amplitude of the dc external magnetic field and the frequency of the rf field are properly renormalized. This equivalence has interesting physical consequences: first, nonlinear ferromagnetic resonance effects can be generated by arbitrarily low rf fields, provided the spin-polarized current is properly tuned; second, phase-locking may occur between current-induced magnetization precession and rf field oscillations.

To show how these conclusions can be reached, we start from Eq. (9.5) and we make the same assumptions as before regarding the uniaxial symmetry of the problem, namely, $D_x = D_y = D_\perp$ and $\mathbf{e}_p \equiv \mathbf{e}_z$. In addition, for the sake of simplicity we limit our analysis to the particular case when $c_p = 0$, i.e.:

$$\frac{\mathrm{d}\mathbf{m}}{\mathrm{d}t} - \alpha\mathbf{m}\times\frac{\mathrm{d}\mathbf{m}}{\mathrm{d}t} = -\mathbf{m}\times\left(\mathbf{h}_{\text{eff}} - \beta\mathbf{m}\times\mathbf{e}_z\right). \tag{9.74}$$

Neglecting inessential terms proportional to $\mathbf{m}$, the effective field appearing in Eq. (9.74) is expressed as:

$$\mathbf{h}_{\text{eff}} = \mathbf{h}_{a\perp}(t) + \left(\mathrm{h}_{az} + \kappa_{\text{eff}}\mathrm{m}_z\right)\mathbf{e}_z, \tag{9.75}$$

where κ_{eff} is given by Eq. (9.66), while the rf component $\mathbf{h}_{a\perp}(t)$ of angular frequency ω is circularly polarized in the (x, y)-plane perpendicular to the

symmetry axis of the problem:

$$\mathbf{h}_{a\perp}(t) = \mathrm{h}_{a\perp}\left(\mathbf{e}_x \cos\omega t + \mathbf{e}_y \sin\omega t\right). \tag{9.76}$$

As previously mentioned, the dynamics (9.74) is identical in structure to the dynamics when no spin-polarized current is present, i.e., $\beta = 0$. This is revealed by expressing the dynamics in the rotating frame in which the rf field is stationary, as was done in Chapter 7. In this reference frame, an additional term contributes to the time derivative of magnetization, as shown by Eq. (7.10), and therefore Eq. (9.74) takes the form:

$$\frac{\mathrm{d}\mathbf{m}}{\mathrm{d}t} - \alpha\mathbf{m}\times\frac{\mathrm{d}\mathbf{m}}{\mathrm{d}t} = -\mathbf{m}\times\left(\mathbf{h}'_{\mathrm{eff}} - \omega'\mathbf{e}_z + \alpha\omega'\mathbf{m}\times\mathbf{e}_z\right), \tag{9.77}$$

where:

$$\mathbf{h}'_{\mathrm{eff}} = \mathrm{h}_{a\perp}\mathbf{e}_a + \left(\mathrm{h}'_{az} + \kappa_{\mathrm{eff}}\mathrm{m}_z\right)\mathbf{e}_z, \tag{9.78}$$

and:

$$\mathrm{h}'_{az} = \mathrm{h}_{az} - \beta/\alpha, \qquad \omega' = \omega - \beta/\alpha. \tag{9.79}$$

Equation (9.77) is identical to the equation (7.11) for the dynamics driven by the rf field only, once the dc magnetic field and the angular frequency of the rf field are redefined as expressed by Eq. (9.79). Therefore, the results obtained in Chapter 7 are immediately applicable to the study of the interplay between spin-transfer effects and rf field. In particular, one finds that the dynamics (9.77) can only result in either periodic modes (**P**-modes) in which the magnetization precesses around the symmetry axis in synchronism with the rf field, or quasi-periodic modes (**Q**-modes), in which a second frequency is superimposed to the frequency of the rf field.

The methods discussed in Chapter 7 can be used equally well to construct the complete stability diagram for the dynamics (9.77). The main difference is that in Chapter 7 the rf field frequency ω was a given constant, which resulted in diagrams in the $(\mathrm{h}_{az}, \mathrm{h}_{a\perp})$ control plane (see, for instance, Fig. 7.12). This is not the case for the problem of interest here, in which three control parameters $(\mathrm{h}'_{az}, \mathrm{h}_{a\perp}, \omega')$ exist. A convenient way to proceed is to fix the value of $\mathrm{h}_{a\perp}$, then to construct the stability diagram in the $\mathrm{h}'_{az}, \omega'$ plane by the methods discussed in Chapter 7, and finally to map this diagram to the $(\mathrm{h}_{az}, \beta/\alpha)$ plane by using the

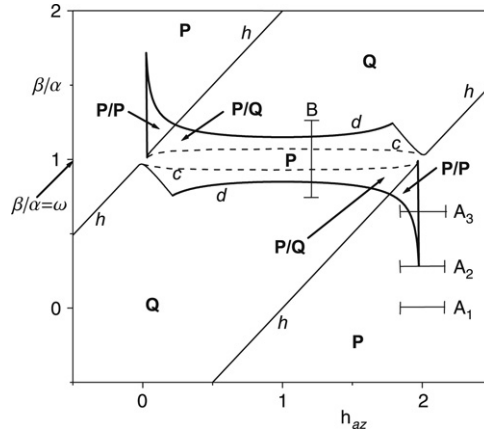

FIGURE 9.9 Stability diagram in the $(\mathrm{h}_{az}, \beta/\alpha)$ control plane (consult text for description of symbols). System parameters: $\alpha = 0.02$, $\kappa_{\mathrm{eff}} = -1$, $\omega = 1$, $\mathrm{h}_{a\perp} = 0.003$. Horizontal bars: field interval considered in Fig. 9.10 for $\beta/\alpha = 0$ (A_1), $\beta/\alpha = 0.28$ (A_2), and $\beta/\alpha = 0.65$ (A_3). Vertical bar B: current interval considered in Fig. 9.11.

transformations (9.79). In Fig. 9.9 we show the result of this analysis for a system with $\alpha = 0.02$ and $\kappa_{\mathrm{eff}} = -1$, when $\omega = 1$ and $\mathrm{h}_{a\perp} = 0.003$. The various dynamic regimes are separated in the diagram by bifurcation lines similar to those discussed in Chapter 7. More precisely, the lines labeled by (d) represent saddle–node bifurcations, when a saddle-node pair of **P**-modes is either created or annihilated. The lines labeled by (h) represent Hopf bifurcations, when one of the **P**-modes changes from stable to unstable or vice versa with the simultaneous appearance or disappearance of a **Q**-mode. Finally, the lines labeled by (c) represent saddle-connection bifurcations, when a **Q**-mode of finite amplitude is created or destroyed. Bold symbols identify the regimes where stable **P**-modes and **Q**-modes are present. The slash notation, i.e., $\mathbf{P}/\mathbf{P}$ or $\mathbf{P}/\mathbf{Q}$, indicates the coexistence of different **P**-modes and **Q**-modes. The stability diagram when no rf field is present, i.e., $\mathrm{h}_{a\perp} = 0$, is shown in the top part of Fig. 9.8 ($c_p = 0$). Comparison between Figs 9.8 and 9.9 reveals that when the rf field is switched on, the parallel (**P**) and antiparallel (**A**) states are changed into **P**-modes, while the self-oscillation (**O**) states are changed into **Q**-modes. In addition, several nontrivial effects emerge as a consequence of the intereference between the action of the rf field and the spin-polarized current. Namely, additional saddle–node and

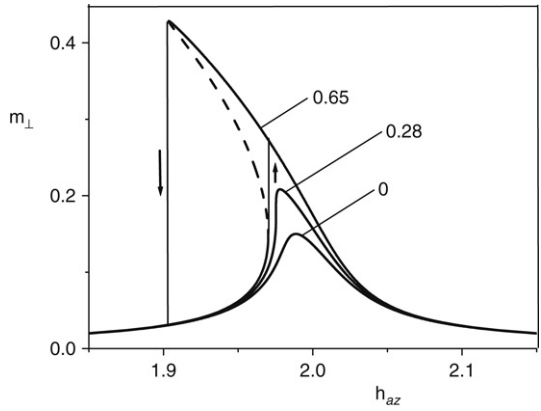

FIGURE 9.10 Magnetization response as a function of the dc field for $h_{a\perp} = 0.003$ and current $\beta/\alpha = 0, 0.28, 0.65$ (A_1, A_2, A_3 intervals in Fig. 9.9). System parameters are those of Fig. 9.9. Continuous lines: stable **P**-modes; dashed line: unstable **P**-mode. Arrows indicate foldover jumps occurring under the largest current.

saddle-connection bifurcation lines as well as the breaking and distortion of Hopf bifurcation lines appear around $\beta/\alpha \simeq \omega$.

Among the various effects predicted by this stability analysis, two of them are of particular physical interest: current-controlled nonlinear ferromagnetic resonance and phase-locking between current-induced magnetization oscillations and rf field.

Let us consider the case where the dc field h_{az} is varied under given current β/α and rf field $h_{a\perp}$. This means that in the diagram shown in Fig. 9.9, we are moving along a horizontal line. The dependence of $m_\perp = (m_x^2 + m_y^2)^{1/2}$ on h_{az} when h_{az} is decreased from large initial values along the intervals A_1, A_2, and A_3 in Fig. 9.9 ($\beta/\alpha = 0, 0.28, 0.65$, respectively) is shown in Fig. 9.10. As discussed in Section 7.5, resonance occurs for $h'_{az} + \kappa_{\text{eff}} = \omega'$, i.e., $h_{az} = \omega - \kappa_{\text{eff}}$. Thus resonance conditions are not modified by the spin-polarized current. However, the current strongly affects the degree of distortion of the magnetization response and, in particular, leads to the onset of foldover instabilities of the type discussed in Section 7.5 even at low rf fields. Foldover occurs in the $\mathbf{P}/\mathbf{P}$ regime in Fig. 9.9, where two stable **P**-modes coexist. The threshold conditions for the appearance of foldover are expressed by Eqs (7.69), (7.43), and (7.21), once $\omega' = \omega - \beta/\alpha$ is used in the place of ω. Whenever $\alpha|\omega'| \ll 1$, the threshold rf field can be computed with good accuracy from the

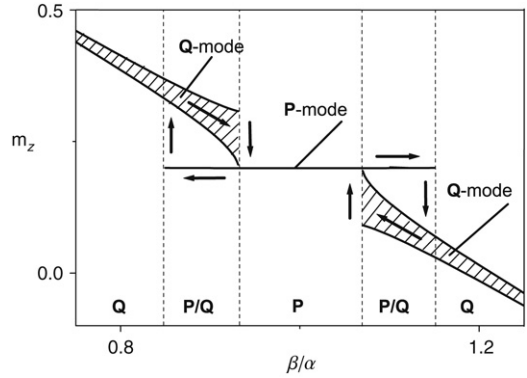

FIGURE 9.11 Magnetization response as a function of current for $h_{az} = 1.2$ (B interval in Fig. 9.9). System parameters are those of Fig. 9.9 (consult text for description of symbols). Vertical dashed lines indicate bifurcation points. Shaded region represents m_z variation in the **Q**-mode. Arrows indicate hysteretic response.

approximate expression (7.70), which yields:

$$h_{a\perp}^2 \simeq \frac{16}{3\sqrt{3}} \frac{\alpha^3 |\omega - \beta/\alpha|^3}{|\kappa_{\text{eff}}|}. \tag{9.80}$$

This equation clearly reveals that the presence of current makes it possible to have foldover for values of $h_{a\perp}$ definitely lower than those expected when $\beta/\alpha = 0$. For a given rf field amplitude $h_{a\perp}$, on the other hand, Eq. (9.80) permits one to estimate the threshold current beyond which foldover will appear. For example, for the system parameters considered in Fig. 9.9, foldover appears for currents larger than $\beta/\alpha \simeq 0.28$ (interval A_2 in Fig. 9.9).

The magnetization response in the **Q** regime in Fig. 9.9 contains basically two frequencies: the frequency of the rf external field and the frequency of the current-induced magnetization precession. Under appropriate conditions, phase-locking may occur between these two frequencies. When the dc field is kept constant and the current is increased from zero in the diagram shown in Fig. 9.9, phase-locking occurs when the current crosses the saddle-connection bifurcation line (c line). At the bifurcation line, the **Q**-mode response becomes unstable and the system jumps to a stable **P**-mode in which the magnetization precesses in synchronism with the rf field. Figure 9.11 illustrates this mechanism when

the current is varied in the B interval shown in Fig. 9.9 ($h_{az} = 1.2$). In the **Q**-mode, the superposition of the mentioned two frequencies results in periodic oscillations of the m_z magnetization component within a certain interval. The dependence of the amplitude of this interval on current is shown by the shashed region in Fig. 9.11. When the system jumps from the **Q**-mode to the **P**-mode and phase-locking takes place, m_z attains a single definite value. Phase-locking persists until the saddle–node bifurcation line is reached (line d in Fig. 9.11). Here, the **P**-mode becomes unstable and the system jumps back to the **Q**-mode response. The arrows in Fig. 9.11 make clear that, in the **P**/**Q** coexistence regime, hysteresis occurs in the magnetization response under increasing or decreasing current.

CHAPTER 10

Stochastic Magnetization Dynamics

10.1 STOCHASTIC LANDAU–LIFSHITZ AND LANDAU–LIFSHITZ–GILBERT EQUATIONS

The dimensions of magnetized devices used in magnetic storage technologies and spintronics are usually rather small (in the submicrometer spatial scale). In these situations, thermal fluctuations play an important role in magnetization dynamics and may induce transitions from one state to another. For this reason, the focus of our discussion in the present chapter is on the study of magnetization dynamics in the presence of thermal fluctuations and noise.

The effects of thermal fluctuations on magnetization dynamics are usually studied by introducing appropriate stochastic terms in the Landau–Lifshitz (LL) or Landau–Lifshitz–Gilbert (LLG) equation [134]. These stochastic terms account for the random fluctuations induced by the interaction of the ferromagnet with the thermal bath. The resulting randomly-perturbed magnetization dynamics is a stochastic process whose properties will be analyzed in detail in this chapter.

To start the discussion, we consider a sufficiently small ferromagnetic object with spatially uniform magnetization. The magnitude of the magnetization vector is constant, but its direction fluctuates because of thermal perturbations. The stochastic term that is usually added to the LL or LLG equation has the form of a random magnetic torque $-\nu \mathbf{m} \times \mathbf{h}_N(t)$, where $\mathbf{h}_N(t)$ is a vector whose components are independent gaussian white-noise processes, and ν is a parameter which measures the intensity of thermal perturbations. The assumption that the thermal noise is gaussian is usually motivated by the central limit theorem. This is because the random fluctuations are the result of a very large number of statistically independent (or weakly correlated) random events, and the sum of their effects tends to have a gaussian (normal) distribution. In addition, the choice of the gaussian distribution leads to results which are consistent with statistical mechanics. On the other hand, the assumption

that the noise has negligible correlation time ("white" noise) reflects the fact that the random perturbations are expected to have a correlation time much shorter than any time constant of magnetization dynamics.

The gaussian white-noise process occupies a special place in the theory of stochastic processes, because this process has the simplest statistical properties. More complex noise processes can be readily obtained by appropriate transformations of gaussian white-noise. On the other hand, the white-noise process is highly irregular in time and this leads to mathematical difficulties in the interpretation of the solutions of differential equations containing the white-noise process. For this reason, the differential equations containing white-noise terms need careful discussion.

As mentioned above, the stochastic magnetization dynamics is usually described by the stochastic LL equation of the form:

$$\frac{\mathrm{d}\mathbf{m}}{\mathrm{d}t} = -\mathbf{m} \times (\mathbf{h}_{\text{eff}} + \nu \mathbf{h}_N(t)) - \alpha \mathbf{m} \times (\mathbf{m} \times \mathbf{h}_{\text{eff}}) \,. \tag{10.1}$$

This equation was considered in the seminal work of Kubo [425]. In this equation the noise term only appears as a perturbation of the precessional term.

An alternative stochastic equation can be obtained from the LL equation when the noise field $\mathbf{h}_N(t)$ is viewed as a random component of the effective field and, consequently, an additional stochastic term is added as follows:

$$\frac{\mathrm{d}\mathbf{m}}{\mathrm{d}t} = -\mathbf{m} \times (\mathbf{h}_{\text{eff}} + \nu \mathbf{h}_N(t)) - \alpha \mathbf{m} \times [\mathbf{m} \times (\mathbf{h}_{\text{eff}} + \nu \mathbf{h}_N(t))] \,. \tag{10.2}$$

The last equation, up to appropriate rescaling of time, is the stochastic differential equation (SDE) that one derives by adding a stochastic term to the effective field in the LLG equation.

Later in this chapter, it will be shown that the stochastic dynamics generated by Eqs (10.1) and (10.2) are in fact equivalent, up to the renormalization of the parameter ν. The appropriate value of this parameter can be determined by considering fluctuation-dissipation relations as it will be discussed in detail in the next section.

The noise field $\mathbf{h}_N(t)$ is introduced in Eqs (10.1) and (10.2) through the cross-product $\mathbf{m} \times (\ldots)$, which leads to random torques that are orthogonal to $\mathbf{m}$. This form of the random terms is used to guarantee the preservation of the magnetization magnitude in stochastic magnetization dynamics. This property is natural because it is expected that at sufficiently

small spatial scales the exchange interaction strongly penalizes spatially nonuniform states. Thus, thermal fluctuations can only perturb the local direction of magnetization but not its magnitude. However, the property of preservation of magnetization magnitude in randomly perturbed dynamics can be formally derived from Eq. (10.1) or Eq. (10.2), only after an appropriate mathematical meaning is attributed to the solutions of these stochastic differential equations.

We start the discussion of this point with the detailed definition of the random field $\mathbf{h}_N(t)$. The gaussian white-noise process can be formally defined as the derivative of the isotropic vector Wiener process (or vector Brownian motion) $\mathbf{W}(t)$ [277]:

$$\mathbf{h}_N(t) = \frac{\mathrm{d}\mathbf{W}(t)}{\mathrm{d}t}, \tag{10.3}$$

where the cartesian components $W_k(t)$ of $\mathbf{W}(t)$ are statistically independent scalar Wiener processes. The scalar Wiener process $W(t)$ is defined by the following properties:

1. $W(t)$ satisfies the following initial condition:

$$W(0) = 0. \tag{10.4}$$

2. $W(t) - W(s)$, with $t > s \geq 0$, is a gaussian random variable with zero mean and variance $t - s$:

$$\langle [W(t_1) - W(s_1)]^2 \rangle = t - s. \tag{10.5}$$

3. $W(t)$ has uncorrelated increments:

$$\langle [W(t_1) - W(s_1)]\,[W(t_2) - W(s_2)] \rangle = 0 \tag{10.6}$$

when $0 \leq s_2 < t_2 \leq s_1 < t_1$.

The brackets $\langle \cdot \rangle$ in Eqs (10.5) and (10.6) denote statistical averages. The last condition means that $[W(t_1) - W(s_1)]$ and $[W(t_2) - W(s_2)]$ are uncorrelated stochastic variables when $0 \leq s_2 < t_2 \leq s_1 < t_1$, which, along with the second condition (i.e., the fact that these variables are gaussian), implies that they are statistically independent. For this reason, one can also express the third condition by saying that the Wiener process has independent increments. Another important property of the Wiener process is that it has continuous trajectories which are not differentiable at

any instant of time (actually, these trajectories satisfy with probability one a Holder condition with any exponent $\alpha < 0.5$, but not with $\alpha \geq 0.5$). To illustrate this, we note that Eq. (10.5) implies that:

$$\lim_{t\to s}\left\langle\left[\frac{W(t)-W(s)}{t-s}\right]^2\right\rangle = \lim_{t\to s}\frac{1}{(t-s)^2}\langle[W(t)-W(s)]^2\rangle = +\infty. \tag{10.7}$$

This means that the ratio $(W(t)-W(s))/(t-s)$, in the limit $t \to s$, does not tend to a finite value, not even in the mean square sense. This fact implies the nondifferentiability of $W(t)$. Indeed, while for differentiable functions of time the differential is first order in $\mathrm{d}t$, in the case of the Wiener process one has:

$$\langle(\mathrm{d}W)^2\rangle = \mathrm{d}t. \tag{10.8}$$

In the case of the isotropic vector Wiener process $\mathbf{W}$, the following result is valid:

$$\langle \mathrm{d}W_h \mathrm{d}W_k\rangle = \delta_{kh}\mathrm{d}t. \tag{10.9}$$

The nondifferentiability of the Wiener process paths results in high irregularity in time of the scalar white-noise process $\mathrm{h}_N(t) = \mathrm{d}W/\mathrm{d}t$. Nevertheless, at least formally, the properties of $\mathrm{h}_N(t)$ can be derived from properties (10.4)–(10.6) of $W(t)$. In this respect, one can start with the integral relation between $\mathrm{h}_N(t)$ and $W(t)$:

$$W(t) = \int_0^t \mathrm{h}_N(\tau)\mathrm{d}\tau, \tag{10.10}$$

and, after appropriate standard manipulations, demonstrate that:

$$\langle \mathrm{h}_N(t)\rangle = 0, \qquad \langle \mathrm{h}_N(t_1)\mathrm{h}_N(t_2)\rangle = \delta(t_1 - t_2), \tag{10.11}$$

where $\delta(\cdot)$ is Dirac's delta function. In the case of the isotropic vectorial white noise $\mathbf{h}_N(t)$, one has:

$$\langle \mathbf{h}_N(t)\rangle = 0, \qquad \langle h_{N,k}(t_1)h_{N,h}(t_2)\rangle = \delta_{kh}\delta(t_1 - t_2), \tag{10.12}$$

where k and h denote cartesian components and δ_{kh} is the Kronecker delta symbol. It is apparent from the above definition that the white noise

process is stationary, which means that its properties are invariant with respect to changes of the time origin.

As mentioned before, the irregular behavior in time of the white-noise process leads to difficulties in the mathematical interpretation of Eqs (10.1) and (10.2). This issue belongs to the branch of mathematics known as stochastic differential calculus. It is beyond the scope of this book to discuss this matter in detail. Only a heuristic introduction to the main points of this calculus will be given, with emphasis on their physical consequences. We shall limit the discussion to Eq. (10.1), but all considerations are also valid for Eq. (10.2).

The first step to deal with the nondifferentiability of $\mathbf{W}(t)$ is to rewrite the differential equation (10.1) as an integral equation:

$$\mathbf{m}(t) - \mathbf{m}(t_0) = \int_{t_0}^{t} \mathbf{v}(\mathbf{m}(\tau))\mathrm{d}\tau + \int_{t_0}^{t} \sigma(\mathbf{m}(\tau)) \cdot \mathrm{d}\mathbf{W}(\tau), \tag{10.13}$$

where the vector field:

$$\mathbf{v}(\mathbf{m}) = -\mathbf{m} \times \mathbf{h}_{\text{eff}} - \alpha \mathbf{m} \times (\mathbf{m} \times \mathbf{h}_{\text{eff}}), \tag{10.14}$$

represents the deterministic drift in the right-hand side of Eq. (10.1), while $\sigma(\mathbf{m})$ is the 3×3 matrix such that $\sigma(\mathbf{m}) \cdot \mathrm{d}\mathbf{W} = -\nu \mathbf{m} \times \mathrm{d}\mathbf{W}$. In terms of cartesian components, one finds:

$$\sigma(\mathbf{m}) = -\nu \begin{pmatrix} 0 & -\mathrm{m}_z & \mathrm{m}_y \\ \mathrm{m}_z & 0 & -\mathrm{m}_x \\ -\mathrm{m}_y & \mathrm{m}_x & 0 \end{pmatrix}. \tag{10.15}$$

The integral equation (10.13) does not contain the derivative of $\mathbf{W}(t)$. However, the integrals on the right-hand side must be properly defined. The first of the two integrals in Eq. (10.13) does not introduce any difficulty and can be interpreted as a usual deterministic integral. The difficulties arise in the interpretation of the second integral, which is usually referred to as a stochastic integral. By using a standard procedure, this integral may be defined by using a set of points $t_0 < t_1 < \cdots < t_{n-1} < t_n = t$ in the interval $[t_0, t]$, and forming an appropriate integral sum:

$$\int_{t_0}^{t} \sigma\left(\mathbf{m}(\tau)\right) \cdot \mathrm{d}\mathbf{W}(\tau) = \lim_{n\to\infty} \sum_{r=1}^{n-1} \sigma\left(\mathbf{m}(\tau_r)\right) \cdot [\mathbf{W}(t_{r+1}) - \mathbf{W}(t_r)], \tag{10.16}$$

where:

$$t_r \leq \tau_r < t_{r+1}. \tag{10.17}$$

The difficulty is in the fact that, due to the highly irregular time behavior of $\mathbf{W}(t)$, the limit on the right-hand side of Eq. (10.16) depends on the positions of τ_r in the intervals (t_r, t_{r+1}). This difficulty can be circumvented by making special definitions of the integral sums, in which the arbitrariness related to the positions of τ_r is removed. In this respect, there are two classical definitions of the integral. The first one is due to Itô [277] and corresponds to the choice $\tau_r = t_r$ in Eq. (10.16):

$$\int_{t_0}^{t} \sigma\left(\mathbf{m}(\tau)\right) \cdot \mathrm{d}\mathbf{W}(\tau) = \lim_{n\to\infty} \sum_{r=1}^{n-1} \sigma\left(\mathbf{m}(t_r)\right) \cdot [\mathbf{W}(t_{r+1}) - \mathbf{W}(t_r)]. \tag{10.18}$$

The second choice is based on the mid-point rule:

$$\int_{t_0}^{t} \sigma\left(\mathbf{m}(\tau)\right) \cdot \mathrm{d}\mathbf{W}(\tau) = \lim_{n\to\infty} \sum_{r=1}^{n-1} \frac{1}{2} \left[\sigma(\mathbf{m}(t_{r+1})) + \sigma(\mathbf{m}(t_r))\right] \cdot [\mathbf{W}(t_{r+1}) - \mathbf{W}(t_r)], \tag{10.19}$$

and is associated with the name of Stratonovich. Since these two different choices lead to different definitions of the stochastic integral and stochastic differential calculus, it is customary in stochastic analysis to speak of Itô or Stratonovich calculus [277,425].

The main advantage of the Itô calculus is that the random quantity $\sigma(\mathbf{m}(t_r))$ (which may depend on the value that the process $\mathbf{W}(t)$ has taken for $t \leq t_r$) is uncorrelated with the Wiener process increment $[\mathbf{W}(t_{r+1}) - \mathbf{W}(t_r)]$. This is a consequence of the fact that $\mathbf{W}(t)$ has independent increments. The absence of correlation between $\sigma(\mathbf{m}(t_r))$ and $[\mathbf{W}(t_{r+1}) - \mathbf{W}(t_r)]$ is instrumental in simplifying the derivation of main formulas. However, Itô calculus has also a major disadvantage: the rules of Itô calculus are different from the rules of ordinary calculus. The Stratonovich calculus, on the other hand, requires more involved derivations, since in each term of the integral sum in Eq. (10.19) the stochastic quantities $[\sigma(\mathbf{m}(t_{r+1})) + \sigma(\mathbf{m}(t_r))]$ and $[\mathbf{W}(t_{r+1}) - \mathbf{W}(t_r)]$ are

in fact correlated. The main advantage of Stratonovich calculus is that its rules coincide with the rules of ordinary calculus. This fact is the main reason why Stratonovich calculus is usually preferred in the physics literature [277].

The difficulty in evaluating stochastic integrals is related to the fact that the matrix $\sigma(\mathbf{m})$ depends on $\mathbf{m}$, which is a stochastic process correlated with $\mathbf{W}(t)$. In this situation, one speaks of multiplicative noise. In the case when the matrix σ does not depend on $\mathbf{m}$, one speaks of additive noise. In this case, no difficulty arises and the limit of the integral sum in Eq. (10.16) does not depend on the choice of τ_r. This also implies that for additive noise the values of Itô and Stratonovich integrals coincide.

The important conclusion of the above discussion is the following: a stochastic differential equation like Eq. (10.13) is not completely defined until one specifies which type of stochastic calculus (e.g. Itô or Stratonovich) is used. For this reason, it is natural to examine whether different interpretations of Eq. (10.13) may lead to different stochastic dynamics for which the magnetization magnitude may or may not be preserved.

In the discussion of this issue, we first introduce the following notation for Eq. (10.13):

$$\mathrm{d}\mathbf{m} = \mathbf{v}(\mathbf{m})\mathrm{d}t + \sigma(\mathbf{m}) \cdot \mathrm{d}\mathbf{W}, \tag{10.20}$$

or in terms of cartesian components:

$$\mathrm{d}m_k = v_k(\mathbf{m})\mathrm{d}t + \sum_h \sigma_{kh}(\mathbf{m})\mathrm{d}W_h. \tag{10.21}$$

The equation is formally written in terms of differentials of stochastic quantities but it has to be understood in the integral sense as Eq. (10.13).

Next, we interpret Eq. (10.20) in Stratonovich sense and we want to find out what type of Itô SDE produces a stochastic process equivalent to the one associated with the Stratonovich SDE (10.20). We illustrate this equivalence by using heuristic arguments based on the following discretized version of the Stratonovich SDE (10.21):

$$\Delta m_k = v_k(\mathbf{m}(t_r))\Delta t + \frac{1}{2}\sum_h \left[\sigma_{kh}(\mathbf{m}(t_{r+1})) + \sigma_{kh}(\mathbf{m}(t_r))\right]\Delta W_h, \tag{10.22}$$

where:

$$\begin{aligned} &\Delta W_h = W_h(t_{r+1}) - W_h(t_r), \qquad \Delta m_k = m_k(t_{r+1}) - m_k(t_r), \\ &\Delta t = t_{r+1} - t_r. \end{aligned} \tag{10.23}$$

By using Taylor expansion in the second term in the right-hand side of (10.22), we derive that:

$$\begin{aligned} &\frac{1}{2}\sum_h \left[\sigma_{kh}(\mathbf{m}(t_{r+1})) + \sigma_{kh}(\mathbf{m}(t_r))\right]\Delta W_h \\ &\quad \approx \sum_h \sigma_{kh}(\mathbf{m}(t_r))\Delta W_h + \frac{1}{2}\sum_{h,l}\left[\frac{\partial \sigma_{kh}}{\partial m_l}\right]_{t_r}\Delta m_l \Delta W_h. \end{aligned} \tag{10.24}$$

In Eq. (10.24) we have neglected terms which are infinitesimal with respect to Δt of order larger than one. The first term on the right-hand side of Eq. (10.24) is just the term corresponding to the Itô interpretation of $\sigma(\mathbf{m})\cdot d\mathbf{W}$. The difference between the Itô and Stratonovich interpretations is related to the second term in this equation. We want to extract from this term all expressions which are of order not larger than Δt. To this end, we substitute Eq. (10.22) into Eq. (10.24) and by using the fact that $\langle \Delta W_k \Delta W_h \rangle \approx \delta_{kh}\Delta t$ for small Δt (see Eq. (10.9)), we arrive at the following equation:

$$\begin{aligned} &\frac{1}{2}\sum_h \left[\sigma_{kh}(\mathbf{m}(t_{r+1})) + \sigma_{kh}(\mathbf{m}(t_r))\right]\Delta W_h \\ &\quad \approx \sum_h \sigma_{kh}(\mathbf{m}(t_r))\Delta W_h + \frac{1}{2}\sum_{h,l}\left[\sigma_{lh}\frac{\partial \sigma_{kh}}{\partial m_l}\right]_{t_r}\Delta t. \end{aligned} \tag{10.25}$$

Now by substituting Eq. (10.25) back into Eq. (10.22), and by passing to the limit $\Delta t \to 0$, we arrive at the following Itô SDE:

$$dm_k = \tilde{v}_k(\mathbf{m})dt + \sum_h \sigma_{kh}(\mathbf{m})dW_h, \tag{10.26}$$

where:

$$\tilde{v}_k(\mathbf{m}) = v_k(\mathbf{m}) + \frac{1}{2}\sum_{h,l}\sigma_{lh}(\mathbf{m})\frac{\partial}{\partial m_l}\sigma_{kh}(\mathbf{m}). \tag{10.27}$$

Thus, for an Itô equation to be equivalent to a Stratonovich equation, their drift terms must be related by Eq. (10.27). By using Eq. (10.15) one finds that:

$$\frac{1}{2}\sum_{h,l}\sigma_{lh}(\mathbf{m})\frac{\partial}{\partial m_l}\sigma_{kh}(\mathbf{m}) = -\nu^2 m_k. \tag{10.28}$$

By substituting Eqs (10.14) and (10.15) back into Eq. (10.20), we conclude that the stochastic LL equation:

$$\mathrm{d}\mathbf{m} = -\left[\mathbf{m}\times\mathbf{h}_{\text{eff}} + \alpha\mathbf{m}\times(\mathbf{m}\times\mathbf{h}_{\text{eff}})\right]\mathrm{d}t - \nu\mathbf{m}\times\mathrm{d}\mathbf{W}(t), \tag{10.29}$$

interpreted in the Stratonovich sense, is equivalent to the stochastic differential equation:

$$\begin{aligned}\mathrm{d}\mathbf{m} = &-\left[\mathbf{m}\times\mathbf{h}_{\text{eff}} + \alpha\mathbf{m}\times(\mathbf{m}\times\mathbf{h}_{\text{eff}})\right]\mathrm{d}t - \nu^2\mathbf{m}\mathrm{d}t\\ &-\nu\mathbf{m}\times\mathrm{d}\mathbf{W}(t),\end{aligned} \tag{10.30}$$

interpreted in the Itô sense.

Having established this equivalence, the discussion of the conservation of the magnetization magnitude is in order. Since in the case of Stratonovich calculus the ordinary rules of calculus apply, one has that $\mathrm{d}|\mathbf{m}|^2/\mathrm{d}t = 2\mathbf{m}\cdot\mathrm{d}\mathbf{m}/\mathrm{d}t = 0$ because, as is clear from Eq. (10.29), $\mathrm{d}\mathbf{m}$ can be written as $\mathrm{d}\mathbf{m} = \mathbf{m}\times(\ldots)$. In the case of Itô calculus, the reasoning is different. The differential of a generic scalar function $f(\mathbf{m}(t))$ of a stochastic process $\mathbf{m}(t)$ governed by the SDE (10.20) is given by the following expression known as the Itô lemma [277]:

$$\mathrm{d}f(\mathbf{m}) = \frac{\partial f(\mathbf{m})}{\partial\mathbf{m}}\cdot\mathrm{d}\mathbf{m} + \sum_{h,l}\frac{1}{2}\sigma_{lh}\frac{\partial^2 f}{\partial m_k\partial m_l}\sigma_{kh}\mathrm{d}t, \tag{10.31}$$

or in matrix form:

$$\mathrm{d}f = \frac{\partial f(\mathbf{m})}{\partial\mathbf{m}}\cdot\mathrm{d}\mathbf{m} + \frac{1}{2}\mathrm{tr}\left(\sigma\cdot\sigma^T\cdot\left[\frac{\partial^2 f}{\partial m_k\partial m_h}\right]\right)\mathrm{d}t, \tag{10.32}$$

where T denotes matrix transposition, and $\mathrm{tr}(\cdot)$ is the trace of the matrix. The additional term on the right-hand side, which is not present in ordinary calculus, can be justified on the basis of the following heuristic

considerations. By using the Taylor expansion of $f(\mathbf{m})$:

$$f(\mathbf{m}+\Delta\mathbf{m}) - f(\mathbf{m}) \approx \frac{\partial f(\mathbf{m})}{\partial \mathbf{m}} \cdot \Delta\mathbf{m} + \frac{1}{2}\sum_{k,l} \frac{\partial^2 f}{\partial m_k \partial m_l} \Delta m_k \Delta m_l, \tag{10.33}$$

then substituting into it the expression $\Delta\mathbf{m} = \mathbf{v}(\mathbf{m})\Delta t + \sigma(\mathbf{m}) \cdot \Delta\mathbf{W}$, and taking into account that $\langle \Delta W_k \Delta W_h \rangle \approx \delta_{kh}\Delta t$, one obtains from the second term in the right-hand side of Eq. (10.33) a term which is of first order in Δt. This term leads to the second term appearing in formula (10.31).

In the case of the LL equation, $\sigma_{kh}(\mathbf{m})$ is defined by Eq. (10.15), and:

$$[\sigma(\mathbf{m}) \cdot \sigma^T(\mathbf{m})]_{kh} = \nu^2(\mathcal{I}\delta_{kh}|\mathbf{m}|^2 - m_k m_h), \tag{10.34}$$

where $\mathcal{I}$ is the identity matrix. Thus, the Itô lemma and the LL equation yield:

$$\begin{aligned} \mathrm{d}f = {} & \frac{\partial f(\mathbf{m})}{\partial(\mathbf{m})} \cdot \mathrm{d}\mathbf{m} + \frac{\nu^2}{2}|\mathbf{m}|^2 \mathrm{tr}\left(\frac{\partial^2 f}{\partial m_k \partial m_h}\right) \mathrm{d}t \\ & - \frac{\nu^2}{2}\mathrm{tr}\left(\sum_r \left[m_k m_r \frac{\partial^2 f}{\partial m_r \partial m_h}\right]\right) \mathrm{d}t. \end{aligned} \tag{10.35}$$

Next, let us apply the Itô lemma to the scalar function:

$$f(\mathbf{m}) = \frac{1}{2}|\mathbf{m}|^2. \tag{10.36}$$

By using Eq. (10.35), one obtains that:

$$\frac{1}{2}\mathrm{d}|\mathbf{m}|^2 = \mathbf{m} \cdot \mathrm{d}\mathbf{m} + \nu^2|\mathbf{m}|^2 \mathrm{d}t. \tag{10.37}$$

Then, by substituting in this equation the expression (10.30) for $\mathrm{d}\mathbf{m}$, one finds:

$$\mathbf{m} \cdot \mathrm{d}\mathbf{m} + \nu^2|\mathbf{m}|^2 \mathrm{d}t = \mathbf{m} \cdot [\mathbf{m} \times (\cdots)]\,\mathrm{d}t - \nu^2 \mathbf{m} \cdot \mathbf{m}\mathrm{d}t + \nu^2|\mathbf{m}|^2 \mathrm{d}t = 0. \tag{10.38}$$

This result confirms that the Itô LL equation (10.30) also preserves the magnetization magnitude. This is expected, given the equivalence between the Itô LL equation (10.30) and the Stratonovich LL equation (10.29).

Finally, it is worthwhile mentioning that, if we interpret Eq. (10.29) in the sense of Itô and we apply again the Itô lemma, then we obtain that:

$$\frac{1}{2}\mathrm{d}|\mathbf{m}|^2 = \nu^2|\mathbf{m}|^2\mathrm{d}t, \tag{10.39}$$

which means that the magnitude of $\mathbf{m}$ is not preserved. This fact clearly indicates that the interpretation of Eq. (10.29) in the sense of Itô leads to stochastic magnetization dynamics which is not the dynamics on the unit sphere associated with the same equation when it is interpreted in the Stratonovich sense.

The analysis presented above is limited to the stochastic Landau–Lifshitz equation expressed by formulas (10.1), (10.2), and (10.29). However, thermal fluctuations may be also present in the generalized magnetization dynamics discussed in Chapter 3. For example, they are important in magnetization dynamics driven by spin-polarized currents. The general strategy that can be followed is the same: given the deterministic equation $\mathrm{d}\mathbf{m}/\mathrm{d}t = \mathbf{v}(\mathbf{m})$ (see Eq. (3.32)), add to it the random precessional torque $-\nu\mathbf{m} \times \mathbf{h}_N(t)$. This leads to the stochastic differential equation of the standard form:

$$\mathrm{d}\mathbf{m} = \mathbf{v}(\mathbf{m})\mathrm{d}t + \sigma(\mathbf{m}) \cdot \mathrm{d}\mathbf{W}, \tag{10.40}$$

where $\sigma(\mathbf{m})$ is given by Eq. (10.15). As discussed in Chapter 3, the deterministic drift $\mathbf{v}(\mathbf{m})$ can be always expressed in the form:

$$\mathbf{v}(\mathbf{m}) = \left[\mathbf{m} \times \frac{\partial g_L}{\partial \mathbf{m}} + \alpha\mathbf{m} \times \left(\mathbf{m} \times \frac{\partial \Phi}{\partial \mathbf{m}}\right)\right], \tag{10.41}$$

where the potential Φ coincides with the free energy g_L when thermal relaxation is the only important relaxation mechanism. It is shown in Chapter 9 that, when magnetization dynamics is driven by spin transfer, one has:

$$\Phi = g_L + \frac{\beta}{\alpha}\frac{\ln(1 + c_p\mathbf{m} \cdot \mathbf{e}_p)}{c_p}, \tag{10.42}$$

where the quantities β, c_p, and $\mathbf{e}_p$ characterize the spin-transfer mechanism.

The two-potential form (10.41) for $\mathbf{v}(\mathbf{m})$ is the most general form in which one can express a vector field on the unit sphere. For this reason, in the sequel, we shall often assume this form for $\mathbf{v}(\mathbf{m})$, as it includes as special cases all types of magnetization dynamics on the unit sphere. By following the same line of reasoning as we have used in the analysis of Eqs (10.1), (10.2) and (10.29), we can conclude that, when Eq. (10.40) is interpreted in the sense of Stratonovich, the magnetization dynamics preserves the magnetization magnitude.

In conclusion of this section, we briefly discuss how the presence of fluctuations affects the analysis carried out in Chapter 7 for a uniformly magnetized uniaxial particle subject to a circularly polarized applied magnetic field. This applied field is rotated around the z axis at the angular velocity ω. It was shown in Chapter 7 that in the analysis of this physical problem it is instrumental to study the dynamics in the rotating reference frame in which the rotating field is stationary. If we start from a stochastic LL equation of the type (10.1) and we pass to the reference frame rotated at the angular velocity ω around the z axis, the stochastic LL equation can be transformed as follows:

$$\frac{\mathrm{d}\mathbf{m}}{\mathrm{d}t} = -\mathbf{m} \times (\mathbf{h}_{\text{eff}} - \omega \mathbf{e}_z) - \alpha \mathbf{m} \times (\mathbf{m} \times \mathbf{h}_{\text{eff}}) - \nu \mathbf{m} \times \mathbf{h}'_N(t), \quad (10.43)$$

where $\mathbf{e}_z$ is the unit vector along the z axis, while:

$$\mathbf{h}'_N(t) = R(t) \cdot \mathbf{h}_N(t), \quad (10.44)$$

where $R(t)$ is the orthogonal matrix representing a rotation through the angle $-\omega t$ around the z axis. After this change of reference frame, the effective field in Eq. (10.43) does not depend explicitly on time anymore. It is important to examine the properties of the stochastic process $\mathbf{h}'_N(t)$. Since $\mathbf{h}'_N(t)$ is a linear transformation of $\mathbf{h}_N(t)$, $\mathbf{h}'_N(t)$ is a gaussian process. It is easy to check that $\mathbf{h}'_N(t)$ has zero statistical average:

$$\langle \mathbf{h}'_N(t) \rangle = R(t) \cdot \langle \mathbf{h}_N(t) \rangle = 0. \quad (10.45)$$

In addition:

$$\begin{aligned}\langle h'_{N,k}(t_1)h'_{N,h}(t_2)\rangle &= \sum_{r,s} R_{kr}(t_1)R_{hs}(t_2)\langle h_{N,r}(t_1)h_{N,s}(t_1)\rangle \\ &= \sum_{r,s} R_{kr}(t_1)R_{hs}(t_2)\delta_{rs}\delta(t_1-t_2) \\ &= \sum_{r} R_{kr}(t_1)R_{hr}(t_1)\delta(t_1-t_2) = \delta_{kh}\delta(t_1-t_2),\end{aligned} \tag{10.46}$$

where the sampling property of the Dirac delta function has been used, as well as the fact that $R(t)$ is an orthogonal matrix:

$$\sum_{r,s} R_{kr}(t)R_{hs}(t) = \delta_{kh}. \tag{10.47}$$

We have thus proved that $\mathbf{h}'_N(t)$ is a white-noise process with the same amplitude as $\mathbf{h}_N(t)$. As a consequence, Eq. (10.43) can be written as a stochastic differential equation of the form:

$$\mathrm{d}\mathbf{m} = [-\mathbf{m}\times(\mathbf{h}_{\text{eff}} - \omega\mathbf{e}_z) - \alpha\mathbf{m}\times(\mathbf{m}\times\mathbf{h}_{\text{eff}})]\,\mathrm{d}t - \nu\mathbf{m}\times\mathrm{d}\mathbf{W}. \tag{10.48}$$

It is worthwhile recalling that also in this case, the deterministic drift can be written in terms of two potentials:

$$\mathbf{v}(\mathbf{m}) = \mathbf{m}\times\frac{\partial\tilde{g_L}}{\partial\mathbf{m}} + \alpha\mathbf{m}\times\left(\mathbf{m}\times\frac{\partial g_L}{\partial\mathbf{m}}\right), \tag{10.49}$$

where $\tilde{g_L} = g_L + \omega\mathbf{e}_z$. In this sense, the general stochastic LL equation (10.40) with $\mathbf{v}(\mathbf{m})$ expressed in terms of two potentials includes as a particular case also the stochastic dynamics in rotating reference frames. More importantly, the nonstationary process describing magnetization dynamics in the laboratory frame is transformed into the stationary process defined by Eq. (10.48) in the rotating frame.

10.2 FOKKER–PLANCK EQUATION FOR STOCHASTIC MAGNETIZATION DYNAMICS

The analysis of stochastic dynamics based on stochastic differential equations (e.g., Eq. (10.20)) leads to a description of the stochastic process in terms of its realizations (paths). There is an alternative and equivalent

approach to the study of stochastic processes, which is based on the analysis of probability distributions and densities associated with the stochastic dynamics. This is the topic discussed in this section.

In general, a stochastic process $\mathbf{m}(t)$ can be fully described by the joint probability densities:

$$w(\mathbf{m}_1, t_1; \mathbf{m}_2, t_2; \ldots; \mathbf{m}_n, t_n) \tag{10.50}$$

of observing the values $\mathbf{m}_1, \mathbf{m}_2, \ldots, \mathbf{m}_n$, at the time instants $t_1 \leq \cdots \leq t_n$. The evolution of the stochastic process can be also characterized by the conditional probability densities:

$$\begin{aligned} &w(\mathbf{m}_n, t_n | \mathbf{m}_1, t_1; \mathbf{m}_2, t_2; \ldots; \mathbf{m}_{n-1}, t_{n-1}) \\ &\quad = \frac{w(\mathbf{m}_1, t_1; \mathbf{m}_2, t_2; \ldots; \mathbf{m}_n, t_n)}{w(\mathbf{m}_1, t_1; \mathbf{m}_2, t_2; \ldots; \mathbf{m}_{n-1}, t_{n-1})} \end{aligned} \tag{10.51}$$

of observing the value $\mathbf{m}_n$ at the time instant t_n under the condition that the process $\mathbf{m}(t)$ has taken values $\mathbf{m}_1, \mathbf{m}_2, \ldots, \mathbf{m}_{n-1}$ at previous time instants $t_1 \leq \cdots \leq t_{n-1}$. Strictly speaking, the complete statistical description of a stochastic process requires the knowledge of the joint distributions (10.50) for all n. In most applications, however, one deals with processes which do not require this complete characterization. In fact, processes generated by stochastic differential equations driven by white noise belong to the important class of Markov processes. Markov processes are characterized by the following property for the conditional probability densities:

$$w(\mathbf{m}_n, t_n | \mathbf{m}_1, t_1; \ldots; \mathbf{m}_{n-1}, t_{n-1}) = w(\mathbf{m}_n, t_n | \mathbf{m}_{n-1}, t_{n-1}), \tag{10.52}$$

for the ordered time instants $t_1 \leq \cdots \leq t_n$. This equation means that the probability density of observing the value $\mathbf{m}_n$ at the instant t_n, given the fact that we have observed values $\mathbf{m}_1, \ldots, \mathbf{m}_{n-1}$ at the previous instants $t_1 \leq t_2 \leq \cdots \leq t_{n-1}$, depends only on the value $\mathbf{m}_{n-1}$ at the time instant t_{n-1} just preceding t_n. By applying iteratively Eq. (10.52), one can prove that:

$$\begin{aligned} &w(\mathbf{m}_1, t_1; \ldots; \mathbf{m}_n, t_n) \\ &\quad = w(\mathbf{m}_n, t_n | \mathbf{m}_{n-1}, t_{n-1}) \cdots w(\mathbf{m}_2, t_2 | \mathbf{m}_1, t_1) w(\mathbf{m}_1, t_1), \end{aligned} \tag{10.53}$$

which demonstrates that the full statistical characterization of a Markov process is given by only two functions, namely, the transition probability

density:

$$w(\mathbf{m}, t|\mathbf{m}_0, t_0), \tag{10.54}$$

and the initial probability density:

$$w(\mathbf{m}_0, t_0). \tag{10.55}$$

Markov processes are the random counterpart of deterministic dynamical systems. A trajectory of a deterministic dynamical system is determined by the initial condition at the initial time instant t_0 and by the evolution rule which defines the state of the system at any subsequent time instant t. The evolution rule is normally specified implicitly through a differential equation. In the case of Markov processes, the evolution is determined by the initial condition, given by the initial probability density (10.55), and by the evolution rule associated with the transition probability density (10.54). In the case of stochastic processes, the evolution rule is usually specified by a partial differential equation whose unknown is the transition probability density (10.54). We shall next discuss this equation.

In the case of a stochastic process with continuous realizations generated by the solution of a stochastic differential equation, it can be shown [277] that the transition probability density satisfies the following diffusion equation:

$$\frac{\partial w}{\partial t} = -\sum_k \frac{\partial}{\partial m_k}[a_k(\mathbf{m}, t)w] + \frac{1}{2}\sum_{k,h} \frac{\partial}{\partial m_k \partial m_h}[b_{kh}(\mathbf{m}, t)w]. \tag{10.56}$$

This equation can be seen as a continuity equation for the conditional probability density:

$$\frac{\partial w}{\partial t} = -\sum_k \frac{\partial}{\partial m_k} J_k = -\nabla \cdot \mathbf{J}, \tag{10.57}$$

where $\mathbf{J}$ is the probability current density, J_k are its cartesian components, $\nabla\cdot$ is the divergence operator, and:

$$J_k = -a_k(\mathbf{m}, t)w + \frac{1}{2}\sum_h \frac{\partial}{\partial m_h}[b_{kh}(\mathbf{m}, t)w]. \tag{10.58}$$

This equation is usually referred to as the forward Kolmogorov equation or Fokker–Planck equation (the first designation is more

common in the mathematical literature). The coefficients $a_k(\mathbf{m}, t)$ and $b_{kh}(\mathbf{m}, t)$ are related to the stochastic dynamics in the manner discussed below. Suppose that the value $\mathbf{m}$ at time instant t is given and consider the stochastic quantity:

$$\Delta\mathbf{m} = \mathbf{m}(t + \Delta t) - \mathbf{m}, \tag{10.59}$$

which is the stochastic displacement of $\mathbf{m}$ during the time interval Δt. It can be shown [277] that the coefficients of the Fokker–Planck equation are related to the stochastic quantity $\Delta\mathbf{m}$ as follows:

$$a_k(\mathbf{m}, t) = \lim_{\Delta t \to 0} \frac{\langle \Delta m_k \rangle}{\Delta t}, \tag{10.60}$$

$$b_{kh}(\mathbf{m}, t) = \lim_{\Delta t \to 0} \frac{\langle \Delta m_k \Delta m_h \rangle}{\Delta t}. \tag{10.61}$$

These two formulas give an explicit procedure to compute the coefficients of the Fokker–Planck equation from the information about the local stochastic dynamics of $\mathbf{m}(t)$. In the case of our interest, the stochastic dynamics of $\mathbf{m}(t)$ is governed by a stochastic differential equation which provides explicit expressions for the stochastic displacements $\Delta\mathbf{m}$ (see Eq. (10.59)). Indeed, if the Itô differential equation (10.26) is used, then:

$$\Delta m_k \approx \tilde{v}_k(\mathbf{m}, t)\Delta t + \sum_h \sigma_{kh}(\mathbf{m}, t)\Delta W_h, \tag{10.62}$$

where:

$$\Delta W_h = \left[W_h(t + \Delta t) - W_h(t) \right]. \tag{10.63}$$

Since $\mathbf{m}$ is here assumed to be a given quantity, one finds:

$$\langle \sigma_{kh}(\mathbf{m}, t)\Delta W_h \rangle = \sigma_{kh}(\mathbf{m}, t)\langle \Delta W_h \rangle = 0. \tag{10.64}$$

By substituting Eq. (10.64) into Eq. (10.62) and into Eq. (10.60), one obtains:

$$a_k(\mathbf{m}, t) = \tilde{v}_k(\mathbf{m}, t). \tag{10.65}$$

In order to compute $b_{kh}(\mathbf{m},t)$, we consider the following covariance matrix:

$$\begin{aligned}\langle \Delta m_k \Delta m_h \rangle \approx & \sum_{r,s} \sigma_{kr}(\mathbf{m},t)\sigma_{hs}(\mathbf{m},t)\langle \Delta W_r \Delta W_s \rangle + \tilde{v}_k(\mathbf{m},t)\tilde{v}_h(\mathbf{m},t)\Delta t^2 \\ & + \tilde{v}_k(\mathbf{m},t)\sum_r \sigma_{hr}(\mathbf{m},t)\langle \Delta W_r \rangle \Delta t \\ & + \tilde{v}_h(\mathbf{m},t)\sum_s \sigma_{ks}(\mathbf{m},t)\langle \Delta W_s \rangle \Delta t. \end{aligned} \tag{10.66}$$

By using the Wiener process properties:

$$\langle \Delta W_k \rangle = 0, \qquad \langle \Delta W_r \Delta W_s \rangle = \delta_{rs}\Delta t, \tag{10.67}$$

and substituting Eq. (10.66) into Eq. (10.61), the following formula is obtained:

$$b_{kh}(\mathbf{m},t) = \sum_r \sigma_{kr}(\mathbf{m},t)\sigma_{hr}(\mathbf{m},t), \tag{10.68}$$

In matrix form, this formula can be written as:

$$b(\mathbf{m},t) = \sigma(\mathbf{m},t)\cdot\sigma^T(\mathbf{m},t), \tag{10.69}$$

where the superscript T denotes the transposed matrix.

The use of the Itô differential equation has led to a simple correspondence between SDE (10.26) and the associated diffusion equation (10.56). The deterministic drift term in the SDE (10.26) corresponds to the drift term in the Fokker–Planck equation (10.56), while the stochastic term in the SDE corresponds to the diffusion term in the Fokker–Planck equation. If one tries to derive the coefficients in Eq. (10.56) by using Eqs (10.60), (10.61), and the Stratonovich SDE (10.21), one has to take into account that:

$$\Delta m_k \approx v_k(\mathbf{m},t)\Delta t + \sum_h \sigma_{kh}(\mathbf{m}+\Delta\mathbf{m}/2,t)\Delta W_h. \tag{10.70}$$

In this case, the second term also contributes to the coefficient $a_k(\mathbf{m},t)$ since it contains terms of the first order in Δt. As expected, after

appropriate manipulations one obtains:

$$a_k(\mathbf{m},t) = v_k(\mathbf{m},t) + \frac{1}{2}\sum_{h,l}\sigma_{lh}(\mathbf{m},t)\frac{\partial}{\partial m_l}\sigma_{kh}(\mathbf{m},t). \tag{10.71}$$

For the coefficients $b_{kh}(\mathbf{m},t)$ the same formula (10.68) is obtained in the Stratonovich case as in the Itô case. It is apparent from Eqs (10.27), (10.65) and (10.71) that the final Fokker–Planck is the same for the Itô and Stratonovich SDE. In fact, while a stochastic process generated by a given SDE is fully defined only after the type of stochastic calculus is specified, the diffusion equation for the transition probability density is in one-to-one correspondence with the statistical properties of the stochastic process. Therefore, no ambiguity must arise when one describes a stochastic process by the associated Fokker–Planck equation.

As a result of the above discussion, we conclude that the Fokker–Planck equation can be written in terms of the vector $\mathbf{v}(\mathbf{m},t)$ and the matrix $\sigma(\mathbf{m},t)$ appearing in the SDE (10.21), as follows:

$$\begin{aligned}\frac{\partial w}{\partial t} = &-\sum_k \frac{\partial}{\partial m_k}\left\{\left[v_k(\mathbf{m},t) + \frac{1}{2}\sum_{h,l}\sigma_{lh}(\mathbf{m},t)\frac{\partial}{\partial m_l}\sigma_{kh}(\mathbf{m},t)\right]w\right\} \\ &+\frac{1}{2}\sum_{k,h}\frac{\partial^2}{\partial m_k \partial m_h}\left[\left(\sum_l \sigma_{kl}(\mathbf{m},t)\sigma_{hl}(\mathbf{m},t)\right)w\right].\end{aligned} \tag{10.72}$$

By rearranging the last two terms on the right-hand side, the equation can be written in the following equivalent form:

$$\begin{aligned}\frac{\partial w}{\partial t} = &-\sum_k \frac{\partial}{\partial m_k}\left[v_k(\mathbf{m},t)w\right] \\ &+\frac{1}{2}\sum_k \frac{\partial}{\partial m_k}\left\{\sum_r \sigma_{kr}(\mathbf{m},t)\sum_h \frac{\partial}{\partial m_h}\left[\sigma_{hr}(\mathbf{m},t)w\right]\right\}.\end{aligned} \tag{10.73}$$

This is a continuity equation of the form:

$$\frac{\partial w}{\partial t} = -\nabla\cdot\mathbf{J}, \tag{10.74}$$

where the cartesian components of the probability current $\mathbf{J}$ are expressed as:

$$J_k = v_k(\mathbf{m}, t)w - \frac{1}{2}\sum_r \sigma_{kr}(\mathbf{m}, t)\sum_h \frac{\partial}{\partial m_h}\left[\sigma_{hr}(\mathbf{m}, t)w\right]. \tag{10.75}$$

By using the expression (10.15) for the matrix $\sigma(\mathbf{m}, t)$, after appropriate algebraic manipulations one finds that:

$$\sum_h \frac{\partial}{\partial m_h}\left[\sigma_{hk}(\mathbf{m}, t)w\right] = \nu\left[\mathbf{m} \times \frac{\partial w}{\partial \mathbf{m}}\right]_k. \tag{10.76}$$

By substituting this last expression into Eq. (10.75), and using the two-potential form (10.41) of $\mathbf{v}$, one obtains the following expression for the probability current:

$$\begin{aligned}\mathbf{J} = &\left[\mathbf{m} \times \frac{\partial g_L}{\partial \mathbf{m}} + \alpha\mathbf{m} \times \left(\mathbf{m} \times \frac{\partial \Phi}{\partial \mathbf{m}}\right)\right] w \\ &+ \frac{\nu^2}{2}\mathbf{m} \times \left(\mathbf{m} \times \frac{\partial w}{\partial \mathbf{m}}\right).\end{aligned} \tag{10.77}$$

Equation (10.77) shows that $\mathbf{J}$ is always orthogonal to $\mathbf{m}$:

$$\mathbf{J} \cdot \mathbf{m} = 0, \tag{10.78}$$

which is the consequence of the fact that stochastic magnetization dynamics preserves the magnetization magnitude. This implies that, if the probability distribution w is initially different from zero only on the unit sphere Σ, its subsequent evolution for $t > t_0$ will take place only on Σ. For this reason, it is legitimate to recast the formulation of the diffusion process as a process taking place on Σ. We regard the vector $\mathbf{m}$ as a vector determining a point on Σ. When $\mathbf{m} \in \Sigma$, we can define the gradient operator on Σ as follows (see also Section 3.3):

$$\nabla_\Sigma f = -\mathbf{m} \times \left(\mathbf{m} \times \frac{\partial f}{\partial \mathbf{m}}\right), \tag{10.79}$$

where f is a generic function of $\mathbf{m}$. The operator (10.79) is the surface gradient operator associated with changes of $\mathbf{m}$ along the unit sphere.

Equations (10.74) and (10.77) can thus be written as:

$$\frac{\partial w}{\partial t} = -\mathrm{div}_{\Sigma}\mathbf{J}, \tag{10.80}$$

$$\mathbf{J} = \left[\mathbf{m} \times \nabla_{\Sigma} g_L - \alpha \nabla_{\Sigma}\Phi\right] w - \frac{\nu^2}{2}\nabla_{\Sigma} w, \tag{10.81}$$

where div_{Σ} represents the divergence operator on the unit sphere. This is the equation that fully describes the stochastic dynamics of $\mathbf{m}$ on Σ in terms of the transition probability density w.

It is important at this point to discuss how this Fokker–Planck equation is affected by the specific way in which noise is added to the deterministic magnetization dynamics. We shall examine this issue by considering the following generalized stochastic LL equation:

$$\begin{aligned} \mathrm{d}\mathbf{m} = &\left[\mathbf{m} \times \frac{\partial g_L}{\partial \mathbf{m}} + \alpha \mathbf{m} \times \left(\mathbf{m} \times \frac{\partial \Phi}{\partial \mathbf{m}}\right)\right] \mathrm{d}t \\ &- \nu_1 \mathbf{m} \times \mathrm{d}\mathbf{W} - \nu_2 \mathbf{m} \times (\mathbf{m} \times \mathrm{d}\mathbf{W}), \end{aligned} \tag{10.82}$$

in which two stochastic terms are present. The stochastic terms have been added in such a way that the stochastic dynamics preserves the magnetization magnitude, provided that the equation is interpreted in the Stratonovich sense. In repeating the same line of reasoning that was followed in the derivation of the Fokker–Planck equation, it must be taken into account that the matrix $\sigma(\mathbf{m})$ multiplying $\mathrm{d}\mathbf{W}$ in Eq. (10.82) is now given by:

$$\sigma(\mathbf{m}) = -\nu_1 \Lambda(\mathbf{m}) - \nu_2 \Lambda^2(\mathbf{m}), \tag{10.83}$$

where $\Lambda(\mathbf{m})$ represents the vector product operation, i.e., $\Lambda(\mathbf{v})\cdot\mathbf{w} = \mathbf{v}\times\mathbf{w}$. In cartesian components:

$$\Lambda(\mathbf{m}) = \begin{pmatrix} 0 & -\mathrm{m}_z & \mathrm{m}_y \\ \mathrm{m}_z & 0 & -\mathrm{m}_x \\ -\mathrm{m}_y & \mathrm{m}_x & 0 \end{pmatrix}. \tag{10.84}$$

Under these conditions, it can be shown that the matrix $b(\mathbf{m}) = \sigma(\mathbf{m}) \cdot \sigma^T(\mathbf{m})$ appearing in the Fokker–Planck equation has the form:

$$\begin{aligned} b(\mathbf{m}) &= \left(-\nu_1 \Lambda(\mathbf{m}) - \nu_2 \Lambda^2(\mathbf{m})\right) \cdot \left(\nu_1 \Lambda(\mathbf{m}) - \nu_2 \Lambda^2(\mathbf{m})\right) \\ &= -(\nu_1^2 + \nu_2^2)\Lambda^2(\mathbf{m}), \end{aligned} \tag{10.85}$$

where we have used the following properties of $\Lambda(\mathbf{m})$:

$$\begin{aligned} &\Lambda^T(\mathbf{m}) = -\Lambda(\mathbf{m}), \qquad \Lambda^2(\mathbf{m}) = \left[\Lambda^2(\mathbf{m})\right]^T, \\ &\Lambda^4(\mathbf{m}) = -\Lambda^2(\mathbf{m}). \end{aligned} \tag{10.86}$$

Equation (10.85) shows that all different choices for the intensity of the noise terms in Eq. (10.82) are physically equivalent up to a renormalization of the parameters ν_1 and ν_2.

Next, we discuss the issue of the equilibrium (stationary) probability associated with the Fokker–Planck Eqs (10.80) and (10.81). When excitation conditions (applied fields, injected currents, etc.) are constant in time, the conditional probability density reaches asymptotically a stationary distribution:

$$\lim_{t\to\infty} w(\mathbf{m}, t|\mathbf{m}_0, t_0) = w^{eq}(\mathbf{m}). \tag{10.87}$$

The probability density $w^{eq}(\mathbf{m})$ is the unique solution of the following stationary problem:

$$\frac{\nu^2}{2}\Delta_\Sigma w^{eq} - \mathrm{div}_\Sigma\left[(\mathbf{m}\times\nabla_\Sigma g_L - \alpha\nabla_\Sigma\Phi)\, w^{eq}\right] = 0, \tag{10.88}$$

where Δ_Σ is the Laplacian on the unit sphere. Equation (10.88) has to be solved under the normalization condition:

$$\oiint_\Sigma w^{eq}(\mathbf{m})\mathrm{d}S = 1. \tag{10.89}$$

The solution of this problem can be obtained in closed form in the special case when:

$$\Phi(\mathbf{m}) = F(g_L(\mathbf{m})), \tag{10.90}$$

where $F(g)$ is some scalar function. Under the condition (10.90), Eq. (10.88) can be written as:

$$\mathrm{div}_\Sigma\left[\frac{\nu^2}{2}\nabla_\Sigma w^{eq} - \alpha w^{eq} F'(g_L)\nabla_\Sigma g_L\right] - [\mathbf{m}\times\nabla_\Sigma g_L]\cdot\nabla_\Sigma w^{eq} = 0. \tag{10.91}$$

Now, we look for $w^{eq}(\mathbf{m})$ in the form:

$$w^{eq}(\mathbf{m}) = W_0(g_L(\mathbf{m})), \tag{10.92}$$

where $W_0(g)$ is an unknown scalar function. By using the last formula and the fact that:

$$[\mathbf{m} \times \nabla_\Sigma g_L] \cdot \nabla_\Sigma w^{eq} = W_0'(g_L)\,[\mathbf{m} \times \nabla_\Sigma g_L] \cdot \nabla_\Sigma g_L = 0, \tag{10.93}$$

Eq. (10.91) is reduced to:

$$\operatorname{div}_\Sigma \left[W_0(g_L) \frac{\mathrm{d}}{\mathrm{d}g_L} \left(\frac{\nu^2}{2} \log W_0 - \alpha F(g_L) \right) \nabla_\Sigma g_L \right] = 0. \tag{10.94}$$

This equation is satisfied for:

$$W_0(g_L) = \frac{1}{Z} \exp\left(-\mu F(g_L)\right), \tag{10.95}$$

where Z is a normalization constant and:

$$\mu = \frac{2\alpha}{\nu^2}. \tag{10.96}$$

The stationary distribution can thus be expressed as:

$$w^{eq}(\mathbf{m}) = \frac{1}{Z} \exp\left(-\mu F(g_L(\mathbf{m}))\right). \tag{10.97}$$

From the normalization condition (10.89), one obtains:

$$Z = \oiint_\Sigma \exp\left(-\mu F(g_L(\mathbf{m}))\right) \mathrm{d}S. \tag{10.98}$$

It is worth remarking that the existence of the closed-form expression (10.97) for the stationary distribution crucially depends on the validity of the condition (10.90). When this is not the case, closed-form solutions are very difficult to obtain.

An important special case where the condition (10.90) holds is when we deal with the classical Landau–Lifshitz stochastic equation (10.29), namely, when the deterministic drift is:

$$\begin{aligned}\mathbf{v}(\mathbf{m}) &= -\mathbf{m}\times\mathbf{h}_{\text{eff}} - \alpha\mathbf{m}\times(\mathbf{m}\times\mathbf{h}_{\text{eff}})\\ &= \mathbf{m}\times\frac{\partial g_L}{\partial\mathbf{m}} + \alpha\mathbf{m}\times(\mathbf{m}\times\frac{\partial g_L}{\partial\mathbf{m}}).\end{aligned} \tag{10.99}$$

In this case, $\Phi = g_L$ and $F(g) = g$. Thus, we have the following stationary probability density for the stochastic magnetization dynamics:

$$w^{eq}(\mathbf{m}) = \frac{1}{Z}\exp\left(-\mu g_L(\mathbf{m})\right), \tag{10.100}$$

with:

$$Z = \oiint_{\Sigma}\exp\left(-\mu g_L(\mathbf{m})\right)\mathrm{d}S. \tag{10.101}$$

From the physical point of view, the stochastic Landau–Lifshitz equation describes the magnetization dynamics in a small ferromagnetic particle driven by fluctuations caused by the contact with the thermal bath. The stationary distribution corresponds to the thermal equilibrium of the magnetic particle with the thermal bath. Under these conditions, it is known from statistical mechanics that the probability density has the form of the Boltzmann distribution:

$$w^{eq}(\mathbf{m}) = \frac{1}{Z}\exp\left(-\frac{G_L(\mathbf{m})}{k_BT}\right), \tag{10.102}$$

where $G_L(\mathbf{m})$ is the free energy of the magnetic particle, while k_B is Boltzmann constant. By comparing Eqs (10.100) and (10.102), one arrives at the following value for the constant μ:

$$\mu = \frac{\mu_0\mathrm{M}_s^2V}{k_BT} \tag{10.103}$$

where V is the volume of the particle, μ_0 is the vacuum permeability, and M_s is the saturation magnetization. The dimensional constant $\mu_0\mathrm{M}_s^2V$ takes into account that the free energy in physical units is given by $G_L(\mathbf{m}) = \mu_0\mathrm{M}_s^2Vg_L(\mathbf{m})$. The condition (10.103) on the constant μ leads to the following formula for the constant ν which controls the noise intensity:

$$\nu^2 = \frac{2\alpha k_BT}{\mu_0\mathrm{M}_s^2V}. \tag{10.104}$$

This relation is often referred to as the "fluctuation-dissipation" relation and it is very important in order to estimate the amplitude of fluctuations.

Strictly speaking, the fluctuation-dissipation relation is only valid for the stochastic Landau–Lifshitz dynamics in the vicinity of equilibrium. However, in the following we assume that the fluctuation-dissipation relation (10.104) remains valid even when the system is forced out of equilibrium by the presence of additional interactions such as the application of time-varying magnetic fields or the injection of electric currents. The justification of this assumption would require a more detailed discussion of the fluctuation-dissipation theorem for out-of-equilibrium processes, which goes beyond the scope of this book. Nevertheless, Eq. (10.104) is a reasonable starting point for the quantitative estimate of the intensity of thermal fluctuations.

We shall now discuss the evolution of the stochastic process $\mathbf{m}(t)$ when the initial condition is different from the stationary distribution we have derived above. To study the dynamics we have to study the evolution equation:

$$\frac{\partial w}{\partial t} = L_{FP} w \tag{10.105}$$

for the Fokker–Planck operator:

$$L_{FP} w = \frac{\nu^2}{2} \Delta_\Sigma w - \operatorname{div}_\Sigma \left[\left(\mathbf{m} \times \nabla_\Sigma g_L - \alpha \nabla_\Sigma \Phi \right) w \right], \tag{10.106}$$

with initial condition:

$$\lim_{t \to t_0} w(\mathbf{m}, t | \mathbf{m}_0, t_0) = \delta_\Sigma(\mathbf{m} - \mathbf{m}_0), \tag{10.107}$$

where $\delta_\Sigma(\mathbf{m} - \mathbf{m}_0)$ is the Dirac delta function on the sphere, defined as:

$$\oiint_\Sigma f(\mathbf{m}) \delta_\Sigma(\mathbf{m} - \mathbf{m}_0) \mathrm{d}S = f(\mathbf{m}_0) \tag{10.108}$$

for all continuous functions $f(\mathbf{m})$.

The solution to this problem can be found by using the classical procedure based on the eigenfunctions of the operator L_{FP} and its adjoint $L_{FP}^\dagger$. To define the adjoint operator, we first define the usual scalar product of two functions $f(\mathbf{m})$ and $g(\mathbf{m})$:

$$(f, g) = \oiint_\Sigma f^*(\mathbf{m}) g(\mathbf{m}) \mathrm{d}S, \tag{10.109}$$

where the symbol * denotes complex conjugate operation. The formal adjoint $L_{FP}^{\dagger}$ of the operator L_{FP} is the operator such that:

$$(f, L_{FP}g) = (L_{FP}^{\dagger}f, g), \tag{10.110}$$

where f and g are two sufficiently regular functions of $\mathbf{m}$. By using Eq. (10.106), and appropriate integration by parts, one can show that the adjoint operator has the following form:

$$L_{FP}^{\dagger}w = \frac{\nu^2}{2}\Delta_{\Sigma}w + [\mathbf{m} \times \nabla_{\Sigma}g_L - \alpha\nabla_{\Sigma}\Phi] \cdot \nabla_{\Sigma}w. \tag{10.111}$$

The solution to Eq. (10.105) can be constructed by using the eigenfunctions of the operators L_{FP} and $L_{FP}^{\dagger}$. In the case when the spectrum of these two operators is discrete, one has:

$$L_{FP}\varphi_r = \lambda_r\varphi_r, \quad r = 1, 2, \ldots \tag{10.112}$$

and

$$L_{FP}^{\dagger}\psi_r = \lambda_r^*\psi_r, \tag{10.113}$$

where φ_r and ψ_r are the right and left eigenfunctions of L_{FP}, respectively. One can readily prove that $(\psi_s, \varphi_r) = 0$ when $r \neq s$. This property is normally referred to as biorthogonality of the two sets of eigenfunctions φ_r and ψ_s. In addition, by appropriate scaling of these functions, it is possible to satisfy the normalization condition:

$$(\psi_s, \phi_r) = \delta_{rs}, \tag{10.114}$$

where δ_{rs} is the Kronecker delta symbol. Finally we assume (and this can be proved under quite general regularity conditions) that the system of biorthogonal eigenfunctions φ_r and ψ_s is complete. This can be expressed mathematically by the following completeness condition:

$$\sum_r \varphi_r(\mathbf{m})\psi_r^*(\mathbf{m}_0) = \delta_{\Sigma}(\mathbf{m} - \mathbf{m}_0), \quad \text{for all } \mathbf{m}, \mathbf{m}_0 \in \Sigma. \tag{10.115}$$

Once we have generated and computed a system of biorthogonal eigenfunctions, the general solution of the Fokker–Planck equation

(10.105) can be written as:

$$w(\mathbf{m},t|\mathbf{m}_0,t_0)=\sum_r \varphi_r(\mathbf{m})\psi_r^*(\mathbf{m}_0)\exp\left[\lambda_r(t-t_0)\right]. \tag{10.116}$$

This can be seen by substituting Eq. (10.116) into Eq. (10.105) and then using Eq. (10.112). In addition, due to the completeness condition (10.115), one can verify that the function in Eq. (10.116) satisfies the correct initial condition (10.107) for the conditional probability density.

It is worthwhile remarking that the first eigenvalue of L_{FP} is $\lambda_0=0$ as a consequence of the fact that the equation $L_{FP}w^{eq}=0$ admits a nonzero solution. The uniqueness of the problem $L_{FP}w^{eq}=0$, as we have discussed above, is enforced by imposing the normalization condition (10.89). It is interesting to note that the left eigenfunction ψ_0 associated with $\lambda_0=0$ is a constant. Then, if we set $\psi_0=1$, in order to satisfy the normalization condition $(\psi_0,\varphi_0)=1$, we have to choose:

$$\varphi_0(\mathbf{m})=w^{eq}(\mathbf{m}). \tag{10.117}$$

An additional property of the spectrum of L_{FP}, which is due to the diffusive nature of this operator, is that the eigenvalues λ_r have negative real part:

$$\mathrm{Re}\{\lambda_r\}\leq 0. \tag{10.118}$$

As a consequence of this property one finds that:

$$\begin{aligned}\lim_{t\to\infty} w(\mathbf{m},t|\mathbf{m}_0,t_0)&=\lim_{t\to\infty}\sum_r \varphi_r(\mathbf{m})\psi_r^*(\mathbf{m}_0)\exp\left[\lambda_r(t-t_0)\right]\\&=\varphi_0(\mathbf{m})=w^{eq}(\mathbf{m}),\end{aligned} \tag{10.119}$$

which is consistent with the fact that $w^{eq}(\mathbf{m})$ is the equilibrium probability density.

An additional property of the eigenfunctions can be derived from the orthogonality condition $(\psi_0,\varphi_r)=0$ for $r\geq 1$, and the fact that $\psi_0=1$. In fact one finds that all $\varphi_r(\mathbf{m})$ with $r\geq 1$ have zero average over the unit sphere:

$$\oiint_\Sigma \varphi_r(\mathbf{m})\mathrm{d}S=0 \quad \text{for all } r\geq 1. \tag{10.120}$$

This property is very important since w has to satisfy the condition:

$$\oiint_{\Sigma} w(\mathbf{m}, t|\mathbf{m}_0, t_0)\mathrm{d}S = 1 \quad \text{for all } t \geq 0, \tag{10.121}$$

where the surface integration is with respect to $\mathbf{m}$. This condition is readily verified by using Eqs (10.116) and (10.120), together with the fact that $\lambda_0 = 0$ and $\psi_0(\mathbf{m}_0) = 1$.

Finally, we briefly discuss the fact that the conditional probability must always satisfy the condition:

$$w(\mathbf{m}, t) = \oiint_{\Sigma} w(\mathbf{m}, t|\mathbf{m}_0, t_0)w^{eq}(\mathbf{m}_0)\mathrm{d}S_0 = w^{eq}(\mathbf{m}), \tag{10.122}$$

where the integration is now with respect to $\mathbf{m}_0$. The meaning of this equation is that if the dynamics starts from the stationary distribution then, at all subsequent instants of time, the probability distribution must coincide with the stationary distribution. This property can be formally established by using the biorthogonality condition (10.114) and Eq. (10.117), together with the fact that $\lambda_0 = 0$ and $\psi_0(\mathbf{m}_0) = 1$.

In conclusion of this section, we discuss how the Fokker–Planck equation (10.80)–(10.81) can be represented in different coordinate systems. We start by expressing the Fokker–Planck equation in terms of spherical coordinates (θ, ϕ), i.e., $\mathrm{m}_x = \sin\theta\cos\phi$, $\mathrm{m}_y = \sin\theta\sin\phi$, $\mathrm{m}_z = \cos\theta$. In this case, Eq. (10.80) can be written as:

$$\frac{\partial w}{\partial t} = -\frac{1}{\sin\theta}\frac{\partial}{\partial\theta}(\sin\theta J_\theta) - \frac{1}{\sin\theta}\frac{\partial J_\phi}{\partial\phi}, \tag{10.123}$$

where the components of the probability current along the unit vectors $\mathbf{e}_\theta$ and $\mathbf{e}_\phi$ are:

$$J_\theta = -\frac{w}{\sin\theta}\frac{\partial g_L}{\partial\phi} - \alpha w\frac{\partial\Phi}{\partial\theta} - \frac{\nu^2}{2}\frac{\partial w}{\partial\theta}, \tag{10.124}$$

$$J_\phi = w\frac{\partial g_L}{\partial\theta} - \frac{\alpha w}{\sin\theta}\frac{\partial\Phi}{\partial\phi} - \frac{\nu^2}{2}\frac{1}{\sin\theta}\frac{\partial w}{\partial\phi}. \tag{10.125}$$

In the above equations, the function w is $w(\theta, \phi, t|\theta_0, \phi_0, t_0)$, i.e., the conditional probability density $w(\mathbf{m}, t|\mathbf{m}_0, t)$ after both $\mathbf{m}$ and $\mathbf{m}_0$ have been expressed in terms of spherical coordinates. This implies that the probability of being inside a certain surface element $\mathrm{d}S$ of the unit

sphere is:

$$w(\mathbf{m}, t|\mathbf{m}_0, t)\mathrm{d}S = w(\theta, \phi, t|\theta_0, \phi_0, t_0)\sin\theta \mathrm{d}\theta\mathrm{d}\phi. \tag{10.126}$$

From this equation it is evident that the conditional probability density associated with the variables (θ, ϕ) is:

$$p(\theta, \phi, t|\theta_0, \phi_0, t_0) = w(\theta, \phi, t|\theta_0, \phi_0, t_0)\sin\theta. \tag{10.127}$$

In terms of p, Eqs (10.123)–(10.125) can be transformed as follows:

$$\frac{\partial p}{\partial t} = -\left(\frac{\partial \mathcal{J}_\theta}{\partial \theta} + \frac{\partial \mathcal{J}_\phi}{\partial \phi}\right), \tag{10.128}$$

where:

$$\mathcal{J}_\theta = \left[-\frac{1}{\sin\theta}\frac{\partial g_L}{\partial \phi} - \alpha\frac{\partial \Phi}{\partial \theta} + \frac{\nu^2}{2}\cot\theta\right]p - \frac{\nu^2}{2}\frac{\partial p}{\partial \theta}, \tag{10.129}$$

$$\mathcal{J}_\phi = \left[\frac{1}{\sin\theta}\frac{\partial g_L}{\partial \theta} - \frac{\alpha}{\sin^2\theta}\frac{\partial \Phi}{\partial \phi}\right]p - \frac{\nu^2}{2}\frac{1}{\sin\theta}\frac{\partial}{\partial \phi}\left(\frac{p}{\sin\theta}\right). \tag{10.130}$$

This form of the Fokker–Planck equation is instrumental in the derivation of the stochastic differential equation for $\mathbf{m}(t)$ on Σ. By using the correspondence between the Fokker–Planck equation and the Stratonovich stochastic differential equation, from Eqs (10.128), (10.129), and (10.130), one obtains the following Stratonovich equations:

$$\mathrm{d}\theta = \left[-\frac{1}{\sin\theta}\frac{\partial g_L}{\partial \phi} - \alpha\frac{\partial \Phi}{\partial \theta} + \frac{\nu^2}{2}\cot\theta\right]\mathrm{d}t + \nu\,\mathrm{d}W_\theta, \tag{10.131}$$

$$\mathrm{d}\phi = \left[\frac{1}{\sin\theta}\frac{\partial g_L}{\partial \theta} - \frac{\alpha}{\sin^2\theta}\frac{\partial \Phi}{\partial \phi}\right]\mathrm{d}t + \frac{\nu}{\sin\theta}\,\mathrm{d}W_\phi, \tag{10.132}$$

where $W_\theta(t)$ and $W_\phi(t)$ are two independent scalar Wiener processes. Equation (10.131) contains the noise-induced drift term $(\nu^2/2)\cot\theta$, the presence of which is not easy to derive when one assumes the stochastic differential equation for $\mathbf{m}$ as the starting point. Such noise-induced drift terms are the consequence of the representation of the sphere by curvilinear coordinates. The presence of these terms can be understood at the level of the stochastic differential equation, without passing through the Fokker–Planck equation, by considering the theory of stochastic

differential equations on manifolds [264]. This topic goes beyond the scope of this book and it is not discussed any further.

It is also useful to express the Fokker–Planck equation in terms of cylindrical coordinates (m_z, ϕ), i.e., $\mathrm{m}_x = \sqrt{1-\mathrm{m}_z^2}\cos\phi$, $\mathrm{m}_y = \sqrt{1-\mathrm{m}_z^2}\sin\phi$. This set of coordinates will be used later in this chapter in the study of uniaxial systems. In order to derive the Fokker–Planck equation in terms of (m_z, ϕ) coordinates, we start from Eqs (10.123)–(10.125), and by using the fact that $\mathrm{d}\mathrm{m}_z = \mathrm{d}(\cos\theta) = -\sin\theta \mathrm{d}\theta$, through appropriate algebraic manipulations, we arrive at the following equation:

$$\frac{\partial w}{\partial t} = -\frac{\partial \mathcal{J}_z}{\partial \mathrm{m}_z} - \frac{\partial \mathcal{J}_\phi}{\partial \phi}, \tag{10.133}$$

where:

$$\begin{aligned}\mathcal{J}_z = &\left[\frac{\partial g_L}{\partial \phi} - \alpha\left[1-\mathrm{m}_z^2\right]\frac{\partial \Phi}{\partial \mathrm{m}_z} - \nu^2 \mathrm{m}_z\right] w \\ &- \frac{\nu^2}{2}\sqrt{1-\mathrm{m}_z^2}\frac{\partial}{\partial \mathrm{m}_z}\left(\sqrt{1-\mathrm{m}_z^2}w\right),\end{aligned} \tag{10.134}$$

$$\begin{aligned}\mathcal{J}_\phi = &\left[-\frac{\partial g_L}{\partial \mathrm{m}_z} - \frac{\alpha}{\left[1-\mathrm{m}_z^2\right]}\frac{\partial \Phi}{\partial \phi}\right] w \\ &- \frac{\nu^2}{2}\frac{1}{\sqrt{1-\mathrm{m}_z^2}}\frac{\partial}{\partial \phi}\left(\frac{1}{\sqrt{1-\mathrm{m}_z^2}}w\right).\end{aligned} \tag{10.135}$$

Here w indicates the probability density in terms of (m_z, ϕ). We note that, since:

$$\begin{aligned}w(\mathbf{m}, t|\mathbf{m}_0, t)\mathrm{d}S &= w(\mathrm{m}_z, \phi, t|\mathrm{m}_{z0}, \phi_0, t_0)\sin\theta \mathrm{d}\theta \mathrm{d}\phi \\ &= -w(\mathrm{m}_z, \phi, t|\mathrm{m}_{z0}, \phi_0, t_0)\mathrm{d}\mathrm{m}_z \mathrm{d}\phi,\end{aligned} \tag{10.136}$$

no metric factor is needed to obtain the probability density. In other terms, $w(\mathrm{m}_z, \phi, t|\mathrm{m}_{z0}, \phi_0, t_0)$ is just the function $w(\mathbf{m}, t|\mathbf{m}_0, t)$ when $\mathbf{m}$ and $\mathbf{m}_0$ are expressed in terms of (m_z, ϕ) coordinates.

Equations (10.133)–(10.135) have the appropriate form to derive the corresponding stochastic differential equations for (m_z, ϕ) coordinates, by taking advantage of the equivalence between the Fokker–Planck equation and the Stratonovich stochastic differential equation. This leads to the following set of Stratonovich equations:

$$\mathrm{d}\mathrm{m}_z = \left[\frac{\partial g_L}{\partial \phi} - \alpha\left[1-\mathrm{m}_z^2\right]\frac{\partial \Phi}{\partial \mathrm{m}_z} - \nu^2 \mathrm{m}_z\right]\mathrm{d}t + \nu\sqrt{1-\mathrm{m}_z^2}\,\mathrm{d}W_z, \tag{10.137}$$

$$\mathrm{d}\phi = \left[-\frac{\partial g_L}{\partial \mathrm{m}_z} - \frac{\alpha}{[1-\mathrm{m}_z^2]}\frac{\partial \Phi}{\partial \phi}\right]\mathrm{d}t + \frac{\nu}{\sqrt{1-\mathrm{m}_z^2}}\mathrm{d}W_\phi. \qquad (10.138)$$

We note that also in this case, Eq. (10.137) contains a noise-induced drift term $-\nu^2 \mathrm{m}_z$.

10.3 ANALYSIS OF MAGNETIZATION DYNAMICS BY USING STOCHASTIC PROCESSES ON GRAPHS

In Chapter 5, it was discussed that two distinct time scales are typically present in magnetization dynamics: the fast time scale of precessional dynamics and the slow time scale of relaxation dynamics. The existence of two time scales was used to develop the averaging technique for the treatment of the slow-time-scale dynamics. These two time scales also exist in the stochastic magnetization dynamics induced by thermal fluctuations. In the general stochastic differential equation for the magnetization dynamics:

$$\mathrm{d}\mathbf{m} = \left[\mathbf{m}\times\frac{\partial g_L}{\partial \mathbf{m}} + \alpha\mathbf{m}\times\left(\mathbf{m}\times\frac{\partial \Phi}{\partial \mathbf{m}}\right)\right]\mathrm{d}t - \nu\mathbf{m}\times\mathrm{d}\mathbf{W}, \quad (10.139)$$

the existence of two time scales is related to the fact that the last two terms in this equation are usually small in comparison with the first term which describes the fast-time-scale precessional dynamics. For example, in the case of stochastic magnetization dynamics in spin-transfer-driven devices, described by the equation:

$$\mathrm{d}\mathbf{m} = \left[-\mathbf{m}\times\mathbf{h}_{\text{eff}} - \alpha\mathbf{m}\times(\mathbf{m}\times\mathbf{h}_{\text{eff}}) + \beta\frac{\mathbf{m}\times(\mathbf{m}\times\mathbf{e}_p)}{1+c_p\mathbf{m}\cdot\mathbf{e}_p}\right]\mathrm{d}t - \nu\mathbf{m}\times\mathrm{d}\mathbf{W}, \qquad (10.140)$$

the two distinct time scales occur because $\alpha \sim \beta \ll 1$ (see Chapter 9) and $\nu^2 \sim \alpha$ (see Eq. (10.104)).

In this section, we investigate how the presence of two distinct time scales can be used in the analysis of stochastic magnetization dynamics. The standard randomly perturbed magnetization dynamic equations, like Eq. (10.140), are written in terms of magnetization components which vary on the fast time scale. For this reason, the slow time scale of magnetization dynamics is concealed and obscured in these formulations. The slow-time-scale magnetization dynamics can be explicitly revealed by using the magnetic free energy as a state variable and by transforming the randomly

perturbed Landau–Lifshitz equation into a stochastic differential equation for the energy.

Some specific difficulties appear in the analysis of generalized Landau–Lifshitz dynamics described by Eq. (10.139), because this magnetization dynamics may exhibit both stable equilibria and stable limit cycles. The time scale of thermal transitions between stable equilibria is controlled by the energy barrier ΔE separating these equilibria. In particular, in the limit of large (with respect to $k_B T$) energy barriers, the time scale of thermal relaxation is given by the Arrhenius formula $\tau = \tau_0 \exp(\Delta E / k_B T)$, where the characteristic time constant τ_0 is typically of the order of 10^{-10}–10^{-11}s [8,275]. When self-oscillations (limit cycles) are present in addition to stationary equilibria, thermal fluctuations may induce switching between these qualitatively different steady states. The main problem is then to define the concept of effective potential barrier between a limit cycle and a stationary equilibrium, or between two limit cycles. It will be shown below that by taking advantage of the presence of two distinct time scales in the dynamics, it is indeed possible to give a precise definition of such effective potential barriers and derive analytical formulas for the description of thermally induced transitions between a limit cycle and an equilibrium state or between two limit cycles.

In order to develop the two-time-scale analysis, it is first necessary to introduce a convenient representation of conservative precessional magnetization dynamics, and then use this representation to compute the effect of damping, spin transfer, and thermal fluctuations by perturbation methods. A detailed analysis of precessional magnetization dynamics has been presented in Chapter 4. The precessional magnetization trajectories form a family of non-intersecting curves on the unit sphere Σ characterized by constant values of free energy. These curves are generated by the equation $g_L(\mathbf{m}) = g$ when g varies in an appropriate interval (see Figs 4.1, 4.7 and 4.9 for some examples). These trajectories define the phase portrait of the conservative dynamics. This phase portrait is completely characterized by the critical points, i.e., points where $\nabla_\Sigma g_L = 0$ (∇_Σ is the gradient operator on Σ). These critical points can be maxima, minima and saddles. The trajectories passing through saddles are called separatrices because they create a natural partition of the phase portrait into different central energy regions.

As discussed in Chapter 4, a natural way to describe the topological properties of the phase portrait of conservative dynamics is to specify the appropriate graph $\mathcal{G}$ (see Fig. 4.2). In this graph, each edge I_k represents a central region and each node corresponds to a saddle equilibrium and

the associated separatrices. The graph nodes will be labeled by using the same notation, $d_1, d_2, \ldots$, as used for saddles. We shall also introduce the following incidence function $I(d_h) = \{k_1, k_2, \ldots\}$, which for each node d_h gives the labels $(k_1, k_2, \ldots)$ of the edges connected to d_h. The edges are associated with the energy intervals $g_k^- < g < g_k^+$ (which will be also denoted as I_k) related to the kth central region. With the help of this graph, one can establish an unambiguous correspondence between magnetization trajectories and the values of the free energy: each magnetization trajectory is associated with one value of energy g and one value k (with $g \in I_k$), which identifies the central region to which the trajectory belongs. We shall use the notation $C_k(g)$ to indicate the closed trajectory on the unit sphere inside the kth central region (kth edge of the graph) for which $g_L(\mathbf{m}) = g$.

Next, we proceed to the study of the effect of perturbations on the precessional magnetization dynamics. Our starting point is the stochastic differential equation (10.139) for magnetization dynamics, and the corresponding Fokker–Planck equation (10.80) for the conditional probability density $w(\mathbf{m}, t|\mathbf{m}_0, t_0)$:

$$\frac{\partial w}{\partial t} = -\mathrm{div}_\Sigma \, \mathbf{J}. \tag{10.141}$$

The probability current density is given by Eq. (10.81), which we shall write in the form:

$$\mathbf{J} = (\mathbf{m} \times \nabla_\Sigma g_L - \alpha \nabla_\Sigma \Phi)\, w - \frac{\alpha}{\mu} \nabla_\Sigma w, \tag{10.142}$$

where $\mu = 2\alpha/\nu^2$. This form has the advantage that α appears explicitly in the second term of the probability current density (10.142). This will be instrumental in subsequent perturbation analysis based on the smallness of α. Equation (10.142) clearly shows that for small α the diffusion term and the nonconservative drift term can be regarded as perturbations of the precessional drift term. Additional small parameters that may be present in Φ are assumed to have the same order of smallness of α. In the specific case of injected spin-polarized currents, the ratio β/α is assumed to be finite. The values of the constants ν and μ are obtained through the fluctuation-dissipation theorem and they are:

$$\nu^2 = \frac{2\alpha k_B T}{\mu_0 \mathrm{M}_s^2 V}, \quad \mu = \frac{\mu_0 \mathrm{M}_s^2 V}{k_B T}, \tag{10.143}$$

as discussed in Section 10.2.

To simplify the notations, we shall omit the dependence of $w(\mathbf{m}, t|\mathbf{m}_0, t_0)$ on the backward coordinates $(\mathbf{m}_0, t_0)$ and we will simply write $w(\mathbf{m}, t)$ to indicate the unknown probability density in the Fokker–Planck equation (10.141)– (10.142). In fact, the backward coordinates appear as parameters and their presence is related to the initial condition imposed on the solution of Eqs (10.141)–(10.142).

To study Eqs (10.141)–(10.142) in the limit of small fluctuations and small nonconservative effects ($\alpha \ll 1$, $\nu \sim \sqrt{\alpha}$), it is convenient to use a coordinate system on the unit sphere in which the energy is one of the coordinate variables. In this coordinate system, the unit vectors:

$$\mathbf{e}_g = \frac{\nabla_\Sigma g_L}{|\nabla_\Sigma g_L|}, \quad \mathbf{e}_\psi = \mathbf{m} \times \mathbf{e}_g, \tag{10.144}$$

are orthogonal and tangential to constant-energy trajectories $C_k(g)$, respectively. The differential displacements $(\mathrm{d}m_g, \mathrm{d}m_\psi)$ along $\mathbf{e}_g$ and $\mathbf{e}_\psi$, associated with infinitesimal changes $(\mathrm{d}g, \mathrm{d}\psi)$ of the coordinates, are respectively given by:

$$\mathrm{d}m_g = \mathbf{e}_g \cdot \mathrm{d}\mathbf{m} = l_g \mathrm{d}g, \qquad \mathrm{d}m_\psi = \mathbf{e}_\psi \cdot \mathrm{d}\mathbf{m} = l_\psi \mathrm{d}\psi, \tag{10.145}$$

where l_g and l_ψ are appropriate metric factors. In particular, from Eq. (10.144) one finds that:

$$l_g = 1/|\nabla_\Sigma g_L|. \tag{10.146}$$

The coordinate system introduced above has the advantage that the two coordinates ψ and g are the fast and slow variables of the problem, respectively. Our goal is now to eliminate the fast variable and derive an approximated diffusion equation for the slow variable g.

The procedure to eliminate the fast variable ψ from the Fokker–Planck equations (10.141)–(10.142) can be devised as follows. We start by integrating both sides of (10.141) over the region of the unit sphere between the two curves $C_k(g + \Delta g)$ and $C_k(g)$. Then, by applying the divergence theorem, dividing both sides by Δg and taking the limit $\Delta g \to 0$, we obtain:

$$\frac{\partial}{\partial t}\rho_k(g, t) = -\frac{\partial}{\partial g} J_k(g), \tag{10.147}$$

where $\rho_k(g,t)$ is defined as:

$$\rho_k(g,t) = \oint_{C_k(g)} \frac{w(\mathbf{m},t)}{|\nabla_\Sigma g_L|} \mathrm{d}m_\psi. \tag{10.148}$$

The quantity:

$$J_k(g) = \oint_{C_k(g)} \mathbf{J}\cdot\mathbf{e}_g \, \mathrm{d}m_\psi \tag{10.149}$$

is the total probability current through the line $C_k(g)$ in the direction of increasing energy. By using Eq. (10.142) and the fact that $(\mathbf{m}\times\nabla_\Sigma g_L)\cdot\mathbf{e}_g = 0$, the probability current $J_k(g)$ can be rewritten as:

$$J_k(g) = -\alpha \oint_{C_k(g)} \left[(\nabla_\Sigma\Phi)w + \frac{1}{\mu}\nabla_\Sigma w\right]\cdot\mathbf{e}_g \, \mathrm{d}l. \tag{10.150}$$

The above Eqs (10.147), (10.149) and (10.150) are exact, and no approximations have been introduced yet. However, $J_k(g)$ is not a linear operator on $\rho_k(g)$ and thus Eq. (10.147) is not an evolution equation for $\rho_k(g)$. This difficulty can be circumvented by utilizing the fact that the actual magnetization dynamics can be regarded as a perturbation of the precessional dynamics. This implies that many precessional oscillations occur before the energy is appreciably affected by nonconservative effects and thermal fluctuations. In this situation, it is natural to consider the following approximation: on the slow time scale the density distribution $w(\mathbf{m},t)$ is almost uniform along each curve $g_L(\mathbf{m}) = g$. Accordingly, on the slow time scale the distribution function depends on $\mathbf{m}$ through $g_L(\mathbf{m})$:

$$w(\mathbf{m},t) \approx w_k(g_L(\mathbf{m}),t), \tag{10.151}$$

where the subscript k is used to indicate the central region to which $\mathbf{m}$ belongs. If we substitute Eq. (10.151) into Eq. (10.148), we obtain:

$$\rho_k(g,t) = w_k(g,t)T_k(g), \tag{10.152}$$

where:

$$T_k(g) = \oint_{C_k(g)} \frac{\mathrm{d}m_\psi}{|\nabla_\Sigma g_L|} \tag{10.153}$$

is the period of the precessional trajectory $C_k(g)$. In addition, from Eqs (10.150) and (10.151) we find that:

$$\begin{aligned} J_k(g) = &-\alpha w_k(g,t) \oint_{C_k(g)} \mathbf{e}_g \cdot \nabla_\Sigma \Phi \, \mathrm{d}m_\psi \\ &- \frac{\alpha}{\mu} \frac{\partial w_k}{\partial g} \oint_{C_k(g)} |\nabla_\Sigma g_L| \, \mathrm{d}m_\psi. \end{aligned} \tag{10.154}$$

The two functions of energy which appear in the right-hand side of Eq. (10.154) are Melnikov functions of the type introduced in Section 5.5:

$$M_k^0(g) = \oint_{C_k(g)} |\nabla_\Sigma g_L| \, \mathrm{d}m_\psi, \tag{10.155}$$

$$M_k(g,\zeta) = \oint_{C_k(g)} \mathbf{e}_g \cdot \nabla_\Sigma \Phi \, \mathrm{d}m_\psi, \tag{10.156}$$

where the parameter ζ generically represents the control parameters that may be present in the potential Φ. We shall assume that $\Phi \equiv g_L$ when $\zeta = 0$, which implies that $M_k(g, \zeta = 0) = M_k^0(g)$. Melnikov functions have been extensively used in our previous analysis of deterministic magnetization dynamics (see Chapters 5 and 9). The function $M_k^0(g)$ is always positive, while $M_k(g,\zeta)$ can be either positive or negative. Indeed, its zeros indicate the presence of limit cycles in the deterministic dynamics in the limit of small α. These functions can be put in the following line integral form:

$$M_k^0(g) = \oint_{C_k(g)} \left(\mathbf{m} \times \frac{\partial g_L}{\partial \mathbf{m}} \right) \cdot \mathrm{d}\mathbf{m}, \tag{10.157}$$

$$M_k(g,\zeta) = \oint_{C_k(g)} \left(\mathbf{m} \times \frac{\partial \Phi}{\partial \mathbf{m}} \right) \cdot \mathrm{d}\mathbf{m}, \tag{10.158}$$

which clearly shows that they depend only on the geometry of precessional trajectories and on the potentials g_L and Φ. By using the Melnikov functions (10.155) and (10.156), the probability current

density in Eq. (10.154) can be rewritten in the following form:

$$J_k(g) = -\alpha M_k(g,\zeta) w_k - \frac{\alpha}{\mu} M_k^0(g) \frac{\partial w_k}{\partial g}, \tag{10.159}$$

which, by using Eq. (10.152), can be expressed in terms of $\rho_k(g)$ as:

$$J_k(g) = -\alpha \left[\frac{M_k(g,\zeta)}{T_k(g)} \rho_k(g,t) + \frac{1}{\mu} M_k^0(g) \frac{\partial}{\partial g} \left(\frac{\rho_k(g,t)}{T_k(g)} \right) \right]. \tag{10.160}$$

By substituting the last equation in Eq. (10.147), we end up with the following diffusion equation for $\rho_k(g,t)$:

$$\frac{\partial}{\partial t} \rho_k(g,t) = \alpha \frac{\partial}{\partial g} \left[\frac{M_k(g,\zeta)}{T_k(g)} \rho_k(g,t) + \frac{1}{\mu} M_k^0(g) \frac{\partial}{\partial g} \left(\frac{\rho_k(g,t)}{T_k(g)} \right) \right], \tag{10.161}$$

which can be also expressed in terms of $w_k(g)$:

$$T_k(g) \frac{\partial}{\partial t} w_k(g,t) = \alpha \frac{\partial}{\partial g} \left[M_k(g,\zeta) w_k(g,t) + \frac{1}{\mu} M_k^0(g) \frac{\partial w_k}{\partial g} \right]. \tag{10.162}$$

The diffusion equations (10.161) and (10.162) are naturally defined on the graph $\mathcal{G}$ and they have to be complemented by appropriate initial, boundary, and normalization conditions. The normalization condition for $\rho_k(g,t)$ is obtained by using Eq. (10.185) in Eq. (10.182). This leads to the condition:

$$\sum_k \int_{I_k} \rho_k(g,t) \, \mathrm{d}g = 1, \tag{10.163}$$

where I_k are the edges of the energy graph $\mathcal{G}$. The normalization condition for $w_k(g,t)$ can be derived from Eq. (10.163) by using Eq. (10.152). One obtains:

$$\sum_k \int_{I_k} T_k(g) w_k(g,t) \, \mathrm{d}g = 1. \tag{10.164}$$

In addition to the normalization conditions (10.163) and (10.164), boundary conditions at the graph nodes are required for the probability distribution and the probability current, in order to solve (10.161) or (10.162) [265]. It is apparent that $w_k(g,t)$ must be continuous on the entire

graph, while the sum of all the incoming probability currents must be zero at each node of the graph. This means that, at the graph nodes:

$$w_{k_i}(g_{d_h}) = w_{k_j}(g_{d_h}), \quad \forall\, k_i, k_j \in I(d_h) \quad h = 1, 2, \ldots, \tag{10.165}$$

where g_{d_h} is the energy of the saddle point d_h and (as previously defined) $I(d_h)$ is the set of labeled edges touching the node d_h. The continuity of probability current (Kirchhoff's law for probability current) at the graph nodes is expressed as:

$$\sum_{k \in I(d_h)} J_k(g_{d_h}) = 0, \tag{10.166}$$

where $J_k(g_{d_h})$ is the current coming from the edge k to the node d_h.

So far, the separation of time scales for the stochastic magnetization dynamics has been accomplished at the level of Fokker–Planck equation, and this has led to the diffusion equation (10.161) for the probability density $\rho_k(g,t)$. The same scale separation can be considered at the level of the stochastic differential equation associated with the diffusion equation (10.161). To this end, we transform Eq. (10.161) to the following standard form:

$$\begin{aligned}\frac{\partial}{\partial t}\rho_k(g,t) = \frac{\partial}{\partial g}\Bigg[\alpha\left(\frac{M_k(g,\zeta)}{T_k(g)} - \frac{1}{\mu T_k(g)}\frac{\partial M_k^0(g)}{\partial g}\right)\rho_k(g,t) \\ + \frac{\alpha}{\mu}\frac{\partial^2}{\partial g^2}\left(\frac{M_k^0(g)}{T_k(g)}\rho_k(g,t)\right)\Bigg].\end{aligned} \tag{10.167}$$

By using the correspondence between Fokker–Planck and stochastic differential equations, one can infer from Eq. (10.167) that on each edge I_k of the graph $\mathcal{G}$ the magnetic free energy $g(t)$ satisfies the following Itô stochastic differential equation:

$$\mathrm{d}g = -\left(\alpha\frac{M_k(g,\zeta)}{T_k(g)} - \frac{\nu^2}{2T_k(g)}\frac{\partial M_k^0(g)}{\partial g}\right)\mathrm{d}t + \nu\sqrt{\frac{M_k^0(g)}{T_k(g)}}\mathrm{d}W, \tag{10.168}$$

where W is the scalar Wiener process. Equation (10.168) defines a Markovian process on the entire graph $\mathcal{G}$, provided the appropriate boundary conditions are imposed on g at each node of $\mathcal{G}$. These conditions are stated in the most general form in [265]. The stochastic differential equation (10.168) reveals the existence of the additional thermally

generated drift term $(\nu^2/2T_k(g))\partial M_k^0(g)/\partial g$, which is concealed in the conventional structure of the stochastic differential equation (10.139) with respect to $\mathbf{m}(t)$. This thermal drift term counteracts the traditional damping-based drift term and this results in measurable effects.

To demonstrate this, let us consider the stochastic dynamics (10.168) near equilibria, under the assumption of small thermal noise. Equation (10.168) can then be linearized around the given stable equilibrium point $g = g_s$. The first-order expansion of the various terms in the right-hand side of Eq. (10.168) can be expressed in a convenient form by using the following formula:

$$\frac{\partial M_k^0(g)}{\partial g} = \oint_{C_k(g)} \frac{\Delta_\Sigma g_L}{|\nabla_\Sigma g_L|} \mathrm{d}l, \tag{10.169}$$

where Δ_Σ is the Laplacian over the unit sphere Σ. The last formula is of interest in its own right. The derivation of this formula can be carried out by using the divergence theorem and it is based on arguments which are similar to ones used in the derivation of Eq. (10.147). One can check that near stable equilibria $\Delta_\Sigma g \approx c_k^0 > 0$. Then, by using formula (10.169) and assuming that $M_k(g,\zeta)$ depends linearly on ζ, as for example is the case for spin-transfer phenomena, we arrive at the following formulas for the linearized quantities:

$$\begin{aligned} M_k(g,\zeta) &\approx [c_k^0 + \zeta c_k^1] T_k(g_s)(g - g_s), \\ \frac{1}{T_k(g)} \frac{\partial M_k^0(g)}{\partial g} &\approx c_k^0 + d_k^0 (g - g_s), \end{aligned} \tag{10.170}$$

where:

$$d_k^0 = \left\{ \frac{\mathrm{d}}{\mathrm{d}g} [(1/T_k(g))(\partial M_k^0(g)/\partial g)] \right\} \Big|_{g=g_s}. \tag{10.171}$$

By using formulas (10.170), the stochastic differential equation (10.168) can be transformed as follows:

$$\frac{\mathrm{d}g}{\mathrm{d}t} + \alpha[c_k^0 + \zeta c_k^1 + (\nu^2/2) d_k^0](g - g_s) = \frac{\nu^2 c_k^0}{2} + \nu \sqrt{c_k^0 (g - g_s)} \frac{\mathrm{d}W_t}{\mathrm{d}t}. \tag{10.172}$$

From Eq. (10.172), we derive the following differential equation for the expected energy value $\overline{g}(t)$:

$$\frac{\mathrm{d}\overline{g}}{\mathrm{d}t} + \alpha c_k(\overline{g} - g_s) = \frac{\nu^2 c_k^0}{2}, \tag{10.173}$$

where $c_k = [c_k^0 + \zeta c_k^1 + (\nu^2/2)d_k^0]$. The solution of the last equation can be written in the form:

$$\overline{g}(t) = g_s + \frac{\nu^2}{2\alpha}\frac{c_k^0}{c_k} + A\exp\left[-\alpha c_k t\right]. \tag{10.174}$$

Formula (10.174) reveals that the thermally generated energy drift results in the shift $\overline{g}_{eq}$ of the expected energy value near equilibria:

$$\begin{aligned}\overline{g}_{eq} &= \frac{[\nu^2/(2\alpha)]}{1 + \zeta c_k^1/c_k^0 + [\nu^2/(2\alpha)](d_k^0/c_k^0)} \\ &= \frac{\frac{k_B T}{\mu_0 \mathrm{M}_s^2 V}}{1 + \zeta c_k^1/c_k^0 + \frac{k_B T}{\mu_0 \mathrm{M}_s^2 V}(d_k^0/c_k^0)},\end{aligned} \tag{10.175}$$

where V is the volume of the magnetic particle. The last equality follows from the fluctuation-dissipation theorem and the normalization of magnetization and effective field. In the absence of nonconservative driving actions ($\zeta = 0$) and for sufficiently small fluctuations, Eq. (10.175) yields $\overline{g}_{eq} = k_B T/\mu_0 \mathrm{M}_s^2 V$ as expected from the equipartition theorem.

In the final part of this section, we discuss how the key assumption (10.151), which has been instrumental in the elimination of fast variables, can be justified in rigorous terms through the perturbation analysis explicitly based on the smallness of α. This leads to a derivation of Eqs (10.161)–(10.162) by using the reasoning which can be traced back to Kramers' treatment of fluctuations in nonlinear oscillators [416] in the limit of small damping and noise.

This analysis starts by rewriting the Fokker–Planck equation (10.141) and (10.142) in terms of the coordinates (g, ψ) and of the index k labeling the appropriate central energy region:

$$\frac{\partial \rho_k}{\partial t} = -\frac{\partial}{\partial g}\left(l_\psi J_{k,g}\right) - \frac{\partial}{\partial \psi}\left(l_g J_{k,\psi}\right), \tag{10.176}$$

where l_g and l_ψ are the metric factors introduced in Eq. (10.145), while:

$$\rho_k(g,\psi,t) = w_k(g,\psi,t) l_g l_\psi \tag{10.177}$$

is the probability density function of (g,ψ). In these equations, $w_k(g,\psi,t)$ is the function $w(\mathbf{m},t)$ expressed in terms of the coordinates (g,ψ), whereas:

$$J_{k,g} = \mathbf{J}\cdot\mathbf{e}_g = -\alpha\left(\frac{w_k}{l_g}\frac{\partial\Phi}{\partial g} + \frac{1}{\mu l_g}\frac{\partial w_k}{\partial g}\right) \tag{10.178}$$

and:

$$J_{k,\psi} = \mathbf{J}\cdot\mathbf{e}_\psi = \frac{w_k}{l_g} - \alpha\left(\frac{w_k}{l_\psi}\frac{\partial\Phi}{\partial\psi} + \frac{1}{\mu l_\psi}\frac{\partial w_k}{\partial\psi}\right) \tag{10.179}$$

are the probability currents along $\mathbf{e}_g$ and $\mathbf{e}_\psi$, respectively. In terms of these coordinates, the Melnikov functions (10.155) and (10.156) can be written as:

$$M_k^0(g) = \oint_{C_k(g)} \frac{1}{l_g}\mathrm{d}m_\psi = \oint_{C_k(g)} |\nabla_\Sigma g|\mathrm{d}m_\psi, \tag{10.180}$$

$$M_k(g,\zeta) = \oint_{C_k(g)} \frac{1}{l_g}\frac{\partial\Phi}{\partial g}\mathrm{d}m_\psi. \tag{10.181}$$

The probability density $\rho_k(g,\psi,t)$ satisfies the usual normalization conditions on the unit sphere:

$$\sum_k \int_{I_k} \mathrm{d}g \int_0^{2\pi} \rho_k(g,\psi,t)\,\mathrm{d}\psi = 1. \tag{10.182}$$

Similarly, $w_k(g,\psi,t)$ has to satisfy the following normalization condition:

$$\sum_k \int_{I_k} \mathrm{d}g \int_0^{2\pi} w_k(g,\psi,t) l_g l_\psi\,\mathrm{d}\psi = 1. \tag{10.183}$$

The starting point for the perturbation analysis is to write the probability density $\rho_k(g,\psi,t)$ as:

$$\rho_k(g,\psi,t) = \rho_k(\psi,t|g)\rho_k(g,t), \tag{10.184}$$

where $\rho_k(\psi, t|g)$ is the conditional probability density and:

$$\rho_k(g,t) = \int_0^{2\pi} \rho_k(\psi, g, t)\mathrm{d}\psi. \tag{10.185}$$

By taking into account Eqs (10.145), (10.146), and (10.177), the last formula can be written in the form:

$$\rho_k(g,t) = \int_0^{2\pi} \rho_k(\psi, g, t)\mathrm{d}\psi = \oint_{C_k(g)} \frac{w(\mathbf{m},t)}{|\nabla_\Sigma g_L|}\mathrm{d}m_\psi. \tag{10.186}$$

In the limit of small α, the energy remains practically constant for a large number of periods of oscillation and appreciable time variations of $\rho_k(g,t)$ are expected to occur only on a time scale of the order of $1/\alpha$. This suggests that $J_{k,g}$ is proportional to α. In fact, by integrating Eq. (10.176) with respect to ψ in the interval $[0, 2\pi]$ and taking into account the periodicity of all quantities with respect to ψ, one obtains that $\partial\rho_k(g,t)/\partial t$ is first-order in α. On the other hand, the conditional distribution $\rho_k(\psi, t|g)$ has a fast time variation regardless of the smallness of α, i.e., $\partial\rho_k(\psi, t|g)/\partial t$ is zeroth order with respect to α. The averaging method is based on the fact that the conditional probability distribution $\rho_k(\psi, t|g)$ reaches equilibrium on the short time scale well before any appreciable change in $\rho_k(g,t)$ occurs [640]. Thus, on the long time scale we have:

$$\rho_k(g, \psi, t) = \rho_k^{eq}(\psi|g)\rho_k(g,t) + \mathcal{O}(\alpha), \tag{10.187}$$

where $\rho_k^{eq}(\psi|g)$ is the equilibrium distribution of $\rho_k(\psi, t|g)$. This equilibrium conditional probability can be found by differentiating Eq. (10.184) with respect to time, then substituting it in Eq. (10.176), and retaining only the zeroth-order terms with respect to α. In this way, we obtain the equation:

$$\frac{\partial}{\partial t}\rho_k(\psi, t|g) = \frac{\partial}{\partial \psi}\left(\frac{\rho_k(\psi, t|g)}{l_g l_\psi}\right). \tag{10.188}$$

The stationary solution $\rho_k^{eq}(\psi|g)$ satisfies the equation:

$$\frac{\partial}{\partial \psi}\left(\frac{\rho_k^{eq}(\psi|g)}{l_g l_\psi}\right) = 0, \tag{10.189}$$

whose solution is:

$$\rho_k^{eq}(\psi|g) = f_k(g) l_g l_\psi, \tag{10.190}$$

where $f_k(g)$ is a function of energy to be determined through the normalization condition:

$$\int_0^{2\pi} \rho_k^{eq}(\psi|g) \mathrm{d}\psi = 1. \tag{10.191}$$

By using Eqs (10.145), (10.146), (10.190), and (10.191), one finds that $c_k(g) = 1/T_k(g)$, which yields:

$$\rho_k^{eq}(\psi|g) = \frac{l_g l_\psi}{T_k(g)}. \tag{10.192}$$

This equation has interesting physical implications. By multiplying both sides of the equation by the differential increment $\mathrm{d}\psi$, we obtain:

$$\rho_k^{eq}(\psi|g)\mathrm{d}\psi = \frac{l_g l_\psi \mathrm{d}\psi}{T_k(g)} = \frac{l_g \mathrm{d}m_\psi}{T_k(g)} = \frac{1}{T_k(g)} \frac{\mathrm{d}m_\psi}{|\nabla_\Sigma g_L|}. \tag{10.193}$$

The ratio $\mathrm{d}m_\psi/|\nabla_\Sigma g_L|$ is equal to the time spent by the precessional trajectory along the arc of length $\mathrm{d}m_\psi$ around the point ψ. Thus, Eq. (10.193) has the following "time" interpretation: the probability of being around a certain point ψ of the precessional trajectory $C_k(g)$ is proportional to the fraction of time that the precessing magnetization spends around ψ. In other terms, the equilibrium conditional probability density on the trajectory $C_k(g)$ is inversely proportional to the velocity of precessional motion along $C_k(g)$.

Equations (10.177), (10.187) and (10.192) imply that $w_k(g, \psi, t)$ is given by:

$$w_k(g, \psi, t) = \frac{\rho_k(g, t)}{T_k(g)} + \mathcal{O}(\alpha), \tag{10.194}$$

where $\mathcal{O}(\alpha)$ denotes terms which are first or higher order in α. Thus, up to first-order terms in α, $w_k(g, \psi, t)$ is in fact independent of ψ. This conclusion justifies the approximation expressed by Eq. (10.151). The function $w_k(g, t)$ in that expression can be interpreted as the dominant part of the expansion of $w_k(g, \psi, t)$ in terms of α. In other words, for small α,

the dependence of $w_k(g, \psi, t)$ on ψ is a higher-order effect. The averaging approximation amounts to neglecting this effect.

10.4 STATIONARY DISTRIBUTIONS AND THERMAL TRANSITIONS

A fundamental role in stochastic magnetization dynamics is played by the stationary distribution asymptotically approached at large times:

$$w_k^{eq}(g) = \lim_{t\to\infty} w_k(g, t). \tag{10.195}$$

To determine $w_k^{eq}(g)$, we rewrite the probability current density (10.159) in the following form:

$$J_k(g) = -\frac{\alpha}{\mu} M_k^0(g) \left(\mu \frac{\partial V_k(g)}{\partial g} w_k(g, t) + \frac{\partial}{\partial g} w_k(g, t) \right), \tag{10.196}$$

where we have introduced the effective potential $V_k(g)$ defined as:

$$\frac{\partial V_k(g)}{\partial g} = \frac{M_k(g, \zeta)}{M_k^0(g)}. \tag{10.197}$$

By integrating this expression along the edge I_k of the graph, we arrive at the following expression:

$$V_k(g) = \int_{g_k^-}^{g} \frac{M_k(u, \zeta)}{M_k^0(u)} \mathrm{d}u + c_k, \tag{10.198}$$

where g_k^- is the lower energy bound on I_k and c_k is some integrating constant. By multiplying both sides of Eq. (10.196) by the integrating factor $\exp(\mu V_k(g))$ we obtain:

$$J_k(g) = -\frac{\alpha}{\mu} M_k^0(g) \exp\left(-\mu V_k(g)\right) \frac{\partial}{\partial g} \left[\exp\left(\mu V_k(g)\right) w_k(g) \right]. \tag{10.199}$$

The stationary distribution function can be derived from the condition $J_k(g) = 0$, which yields:

$$w_k^{eq}(g) = A_k \exp\left(-\mu V_k(g)\right), \tag{10.200}$$

as immediately apparent from Eq. (10.199). It follows from this expression that Eq. (10.166) is satisfied, since all the currents $J_k(g)$ are identically zero. The constant A_k should be chosen in order to fulfill the normalization condition (10.164) and the continuity conditions (10.165) at the graph nodes. The constants c_k in Eq. (10.198) can be used for this purpose. First, we note that, with no lack of generality, $w_k^{eq}(g)$ can be represented in the form:

$$w_k^{eq}(g) = A_0 \exp\left(-\mu V_k(g)\right), \tag{10.201}$$

where A_0 is the same for all I_k in $\mathcal{G}$. The condition (10.165) can be satisfied if we choose the constants c_k in the expression for V_k in such a way that:

$$V_{k_i}(g_{d_h}) = V_{k_j}(g_{d_h}), \quad \forall k_i, k_j \in I(d_h) \quad h = 1, 2, \ldots. \tag{10.202}$$

It remains to determine the value of A_0. This constant can be found from the normalization condition (10.164), which leads to the following result:

$$\frac{1}{A_0} = Z(\mu) = \sum_k \int_{I_k} \exp\left(-\mu V_k(g)\right) T_k(g)\, \mathrm{d}g, \tag{10.203}$$

where $Z(\mu)$ is a sort of partition function. Thus, the stationary distribution function can be written in the following form:

$$w_k^{eq}(g) = \frac{1}{Z(\mu)} \exp\left(-\mu V_k(g)\right). \tag{10.204}$$

The expression (10.204) for $w_k^{eq}(g)$ is formally coincident with the canonical Boltzmann distribution, with $Z(\mu)$ and $V_k(g)$ playing the role of partition function and potential energy, respectively. The functions $Z(\mu)$ and $V_k(g)$ depend on the Melnikov function $M_k(g, \zeta)$, which is related to the potential Φ (see Eq. (10.158)). When thermal relaxation is the only important mechanism, then $\Phi(\mathbf{m}) = g_L(\mathbf{m})$ and the Melnikov function $M_k(g, \zeta)$ is reduced to $M_k^0(g)$ (see Eq. (10.157)). In this case, one finds from formulas (10.198) and (10.202) that $V_k(g) = g$ for all edges of the graphs, which implies that $Z(\mu)$ and $w_k(g)$ take indeed their usual meaning of partition function and canonical distribution function, respectively. However, under the presence of additional nonconservative driving actions, $\Phi(\mathbf{m}) \neq g_L(\mathbf{m})$, $V_k(g) \neq g$, and the distribution $w_k^{eq}(g)$ cannot be interpreted as an equilibrium distribution anymore. In those

cases, it rather represents the steady-state out-of-equilibrium distribution induced by the driving actions accounted for by the potential $\Phi(\mathbf{m})$.

In general, the stationary distribution for the randomly perturbed magnetization dynamics driven by two potentials g_L and Φ can be determined in closed form only in very special cases. Equation (10.204) shows that by using the technique of stochastic processes on graphs, one can obtain closed form (albeit approximate) solutions under more general conditions.

It is beneficial to gain some insight into the qualitative properties of the potential function $V_k(g)$ and the related properties of the stationary distribution (10.204). The function $V_k(g)$ plays the role of effective potential governing the stochastic dynamics. This fact is better appreciated by comparing it with the potential $U_k(g)$ introduced in the analysis of deterministic dynamics (see Eq. (5.150)) in the framework of the averaging technique. We recall that the slow deterministic dynamics of energy can be described by the equation:

$$\frac{\mathrm{d}g}{\mathrm{d}t} = -\alpha \frac{\partial U_k}{\partial g}, \tag{10.205}$$

where the effective potential $U_k(g)$ is defined, up to a constant, as:

$$U_k(g) = \int_{g_k^-}^{g} \frac{M_k(u,\zeta)}{T_k(u)} \mathrm{d}u. \tag{10.206}$$

By comparing Eq. (10.206) with Eq. (10.197), we find that the potentials V_k and U_k are connected by the following relation:

$$\frac{\partial V_k(g)}{\partial g} = \frac{T_k(g)}{M_k^0(g)} \frac{\partial U_k(g)}{\partial g}. \tag{10.207}$$

Since both M_k^0 and T_k are positive-definite, V_k and U_k exhibit the same maxima and minima. Therefore, according to Eq. (10.204), the stationary distribution function w_k^{eq} is peaked around the stable states of the deterministic dynamics, which can be either fixed points (stationary states) or limit cycles (self-oscillation states).

To be more specific, let us consider the case of spin-polarized current injection. In this case (see Chapter 9 for the definition of the various parameters):

$$\Phi(\mathbf{m}) = g_L(\mathbf{m}) + \frac{\beta}{\alpha} \frac{\ln(1 + c_p \mathbf{m} \cdot \mathbf{e}_p)}{c_p}. \tag{10.208}$$

By substituting Eq. (10.208) into Eq. (10.158), we get the following expression for the Melnikov function:

$$M_k(g, \beta/\alpha) = M_k^0(g) + \frac{\beta}{\alpha} M_k^1(g), \tag{10.209}$$

where:

$$M_k^1(g) = \oint_{C_k(g)} \frac{\mathbf{m} \times (\mathbf{m} \times \mathbf{e}_p)}{1 + c_p \mathbf{m} \cdot \mathbf{e}_p} \cdot \mathbf{e}_g \mathrm{d}m_\psi. \tag{10.210}$$

This implies that the effective potential can be written as:

$$V_k(g) = g + \frac{\beta}{\alpha} \int_{g_k^-}^{g} \frac{M_k^1(u)}{M_k^0(u)} \mathrm{d}u + c_k - g_k^-, \tag{10.211}$$

where again c_k can be chosen to make $V_k(g)$ continuous on the entire graph $\mathcal{G}$.

As discussed in Chapter 9, the Melnikov functions $M_k^0(g)$ and $M_k(g, \beta/\alpha)$ can be computed analytically by using the analytical solutions of the conservative magnetization dynamics (see Chapter 4). Then, through Eq. (10.211), one can compute the effective potential governing the probability distribution $w_k^{eq}(g)$ of the problem. We present here an example of such computations for the case shown in Fig. 10.1. The applied field is along the easy axis of the particle (x axis) and its value is such that the phase portrait of the conservative dynamics is partitioned into three central regions, with two energy maxima and one energy minimum. The two central regions corresponding to the energy maxima are symmetric and, therefore, correspond to the same range of energy values. The associated graph has three edges, with one node. In Fig. 10.2, the computed Melnikov functions for each edge, the effective potential and the stationary distribution are represented. As expected, the distribution w^{eq} is peaked around the minima of the effective potential and depressed around the maxima.

Figure 10.3(a)–(d) illustrates how the effective potential and the stationary distribution are affected by changes of the injected spin-polarized current (i.e., of the parameter β/α). Under increasing spin-polarized current, one peak of the distribution is decreased while another is increased. At intermediate current values, w^{eq} is characterized by two peaks (see Fig. 10.3(b)). Multiple peaks in the stationary distribution indicate the presence of multiple stable steady states. For example, in the case of Fig. 10.2, there is a stable fixed point at the energy g_s and

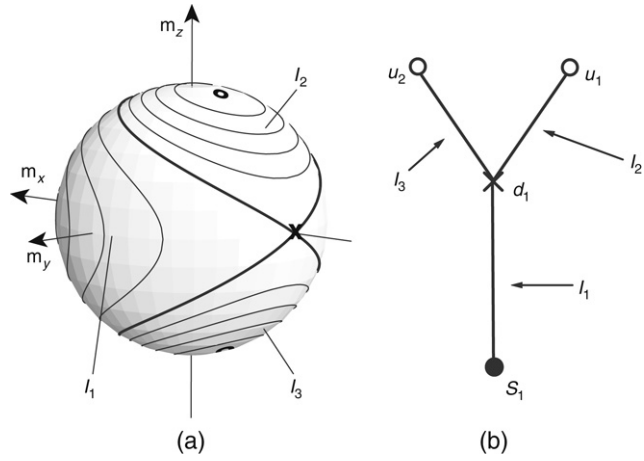

FIGURE 10.1 (a) Phase portrait of the conservative magnetization dynamics on the unit sphere for $\mathbf{h}_a = \mathrm{h}_{ax}\mathbf{e}_x$. black dot: energy minimum; white dot: energy maximum; cross: energy saddle; bold lines: separatrices. System parameters: $D_x = -0.034$, $D_y = 0$, $D_z = 0.68$, $\mathrm{h}_{ax} = 0.2$. (b) Corresponding graph. s_1: minimum; d_1: saddle; u_1, u_2: maxima; I_1, I_2, I_3: central energy regions.

a stable limit cycle at the energy g_a. These two stable steady states are separated by an unstable limit cycle at $g = g_r$. This is a very interesting situation, where the possibility of thermally induced transitions between a stable limit cycle and a stable fixed point appears. The question is whether these transitions are governed by some properly defined potential barrier separating these two stable steady states. We shall show in the sequel that this potential barrier can indeed be defined in terms of the effective potential $V_k(g)$ in the following way:

$$\Delta V_k = V_k(g_{\max}) - V_k(g_{\min}), \tag{10.212}$$

where $g_{\max}$ and $g_{\min}$ respectively denote the energy values corresponding to the maximum and minimum of $V(g)$ for the transition of interest. This is what one would naturally expect from the fact that stable and unstable states of the deterministic dynamics respectively correspond to minima and maxima of $V_k(g)$. On the other hand, it is worth stressing that the potential barrier is defined for the energy dynamics, which means that it has no inherent connection with barriers that may be present in the free energy g_L as a function of $\mathbf{m}$. An example is the case presented in Fig. 10.2(b), where an unstable limit cycle exists between a stable limit

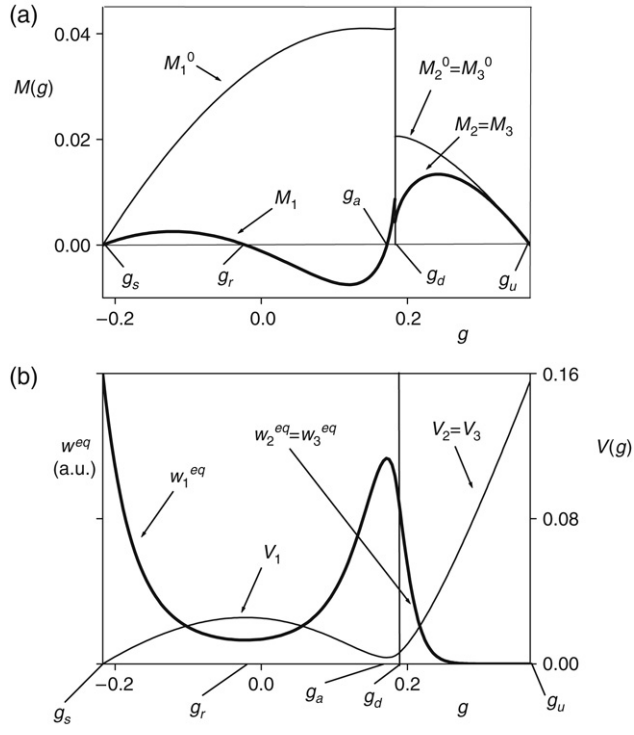

FIGURE 10.2 (a) Melnikov functions corresponding to the central energy regions I_k shown in Fig. 10.1. (b) Effective potential $V(g)$ and equilibrium probability distribution w^{eq}. g_s: energy minimum; g_r: energy of unstable limit cycle; g_a: energy of stable limit cycle; g_d: energy saddle; g_u: energy maximum. System parameters: $D_x = -0.034$, $D_y = 0$, $D_z = 0.68$, $\alpha = 0.014$, $P = 0.3$, $V = 5 \cdot 10^{-25}$ m^3, $\mu_0 \mathrm{M}_s = 1.76$ T, $T = 300$ K, $\mathbf{h}_a = 0.2\mathbf{e}_x$, $\beta/\alpha = 0.675$.

cycle and a stable equilibrium in the energy region I_1. As a result, the potential barrier for the exit from the basin of attraction around the stable equilibrium is given by $V_1(g_r) - V_1(g_s)$, whereas the potential barrier for the exit from the basin of attraction around the stable limit cycle is $V_1(g_r) - V_1(g_a)$, where g_s, g_a, and g_r denote the energy values of the stable equilibrium, the stable limit cycle, and the unstable limit cycle, respectively. The dependence of the potential barriers $V_k(g_r) - V_k(g_s)$ and $V_k(g_r) - V_k(g_a)$ on the injected spin-polarized current is far from straightforward, since the limit-cycle energies g_a and g_r are zeros of $M_k(g, \beta/\alpha)$: $M_k(g_a, \beta/\alpha) = 0$ and $M_k(g_r, \beta/\alpha) = 0$. When the transition from a stable fixed point to a stable state in another energy region is of

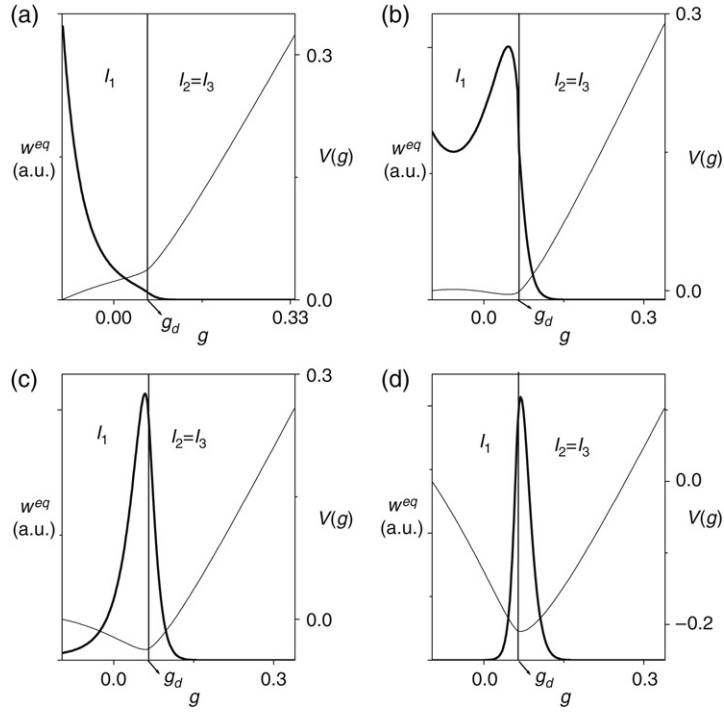

FIGURE 10.3 Modifications of stationary distribution w^{eq} (bold lines) and effective potential $V_k(g)$ (thin lines) under increasing spin-polarized current and fixed external field. Energy intervals corresponding to $I_k (k = 1, 2, 3)$ are indicated. System parameters: $D_x = -0.034$, $D_y = 0$, $D_z = 0.68$, $\alpha = 0.014$, $P = 0.3$, $V = 5 \cdot 10^{-25}$ m^3, $\mu_0 \mathrm{M}_s = 1.76$ T, $T = 300$ K, $\mathbf{h}_a = 0.08\mathbf{e}_x$. g_d: energy saddle. (a) $\beta/\alpha = 0.5$; (b) $\beta/\alpha = 0.66$; (c) $\beta/\alpha = 0.8$; (d) $\beta/\alpha = 1.5$.

interest, the potential barrier is $V_k(g_d) - V_k(g_s)$, where g_d is the energy value of the saddle, which is current independent. In this case, by taking into account that β/α is proportional to the spin-polarized current density J_e, one finds from Eq. (10.211) that the potential barrier can be written in the form:

$$V_1(g_d) - V_1(g_s) = (g_d - g_s)\,(1 - J_e/J_c)\,, \tag{10.213}$$

where J_c is a constant with the dimensions of electric current density. This linear dependence of the potential barrier on injected spin-polarized

current is in agreement with the results of experiments concerning spin-polarized current-induced switching in nanopillar devices [691,23].

The notion of potential barrier in the energy dynamics emerges in a neat way when one investigates the transient solutions to Eq. (10.162) (or equivalently Eq. (10.161)) in the limit of low temperatures where $\mu\Delta V_k \gg 1$. In this limit, one can follow the approach introduced by Brown [135] to calculate the expression for the transition rate from one basin of attraction to another [598]. To illustrate this method, we consider the situation shown in Fig. 10.2, where two steady states exist in the central region I_1 of the graph $\mathcal{G}$. The low-temperature limit implies that:

$$\mu(V_1(g_r) - V_1(g_a)) \gg 1, \qquad \mu(V_1(g_r) - V_1(g_s)) \gg 1. \tag{10.214}$$

This is a case of strong interest in applications, where devices are designed to be relatively stable against thermal fluctuations. Under these conditions, equilibrium will be reached within each potential well much faster than equilibrium between different potential wells. It is then legitimate to assume that the distributions about the minima of $V_k(g)$ are of the form:

$$w_1(g,t) = w_1(g_s,t)\exp\left[-\mu[V_1(g) - V_1(g_s)]\right], \quad g \in [g_s, g_r'], \tag{10.215}$$
$$w_1(g,t) = w_1(g_a,t)\exp\left[-\mu[V_1(g) - V_1(g_a)]\right], \quad g \in [g_r'', g_d], \tag{10.216}$$

where the potential wells around g_s and g_a cover the energy ranges $[g_s, g_r']$ and $[g_r'', g_d]$, respectively. According to the assumption (10.214), $w_1(g,t)$ is practically vanishing outside these two energy intervals.

With the above simplifications, the study of the energy dynamics is reduced to the determination of the relative portions $n_a(t)$ and $n_s(t)$ of the distribution near g_a and g_s, respectively. These portions are defined as:

$$\begin{aligned} n_s(t) &= \int_{g_s}^{g_r'} w_1(g,t)T_1(g)\,\mathrm{d}g, \\ n_a(t) &= \int_{g_r''}^{g_d} w_1(g,t)T_1(g)\,\mathrm{d}g. \end{aligned} \tag{10.217}$$

The problem can be dealt with by using Kramers' treatment of particle escape from a potential barrier [322]. By using the approximations (10.215)

and (10.216) in Eq. (10.217), we obtain the relations:

$$\begin{aligned} n_s(t) &= Z_s w_1(g_s, t) \exp\left[\mu V_1(g_s)\right], \\ n_a(t) &= Z_a w_1(g_a, t) \exp\left[\mu V_1(g_a)\right], \end{aligned} \tag{10.218}$$

where:

$$\begin{aligned} Z_s &= \int_{g_s}^{g_r'} \exp\left[-\mu V_1(g)\right] T(g)\, \mathrm{d}g, \\ Z_a &= \int_{g_r''}^{g_d} \exp\left[-\mu V_1(g)\right] T(g)\, \mathrm{d}g. \end{aligned} \tag{10.219}$$

The letter Z is used in these equations to stress the fact that the integrals represent portions of the partition function $Z(\mu)$ (see Eq. (10.203)). In the energy interval $[g_r', g_r'']$, $w_1(g, t)$ is very small. Nevertheless, there must be a net flow of probability through this region from the overpopulated to the underpopulated well. Following Kramers, we assume that the probability current in this region is constant:

$$J_1(g, t) = J_1(g_r, t), \quad \forall g \in [g_r', g_r''], \tag{10.220}$$

and, consequently, divergence-free:

$$\frac{\partial}{\partial g} J_1(g, t) = 0, \quad \forall g \in [g_r', g_r'']. \tag{10.221}$$

In addition, we assume that there is negligbile probability current in the direction of the high-energy regions I_2 and I_3, which implies:

$$J_1(g_d, t) = 0. \tag{10.222}$$

The above assumptions imply that, during relaxation toward equilibrium, there will be no appreciable change in the probability density $w_k(g, t)$ in the regions $[g_r', g_r'']$ and $[g_d, g_u]$, where $w_k(g, t)$ is vanishingly small. Therefore, $n_a(t) + n_s(t) = 1$ and the increase in $n_a(t)$ results in the corresponding decrease in $n_s(t)$ (or vice versa) and the exchange of probability density occurs through the constant probability current flow in the region $[g_r', g_r'']$.

The rate equations for $n_s(t)$ and $n_a(t)$ are obtained by integrating the Fokker–Planck equation (10.162) for the energy in the intervals $[g_s, g_r']$ and

$[g_r'', g_d]$, and by using Eqs (10.217), (10.220) and (10.222). By also taking into account that $J_1(g_s, t) = 0$ because $M_1^0(g_s) = 0$), we end up with the following equations:

$$\frac{\mathrm{d}}{\mathrm{d}t} n_s(t) = -J_1(g_r, t), \qquad \frac{\mathrm{d}}{\mathrm{d}t} n_a(t) = J_1(g_r, t). \tag{10.223}$$

The quantity $J_1(g_r, t)$ can be expressed in terms of $n_a(t)$ and $n_s(t)$. To this end, we rewrite Eq. (10.199) in the form:

$$\frac{\mu}{\alpha} \frac{J_1(g_r, t)}{M_1^0(g)} \exp\left[\mu V_1(g)\right] = -\frac{\partial}{\partial g}\left[w_1(g, t) \exp\left[\mu V_1(g)\right]\right], \quad \forall g \in [g_r', g_r''], \tag{10.224}$$

and then integrate this equation between $[g_r', g_r'']$. We obtain:

$$w_1(g_r', t) \exp\left[\mu V_1(g_r')\right] - w_1(g_r'', t) \exp\left[\mu V_1(g_r'')\right] = \frac{\mu}{\alpha} J_1(g_r, t) S_r, \tag{10.225}$$

where:

$$S_r = \int_{g_r'}^{g_r''} \frac{\exp\left[\mu V_1(g)\right]}{M_1^0(g)} \, \mathrm{d}g. \tag{10.226}$$

Now, by using Eqs (10.215), (10.216) and (10.218), we obtain:

$$w_1(g_r', t) \exp\left[\mu V_1(g_r')\right] = w_1(g_s, t) \exp\left[\mu V_1(g_s)\right] = \frac{n_s(t)}{Z_s}, \tag{10.227}$$

$$w_1(g_r'', t) \exp\left[\mu V_1(g_r'')\right] = w_1(g_a, t) \exp\left[\mu V_1(g_a)\right] = \frac{n_a(t)}{Z_a}. \tag{10.228}$$

Then, by substituting Eqs (10.227)–(10.228) into Eq. (10.225), and by using formulas (10.223) and (10.96), we end up with the following form of the rate equation:

$$\frac{\mathrm{d}}{\mathrm{d}t} n_s(t) = -\frac{\mathrm{d}}{\mathrm{d}t} n_a(t) = \frac{\nu^2}{2} \left(\frac{n_a(t)}{Z_a} - \frac{n_s(t)}{Z_s} \right) \frac{1}{S_r}. \tag{10.229}$$

The last equation can be transformed into the canonical form:

$$\frac{\mathrm{d}}{\mathrm{d}t}n_s(t) = -\frac{\mathrm{d}}{\mathrm{d}t}n_a(t) = \frac{1}{\tau_{as}}n_a(t) - \frac{1}{\tau_{sa}}n_s(t), \tag{10.230}$$

where:

$$\frac{1}{\tau_{as}} = \frac{1}{S_r Z_a}\frac{\nu^2}{2}, \qquad \frac{1}{\tau_{sa}} = \frac{1}{S_r Z_s}\frac{\nu^2}{2}. \tag{10.231}$$

These expressions represent the transition rates from the limit cycle to the fixed point and from the fixed point to the limit cycle, respectively.

The quantities Z_a, Z_s and S_r appearing in the transition rates (10.231) can be approximately computed by using the approximations inherent in the above derivation. Let us start with Z_s (see Eq. (10.219)). Since the exponential function is strongly attenuated for values of g away from g_s, we can make the following approximation:

$$\begin{aligned} Z_s &\approx \int_{g_s}^{+\infty} \exp\left[-\mu V_1(g)\right] T(g)\, \mathrm{d}g \\ &\approx T(g_s) \int_{g_s}^{+\infty} \exp\left[-\mu[V_1(g_s) + V_1'(g_s)(g-g_s)]\right]\, \mathrm{d}g \\ &\approx T(g_s)\exp\left[-\mu V_1(g_s)\right] \int_{g_s}^{+\infty} \exp\left[-\mu V_1'(g_s)(g-g_s)\right]\, \mathrm{d}g \\ &= \frac{T(g_s)\exp\left[-\mu V_1(g_s)\right]}{\mu V_1'(g_s)}, \end{aligned} \tag{10.232}$$

where $V_1'(g)$ is the derivative of $V_1(g)$. By using the same line of reasoning and taking into account that $V_1'(g_a) = 0$, we obtain:

$$\begin{aligned} Z_a &\approx T(g_a) \int_{-\infty}^{+\infty} \exp\left[-\mu[V_1(g_a) + \frac{1}{2}V_1''(g_a)(g-g_a)^2]\right] \mathrm{d}g \\ &= T(g_a)\exp\left[-\mu V_1(g_a)\right] \sqrt{\frac{2\pi}{\mu V_1''(g_a)}}, \end{aligned} \tag{10.233}$$

where $V_1''(g)$ is the second derivative of $V_1(g)$. Finally, by using Eq. (10.226), we find:

$$S_r \approx \frac{1}{M_1^0(g_r)} \int_{-\infty}^{+\infty} \exp\left[\mu[V_1(g_r) - \frac{1}{2}|V_1''(g_r)|(g-g_r)^2]\right] \mathrm{d}g$$
$$= \frac{\exp\left[\mu V_1(g_r)\right]}{M_1^0(g_r)} \sqrt{\frac{2\pi}{\mu|V_1''(g_r)|}}. \tag{10.234}$$

By using the last three equations in formulas (10.231), we arrive at:

$$\frac{1}{\tau_{as}} = \frac{1}{S_r Z_a}\frac{\nu^2}{2}$$
$$= \frac{\alpha M_1^0(g_r)}{2\pi T_1(g_a)} \sqrt{V_1''(g_a)|V_1''(g_r)|}\exp\left[-\mu[V_1(g_r) - V_1(g_a)]\right], \tag{10.235}$$

$$\frac{1}{\tau_{sa}} = \frac{1}{S_r Z_s}\frac{\nu^2}{2}$$
$$= \alpha M_1^0(g_r)\frac{V_1'(g_s)}{T_1(g_s)} \sqrt{\frac{\mu|V_1''(g_r)|}{2\pi}}\exp\left[-\mu[V_1(g_r) - V_1(g_s)]\right]. \tag{10.236}$$

The previous expressions for the transition rates can be written in the classical Arrhenius form:

$$\begin{aligned} \frac{1}{\tau_{sa}} &= c_{sa}\exp\left[-\mu[V_1(g_r) - V_1(g_s)]\right], \\ \frac{1}{\tau_{as}} &= c_{as}\exp\left[-\mu[V_1(g_r) - V_1(g_a)]\right], \end{aligned} \tag{10.237}$$

where the coefficients c_{sa} and c_{as} can be ascertained from Eqs (10.235) and (10.236). It is worth observing that the various quantities related to $V_1(g)$ in Eqs (10.235) and (10.236) can be expressed in terms of the Melnikov functions:

$$V_1'(g) = \frac{M_1(g,\beta/\alpha)}{M_1^0(g)}, \qquad V_1''(g) = \frac{\partial}{\partial g}\left[\frac{M_1(g,\beta/\alpha)}{M_1^0(g)}\right]. \tag{10.238}$$

Since both $M_1(g, \beta/\alpha)$ and $M_1^0(g)$ are zero at $g = g_s$, the value $V_1'(g_s)$ has to be understood as a limit:

$$V_1'(g_s) = \lim_{g \to g_s} \frac{M_1(g, \beta/\alpha)}{M_1^0(g)}. \tag{10.239}$$

The rate equations previously derived are valid when the temperature is sufficiently small. When this condition is not satisfied, the energy diffusion equation (10.162) must be solved by more general methods. We outline here a possible approach based on eigenfunction expansions. To this end, it is convenient to use the form (10.199) of the probability current density. This leads to the following form of the Fokker–Planck equation:

$$\begin{aligned} &T_k(g) \frac{\partial}{\partial t} w_k(g,t) \\ &\quad = \frac{\nu^2}{2} \frac{\partial}{\partial g} \left\{ M_k^0(g) \exp\left[-\mu V_k(g)\right] \frac{\partial}{\partial g} \left[\exp\left[\mu V_k(g)\right] w_k(g)\right] \right\}. \end{aligned} \tag{10.240}$$

Let us introduce the new unknown:

$$\phi_k(g,t) = w_k(g,t) \exp\left[\mu V_k(g)\right]. \tag{10.241}$$

In terms of this unknown, Eq. (10.240) becomes:

$$\begin{aligned} &T_k(g) \exp\left[-\mu V_k(g)\right] \frac{\partial}{\partial t} \phi_k(g,t) \\ &\quad = \frac{\nu^2}{2} \frac{\partial}{\partial g} \left\{ M_k^0(g) \exp\left[-\mu V_k(g)\right] \frac{\partial}{\partial g} \phi_k(g,t) \right\}, \end{aligned} \tag{10.242}$$

and the function $\phi_k(g,t)$ has to satisfy the previously discussed boundary conditions at the graph nodes:

$$\phi_{k_i}(g_{d_h}, t) = \phi_{k_j}(g_{d_h}, t), \quad \forall\, k_i, k_j \in I(d_h), \quad h = 1, 2, \ldots, \tag{10.243}$$

$$\begin{aligned} \sum_{k \in I(d_h)} J_k(g_{d_h}) &= \sum_{k \in I(d_h)} \left[\frac{\nu^2}{2} M_k^0(g_{d_h}) \exp\left[-\mu V_k(g_{d_h})\right] \frac{\partial}{\partial g} \phi_k(g_{d_h}, t) \right] \\ &= 0. \end{aligned} \tag{10.244}$$

By taking into account that:

$$\sum_{k\in I(d_h)} M_k^0(g_{d_h}) = 0, \tag{10.245}$$

one obtains from Eq. (10.244) that:

$$\frac{\partial \phi_{k_i}}{\partial g}(g_{d_h}, t) = \frac{\partial \phi_{k_j}}{\partial g}(g_{d_h}, t), \quad \forall\, k_i, k_j \in I(d_h), \quad h = 1, 2, \ldots. \tag{10.246}$$

Equations (10.243) and (10.246) suggest that $\phi_k(g,t)$ is continuously differentiable on the entire graph.

Equation (10.242) can be solved for any initial condition by using the following eigenfunction expansion:

$$\phi_k(g,t) = A_0 + \sum_{n=1}^{\infty} A_n \phi_k^{(n)}(g) \exp\left[-\lambda_n t\right], \tag{10.247}$$

where $\phi_k^{(n)}$ are the solution of the following eigenvalue problem:

$$\begin{aligned} &\frac{\partial}{\partial g}\left\{ M_k^0(g) \exp\left[-\mu V_k(g)\right] \frac{\partial}{\partial g}\phi_k^{(n)}(g) \right\} \\ &\quad + \lambda_n T_k(g) \exp\left[-\mu V_k(g)\right] \phi_k^{(n)}(g) = 0. \end{aligned} \tag{10.248}$$

The above eigenvalue problem for $\phi_k^{(n)}(g)$ can be formulated in terms of minimization of the quadratic functional:

$$D[\phi_k(g)] = \frac{\nu^2}{2} \sum_k \int_{I_k} \left\{ M_k^0(g) \exp\left[-\mu V_k(g)\right] \left[\frac{\partial}{\partial g}\phi_k(g)\right]^2 \right\} \mathrm{d}g, \tag{10.249}$$

under the constraint:

$$\begin{aligned} H[\phi_k(g), \phi_k(g)] &= \sum_k \int_{I_k} \left\{ T_k(g) \exp\left[-\mu V_k(g)\right] \left[\phi_k(g)\right]^2 \right\} \mathrm{d}g \\ &= \text{const}. \end{aligned} \tag{10.250}$$

and the orthogonality conditions:

$$H[\phi_k(g), \phi_k^{(m)}(g)] = \sum_k \int_{I_k} \left\{ T_k(g) \exp\left[-\mu V_k(g)\right] \left[\phi_k(g)\phi_k^{(m)}(g)\right] \right\} \mathrm{d}g = 0, \tag{10.251}$$

for $m = 0, 1, \ldots, n-1$. Once this problem is solved, the eigenvalue λ_n is given by:

$$\lambda_n = \frac{D[\phi_k^{(n)}(g)]}{H[\phi_k^{(n)}(g), \phi_k^{(n)}(g)]}. \tag{10.252}$$

It must be remarked that one eigenvalue is always $\lambda_0 = 0$, which corresponds to the stationary solution $\phi_k^{(0)} = A_0 = 1/Z(\mu)$. In many applications, one is mostly interested in the next eigenfunction $\phi_k^{(1)}$ and the corresponding eigenvalue λ_1. The constraint (10.251) yields:

$$\sum_k \int_{I_k} T_k(g) \exp\left[-\mu V_k(g)\right] \phi_k(g) \, \mathrm{d}g = 0. \tag{10.253}$$

The outlined procedure can be implemented to compute λ_n and $\phi_k^{(n)}$.

10.5 STOCHASTIC MAGNETIZATION DYNAMICS IN UNIAXIAL SYSTEMS

The results discussed in the previous sections acquire a particularly simple form when the problem exhibits uniaxial symmetry, i.e., when geometrical and physical properties are invariant with respect to rotations around a given axis. The deterministic magnetization dynamics in uniaxial systems has been analyzed from various perspectives in Chapters 5 and 7–9. We state now the symmetry condition for the stochastic dynamics. Consider Eqs (10.40) and (10.41) for the generalized stochastic magnetization dynamics:

$$\mathrm{d}\mathbf{m} = \left[\mathbf{m} \times \frac{\partial g_L}{\partial \mathbf{m}} + \alpha \mathbf{m} \times \left(\mathbf{m} \times \frac{\partial \Phi}{\partial \mathbf{m}} \right) \right] \mathrm{d}t - \nu \mathbf{m} \times \mathrm{d}\mathbf{W}, \tag{10.254}$$

where $\mathbf{W}(t)$ is the standard vector isotropic Wiener process. It is assumed below that the z axis of the chosen cartesian reference frame is along the

symmetry axis. Then, the system (or particle) has uniaxial symmetry if the two potentials g_L and Φ depend only on m_z:

$$g_L = g_L(\mathrm{m}_z), \qquad \Phi = \Phi(\mathrm{m}_z). \tag{10.255}$$

The equation governing the deterministic magnetization dynamics in uniaxial systems can be obtained from Eqs (10.254) and (10.255) by setting $\nu = 0$ in Eq. (10.254). In cylindrical coordinates (m_z, ϕ), one obtains the following equations:

$$\frac{\mathrm{d}\mathrm{m}_z}{\mathrm{d}t} = -\alpha \frac{\partial \Phi}{\partial \mathrm{m}_z}(1 - \mathrm{m}_z^2), \tag{10.256}$$

$$\frac{\mathrm{d}\phi}{\mathrm{d}t} = -\frac{\partial g_L}{\partial \mathrm{m}_z} = \omega_0(\mathrm{m}_z). \tag{10.257}$$

As a consequence of uniaxial symmetry, the equation for m_z is decoupled from the equation for the azimuthal angle ϕ. Steady states of deterministic magnetization dynamics (fixed points and steady-state precessions) are found by solving the above equation for the case of $\mathrm{d}\mathrm{m}_z/\mathrm{d}t = 0$. One finds that there are always two fixed points at $\mathrm{m}_z = \pm 1$. Steady-state precessions around the symmetry axis correspond to solutions m_{z0} of the equation $\partial\Phi/\partial \mathrm{m}_z = 0$, and have angular frequency $\omega_0(\mathrm{m}_{z0})$. By studying the stability of these steady-state solutions, it is possible to construct the complete stability diagram of deterministic dynamics.

A particularly interesting case is the spin-transfer-driven magnetization dynamics discussed in Section 9.6. In that case, uniaxial symmetry is present when the free-layer easy axis, the fixed-layer easy axis, and the external magnetic field directions are all along the z axis perpendicular to the layer plane, while the layer properties show uniaxial symmetry around the same axis. The two potentials in Eq. (10.255) are given by the formulas:

$$g_L(\mathrm{m}_z; \mathrm{h}_{az}) = -\kappa_{\text{eff}} \frac{\mathrm{m}_z^2}{2} - \mathrm{h}_{az}\mathrm{m}_z, \tag{10.258}$$

$$\Phi(\mathrm{m}_z; \mathrm{h}_{az}, \beta/\alpha) = g_L(\mathrm{m}_z; \mathrm{h}_{az}) + \frac{\beta}{\alpha}\frac{\ln(1 + c_p \mathrm{m}_z)}{c_p}, \tag{10.259}$$

where $\kappa_{\text{eff}} = D_\perp - D_z$ and all the notations used have been defined in Section 9.6. The stability diagram can be constructed in the control plane $(\mathrm{h}_{az}, \beta/\alpha)$, as shown in Fig. 9.8.

When thermal fluctuations are present, stochastic magnetization dynamics can be studied by using the Fokker–Planck equation in

cylindrical coordinates for the conditional probability density $w = w(\mathrm{m}_z, \phi, t|\mathrm{m}_{z0}, \phi_0, t_0)$ [277]. By using the fact that g_L and Φ do not depend on ϕ, we arrive at the following equation:

$$\frac{\partial}{\partial t} w = \frac{\nu^2}{2} \Delta_\Sigma w + \alpha \frac{\partial}{\partial \mathrm{m}_z} \left([1 - \mathrm{m}_z^2] \frac{\partial \Phi}{\partial \mathrm{m}_z} w \right) - \omega_0 \frac{\partial w}{\partial \phi}, \tag{10.260}$$

where Δ_Σ is the Laplacian operator on the unit sphere:

$$\Delta_\Sigma w = \frac{\partial}{\partial \mathrm{m}_z} \left\{ [1 - \mathrm{m}_z^2] \frac{\partial w}{\partial \mathrm{m}_z} \right\} + \frac{1}{1 - \mathrm{m}_z^2} \frac{\partial^2 w}{\partial \phi^2}, \tag{10.261}$$

and w has to satisfy the initial condition:

$$\lim_{t \to t_0} w = \delta(\mathrm{m}_z - \mathrm{m}_{z0}) \delta(\phi - \phi_0), \tag{10.262}$$

where $\delta(\cdot)$ is Dirac delta function.

Since for uniaxial systems $\nabla_\Sigma g_L$ is everywhere aligned with $\nabla_\Sigma \Phi$, it is possible to derive the stationary distribution $w^{eq}(\mathrm{m}_z, \phi)$ in closed form. By carrying out usual algebraic manipulations, one derives that due to the axial symmetry w^{eq} does not depend on ϕ and it is given by:

$$w^{eq}(\mathrm{m}_z) = \frac{1}{Z} \exp\left[-\mu \Phi(\mathrm{m}_z) \right], \tag{10.263}$$

where $\mu = 2\alpha/\nu^2$, while:

$$Z = 2\pi \int_{-1}^{1} \exp(-\mu \Phi) \mathrm{d}\mathrm{m}_z. \tag{10.264}$$

As before, the value of μ is determined from the fluctuation-dissipation relation:

$$\frac{\nu^2}{2\alpha} = \frac{k_B T}{\mu_0 \mathrm{M}_s^2 V}, \tag{10.265}$$

where V is the volume of the magnetic particle.

It must be remarked again that Eq. (10.263) is not the equilibrium Boltzmann distribution, although it is formally similar to it. This can be seen from the fact that the exponential contains the generalized potential

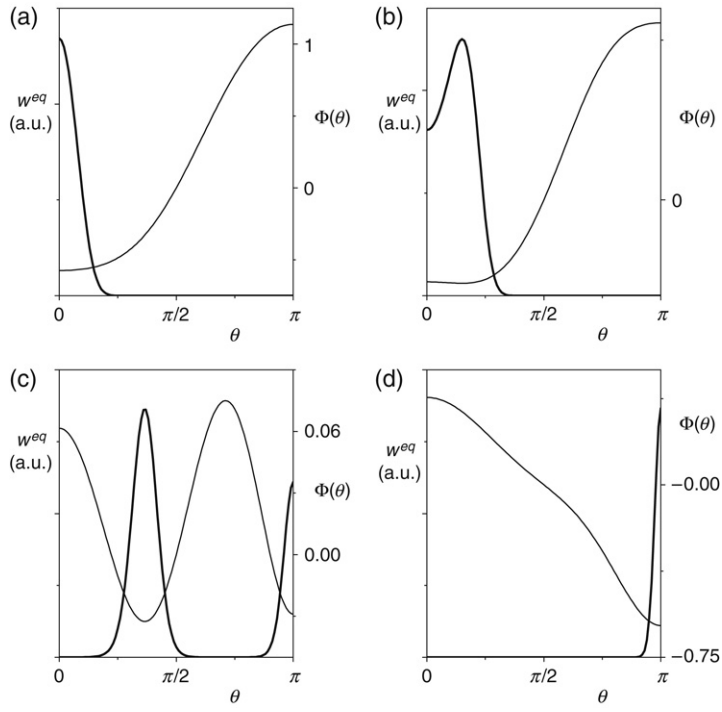

FIGURE 10.4 Modifications of w^{eq} (bold line) and Φ (thin line) under increasing spin-polarized current and fixed external field. System parameters: $D_z = 1$, $D_\perp = 0$, $\alpha = 0.01$, $P = 0.3$, $V = 5 \cdot 10^{-25}$ m^3, $\mathrm{M}_s = 800$ kAm^{-1}, $T = 300$ K, $\mathrm{h}_{az} = 1.6$. (a) $\beta/\alpha = 0.66$; (b) $\beta/\alpha = 1.06$; (c) $\beta/\alpha = 1.46$; (d) $\beta/\alpha = 1.86$.

Φ instead of the free energy of the system. This distribution has to be viewed as a stationary out-of-equilibrium distribution for a system driven by external excitations. Consider, for example, the case of spin-transfer-driven systems. In this case, Φ is given by Eq. (10.259) and is a function of the injected current density. This reflects the fact that w^{eq} is the stationary distribution of an open system driven out-of-equilibrium by the injection of the spin-polarized current. The dependence of w^{eq} on the current, i.e., β/α, is presented in Fig. 10.4. In this figure, distributions are plotted as a function of the polar angle θ defined as:

$$\cos\theta = \mathrm{m}_z. \tag{10.266}$$

In the case shown in Fig. 10.4(c), $\theta = \pi$ is a stable state while $\theta = 0$ is not, which means that despite the large positive field $\mathrm{h}_{az} = 1.6$ acting on the nanomagnet, the effect of the spin-polarized current is strong enough to destroy the stability of the $\theta = 0$ state. Two limit cycles exist for $\theta_0 \simeq 1.15$ and $\theta_0 \simeq 2.23$, of which the former is stable while the latter is unstable. The barrier $\Delta\Phi$ separating these two stable states is $\Delta\Phi \approx 0.1$, corresponding to an energy barrier of the order of $10\ k_B T$.

The presence of uniaxial symmetry implies that one is often interested only in the dynamics of the angle θ. This dynamics is described by the reduced Fokker–Planck equation which is obtained by integrating Eq. (10.260) with respect to ϕ and by taking into account that g_L and Φ are independent of ϕ because of symmetry. As a result, one obtains the following equation:

$$\frac{\partial \overline{P}}{\partial t} = \frac{\partial}{\partial \theta}\left[\left(\alpha \frac{\partial \Phi}{\partial \theta} - \frac{\nu^2}{2}\cot\theta\right)\overline{P} + \frac{\nu^2}{2}\frac{\partial \overline{P}}{\partial \theta}\right], \tag{10.267}$$

for the reduced probability density $\overline{P}(\theta)$, defined as:

$$\overline{P} = \sin\theta \int_0^{2\pi} w\ \mathrm{d}\phi. \tag{10.268}$$

The Fokker–Planck equation (10.267) corresponds to the following Langevin-type equation for θ:

$$\mathrm{d}\theta = \left[-\alpha \frac{\partial \Phi}{\partial \theta} + \frac{\nu^2}{2}\cot\theta\right]\mathrm{d}t + \nu \mathrm{d}W(t), \tag{10.269}$$

where $W(t)$ represents the scalar Wiener process. Equation (10.269) reveals an additional drift term related to the description of the magnetization state in terms of θ.

Two important remarks are in order. First, the angle θ is directly related to the energy g_L and is itself a slow variable for the magnetization dynamics. Equations (10.267) and (10.269) describe the stochastic dynamics of this slow variable with no approximations. In other words, in uniaxial systems the separation of slow and fast time scales is exact and it is valid for any value of α. Second, the dynamics of θ is the classical relaxation dynamics governed by the potential Φ. Thus, one can use Kramer's approach in the limit of high-energy barriers [135] to derive the expression for the transition rate $1/\tau_{ij}$ from one stable state (θ_i) to another

stable state (θ_j). One obtains:

$$\frac{1}{\tau_{ij}} = \alpha k_i \sin\theta_m \sqrt{\frac{\alpha k_m}{\pi\nu^2}}\, \exp\left[-\mu\left(\Phi(\theta_m) - \Phi(\theta_i)\right)\right], \tag{10.270}$$

where the maximum of Φ is achieved at θ_m ($\theta_i < \theta_m < \theta_j$), while $k_i = \Phi''(\theta_i)$, and $k_m = -\Phi''(\theta_m)$. For the case shown in Fig. 10.4(c), the two stable states are $\theta_1 \simeq 1.15$ and $\theta_2 = \pi$, whereas the maximum corresponds to the unstable limit cycle at $\theta_m \simeq 2.23$. In physical units, the transition frequencies are $f_{12} \approx 40$ kHz and $f_{21} \approx 100$ kHz.

The fact that in the uniaxial case the coefficients of the Fokker–Planck equation (10.260) do not depend on ϕ can be used to simplify the solution of this equation. Indeed, instead of using the expansion of the solution in terms of the eigenfunctions of the entire Fokker–Planck operator L_{FP} (see Section 10.2), one can use Fourier series to represent the dependence of w on ϕ and ϕ_0:

$$w = \frac{1}{2\pi}\sum_n w_n(\mathrm{m}_z, t|\mathrm{m}_{z0}, t_0)\exp\left[in(\phi - \phi_0)\right]. \tag{10.271}$$

The factor $1/2\pi$ is due to the identity:

$$\delta(\phi - \phi_0) = \frac{1}{2\pi}\sum_n \exp\left[in(\phi - \phi_0)\right]. \tag{10.272}$$

The substitution of Eq. (10.271) into Eqs (10.260)–(10.261) leads to the sequence of equations:

$$\frac{\partial w_n}{\partial t} = \mathcal{A}_n w_n, \tag{10.273}$$

where the differential operators $\mathcal{A}_n$ are defined as:

$$\mathcal{A}_n w_n = \frac{\nu^2}{2}\mathcal{L}_n w_n + \alpha\frac{\partial}{\partial \mathrm{m}_z}\left([1 - \mathrm{m}_z^2]\frac{\partial \Phi}{\partial \mathrm{m}_z} w_n\right) - in\omega_0 w_n, \tag{10.274}$$

with:

$$\mathcal{L}_n w_n = \frac{\partial}{\partial \mathrm{m}_z}\left\{[1 - m_z^2]\frac{\partial w_n}{\partial \mathrm{m}_z}\right\} - \frac{n^2}{1 - \mathrm{m}_z^2} w_n. \tag{10.275}$$

The functions w_n have to satisfy the initial condition:

$$\lim_{t \to t_0} w_n(\mathrm{m}_z, t|\mathrm{m}_{z0}, t_0) = \delta(\mathrm{m}_z - \mathrm{m}_{z0}). \tag{10.276}$$

We denote by $\mathcal{A}_n^\dagger$ the operator adjoint to $\mathcal{A}_n$ with respect to the inner product:

$$(f, g) = \int_{-1}^{+1} f^*(\mathrm{m}_z) g(\mathrm{m}_z) \mathrm{d}\mathrm{m}_z, \tag{10.277}$$

where the symbol $*$ denotes complex conjugate operation. The general solution to the problem (10.273)–(10.276) is given by the following expansion [277]:

$$w_n(\mathrm{m}_z, t|\mathrm{m}_{z0}, t_0) = \sum_k \varphi_{n,k}(\mathrm{m}_z) \psi_{n,k}^*(\mathrm{m}_{z0}) \exp\left[\lambda_{n,k}(t - t_0)\right], \tag{10.278}$$

where $\lambda_{n,k}$, $\varphi_{n,k}$ and $\psi_{n,k}$ are solutions of the following (adjoint) eigenvalue problems:

$$\mathcal{A}_n \varphi_{n,k} = \lambda_{n,k} \varphi_{n,k}, \tag{10.279}$$

$$\mathcal{A}_n^\dagger \psi_{n,k} = \lambda_{n,k}^* \psi_{n,k}. \tag{10.280}$$

The expansion (10.278) is based on the assumption that $\varphi_{n,k}$ and $\psi_{n,k}$ form a complete set of biorthogonal functions, which means that $(\psi_{n,k_1}, \varphi_{n,k_2}) = \delta_{k_1,k_2}$ ($\delta_{k,h}$ is the Kronecker symbol), and:

$$\sum_k \varphi_{n,k}(\mathrm{m}_z) \psi_{n,k}^*(\mathrm{m}_{z0}) = \delta(\mathrm{m}_z - \mathrm{m}_{z0}). \tag{10.281}$$

Indeed, if one considers the limit of (10.278) for $t \to t_0$, and one takes into account (10.281), one easily checks that w_n satisfies the initial condition (10.276).

By combining the expansions (10.271) and (10.278), we arrive at the following solution of the Fokker–Planck equation for the conditional probability density:

$$w = \frac{1}{2\pi} \sum_n \sum_k \varphi_{n,k}(\mathrm{m}_z) \psi^*_{n,k}(\mathrm{m}_{z0}) \exp\left[in(\phi - \phi_0)\right] \times \exp\left[\lambda_{n,k}(t - t_0)\right]. \tag{10.282}$$

This formula shows that the derivation of the complete information concerning the magnetization stochastic process for uniaxial magnetic systems requires the solution of the eigenvalue problems (10.279) and (10.280). These are one-dimensional eigenvalue problems in terms of m_z.

10.6 AUTOCORRELATION FUNCTION AND POWER SPECTRAL DENSITY

In this section, the mathematical machinery of the Fokker–Planck equation will be used for the calculation of the autocorrelation function and the power spectral density (PSD) of the stochastic magnetization dynamics. The latter quantity is of special interest, because it is directly accessible to measurements.

The autocorrelation function of the scalar function $f(\mathbf{m})$ of the stationary stochastic process $\mathbf{m}(t)$ is defined as follows:

$$C_f(\tau) = \langle [f(\mathbf{m}(t_0 + \tau)) - \langle f(\mathbf{m}) \rangle] [f(\mathbf{m}(t_0)) - \langle f(\mathbf{m}) \rangle] \rangle, \tag{10.283}$$

where the symbol $\langle \cdot \rangle$ denotes statistical averages. The average $\langle f(\mathbf{m}) \rangle$ can be computed by using the stationary distribution w^{eq}:

$$\langle f(\mathbf{m}) \rangle = \iint_\Sigma f(\mathbf{m}) w^{eq}(\mathbf{m}) \mathrm{d}S. \tag{10.284}$$

The computation of the autocorrelation function is performed by using the joint distribution function $w(\mathbf{m}, t_0 + \tau; \mathbf{m}_0, t_0)$ as follows:

$$C_f(\tau) = \iint_\Sigma \iint_\Sigma [f(\mathbf{m}) - \langle f(\mathbf{m}) \rangle] [f(\mathbf{m}_0) - \langle f(\mathbf{m}) \rangle] w(\mathbf{m}, t_0 + \tau; \mathbf{m}_0, t_0) \mathrm{d}S \mathrm{d}S_0. \tag{10.285}$$

where $\mathrm{d}S\mathrm{d}S_0$ is a concise notation for the elements of surface integration with respect to $\mathbf{m}$ and $\mathbf{m}_0$. The independence of this quantity from t_0 is a consequence of the stationarity of the process. Since:

$$w(\mathbf{m}, t_0 + \tau; \mathbf{m}_0, t_0) = w(\mathbf{m}, \tau | \mathbf{m}_0, 0) w^{eq}(\mathbf{m}_0), \tag{10.286}$$

the autocorrelation function can be expressed as follows:

$$C_f(\tau) = \oiint_{\Sigma} f(\mathbf{m}) \left\{ \oiint_{\Sigma} f(\mathbf{m}_0) \left[w(\mathbf{m}, \tau | \mathbf{m}_0, 0) - w^{eq}(\mathbf{m}) \right] w^{eq}(\mathbf{m}_0) \mathrm{d}S_0 \right\} \mathrm{d}S. \tag{10.287}$$

As discussed in Section 10.2, the general solution of the Fokker–Planck equation can be written as the following expansion:

$$w(\mathbf{m}, t | \mathbf{m}_0, t_0) = \sum_r \varphi_r(\mathbf{m}) \psi_r^*(\mathbf{m}_0) \exp\left[\lambda_r (t - t_0)\right], \tag{10.288}$$

where the symbol * denotes complex conjugate operation, $\varphi_r(\mathbf{m})$ and $\psi_r(\mathbf{m}_0)$ are right and left eigenfunctions associated with the eigenvalue λ_r of the Fokker–Planck operator:

$$L_{FP} w = \frac{\nu^2}{2} \Delta_\Sigma w - \mathrm{div}_\Sigma \left[(\mathbf{m} \times \nabla_\Sigma g_L - \alpha \nabla_\Sigma \Phi) w \right]. \tag{10.289}$$

Thus, in principle, by solving the eigenvalue problem for L_{FP}, and by using Eq. (10.288) in Eq. (10.287), it is possible to compute the autocorrelation function.

There is an alternative approach to the computation of the autocorrelation function, which takes advantage of the structure of formula (10.287). This approach is based on the use of the following auxiliary function:

$$p(\mathbf{m}, \tau) = \oiint_{\Sigma} f(\mathbf{m}_0) \left[w(\mathbf{m}, \tau | \mathbf{m}_0, 0) - w^{eq}(\mathbf{m}) \right] w^{eq}(\mathbf{m}_0) \mathrm{d}S_0. \tag{10.290}$$

This function depends on the forward coordinates $(\mathbf{m}, \tau)$ through the conditional probability density $w(\mathbf{m}, \tau | \mathbf{m}_0, 0)$ and, for this reason, this function is a solution of the Fokker–Planck equation:

$$\frac{\partial p}{\partial \tau} = L_{FP} p. \tag{10.291}$$

The initial condition for $p(\mathbf{m}, \tau)$ can be determined by using the initial condition for w. One obtains:

$$\begin{aligned} p(\mathbf{m}, 0) &= \oiint_{\Sigma} f(\mathbf{m}_0) \left[\delta(\mathbf{m} - \mathbf{m}_0) - w^{eq}(\mathbf{m}) \right] w^{eq}(\mathbf{m}_0) \mathrm{d}S_0 \\ &= w^{eq}(\mathbf{m}) \left[f(\mathbf{m}) - \langle f(\mathbf{m}) \rangle \right]. \end{aligned} \tag{10.292}$$

Unlike probability densities, $p(\mathbf{m},\tau)$ is not positive-definite, and it actually satisfies the condition:

$$\oiint_{\Sigma} p(\mathbf{m},\tau)\mathrm{d}S = 0. \tag{10.293}$$

This relation is true for the initial condition (10.292) and it remains true at subsequent times because the Fokker–Planck equation preserves the integral (10.293) during the time evolution.

Once the initial value problem defined by Eqs (10.291) and (10.292) has been solved (this can be again accomplished by using eigenfunction expansions), the autocorrelation function can be computed through the formula:

$$C_f(\tau) = \oiint_{\Sigma} f(\mathbf{m})p(\mathbf{m},t)\mathrm{d}S, \tag{10.294}$$

which is the consequence of Eqs (10.287) and (10.290). The main advantage of the outlined technique is that one has to solve the FP equation for only one initial condition (10.292), while the direct use of Eq. (10.287) requires the solution of the Fokker–Planck equation for $w(\mathbf{m},\tau|\mathbf{m}_0,0)$ for any $\mathbf{m}_0$ in the initial condition.

Having found the autocorrelation function, the power spectral density (PSD) can be immediately computed by using the fact that the Fourier transform of the autocorrelation function:

$$S_f(\omega) = \int_{-\infty}^{+\infty} C_f(\tau)\exp\left(-i\omega\tau\right)\mathrm{d}\tau. \tag{10.295}$$

In the case when the auxiliary function (10.290) is used, the PSD can be found from the following equation:

$$S_f(\omega) = \oiint_{\Sigma} f(\mathbf{m})P(\mathbf{m},\omega)\ \mathrm{d}S, \tag{10.296}$$

where $P(\mathbf{m},\omega)$ is the Fourier transform of $p(\mathbf{m},\tau)$:

$$P(\mathbf{m},\omega) = \int_{-\infty}^{+\infty} p(\mathbf{m},\tau)\exp\left(-i\omega\tau\right)\mathrm{d}\tau. \tag{10.297}$$

The function $P(\mathbf{m},\omega)$ can be directly computed by using the equation:

$$i\omega P(\mathbf{m},\omega) - L_{FP}P(\mathbf{m},\omega) = w^{eq}(\mathbf{m})\left[f(\mathbf{m}) - \langle f(\mathbf{m})\rangle\right], \tag{10.298}$$

which is derived from the Fokker–Planck equation (10.291) and the initial condition (10.292). The last equation can be concurrently solved for various values of ω.

In the sequel, we shall apply the above general considerations to two special cases of stochastic magnetization dynamics in spin-transfer-driven devices: (i) computation of power spectral density in uniaxial systems; and (ii) computation of power spectral density in the framework of stochastic processes on graphs. In the first case we shall use the technique based on the eigenfunction expansion, while in the second case we shall make use of the auxiliary function technique outlined above. It will be apparent that the discussion is quite general in nature and is applicable to more complicated situations as well.

We begin with the discussion of uniaxial spin-transfer systems in which the symmetry axis, the anisotropy axis, and the magnetization direction in the fixed layer are all parallel to the z axis. This case has been discussed in the previous section. The magnetization dynamics in the free layer is described by Eq. (10.254), where the two potentials g_L and Φ depend only on m_z and have the analytical form given by Eqs (10.258)–(10.259). The study of stochastic magnetization dynamics can be carried out by solving the Fokker–Planck equation (10.260)–(10.261) for the conditional probability density $w = w(\mathrm{m}_z, \phi, t|\mathrm{m}_{z0}, \phi_0, t_0)$. The general solution is given by the Fourier series (10.271), where the expansion (10.278) is valid for the coefficients w_n of the series. The stationary probability density $w^{eq}(\mathrm{m}_z)$ is given by Eq. (10.263).

Once the conditional probability density is found, the joint probability distribution can be obtained as $w(\mathrm{m}_z, \phi, \tau|\mathrm{m}_{z0}, \phi_0, 0)w^{eq}(\mathrm{m}_{z0})$ and then can be used to compute the correlation functions of the components of $\mathbf{m}(t)$. Here, we limit ourself to the analysis of the component $\mathrm{m}_x(t)$. The autocorrelation of m_x is given by:

$$R_{\mathrm{m}_x}(t - t_0) = \langle \sin\theta \cos\phi \sin\theta_0 \cos\phi_0 \rangle, \tag{10.299}$$

where it has been taken into account that $\mathrm{m}_x = \sin\theta\cos\phi$ and $\langle \mathrm{m}_x \rangle = 0$ due to the uniaxial symmetry. Since in the expansion (10.271) only the terms with $n = \pm 1$ give rise to nonzero averages, Eq. (10.299) yields:

$$R_{\mathrm{m}_x}(t - t_0) = \sum_k \mathcal{R}e \left\{ \frac{1}{2} a_k \exp\left[\lambda_{1,k}(t - t_0)\right] \right\}, \tag{10.300}$$

where:

$$a_k = \left[\int_{-1}^{+1} \sqrt{1-\mathrm{m}_z^2}\,\varphi_{1,k}(\mathrm{m}_z)\mathrm{d}\mathrm{m}_z\right] \times \left[\int_{-1}^{+1} \sqrt{1-\mathrm{m}_{z0}^2}\,\psi_{1,k}(\mathrm{m}_{z0})w^{eq}(\mathrm{m}_{z0})\mathrm{d}\mathrm{m}_{z0}\right]. \quad (10.301)$$

From Eq. (10.300), the power spectral density can be computed by taking the Fourier transform.

The most difficult step in the outlined procedure is the solution of the eigenvalues problems (10.279)–(10.280) for the operators $\mathcal{A}_n$ and $\mathcal{A}_n^\dagger$. We addressed this problem numerically, by using the Chebychev pseudo-spectral method to compute a matrix approximation of the operator $\mathcal{A}_n$. After obtaining this matrix, we numerically computed the eigenvalues along with the associated right and left eigenvectors, and this allowed us to arrive at an approximate expression for the autocorrelation (10.300). In Fig. 10.5, we present the computed power spectral density or three different values of β/α. Peaks in the PSD correspond to stable steady states, which can be one of the fixed points $\mathrm{m}_z = \pm 1$ (with free precessional frequencies of 4.6 and 27.4 GHz, respectively), or a steady-state precession at a frequency in between those associated with $\mathrm{m}_z = \pm 1$. In Fig. 10.6, the linewidths of the various peaks are reported: the linewidths are in the order of 0.1–1 GHz, in reasonable agreement with experiments in nanopillars [398,578]. In the case of point-contact devices [558,378], the measured linewidths are usually smaller. This can be partly ascribed to the fact that in point-contact devices the volume of the free layer is not precisely defined.

Now, we turn to the problem of computing the autocorrelation function and the power spectral density in the framework of stochastic processes on graphs. It has been shown that the vectorial stochastic differential equation (10.139) is reduced to the following scalar stochastic differential equation for the energy on the graph edge I_k (see Eq. (10.168)):

$$\mathrm{d}g = b_k(g)\mathrm{d}t + \nu\sigma_k(g)\mathrm{d}W, \quad (10.302)$$

where $W(t)$ is the standard scalar Wiener process, while the coefficients $b_k(g)$ and $\sigma_k(g)$ are obtained through the appropriate averaging of the right-hand side of Eq. (10.139) along curves $C_k(g)$. Namely, these

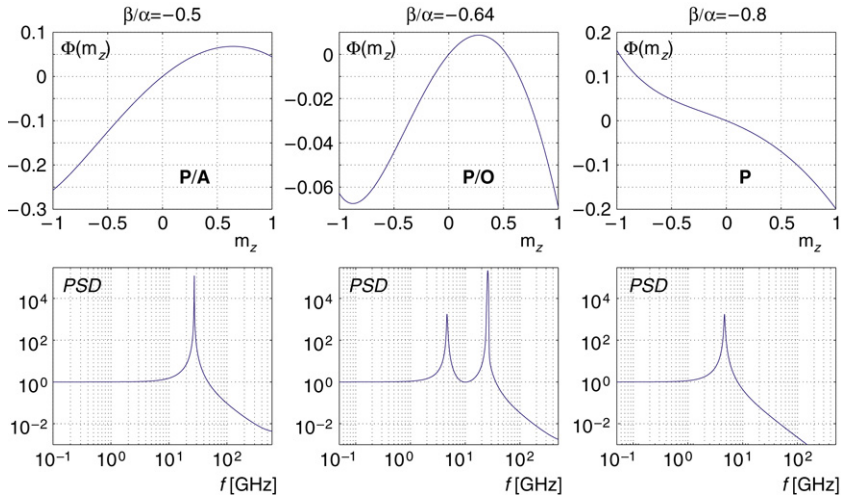

FIGURE 10.5 Effective potentials $\Phi(\mathrm{m}_z)$ (upper plots) and corresponding power spectral densities (lower plots, presented in log-log scale) for a uniaxial spin-transfer device, for three values of injected spin-polarized current: $\beta/\alpha = -0.5, -0.64, -0.8$. System parameters: $\mathrm{h}_{az} = -0.7$, $\kappa_{\mathrm{eff}} = 0.5$, $c_p = 0.5$, $\alpha = 0.01$, $T = 300$ K, $\mathrm{M}_s = 6.5 \cdot 10^5$ A/m, $V = 80 \times 40 \times 3.125\,\mathrm{nm}^3 = 10^{-23}$ m^3. Bold symbols **P**, **A**, **O** have same meanings as in Fig. 9.8.

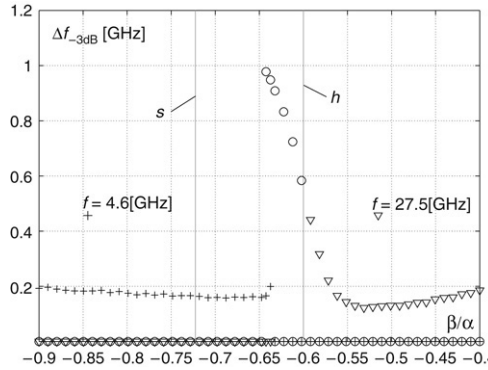

FIGURE 10.6 −3dB linewidth of power spectral density peaks versus β/α. "+": linewidth of peaks associated with the state $\mathrm{m}_z = +1$; "∇": linewidth of peaks associated with state $\mathrm{m}_z = -1$; "$\circ$": linewidth of peaks associated with self-oscillations. Applied field and other system parameters are the same as in Fig. 10.5. The frequencies denoted as f_+ and f_∇ are the values of Kittel frequency around states $\mathrm{m}_z = +1$ and $\mathrm{m}_z = -1$, respectively. When a peak is not present the linewidth is set to zero.

coefficients are given by the formulas:

$$b_k(g) = -\alpha \frac{M_k(g)}{T_k(g)} + \frac{\nu^2}{2T_k(g)} \frac{\partial M_k^0(g)}{\partial g}, \tag{10.303}$$

$$\sigma_k(g) = \sqrt{\frac{M_k^0(g)}{T_k(g)}}, \tag{10.304}$$

where:

$$T_k(g) = \oint_{C_k(g)} \frac{\mathrm{d}l}{|\nabla_\Sigma g|}, \qquad M_k^0(g) = \oint_{C_k(g)} |\nabla_\Sigma g_L| \mathrm{d}l, \tag{10.305}$$

$$M_k(g, \beta/\alpha) = M_k^0(g) + \frac{\beta}{\alpha} \oint_{C_k(g)} \left[\frac{\mathbf{m} \times (\mathbf{m} \times \mathbf{e}_p)}{1 + c_p \mathbf{m} \cdot \mathbf{e}_p} \cdot \mathbf{n} \right] \mathrm{d}l. \tag{10.306}$$

The stochastic differential equation (10.302) defines a Markov process on the entire graph, provided the appropriate gluing (boundary) conditions [265,266] are imposed at each node (vertex) of the graph $\mathcal{G}$.

Next, we proceed to the discussion of calculation of the autocorrelation function and the power spectral density of some function $f(g)$. It can be shown that the calculation of the autocorrelation and spectral density of some measurable quantity $F(\mathbf{m})$ is reduced to the calculation of the autocorrelation and power spectral density of the following function defined on the graph $\mathcal{G}$:

$$f(g) = \frac{1}{T_k(g)} \int_{C_k(g)} F(\mathbf{m}) \frac{\mathrm{d}l}{|\nabla_\Sigma g|}. \tag{10.307}$$

By definition, the autocorrelation $C_f(\tau)$ of $f(g)$ is:

$$C_f(\tau) = \langle [f(g) - \langle f(g) \rangle] [f(g') - \langle f(g') \rangle] \rangle, \tag{10.308}$$

where g and g' are the energy values at times $t = \tau$ and $t = 0$, respectively, while as before the notation $\langle \cdot \rangle$ is used for (statistical) expected values. Autocorrelation $C_f(\tau)$ can be expressed in the integral form as follows:

$$C_f(\tau) = \int \int f(g) f(g') \left[\rho(g, \tau; g', 0) - \rho^{eq}(g) \rho^{eq}(g') \right] \mathrm{d}g \mathrm{d}g', \tag{10.309}$$

where $\rho(g,\tau;g',0)$ is the joint probability density function, $\rho^{eq}(g)$ is the stationary distribution function, while integration with respect to g and g' are performed over the entire graph $\mathcal{G}$.

The joint probability is given by:

$$\rho(g,\tau;g',0) = \rho(g,\tau|g',0)\rho^{eq}(g'), \tag{10.310}$$

where $\rho(g,\tau|g',0)$ is the transition probability function. This function satisfies the following Fokker–Planck equation on each edge I_k of the graph:

$$\frac{\partial}{\partial\tau}\rho_k(g,\tau|g',0) = \hat{L}_g^{(k)}\rho_k(g,\tau|g',0), \tag{10.311}$$

where:

$$\hat{L}_g^{(k)}\rho_k = -\frac{\partial}{\partial g}\left[b_k(g)\rho_k(g)\right] + \frac{\nu^2}{2}\frac{\partial^2}{\partial g^2}\left[\sigma_k^2(g)\rho_k(g)\right]. \tag{10.312}$$

The transition probability function satisfies the following initial condition:

$$\rho_k(g,\tau;g',0)|_{\tau=0} = \delta(g-g'), \tag{10.313}$$

and special boundary conditions at each vertex of the graph. These boundary conditions express the conservation of probability current at each vertex as well as the continuity of the transition probability normalized by $T_k(g)$. For instance, this transition probability continuity at the vertex d_1 in Fig. 4.2(b) is expressed as follows:

$$\frac{\rho_1(g_{d_1})}{T_1(g_{d_1})} = \frac{\rho_2(g_{d_1})}{T_2(g_{d_1})} = \frac{\rho_3(g_{d_1})}{T_3(g_{d_1})}, \tag{10.314}$$

where g_{d_1} is the energy value corresponding to the saddle d_1.

The stationary distribution function $\rho^{eq}(g)$ satisfies the stationary Fokker–Planck equation:

$$\hat{L}_g^{(k)}\rho_k^{eq}(g) = 0. \tag{10.315}$$

We note from Eqs (10.309) and (10.310) that, in order to compute the autocorrelation $C_f(\tau)$, the transition probability function $\rho(g,\tau|g',0)$ needs to be computed for all initial conditions g' (see formula (10.313)).

However, this deficiency can be completely circumvented by introducing an appropriately defined auxiliary ("effective") distribution function. To this end, by using Eq. (10.310), we shall rewrite formula (10.309) as follows:

$$C_f(\tau) = \int f(g) \left\{ \int f(g') \left[\rho(g, \tau | g', 0) - \rho_s(g) \right] \rho_s(g') \mathrm{d}g' \right\} \mathrm{d}g. \tag{10.316}$$

Now, we introduce the effective distribution function $p(g, \tau)$:

$$p(g, \tau) = \int f(g') \left[\rho(g, \tau | g', 0) - \rho_s(g) \right] \rho_s(g') \, \mathrm{d}g', \tag{10.317}$$

and write formula (10.316) in the form:

$$C_f(\tau) = \int f(g) p(g, \tau) \, \mathrm{d}g. \tag{10.318}$$

Thus, if the effective distribution $p(g, \tau)$ is somehow found, then $C_f(\tau)$ can be easily computed. Next, we shall derive the initial-boundary value problem for $p(g, \tau)$. It is clear from Eqs (10.312) and (10.315) that the difference $\rho(g, \tau | g', 0) - \rho^{eq}(g)$ satisfies Eq. (10.311). By replacing $\rho(g, \tau | g', 0)$ by $\rho(g, \tau | g', 0) - \rho^{eq}(g)$ in Eq. (10.311), multiplying the latter equation by $f(g')\rho_s(g')$, and next integrating it with respect to the "backward" variable g' over the graph $\mathcal{G}$, we derive the following equation for $p(g, \tau)$:

$$\frac{\partial}{\partial \tau} p_k(g, \tau) = \hat{L}_g^{(k)} p_k(g, \tau). \tag{10.319}$$

Next, by substituting the initial condition (10.313) into formula (10.317), we derive the following initial condition for the effective distribution function:

$$p_k(g, 0) = \left[f(g) - \langle f(g) \rangle \right] \rho_k^{eq}(g). \tag{10.320}$$

It is also clear that the boundary conditions for $p(g, \tau)$ at the vertices of the graph $\mathcal{G}$ will be the same as the boundary conditions for $\rho(g, \tau | g', 0)$. This is because these boundary conditions are formulated in terms of the "forward" variable g, while the transformation (10.317) from the transition

probability function to the "effective" probability function involves only integration over the "backward" variable g'.

Thus, appreciable simplification of computation of $C_f(\tau)$ has been achieved. Indeed, the initial boundary value problem (10.319)–(10.320) needs to be solved only once, and then $C_f(\tau)$ can be computed by using formula (10.318), i.e., by means of only one integration. This simplification can be translated into the simplification of computation of power spectral density $S_f(\omega)$, which is related to $C_f(\tau)$ as follows:

$$S_f(\omega) = \int_{-\infty}^{+\infty} C_f(\tau) \exp(-i\omega\tau)\, \mathrm{d}\tau. \tag{10.321}$$

By using formulas (10.318) and (10.321), we derive:

$$S_f(\omega) = \int_{-\infty}^{+\infty} f(g) P(g,\omega)\, \mathrm{d}g, \tag{10.322}$$

where:

$$P(g,\omega) = \int_{-\infty}^{+\infty} p(g,\tau) \exp(-i\omega\tau)\, \mathrm{d}\tau. \tag{10.323}$$

From the definition (10.323) and the initial-boundary value problem (10.319)–(10.320), we derive the following ordinary differential equations for $P(g,\omega)$ on the graph edges:

$$i\omega P_k(g,\omega) + \hat{L}_g^{(k)} P_k(g,\omega) = [f(g) - \langle f(g)\rangle]\, \rho_k^{eq}(g). \tag{10.324}$$

Thus, by solving the ordinary differential equations (10.324) subject to the same boundary vertex conditions, the function $P(g,\omega)$ can be calculated. Then by using formula (10.322), the power spectral density of $f(g)$ is computed.

To illustrate the presented technique, we apply it to the uniaxial spin-transfer device considered in Section 10.5, for which anisotropy axis, applied field, and spin polarization are all aligned along the symmetry axis $\mathbf{e}_z$. The energy of the system is given by Eq. (10.258), where the constant $\kappa_{\text{eff}} = D_\perp - D_z$ takes into account both crystalline and shape anisotropies, while h_{az} is the amplitude of the external magnetic field applied along the z axis. In this case the graph has two branches. The magnetization component m_z is a one-to-one function of g on each edge

of the graph:

$$\mathrm{m}_z = \mathrm{m}_{z,k}(g) = \left(-\mathrm{h}_{az} \pm \sqrt{\mathrm{h}_{az}^2 - 2\kappa_{\text{eff}} g}\right)/D_z, \quad k = \{1,2\}, \quad (10.325)$$

where the two values of k correspond to "+" and "−" signs, respectively. Note that the energy intervals associated with the two edges of the graph are $-(\mathrm{h}_{az} + \kappa_{\text{eff}}/2) \leq g \leq \mathrm{h}_{az}^2/(2\kappa_{\text{eff}})$, and $\mathrm{h}_{az} - \kappa_{\text{eff}}/2 \leq g \leq \mathrm{h}_{az}^2/(2\kappa_{\text{eff}})$, respectively. The potential Φ for spin-transfer effects is given by Eq. (10.259).

After appropriate algebraic manipulations of Eqs (10.305)–(10.306), it can be shown that:

$$T_k(g) = \frac{2\pi}{|\kappa_{\text{eff}}\mathrm{m}_{z,k}(g) + \mathrm{h}_{az}|} = 2\pi s_k \left[\frac{\partial g_L}{\partial \mathrm{m}_z}(\mathrm{m}_{z,k}(g))\right]^{-1}, \quad (10.326)$$

$$\begin{aligned} M_k^0(g) &= 2\pi \left[1 - \mathrm{m}_{z,k}(g)\right]^2 |\kappa_{\text{eff}}\mathrm{m}_{z,k}(g) + \mathrm{h}_{az}| \\ &= \left[1 - \mathrm{m}_{z,k}(g)\right]^2 2\pi s_k \left[\frac{\partial g_L}{\partial \mathrm{m}_z}(\mathrm{m}_{z,k}(g))\right], \end{aligned} \quad (10.327)$$

$$\begin{aligned} M_k(g, \beta/\alpha) &= M_k^0(g) + \frac{\beta}{\alpha}\left[1 - \mathrm{m}_{z,k}(g)\right]^2 \frac{2\pi s_k}{(1 + c_p \mathrm{m}_{z,k}(g))} \\ &= \left[1 - \mathrm{m}_{z,k}(g)\right]^2 2\pi s_k \frac{\partial \Phi}{\partial \mathrm{m}_z}(\mathrm{m}_{z,k}(g)), \end{aligned} \quad (10.328)$$

where s_k is the sign of $\partial g_L/\partial \mathrm{m}_z$.

The functions in Eqs (10.326)–(10.328) are continuous on the entire graph due to the continuity of the function $\mathrm{m}_{z,k}(g)$. By substituting Eqs (10.326)–(10.328) into Eqs (10.303), (10.304) and (10.312), one obtains the following Fokker–Planck equation:

$$\begin{aligned} \frac{\partial \rho_k}{\partial t} &= \alpha \frac{\partial}{\partial g}\left\{\left(\frac{\partial g_L}{\partial \mathrm{m}_z}(\mathrm{m}_{z,k}(g))\right)\left[1 - \mathrm{m}_{z,k}(g)\right]^2 \frac{\partial \Phi}{\partial \mathrm{m}_z}(\mathrm{m}_{z,k}(g))\rho_k\right\} \\ &\quad + \frac{\nu^2}{2}\frac{\partial}{\partial g}\left\{\left|\frac{\partial g_L}{\partial \mathrm{m}_z}(\mathrm{m}_{z,k}(g))\right|\left[1 - \mathrm{m}_{z,k}(g)\right]^2 \right. \\ &\quad \left. \times \frac{\partial}{\partial g}\left(\left|\frac{\partial g_L}{\partial \mathrm{m}_z}(\mathrm{m}_{z,k}(g))\right|\rho_k\right)\right\}. \end{aligned} \quad (10.329)$$

One can derive the stationary probability, which is given by:

$$\rho_k^{eq}(g) = \frac{1}{Z}\left|\frac{\partial g_L}{\partial \mathrm{m}_z}(\mathrm{m}_{z,k}(g))\right|^{-1} \exp\left[-\mu\Phi(\mathrm{m}_{z,k}(g))\right], \quad (10.330)$$

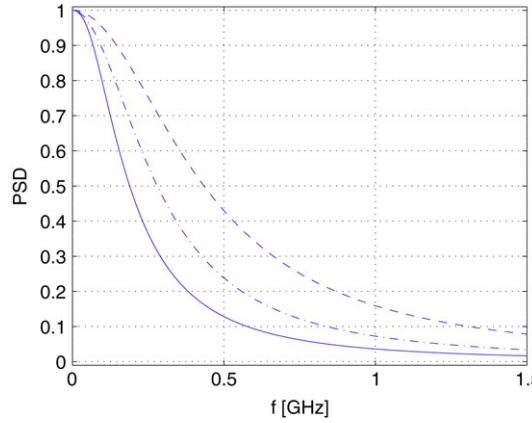

FIGURE 10.7 Power spectral density of the stochastic process $\mathrm{m}_z(g)$ for the three values of β/α: $\beta/\alpha = -1.0$ (dash-dotted line), $\beta/\alpha = 0$ (dashed line), $\beta/\alpha = 0.5$ (continuous lines). Other parameters: $\mathrm{h}_{az} = -0.2$, $\kappa_{\text{eff}} = 0.5$, $c_p = 0.5$, $\alpha = 0.01$, $T = 300$ K, $V = 4.8 \cdot 10^{-24}\mathrm{m}^3$, $\mathrm{M}_s = 6.5 \cdot 10^5$ A/m.

where $\mu = 2\alpha/\nu^2$ and Z is a normalizing constant such that the integral of ρ_k^{eq} over the entire graph is one.

By using the technique described above, we have computed the power spectral density of the function $\mathrm{m}_z(g)$ for three different values of the spin-polarized injected current, i.e., β/α. The results are presented in Fig. 10.7. They reveal that the linewidth tends to decrease as a result of the current injection.

10.7 STOCHASTIC MAGNETIZATION DYNAMICS IN NONUNIFORMLY MAGNETIZED FERROMAGNETS

In this section, we consider the problem of thermal fluctuations of magnetization in nonuniformly magnetized objects. In this case, the magnetic state is described by the magnetization vector field $\mathbf{m}(\mathbf{r}, t)$ and the equation governing the stochastic dynamics of $\mathbf{m}(\mathbf{r}, t)$ is obtained by adding a spatially distributed random magnetic torque to the deterministic equation. This leads to the following stochastic equation:

$$\frac{\partial \mathbf{m}}{\partial t} = -\mathbf{m} \times \mathbf{h}_{\text{eff}} - \alpha \mathbf{m} \times (\mathbf{m} \times \mathbf{h}_{\text{eff}}) - \nu \mathbf{m} \times \mathbf{h}_N(\mathbf{r}, t), \quad (10.331)$$

where $\mathbf{h}_N(\mathbf{r}, t)$ is a random field and ν is the constant measuring the intensity of thermal fluctuations. We recall that, in the case of spatially

distributed magnetic systems, $\mathbf{h}_{\text{eff}}$ is an operator which is defined as the variational derivative of the free energy functional $g_L(\mathbf{m}(.); \mathbf{h}_a)$:

$$\mathbf{h}_{\text{eff}} = -\frac{\delta g_L}{\delta \mathbf{m}}, \tag{10.332}$$

where:

$$g_L(\mathbf{m}(.); \mathbf{h}_a) = \frac{1}{V}\int_\Omega \left[\frac{1}{2}|\nabla \mathbf{m}|^2 + \varphi_{AN}(\mathbf{m}) - \frac{1}{2}\mathbf{h}_M \cdot \mathbf{m} - \mathbf{h}_a \cdot \mathbf{m}\right] \mathrm{d}V. \tag{10.333}$$

In this equation, $\varphi_{AN}(\mathbf{m})$ is the anisotropy energy density, $\mathbf{h}_M$ and $\mathbf{h}_a$ are the demagnetizing and applied fields, Ω indicates the region occupied by the object, and lengths are measured in units of the exchange length $l_{EX} = \sqrt{2A/\mu_0 \mathrm{M}_s^2}$. In particular, V represents the normalized volume of the object, measured in units of l_{EX}^3. Finally, homogeneous Neumann boundary conditions $\partial \mathbf{m}/\partial \mathbf{n} = 0$ are imposed at the boundary of Ω.

The random field $\mathbf{h}_N(\mathbf{r}, t)$ is assumed to be a normalized Gaussian white-noise random field characterized by the following mean value and autocorrelation function:

$$\begin{aligned} &\langle \mathbf{h}_N(\mathbf{r}, t)\rangle = 0, \\ &\langle h_{N,i}(\mathbf{r}, t) h_{N,j}(\mathbf{r}', t')\rangle = \delta_{ij}\delta(t - t')\delta(\mathbf{r} - \mathbf{r}'), \end{aligned} \tag{10.334}$$

where i, j are indexes labeling cartesian components.

The stochastic dynamics (10.331) driven by the white noise (10.334) is defined in an infinite-dimensional space. The mathematical theory of infinite-dimensional SDEs is not completely established and it is very difficult to give an appropriate mathematical meaning to the solutions of such stochastic differential equations. For this reason, instead of the continuous stochastic process (10.331), a finite-dimensional formulation will be introduced in terms of an appropriate finite dimensional representation of the vector field $\mathbf{m}(\mathbf{r})$. In this representation, $\mathbf{m}(\mathbf{r})$ is specified in a finite number of points in space, and values in intermediate points are computed by interpolation. Other types of discretization might be devised as well, by using, for example, spectral representations of $\mathbf{m}(\mathbf{r})$ by means of a truncated Fourier series. As it is often done, the discretization will be used under the tacit assumption that the discretized equation can approximate the evolution of the actual vector field $\mathbf{m}(\mathbf{r}, t)$

with the desired accuracy, even though this assumption cannot be given a rigorous mathematical justification.

In accordance with the above discussion, we introduce the following discretized version of Eq. (10.331). We consider a partition of the region Ω in N cells Ω_k with volume V_k. The vector field $\mathbf{m}(\mathbf{r}, t)$ is described by the collection of vectors $\boldsymbol{\mathcal{M}}_k(t)$ representing the integrals of $\mathbf{m}(\mathbf{r}, t)$ over each cell:

$$\boldsymbol{\mathcal{M}}_k(t) = \int_{\Omega_k} \mathbf{m}(\mathbf{r}, t) \mathrm{d}V. \tag{10.335}$$

Similarly, the discretized effective field is defined as the collection of the average effective fields over each cell:

$$\mathbf{h}_{\text{eff};k} = \frac{1}{V_k} \int_{\Omega_k} \mathbf{h}_{\text{eff}}(\mathbf{r}, t) \mathrm{d}V. \tag{10.336}$$

We note that $\boldsymbol{\mathcal{M}}_k(t)$ has the meaning of the normalized magnetic moment associated with the cell Ω_k. It is also assumed that the cells Ω_k are small enough that $\mathbf{m}(\mathbf{r}, t)$ can be considered spatially uniform in Ω_k. It is usually expected that $\mathbf{m}(\mathbf{r}, t)$ is spatially uniform over spatial scales comparable with the exchange length l_{EX}. Thus, the uniformity assumption implies that the cells should have a diameter in the order of unity or smaller.

The uniformity assumption and the fact that $|\mathbf{m}(\mathbf{r}, t)| = 1$ lead to the following constraint on the magnitude of the vectors $\boldsymbol{\mathcal{M}}_k(t)$:

$$|\boldsymbol{\mathcal{M}}_k(t)| = V_k. \tag{10.337}$$

Next, we proceed to the careful discussion of the discretization of the thermal field $\mathbf{h}_N(\mathbf{r}, t)$. The discretized random field $\mathbf{h}_{N;k}(t)$ is introduced as the spatial average of the continuous random field over the cell Ω_k. Namely, the following definition is adopted:

$$\nu_k \mathbf{h}_{N;k}(t) = \frac{1}{V_k} \int_{\Omega_k} \nu \mathbf{h}_N(\mathbf{r}, t) \mathrm{d}V, \tag{10.338}$$

where the constants ν_k are to be determined. From Eq. (10.334), one can readily show that the processes $\mathbf{h}_{N;k}(t)$ are zero-mean gaussian white-noise stochastic processes in time. In addition, the stochastic processes $\mathbf{h}_{N;k}(t)$ and $\mathbf{h}_{N;h}(t)$ associated with two distinct cells are statistically

independent. We shall use the following normalization conditions:

$$\langle h_{N;k,i}(t) h_{N;h,j}(t') \rangle = \delta_{kh} \delta_{ij} \delta(t - t'). \tag{10.339}$$

In this equation, k and h are indexes denoting cells, while i and j denote cartesian components. To guarantee that the conditions (10.339) are satisfied, we have to choose the appropriate value of ν_k in Eq. (10.338). To this end, let us consider the following identity, which can be readily derived from Eq. (10.334):

$$\left\langle \int_{\Omega_k} h_{N,i}(\mathbf{r}, t) \mathrm{d}V \int_{\Omega_h} h_{N,j}(\mathbf{r}', t') \mathrm{d}V' \right\rangle = V_k \delta_{kh} \delta_{ij} \delta(t - t'). \tag{10.340}$$

By comparing the last equation with Eqs (10.338) and (10.339), one obtains the value of the constant ν_k:

$$\nu_k^2 = \frac{\nu^2}{V_k^2} V_k \Longrightarrow \nu_k = \frac{\nu}{\sqrt{V_k}}. \tag{10.341}$$

By using the discretization outlined above, we arrive at the following set of discretized stochastic equations:

$$\begin{aligned} \frac{\mathrm{d}\boldsymbol{\mathcal{M}}_k}{\mathrm{d}t} = & -\boldsymbol{\mathcal{M}}_k \times \mathbf{h}_{\text{eff};k} - \frac{\alpha}{V_k} \boldsymbol{\mathcal{M}}_k \times (\boldsymbol{\mathcal{M}}_k \times \mathbf{h}_{\text{eff};k}) \\ & - \frac{\nu}{\sqrt{V_k}} \boldsymbol{\mathcal{M}}_k \times \mathbf{h}_{N;k}(t). \end{aligned} \tag{10.342}$$

The analysis of the coupled stochastic differential equations (10.342) can be carried out in the same way as the one presented in Section 10.1 for the stochastic magnetization dynamics in uniformly magnetized objects. Equation (10.342) can be rewritten in a different form by dividing both sides by V_k. This yields:

$$\begin{aligned} \frac{\mathrm{d}\mathbf{m}_k}{\mathrm{d}t} = & -\mathbf{m}_k \times \mathbf{h}_{\text{eff};k} - \alpha \mathbf{m}_k \times (\mathbf{m}_k \times \mathbf{h}_{\text{eff};k}) \\ & - \frac{\nu}{\sqrt{V_k}} \mathbf{m}_k \times \mathbf{h}_{N;k}(t), \end{aligned} \tag{10.343}$$

where $\mathbf{m}_k(t)$ represents the average magnetization in the kth cell:

$$\mathbf{m}_k(t) = \frac{1}{V_k} \int_{\Omega_k} \mathbf{m}(\mathbf{r}, t) \mathrm{d}V. \tag{10.344}$$

This quantity satisfies the normalization condition:

$$|\mathbf{m}_k(t)| = 1. \tag{10.345}$$

Discretized LL equations in the form Eq. (10.343) are commonly used as the starting point in computational micromagnetics studies. The form (10.342), on the other hand, turns out to be more convenient for the theoretical considerations that are presented in the sequel. This convenience is due to the presence of the factors $1/V_k$ and $1/\sqrt{V_k}$ respectively in the damping and fluctuation terms in Eq. (10.342). The specific form of these factors simplifies the derivation of fluctuation-dissipation relations.

The discretized free energy $G_L(\boldsymbol{\mathcal{M}}_1, \ldots, \boldsymbol{\mathcal{M}}_N; \mathbf{h}_a)$ for the model must be defined in such a way that its gradient yields the discretized effective field, namely:

$$h_{\text{eff};k,i} = -\frac{\partial G_L}{\partial \mathcal{M}_{k,i}}, \tag{10.346}$$

where i labels the cartesian components. The energy G_L is an approximation of the free energy functional $g_L(\mathbf{m}; \mathbf{h}_a)$:

$$G_L(\boldsymbol{\mathcal{M}}_1, \ldots, \boldsymbol{\mathcal{M}}_N; \mathbf{h}_a) \approx V g_L(\mathbf{m}(.); \mathbf{h}_a), \tag{10.347}$$

where V is the volume of the magnetic object. To write formula (10.346) in concise vector form, we introduce the following vectors in the $\mathbb{R}^{3N}$ Euclidean space:

$$\begin{aligned}
\underline{\boldsymbol{\mathcal{M}}} &= (\boldsymbol{\mathcal{M}}_1^T, \ldots, \boldsymbol{\mathcal{M}}_N^T)^T \\
&= (\mathcal{M}_{1,1}, \mathcal{M}_{1,2}, \mathcal{M}_{1,3}, \ldots, \mathcal{M}_{N,1}, \mathcal{M}_{N,2}, \mathcal{M}_{N,3})^T, && (10.348)\\
\underline{\boldsymbol{\mathcal{H}}}_{\text{eff}} &= (\mathbf{h}_{\text{eff};1}^T, \ldots, \mathbf{h}_{\text{eff};N}^T)^T \\
&= (h_{\text{eff};1,1}, h_{\text{eff};1,2}, h_{\text{eff};1,3}, \ldots, h_{\text{eff};N,1}, h_{\text{eff};N,2}, h_{\text{eff};N,3})^T, && (10.349)\\
\underline{\boldsymbol{\mathcal{H}}}_N &= (\mathbf{h}_{N;1}^T, \ldots, \mathbf{h}_{N;N}^T)^T \\
&= (h_{N;1,1}, h_{N;1,2}, h_{N;1,3}, \ldots, h_{N;N,1}, h_{N;N,2}, h_{N;N,3})^T, && (10.350)
\end{aligned}$$

where superscript T indicates transposition. With these notations, Eq. (10.346) can be written as:

$$\underline{\boldsymbol{\mathcal{H}}}_{\text{eff}} = -\frac{\partial}{\partial \underline{\boldsymbol{\mathcal{M}}}} G_L(\underline{\boldsymbol{\mathcal{M}}}). \tag{10.351}$$

In addition, we introduce the following block-diagonal matrices:

$$\underline{\Lambda}(\underline{\boldsymbol{\mathcal{M}}}) = \begin{pmatrix} \Lambda(\boldsymbol{\mathcal{M}}_1) & 0 & \cdots & 0 \\ 0 & \Lambda(\boldsymbol{\mathcal{M}}_2) & 0 \dots & 0 \\ \vdots & & \ddots & \\ 0 & \cdots & 0 & \Lambda(\boldsymbol{\mathcal{M}}_N) \end{pmatrix}, \tag{10.352}$$

$$D = \begin{pmatrix} V_1\mathcal{I}_3 & 0 & \cdots & 0 \\ 0 & V_2\mathcal{I}_3 & 0 \dots & 0 \\ \vdots & & \ddots & \\ 0 & \cdots & 0 & V_N\mathcal{I}_3 \end{pmatrix}, \tag{10.353}$$

where $\Lambda(\cdot)$ represents the vector product:

$$\Lambda(\mathbf{v}) = \begin{pmatrix} 0 & -v_z & v_y \\ v_z & 0 & -v_x \\ -v_y & v_x & 0 \end{pmatrix}, \tag{10.354}$$

while $\mathcal{I}_3$ is the 3×3 identity matrix.

By using the above notations, the discretized Eq. (10.342) can be written as an evolution equation in $\mathbb{R}^{3N}$ Euclidean space:

$$\begin{aligned} \frac{\mathrm{d}}{\mathrm{d}t}\underline{\boldsymbol{\mathcal{M}}} = \Lambda(\underline{\boldsymbol{\mathcal{M}}}) \cdot \frac{\partial G_L}{\partial \underline{\boldsymbol{\mathcal{M}}}} + \alpha D^{-1} \cdot \underline{\Lambda}^2(\underline{\boldsymbol{\mathcal{M}}}) \\ \cdot \frac{\partial G_L}{\partial \underline{\boldsymbol{\mathcal{M}}}} - \nu D^{-1/2} \cdot \underline{\Lambda}(\underline{\boldsymbol{\mathcal{M}}}) \cdot \underline{\boldsymbol{\mathcal{H}}}_N, \end{aligned} \tag{10.355}$$

where we recall that $\underline{\boldsymbol{\mathcal{H}}}_N$ is a $3N$-dimensional normalized white-noise stochastic process. Equation (10.355) can be written in the usual SDE notation:

$$\mathrm{d}\underline{\boldsymbol{\mathcal{M}}} = \underline{\mathbf{V}}\,(\underline{\boldsymbol{\mathcal{M}}})\,\mathrm{d}t + \sigma(\underline{\boldsymbol{\mathcal{M}}}) \cdot \mathrm{d}\underline{\boldsymbol{\mathcal{W}}}(t), \tag{10.356}$$

where:

$$\underline{\mathbf{V}}\,(\underline{\boldsymbol{\mathcal{M}}}) = \underline{\Lambda}(\underline{\boldsymbol{\mathcal{M}}}) \cdot \frac{\partial G_L}{\partial \underline{\boldsymbol{\mathcal{M}}}} + \alpha D^{-1} \cdot \underline{\Lambda}^2(\underline{\boldsymbol{\mathcal{M}}}) \cdot \frac{\partial G_L}{\partial \underline{\boldsymbol{\mathcal{M}}}}, \tag{10.357}$$

$$\sigma(\underline{\boldsymbol{\mathcal{M}}}) = -\nu D^{-1/2} \cdot \underline{\Lambda}(\underline{\boldsymbol{\mathcal{M}}}). \tag{10.358}$$

In Eq. (10.356), the vector field $\underline{\mathbf{V}}\left(\underline{\boldsymbol{\mathcal{M}}}\right)$ represents the deterministic drift term, while $\underline{\boldsymbol{\mathcal{W}}}(t)$ is the standard $3N$-dimensional Wiener process with uncorrelated components.

Equation (10.356) is formally similar to Eq. (10.40), which describes the stochastic magnetization dynamics in uniformly magnetized objects. Thus, all the considerations of Section 10.1 related to the multiplicative nature of the noise and the necessity of specifying the type of stochastic calculus (Itô's or Stratonovich's) are applicable to Eq. (10.356) as well. In particular, if we require that the stochastic dynamics described by Eq. (10.356) has to preserve the constraint $|\underline{\boldsymbol{\mathcal{M}}}_k| = V_k$, we have to adopt the Stratonovich calculus. With this adoption, the stochastic dynamics of $\underline{\boldsymbol{\mathcal{M}}}$ described by Eq. (10.356) takes place on the following $2N$-dimensional manifold (immersed in $\mathbb{R}^{3N}$):

$$\Sigma_{\mathcal{M}}^{N} = \Sigma(V_1) \otimes \Sigma(V_2) \otimes \cdots \otimes \Sigma(V_N), \tag{10.359}$$

where $\Sigma(R)$ denotes the ordinary two-dimensional sphere with radius R, while "$\otimes$" denotes the cartesian product. In other terms, we have that:

$$\underline{\boldsymbol{\mathcal{M}}} \in \Sigma_{\mathcal{M}}^{N} \Longrightarrow \boldsymbol{\mathcal{M}}_1 \in \Sigma(V_1), \boldsymbol{\mathcal{M}}_2 \in \Sigma(V_2), \ldots, \boldsymbol{\mathcal{M}}_N \in \Sigma(V_N). \tag{10.360}$$

By using the correspondence between the Stratonovich SDE and the Fokker–Planck equation, we arrive at the following Fokker–Planck equation:

$$\frac{\partial w}{\partial t} = -\mathrm{div}_{\underline{\boldsymbol{\mathcal{M}}}}\, \underline{\boldsymbol{\mathcal{J}}}. \tag{10.361}$$

The probability current $\underline{\boldsymbol{\mathcal{J}}}$ is defined as:

$$\underline{\boldsymbol{\mathcal{J}}} = \underline{\mathbf{V}}\left(\underline{\boldsymbol{\mathcal{M}}}\right) w - \frac{1}{2}\sigma\left(\underline{\boldsymbol{\mathcal{M}}}\right) \cdot \left\{\mathrm{div}_{\underline{\boldsymbol{\mathcal{M}}}}\left[\sigma\left(\underline{\boldsymbol{\mathcal{M}}}\right) w\right]\right\}^{T}, \tag{10.362}$$

where T denotes matrix transposition, while w is the conditional probability density:

$$w = w\left(\underline{\boldsymbol{\mathcal{M}}}, t | \underline{\boldsymbol{\mathcal{M}}}_0, t_0\right). \tag{10.363}$$

The divergence $\mathrm{div}_{\underline{\boldsymbol{\mathcal{M}}}}\underline{\boldsymbol{\mathcal{J}}}$ can be written as:

$$\mathrm{div}_{\underline{\boldsymbol{\mathcal{M}}}}\underline{\boldsymbol{\mathcal{J}}} = \sum_{k,i} \frac{\partial}{\partial \mathcal{M}_{k,i}} \mathcal{J}_{k,i} = \sum_{k} \mathrm{div}_{\boldsymbol{\mathcal{M}}_k} \boldsymbol{\mathcal{J}}_k, \tag{10.364}$$

where $\boldsymbol{\mathcal{J}}_k$ is the three-dimensional vector:

$$\boldsymbol{\mathcal{J}}_k = (\mathcal{J}_{k,1}, \mathcal{J}_{k,2}, \mathcal{J}_{k,3})^T. \tag{10.365}$$

By using the specific mathematical forms of $\underline{\mathbf{V}}(\underline{\boldsymbol{\mathcal{M}}})$ and $\sigma(\underline{\boldsymbol{\mathcal{M}}})$ (see Eqs (10.357)–(10.358)) in Eq. (10.362), we arrive at the following expression for the probability currents $\underline{\boldsymbol{\mathcal{J}}}_k$:

$$\begin{aligned}\boldsymbol{\mathcal{J}}_k = &\left[\boldsymbol{\mathcal{M}}_k \times \frac{\partial G_L}{\partial \boldsymbol{\mathcal{M}}_k} + \frac{\alpha}{\Omega_k}\boldsymbol{\mathcal{M}}_k \times \left(\boldsymbol{\mathcal{M}}_k \times \frac{\partial G_L}{\partial \boldsymbol{\mathcal{M}}_k}\right)\right] w \\ &+ \frac{\nu^2}{2\Omega_k}\boldsymbol{\mathcal{M}}_k \times \left(\boldsymbol{\mathcal{M}}_k \times \frac{\partial w}{\partial \boldsymbol{\mathcal{M}}_k}\right),\end{aligned} \tag{10.366}$$

which can be summarized in the vector formula:

$$\begin{aligned}\underline{\boldsymbol{\mathcal{J}}} = \Lambda(\underline{\boldsymbol{\mathcal{M}}}) \cdot \Bigg[&\left(\frac{\partial G_L}{\partial \underline{\boldsymbol{\mathcal{M}}}} + \alpha D^{-1} \cdot \Lambda(\underline{\boldsymbol{\mathcal{M}}}) \cdot \frac{\partial G_L}{\partial \underline{\boldsymbol{\mathcal{M}}}}\right) w \\ &+ \frac{\nu^2}{2} D^{-1} \cdot \left(\mathrm{div}_{\underline{\boldsymbol{\mathcal{M}}}}\left(\cdot \Lambda(\underline{\boldsymbol{\mathcal{M}}}) w\right)\right)^T\Bigg].\end{aligned} \tag{10.367}$$

The probability current $\underline{\boldsymbol{\mathcal{J}}}(\underline{\boldsymbol{\mathcal{M}}})$ is tangential to the manifold $\Sigma^N_{\mathcal{M}}$ (see Eq. (10.359)). Indeed, it can be verified that there are N linearly independent vectors, orthogonal to the tangent space of the manifold at the point $\underline{\boldsymbol{\mathcal{M}}} = (\boldsymbol{\mathcal{M}}_1, \ldots, \boldsymbol{\mathcal{M}}_N)$, given by:

$$\begin{aligned}&\underline{\mathbf{f}}_1(\underline{\boldsymbol{\mathcal{M}}}) = (\boldsymbol{\mathcal{M}}_1, \ldots, \mathbf{0}), \\ &\underline{\mathbf{f}}_2(\underline{\boldsymbol{\mathcal{M}}}) = (\mathbf{0}, \boldsymbol{\mathcal{M}}_2, \ldots, \mathbf{0}), \\ &\qquad\qquad\qquad\qquad \ldots, \\ &\underline{\mathbf{f}}_N(\underline{\boldsymbol{\mathcal{M}}}) = (\mathbf{0}, \ldots, \boldsymbol{\mathcal{M}}_N).\end{aligned} \tag{10.368}$$

Thus, $\underline{\mathbf{f}}_1(\underline{\boldsymbol{\mathcal{M}}}), \ldots, \underline{\mathbf{f}}_N(\underline{\boldsymbol{\mathcal{M}}})$ is a basis of the vector space orthogonal (in the $3N$-dimensional Euclidean space) to the tangent space of the manifold $\Sigma^N_{\mathcal{M}}$ at $\underline{\boldsymbol{\mathcal{M}}} = (\boldsymbol{\mathcal{M}}_1, \ldots, \boldsymbol{\mathcal{M}}_N)$. To verify that the vector $\underline{\boldsymbol{\mathcal{J}}}(\underline{\boldsymbol{\mathcal{M}}})$ is tangential to $\Sigma^N_{\mathcal{M}}$, it is sufficient to check that it is orthogonal to all $\underline{\mathbf{f}}_1, \ldots, \underline{\mathbf{f}}_N$. Indeed:

$$f_k(\underline{\boldsymbol{\mathcal{M}}}) \cdot \underline{\boldsymbol{\mathcal{J}}}(\underline{\boldsymbol{\mathcal{M}}}) = 0, \quad k = 1, 2, \ldots, N, \tag{10.369}$$

because:

$$\underline{\mathbf{f}}_k(\underline{\boldsymbol{\mathcal{M}}}) \cdot \underline{\Lambda}(\underline{\boldsymbol{\mathcal{M}}}) = 0, \quad k = 1, 2, \ldots, N. \tag{10.370}$$

The above result shows that the vectors $\underline{\mathbf{f}}_1(\underline{\boldsymbol{\mathcal{M}}}), \ldots, \underline{\mathbf{f}}_N(\underline{\boldsymbol{\mathcal{M}}})$ are a basis of the kernel of the matrix $\underline{\Lambda}(\underline{\boldsymbol{\mathcal{M}}})$. This reveals an important property of the Fokker–Planck equation: if the distribution w is different from zero only at points on the manifold $\Sigma^N_{\mathcal{M}}$, the evolution equations (10.361)–(10.367) for w will preserve this property. In other terms, there will be no diffusion of probability density outside the manifold. This fact has important consequences in the statistical mechanics of the problem. In fact, one can prove that:

$$\oiint_{\Sigma^N_{\mathcal{M}}} w(\underline{\boldsymbol{\mathcal{M}}}, t)\mathrm{d}S^N = \oiint_{\Sigma^N_{\mathcal{M}}} w(\underline{\boldsymbol{\mathcal{M}}}, t=0)\mathrm{d}S^N, \tag{10.371}$$

for any time instant $t > 0$. Therefore, one can impose the following normalization condition on w:

$$\oiint_{\Sigma^N_{\mathcal{M}}} w(\underline{\boldsymbol{\mathcal{M}}}, t)\mathrm{d}S^N = 1. \tag{10.372}$$

The stationary solution to the Fokker–Planck equation (10.361)–(10.367) is obtained by solving the equation:

$$\mathrm{div}_{\underline{\boldsymbol{\mathcal{M}}}}\underline{\boldsymbol{\mathcal{J}}} = 0. \tag{10.373}$$

We shall look for a solution in the form:

$$w^{eq}(\underline{\boldsymbol{\mathcal{M}}}) = F\left(G_L(\underline{\boldsymbol{\mathcal{M}}}) + \sum_k \frac{\lambda_k}{2}|\boldsymbol{\mathcal{M}}_k|^2\right) = F\left(H_L(\underline{\boldsymbol{\mathcal{M}}})\right), \tag{10.374}$$

where:

$$H_L(\underline{\boldsymbol{\mathcal{M}}}) = G_L(\underline{\boldsymbol{\mathcal{M}}}) + \sum_k \frac{\lambda_k}{2}|\boldsymbol{\mathcal{M}}_k|^2, \tag{10.375}$$

while λ_k are arbitrary multipliers related to the constraints $|\boldsymbol{\mathcal{M}}_k| = V_k$. Consider the conservative part of the drift:

$$\underline{\mathbf{V}}_0\left(\underline{\boldsymbol{\mathcal{M}}}\right) = \Lambda(\underline{\boldsymbol{\mathcal{M}}}) \cdot \frac{\partial G_L}{\partial \underline{\boldsymbol{\mathcal{M}}}}. \tag{10.376}$$

First, we intend to prove that:

$$\begin{aligned}\mathrm{div}_{\underline{\boldsymbol{\mathcal{M}}}}\left[\underline{\mathbf{V}}_0\left(\underline{\boldsymbol{\mathcal{M}}}\right) w^{eq}\right] &= w^{eq}\mathrm{div}_{\underline{\boldsymbol{\mathcal{M}}}}\underline{\mathbf{V}}_0\left(\underline{\boldsymbol{\mathcal{M}}}\right) + \underline{\mathbf{V}}_0\left(\underline{\boldsymbol{\mathcal{M}}}\right) \\ &\cdot \mathrm{grad}_{\underline{\boldsymbol{\mathcal{M}}}} w^{eq} = w^{eq}\mathrm{div}_{\underline{\boldsymbol{\mathcal{M}}}}\underline{\mathbf{V}}_0\left(\underline{\boldsymbol{\mathcal{M}}}\right). \end{aligned} \tag{10.377}$$

The proof proceeds as follows. According to Eq. (10.374), we have:

$$\mathrm{grad}_{\underline{\boldsymbol{\mathcal{M}}}} w^{eq} = F'\left(H_L(\underline{\boldsymbol{\mathcal{M}}})\right) \mathrm{grad}_{\underline{\boldsymbol{\mathcal{M}}}} H_L, \tag{10.378}$$

which implies that:

$$\underline{\mathbf{V}}_0\left(\underline{\boldsymbol{\mathcal{M}}}\right) \cdot \mathrm{grad}_{\underline{\boldsymbol{\mathcal{M}}}} H_L = \left(\frac{\partial H_L}{\partial \underline{\boldsymbol{\mathcal{M}}}}\right)^T \cdot \Lambda(\underline{\boldsymbol{\mathcal{M}}}) \cdot \frac{\partial G_L}{\partial \underline{\boldsymbol{\mathcal{M}}}} = 0. \tag{10.379}$$

The last equality is established by using the antisymmetric nature of $\Lambda(\underline{\boldsymbol{\mathcal{M}}})$, Eq. (10.370), and the identity:

$$\frac{\partial}{\partial \underline{\boldsymbol{\mathcal{M}}}}\left(\frac{1}{2}\sum_k |\boldsymbol{\mathcal{M}}_k|^2\right) = \underline{\mathbf{f}}_k(\underline{\boldsymbol{\mathcal{M}}}). \tag{10.380}$$

Since the diagonal blocks of the matrix Λ represent cross-products, from formula (10.376) we derive:

$$\mathrm{div}_{\underline{\boldsymbol{\mathcal{M}}}}\underline{\mathbf{V}}_0\left(\underline{\boldsymbol{\mathcal{M}}}\right) = \sum_k \mathrm{div}_{\boldsymbol{\mathcal{M}}_k}\left(\boldsymbol{\mathcal{M}}_k \times \frac{\partial G_L}{\partial \boldsymbol{\mathcal{M}}_k}\right) = 0. \tag{10.381}$$

By using this formula in Eq. (10.377), we find:

$$\mathrm{div}_{\underline{\boldsymbol{\mathcal{M}}}}\left[\underline{\mathbf{V}}_0\left(\underline{\boldsymbol{\mathcal{M}}}\right) w^{eq}\right] = 0. \tag{10.382}$$

Thus, the problem of finding the stationary solution of Eq. (10.361) is reduced to the solution of the following equation:

$$\begin{aligned}\mathrm{div}_{\underline{\boldsymbol{\mathcal{M}}}}\Bigg\{&\left[\alpha D^{-1} \cdot \underline{\Lambda}^2(\underline{\boldsymbol{\mathcal{M}}}) \cdot \frac{\partial G_L}{\partial \underline{\boldsymbol{\mathcal{M}}}} w^{eq}\right] \\ &+ \frac{\nu^2}{2} D^{-1} \cdot \underline{\Lambda}(\underline{\boldsymbol{\mathcal{M}}}) \cdot \left[\mathrm{div}_{\underline{\boldsymbol{\mathcal{M}}}}\left(\Lambda(\underline{\boldsymbol{\mathcal{M}}}) w^{eq}\right)\right]^T\Bigg\} = 0. \end{aligned} \tag{10.383}$$

It is demonstrated below that this solution is given by the function (10.374) because this function satisfies the following "detailed balance" equation:

$$\left[\alpha D^{-1}\cdot\underline{\Lambda}^2(\underline{\boldsymbol{\mathcal{M}}})\cdot\frac{\partial G_L}{\partial\underline{\boldsymbol{\mathcal{M}}}}w^{eq}\right] + \frac{\nu^2}{2}D^{-1}\cdot\underline{\Lambda}(\underline{\boldsymbol{\mathcal{M}}})\cdot\left[\mathrm{div}_{\underline{\boldsymbol{\mathcal{M}}}}\left(\Lambda(\underline{\boldsymbol{\mathcal{M}}})w^{eq}\right)\right]^T=0. \tag{10.384}$$

We first observe that:

$$\mathrm{div}_{\underline{\boldsymbol{\mathcal{M}}}}\left(\underline{\Lambda}(\underline{\boldsymbol{\mathcal{M}}})w^{eq}\right)=\sum_k\mathrm{div}_{\boldsymbol{\mathcal{M}}_k}\left(\Lambda(\boldsymbol{\mathcal{M}}_k)w^{eq}\right) = w^{eq}\sum_k\mathrm{div}_{\boldsymbol{\mathcal{M}}_k}\Lambda(\boldsymbol{\mathcal{M}}_k)+\sum_k\Lambda(\boldsymbol{\mathcal{M}}_k)\cdot\frac{\partial w^{eq}}{\partial\boldsymbol{\mathcal{M}}_k}. \tag{10.385}$$

Then, by using the fact that:

$$\mathrm{div}_{\boldsymbol{\mathcal{M}}_k}\Lambda(\boldsymbol{\mathcal{M}}_k)=0, \tag{10.386}$$

and by taking into account formulas (10.374) and (10.385), Eq. (10.384) can be rewritten in the form:

$$D^{-1}\cdot\Lambda^2(\underline{\boldsymbol{\mathcal{M}}})\cdot\left(\alpha\frac{\partial G_L}{\partial\underline{\boldsymbol{\mathcal{M}}}}F\left(H_L\right)+\frac{\nu^2}{2}\frac{\partial F\left(H_L\right)}{\partial\underline{\boldsymbol{\mathcal{M}}}}\right)=0. \tag{10.387}$$

By factoring out $F\left(H_L\right)$, one arrives at the equation:

$$F\left(H_L\right)D^{-1}\cdot\Lambda^2(\underline{\boldsymbol{\mathcal{M}}})\cdot\left(\alpha\frac{\partial G_L}{\partial\underline{\boldsymbol{\mathcal{M}}}}+\frac{\nu^2}{2}\frac{\partial\log\left(F\left(H_L\right)\right)}{\partial\underline{\boldsymbol{\mathcal{M}}}}\right)=0, \tag{10.388}$$

i.e.:

$$\alpha\frac{\partial G_L}{\partial\underline{\boldsymbol{\mathcal{M}}}}+\frac{\nu^2}{2}\frac{\partial\log\left(F\left(H_L\right)\right)}{\partial\underline{\boldsymbol{\mathcal{M}}}}=\sum_k\lambda_k\underline{\mathbf{f}}_k(\underline{\boldsymbol{\mathcal{M}}}), \tag{10.389}$$

where the fact has been used that the vectors $\underline{\mathbf{f}}_k$ form a basis of the kernel of the matrix $\Lambda(\underline{\boldsymbol{\mathcal{M}}})$. This finally yields the solution:

$$\begin{aligned} w^{eq}(\underline{\boldsymbol{\mathcal{M}}}) &= F\left(H_L(\underline{\boldsymbol{\mathcal{M}}})\right) \\ &= C\exp\left[-\mu G_L(\underline{\boldsymbol{\mathcal{M}}}) + \sum_k \frac{\lambda_k}{2}|\boldsymbol{\mathcal{M}}_k|^2\right], \end{aligned} \tag{10.390}$$

where $\mu = 2\alpha/\nu^2$.

The constant C is obtained from the normalization condition:

$$\oiint_{\Sigma^N_{\mathcal{M}}} w^{eq}(\underline{\boldsymbol{\mathcal{M}}})\mathrm{d}S^N = 1. \tag{10.391}$$

The quantities $|\boldsymbol{\mathcal{M}}_k|^2$ in Eq. (10.390) are all constants and thus they can be included into the constant C itself. By using Eq. (10.391), we conclude that the distribution function can be written in the form:

$$w^{eq}(\underline{\boldsymbol{\mathcal{M}}}) = \frac{1}{Z(\mu)}\exp\left[-\mu G_L(\underline{\boldsymbol{\mathcal{M}}})\right], \tag{10.392}$$

where $Z(\mu)$ is the "partition function":

$$Z(\mu) = \int_{\Sigma^N_{\mathcal{M}}} \exp\left[-\mu G_L(\underline{\boldsymbol{\mathcal{M}}})\right]\mathrm{d}S. \tag{10.393}$$

The stationary distribution (10.392) must coincide with the Boltzmann distribution:

$$w_B(\underline{\boldsymbol{\mathcal{M}}}) = C\exp\left[-\frac{\mu_0 \mathrm{M}_s^2 l_{EX}^3}{k_B T} G_L(\underline{\boldsymbol{\mathcal{M}}})\right], \tag{10.394}$$

where the normalization constant $\mu_0\mathrm{M}_s^2$ has been included to measure energy in physical units. By comparing Eqs (10.392) and (10.394), we end up with the following fluctuation-dissipation relation:

$$\nu^2 = \frac{2\alpha k_B T}{\mu_0 \mathrm{M}_s^2 l_{EX}^3}, \tag{10.395}$$

which permits one to determine the noise intensity in the original LLG equation. This result is completely *independent* of the discretization

procedure, because formula (10.395) does not contain any quantity related to the cell partition. This is consistent with the meaning of the quantity ν.

Finally, by using Eq. (10.395) in Eq. (10.341), one finds:

$$\nu_k = \sqrt{\frac{2\alpha k_B T}{\mu_0 \mathrm{M}_s^2 l_{EX}^3 V_k}}, \tag{10.396}$$

where $l_{EX}^3 V_k$ is the volume of the kth cell in physical units. This formula gives the intensity of the noise terms in the spatially discretized LLG equation.

The analysis of the evolution of the conditional probability density through the solution of the Fokker–Planck equation is quite difficult, due to the very high dimensionality of the state space. The study of fluctuations in nonuniformly magnetized bodies can be carried out by direct numerical integration of Eqs (10.356)–(10.358). In applications, ferromagnetic devices are designed to be relatively stable against thermal fluctuations. This means that stable magnetization states are separated by large energy barriers and thermally activated transitions between these states occur on very long time scales. Under these conditions, magnetization dynamics has very different time scales of evolution: stochastically perturbed precessional dynamics occurs on the picosecond time scale, while thermally activated dynamics may occur on the microsecond or millisecond time scales. Since a correct stochastic time integration requires an accurate description also of the fast time scale, direct numerical simulations of magnetization dynamics may become computationally very expensive. The study of thermally activated transitions under these weak noise conditions can be carried out by using appropriate asymptotic techniques, such as nudged elastic band method [223], string method [235], and action functional method [412]. These techniques provide estimates for the probability of certain transitions. The probability is estimated in terms of exponential factors which can be computed by determining the most probable dynamic path to realize the transition under investigation. This issue is related to the area of mathematics referred to as large deviation theory. A discussion of this issue goes beyond the scope of this book.

CHAPTER 11

Numerical Techniques for Magnetization Dynamics Analysis

11.1 MID-POINT FINITE-DIFFERENCE SCHEMES

Due to the nonlinear nature of the Landau–Lifshitz–Gilbert or Landau–Lifshitz equation, analytical solutions can be derived in very few special cases [394,459,81]. For this reason, the most general and mostly used method to study magnetization dynamics is to solve the LLG equation numerically. Typically, the dynamic problem is first discretized in space by using finite-difference or finite element methods [258]. This leads to a discretized version of the micromagnetic free energy and to a corresponding system of ordinary differential equations (ODEs). Then, this system of ODEs is numerically integrated by using appropriate time-stepping techniques. While the spatial discretization is carried out by preserving the main properties of the energy functional $g_L(\mathbf{m}(.); \mathbf{h}_a)$, little attention is paid to the preservation of the unique features of LLG dynamics. In this regard, the main emphasis in this chapter is on the derivation of finite-difference schemes that preserve the qualitative features of time-continuous magnetization dynamics. The main structural feature of LLG dynamics which is important to preserve is the conservation of magnetization magnitude. In addition, it is desirable to preserve other intrinsic properties of the dynamics such as the monotonic decrease of free energy under constant external fields, or the Hamiltonian structure in the limit of zero damping. It is demonstrated in this chapter that this can be achieved by using "mid-point" finite-difference schemes. These schemes are unconditionally stable and of second-order accuracy. They also preserve the fundamental structural properties of LLG dynamics [193].

The problem of designing time-stepping techniques which preserve structural properties of LLG dynamics has been largely overlooked in magnetization dynamics studies. In fact, most researchers use

"off-the-shelf" algorithms such as Euler, linear multi-step methods (e.g., Adams-Bashforth, Adams-Moulton, Crank-Nicholson, Backward Differentiation Formulas (BDF)) or Runge–Kutta methods [499,585]. This is partly due to the fact that the main emphasis has been on static micromagnetics and on obtaining accurate approximations of the free energy landscape. This goal has been generally achieved by using sufficiently accurate spatial discretizations. On the other hand, when magnetization dynamics has to be investigated, the issue of accurate numerical time integration techniques becomes crucial.

Existing discretization techniques (e.g., fourth- or higher-order explicit Runge–Kutta, predictor-corrector, etc.), when applied to the LLG or LL equation, usually corrupt the conservation of magnetization magnitude in time. For this reason, it is very important to develop finite-difference schemes that preserve this property, especially when the long-term dynamical behavior of the system has to be investigated. It is also desirable to have discretization schemes that lead to finite-difference equations that are not spatially coupled. For such schemes, magnetization at each spatial mesh point can be updated in time independently of other spatial mesh points. In addition, it is beneficial to have finite-difference schemes that are linear and of second-order accuracy as far as truncation error is concerned. A finite-difference two-step scheme that fulfills the above requirements is presented below. The property of conservation of magnetization magnitude in the numerical integration is achieved by using the mid-point rule. In fact, the use of the mid-point rule to devise numerical schemes that preserve dynamic invariants (e.g., magnetization, energy, angular momentum, etc.) has been extensively explored in the area of Hamiltonian dynamics [161,417]. It is important to observe that the application of the standard mid-point rule to the Landau–Lifshitz equation would produce spatially coupled finite-difference equations that would require the inversion of a large system of nonlinear equations at each integration step. The finite-difference scheme discussed below is based on the coupling of the mid-point rule with an appropriate two-step extrapolation formula which leads to spatially uncoupled difference equations.

For the sake of simplicity and clarity, the formulas in this section are derived in the case of uniformly magnetized objects. Later in this chapter, these formulas are extended to the case of nonuniformly magnetized ferromagnets.

We start the discussion by writing the Landau–Lifshitz–Gilbert equation in the form:

$$\frac{\mathrm{d}\mathbf{m}}{\mathrm{d}t} = -\mathbf{m} \times \boldsymbol{\mathcal{H}}(\mathbf{m}, t), \tag{11.1}$$

where $\boldsymbol{\mathcal{H}}$ is a generalized effective field which takes into account all effects driving the dynamics of $\mathbf{m}$. In the case of the Landau–Lifshitz equation $\boldsymbol{\mathcal{H}}$ takes the following form:

$$\boldsymbol{\mathcal{H}} = (\mathbf{h}_{\text{eff}} + \alpha \mathbf{m} \times \mathbf{h}_{\text{eff}}) . \tag{11.2}$$

More generally, if one considers effects due to spin transfer or effects due to rotating fields, $\boldsymbol{\mathcal{H}}$ can be written in the following two-scalar-potential form (see Chapter 3):

$$\boldsymbol{\mathcal{H}} = \frac{\partial g_L}{\partial \mathbf{m}} + \alpha \mathbf{m} \times \frac{\partial \Phi}{\partial \mathbf{m}}. \tag{11.3}$$

In order to develop a numerical integration scheme for Eq. (11.1), we consider the temporal mesh consisting of the sequence of time instants $t_1, t_2, t_3, \ldots$, which, for the sake of simplicity, are uniformly spaced, i.e., $t_{k+1} - t_k = \Delta t$. A numerical time-stepping scheme is a map:

$$\mathbf{m}^{(k+1)} = F_k(\Delta t, \mathbf{m}^{(k)}, \mathbf{m}^{(k-1)}, \ldots), \quad k = 1, 2, \ldots, \tag{11.4}$$

which generates a sequence of approximate values $\mathbf{m}^{(k)}$ of the unknown solution $\mathbf{m}(t)$ of the LLG equation at the time instants t_k.

The first point to be addressed is whether there are techniques which preserve the magnetization magnitude in the numerical integration. It is shown below that the conservation of $|\mathbf{m}|$ can be achieved by using the following mid-point rule formulas:

$$\frac{\mathrm{d}\mathbf{m}}{\mathrm{d}t}(t_k + \Delta t/2) = \frac{\mathbf{m}(t_{k+1}) - \mathbf{m}(t_k)}{\Delta t} + \mathcal{O}\left(\Delta t^2\right), \tag{11.5}$$

$$\mathbf{m}(t_k + \Delta t/2) = \frac{\mathbf{m}(t_{k+1}) + \mathbf{m}(t_k)}{2} + \mathcal{O}\left(\Delta t^2\right). \tag{11.6}$$

By substituting Eqs (11.5) and (11.6) in Eq. (11.1), we obtain:

$$\frac{\mathbf{m}(t_{k+1}) - \mathbf{m}(t_k)}{\Delta t} = -\left(\frac{\mathbf{m}(t_{k+1}) + \mathbf{m}(t_k)}{2}\right) \times \boldsymbol{\mathcal{H}}(t_k + \Delta t/2) + \mathcal{O}\left(\Delta t^2\right). \tag{11.7}$$

To arrive at the final form of the finite-difference scheme, we have to express $\boldsymbol{\mathcal{H}}(t_k + \Delta t/2)$ in terms of values of $\boldsymbol{\mathcal{H}}$ at the mesh points. This can be done by using different techniques. However, the conservation of

magnetization magnitude does not depend on a particular formula by which $\boldsymbol{\mathcal{H}}(t_k + \Delta t/2)$ is approximated. By using any formula $\mathbf{H}^{(k)}$ of the second order of accuracy in time, we will arrive at the expression:

$$\boldsymbol{\mathcal{H}}(t_k + \Delta t/2) = \mathbf{H}^{(k)}\left(\mathbf{m}(t_{k+1}), \mathbf{m}(t_k), \mathbf{m}(t_{k-1}), \ldots\right) + \mathcal{O}\left(\Delta t^2\right). \quad (11.8)$$

By using Eqs (11.7) and (11.8), we can devise the following second-order-accuracy time-stepping scheme:

$$\mathbf{m}^{(k+1)} - \mathbf{m}^{(k)} = -\frac{\Delta t}{2}\left(\mathbf{m}^{(k+1)} + \mathbf{m}^{(k)}\right) \times \boldsymbol{\mathcal{H}}^{\left(k+\frac{1}{2}\right)}, \quad (11.9)$$

where:

$$\boldsymbol{\mathcal{H}}^{\left(k+\frac{1}{2}\right)} = \mathbf{H}^{(k)}\left(\mathbf{m}^{(k+1)}, \mathbf{m}^{(k)}, \mathbf{m}^{(k-1)}, \ldots\right). \quad (11.10)$$

The remarkable property of the scheme (11.9)–(11.10) is that it preserves the magnetization magnitude. Indeed, by computing the dot products of both sides of equation (11.9) with the vector $\mathbf{m}^{(k+1)} + \mathbf{m}^{(k)}$, we obtain:

$$\left(\mathbf{m}^{(k+1)} + \mathbf{m}^{(k)}\right) \cdot \left(\mathbf{m}^{(k+1)} - \mathbf{m}^{(k)}\right) = 0, \quad (11.11)$$

which is equivalent to:

$$|\mathbf{m}^{(k+1)}|^2 = |\mathbf{m}^{(k)}|^2 = \text{const}. \quad (11.12)$$

This conservation property is valid for any form of the function $\mathbf{H}^{(k)}$ used in Eq. (11.8). Furthermore, this property of the scheme is valid for any excitation conditions (constant or time-varying applied fields, constant or time-varying spin-transfer effects, various anisotropy properties, etc.).

The numerical scheme (11.9) is implicit in nature since it contains $\mathbf{m}^{(k+1)}$ on both sides. However, we can use explicit extrapolation formulas in Eq. (11.10). This implies the choice of functions $\mathbf{H}^{(k)}$ which do not depend on $\mathbf{m}^{(k+1)}$ but only on $\mathbf{m}$ at previous time steps. Then, the computation of $\mathbf{m}^{(k+1)}$ in Eq. (11.9) requires only the solution of a linear equation. It is convenient to rewrite the finite-difference scheme (11.9) as follows:

$$\mathbf{m}^{(k+1)} + \frac{\Delta t}{2}\mathbf{m}^{(k+1)} \times \boldsymbol{\mathcal{H}}^{\left(k+\frac{1}{2}\right)} = \mathbf{m}^{(k)} - \frac{\Delta t}{2}\mathbf{m}^{(k)} \times \boldsymbol{\mathcal{H}}^{\left(k+\frac{1}{2}\right)}. \quad (11.13)$$

The last formula can be interpreted as a linear vector equation for $\mathbf{m}^{(k+1)}$ (or as three simultaneous linear equations for the cartesian components of $\mathbf{m}^{(k+1)}$).

A convenient second-order finite-difference scheme can be devised by using the following Adams extrapolation formula:

$$\boldsymbol{\mathcal{H}}(t_k + \Delta t/2) = \frac{3}{2}\boldsymbol{\mathcal{H}}\left(\mathbf{m}(t_k), t_k\right) - \frac{1}{2}\boldsymbol{\mathcal{H}}\left(\mathbf{m}(t_{k-1}), t_{k-1}\right) + \mathcal{O}\left(\Delta t^2\right). \tag{11.14}$$

This leads to the following expression for the field $\boldsymbol{\mathcal{H}}^{\left(k+\frac{1}{2}\right)}$ in Eq. (11.9):

$$\boldsymbol{\mathcal{H}}^{\left(k+\frac{1}{2}\right)} = \frac{3}{2}\boldsymbol{\mathcal{H}}\left(\mathbf{m}^{(k)}, t_k\right) - \frac{1}{2}\boldsymbol{\mathcal{H}}\left(\mathbf{m}^{(k-1)}, t_{k-1}\right). \tag{11.15}$$

The resulting finite-difference scheme is fast and quite simple to implement. It is also very convenient for the analysis of spatially nonuniform dynamics, where the extrapolation formula given by Eq. (11.15) can be used at each spatial location by using the values of $\mathbf{m}^{(k)}$ and $\boldsymbol{\mathcal{H}}^{(k)}$ at previous time instants at the same location. In this way, by using the two-step structure of the scheme, it is possible to achieve a complete decoupling in spatially nonuniform magnetization dynamics analysis. This two-step scheme presents a minor difficulty for the calculation of $\boldsymbol{\mathcal{H}}^{\left(\frac{1}{2}\right)}$ at the first step. This difficulty can be circumvented by using the second-order Runge–Kutta method to compute $\mathbf{m}^{\left(\frac{1}{2}\right)}$ needed for the calculation of $\boldsymbol{\mathcal{H}}^{\left(\frac{1}{2}\right)}$.

Next, we shall investigate the mid-point rule for the preservation of the energy balance properties of LLG dynamics in numerical computations. The preservation of the magnetization magnitude by the mid-point rule is valid for any excitation conditions and it is only based on the cross-product structure of the equation of motion. On the other hand, in the study of the energy balance property we need to be more specific about the excitation conditions. We start our discussion with the case of a uniformly magnetized ferromagnet subject to a constant-in-time applied field. It is convenient to use the Gilbert form of the magnetization dynamics equation, namely Eq. (11.1) with:

$$\boldsymbol{\mathcal{H}} = \mathbf{h}_{\text{eff}} - \alpha\frac{\mathrm{d}\mathbf{m}}{\mathrm{d}t}. \tag{11.16}$$

The effective field $\mathbf{h}_{\text{eff}}$ has the following form:

$$\mathbf{h}_{\text{eff}} = -D \cdot \mathbf{m} + \mathbf{h}_a, \tag{11.17}$$

where D is the 3×3 symmetric matrix describing anisotropies, and $\mathbf{h}_a$ is the constant applied field. Under these conditions, the energy is a quadratic function of $\mathbf{m}$:

$$g_L = \frac{1}{2}\mathbf{m} \cdot D \cdot \mathbf{m} - \mathbf{h}_a \cdot \mathbf{m}. \tag{11.18}$$

Furthermore, the energy satisfies the following energy balance equation (see Chapter 3):

$$\frac{\mathrm{d}g_L}{\mathrm{d}t} = -\alpha \left| \frac{\mathrm{d}\mathbf{m}}{\mathrm{d}t} \right|^2. \tag{11.19}$$

It has been shown above that the following finite-difference scheme preserves the magnetization magnitude:

$$\begin{aligned} \frac{\mathbf{m}(t_{k+1}) - \mathbf{m}(t_k)}{\Delta t} = &- \left(\frac{\mathbf{m}(t_{k+1}) + \mathbf{m}(t_k)}{2} \right) \\ &\times \boldsymbol{\mathcal{H}}(t_k + \Delta t/2) + \mathcal{O}\left(\Delta t^2\right). \end{aligned} \tag{11.20}$$

The mathematical form of the evolution equation (11.19) for the free energy can be mimicked by using the following mid-point formula for $\boldsymbol{\mathcal{H}}(t_k + \Delta t/2)$:

$$\begin{aligned} \boldsymbol{\mathcal{H}}(t_k + \Delta t/2) = &-D \cdot \left[\frac{\mathbf{m}(t_{k+1}) + \mathbf{m}(t_k)}{2} \right] + \mathbf{h}_a \\ &- \alpha \frac{\mathbf{m}(t_{k+1}) - \mathbf{m}(t_k)}{\Delta t} + \mathcal{O}(\Delta t^2). \end{aligned} \tag{11.21}$$

The last two formulas lead to the following mid-point scheme for Eq. (11.1):

$$\mathbf{m}^{(k+1)} - \mathbf{m}^{(k)} = -\frac{\Delta t}{2} \left(\mathbf{m}^{(k+1)} + \mathbf{m}^{(k)} \right) \times \boldsymbol{\mathcal{H}}^{\left(k+\frac{1}{2}\right)}, \tag{11.22}$$

with:

$$\boldsymbol{\mathcal{H}}^{\left(k+\frac{1}{2}\right)} = -D \cdot \left[\frac{\mathbf{m}^{(k+1)} + \mathbf{m}^{(k)}}{2}\right] + \mathbf{h}_a - \alpha \frac{\mathbf{m}^{(k+1)} - \mathbf{m}^{(k)}}{\Delta t}. \quad (11.23)$$

By dot-multiplying both sides of Eq. (11.22) by $\boldsymbol{\mathcal{H}}^{\left(k+\frac{1}{2}\right)}$, we obtain $\boldsymbol{\mathcal{H}}^{\left(k+\frac{1}{2}\right)} \cdot (\mathbf{m}^{(k+1)} - \mathbf{m}^{(k)})/\Delta t = 0$. Then, by substituting formula (11.23) for $\boldsymbol{\mathcal{H}}^{\left(k+\frac{1}{2}\right)}$ in the last identity and by using the symmetry of the matrix D and formula (11.18), we find the following energy balance for the discretized dynamics:

$$\frac{g_L^{(k+1)} - g_L^{(k)}}{\Delta t} = -\alpha \left| \frac{\mathbf{m}^{(k+1)} - \mathbf{m}^{(k)}}{\Delta t} \right|^2, \quad (11.24)$$

where $g_L^{(k)} = g_L(\mathbf{m}^{(k)})$.

Equation (11.24) has very important consequences. First, it shows that the mid-point rule is an unconditionally stable algorithm which reproduces the relaxation behavior in LLG discretized dynamics for any choice of the time step. In addition, for $\alpha = 0$ the energy is exactly preserved regardless of the time step. This property indicates that for slightly dissipative systems the mid-point rule will tend to reproduce correctly the time-evolution of the energy during the LLG dynamics.

In order to test the accuracy of the finite-difference scheme (11.13) and (11.15), we have studied the magnetization dynamics in the case of a uniformly magnetized thin film subjected to an in-plane and circularly polarized magnetic field as well as to a dc magnetic field normal to the film plane. For this case exact analytical time-harmonic solutions (**P**-modes) can be found (see Chapter 7). These exact solutions are compared with numerical solutions in Figs 11.1 and 11.2. These figures demonstrate that the numerical solution converges after some transient to a periodic (uniformly rotating) solution for which $|\mathbf{m}_\perp|$ as well as the angle between $\mathbf{h}_{a\perp}$ and $\mathbf{m}_\perp$ are constant (the subscript $\perp$ denotes components in the film plane). The calculations were performed near ferromagnetic resonance conditions, by using the following data: $\mathrm{M}_s = 8 \times 10^5$ A/m, $\alpha = 0.01$, dc field $\mathrm{h}_{az} = \mathrm{H}_{az}/\mathrm{M}_s = 1.1$, in-plane rotating ac field with amplitude $\mathrm{h}_{a\perp} = \mathrm{H}_{a\perp}/\mathrm{M}_s = 5 \times 10^{-4}$ and with normalized angular frequency $\omega = 0.103$, which is equivalent to 1.82×10^{10} Hz. Under these conditions, the magnetization dynamics exhibits the foldover effect (see Section 7.5) and there are two possible stable uniformly rotating steady-state solutions. In Figs 11.1 and 11.2, two time-evolutions of magnetization are reported which eventually reach the two different stable steady-state regimes. These evolutions can be obtained by choosing the initial conditions

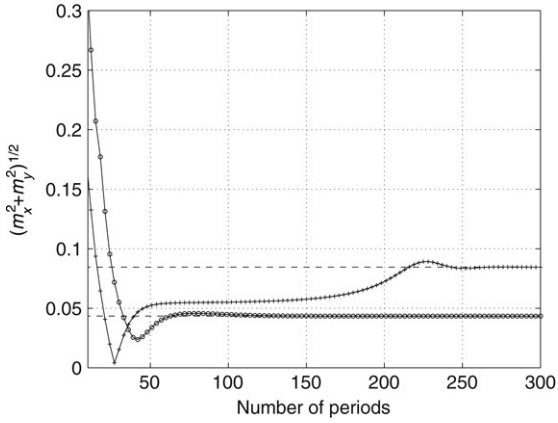

FIGURE 11.1 Comparison between analytical and numerical solutions for $|\mathbf{m}_\perp|$. Dashed lines represent the analytically computed **P**-mode solutions. Symbol "$\circ$" indicates time evolution starting at $t = 0$ from $\mathbf{m}(0) = (0.5774, 0.5774, -0.5774)$; values of the parameters: $\mathrm{M}_s = 8 \times 10^5$ A/m, $\alpha = 0.01$. Symbol "$+$" indicates time evolution starting at $t = 0$ from $\mathbf{m}(0) = (0.2357, 0.2357, 0.9428)$; values of parameters: $\omega = 0.103$, $\mathrm{h}_{az} = 1.1$, $\mathrm{h}_{a\perp} = 1 \times 10^{-4}$.

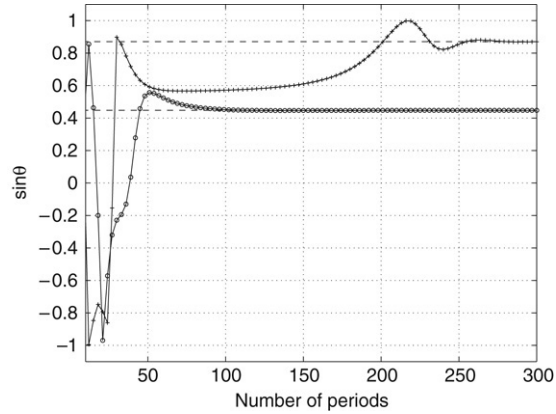

FIGURE 11.2 Comparison between analytical and numerical solutions for $\sin\theta$ where θ is the angle between $\mathbf{h}_{a\perp}$ and $\mathbf{m}_\perp$. Dashed lines represent the analytically computed **P**-mode solutions. Symbols and values of the parameters are the same as in Fig. 11.1.

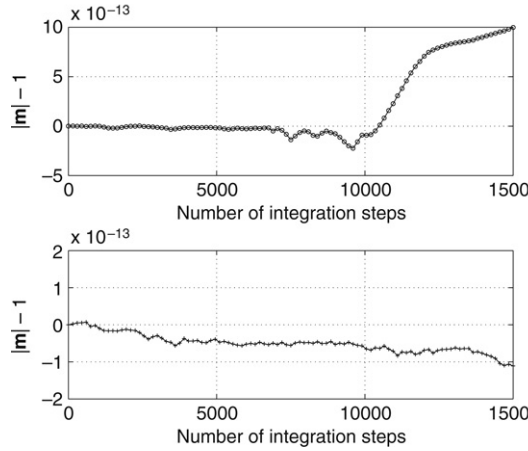

FIGURE 11.3 Relative error in the magnetization amplitude for the simulations reported in Figs 11.1–11.2.

$\mathbf{m}(0) = (0.5774, 0.5774, -0.5774)$ (results are indicated with the symbol "$\circ$" in Figs 11.1 and 11.2) and $\mathbf{m}(0) = (0.2357, 0.2357, 0.9428)$ (indicated with the symbol "$+$" in Figs 11.1 and 11.2), respectively. Figure 11.3 demonstrates that the magnitude of magnetization $|\mathbf{M}(t)|$ is conserved for both simulations with high accuracy (relative error is smaller than 10^{-12} after 15 000 time steps).

11.2 MID-POINT FINITE-DIFFERENCE SCHEMES FOR STOCHASTIC MAGNETIZATION DYNAMICS

The mid-point rule is also very effective in time-stepping schemes for solving the Landau–Lifshitz–Gilbert equation in the presence of noise. In this situation, the equation of magnetization dynamics is a stochastic differential equation. As we discussed in Chapter 10, special attention must be paid to the mathematical interpretation of the solution of this kind of equation. These mathematical facts are also important in the numerical integration of this equation since different time-stepping techniques may be compatible, in the limit of vanishing time step, with different interpretations (i.e., Itô's or Stratonovich's) of the stochastic differential equation. In this respect, it is interesting to demonstrate that the mid-point scheme (11.22)–(11.23) is compatible with the Stratonovich interpretation.

To start the discussion, we recall the basic facts concerning magnetization dynamics in uniformly magnetized particles in the

presence of thermal fluctuations. The equation governing magnetization dynamics is the Landau–Lifshitz equation:

$$\frac{\mathrm{d}\mathbf{m}}{\mathrm{d}t} = -\mathbf{m} \times (\mathbf{h}_{\text{eff}} + \nu \mathbf{h}_N) - \alpha \mathbf{m} \times [\mathbf{m} \times (\mathbf{h}_{\text{eff}} + \nu \mathbf{h}_N)], \qquad (11.25)$$

where the random thermal field $\nu \mathbf{h}_N(t)$ is an isotropic vector gaussian white-noise process with variance ν^2. As a consequence, $\mathbf{h}_N(t)$ can be expressed in terms of the Wiener process as follows:

$$\mathbf{h}_N(t)\mathrm{d}t = \mathrm{d}\mathbf{W}(t), \qquad (11.26)$$

where $\mathbf{W}(t)$ is the isotropic vector Wiener process characterized by $\langle |\mathrm{W}_i(t) - \mathrm{W}_i(s)|^2 \rangle = t - s$ ($\langle \cdot \rangle$ means statistical average).

As discussed in Chapter 10, the fact that we describe the thermal fluctuations by a multiplicative white-noise process produces the so-called Itô–Stratonovich dilemma [277]. This means that Eq. (11.25) has to be complemented by the specification of the type of stochastic calculus to be used. In this respect, following Brown [135] and Kubo [425], we interpret Eq. (11.25) in the sense of Stratonovich. Since in this interpretation the ordinary rules of calculus apply, one can immediately derive from Eq. (11.25) that:

$$\mathrm{d}(|\mathbf{m}|^2) = 2\mathbf{m} \cdot \mathrm{d}\mathbf{m} = 0, \qquad (11.27)$$

which means that SDE (11.25) generates a stochastic process on the unit sphere (this is not strictly true if one interprets (11.25) in Itô sense). We now rewrite Eq. (11.25) as follows:

$$\mathrm{d}\mathbf{m} = \mathbf{v}(\mathbf{m}, t)\mathrm{d}t - \mathbf{m} \times (\nu \mathrm{d}\mathbf{W} + \alpha\nu \mathbf{m} \times \mathrm{d}\mathbf{W}), \qquad (11.28)$$

where $\mathbf{v}(\mathbf{m}) = -\mathbf{m} \times (\mathbf{h}_{\text{eff}} + \alpha \mathbf{m} \times \mathbf{h}_{\text{eff}})$. The SDE (11.28) can be also transformed into the alternative Itô SDE by adding the noise-induced drift term [264] (see Section 10.1):

$$\mathrm{d}\mathbf{m} = \left[\mathbf{v}(\mathbf{m}, t) - \nu^2 \mathbf{m}\right] \mathrm{d}t - \mathbf{m} \times (\nu \mathrm{d}\mathbf{W} + \alpha\nu \mathbf{m} \times \mathrm{d}\mathbf{W}). \qquad (11.29)$$

Equation (11.28) in the sense of Stratonovich and Eq. (11.29) in the sense of Itô are statistically equivalent and describe the same stochastic process $\mathbf{m}(t)$ on the unit sphere $|\mathbf{m}|^2 = 1$. Indeed, it has been shown in Section 10.2 that the Fokker–Planck equations associated with these two

SDEs are the same and can be written in the form:

$$\frac{\partial w}{\partial t} = -\nabla_{\Sigma} \cdot \mathbf{J}, \tag{11.30}$$

where $\mathbf{J} = \mathbf{v}(\mathbf{m}, t)\, w(\mathbf{m}, t) - \left(\nu^2/2\right) \nabla_{\Sigma} w(\mathbf{m}, t)$, while $w(\mathbf{m}, t)$ is the probability density of $\mathbf{m}$ on the unit sphere Σ and ∇_{Σ} is the gradient operator on Σ. The value of the constant ν can be derived from the fluctuation-dissipation theorem. This leads to the following expression:

$$\nu^2 = \frac{2\alpha k_B T}{\mu_0 \mathrm{M}_s^2 V}, \tag{11.31}$$

where V is the volume of the particle. This expression is consistent with the one derived by Brown [135] and later by Garcia-Palacios [275] and Fredkin [264] (see Chapter 10).

The choice of specific interpretations of the solution of the stochastic LLG equation requires the use of specific numerical schemes for its integration. For instance, if one considers Eq. (11.28) in the sense of Stratonovich, one has to choose a numerical scheme that in the limit of time step $\Delta t \to 0$ converges to the Stratonovich solution. Similarly, considering Eq. (11.29) in the sense of Itô, one has to choose specific numerical schemes converging to the Itô solution for $\Delta t \to 0$. In the case of Itô SDE, this is generally achieved by using methods such as the forward Euler and Milstein methods [585], whereas in the case of Stratonovich SDE one has to adopt numerical schemes such as Heun [275, 585] or methods based on the mid-point rule [492]. The most common choice for the integration of stochastic LLG equation is the adoption of explicit integration methods like forward Euler and Heun. However, despite the fact that the Euler (Heun) numerical solution converges to the Itô (Stratonovich) solution with mean square error of order $1/2$ (m.s. error of order 1 for the Heun scheme) for $\Delta t \to 0$, for finite Δt the use of these explicit methods does not preserve magnetization magnitude. In order to circumvent this problem, some researchers use the naive approach of renormalizing the magnitude of the magnetization computed with the forward Euler (Heun) method at each time step. This is a nonlinear modification of the forward Euler (Heun) scheme for which the convergence towards the Itô (Stratonovich) solution should yet be proved. In addition, explicit methods have to deal with numerical stability requirements which impose the constraints of very small time steps.

Conversely, it has been proved [492] that the implicit mid-point rule scheme converges to the Stratonovich solution of Eq. (11.28) with mean

square error of order $1/2$. It has been also demonstrated that this scheme has clear advantages in the numerical integration of the deterministic LLG equation [591,193]. In fact, despite the implicit nature of the scheme requiring the solution of a nonlinear system of coupled equations at each time step, the computational cost of the mid-point rule is comparable to that of explicit methods since one can choose considerably larger time steps due to the unconditional stability (details on the analysis of the computational cost can be found in Ref. [193]). It is shown below that these advantages are even more pronounced in the numerical integration of the stochastic LLG equation.

The mid-point discretized version of Eq. (11.28) is given by:

$$\begin{aligned}\mathbf{m}^{(k+1)} - \mathbf{m}^{(k)} = &-\mathbf{m}^{(k+\frac{1}{2})} \times (\mathbf{h}_{\text{eff}}^{(k+\frac{1}{2})} + \alpha \mathbf{m}^{(k+\frac{1}{2})} \times \mathbf{h}_{\text{eff}}^{(k+\frac{1}{2})})\Delta t \\ &- \mathbf{m}^{(k+\frac{1}{2})} \times [\nu(\mathbf{W}^{(k+1)} - \mathbf{W}^{(k)}) + \alpha\nu \mathbf{m}^{(k+\frac{1}{2})} \\ &\times (\mathbf{W}^{(k+1)} - \mathbf{W}^{(k)})], \end{aligned} \tag{11.32}$$

where $\mathbf{m}^{(k+\frac{1}{2})} = (\mathbf{m}^{(k+1)} + \mathbf{m}^{(k)})/2$ and $\mathbf{h}_{\text{eff}}^{(k+\frac{1}{2})} = \mathbf{h}_{\text{eff}}(\mathbf{m}^{(k+\frac{1}{2})})$. Now, by dot-multiplying both sides of Eq. (11.32) by $\mathbf{m}^{(k+\frac{1}{2})}$, one can verify that:

$$|\mathbf{m}^{(k+1)}|^2 - |\mathbf{m}^{(k)}|^2 = 0. \tag{11.33}$$

This means that the magnetization magnitude is conserved unconditionally, i.e., for any choice of Δt. This reveals that the discrete-time stochastic process $\mathbf{m}^{(k)}$ evolves on the unit sphere.

It is also interesting to study the energy balance properties of mid-point discretized stochastic dynamics. For the sake of simplicity, we assume that the applied field $\mathbf{h}_a$ is constant in time. By dot-multiplying both sides of Eq. (11.32) by $[\mathbf{h}_{\text{eff}}^{(k+\frac{1}{2})}\Delta t + \nu(\mathbf{W}^{(k+1)} - \mathbf{W}^{(k)})]$, and by taking into account that $\mathbf{h}_{\text{eff}}^{(k+\frac{1}{2})} = -D \cdot \mathbf{m}^{(k+\frac{1}{2})} + \mathbf{h}_a$ and $g_L(\mathbf{m}) = (\mathbf{m} \cdot D \cdot \mathbf{m})/2 - \mathbf{h}_a \cdot \mathbf{m}$ (the matrix $D = \text{diag}[D_x, D_y, D_z]$), one obtains:

$$\begin{aligned} g_L^{(k+1)} - g_L^{(k)} - \left(\mathbf{m}^{(k+1)} - \mathbf{m}^{(k)}\right) \cdot \left(\nu \frac{\mathbf{W}^{(k+1)} - \mathbf{W}^{(k)}}{\Delta t}\right) \\ = -\alpha \left| \mathbf{m}^{(k+\frac{1}{2})} \times \left(\mathbf{h}_{\text{eff}}^{(k+\frac{1}{2})} + \nu \frac{\mathbf{W}^{(k+1)} - \mathbf{W}^{(k)}}{\Delta t}\right)\right|^2 \Delta t, \end{aligned} \tag{11.34}$$

where $g_L^{(k+1)} = g_L(\mathbf{m}^{(k+1)})$ and $g_L^{(k)} = g_L(\mathbf{m}^{(k)})$. As a consequence of Eq. (11.34), one finds:

$$g_L^{(k+1)} - g_L^{(k)} \leq \left(\mathbf{m}^{(k+1)} - \mathbf{m}^{(k)}\right) \cdot \left(\nu \frac{\mathbf{W}^{(k+1)} - \mathbf{W}^{(k)}}{\Delta t}\right). \quad (11.35)$$

The last inequality implies that for any finite Δt the variation of the free energy cannot exceed the average work performed by the thermal field on the magnetization. From Eqs (11.34)–(11.35) it follows that: (i) in the deterministic case ($\nu = 0$), the free energy is always a decreasing function of time; (ii) in the conservative case ($\alpha = 0$, $\nu = 0$), the discretized free energy is exactly preserved. Both (i) and (ii) are fulfilled unconditionally. The property (i) is a consequence of the unconditional stability of the mid-point rule, which allows one to choose the time step Δt only for accuracy reasons, whereas explicit methods have to deal with strict numerical stability constraints. The property (ii) guarantees an accurate reproduction of the precessional magnetization dynamics. This property is very important for stochastic dynamics with moderately low noise, in which the magnetization motion is mainly driven by the precession and the influence of thermal fluctuations occurs on a much longer time scale. As far as the actual solving of Eq. (11.32) is concerned, it can be performed by using a quasi-Newton technique similar to the one described in Ref. [193].

To test the effectiveness of the mid-point rule numerical technique, we have simulated the thermal relaxation of a cobalt spheroidal particle to the superparamagnetic state. In the simulations, the x, y, z half-axis lengths have been respectively chosen as 2 nm, 2 nm, 4 nm, while the choice of material parameters has been as follows: $\mathrm{M}_s = 1.42 \times 10^6$ A/m, $K_1 = 10^5$ J/m^3 ($D_z = N_z - 2K_1/(\mu_0 \mathrm{M}_s^2)$, $D_x = N_x, D_y = N_y$, $D_x = D_y = D_\perp$, N_x, N_y, N_z are the demagnetizing factors along x, y, z directions), $\alpha = 0.005$. It has been assumed that the temperature $T = 300$ K and there is no external applied field. In Fig. 11.4(a) the plot of the time evolution of m_z is presented, while the plot of $1 - |\mathbf{m}|$ as a function of time is given in Fig. 11.4(b). One can clearly observe that the property (11.33) is fulfilled with computer precision. Next, we analyze the system in the superparamagnetic state. In this state, the equilibrium expression for $w^{eq}(\mathbf{m})$ has the following Boltzmann-like form [135] (see Section 10.4):

$$w^{eq}(\mathbf{m}) = \frac{1}{Z(\mu)} \exp(-\mu g_L(\mathbf{m})), \qquad Z(\mu) = \oiint_\Sigma w^{eq}(\mathbf{m}) \mathrm{d}S, \quad (11.36)$$

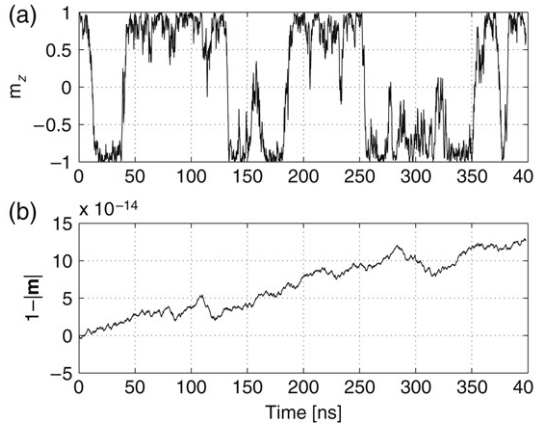

FIGURE 11.4 Numerical results for thermal fluctuations of magnetization in a spheroidal Co particle under zero external field. (a) Plot of the time evolution of m_z. (b) Plot of $1 - |\mathbf{m}|$ as a function of time. Simulation parameters: $D_z = 0.0946$, $D_x = D_y = 0.4132$, $\alpha = 0.005$, $\mathrm{M}_s = 1.42 \times 10^6$ A/m, $T = 300$ K.

where $\mu = 2\alpha/\nu^2 = \mu_0 \mathrm{M}_s^2 V/k_B T$. In the case of spheroidal particles, Eq. (11.36) is reduced to the following simple function of m_z:

$$w^{eq}(\mathbf{m}) = \frac{1}{Z(\mu)} \exp(-\mu(D_z \mathrm{m}_z^2 + D_\perp(1 - \mathrm{m}_z^2))/2), \tag{11.37}$$

which is presented in Fig. 11.5 by the solid line. Since the distribution $w^{eq}(\mathrm{m}_z)$ is symmetric with respect to zero, it is clear that at thermodynamic equilibrium $\langle \mathrm{m}_z \rangle = 0$. In order to compute the equilibrium distribution by using numerical simulations, we have proceeded as follows: an ensemble of N particles with magnetization initially aligned along the easy axis has been used, then Eq. (11.32) has been repeatedly solved until the ensemble average stabilized at zero. Afterwards, the histogram of the N final values of m_z has been computed. This histogram, after appropriate normalization to N, is an approximation of the probability distribution function $w^{eq}(\mathrm{m}_z)$. The results of this calculation are presented in Fig. 11.5 by the dashed line with black dots. It can be observed that the agreement with Eq. (11.37) is quite good. The time step used in the simulations was such that $(\gamma \mathrm{M}_s)^{-1} \Delta t = 1.6$ ps, which is considerably larger than the time step used with explicit methods, but comparable with the time scale of actual magnetization dynamics phenomena.

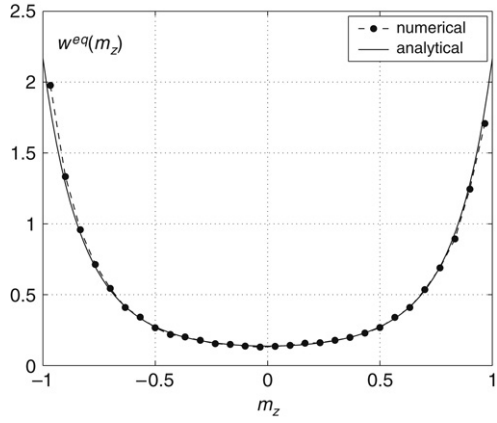

FIGURE 11.5 Equilibrium distribution function $w^{eq}(\mathrm{m}_z)$. Solid line refers to the analytical expression (11.37). Dashed line with black dots refers to the numerically computed equilibrium distribution. The simulation parameters are the same as in Fig. 11.4. The number of simulated particles is $N = 100\,000$.

11.3 NUMERICAL TECHNIQUES FOR NONUNIFORMLY MAGNETIZED PARTICLES

To treat the case of nonuniformly magnetized ferromagnets, we shall first introduce a spatially discretized version of the Landau–Lifshitz–Gilbert dynamics. The spatial discretization of magnetization dynamics has been already introduced in Section 10.7 in connection with the study of thermal fluctuations in nonuniformly magnetized objects. The discussion here follows the same line of reasoning and it is briefly summarized here for the reader's convenience. It is important to stress that we tacitly assume that the spatially discretized LLG equation can approximate the continuous problem with any degree of accuracy by appropriately increasing the number of discretization cells. Although a formal proof of this convergence result is not available (to our knowledge), this assumption justifies the use of numerical techniques to analyze the spatially nonuniform LLG dynamics. The discussion presented below is quite general and applicable to all spatial discretization techniques such as finite difference or finite elements [193,258].

We start our discussion by recalling the Landau–Lifshitz–Gilbert equation for nonuniformly magnetized bodies. This equation can be

written in the following form:

$$\frac{\partial \mathbf{m}}{\partial t} - \alpha \mathbf{m} \times \frac{\partial \mathbf{m}}{\partial t} = -\mathbf{m} \times \mathbf{h}_{\text{eff}}, \tag{11.38}$$

or equivalently (up to appropriate rescaling of time) as:

$$\frac{\partial \mathbf{m}}{\partial t} = -\mathbf{m} \times \mathbf{h}_{\text{eff}} - \alpha \mathbf{m} \times (\mathbf{m} \times \mathbf{h}_{\text{eff}}), \tag{11.39}$$

where:

$$\mathbf{h}_{\text{eff}} = -\frac{\delta g_L}{\delta \mathbf{m}}, \tag{11.40}$$

$$g_L(\mathbf{m}(.); \mathbf{h}_a) = \frac{1}{V} \int_\Omega \left[\frac{1}{2} |\nabla \mathbf{m}|^2 + \varphi_{AN}(\mathbf{m}) - \frac{1}{2} \mathbf{h}_M \cdot \mathbf{m} - \mathbf{h}_a \cdot \mathbf{m} \right] \mathrm{d}V. \tag{11.41}$$

Here, $\varphi_{AN}(\mathbf{m})$ is the anisotropy energy density (which for the sake of simplicity is assumed to be uniaxial), $\mathbf{h}_M$ and $\mathbf{h}_a$ are the demagnetizing and applied fields, Ω indicates the region occupied by the ferromagnet, and V is the volume of the region. In addition, homogeneous Neumann boundary conditions $\partial \mathbf{m}/\partial \mathbf{n} = 0$ are imposed at the object surface. We also remind that, in the equations above, time is measured in units of $(\gamma \mathrm{M}_s)^{-1}$ and space in units of the exchange length l_{EX}. Thus, the volume in physical units of the region occupied by the ferromagnet is $V l_{EX}^3$.

The spatial discretization is achieved by subdividing the magnetic object in N cells or finite elements. We denote the magnetization vector associated with the kth cell or node by $\mathbf{m}_k(t) \in \mathbb{R}^3$. Analogously, the effective and the applied fields at each cell will be denoted as $\mathbf{h}_{\text{eff};k}(t)$ and $\mathbf{h}_{a;k}(t)$, respectively. In addition to the vectors associated with the cells, we introduce vectors associated with the entire mesh. These are $\mathbb{R}^{3N}$ vectors formed by the collection of all cell vectors. We will indicate the mesh vectors associated with $\mathbf{m}, \mathbf{h}_{\text{eff}}, \mathbf{h}_a$ by the notations $\underline{\mathbf{m}}$, $\underline{\mathbf{h}}_{\text{eff}}$, $\underline{\mathbf{h}}_{\text{a}}$. These vectors are as follows:

$$\underline{\mathbf{m}} = \begin{pmatrix} \mathbf{m}_1 \\ \vdots \\ \mathbf{m}_N \end{pmatrix} \qquad \underline{\mathbf{h}}_{\text{eff}} = \begin{pmatrix} \mathbf{h}_{\text{eff};1} \\ \vdots \\ \mathbf{h}_{\text{eff};N} \end{pmatrix} \qquad \underline{\mathbf{h}}_{\text{a}} = \begin{pmatrix} \mathbf{h}_{a;1} \\ \vdots \\ \mathbf{h}_{a;N} \end{pmatrix}. \tag{11.42}$$

We assume that the discretization cells are small enough that for the magnetization vector $\mathbf{m}_k$ associated with each discretization cell we can

assume the validity of fundamental micromagnetics constraint:

$$|\mathbf{m}_k| = 1. \tag{11.43}$$

This means that the $\mathbb{R}^{3N}$ vector $\underline{\mathbf{m}}$ is associated with a point of the $2N$-dimensional manifold (embedded in $\mathbb{R}^{3N}$):

$$\Sigma^N = \Sigma \otimes \cdots \otimes \Sigma, \tag{11.44}$$

where Σ denotes the ordinary two-dimensional sphere with unit radius, and "$\otimes$" denotes the cartesian product. In other terms, we have:

$$\underline{\mathbf{m}} \in \Sigma^N \Longrightarrow \mathbf{m}_1 \in \Sigma, \mathbf{m}_2 \in \Sigma, \ldots, \mathbf{m}_N \in \Sigma. \tag{11.45}$$

Next, we discuss the form of the free energy and the effective fields which appear in the spatially discretized equations. Usual spatial discretization techniques [258] (e.g., finite elements and finite differences) quite naturally lead to a discretized version of the free energy (11.41), which has the form:

$$\underline{g}_L(\underline{\mathbf{m}}; \underline{\mathbf{h}}_a) = \frac{1}{2}\underline{\mathbf{m}} \cdot \underline{\mathrm{C}} \cdot \underline{\mathbf{m}} - \underline{\mathbf{h}}_a \cdot \underline{\mathbf{m}}, \tag{11.46}$$

where $\underline{\mathrm{C}}$ is now a $3N \times 3N$ symmetric matrix [585] which describes exchange, (uniaxial) anisotropy and magnetostatic interactions. Once the discretized free energy has been defined, the corresponding spatially discretized effective field $\underline{\mathbf{h}}_{\text{eff}}(\underline{\mathbf{m}}, t)$ can be obtained as:

$$\underline{\mathbf{h}}_{\text{eff}}(\underline{\mathbf{m}}, t) = -\frac{\partial \underline{g}_L}{\partial \underline{\mathbf{m}}} = -\underline{\mathrm{C}} \cdot \underline{\mathbf{m}} + \underline{\mathbf{h}}_a(t). \tag{11.47}$$

The matrix $\underline{\mathrm{C}}$ can be naturally decomposed into the sum of the three terms $\underline{\mathrm{C}}_{\text{ex}}$, $\underline{\mathrm{C}}_{\text{m}}$, $\underline{\mathrm{C}}_{\text{an}}$, which correspond to discretized exchange, magnetostatic and anisotropy interactions:

$$\underline{\mathrm{C}} = \underline{\mathrm{C}}_{\text{ex}} + \underline{\mathrm{C}}_{\text{m}} + \underline{\mathrm{C}}_{\text{an}}. \tag{11.48}$$

It can be observed that $\underline{\mathrm{C}}_{\text{ex}}$ and $\underline{\mathrm{C}}_{\text{an}}$ are sparse matrices since the exchange and anisotropy interactions have a local character, whereas $\underline{\mathrm{C}}_{\text{m}}$ is a fully populated matrix due to the long-range nature of magnetostatic interactions.

In the above notations, the spatially discretized LLG equations form a coupled set of $3N$ ODEs, which for a generic kth cell can be written as follows:

$$\frac{\mathrm{d}}{\mathrm{d}t}\mathbf{m}_k = -\mathbf{m}_k \times \left[\mathbf{h}_{\mathrm{eff};k}(\underline{\mathbf{m}}, t) - \alpha \frac{\mathrm{d}}{\mathrm{d}t}\mathbf{m}_k\right]. \tag{11.49}$$

The entire set of ODEs is:

$$\frac{\mathrm{d}}{\mathrm{d}t}\underline{\mathbf{m}} = -\underline{\Lambda}(\underline{\mathbf{m}}) \cdot \left[\underline{\mathbf{h}}_{\mathrm{eff}}(\underline{\mathbf{m}}, t) - \alpha \frac{\mathrm{d}}{\mathrm{d}t}\underline{\mathbf{m}}\right], \tag{11.50}$$

where $\underline{\Lambda}(\underline{\mathbf{m}})$ is a block-diagonal matrix:

$$\underline{\Lambda}(\underline{\mathbf{m}}) = \mathrm{diag}(\Lambda(\mathbf{m}_1), \ldots, \Lambda(\mathbf{m}_N)), \tag{11.51}$$

with blocks $\Lambda(\cdot) \in \mathbb{R}^{3\times 3}$ such that $\Lambda(\mathbf{v}) \cdot \mathbf{w} = \mathbf{v} \times \mathbf{w}$, for any $\mathbf{v}, \mathbf{w} \in \mathbb{R}^3$. We also observe that $\underline{\Lambda}(\underline{\mathbf{m}})$ is linearly dependent on $\underline{\mathbf{m}}$:

$$\underline{\Lambda}(\underline{\mathbf{m}}) = \underline{\Gamma} \cdot \underline{\mathbf{m}}, \tag{11.52}$$

where tensor $\underline{\Gamma}$ has N diagonal $3 \times 3 \times 3$ third-order permutation tensors and the dot product in Eq. (11.52) represents an index contraction. The meaning of this contraction can be inferred by observing that the component of the vector $\underline{\mathbf{v}} \cdot (\underline{\Gamma} \cdot \underline{\mathbf{w}})$ corresponding to the kth cell is given by:

$$(\underline{\mathbf{v}} \cdot (\underline{\Gamma} \cdot \underline{\mathbf{w}}))_k = \mathbf{v}_k \times \mathbf{w}_k, \tag{11.53}$$

where we have used the notation introduced above for mesh vectors $\underline{\mathbf{v}}$, $\underline{\mathbf{w}}$ and cell vectors $\mathbf{v}_k$, $\mathbf{w}_k$. The semi-discretized LLG equation can be transformed to the following Landau–Lifshitz form:

$$\frac{\mathrm{d}}{\mathrm{d}t}\underline{\mathbf{m}} = -\underline{\Lambda}(\underline{\mathbf{m}}) \cdot \underline{\mathbf{h}}_{\mathrm{eff}}(\underline{\mathbf{m}}, t) - \alpha \underline{\Lambda}(\underline{\mathbf{m}}) \cdot (\underline{\Lambda}(\underline{\mathbf{m}}) \cdot \underline{\mathbf{h}}_{\mathrm{eff}}(\underline{\mathbf{m}}, t)). \tag{11.54}$$

Now, we briefly describe the properties of the semi-discretized LLG (11.49)–(11.50). These properties are similar to the properties of the continuous equation (11.38). First, it can be easily proved that:

$$|\mathbf{m}_k(t)| = |\mathbf{m}_k(t_0)|, \tag{11.55}$$

for any $t \geq t_0, k = 1, \ldots, N$. If $|\mathbf{m}_k(t_0)| = 1$, then each cell vector evolves on the two-dimensional unit sphere Σ. In other words, LLG dynamics takes place on the $2N$-dimensional manifold Σ^N (see Eq. (11.45)). It is worthwhile to point out that the rich topological structure of this manifold is responsible for the multiplicity of metastable states which, in turn, leads to the complexity of LLG dynamics.

As far as the energy balance is concerned, one obtains:

$$\begin{aligned} \frac{\mathrm{d}}{\mathrm{d}t}\underline{\mathbf{g}}_L(\underline{\mathbf{m}}(t); \underline{\mathbf{h}}_a(t)) &= -\alpha \left| \frac{\mathrm{d}\underline{\mathbf{m}}}{\mathrm{d}t} \right|^2 - \underline{\mathbf{m}} \cdot \frac{\mathrm{d}\underline{\mathbf{h}}_a}{\mathrm{d}t} \\ &= -\sum_{k=1}^{N} \alpha \left| \frac{\mathrm{d}\mathbf{m}_k}{\mathrm{d}t} \right|^2 - \sum_{k=1}^{N} \mathbf{m}_k \cdot \frac{\mathrm{d}\mathbf{h}_{a;k}}{\mathrm{d}t}. \end{aligned} \tag{11.56}$$

In the case of constant applied field, one derives:

$$\frac{\mathrm{d}}{\mathrm{d}t}\underline{\mathbf{g}}(\underline{\mathbf{m}}(t); \underline{\mathbf{h}}_a) = -\alpha \left| \frac{\mathrm{d}\underline{\mathbf{m}}}{\mathrm{d}t} \right|^2 = -\sum_{k=1}^{N} \alpha \left| \frac{\mathrm{d}\mathbf{m}_k}{\mathrm{d}t} \right|^2, \tag{11.57}$$

which reveals the relaxation dynamics toward an energy minimum.

As a final remark, we observe that semi-discretized magnetization dynamics equations can be put in the form:

$$\frac{\mathrm{d}}{\mathrm{d}t}\underline{\mathbf{m}} = -\underline{\Lambda}(\underline{\mathbf{m}}) \cdot \mathcal{H}(\underline{\mathbf{m}}, t), \tag{11.58}$$

where:

$$\mathcal{H}(\underline{\mathbf{m}}, t) = \underline{\mathbf{h}}_{\text{eff}}(\underline{\mathbf{m}}, t) + \underline{\mathbf{h}}_{\text{dis}}(\underline{\mathbf{m}}, t), \tag{11.59}$$

and $\underline{\mathbf{h}}_{\text{dis}}(\underline{\mathbf{m}}, t)$ is a term which takes into account dissipative effects. In the case of the LLG equation (11.50), one has:

$$\mathcal{H}(\underline{\mathbf{m}}, t) = \underline{\mathbf{h}}_{\text{eff}}(\underline{\mathbf{m}}, t) - \alpha \frac{\mathrm{d}}{\mathrm{d}t}\underline{\mathbf{m}}, \tag{11.60}$$

while for the LL form (11.54), one finds:

$$\mathcal{H}(\underline{\mathbf{m}}, t) = \underline{\mathbf{h}}_{\text{eff}}(\underline{\mathbf{m}}, t) + \alpha \underline{\Lambda}(\underline{\mathbf{m}}) \cdot \underline{\mathbf{h}}_{\text{eff}}(\underline{\mathbf{m}}, t). \tag{11.61}$$

Now, we proceed to the discussion of the numerical integration of spatially discretized LLG equations. In order to develop a numerical integration scheme for Eq. (11.50), we consider the temporal mesh consisting of the sequence of time instants $t_1, t_2, t_3, \ldots$, which, for the sake of simplicity, are uniformly distributed, i.e., $t_{k+1} - t_k = \Delta t$. As we discussed in previous sections, a numerical time-stepping scheme is a map:

$$\underline{\mathbf{m}}^{(k+1)} = F_k(\Delta t, \underline{\mathbf{m}}^{(k)}, \underline{\mathbf{m}}^{(k-1)}, \ldots), \quad k = 1, 2, \ldots, \tag{11.62}$$

which generates a sequence of approximate values $\underline{\mathbf{m}}^{(k)}$ of the unknown solution $\underline{\mathbf{m}}(t)$ of the LLG equation at the time instants t_k. The first issue that we address is the conservation of magnetization amplitude in each computational cell. By following the same line of reasoning as in Section 11.1, we start with Eq. (11.58), and we shall use the following mid-point formulas:

$$\frac{\mathrm{d}\underline{\mathbf{m}}}{\mathrm{d}t}(t_k + \Delta t/2) = \frac{\underline{\mathbf{m}}(t_{k+1}) - \underline{\mathbf{m}}(t_k)}{\Delta t} + \mathcal{O}\left(\Delta t^2\right), \tag{11.63}$$

$$\underline{\mathbf{m}}(t_k + \Delta t/2) = \frac{\underline{\mathbf{m}}(t_{k+1}) + \underline{\mathbf{m}}(t_k)}{2} + \mathcal{O}\left(\Delta t^2\right). \tag{11.64}$$

By substituting Eqs (11.63) and (11.64) in Eq. (11.58), and considering the equation for the lth cell, we obtain:

$$\frac{\mathbf{m}_l(t_{k+1}) - \mathbf{m}_l(t_k)}{\Delta t} = -\left(\frac{\mathbf{m}_l(t_{k+1}) + \mathbf{m}_l(t_k)}{2}\right) \times \boldsymbol{\mathcal{H}}_l(t_k + \Delta t/2) + \mathcal{O}\left(\Delta t^2\right). \tag{11.65}$$

To arrive at the final form of the finite-difference scheme, we have to express $\boldsymbol{\mathcal{H}}_l(t_k + \Delta t/2)$ in terms of values of $\underline{\mathbf{m}}$ at the time instants t_k. This can be done by using the formula:

$$\boldsymbol{\mathcal{H}}(t_k + \Delta t/2) = \mathbf{H}^{(k)}\left(\underline{\mathbf{m}}(t_{k+1}), \underline{\mathbf{m}}(t_k), \underline{\mathbf{m}}(t_{k-1}), \ldots\right) + \mathcal{O}\left(\Delta t^2\right), \tag{11.66}$$

where $\mathbf{H}^{(k)}$ is a function which provides a second-order approximation to $\boldsymbol{\mathcal{H}}(t_k + \Delta t/2)$ in terms of $\underline{\mathbf{m}}^{(k+1)}$, $\underline{\mathbf{m}}^{(k)}$, $\underline{\mathbf{m}}^{(k-1)}$, etc. By using Eqs (11.65) and (11.66), we arrive at the following second-order-accuracy

time-stepping scheme:

$$\mathbf{m}_l^{(k+1)} - \mathbf{m}_l^{(k)} = -\frac{\Delta t}{2}\left(\mathbf{m}_l^{(k+1)} + \mathbf{m}_l^{(k)}\right) \times \boldsymbol{\mathcal{H}}_l^{\left(k+\frac{1}{2}\right)}, \tag{11.67}$$

which can be written for the entire spatial mesh as follows:

$$\underline{\mathbf{m}}^{(k+1)} - \underline{\mathbf{m}}^{(k)} = -\frac{\Delta t}{2}\underline{\Lambda}\left(\underline{\mathbf{m}}^{(k+1)} + \underline{\mathbf{m}}^{(k)}\right) \cdot \boldsymbol{\mathcal{H}}^{\left(k+\frac{1}{2}\right)}, \tag{11.68}$$

where the following notation has been adopted:

$$\boldsymbol{\mathcal{H}}^{\left(k+\frac{1}{2}\right)} = \mathbf{H}^{(k)}\left(\underline{\mathbf{m}}^{(k+1)}, \underline{\mathbf{m}}^{(k)}, \underline{\mathbf{m}}^{(k-1)}, \ldots\right). \tag{11.69}$$

One can prove that the numerical scheme specified by Eqs (11.67)–(11.69) preserves the magnetization magnitude associated with each spatial cell. Indeed, by taking the dot products of both sides of Eq. (11.67) with the vector $\mathbf{m}_l^{(k+1)} + \mathbf{m}_l^{(k)}$, we obtain:

$$\left(\mathbf{m}_l^{(k+1)} + \mathbf{m}_l^{(k)}\right) \cdot \left(\mathbf{m}_l^{(k+1)} - \mathbf{m}_l^{(k)}\right) = 0, \tag{11.70}$$

which is equivalent to:

$$\left|\mathbf{m}_l^{(k+1)}\right|^2 = \left|\mathbf{m}_l^{(k)}\right|^2 = \text{const}. \tag{11.71}$$

This conservation property is valid regardless of the choice of the function $\mathbf{H}^{(k)}$ used in Eq. (11.66) to approximate $\boldsymbol{\mathcal{H}}(t_k + \Delta t/2)$. The conservation of $|\mathbf{m}|$ is also valid regardless of which expression, either (11.60) or (11.61), is used for $\boldsymbol{\mathcal{H}}$, and for even more general situations when $\boldsymbol{\mathcal{H}}$ accounts for effects due to spin-transfer injection or other nonconservative excitation effects.

The numerical scheme (11.67) is implicit in nature since it contains $\mathbf{m}_l^{(k+1)}$ on both sides of the equation. By using the linearity of $\underline{\Lambda}(\underline{\mathbf{m}})$ with respect to $\underline{\mathbf{m}}$, it is possible to rewrite the finite-difference scheme as follows:

$$\underline{\mathbf{m}}^{(k+1)} + \frac{\Delta t}{2}\underline{\Lambda}\left(\underline{\mathbf{m}}^{(k+1)}\right) \cdot \boldsymbol{\mathcal{H}}^{\left(k+\frac{1}{2}\right)} = \underline{\mathbf{m}}^{(k)} - \frac{\Delta t}{2}\underline{\Lambda}\left(\underline{\mathbf{m}}^{(k)}\right) \cdot \boldsymbol{\mathcal{H}}^{\left(k+\frac{1}{2}\right)}. \tag{11.72}$$

If explicit extrapolation formulas are used in Eq. (11.69), then the determination of $\underline{\mathbf{m}}^{(k+1)}$ in Eq. (11.67) requires only the inversion of 3×3 linear equations. This is evident by writing (11.72) for the lth cell as follows:

$$\mathbf{m}_l^{(k+1)} + \frac{\Delta t}{2}\mathbf{m}_l^{(k+1)} \times \boldsymbol{\mathcal{H}}_l^{\left(k+\frac{1}{2}\right)} = \mathbf{m}_l^{(k)} - \frac{\Delta t}{2}\mathbf{m}_l^{(k)} \times \boldsymbol{\mathcal{H}}_l^{\left(k+\frac{1}{2}\right)}. \quad (11.73)$$

When $\boldsymbol{\mathcal{H}}^{\left(k+\frac{1}{2}\right)}$ does not depend on $\underline{\mathbf{m}}^{(k+1)}$, the last formula can be interpreted as a linear system of $3N$ equations composed of N decoupled 3×3 linear equations. In other words, by choosing $\mathbf{H}^{(k)}$ in such a way that it does not depend on $\underline{\mathbf{m}}^{(k+1)}$, one obtains a complete spatial decoupling in the time-stepping calculations.

A very effective explicit second-order extrapolation formula to achieve this spatial decoupling is the one used in Section 11.1:

$$\begin{aligned}\boldsymbol{\mathcal{H}}(t_k + \Delta t/2) = \frac{3}{2}\boldsymbol{\mathcal{H}}\left(\underline{\mathbf{m}}(t_k), t_k\right) - \frac{1}{2}\boldsymbol{\mathcal{H}}\left(\underline{\mathbf{m}}(t_{k-1}), t_{k-1}\right) \\ + \mathcal{O}\left(\Delta t^2\right). \end{aligned} \quad (11.74)$$

This leads to the following expression for $\boldsymbol{\mathcal{H}}^{\left(k+\frac{1}{2}\right)}$ in Eq. (11.68):

$$\boldsymbol{\mathcal{H}}^{\left(k+\frac{1}{2}\right)} = \frac{3}{2}\boldsymbol{\mathcal{H}}\left(\underline{\mathbf{m}}^{(k)}, t_k\right) - \frac{1}{2}\boldsymbol{\mathcal{H}}\left(\underline{\mathbf{m}}^{(k-1)}, t_{k-1}\right). \quad (11.75)$$

Next, we shall discuss another scheme which accurately replicates the energy time-evolution during the magnetization dynamics. We shall use the Gilbert form (11.60) of $\boldsymbol{\mathcal{H}}$ and the following mid-point formula:

$$\begin{aligned}\boldsymbol{\mathcal{H}}(t_k + \Delta t/2) = \underline{\mathrm{C}} \cdot \left[\frac{\underline{\mathbf{m}}(t_{k+1}) + \underline{\mathbf{m}}(t_k)}{2}\right] + \underline{\mathbf{h}}_a \\ - \alpha \frac{\underline{\mathbf{m}}(t_{k+1}) - \underline{\mathbf{m}}(t_k)}{\Delta t} + \mathcal{O}(\Delta t^2), \end{aligned} \quad (11.76)$$

where $\underline{\mathbf{h}}_a$ is assumed to be constant and the fact that $\underline{\mathbf{h}}_{\text{eff}}(\underline{\mathbf{m}}, t) = -\underline{\mathrm{C}} \cdot \underline{\mathbf{m}} + \underline{\mathbf{h}}_a$ has been used. This leads to the following expression for the field $\boldsymbol{\mathcal{H}}^{\left(k+\frac{1}{2}\right)}$ in Eq. (11.68):

$$\boldsymbol{\mathcal{H}}^{\left(k+\frac{1}{2}\right)} = -\underline{\mathrm{C}} \cdot \left[\frac{\underline{\mathbf{m}}^{(k+1)} + \underline{\mathbf{m}}^{(k)}}{2}\right] + \underline{\mathbf{h}}_a - \alpha \frac{\underline{\mathbf{m}}^{(k+1)} - \underline{\mathbf{m}}^{(k)}}{\Delta t}. \quad (11.77)$$

By multiplying both sides of Eq. (11.68) by $\boldsymbol{\mathcal{H}}^{\left(k+\frac{1}{2}\right)}$, we obtain $\boldsymbol{\mathcal{H}}^{\left(k+\frac{1}{2}\right)} \cdot (\underline{\mathbf{m}}^{(k+1)} - \underline{\mathbf{m}}^{(k)})/\Delta t = 0$. Then, by substituting formula (11.77) for $\boldsymbol{\mathcal{H}}^{\left(k+\frac{1}{2}\right)}$ in the last identity and by using the symmetry of the matrix $\underline{\mathrm{C}}$ and formula (11.46), one can derive the following equation for the time-discrete dynamics:

$$\frac{\underline{\mathbf{g}}_L^{(k+1)} - \underline{\mathbf{g}}_L^{(k)}}{\Delta t} = -\alpha \left| \frac{\underline{\mathbf{m}}^{(k+1)} - \underline{\mathbf{m}}^{(k)}}{\Delta t} \right|^2. \tag{11.78}$$

Equation (11.78) has important implications. First, it shows that the mid-point rule is an unconditionally stable algorithm which reproduces the relaxation behavior in LLG discretized dynamics for any choice of the time step. In addition, for $\alpha = 0$ the energy is exactly conserved regardless of the time step. This property indicates that for slightly dissipative systems the mid-point rule will tend to reproduce accurately the time-evolution of energy during the LLG dynamics.

In the following, we discuss the implementation of the mid-point scheme defined by Eqs (11.72) and (11.77) for micromagnetic switching problems. Since this scheme is implicit, we have to solve at each time step the following system of $3N$ nonlinear equations with respect to the $3N$ unknowns $\underline{\mathbf{m}}^{(k+1)}$:

$$\boldsymbol{\mathcal{F}}^{(k)}(\underline{\mathbf{m}}^{(k+1)}) = \mathbf{0}, \tag{11.79}$$

where $\boldsymbol{\mathcal{F}}^{(k)}(\underline{\mathbf{y}}) : \mathbb{R}^{3N} \to \mathbb{R}^{3N}$ is the following vector function:

$$\boldsymbol{\mathcal{F}}^{(k)}(\underline{\mathbf{y}}) = \left[\underline{\mathrm{I}} - \alpha \underline{\Lambda} \left(\frac{\underline{\mathbf{y}} + \underline{\mathbf{m}}^{(k)}}{2} \right) \right] \left(\underline{\mathbf{y}} - \underline{\mathbf{m}}^{(k)} \right) - \Delta t \mathbf{f}^{(k)} \left(\frac{\underline{\mathbf{y}} + \underline{\mathbf{m}}^{(k)}}{2} \right), \tag{11.80}$$

and:

$$\begin{aligned} \mathbf{f}^{(k)}(\underline{\mathbf{m}}) &= -\underline{\Lambda}(\underline{\mathbf{m}}) \cdot \underline{\mathbf{h}}_{\text{eff}} \left(\underline{\mathbf{m}}, t_k + \frac{\Delta t}{2} \right) \\ &= \underline{\Lambda}(\underline{\mathbf{m}}) \cdot \frac{\partial \underline{\mathbf{g}}}{\partial \underline{\mathbf{m}}} \left(\underline{\mathbf{m}}; \underline{\mathbf{h}}_a \left(t^{(k)} + \frac{\Delta t}{2} \right) \right). \end{aligned} \tag{11.81}$$

The solution of the system of equations (11.79) can be obtained by using the Newton–Raphson (NR) algorithm. To this end, we derive the Jacobian

matrix $\underline{\mathrm{J}}_{\mathrm{F}}^{(k)}(\underline{\mathbf{y}})$ of the vector function $\boldsymbol{\mathcal{F}}^{(k)}(\underline{\mathbf{y}})$, which can be written in the following form:

$$\underline{\mathrm{J}}_{\mathrm{F}}^{(k)}(\underline{\mathbf{y}}) = \underline{\mathrm{I}} - \alpha\underline{\Lambda}(\underline{\mathbf{m}}^{(k)}) - \frac{\Delta t}{2}\underline{\mathrm{J}}_{\mathrm{f}}^{(k)}\left(\frac{\underline{\mathbf{y}} + \underline{\mathbf{m}}^{(k)}}{2}\right), \tag{11.82}$$

where $\underline{\mathrm{J}}_{\mathrm{f}}^{(k)}$ is the Jacobian matrix for $\mathbf{f}^{n}(\underline{\mathbf{m}})$. By using Eqs (11.52) and (11.81), one obtains:

$$\begin{aligned}\underline{\mathrm{J}}_{\mathrm{f}}^{(k)}(\underline{\mathbf{m}}) &= \frac{\partial \mathbf{f}^{(k)}}{\partial \underline{\mathbf{m}}}(\underline{\mathbf{m}}) \\ &= \underline{\Lambda}(\underline{\mathbf{m}}) \cdot \underline{\mathrm{C}} + \underline{\Gamma} \cdot \left[-\underline{\mathrm{C}} \cdot \underline{\mathbf{m}} + \underline{\mathbf{h}}_{a}\left(t_k + \frac{\Delta t}{2}\right)\right].\end{aligned} \tag{11.83}$$

The main difficulty in applying the NR method is that the Jacobian $\underline{\mathrm{J}}_{\mathrm{F}}^{(k)}(\underline{\mathbf{y}})$ of $\boldsymbol{\mathcal{F}}^{(k)}(\underline{\mathbf{y}})$ is a fully populated matrix, due to the long-range nature of magnetostatic interactions. It can be also observed that the damping term affects only a small sparse component of the Jacobian $\underline{\mathrm{J}}_{\mathrm{F}}^{(k)}(\underline{\mathbf{y}})$ and thus does not introduce any additional difficulty.

Since the matrix $\underline{\mathrm{J}}_{\mathrm{F}}^{(k)}(\underline{\mathbf{y}})$ is fully populated, the use of the NR method would require an appreciable computational cost. This problem can be circumvented by using a quasi-Newton method, which is based on a sparse approximation of the Jacobian. Detailed discussion of this method can be found in Ref. [193].

Since the time-stepping equations are solved through an iterative procedure, the conservation properties of the mid-point rule are fulfilled only within a certain accuracy. For this reason, it is important to test the accuracy of the conservation properties during the computation.

As far as magnetization magnitude conservation is concerned, we control its accuracy with the following quantities:

$$\mathrm{m}_{\mathrm{av}} = \frac{1}{N}\sum_{l=1}^{N}|\mathbf{m}_l|, \quad \sigma_{\mathrm{m}}^2 = \frac{1}{N}\sum_{l=1}^{N}(|\mathbf{m}_l| - \mathrm{m}_{\mathrm{av}})^2, \tag{11.84}$$

which are mean value and variance of the magnetization magnitude over the cells of the mesh, respectively.

As far as the energy balance equation is concerned, we use the self-consistency criterion proposed by Albuquerque and coworkers [16]. This criterion is valid for constant applied field and is based on Eq. (11.57)

rewritten in the following form:

$$\alpha = \left(\frac{\mathrm{d}}{\mathrm{d}t} \underline{\mathbf{g}}(\underline{\mathbf{m}}(t); \underline{\mathbf{h}}_a) \right) \Big/ \left| \frac{\mathrm{d}\underline{\mathbf{m}}}{\mathrm{d}t} \right|^2 . \tag{11.85}$$

To test the conservation of energy in numerical computation, we consider the value:

$$\hat{\alpha}^{(k)} = - \left(\frac{\underline{\mathbf{g}}(\underline{\mathbf{m}}^{(k+1)}; \underline{\mathbf{h}}_a) - \underline{\mathbf{g}}(\underline{\mathbf{m}}^{(k)}; \underline{\mathbf{h}}_a)}{\Delta t} \right) \Big/ \left| \frac{\underline{\mathbf{m}}^{(k+1)} - \underline{\mathbf{m}}^{(k)}}{\Delta t} \right|^2 , \tag{11.86}$$

computed at each time step, and we have compared it with the constant α. It can be observed that if we could exactly invert the nonlinear system of equations (11.79), then $\hat{\alpha}^{(k)}$ would be constant and equal to α. When an iterative procedure is used, $\hat{\alpha}^{(k)}$ are nonconstant and exhibit an oscillatory behavior. In particular, unstable behavior corresponds to negative $\hat{\alpha}^{(k)}$.

For the conservative dynamics, the discretized energy is conserved:

$$\underline{\mathbf{g}}(\underline{\mathbf{m}}^{(k+1)}; \underline{\mathbf{h}}_a) = \underline{\mathbf{g}}(\underline{\mathbf{m}}^{(k)}; \underline{\mathbf{h}}_a), \tag{11.87}$$

regardless of the time step. One can test the accuracy of the scheme by recording the deviation of the total energy from its initial value. Again, one cannot expect that this property will be exactly fulfilled with an iterative procedure. For this reason, we will verify *a posteriori* that the energy conservation is guaranteed with sufficient precision by computing the relative error e_{g} of $\underline{\mathbf{g}}(\underline{\mathbf{m}}^{(k)}; \underline{\mathbf{h}}_a)$ with respect to the initial energy $\underline{\mathbf{g}}(\underline{\mathbf{m}}^{(0)}; \underline{\mathbf{h}}_a)$:

$$e_{\mathrm{g}}^{(k)} = \frac{\underline{\mathbf{g}}(\underline{\mathbf{m}}^{(k)}; \underline{\mathbf{h}}_a) - \underline{\mathbf{g}}(\underline{\mathbf{m}}^{(0)}; \underline{\mathbf{h}}_a)}{\underline{\mathbf{g}}(\underline{\mathbf{m}}^{(0)}; \underline{\mathbf{h}}_a)}, \tag{11.88}$$

and checking that the sequence $e_{\mathrm{g}}^{(k)}$ remains within the desired tolerance.

Up to this point the discussion of the implementation of mid-point rule was rather independent of the chosen spatial discretization. To test the method, we have chosen a finite-differences spatial discretization method. In this method, the magnetic object is subdivided into rectangular prisms with edges parallel to the coordinate axes and edge lengths d_x, d_y, d_z. It is convenient to identify each cell by three indices i, j, k. The magnetization $\mathbf{m}_{i,j,k}$ is assumed to be uniform within a generic (i, j, k)

cell. With this notation, the effective field in the generic (i, j, k) cell can be expressed as follows:

$$\mathbf{h}_{\text{eff};i,j,k} = \mathbf{h}_{\text{ex};i,j,k} + \mathbf{h}_{\text{m};i,j,k} + \mathbf{h}_{\text{an};i,j,k} + \mathbf{h}_{a;i,j,k}. \tag{11.89}$$

The exchange field $\mathbf{h}_{\text{ex};i,j,k}$ is computed by means of a 7-point Laplacian discretization, which is second order of accuracy. For interior cells, it can be expressed as follows:

$$\mathbf{h}_{\text{ex};i,j,k} = \frac{2A}{\mu_0 \mathrm{M}_s^2}\left[\frac{\mathbf{m}_{i+1,j,k} + \mathbf{m}_{i-1,j,k}}{d_y^2} + \frac{\mathbf{m}_{i,j+1,k} + \mathbf{m}_{i,j-1,k}}{d_x^2} + \frac{\mathbf{m}_{i,j,k+1} + \mathbf{m}_{i,j,k-1}}{d_z^2} - \left(\frac{2}{d_y^2} + \frac{2}{d_x^2} + \frac{2}{d_z^2}\right)\mathbf{m}_{i,j,k}\right]. \tag{11.90}$$

A similar expression holds for the boundary cells, where the Neumann boundary condition has to be taken into account. Since the exchange interaction is a next-neighbor interaction, one can easily observe that the matrix $\underline{\mathrm{C}}_{\text{ex}}$ is a block-diagonal matrix.

The magnetostatic field $\mathbf{h}_{\text{m};i,j,k}$ can be expressed as discrete convolution [582,754]:

$$\mathbf{h}_{\text{m};i,j,k} = \sum_{i' \neq i} \sum_{j' \neq j} \sum_{k' \neq k} N_{i-i',j-j',k-k'} \cdot \mathbf{m}_{i',j',k'} d_x d_y d_z, \tag{11.91}$$

where $N_{i-i',j-j',k-k'}$ is the 3×3 block of the matrix $\underline{\mathrm{C}}_{\text{m}}$ which describes the magnetostatic interaction between the cells i, j, k and i', j', k'. The discrete convolution (11.91) is computed by means of the 3D fast Fourier transform (FFT) by using the zero-padding algorithm [73]. The kernel of the convolution is obtained by generalizing the formulas proposed in Ref. [582] for cubic cells to prisms.

As far as anisotropy is concerned, we assume that the anisotropy field is:

$$\mathbf{h}_{\text{an};i,j,k} = \frac{2K_1}{\mu_0 \mathrm{M}_s^2}(\mathbf{m}_{i,j,k} \cdot \mathbf{e}_{\text{an}})\mathbf{e}_{\text{an}}, \tag{11.92}$$

and the matrix $\underline{\mathrm{C}}_{\text{an}}$ is a diagonal matrix.

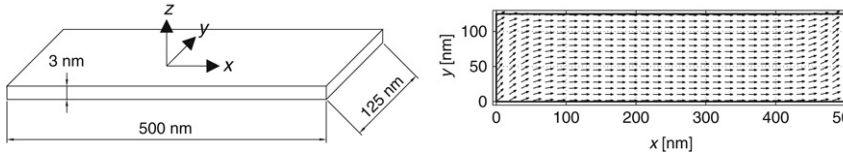

FIGURE 11.6 (Left) Thin-film geometry for μ-mag standard problem n. 4. (Right) Initial equilibrium S-state.

11.4 MICROMAGNETIC SIMULATIONS OF MAGNETIZATION REVERSAL AND SPIN-WAVE EXCITATION

A stringent test of the above numerical techniques is to apply them to the so-called μ-mag standard problems [499]. We have used them to solve the standard problem n. 4. This problem is concerned with the study of magnetization reversal dynamics in a permalloy thin film subject to a constant and spatially uniform external field, applied almost antiparallel to the initial magnetization. The geometry of the medium is sketched in Fig. 11.6(a). The material parameters are $A = 1.3 \times 10^{-11}$ J/m, $\mathrm{M}_s = 8.0 \times 10^5$ A/m, $K_1 = 0$ J/m^3, and $\alpha = 0.02$. The initial state is an equilibrium "S-state" (see Ref. [499] and Fig. 11.6(b)) which is obtained by slowly reducing a saturating field along the $[1, 1, 1]$ direction to zero. In all the numerical simulations, the magnetization is assumed to have reached equilibrium when:

$$\max_{l=1,\ldots,N} \left| \frac{\mathbf{m}_l^{(k+1)} - \mathbf{m}_l^{(k)}}{\Delta t} \right| < \varepsilon_{\text{torque}}, \tag{11.93}$$

i.e., the maximum of the (normalized) torque across the body is less than a chosen tolerance $\varepsilon_{\text{torque}}$. In our computations, $\varepsilon_{\text{torque}} = 10^{-5}$. Moreover, the stopping criterion of the quasi-Newton iterative procedure has been chosen as:

$$\max_{q=1,\ldots,3N} |\mathrm{F}_q^{(k)}(\underline{\mathbf{y}}_n)| < 10^{-14}, \tag{11.94}$$

where $\mathrm{F}_q^{(k)}(\underline{\mathbf{y}}_n)$ is the qth components of the vector $\boldsymbol{\mathcal{F}}^{(k)}(\underline{\mathbf{y}}_n)$, and the index n indicates the number of quasi-Newton iterations.

Two switching events have been calculated using fields applied in the x–y-plane of different magnitude and direction. In the first case the

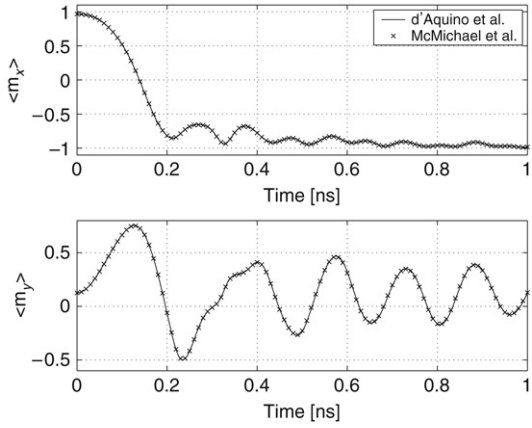

FIGURE 11.7 Comparison between solutions of μ-mag standard problem no. 4. Plots of $\langle \mathrm{m}_x \rangle$ and $\langle \mathrm{m}_y \rangle$ versus time. The external field is applied at the angle of 170° with respect to the x axis.

external field is applied at the angle of 170° with respect to the x axis with the components $\mu_0 \mathrm{M}_s \mathrm{h}_{ax} = -24.6\ \mathrm{mT}$ and $\mu_0 \mathrm{M}_s \mathrm{h}_{ay} = 4.3\ \mathrm{mT}$. In the second case the external field is applied at the angle of 190° with respect to the x axis with the components $\mu_0 \mathrm{M}_s \mathrm{h}_{ax} = -35.5\ \mathrm{mT}$ and $\mu_0 \mathrm{M}_s \mathrm{h}_{ay} = -6.3\ \mathrm{mT}$. In both cases the cell edges are $d_x = 3.125$ nm, $d_y = 3.125$ nm, $d_z = 3$ nm and, therefore, the number of cells is $N = 160 \times 40 \times 1 = 6400$.

Next, we report the comparison between the solution obtained using the above numerical technique and the solutions submitted by other researchers [499] to the μ-mag website. The time step of the mid-point numerical algorithm is constant and it is such that $(\gamma \mathrm{M}_s)^{-1} \Delta t = 2.5$ ps. This value has been chosen only on the basis of accuracy, since the mid-point rule is unconditionally stable. In this respect, we observe that the time steps chosen in the other submitted computations (see Ref. [499]) are considerably smaller (from tens of femtoseconds to 0.2 picoseconds). These small time steps are presumably due to numerical stability requirements. In the results presented in the sequel, we plot average value of magnetization components. For instance, the average value $\langle \mathrm{m}_x \rangle$ of the m_x component is computed as:

$$\langle \mathrm{m}_x \rangle = \frac{1}{N} \sum_{i,j,k} m_{x;i,j,k}. \tag{11.95}$$

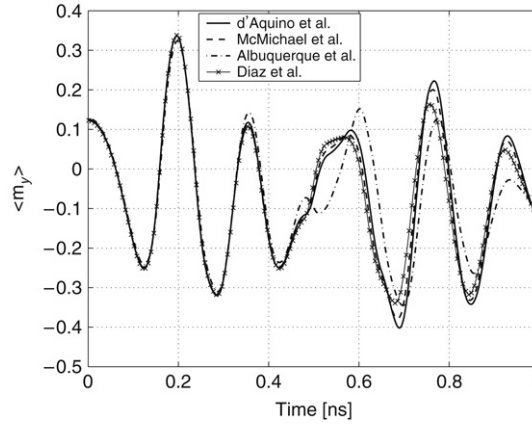

FIGURE 11.8 Comparison between solutions of μ-mag standard problem no. 4. Plots of $\langle m_y \rangle$ versus time. The external field is applied at the angle of 190° with respect to the x axis.

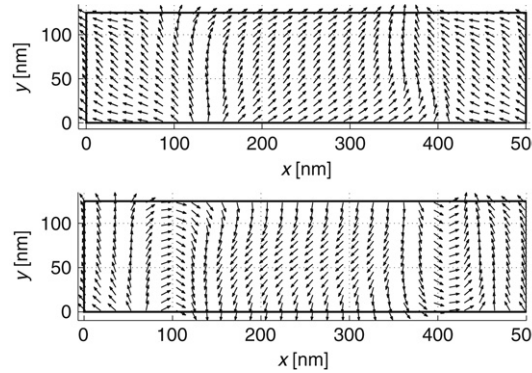

FIGURE 11.9 Numerical results for μ-mag standard problem no. 4. Snapshot of magnetization vector field when the average $\langle m_x \rangle$ crosses zero for the first time. The external field is applied at the angle of 170° (up) and 190° (down) with respect to the x axis.

In Figs 11.7 and 11.8 plots of $\langle m_x \rangle$ and $\langle m_y \rangle$ as a function of time are reported. We observe that in the first case (Fig. 11.7) there is good agreement between different submitted solutions (see Ref. [499]) and, for this reason, we report only the solution proposed by McMichael and

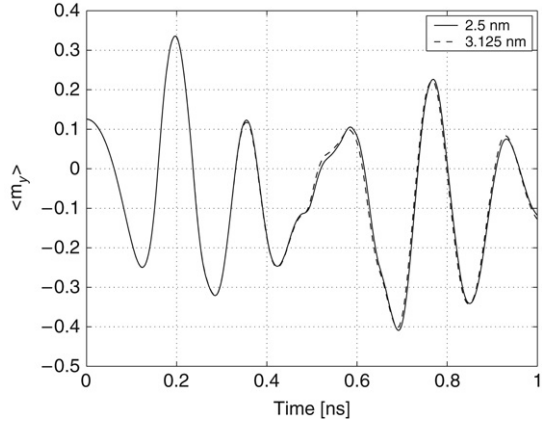

FIGURE 11.10 Numerical results for μ-mag standard problem no. 4. Plots of $\langle \mathrm{m}_y \rangle$ versus time for two different sizes of the mesh edge length. The external field is applied at the angle of 190° with respect to the x axis.

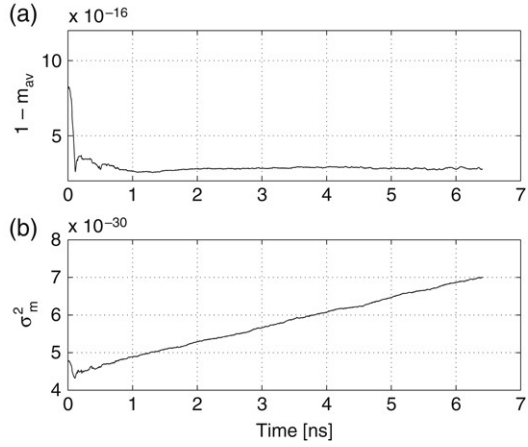

FIGURE 11.11 Numerical results for μ-mag standard problem no. 4. (a) Plot of $1 - \mathrm{m}_{\mathrm{av}}$ as a function of time. (b) Plot of the variance σ^2_{m} as a function of time. In both plots $\delta = 190^\circ$, $N = 6400$.

coworkers. In Fig. 11.9 the plots of magnetization vector field when $\langle \mathrm{m}_x \rangle$ crosses zero for the first time are reported. To check whether the numerical solution depends on the cell's size, numerical simulations of the same

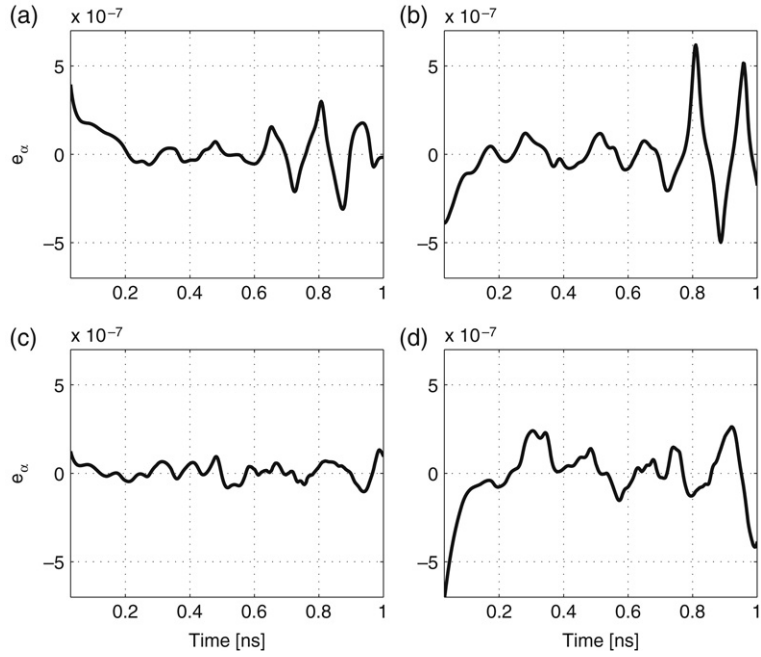

FIGURE 11.12 Numerical results for μ-mag standard problem no. 4. Plot of the relative error $e_\alpha^{(k)} = (\hat{\alpha}^{(k)} - \alpha)/\alpha$ as a function of time. (a) $\delta = 170^\circ$, $N = 6400$. (b) $\delta = 170^\circ$, $N = 10\,000$. (c) $\delta = 190^\circ$, $N = 6400$. (d) $\delta = 190^\circ$, $N = 10\,000$.

problem were performed with a smaller cell edge (2.5 nm, number of cells $N = 10\,000$). The results reported in Fig. 11.10 for the two different mesh sizes are almost coincident. As far as the accuracy is concerned, the self-consistency conditions mentioned above have been verified by means of the computation of the values $\mathrm{m_{av}}$, σ_{m}^2 and $\hat{\alpha}^n$. The results of these computations are reported in Figs 11.11–11.12. One can observe from Fig. 11.11 that the magnetization magnitude is very well preserved, since the mean value $\mathrm{m_{av}} \sim 1 \pm 10^{-16}$ and the variance σ_{m}^2 is in the order of 10^{-30}. It is remarkable that the accuracy in magnetization magnitude conservation is within machine precision. Moreover, one can see from Fig. 11.12 that the relative error $e_\alpha^{(k)} = (\hat{\alpha}^{(k)} - \alpha)/\alpha$ is on the order of 10^{-7} in all cases.

To analyze the conservative dynamics, the same problem has been simulated with $\alpha = 0$. The results, reported in Fig. 11.13, show that the reversal of the thin film occurs, in the sense that the average magnetiza-

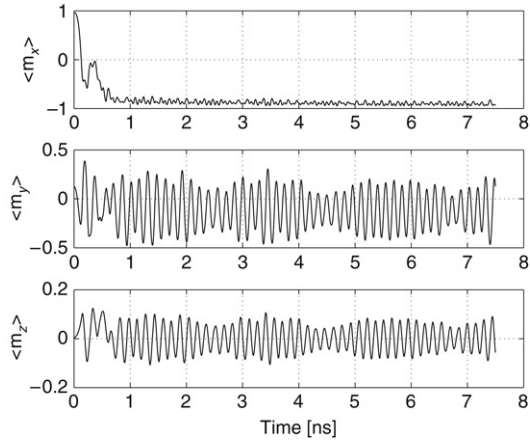

FIGURE 11.13 Numerical results for μ-mag standard problem no. 4 in the conservative case $\alpha = 0$. Plot of $\langle \mathrm{m}_x \rangle$ (top), $\langle \mathrm{m}_y \rangle$ (middle), $\langle \mathrm{m}_z \rangle$ (bottom) as functions of time; $\delta = 190^\circ$, $N = 6400$.

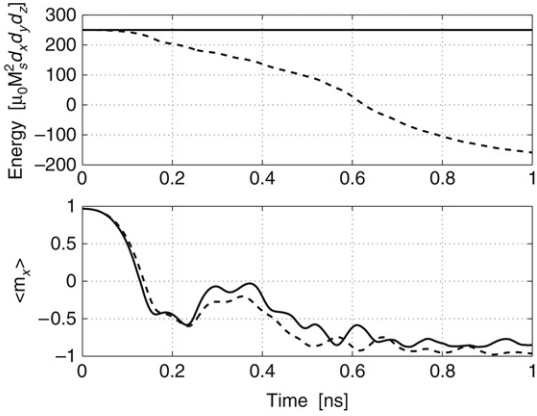

FIGURE 11.14 Comparison of numerical results for μ-mag standard problem no. 4 in the conservative and dissipative case. Solid lines refer to the conservative case $\alpha = 0$, dashed lines refer to the dissipative case $\alpha = 0.02$. Plot of the free energy $\underline{\mathrm{g}}$ (top), $\langle \mathrm{m}_x \rangle$ (bottom) as functions of time. $\delta = 190^\circ$, $N = 6400$.

tion exhibits a persistent oscillation around the reversed state. In fact, by comparing the conservative and dissipative dynamics, reported in

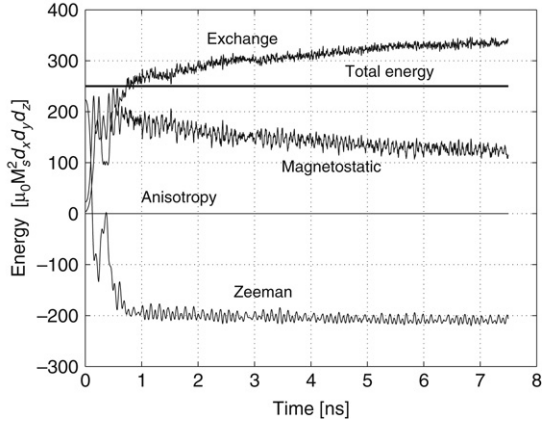

FIGURE 11.15 Numerical results for μ-mag standard problem no. 4 in the conservative case $\alpha = 0$. Plots of exchange, anisotropy, magnetostatic, Zeeman and total free energy as functions of time. $\delta = 190^\circ$, $N = 6400$.

Fig. 11.14, one can observe that on a short time scale ($0 < t < 0.2$ ns), the conservative and dissipative dynamics are quite close. This means that the precessional effects are prevalent with respect to the damping effects in the reversal process. One can see from Fig. 11.15 that the free energy is conserved. In this numerical experiment, we have checked that the relative error e_g of the free energy with respect to its initial value is in the order of 10^{-8} as one can see from Fig. 11.16. We observe that the conservative switching process occurs mainly through a transfer of energy from magnetostatic form to exchange form. This transfer of energy process is connected to the generation of spin-waves with decreasing wavelength [574].

Finally, we shall apply the numerical techniques of the previous section to the simulation of spin-wave excitation in the case of an ultrathin (few nm thickness) uniaxial ferromagnetic disk subjected to circularly polarized and spatially uniform external fields (see Fig. 11.17). This case was analyzed in detail in Section 8.5. For small disk dimensions (diameter $D \approx 100 l_{EX}$ and thickness $d \approx l_{EX}$) and under spatially uniform excitation conditions, spatially uniform modes are expected to be the main dynamic modes: either periodic **P**-modes or quasi-periodic **Q**-modes (see Chapter 7). We recall that **P**-modes can be determined analytically. Each **P**-mode is identified by the angle θ_0 of $\mathbf{m}$ with respect to $\mathbf{e}_z$ and by the lag

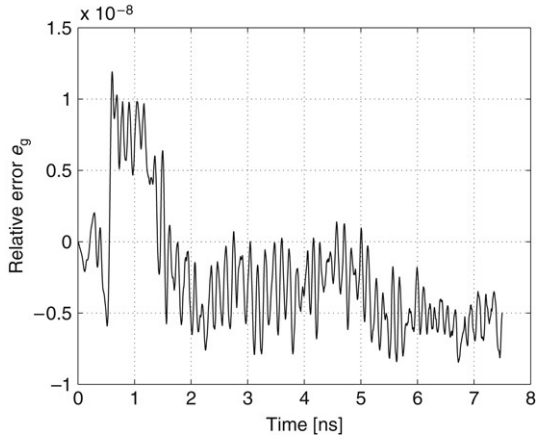

FIGURE 11.16 Numerical results for μ-mag standard problem no. 4 in the conservative case $\alpha = 0$. Plot of the relative error $e_{\underline{\mathbf{g}}}^{(k)} = (\underline{\mathbf{g}}(\underline{\mathbf{m}}^{(k)}; \underline{\mathbf{h}}_a) - \underline{\mathbf{g}}(\underline{\mathbf{m}}^{(0)}; \underline{\mathbf{h}}_a))/\underline{\mathbf{g}}(\underline{\mathbf{m}}^{(0)}; \underline{\mathbf{h}}_a)$ as a function of time. $\delta = 190°$, $N = 6400$.

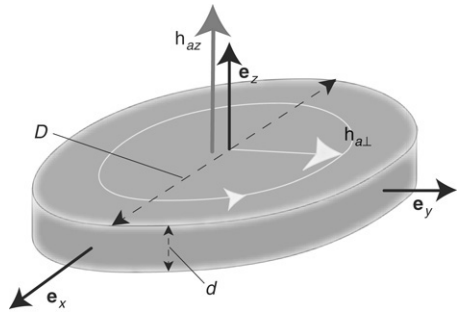

FIGURE 11.17 Sketch of thin-disk geometry and exitation conditions.

angle ϕ_0 of $\mathbf{m}_\perp$ with respect to $\mathbf{h}_{a\perp}$. These angles satisfy the equations:

$$\nu_0 = \frac{\mathrm{h}_{az} - \omega}{\cos\theta_0} + \kappa_{\text{eff}}, \qquad \nu_0^2 = \frac{\mathrm{h}_{a\perp}^2}{\sin^2\theta_0} - \alpha^2\omega^2, \tag{11.96}$$

where $\nu_0 = \alpha\omega\cot\phi_0$ and $\kappa_{\text{eff}} = \kappa + N_\perp - N_z$ (N_z and $N_\perp$ are the disk demagnetizing factors). The angle ϕ_0 is in one-to-one correspondence with

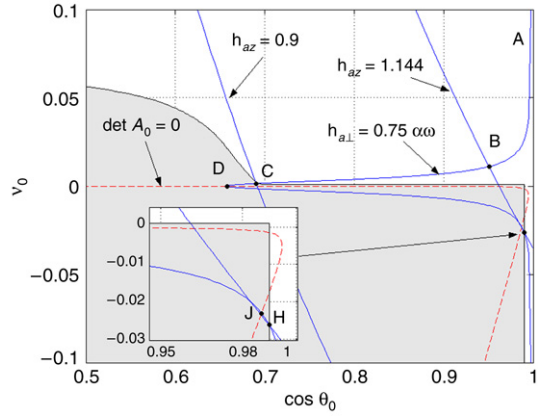

FIGURE 11.18 Portion of the spin-wave instability (shaded) region in the $(\cos\theta_0, \nu_0)$-plane. The inset is a magnification of a portion of the diagram. The value of parameters are $\mu_0 M_s = 1$ T, $\alpha = 0.02$, $\omega = 0.25$ (which corresponds to 7 GHz), $l_{EX} = 5.71$ nm, $d = 3$ nm, $N_z = 0.9498$, $\kappa_{\text{eff}} = -0.9248$. The lines labeled with values of $h_{a\perp}$ and values of h_{az} are lines of the $(\cos\theta_0, \nu_0)$-plane characterized by constant values of $h_{a\perp}$ and h_{az}, respectively. The analytical form of these lines can be derived by Eq. (11.96). The line labeled with $\det A_0 = 0$ correspond to instability due to spatially uniform perturbations (**P**-mode foldover phenomenon). The points A, B, C, D, J, H are indicated in order to compare this figure with Fig. 11.19.

ν_0 because $0 \leq \phi_0 \leq \pi$ under all circumstances. The plane $(\cos\theta_0, \nu_0)$ is the natural plane for the representation of **P**-modes (see Fig. 7.3).

P-modes can become unstable as a consequence of spatially uniform or spatially nonuniform perturbations. Stability with respect to uniform perturbations is governed by Eqs (7.38)–(7.41). Instabilities occur when the determinant $\det A_0$ changes from positive to negative (the critical condition is $\det A_0 = 0$, which corresponds to a saddle–node bifurcation) or when the trace $\text{tr } A_0$ changes from negative to positive (the critical condition is $\text{tr } A_0 = 0$, which corresponds to a Hopf bifurcation). On the other hand, as discussed in Section 8.5, in ultra-thin films **P**-mode stability with respect to plane-wave (spin-wave) nonuniform perturbations can be investigated under the assumption that the magnetization vector is uniform across the film thickness. The amplitudes of the spin-wave perturbation of wave-vector q satisfy the set of equations (8.126)–(8.130). The key information about spin-wave instabilities is provided by the one-period map associated with Eq. (8.126). Given the matrix solution $\Phi_q(t)$ of Eq. (8.126), with $\Phi_q(0) = \delta_{ij}$, the one-period map M_q is defined as $M_q =$

$\Phi_q(2\pi/\omega)$. Stability is controlled by the eigenvalues $\mu_\pm$ of M_q. Instability occurs whenever $|\mu_+| > 1$ or $|\mu_-| > 1$. Therefore, one can immediately determine the stability of all **P**-modes with respect to any particular spin-wave perturbation by numerical integration of Eq. (8.126) for all possible values of q (see Fig. 11.18). The integration is performed for any value of $(\cos\theta_0, \nu_0)$ and for $q \geq q_{\min}$, where $q_{\min} = \pi l_{EX}/D$. The shaded region in Fig. 11.18 is the region in the $(\cos\theta_0, \nu_0)$-plane corresponding to **P**-modes which are unstable for at least one value of q. This figure should be compared with Fig. 8.2, which was computed for the case of spin-wave instabilities in bulk systems.

We have performed numerical simulations of spin-wave excitation in an ultra-thin permalloy disk ($l_{EX} = 5.71$ nm, $\mu_0 \mathrm{M}_s = 1$ T, $d = 3$ nm, $D = 200$ nm). The disk is subdivided into rectangular prisms with dimensions $5 \times 5 \times 3$ nm with edges parallel to the coordinate axes. The magnetization is assumed uniform within each cell. As previously discussed, the exchange field is computed using a 7-point finite-difference Laplacian approximation. The magnetostatic field is expressed as a discrete convolution and this convolution is evaluated by means of the 3D fast Fourier transform (FFT). The time-integration of the LLG equation is performed by using the mid-point rule scheme. The preservation of the main qualitative properties of the magnetization dynamics is particularly important in the present case, where very long simulation times are required. c

The numerical results are reported in Fig. 11.19. The dc field h_{az} is changed in a step-wise fashion from 1.3 to 0.8 and then back to 1.3. After each step, a time interval of 10 ns is needed (50 ns along the branch FEG) for the magnetization to approach a steady state. Then the maximum value (in time) of the quantity $m_\perp = (\langle \mathrm{m}_x \rangle^2 + \langle \mathrm{m}_y \rangle^2)^{1/2}$ is stored ($\langle \cdot \rangle$ denotes spatial average over the disk). The total simulation time is almost 600 ns and the time step is 5 ps.

The spatial uniformity is monitored during the simulations. It is found that the value of $(\langle \mathrm{m}_x \rangle^2 + \langle \mathrm{m}_y \rangle^2 + \langle \mathrm{m}_z \rangle^2)^{1/2}$ usually deviated from 1 by a few percent except at the irreversible jumps CE and JB, as well as along the branch HJ, where the deviation from 1 is between 10 and 20 percent. In the first part of the simulation the branch ABC is traced, where **P**-modes are observed. The numerical solution is reasonably close to the curve (dotted line) given by **P**-mode theory. However, the irreversible jump CE occurs at a value of the field ($\mathrm{h}_{az} \approx 0.9$) higher than the field for foldover switching (point D). This instability can be justified by taking into account that the point C represented in the $(\cos\theta_0, \nu_0)$-plane (see Fig. 11.18) is just inside the spin-wave instability region. After the jump the system reaches **Q**-modes regimes (branch FEG) which disappear through a Hopf bifurcation

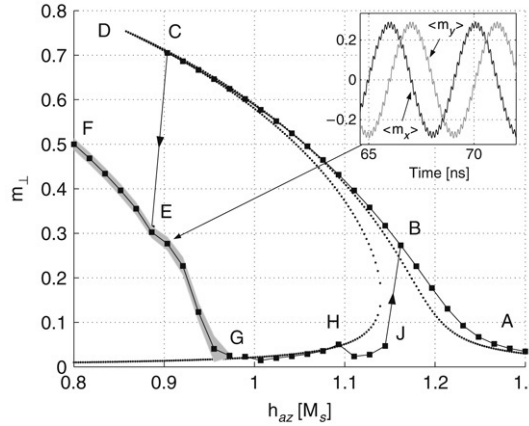

FIGURE 11.19 Numerical simulations of foldover and instability processes. On the vertical axis the maximum (in time) value of $\mathrm{m}_\perp = (\langle \mathrm{m}_x \rangle^2 + \langle \mathrm{m}_y \rangle^2)^{1/2}$ is represented ($\langle\cdot\rangle$ denotes spatial average) after the system has reached a steady state. The RF field has values $h_{a\perp} = 0.75\alpha\omega$, while the field h_{az} (plotted along the horizontal axis) is changed from 1.3 to 0.8 and then back to 1.3. All other parameters are the same as in Fig. 11.18. The continuous line with symbol "■" represents numerical simulations. The dotted line represents the spatially uniform **P**-mode foldover theoretical curve. The points A, B, C, D, H, J are also indicated in Fig. 11.18. The shaded region around the branch F, E, G indicates numerically observed **Q**-modes. In the inset, spatially averaged m_x and m_y versus time in the case of a **Q**-mode.

at the value of $\mathrm{h}_{az} \approx 0.95$. This is slightly larger than the value predicted by the theory $\mathrm{h}_{az} = -\kappa_{\text{eff}} \approx 0.92$, but still in a very reasonable agreement. In the branch GH the solution follows the **P**-mode foldover lower branch up to the point H where again the system (see Fig. 11.18) enters in the spin-wave instability region and the solution is driven into a new regime in which spatial nonuniformity is pronounced. It is interesting to note that magnetization jumps back to the foldover upper branch at point J, exactly at the point where the jump is expected to be according to the **P**-mode theory.

We can conclude that, despite the approximations inherent in the spin-wave theory and in the numerical treatment of the problem, the quantitative comparison between theoretical predictions and numerical simulations is reasonably good. This means that the spin-wave theory applied to ultra-thin disks can reasonably predict the excitation conditions for which deviations from **P**-modes theory have to be expected.

11.5 MICROMAGNETIC SIMULATIONS OF CHAOTIC DYNAMICS

In the case when the frequency of the driving field approaches the characteristic frequency of precession of the spin around the applied dc field, various nonlinear phenomena can be observed and the dynamics of spins may become very complicated. For example, chaotic dynamics has been studied and observed experimentally in ferrites and in conducting ferromagnetic thin films. In these cases, complex dynamics is attributed to the nonlinear coupling of the spatially nonuniform magnetization modes.

In this section, the case of a uniformly magnetized sample is considered. Therefore, the possible excitation of nonuniform modes is not taken into account. Nevertheless, it is shown that in this simple case the spin dynamics may exhibit complicated nonlinear phenomena such as spontaneous symmetry breaking, bifurcations, quasi-periodicity and chaotic behavior.

We shall consider the magnetization dynamics of a uniformly magnetized ferromagnetic spheroidal particle with uniaxial anisotropy. The easy axis is coincident with the symmetry axis and they are both oriented along the z axis of the cartesian reference frame. The applied rf field $\mathbf{H}_{a\perp}(t)$ is elliptically polarized and its polarization is characterized by using the Poincaré sphere and the following Stokes parameters:

$$I = H_{ax}^2 + H_{ay}^2, \qquad Q = H_{ax}^2 - H_{ay}^2 \tag{11.97}$$

$$U = 2H_{ax}H_{ay}\cos\theta_0, \qquad V = -2H_{ax}H_{ay}\sin\theta_0, \tag{11.98}$$

where $\theta_0 = \theta_x - \theta_y$. The last two parameters U and V characterize the orientation of the polarization ellipse in the (x, y)-plane and can be arbitrarily chosen since the ferromagnetic particle is isotropic in the (x, y)-plane. For the sake of simplicity, we shall assume $\theta_x = \theta_y = \theta_0 = 0$.

As was discussed in Chapter 7, when all the equilibria are unstable the steady state of the system is a limit cycle on the sphere which, in the original frame of reference, corresponds to a quasi-periodic solution (see Fig. 11.20). The emergence of quasi-periodic solutions in the case of a circularly polarized applied magnetic field can be seen as a manifestation of spontaneous symmetry breaking. In fact, the solution shown in Fig. 11.20 is only one of a continuous set of quasi-periodic solutions which can be obtained from each other by a rotation around the z axis. Therefore, after the bifurcation which leads to the appearance of quasi-periodic solutions, the symmetry of the system is reflected in the symmetry of the whole set of solutions rather than in individual solutions.

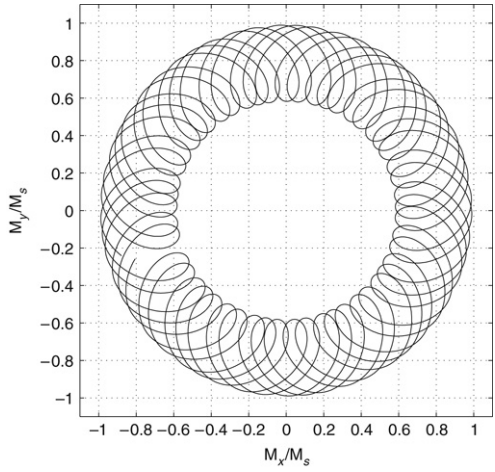

FIGURE 11.20 $\mathrm{M}_y/\mathrm{M}_s$ vs $\mathrm{M}_x/\mathrm{M}_s$ for the quasi-periodic steady-state LLG dynamics subject to a rotating applied field. Value of the parameters: $b_z = -2.825$, $a_\perp = 35.4$, $\Omega = 2.825 \cdot 10^{-2}$, $\alpha = 0.01$ and $\kappa_{\text{eff}} = -1$.

An important consequence of the reduction of the LLG equation to the autonomous form on the sphere in the case of the circularly polarized rf field is that the system cannot exhibit chaotic behavior for this polarization of the applied field (see Chapter 7). This is because chaotic motion may occur only in dynamical systems evolving on manifolds with at least three dimensions. On the other hand, it has been reported that the system may exhibit chaotic behavior in the case of a linearly polarized magnetic field [250]. This suggests the detailed study of the route to chaos through the gradual change of polarization of the $\mathbf{H}_{a\perp}(t)$ field from circular to linear.

In the case when $H_{ax} \neq H_{ay}$, the mathematical formulation of the problem is not rotationally symmetric in the (x, y)-plane. However, it can be easily verified that the mathematical formulation of the problem is invariant with respect to reflection around the origin of the (x, y)-plane.

This kind of symmetry is inherited by the solutions of the problem in a certain range of parameters. This fact is shown in Fig. 11.21(a) where the projections on the (m_y, m_x)-plane of two period-1 (i.e., period $T = 2\pi/\omega$) solutions corresponding to two different values of the parameter $a_p = Q/I$ (which characterizes the polarization of $\mathbf{H}_{a\perp}(t)$), are presented. The two figures show that the above solutions are symmetric with respect to the origin of the reference axes. In Fig. 11.21(b), two period-1 solutions are shown for an increased value of a_p. These periodic solutions are obtained

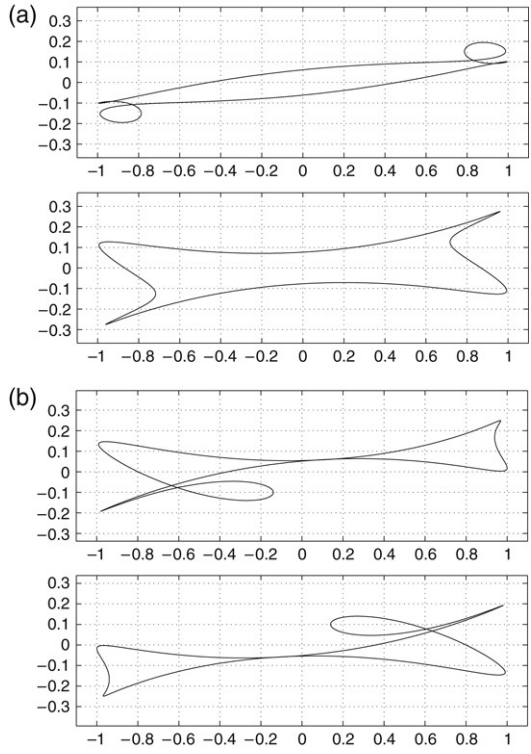

FIGURE 11.21 M_x/M_s vs M_y/M_s for period-1 solutions in the case of elliptically polarized applied field. Value of the parameters: $a_\perp = 35.35$, $\Omega = 0.05$, $b_z = 0.9$, $\alpha = 0.05$, $\kappa_{\text{eff}} = 0.1$, (a) $a_p = 0.75$ and $a_p = 0.91$, (b) in both figures $a_p = 0.96$ but the two solutions are obtained from two different and symmetric (with respect to the origin) initial conditions.

for the same value of a_p by solving the LL equations starting from two initial conditions symmetric with respect to the origin. It is evident that the steady-state solutions are not symmetric. However, these two solutions can be mapped into one another by reflection with respect to the origin. This demonstrates that for some critical value of the parameters a_p there is symmetry breaking bifurcation which leads to the set of two nonsymmetric solutions. These solutions together reflect the symmetry of the dynamical system with respect to the origin.

The possible bifurcations of the period-1 solution under the change of polarization, i.e., under the change of a_p, strongly depend on the values of the chosen parameters. We have also observed subharmonic steady states

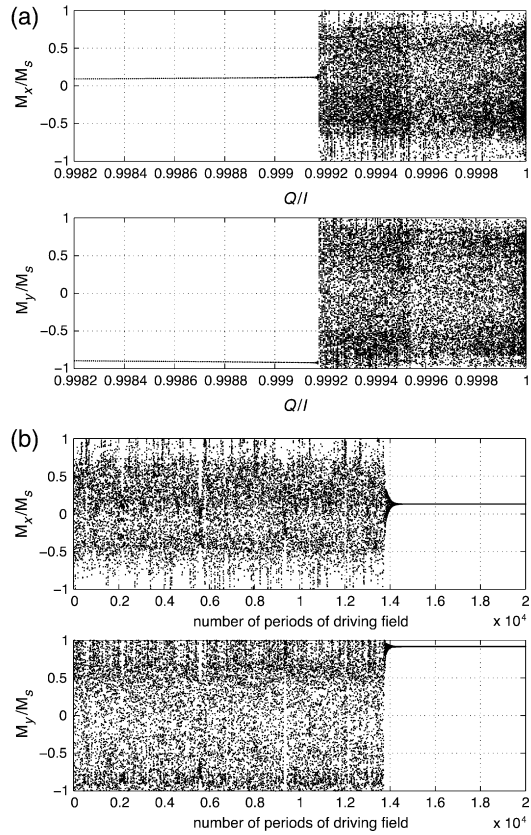

FIGURE 11.22 (a) Bifurcation diagram for $\mathrm{M}_x/\mathrm{M}_s$ and $\mathrm{M}_y/\mathrm{M}_s$ vs $a_p = Q/I$ for period-1 solutions; (b) example of chaotic transient: Poincaré map of $\mathrm{M}_x/\mathrm{M}_s$ and $\mathrm{M}_y/\mathrm{M}_s$ vs number of period. Value of the parameters: $a_\perp = 35.35$, $\Omega = 0.05$, $\Omega_z = 0.9$.

in certain regions of the parameter space (often coexisting with the period-1 periodic solutions) which can be reached by an appropriate choice of the initial condition. In this section, however, we shall limit ourselves to the discussion of the case of period-1 solutions.

In the sequel, we consider the bifurcation of the period-1 solutions for the values of the parameters $a_\perp = 35.35$, $\Omega = 0.05$, $b_z = 0.9$, $\alpha = 0.05$ and $\kappa_{\text{eff}} = 0.1$ (which coincide with those corresponding to the solutions shown in Fig. 11.21). These values are such that in the case of linearly polarized fields, i.e., $a_p = 1$, the system has chaotic behavior according

to the results reported in Ref. [250]. For these values of the parameters the bifurcation diagram displays an interesting behavior: the period-1 solution exists and it is stable for almost any value of a_p up to a critical value (determined up to intrinsic numerical uncertainties) $\tilde{a}_p \approx 0.999\,18$, where it loses its stability and the system enters a chaotic region. The bifurcation diagram (see Fig. 11.22(a)) is created through the following procedure. The value of $a_p = Q/I$ is increased by small steps starting from the $Q/I = 0$, which correspond to the case of a circular polarization. After each change in a_p, we numerically solved the LLG equation for a number of periods without recording the results. This is necessary to let the system reach a steady state. After this transient is faded, we start to sample the value of magnetization each $T = 2\pi/\omega$ s. In other words, we extract a Poincaré map by sampling the time at multiple of the period of the periodic driving field. The presence of only one point for each value of Q/I has to be read as the existence of period-1 solutions, while a period-n solution would show up as n points for the same value of Q/I.

From our numerical simulations, it is reasonable to conjecture that the transition to chaos occurs through the so-called chaotic transient. Indeed, we have found that when a_p approaches the critical point, the average time necessary to reach the period-1 solution increases progressively. In Fig. 11.22(b) an example of a chaotic transient is reported for $a_p = 0.998\,775$. The value of magnetization is sampled at multiples of the period $2\pi/\omega$. The trajectory eventually reaches a period-1 solution, but for almost $1.4 \cdot 10^4$ periods the trajectory has a chaotic behavior. It must be remarked that the final values of $\mathrm{M}_x/\mathrm{M}_s$ and $\mathrm{M}_y/\mathrm{M}_s$ in Fig. 11.22(b) do not coincide with the corresponding values in Fig. 11.22(a) because the period-1 solution is sampled at different time instants in the two cases.

References

[1] C. Abraham, "Model for lowering the nucleation field of ferromagnetic materials", *Phys. Rev.*, **135**, A1269–A1272 (1964).

[2] J.A. Acebron, L.L. Bonilla, C.J. Perez-Vicente, F. Ritort, and R. Spigler, "The Kuramoto model: A simple paradigm for synchronization phenomena", *Rev. Mod. Phys.*, **77**, 137–185 (2005).

[3] Y. Acremann, C.H. Back, M. Buess, O. Portmann, A. Vaterlaus, D. Pescia, and H. Melchior, "Imaging precessional motion of the magnetization vector", *Science*, **290**, 492–495 (2000).

[4] Y. Acremann, C.H. Back, M. Buess, D. Pescia, and V. Pokrovsky, "Bifurcation in precessional switching", *Appl. Phys. Lett.*, **79**, 2228–2230 (2001).

[5] A. Aharoni and S. Shtrikman, "Magnetization curve of the infinite cylinder", *Phys. Rev.*, **109**, 1522–1528 (1958).

[6] A. Aharoni, "Complete eigenvalue spectrum for the nucleation in a ferromagnetic prolate spheroid", *Phys. Rev.*, **131**, 1478–1482 (1963).

[7] A. Aharoni, "Thermal agitation of single domain particles", *Phys. Rev.*, **135**, A447–A449 (1964).

[8] A. Aharoni, "Effect of a magnetic field on the superparamagnetic relaxation time", *Phys. Rev.*, **177**, 793–796 (1969).

[9] A. Aharoni, "Exchange resonance modes in a ferromagnetic sphere", *J. Appl. Phys.*, **69**, 7762–7764 (1991).

[10] A. Aharoni, *Introduction to the Theory of Ferromagnetism*, Oxford University Press, Oxford, 1996.

[11] A. Aharoni, "The special role of magnetization curling in nanoparticles", *Phys. Stat. Sol. (a)*, **189**, 545–553 (2002).

[12] A. Aharoni, "'Local' demagnetization in a rectangular ferromagnetic prism", *Phys. Stat. Sol. (b)*, **229**, 1413–1416 (2002).

[13] A. Aharoni, "Exchange resonance modes in a hollow sphere", *Phys. Stat. Sol. (b)*, **231**, 547–553 (2002).

[14] F.J. Albert, J.A. Katine, R.A. Buhrman, and D.C. Ralph, "Spin-polarized current switching of a Co thin film nanomagnet", *Appl. Phys. Lett.*, **77**, 3809–3811 (2000).

[15] F.J. Albert, N.C. Emley, E.B. Myers, D.C. Ralph, and R.A. Buhrman, "Quantitative study of magnetization reversal by spin-polarized current in magnetic multilayer nanopillars", *Phys. Rev. Lett.*, **89**, 226802 (2002).

[16] G. Albuquerque, J. Miltat, and A. Thiaville, "Self-consistency based control scheme for magnetization dynamics", *J. Appl. Phys.*, **89**, 6719–6721 (2001).

[17] S. Alexander, J. Bernasconi, W.R. Schneider, and R. Orbach, "Excitation dynamics in random one-dimensional systems", *Rev. Mod. Phys.*, **53**, 175–198 (1981).

[18] D.A. Allwood, G. Xiong, M.D. Cooke, C.C. Faulkner, D. Atkinson, N. Vernier, and R.P. Cowburn, "Submicrometer ferromagnetic NOT gate and shift register", *Science*, **296**, 2003–2006 (2002).

[19] D.A. Allwood, G. Xiong, and R.P. Cowburn, "Domain wall diodes in ferromagnetic planar nanowires", *Appl. Phys. Lett.*, **85**, 2848–2850 (2004).

[20] W.S. Ament and G.T. Rado, "Electromagnetic effects of spin wave resonance in ferromagnetic metals", *Phys. Rev.*, **97**, 1558–1566 (1955).

[21] P.W. Anderson and P.R. Weiss, "Exchange narrowing in paramagnetic resonance", *Rev. Mod. Phys.*, **25**, 269–276 (1953).

[22] P.W. Anderson and H. Suhl, "Instability in the motion of ferromagnets at high microwave power levels", *Phys. Rev.*, **100**, 1788–1789 (1955).

[23] D.M. Apalkov and P.B. Visscher, "Slonczewski spin-torque as negative damping: Fokker–Planck computation of energy distribution", *J. Magn. Magn. Mater.*, **286**, 370–374 (2005).

[24] D.M. Apalkov and P.B. Visscher, "Spin-torque switching: Fokker–Planck rate calculation", *Phys. Rev. B*, **72**, 180405(R) (2005).

[25] R. Arias and D.L. Mills, "Extrinsic contributions to the ferromagnetic resonance response of ultrathin films", *Phys. Rev. B*, **60**, 7395–7409 (1999).

[26] R. Arias and D.L. Mills, "Extrinsic contributions to the ferromagnetic resonance response of ultrathin films", *J. Appl. Phys.*, **87**, 5455–5456 (2000).

[27] R. Arias and D.L. Mills, "Theory of spin excitations and the microwave response of cylindrical ferromagnetic nanowires", *Phys. Rev. B*, **63**, 134439 (2001).

[28] R. Arias and D.L. Mills, "Theory of collective spin waves and microwave response of ferromagnetic nanowire arrays", *Phys. Rev. B*, **67**, 094423 (2003).

[29] R. Arias and D.L. Mills, "Magnetostatic modes in ferromagnetic nanowires", *Phys. Rev. B*, **70**, 094414 (2004).

[30] R. Arias and D.L. Mills, "Theory of collective spin-wave modes of interacting ferromagnetic spheres", *Phys. Rev. B*, **70**, 104425 (2004).

[31] R. Arias and D.L. Mills, "Dipole exchange spin waves and microwave response of ferromagnetic spheres", *Phys. Rev. B*, **71**, 224410 (2005).

[32] R. Arias and D.L. Mills, "Magnetostatic modes in ferromagnetic nanowires. II. A method for cross sections with very large aspect ratio", *Phys. Rev. B*, **72**, 104418 (2005).

[33] V.I. Arnold, *Mathematical Methods of Classical Mechanics*, Springer, Berlin, 1989.

[34] V.I. Arnold, V.V. Kozlov, and A.I. Neishtadt, *Mathematical Aspects of Classical and Celestial Mechanics*, Springer, Berlin, 2006.

[35] G. Asti, M. Solzi, M. Ghidini, and F.M. Neri, "Micromagnetic analysis of exchange-coupled hard-soft planar nanocomposites", *Phys. Rev. B*, **69**, 174401 (2004).

[36] M.A. Austin and P.S. Krishnaprasad, "Almost Poisson integration of rigid body systems", *J. Comput. Phys.*, **107**, 105 (1993).

[37] K.L. Babcock and R.M. Westervelt, "Avalanches and self-organization in cellular magnetic-domain patterns", *Phys. Rev. Lett.*, **64**, 2168–2171 (1990).

[38] C.H. Back, D. Weller, J. Heidmann, D. Mauri, D. Guarisco, E.L. Garwin, and H.C. Siegmann, "Magnetization reversal in ultrashort magnetic field pulses", *Phys. Rev. Lett.*, **81**, 3251–3254 (1998).

[39] C.H. Back, R. Allenspach, W. Weber, S.S.P. Parkin, D. Weller, E.L. Garwin, and H.C. Siegmann, "Minimum field strength in precessional magnetization reversal", *Science*, **285**, 864–867 (1999).

[40] M.N. Baibich, J.M. Broto, A. Fert, F. NguyenVanDau, and F. Petroff, "Giant magnetoresistance of (001)Fe/(001)Cr magnetic superlattices", *Phys. Rev. Lett.*, **61**, 2472–2475 (1988).

[41] P. Bak and H. Flyvbjerg, "Self-organization of cellular magnetic-domain patterns", *Phys. Rev. A*, **45**, 2192–2200 (1992).

[42] R. Balescu, *Equilibrium and Nonequilibrium Statistical Mechanics*, Wiley, New York, 1975.

[43] V. Barcilon, "Singular perturbation analysis of the Fokker–Planck equation: Kramers' underdamped problem", *SIAM J. Appl. Math.*, **56**, 446–479 (1996).

[44] A. Barman, V.V. Kruglyak, R.J. Hicken, C.H. Marrows, M. Ali, A.T. Hindmarch, and B.J. Hickey, "Characterization of spin valves fabricated on opaque substrates by optical ferromagnetic resonance", *Appl. Phys. Lett.*, **81**, 1468–1470 (2002).

[45] A. Barman, V.V. Kruglyak, R.J. Hicken, A. Kundrotaite, and M. Rahman, "Anisotropy, damping, and coherence of magnetization dynamics in a 10 μm square $Ni_{81}Fe_{19}$ element", *Appl. Phys. Lett.*, **82**, 3065–3067 (2003).

[46] A. Barman, V.V. Kruglyak, R.J. Hicken, A. Kundrotaite, and M. Rahman, "Observation of incoherent picosecond magnetisation dynamics in micron sized $Ni_{81}Fe_{19}$ elements by time resolved scanning Kerr effect microscopy", *IEE Proc.-Sci. Meas. Technol.*, **150**, 260–263 (2003).

[47] S.E. Barnes and S. Maekawa, "Current-spin coupling for ferromagnetic domain walls in fine wires", *Phys. Rev. Lett.*, **95**, 107204 (2005).

[48] D.S. Bartran, "Limitations of coherent precession models", *IEEE Trans. Magn.*, **42**, 1958–1962 (2006).

[49] V.G. Baryakhtar, B.A. Ivanov, A.L. Sukstanskii, and E.Y. Melikhov, "Soliton relaxation in magnets", *Phys. Rev. B*, **56**, 619–635 (1997).

[50] V.G. Baryakhtar, "The phenomenological theory of relaxation processes in magnets", In *Frontiers in Magnetism of Reduced Dimension Systems*, (V.G. Baryakhtar, ed.), pp. 63–94, Kluwer, Dordrecht, 1998.

[51] I.V. Baryakhtar and V.G. Baryakhtar, "A motion equation for magnetization: dynamics and relaxation", *Ukr. Fiz. Zh.*, **43**, 1433–1448 (1998).

[52] J. Bass and W.P. Pratt Jr, "Current-perpendicular (CPP) magnetoresistance in magnetic metallic multilayers", *J. Magn. Magn. Mater.*, **200**, 274–289 (1999).

[53] V. Basso, C. Beatrice, M. LoBue, P. Tiberto, and G. Bertotti, "Connection between hysteresis and thermal relaxation in magnetic materials", *Phys. Rev. B*, **61**, 1278–1285 (2000).

[54] M. Bauer, J. Fassbender, B. Hillebrands, and R.L. Stamps, "Switching behavior of a Stoner particle beyond the relaxation time limit", *Phys. Rev. B*, **61**, 3410–3416 (2000).

[55] G.E.W. Bauer, Y. Tserkovnyak, D. Huertas-Hernando, and A. Brataas, "Universal angular magnetoresistance and spin torque in ferromagnetic/normal metal hybrids", *Phys. Rev. B*, **67**, 094421 (2003).

[56] Y.B. Bazaliy, B.A. Jones, and S.C. Zhang, "Modification of the Landau–Lifshitz equation in the presence of a spin-polarized current in colossal- and giant-magnetoresistive materials", *Phys. Rev. B*, **57**, R3213–R3216 (1998).

[57] Y.B. Bazaliy, B.A. Jones, and S.C. Zhang, "Towards metallic magnetic memory: how to interpret experimental results on magnetic switching induced by spin", *J. Appl. Phys.*, **89**, 6793–6795 (2001).

[58] Y.B. Bazaliy and B.A. Jones, "Magnetization rotation or generation of incoherent spin waves? Suggestions for a spin-transfer effect experiment", *Physica B*, **329–333**, 1290–1291 (2003).

[59] Y.B. Bazaliy, B.A. Jones, and S.C. Zhang, "Current-induced magnetization switching in small domains of different anisotropies", *Phys. Rev. B*, **69**, 094421 (2004).

[60] Y.B. Bazaliy, "Magnetization dynamics in planar spin transfer devices and stabilization by repulsion in a spin-flip transistor", *Appl. Phys. Lett.*, **91**, 262510 (2007).

[61] J.M.L. Beaujour, W. Chen, A.D. Kent, and J.Z. Sun, "Ferromagnetic resonance study of polycrystalline cobalt ultrathin films", *J. Appl. Phys.*, **99**, 08N503 (2006).

[62] E. Beaurepaire, J.C. Merle, A. Daunois, and J.Y. Bigot, "Ultrafast spin dynamics in ferromagnetic nickel", *Phys. Rev. Lett.*, **76**, 4250–4253 (1996).

[63] M. Belmeguenai, T. Devolder, and C. Chappert, "Analytical solution for precessional magnetization switching in exchange biased high perpendicular anisotropy nanostructures", *J. Phys. D: Appl. Phys.*, **39**, 1–5 (2006).

[64] L. Berger, "Low-field magnetoresistance and domain drag in ferromagnets", *J. Appl. Phys.*, **49**, 2156–2161 (1978).

[65] L. Berger, "Exchange interaction between ferromagnetic domain wall and electric current in very thin metallic films", *J. Appl. Phys.*, **55**, 1954–1956 (1984).

[66] L. Berger, "Possible existence of a Josephson effect in ferromagnets", *Phys. Rev. B*, **33**, 1572–1578 (1986).

[67] L. Berger, "Precession of conduction-electron spins near an interface between normal and magnetic metals", *IEEE Trans. Magn.*, **31**, 3871–3873 (1995).

[68] L. Berger, "Emission of spin waves by a magnetic multilayer traversed by a current", *Phys. Rev. B*, **54**, 9353–9358 (1996).

[69] L. Berger, "Multilayers as spin-wave emitting diodes", *J. Appl. Phys.*, **81**, 4880–4882 (1997).

[70] L. Berger, "Spin-wave emitting diodes and spin diffusion in magnetic multilayers", *IEEE Trans. Magn.*, **34**, 3837–3841 (1998).

[71] A. Berger, A. Inomata, J.S. Jiang, J.E. Pearson, and S.D. Bader, "Experimental observation of disorder-driven hysteresis-loop criticality", *Phys. Rev. Lett.*, **85**, 4176–4179 (2000).

[72] L. Berger, "Multilayer configuration for experiments of spin precession induced by a dc current", *J. Appl. Phys.*, **93**, 7693–7695 (2003).

[73] D.V. Berkov, K. Ramstock, and A. Hubert, "Solving micromagnetic problems: towards an optimal numerical method", *Phys. Stat. Sol. (a)*, **137**, 207 (1993).

[74] D.V. Berkov, "Numerical calculation of the energy barrier distribution in disordered many-particle systems: the path integral method", *J. Magn. Magn. Mater.*, **186**, 199–213 (1998).

[75] D.V. Berkov and N.L. Gorn, "Thermally activated processes in magnetic systems consisting of rigid dipoles: Equivalence of the Ito and Stratonovich stochastic calculus", *J. Phys.: Condens. Matter*, **14**, L281–L287 (2002).

[76] D.V. Berkov and N.L. Gorn, "Transition from the macrospin to chaotic behavior by a spin-torque driven magnetization precession of a square nanoelement", *Phys. Rev. B*, **71**, 052403 (2005).

[77] D.V. Berkov and N.L. Gorn, "Micromagnetic simulations of the magnetization precession induced by a spin-polarized current in a point-contact geometry", *J. Appl. Phys.*, **99**, 08Q701 (2006).

[78] G. Bertotti, "Energetic and thermodynamic aspects of hysteresis", *Phys. Rev. Lett.*, **76**, 1739–1742 (1996).

[79] G. Bertotti, *Hysteresis in Magnetism*, Academic Press, Boston, 1998.

[80] G. Bertotti, I.D. Mayergoyz, V. Basso, and A. Magni, "Functional integration approach to hysteresis", *Phys. Rev. E*, **60**, 1428–1440 (1999).

[81] G. Bertotti, C. Serpico, and I.D. Mayergoyz, "Nonlinear magnetization dynamics under circularly polarized field", *Phys. Rev. Lett.*, **86**, 724–727 (2001).

[82] G. Bertotti, I.D. Mayergoyz, and C. Serpico, "Spin-wave instabilities in large-scale nonlinear magnetization dynamics", *Phys. Rev. Lett.*, **87**, 217203 (2001).

[83] G. Bertotti, A. Magni, I.D. Mayergoyz, and C. Serpico, "Bifurcation analysis of Landau–Lifshitz–Gilbert dynamics under circularly polarized field", *J. Appl. Phys.*, **89**, 6710–6712 (2001).

[84] G. Bertotti, I.D. Mayergoyz, and C. Serpico, "Perturbation technique for Landau–Lifshitz–Gilbert equation under elliptically polarized fields", *Physica B*, **306**, 47–51 (2001).

[85] G. Bertotti, A. Magni, I.D. Mayergoyz, and C. Serpico, "Landau–Lifshitz magnetization dynamics and eddy currents in metallic thin films", *J. Appl. Phys.*, **91**, 7559–7561 (2002).

[86] G. Bertotti, I.D. Mayergoyz, and C. Serpico, "Perturbation technique for LLG dynamics in uniformly magnetized bodies subject to rf fields", *IEEE Trans. Magn.*, **38**, 2403–2405 (2002).

[87] G. Bertotti, I.D. Mayergoyz, and C. Serpico, "Generalized notion of spin-wave for large magnetization motion", *J. Appl. Phys.*, **91**, 8656–8658 (2002).

[88] G. Bertotti, I.D. Mayergoyz, and C. Serpico, "Analysis of instabilities in nonlinear Landau–Lifshitz–Gilbert dynamics under circularly polarized fields", *J. Appl. Phys.*, **91**, 7556–7558 (2002).

[89] G. Bertotti, I.D. Mayergoyz, C. Serpico, and M. Dimian, "Comparison of analytical solutions of Landau–Lifshitz equation for 'damping' and 'precessional' switchings", *J. Appl. Phys.*, **93**, 6811–6813 (2003).

[90] G. Bertotti, R. Bonin, I.D. Mayergoyz, and C. Serpico, "Generalized magnetostatic modes around large magnetization motions", *J. Appl. Phys.*, **95**, 7046–7048 (2004).

[91] G. Bertotti, I.D. Mayergoyz, and C. Serpico, "Analytical solutions of Landau–Lifshitz equation for precessional dynamics", *Physica B*, **343**, 325–330 (2004).

[92] G. Bertotti, I.D. Mayergoyz, and C. Serpico, "Averaging technique for the analysis of magnetization relaxations", *J. Appl. Phys.*, **95**, 6598–6600 (2004).

[93] G. Bertotti, I.D. Mayergoyz, and C. Serpico, "Analytical solutions of Landau–Lifshitz equation for precessional dynamics", *Physica B*, **343**, 325–330 (2004).

[94] G. Bertotti, C. Serpico, I.D. Mayergoyz, A. Magni, M. d'Aquino, and R. Bonin, "Magnetization switching and microwave oscillations in nanomagnets driven by spin-polarized currents", *Phys. Rev. Lett.*, **94**, 127206 (2005).

[95] G. Bertotti, A. Magni, R. Bonin, I.D. Mayergoyz, and C. Serpico, "Analytical description of magnetization relaxation to equilibrium", *J. Appl. Phys.*, **97**, 10E315 (2005).

[96] G. Bertotti, R. Bonin, A. Magni, I.D. Mayergoyz, and C. Serpico, "Energy equation for the analysis of magnetization relaxation to equilibrium", *J. Magn. Magn. Mater.*, **286**, 282–285 (2005).

[97] G. Bertotti, A. Magni, R. Bonin, I.D. Mayergoyz, and C. Serpico, "Bifurcation analysis of magnetization dynamics driven by spin transfer", *J. Magn. Magn. Mater.*, **290–291**, 522–525 (2005).

[98] G. Bertotti, C. Serpico, I.D. Mayergoyz, R. Bonin, A. Magni, and M. d'Aquino, "Magnetization self-oscillations induced by spin-polarized currents", *IEEE Trans. Magn.*, **41**, 2574–2576 (2005).

[99] G. Bertotti and I.D. Mayergoyz, *The Science of Hysteresis*, Elsevier, Oxford, 2006.

[100] G. Bertotti, V. Basso, M. LoBue, and A. Magni, "Thermodynamics, hysteresis, and micromagnetics", In *The Science of Hysteresis. Volume II: Physical Modeling, Micromagnetics, and Magnetization Dynamics*, (G. Bertotti and I.D. Mayergoyz, eds), p. 106, Elsevier, Oxford, 2006.

[101] G. Bertotti, I.D. Mayergoyz, and C. Serpico, "Nonlinear magnetization dynamics. Switching and relaxation phenomena", In *The Science of Hysteresis. Volume II: Physical Modeling, Micromagnetics, and Magnetization Dynamics*, (G. Bertotti and I.D. Mayergoyz, eds), pp. 435–566, Elsevier, Oxford, 2006.

[102] G. Bertotti, I.D. Mayergoyz, and C. Serpico, "Nonlinear magnetization dynamics. Magnetization modes and spin waves under rotating fields", In *The Science of Hysteresis. Volume II: Physical Modeling, Micromagnetics, and Magnetization Dynamics*, (G. Bertotti and I.D. Mayergoyz, eds), pp. 567–642, Elsevier, Oxford, 2006.

[103] G. Bertotti, I.D. Mayergoyz, and C. Serpico, "Analysis of random Landau–Lifshitz dynamics by using stochastic processes on graphs", *J. Appl. Phys.*, **99**, 08F301 (2006).

[104] G. Bertotti, C. Serpico, I.D. Mayergoyz, R. Bonin, and M. d'Aquino, "Current-induced magnetization dynamics in nanomagnets", *J. Magn. Magn. Mater.*, **316**, 285–290 (2007).

[105] J.J. Binney, N.J. Dowrick, A.J. Fisher, and M.E.J. Newman, *The Theory of Critical Phenomena*, Oxford University Press, Oxford, 1993.

[106] F. Bloch, "Nuclear induction", *Phys. Rev.*, **70**, 460–474 (1946).

[107] F. Bloch, "Dynamical theory of nuclear induction. II", *Phys. Rev.*, **102**, 104–135 (1956).

[108] F. Bloch, "Generalized theory of relaxation", *Phys. Rev.*, **105**, 1206–1222 (1957).

[109] A. Bloch, P.S. Krishnaprasad, J.E. Marsden, and T.S. Ratiu, "The Euler–Poincaré equations and double bracket dissipation", *Commun. Math. Phys.*, **175**, 1–42 (1996).

[110] N. Bloembergen, "On the ferromagnetic resonance in nickel and supermalloy", *Phys. Rev.*, **78**, 572–580 (1950).

[111] N. Bloembergen and R.W. Damon, "Relaxation effects in ferromagnetic resonance", *Phys. Rev.*, **85**, 699 (1952).

[112] N. Bloembergen and S. Wang, "The influence of anisotropy on ferromagnetic relaxation", *Phys. Rev.*, **87**, 392–393 (1952).

[113] N. Bloembergen and S. Wang, "Relaxation effects in para- and ferromagnetic relaxation", *Phys. Rev.*, **93**, 72–83 (1954).

[114] H.J. Blythe, V.M. Fedosyuk, O.I. Kasyutich, and W. Schwarzacher, "SQUID studies of Co–Cu heterogeneous alloy nanowires", *J. Magn. Magn. Mater.*, **208**, 251–254 (2000).

[115] S. Bobbio, *Electrodynamics of Materials*, Academic Press, San Diego, 2000.

[116] R. Bonin, G. Bertotti, I.D. Mayergoyz, and C. Serpico, "Spin-torque driven magnetization dynamics in nanomagnets subject to magnetic fields perpendicular to the sample plane", *J. Appl. Phys.*, **99**, 08G508 (2006).

[117] R. Bonin, G. Bertotti, C. Serpico, I.D. Mayergoyz, and M. d'Aquino, "Model of phase locking in spin-transfer-driven magnetization dynamics", *J. Appl. Phys.*, **101**, 09A506 (2007).

[118] R. Bonin, C. Serpico, G. Bertotti, I.D. Mayergoyz, and M. d'Aquino, "Analytical study of magnetization dynamics driven by spin-polarized currents", *Eur. Phys. J. B*, **59**, 435–445 (2007).

[119] R. Bonin, G. Bertotti, C. Serpico, I.D. Mayergoyz, and M. d'Aquino, "Effect of thermal fluctuations in spin-torque driven magnetization dynamics", *J. Magn. Magn. Mater.*, **316**, e919–e922 (2007).

[120] F.J. Bourland and R. Haberman, "Separatrix crossing: time-invariant potentials with dissipation", *SIAM J. Appl. Math.*, **50**, 1716–1744 (1990).

[121] A. Bossavit, *Computational Electromagnetism*, Academic Press, San Diego, 1998.

[122] O. Bottauscio, A. Manzin, V. Chiadó-Piat, M. Codegone, and M. Chiampi, "Electromagnetic phenomena in heterogeneous media: effective properties and local behavior", *J. Appl. Phys.*, **100**, 044902 (2006).

[123] O. Bottauscio, V. Chiadó-Piat, M. Chiampi, M. Codegone, and A. Manzin, "Evaluation of effective electromagnetic properties in heterogeneous media", *Eur. Phys. J. Appl. Phys.*, **39**, 113–118 (2007).

[124] O. Boulle, V. Cros, J. Grollier, L.G. Pereira, C. Deranlot, F. Petroff, G. Faini, J. Barnas, and A. Fert, "Shaped angular dependence of the spin-transfer torque and microwave generation without magnetic field", *Nature Physics*, **3**, 492–497 (2007).

[125] A. Brandt, "Multiscale solvers and systematic upscaling in computational physics", *Comput. Phys. Commun.*, **169**, 438–441 (2005).

[126] J.P. Braselton, M.L. Abell, and L.M. Braselton, "Generalized Walker solutions to the Landau–Lifshitz–Gilbert equations", *Int. J. Non-linear Mech.*, **36**, 571–579 (2001).

[127] H.B. Braun, "Thermally activated magnetization reversal in elongated ferromagnetic particles", *Phys. Rev. Lett.*, **71**, 3557–3560 (1993).

[128] A.J. Bray and A.J. McKane, "Instanton calculation of the escape rate for activation over a potential barrier driven by colored noise", *Phys. Rev. Lett.*, **62**, 493–496 (1989).

[129] M. Brokate and J. Sprekels, *Hysteresis and Phase Transitions*, Springer, New York, 1996.

[130] W.F. Brown, "Virtues and weaknesses of the domain concept", *Rev. Mod. Phys.*, **17**, 15–19 (1945).

[131] W.F. Brown, "Criterion for uniform micromagnetization", *Phys. Rev.*, **105**, 1479–1482 (1957).

[132] W.F. Brown, "Micromagnetics, domains, and resonance", *J. Appl. Phys.*, **30**, 62S–69S (1959).

[133] W.F. Brown, *Magnetostatic principles in ferromagnetism*, North-Holland, Amsterdam, 1962.

[134] W.F. Brown, *Micromagnetics*, Krieger Publishing Co., New York, 1963.

[135] W.F. Brown, "Thermal fluctuations of a single-domain particle", *Phys. Rev.*, **130**, 1677–1686 (1963).

[136] W.F. Brown, "Magnetic interactions of superparamagnetic particles", *J. Appl. Phys.*, **38**, 1017–1018 (1967).

[137] P. Bruno, "Geometrically constrained magnetic wall", *Phys. Rev. Lett.*, **83**, 2425–2428 (1999).

[138] P. Bryant, C. Jeffries, and K. Nakamura, "Spin-wave nonlinear dynamics in an yttrium iron garnet sphere", *Phys. Rev. Lett.*, **60**, 1185–1188 (1988).

[139] P. Bryant, C. Jeffries, and K. Nakamura, "Spin-wave dynamics in a ferrimagnetic sphere", *Phys. Rev. A*, **38**, 4223–4240 (1988).

[140] P. Bryant and H. Suhl, "Thin-film magnetic patterns in an external field", *Appl. Phys. Lett.*, **54**, 2224–2226 (1989).

[141] K.S. Buchanan, P.E. Roy, F.Y. Fradin, K.Y. Guslienko, M. Grimsditch, S.D. Bader, and V. Novosad, "Vortex dynamics in patterned ferromagnetic ellipses", *J. Appl. Phys.*, **99**, 08C707 (2006).

[142] J.D. Burton, A. Kashyap, M.Y. Zhuravlev, R. Skomski, E.Y. Tsymbal, S.S. Jaswal, O.N. Mryasov, and R.W. Chantrell, "Field-controlled domain-wall resistance in magnetic nanojunctions", *Appl. Phys. Lett.*, **85**, 251–253 (2004).

[143] K. Bussmann, G.A. Prinz, S.F. Cheng, and D. Wang, "Switching of vertical giant magnetoresistance devices by current through the device", *Appl. Phys. Lett.*, **75**, 2476–2478 (1999).

[144] G.G. Cabrera and L.M. Falicov, "Spin-dependent scattering, transport properties, and magnetic breakdown in ferromagnetic metals", *Phys. Rev. B*, **11**, 2651–2659 (1975).

[145] H.B. Callen and T.A. Welton, "Irreversibility and generalized noise", *Phys. Rev.*, **83**, 34–40 (1951).

[146] H.B. Callen and R.F. Greene, "On a theorem of irreversible thermodynamics", *Phys. Rev.*, **86**, 702–710 (1952).

[147] H.B. Callen, "A ferromagnetic dynamical equation", *J. Phys. Chem. Solids*, **4**, 256–270 (1958).

[148] H.B. Callen, *Thermodynamics and an Introduction to Thermostatistics*, Wiley, New York, 1985.

[149] J. Camarero, Y. Pennec, M. Bonfim, J. Vogel, S. Pizzini, A. Fontaine, M. Cartier, F. Fettar, and B. Dieny, "Magnetization reversal dynamics in exchange-coupled NiO–Co bilayers", *J. Appl. Phys.*, **89**, 6585–6587 (2001).

[150] F.F. Cap, "Averaging method for the solution of non-linear differential equations with periodic non-harmonic solutions", *Int. J. Non-Linear Mechanics*, **9**, 441–450 (1974).

[151] T.L. Carroll, L.M. Pecora, and F.J. Rachford, "Chaotic transients and multiple attractors in spin-wave experiments", *Phys. Rev. Lett.*, **59**, 2891–2894 (1987).

[152] T.L. Carroll, L.M. Pecora, and F.J. Rachford, "Chaos and chaotic transients in yttrium iron garnet", *J. Appl. Phys.*, **64**, 5396–5400 (1988).

[153] T.L. Carroll, F.J. Rachford, and L.M. Pecora, "Occurrence of chaotic transients during transitions between quasiperiodic states in yttrium iron garnet", *Phys. Rev. B*, **38**, 2938–2940 (1988).

[154] T.L. Carroll, L.M. Pecora, and F.J. Rachford, "Chaos and chaotic transients in an yttrium iron garnet sphere", *Phys. Rev. A*, **40**, 377–386 (1989).

[155] T.L. Carroll, L.M. Pecora, and F.J. Rachford, "Chaos in magnetostatic modes in an yttrium iron garnet film between 2 and 4 GHz", *J. Appl. Phys.*, **67**, 5630–5632 (1990).

[156] T.L. Carroll, L.M. Pecora, and F.J. Rachford, "Characterizing chaos in magnetostatic modes", *J. Appl. Phys.*, **69**, 5727–5729 (1991).

[157] T.L. Carroll, L.M. Pecora, and F.J. Rachford, "Using nonlinear dynamics to understand spin wave interactions", *IEEE Trans. Magn.*, **27**, 5441–5443 (1991).

[158] F.J. Castano, C.A. Ross, C. Frandsen, A. Eilez, D. Gil, H.I. Smith, M. Redjdal, and F.B. Humphrey, "Metastable states in magnetic nanorings", *Phys. Rev. B*, **67**, 184425 (2003).

[159] S. Chandrasekhar, "Stochastic problems in physics and astronomy", *Rev. Mod. Phys.*, **15**, 1–89 (1943).

[160] C.R. Chang and C.M. Lee, "Coupling of reversal modes for an infinite ferromagnetic cylinder", *J. Appl. Phys.*, **83**, 6593–6595 (1998).

[161] P.J. Channel and J.C. Scovel, "Symplectic integration of Hamiltonian systems", *Nonlinearity*, **3**, 231–259 (1990).

[162] C. Chappert, K. LeDang, P. Beauvillain, H. Hurdequint, and D. Renard, "Ferromagnetic resonance studies of very thin cobalt films on a gold substrate", *Phys. Rev. B*, **34**, 3192–3197 (1986).

[163] X. Che and H. Suhl, "Magnetic domain patterns as self-organized critical systems", *Phys. Rev. Lett.*, **64**, 1670–1673 (1990).

[164] K. Chen and D.P. Landau, "Spin-dynamics study of the dynamic critical behavior of the three-dimensional classical Heisenberg ferromagnet", *Phys. Rev. B*, **49**, 3266–3274 (1994).

[165] W. Chen, J.M.L. Beaujour, G. deLoubens, and A.D. Kent, "Spin-torque driven ferromagnetic resonance of Co/Ni synthetic layers in spin valves", *Appl. Phys. Lett.*, **92**, 012507 (2008).

[166] W. Chen, G. deLoubens, J.M.L. Beaujour, A.D. Kent, and J.Z. Sun, "Finite size effects on spin-torque driven ferromagnetic resonance in spin valves with a Co/Ni synthetic free layer", *J. Appl. Phys.*, **103**, 07A502 (2008).

[167] S.B. Choe, Y. Acremann, A. Scholl, A. Bauer, A. Doran, J. Stohr, and H.A. Padmore, "Vortex core-driven magnetization dynamics", *Science*, **304**, 420–422 (2004).

[168] B.C. Choi, M. Belov, W.K. Hiebert, G.E. Ballentine, and M.R. Freeman, "Ultrafast magnetization reversal dynamics investigated by time domain imaging", *Phys. Rev. Lett.*, **86**, 728–731 (2001).

[169] S. Choi and S. Kim, "Double-contact spin-torque nano-oscillator with optimized spin-wave coupling: micromagnetic modeling", *Appl. Phys. Lett.*, **90**, 083114 (2007).

[170] O.A. Chubykalo, B. Lengsfield, B. Jones, J. Kaufman, J.M. Gonzalez, R.W. Chantrell, and R. Smirnov-Rueda, "Micromagnetic modelling of thermal decay in interacting systems", *J. Magn. Magn. Mater.*, **221**, 132–136 (2000).

[171] O. Chubykalo, J.D. Hannay, M. Wongsam, R.W. Chantrell, and J.M. Gonzalez, "Langevin dynamic simulation of spin waves in a micromagnetic model", *Phys. Rev. B*, **65**, 184428 (2002).

[172] S.H. Chun, M.B. Salamon, Y. Lyanda-Geller, P.M. Goldbart, and P.D. Han, "Magnetotransport in manganites and the role of quantal phases: theory and experiment", *Phys. Rev. Lett.*, **84**, 757–760 (2000).

[173] I. Cimrak and M. Slodicka, "An iterative approximation scheme for the Landau–Lifshitz–Gilbert equation", *J. Comput. Appl. Math.*, **169**, 17–32 (2004).

[174] I. Cimrak and M. Slodicka, "Optimal convergence rate for Maxwell–Landau–Lifshitz system", *Physica B*, **343**, 236–240 (2004).

[175] D. Cioranescu and P. Donato, *An Introduction to Homogenization*, Oxford University Press, Oxford, 1999.

[176] F. Ciubotaru, A. Stancu, and L. Stoleriu, "LLG study of the precessional switching process in pulsed magnetic fields", *J. Optoelectr. Adv. Mater.*, **6**, 1017–1021 (2004).

[177] P. Cizeau, S. Zapperi, G. Durin, and H.E. Stanley, "Dynamics of a ferromagnetic domain wall and the Barkhausen effect", *Phys. Rev. Lett.*, **79**, 4669–4672 (1997).

[178] A.M. Clogston, H. Suhl, L.R. Walker, and P.W. Anderson, "Possible source of line width in ferromagnetic resonance", *Phys. Rev.*, **101**, 903–905 (1956).

[179] W.T. Coffey, D.S.F. Crothers, J.L. Dormann, Y.P. Kalmykov, E.C. Kennedy, and W. Wernsdorfer, "Thermally activated relaxation time of a single domain ferromagnetic particle subjected to a uniform field at an oblique angle to the easy axis: comparison with experimental observations", *Phys. Rev. Lett.*, **80**, 5655–5658 (1998).

[180] W.T. Coffey, Y.P. Kalmykov, and J.T. Waldron, *The Langevin Equation*, World Scientific, Singapore, 2004.

[181] F. Colaiori, G. Durin, and S. Zapperi, "Loss separation for dynamic hysteresis in ferromagnetic thin films", *Phys. Rev. Lett.*, **97**, 257203 (2006).

[182] G. Consolo, L. Lopez-Diaz, L. Torres, and B. Azzerboni, "Boundary conditions for spin-wave absorption based on different site-dependent damping functions", *IEEE Trans. Magn.*, **43**, 2974–2976 (2007).

[183] G. Counil, J.V. Kim, T. Devolder, C. Chappert, K. Shigeto, and Y. Otani, "Spin wave contributions to the high-frequency magnetic response of thin films obtained with inductive methods", *J. Appl. Phys.*, **95**, 5646–5652 (2004).

[184] M. Covington, M. AlHajDarwish, Y. Ding, N.J. Gokemeijer, and M.A. Seigler, "Current-induced magnetization dynamics in current perpendicular to plane spin valves", *Phys. Rev. B*, **69**, 184406 (2004).

[185] B. Cowan, *Topics in Statistical Mechanics*, Imperial College Press, London, 2005.

[186] R.P. Cowburn, D.K. Kolstov, A.O. Adeyeye, and M.E. Welland, "Single-domain circular nanomagnets", *Phys. Rev. Lett.*, **83**, 1042–1045 (1999).

[187] R.T. Cox, "The statistical method of gibbs in irreversible change", *Rev. Mod. Phys.*, **22**, 238–248 (1950).

[188] J.D. Crawford, "Introduction to bifurcation theory", *Rev. Mod. Phys.*, **63**, 991–1037 (1991).

[189] T. Crawford, P. Kabos, and T. Silva, "Coherent control of precessional dynamics in thin film permalloy", *Appl. Phys. Lett.*, **76**, 2113–2115 (2000).

[190] R. Damon, "Relaxation effects in the ferromagnetic resonance", *Rev. Mod. Phys.*, **25**, 239–245 (1953).

[191] R.W. Damon and J.R. Eshbach, "Magnetostatic modes of ferromagnetic slab", *J. Phys. Chem. Solids*, **19**, 308 (1961).

[192] M. d'Aquino, C. Serpico, G. Miano, I.D. Mayergoyz, and G. Bertotti, "Numerical integration of Landau–Lifshitz–Gilbert equation based on the midpoint rule", *J. Appl. Phys.*, **97**, 10E319 (2005).

[193] M. d'Aquino, C. Serpico, and G. Miano, "Geometrical integration of Landau–Lifshitz–Gilbert equation based on the mid-point rule", *J. Comput. Phys.*, **209**, 730–753 (2005).

[194] M. d'Aquino, C. Serpico, G. Coppola, I.D. Mayergoyz, and G. Bertotti, "Midpoint numerical technique for stochastic Landau–Lifshitz–Gilbert dynamics", *J. Appl. Phys.*, **99**, 08B905 (2006).

[195] M. d'Aquino, G. Bertotti, C. Serpico, I.D. Mayergoyz, and R. Bonin, "Foldover, quasi-periodicity, and spin-wave instabilities in ultra-thin magnetic films", *IEEE Trans. Magn.*, **42**, 3195–3197 (2006).

[196] M. d'Aquino, G. Bertotti, C. Serpico, I.D. Mayergoyz, R. Bonin, and G. Guida, "Foldover, quasi-periodicity, spin-wave instabilities in ultra-thin films subject to RF fields", *J. Magn. Magn. Mater.*, **316**, e523–e525 (2007).

[197] M. d'Aquino, C. Serpico, G. Miano, G. Bertotti, and I.D. Mayergoyz, "Magnetization normal oscillation modes in saturated ferromagnetic particles", *Physica B*, **403**, 242–244 (2008).

[198] A. Deac, K.J. Lee, Y. Liu, O. Redon, M. Li, P. Wang, J.P. Nozieres, and B. Dieny, "Spin transfer effects in exchange-biased spin-valves for current-perpendicular-to-plane magnetoresistive heads", *J. Magn. Magn. Mater.*, **290-291**, 42–47 (2005).

[199] A. Deac, K.J. Lee, Y. Liu, O. Redon, M. Li, P. Wang, J.P. Nozieres, and B. Dieny, "Current-induced magnetization switching in exchange-biased spin valves for current-perpendicular-to-plane giant magnetoresistance heads", *Phys. Rev. B*, **73**, 064414 (2006).

[200] F.M. de Aguiar and S.M. Rezende, "Observation of subharmonic routes to chaos in parallel-pumped spin waves in yttrium iron garnet", *Phys. Rev. Lett.*, **56**, 1070–1073 (1986).

[201] F.M. de Aguiar, A. Azevedo, and S.M. Rezende, "Nonlinear dynamics of spin-injected magnons in magnetic nanostructures", *J. Appl. Phys.*, **91**, 8046–8048 (2002).

[202] E. della Torre, *Magnetic Hysteresis*, Wiley-IEEE Press, New York, 2000.

[203] H. Dekker, "Functional integration and the Onsager-Machlup Lagrangian for continuous Markov processes in Riemannian geometries", *Phys. Rev. A*, **19**, 2102–2111 (1979).

[204] S.R. deGroot and P. Mazur, *Non-Equilibrium Thermodynamics*, Dover, New York, 1984.

[205] V.E. Demidov, U.H. Hansen, and S.O. Demokritov, "Spin-wave eigenmodes of a saturated magnetic square at different precession angles", *Phys. Rev. Lett.*, **98**, 157203 (2007).

[206] A. Demir, A. Mehrotra, and J. Roychowdhury, "Phase noise in oscillators: a unifying theory and numerical methods for characterization", *IEEE Trans. Circuits Syst.*, **47**, 655–674 (2000).

[207] S.I. Denisov, T.V. Lyutyy, P. Hanggi, and K.N. Trohidou, "Dynamical and thermal effects in nanoparticle systems driven by a rotating magnetic field", *Phys. Rev. B*, **74**, 104406 (2006).

[208] S.I. Denisov, T.V. Lyutyy, and P. Hanggi, "Magnetization of nanoparticle systems in a rotating magnetic field", *Phys. Rev. Lett.*, **97**, 227202 (2006).

[209] S.I. Denisov, K. Sakmann, P. Talkner, and P. Hanggi, "Rapidly driven nanoparticles: mean first-passage times and relaxation of the magnetic moment", *Phys. Rev. B*, **75**, 184432 (2007).

[210] A. deSimone, "Energy minimizers for large ferromagnetic bodies", *Arch. Ration. Mech. Anal.*, **125**, 99 (1993).

[211] A. deSimone, R.V. Kohn, S. Mueller, and F. Otto, "A reduced theory for thin-film micromagnetics", *Commun. Pure Appl. Math.*, **55**, 1408 (2002).

[212] A. deSimone, R.V. Kohn, S. Mueller, and F. Otto, "Recent analytical developments in micromagnetics", In *The Science of Hysteresis. Volume II: Physical Modeling, Micromagnetics, and Magnetization Dynamics*, (G. Bertotti and I.D. Mayergoyz, eds), pp. 269–381, Elsevier, Oxford, 2006.

[213] J.M. Deutsch and O. Narayan, "Subharmonics and aperiodicity in hysteresis loops", *Phys. Rev. Lett.*, **91**, 200601 (2003).

[214] J.M. Deutsch, A. Dhar, and O. Narayan, "Return to return point memory", *Phys. Rev. Lett.*, **92**, 227203 (2004).

[215] J.M. Deutsch and O. Narayan, "Energy dissipation and fluctuation response for particles in fluids", *Phys. Rev. E*, **74**, 026112 (2006).

[216] J.M. Deutsch and A. Berger, "Spin precession and avalanches", *Phys. Rev. Lett.*, **99**, 027207 (2007).

[217] T. Devolder and C. Chappert, "Precessional switching of thin nanomagnets: analytical study", *Eur. Phys. J. B*, **36**, 57–64 (2003).

[218] T. Devolder and C. Chappert, "Cell writing selection when using precessional switching in a magnetic random access memory", *J. Appl. Phys.*, **95**, 1933–1941 (2004).

[219] T. Devolder and C. Chappert, "Spectral analysis of the precessional switching of the magnetization in an isotropic thin film", *Sol. State Comm.*, **129**, 97–101 (2004).

[220] T. Devolder, P. Crozat, C. Chappert, J. Miltat, A. Tulapurkar, Y. Suzuki, and K. Yagami, "Instability threshold versus switching threshold in spin-transfer-induced magnetization switching", *Phys. Rev. B*, **71**, 184401 (2005).

[221] R.E. deWames and T. Wolfram, "Dipole-exchange spin waves in ferromagnetic films", *J. Appl. Phys.*, **41**, 987–993 (1970).

[222] D. D'Humieres, M.R. Beasley, B.A. Huberman, and A. Libchaber, "Chaotic states and routes to chaos in the forced pendulum", *Phys. Rev. A*, **26**, 3483–3496 (1982).

[223] R. Dittrich, T. Schrefl, D. Suess, W. Scholtz, H. Forster, and J. Fidler, "A path method for finding energy barriers and minimum energy paths in complex micromagnetic systems", *J. Magn. Magn. Mater.*, **250**, L12–L19 (2002).

[224] R. Dittrich, J. Fidler, D. Suess, W. Scholtz, H. Forster, and T. Schrefl, "Computational aspects of micromagnetics", In *The Science of Hysteresis. Volume II: Physical Modeling, Micromagnetics, and Magnetization Dynamics*, (G. Bertotti and I.D. Mayergoyz, eds), pp. 383–433, Elsevier, Oxford, 2006.

[225] A.Y. Dobin and R.H. Victora, "Intrinsic nonlinear ferromagnetic relaxation in thin metallic films", *Phys. Rev. Lett.*, **90**, 167203 (2003).

[226] V.V. Dobrovitski, M.I. Katsnelson, and B.N. Harmon, "Statistical coarse-graining as an approach to multiscale problems in magnetism", *J. Magn. Magn. Mater.*, **221**, L235–L242 (2000).

[227] V.V. Dobrovitski, M.I. Katsnelson, and B.N. Harmon, "Length scale coupling for nonlinear dynamical problems in magnetism", *Phys. Rev. Lett.*, **90**, 067201 (2003).

[228] M.J. Donahue and D.G. Porter, "Analysis of switching in uniformly magnetized bodies", *IEEE Trans. Magn.*, **38**, 2468–2470 (2002).

[229] W.D. Doyle and L. He, "The effect of DC bias fields on the switching speed in magnetic particulate media", *IEEE Trans. Magn.*, **29**, 3634 (1993).

[230] V.K. Dugaev, J. Barnas, A. Lusakowski, and L.A. Turski, "Accumulation of spin and charge and transport properties of ferromagnets with domain walls", *Phys. Stat. Sol. (a)*, **196**, 177–180 (2003).

[231] P. Dutta and P.M. Horn, "Low-frequency fluctuations in solids: 1/f noise", *Rev. Mod. Phys.*, **53**, 497–516 (1981).

[232] F.J. Dyson, "General theory of spin-wave interactions", *Phys. Rev.*, **102**, 1217–1230 (1956).

[233] F.J. Dyson, "Thermodynamic behavior of an ideal ferromagnet", *Phys. Rev.*, **102**, 1230–1244 (1956).

[234] W. E and X.P. Wang, "Numerical methods for the Landau–Lifshitz equation", *SIAM J. Numer. Analysis*, **38**, 1647–1665 (2000).

[235] W. E, W. Ren, and E. Vanden-Eijnden, "Energy landscape and thermally activated switching of submicron-sized ferromagnetic elements", *J. Appl. Phys.*, **93**, 2275–2282 (2003).

[236] W. E, W. Ren, and E. Vanden-Eijnden, "Minimum action method for the study of rare events", *Commun. Pure Appl. Math*, **57**, 637–656 (2004).

[237] W. E., B. Engquist, X. Li, W. Ren, and E. Vanden-Eijnden, "Heterogeneous multiscale methods: a review", *Commun. Comput. Phys.*, **2**, 367–450 (2007).

[238] W. Ebeling and I.M. Sokolov, *Statistical Thermodynamics and Stochastic Theory of Nonequilibrium Systems*, World Scientific, Singapore, 2005.

[239] U. Ebels, A. Radulescu, Y. Henry, L. Piraux, and K. Ounadjela, "Spin accumulation and domain wall magnetoresistance in 35 nm co wires", *Phys. Rev. Lett.*, **84**, 983–986 (2000).

[240] J.P. Eberhard, "Upscaling for the time-harmonic Maxwell equations with heterogenous magnetic materials", *Phys. Rev. E*, **72**, 036616 (2005).

[241] R.J. Elliott, E.M. Epshtein, Y.V. Gulyaev, and P.E. Zilberman, "Magnetization reversal and current hysteresis due to spin injection in magnetic junction", *J. Magn. Magn. Mater.*, **271**, 88–96 (2004).

[242] J.R. Eshbach and R.W. Damon, "Surface magnetostatic modes and surface spin waves", *Phys. Rev.*, **118**, 1208–1210 (1960).

[243] D.J. Evans, E.G.D. Cohen, and G.P. Morriss, "Probability of second law violations in shearing steady states", *Phys. Rev. Lett.*, **71**, 2401–2404 (1993).

[244] P.R. Evans, G. Yi, and W. Schwarzacher, "Current perpendicular to plane giant magnetoresistance of multilayered nanowires electrodeposited in anodic aluminum oxide membranes", *Appl. Phys. Lett.*, **76**, 481–483 (2000).

[245] D.J. Evans and D.J. Searles, "The fluctuation theorem", *Advances in Physics*, **51**, 1529–1585 (2002).

[246] A. Fabian, C. Terrier, S. Serrano-Guisan, X. Hoffer, M. Dubey, L. Gravier, and J.P. Ansermet, "Current-induced two-level fluctuations in pseudo-spin-valve (Co/Cu/Co) nanostructures", *Phys. Rev. Lett.*, **91**, 257209 (2003).

[247] J. Fabian, I. Zutic, and S. das Sarma, "Magnetic bipolar transistor", *Appl. Phys. Lett.*, **84**, 85–87 (2004).

[248] M. Farle, "Ferromagnetic resonance of ultrathin metallic layers", *Rep. Prog. Phys.*, **61**, 755–826 (1998).

[249] X. Feng and P.B. Visscher, "Coarse-graining Landau–Lifshitz damping", *J. Appl. Phys.*, **89**, 6988–6990 (2001).

[250] L. Fernandez-Alvarez, O. Pla, and O. Chubykalo, "Quasiperiodicity, bistability, and chaos in the Landau–Lifshitz equation", *Phys. Rev. B*, **61**, 11613–11617 (2000).

[251] J. Fernandez-Rossier, M. Braun, A.S. Nunez, and A.H. MacDonald, "Influence of a uniform current on collective magnetization dynamics in a ferromagnetic metal", *Phys. Rev. B*, **69**, 174412 (2004).

[252] A. Fert, J.L. Duvail, and T. Valet, "Spin relaxation effects in the perpendicular magnetoresistance of magnetic multilayers", *Phys. Rev. B*, **52**, 6513–6521 (1995).

[253] A. Fert, A. Barthelemy, J.B. Joussef, J.P. Contour, V. Cros, J.M. deTeresa, A. Hamzic, J.M. George, G. Faini, J. Grollier, H. Jaffres, H. leGall, F. Montaigne, F. Pailloux, and F. Petroff, "Review of recent results on spin polarized tunneling and magnetic switching by spin injection", *Mat. Sci. Eng. B*, **84**, 1–9 (2001).

[254] Y.K. Fetisov, C.E. Patton, and V.T. Sygonach, "Nonlinear ferromagnetic resonance and foldover in yttrium iron garnet thin films – inadequacy of the classical model", *IEEE Trans. Magn.*, **35**, 4511–4521 (1999).

[255] Y.K. Fetisov and C.E. Patton, "Thermal microwave foldover and bistability in ferromagnetic resonance", *IEEE Trans. Magn.*, **40**, 473–482 (2004).

[256] Y.K. Fetisov, C.E. Patton, and V.T. Sygonach, "Envelope solitons in a medium with strong nonlinear damping", *JETP Lett.*, **83**, 488–492 (2006).

[257] R.P. Feynman, *Statistical Mechanics*, Addison Wesley, Reading, 1998.

[258] J. Fidler and T. Schrefl, "Micromagnetic modeling – the current state of the art", *J. Phys. D: Appl. Phys.*, **33**, R135–R156 (2000).

[259] G. Finocchio, I. Krivorotov, M. Carpentieri, G. Consolo, B. Azzerboni, L. Torres, E. Martinez, and L. Lopez-Diaz, "Magnetization dynamics driven by the combined action of ac magnetic field and dc spin-polarized current", *J. Appl. Phys.*, **99**, 08G507 (2006).

[260] G. Finocchio, M. Carpentieri, B. Azzerboni, L. Torres, E. Martinez, and L. Lopez-Diaz, "Micromagnetic simulations of nanosecond magnetization reversal processes in magnetic nanopillar", *J. Appl. Phys.*, **99**, 08G522 (2006).

[261] F. Fiorillo, *Measurement and Characterization of Magnetic Materials*, Elsevier, Amsterdam, 2004.

[262] P.C. Fletcher and R.O. Bell, "Ferrimagnetic resonance modes in spheres", *J. Appl. Phys.*, **30**, 687–698 (1959).

[263] D.R. Fredkin and A. Ron, "Microscopic derivation of the Landau-Lifschitz equation for ferromagnetic relaxation", *Phys. Rev. B*, **61**, 8654–8655 (2000).

[264] D.R. Fredkin, "Brownian motion on manifolds, with application to thermal magnetization reversal", *Physica B*, **306**, 26–32 (2001).

[265] M.I. Freidlin and A.D. Wentzell, "Random perturbations of Hamiltonian systems", *Mem. Am. Math. Soc.*, **109**, 523 (1994).

[266] M.I. Freidlin and A.D. Wentzell, *Random Perturbations of Dynamical Systems*, Springer, New York, 1998.

[267] G. Gallavotti and E.G.D. Cohen, "Dynamical ensembles in nonequilibrium statistical mechanics", *Phys. Rev. Lett.*, **74**, 2694–2697 (1995).

[268] L. Gammaitoni, P. Hanggi, and P. Jung, "Stochastic resonance", *Rev. Mod. Phys.*, **70**, 223–287 (1998).

[269] F.R. Gantmacher, *Lectures in Analytical Mechanics*, Mir Publications, Moscow, 1975.

[270] D.A. Garanin, "Fokker–Planck and Landau–Lifshitz-Bloch equations for classical ferromagnets", *Phys. Rev. B*, **55**, 3050–3057 (1997).

[271] D.A. Garanin and O. Chubykalo-Fesenko, "Thermal fluctuations and longitudinal relaxation of single-domain magnetic particles at elevated temperatures", *Phys. Rev. B*, **70**, 212409 (2004).

[272] N. Garcia, M. Munoz, and Y.W. Zhao, "Magnetoresistance in excess of 200 percent in ballistic Ni nanocontacts at room temperature and 100 Oe", *Phys. Rev. Lett.*, **82**, 2923–2926 (1999).

[273] N. Garcia, M. Munoz, and Y.W. Zhao, "Ballistic magnetoresistance in transition-metal nanocontacts: the case of iron", *Appl. Phys. Lett.*, **76**, 2586–2587 (2000).

[274] C.J. Garcia-Cervera and W. E, "Effective dynamics for ferromagnetic thin films", *J. Appl. Phys.*, **90**, 370–374 (2001).

[275] J.L. Garcia-Palacios and F.J. Lazaro, "Langevin-dynamics study of the dynamical properties of small magnetic particles", *Phys. Rev. B*, **58**, 14937–14958 (1998).

[276] J.L. Garcia-Palacios and P. Svedlindh, "Large nonlinear dynamical response of superparamagnets: interplay between precession and thermoactivation in the stochastic Landau–Lifshitz Equation", *Phys. Rev. Lett.*, **85**, 3724–3727 (2000).

[277] C.W. Gardiner, *Handbook of Stochastic Methods*, Springer, Berlin, 1985.

[278] N. Garnier and S. Ciliberto, "Nonequilibrium fluctuations in a resistor", *Phys. Rev. E*, **71**, 060101(R) (2005).

[279] I.M. Gelfand and A.M. Yaglom, "Integration in functional spaces and its applications in quantum physics", *J. Math. Phys.*, **1**, 48–69 (1960).

[280] T. Gerrits, H.A.M. van den Berg, J. Hohlfeld, L. Bar, and T. Rasing, "Ultrafast precessional magnetization reversal by picosecond magnetic field pulse shaping", *Nature*, **418**, 509–512 (2002).

[281] T. Gerrits, M.L. Schneider, A.B. Kos, and T.J. Silva, "Large-angle magnetization dynamics measured by time-resolved ferromagnetic resonance", *Phys. Rev. B*, **73**, 094454 (2006).

[282] T. Gerrits, P. Krivosik, M.L. Schneider, C.E. Patton, and T.J. Silva, "Direct detection of nonlinear ferromagnetic resonance in thin films by the magneto-optical Kerr effect", *Phys. Rev. Lett.*, **98**, 207602 (2007).

[283] G. Gibson and C. Jeffries, "Observation of period doubling and chaos in spin-wave instabilities in yttrium iron garnet", *Phys. Rev. A*, **29**, 811–818 (1984).

[284] T.L. Gilbert, "Abstract", *Phys. Rev.*, **100**, 1245 (1955).

[285] T.L. Gilbert, "A phenomenological theory of damping in ferromagnetic materials", *IEEE Trans. Magn.*, **40**, 3443–3449 (2004).

[286] A Goriely, *Integrability and Nonintegrability of Dynamical Systems*, World Scientific, Singapore, 2001.

[287] J. Goulon, A. Rogalev, F. Wilhem, N. Jaouen, C. Goulon-Ginet, and C. Brouder, "X-ray detected ferromagnetic resonance in thin films", *Eur. Phys. J. B*, **53**, 169–184 (2006).

[288] J. Goulon, A. Rogalev, F. Wilhem, C. Goulon-Ginet, and G. Goujon, "Element-selective X-ray detected magnetic resonance: a novel application of synchrotron radiation", *J. Synchrotron Rad.*, **14**, 257–271 (2007).

[289] R. Graham, "Path integral formulation of general diffusion processes", *Z. Physik B*, **26**, 281–290 (1977).

[290] R. Graham, "Covariant formulation of non-equilibrium statistical thermodynamics", *Z. Physik B*, **26**, 397–405 (1977).

[291] R. Graham and T. Tel, "Existence of a potential for dissipative dynamical systems", *Phys. Rev. Lett.*, **52**, 9–12 (1984).

[292] R. Graham and T. Tel, "Weak-noise limit of Fokker–Planck models and nondifferentiable potentials for dissipative dynamical systems", *Phys. Rev. A*, **31**, 1109–1122 (1985).

[293] J.F. Gregg, W. Allen, K. Ounadjela, M. Viret, M. Hehn, S.M. Thompson, and J.M.D. Coey, "Giant magnetoresistive effects in a single element magnetic thin film", *Phys. Rev. Lett.*, **77**, 1580–1583 (1996).

[294] A. Greven, G. Keller, and G. Warnecke (eds), *Entropy*, Princeton University Press, Princeton, 2003.

[295] G. Grinstein and R.H. Koch, "Coarse graining in micromagnetics", *Phys. Rev. Lett.*, **90**, 207201 (2003).

[296] G. Grinstein and R.H. Koch, "Switching probabilities for single-domain magnetic particles", *Phys. Rev. B*, **71**, 184427 (2005).

[297] J. Grollier, V. Cros, A. Hamzic, J.M. George, H. Jaffres, A. Fert, G. Faini, J.B. Youssef, and H. leGall, "Spin-polarized current induced switching in Co/Cu/Co pillars", *Appl. Phys. Lett.*, **78**, 3663–3665 (2001).

[298] J. Grollier, V. Cros, H. Jaffres, A. Hamzic, J.M. George, G. Faini, J.B. Youssef, H. LeGall, and A. Fert, "Field dependence of magnetization reversal by spin transfer", *Phys. Rev. B*, **67**, 174402 (2003).

[299] J. Grollier, P. Boulenc, V. Cros, A. Hamzic, A. Vaures, A. Fert, and G. Faini, "Switching a spin valve back and forth by current-induced domain wall motion", *Appl. Phys. Lett.*, **83**, 509–511 (2003).

[300] J. Grollier, V. Cros, and A. Fert, "Synchronization of spin-transfer oscillators driven by stimulated microwave currents", *Phys. Rev. B*, **73**, 060409(R) (2006).

[301] G. Gubbiotti, M. Madami, S. Tacchi, C. Carlotti, H. Tanigawa, T. Ono, L. Giovannini, F. Montoncello, and F. Nizzoli, "Splitting of spin excitations in nanometric rings induced by a magnetic field", *Phys. Rev. Lett.*, **97**, 247203 (2006).

[302] G. Gubbiotti, M. Madami, S. Tacchi, C. Carlotti, and T. Okuno, "Normal mode splitting in interacting arrays of cylindrical permalloy dots", *J. Appl. Phys.*, **99**, 08C701 (2006).

[303] G. Gubbiotti, M. Madami, S. Tacchi, C. Carlotti, M. Pasquale, N. Singh, S. Goolaup, and A.O. Adeyeye, "Field evolution of the magnetic normal modes in elongated permalloy nanometric rings", *J. Phys.: Condens. Matter*, **19**, 406229 (2007).

[304] J. Guckenheimer and P. Holmes, *Nonlinear Oscillations, Dynamical Systems, and Bifurcations of Vector Fields*, Springer, New York, 1997.

[305] A.P. Guimaraes, *Magnetism and Magnetic Resonance in Solids*, Wiley, New York, 1998.

[306] A.G. Gurevich and G.A. Melkov, *Magnetization Oscillations and Waves*, CRC Press, Boca Raton, 1996.

[307] K.Y. Guslienko, "Magnetostatic interdot coupling in two-dimensional magnetic dot arrays", *Appl. Phys. Lett.*, **75**, 394–396 (1999).

[308] K.Y. Guslienko and K.L. Metlov, "Evolution and stability of a magnetic vortex in a small cylindrical ferromagnetic particle under applied field", *Phys. Rev. B*, **63**, 100403(R) (2001).

[309] K.Y. Guslienko, V. Novosad, Y. Otani, H. Shima, and K. Fukamichi, "Magnetization reversal due to vortex nucleation, displacement, and annihilation in submicron ferromagnetic dot arrays", *Phys. Rev. B*, **65**, 024414 (2001).

[310] K.Y. Guslienko, V. Novosad, Y. Otani, H. Shima, and K. Fukamichi, "Field evolution of magnetic vortex state in ferromagnetic disks", *Appl. Phys. Lett.*, **78**, 3848–3850 (2001).

[311] K.Y. Guslienko, B.A. Ivanov, V. Novosad, Y. Otani, H. Shima, and K. Fukamichi, "Eigenfrequencies of vortex state excitations in magnetic submicron-size disks", *J. Appl. Phys.*, **91**, 8037–8039 (2002).

[312] K.Y. Guslienko, S.O. Demokritov, B. Hillebrands, and A.N. Slavin, "Effective dipolar boundary conditions for dynamic magnetization in thin magnetic stripes", *Phys. Rev. B*, **66**, 132402 (2002).

[313] K.Y. Guslienko, R.W. Chantrell, and A.N. Slavin, "Dipolar localization of quantized spin-wave modes in thin rectangular magnetic elements", *Phys. Rev. B*, **68**, 024422 (2003).

[314] K.Y. Guslienko, O. Chubykalo-Fesenko, O. Mryasov, R. Chantrell, and D. Weller, "Magnetization reversal via perpendicular exchange spring in FePt/FeRh bilayer films", *Phys. Rev. B*, **70**, 104405 (2004).

[315] K.Y. Guslienko, K.S. Buchanan, S.D. Bader, and V. Novosad, "Dynamics of coupled vortices in layered magnetic nanodots", *Appl. Phys. Lett.*, **86**, 223112 (2005).

[316] K.Y. Guslienko, X.F. Han, D.J. Keavney, R. Divan, and S.D. Bader, "Magnetic vortex core dynamics in cylindrical ferromagnetic dots", *Phys. Rev. Lett.*, **96**, 0672005 (2006).

[317] J.K. Ha, R. Hertel, and J. Kirschner, "Micromagnetic study of magnetic configurations in submicron permalloy disks", *Phys. Rev. B*, **67**, 224432 (2003).

[318] J.K. Ha, R. Hertel, and J. Kirschner, "Configurational stability and magnetization processes in submicron permalloy disks", *Phys. Rev. B*, **67**, 064418 (2003).

[319] J. Hale and H. Kocak, *Dynamics and Bifurcations*, Springer, Berlin, 1991.

[320] J.K. Hale, *Oscillations in Nonlinear Systems*, Dover, New York, 1992.

[321] H. Hancock, *Elliptic Integrals*, Dover, New York, 1958.

[322] P. Hanggi, P. Talkner, and M. Borkovec, "Reaction-rate theory: fifty years after Kramers", *Rev. Mod. Phys.*, **62**, 251–341 (1990).

[323] T. Harada and S. Sasa, "Equality connecting energy dissipation with a violation of the fluctuation-response relation", *Phys. Rev. Lett.*, **95**, 130602 (2005).

[324] S. Havlin and D. Ben-Avraham, "Diffusion in disorderd media", *Advances in Physics*, **36**, 695–798 (1987).

[325] L. He, W.D. Doyle, and H. Fujiwara, "High speed coherent switching below the Stoner-Wohlfarth limit", *IEEE Trans. Magn.*, **30**, 4086–4088 (1994).

[326] L. He and W.D. Doyle, "A theoretical description of magnetic switching experiments in picosecond field pulses", *J. Appl. Phys.*, **79**, 6489–6491 (1996).

[327] J. He, Z. Li, and S. Zhang, "Effects of current on vortex and transverse domain walls", *J. Appl. Phys.*, **99**, 08G509 (2006).

[328] C. Heide, R.J. Elliott, and N.S. Wingreen, "Spin-polarized tunnel current in magnetic-layer systems and its relation to the interlayer exchange interaction", *Phys. Rev. B*, **59**, 4287–4304 (1999).

[329] C. Heide and P.E. Zilberman, "Dynamic equations for individual spins in materials with magnetic order: the ideal ferromagnet", *Phys. Rev. B*, **60**, 14756–14770 (1999).

[330] C. Heide, P.E. Zilberman, and R.J. Elliott, "Current-driven switching of magnetic layers", *Phys. Rev. B*, **63**, 064424 (2001).

[331] C. Heide, "Spin currents in magnetic films", *Phys. Rev. Lett.*, **87**, 197201 (2001).

[332] C. Heide, "Effects of spin accumulation in magnetic multilayers", *Phys. Rev. B*, **65**, 054401 (2002).

[333] B. Heinrich, K.B. Urquhart, A.S. Arrott, J.F. Cochran, K. Myrtle, and S.T Purcell, "Ferromagnetic-resonance study of ultrathin bcc Fe(100) films grown epitaxially on fcc Ag(100) substrates", *Phys. Rev. Lett.*, **59**, 1756–1759 (1987).

[334] B. Heinrich, Y. Tserkovnyak, G. Woltersdorf, A. Brataas, R. Urban, and G.E.W. Bauer, "Dynamic exchange coupling in magnetic bilayers", *Phys. Rev. Lett.*, **90**, 187601 (2003).

[335] S. Helgason, *Differential Geometry, Lie Groups, and Symmetric Spaces*, Academic Press, New York, 1978.

[336] M. Henkel, M. Pleimling, C. Godreche, and J.M. Luck, "Aging, phase ordering, and conformal invariance", *Phys. Rev. Lett.*, **87**, 265701 (2001).

[337] M. Henkel and M. Pleimling, "Local scale invariance as dynamical space-time symmetry in phase-ordering kinetics", *Phys. Rev. E*, **68**, 065101(R) (2003).

[338] C. Herring and C. Kittel, "On the theory of spin waves in ferromagnetic media", *Phys. Rev.*, **81**, 869–880 (1951).

[339] R. Hertel and J. Kirschner, "Dynamics of solenoidal magnetic structures in soft magnetic thin-film elements", *J. Magn. Magn. Mater.*, **270**, 364–370 (2004).

[340] R.J. Hicken, A. Barman, V.V. Kruglyak, and S. Ladak, "Optical ferromagnetic resonance studies of thin film magnetic structures", *J. Phys. D: Appl. Phys.*, **36**, 2183–2192 (2003).

[341] W.K. Hiebert, G.E. Ballentine, and M.R. Freeman, "Comparison of experimental and numerical micromagnetic dynamics in coherent precessional switching and modal oscillations", *Phys. Rev. B*, **65**, 140404(R) (2002).

[342] B. Hillebrands and K. Ounadjela (eds), *Spin Dynamics in Confined Magnetic Structures I*, Springer, Berlin, 2001.

[343] B. Hillebrands and K. Ounadjela (eds), *Spin Dynamics in Confined Magnetic Structures II*, Springer, Berlin, 2003.

[344] B. Hillebrands and A. Thiaville (eds), *Spin Dynamics in Confined Magnetic Structures III*, Springer, Berlin, 2006.

[345] E.J. Hinch, *Perturbation Methods*, Cambridge University Press, Cambridge, 1991.

[346] D. Hinzke and U. Nowak, "Magnetization switching in a Heisenberg model for small ferromagnetic particles", *Phys. Rev. B*, **58**, 265–272 (1998).

[347] D. Hinzke and U. Nowak, "Magnetic relaxation in a classical spin chain", *Phys. Rev. B*, **61**, 6734–6740 (2000).

[348] A. Hirohata, Y.B. Xu, C.C. Yao, H.T. Leung, W.Y. Lee, S.M. Gardiner, D.G. Hasko, and J.A.C. Bland, "Domain wall trapping in controlled submicron ferromagnetic elements", *J. Appl. Phys.*, **87**, 4727–4729 (2000).

[349] A. Hirohata, Y.B. Xu, C.C. Yao, H.T. Leung, W.Y. Lee, S.M. Gardiner, D.G. Hasko, J.A.C. Bland, and S.N. Holmes, "Domain-wall trapping in controlled mesoscopic ferromagnetic wire junctions", *J. Magn. Magn. Mater.*, **226–230**, 1845–1847 (2001).

[350] L.L. Hirst, *Spin Transport in Ferromagnetic Metals*, *Phys. Rev.*, **141**, 503–506 (1966).

[351] M.A. Hoefer, M.J. Ablowitz, B. Ilan, M.R. Pufall, and T.J. Silva, "Theory of magnetodynamics induced by spin torque in perpendicularly magnetized thin films", *Phys. Rev. Lett.*, **95**, 267206 (2005).

[352] P. Holmes, "A nonlinear oscillator with a strange attractor", *Phil. Trans. Roy. Soc. London A*, **292**, 419–448 (1979).

[353] T. Holstein and H. Primakoff, "Field Dependence of the Intrinsic Domain Magnetization of a Ferromagnet", *Phys. Rev.*, **58**, 1098–1113 (1940).

[354] T.Y. Hou and X.H. Wu, "A multiscale finite element method for elliptic problems in composite materials and porous media", *J. Comp. Phys.*, **134**, 169–189 (1997).

[355] T.Y. Hou, X.H. Wu, and Z. Cai, "Convergence of a multiscale finite element method for elliptic problems with rapidly oscillating coefficients", *Mathematics of Computation*, **68**, 913–943 (1999).

[356] D. Houssameddine, U. Ebels, B. Delaet, B. Rodmacq, I. Firastrau, F. Ponthenier, M. Brunet, C. Thirion, J.P. Michel, L. Prejbeanu-Buda, M.C. Cyrille, and B. Dieny, "Spin-torque oscillator using a perpendicular polarizer and a planar free layer", *Nature Materials*, **6**, 447–453 (2007).

[357] K. Huang, *Statistical Mechanics*, Wiley, New York, 1987.

[358] J.H. Hubbard and B.H. West, *Differential Equations: A Dynamical Systems Approach*, Springer, New York, 1995.

[359] A. Hubert and R. Schäefer, *Magnetic Domains*, Springer-Verlag, Berlin, 1998.

[360] K.L.C. Hunt and J. Ross, "Path integral solutions of stochastic equations for nonlinear irreversible processes: the uniqueness of the thermodynamic Lagrangian", *J. Chem. Phys.*, **75**, 976–984 (1981).

[361] M.J. Hurben and C.E. Patton, "Theory of two magnon scattering microwave relaxation and ferromagnetic resonance linewidth in magnetic thin films", *J. Appl. Phys.*, **83**, 4344–4365 (1998).

[362] O. Iglesias and A. Labarta, "Magnetic history dependence of metastable states in thin films with dipolar interactions", *J. Magn. Magn. Mater.*, **221**, 149–157 (2000).

[363] H. Imamura, N. Kobayashi, S. Takahashi, and S. Maekawa, "Conductance quantization and magnetoresistance in magnetic point contacts", *Phys. Rev. Lett.*, **84**, 1003–1006 (2000).

[364] A. Imparato and L. Peliti, "Work-probability distribution in systems driven out of equilibrium", *Phys. Rev. E*, **72**, 046114 (2005).

[365] K. Itô, T. Devolder, C. Chappert, M.J. Carey, and J.A. Katine, "Probabilistic behavior in subnanosecond spin transfer torque switching", *J. Appl. Phys.*, **99**, 08G519 (2006).

[366] Y. Jaccard, P. Guittienne, D. Kelly, J.E. Wegrowe, and J.P. Ansermet, "Uniform magnetization rotation in single ferromagnetic nanowires", *Phys. Rev. B*, **62**, 1141–1147 (2000).

[367] A.G.M. Jansen, A.P. van Gelder, and P. Wyder, "Point-contact spectroscopy in metals", *J. Phys. C*, **13**, 6073–6118 (1980).

[368] C. Jarzynski, "Nonequilibrium equality for free energy differences", *Phys. Rev. Lett.*, **78**, 2690–2693 (1997).

[369] C. Jarzynski, "Rare events and the convergence of exponentially averaged work values", *Phys. Rev. E*, **73**, 046105 (2006).

[370] Y. Ji, C.L. Chien, and M.D. Stiles, "Current-induced spin-wave excitations in a single ferromagnetic layer", *Phys. Rev. Lett.*, **90**, 106601 (2003).

[371] D.C. Jiles, *Introduction to Magnetism and Magnetic Materials*, Chapman and Hall, London, 1990.

[372] D.C. Jiles, "Hysteresis models: non-linear magnetism on length scales from the atomistic to the macroscopic", *J. Magn. Magn. Mater.*, **242–245**, 116–124 (2002).

[373] M. Johnson, "The bipolar spin transistor", *J. Magn. Magn. Mater.*, **140–144**, 21–24 (1995).

[374] J. Jorzick, S.O. Demokritov, B. Hillebrands, M. Bailleul, C. Fermon, K.Y. Guslienko, A.N. Slavin, D.V. Berkov, and N.L. Gorn, "Effective dipolar boundary conditions for dynamic magnetization in thin magnetic stripes", *Phys. Rev. Lett.*, **88**, 047204 (2002).

[375] J.V. José and E.J. Saletan, *Classical Dynamics: A Contemporary Approach*, Cambridge University Press, Cambridge, 2002.

[376] M.I. Kaganov, "Excitation of standing spin waves in a film", *Sov. Phys. JETP*, **12**, 114–116 (1960).

[377] S. Kaka and S.E. Russek, "Precessional switching of submicrometer spin valves", *Appl. Phys. Lett.*, **80**, 2958–2960 (2002).

[378] S. Kaka, M.R. Pufall, W.H. Rippard, T.J. Silva, S.E. Russek, and J.A. Katine, "Mutual phase-locking of microwave spin torque nano-oscillators", *Nature*, **437**, 389–392 (2005).

[379] G.N. Kakazei, A.F. Kravets, N.A. Lesnik, M.M.P. de Azevedo, Y.G. Pogorelov, and J.B. Sousa, "Ferromagnetic resonance in granular thin films", *J. Appl. Phys.*, **85**, 5654–5656 (1999).

[380] G.N. Kakazei, P.E. Wigen, K.Y. Guslienko, V. Novosad, A.N. Slavin, V.O. Golub, N.A. Lesnik, and Y. Otani, "Spin-wave spectra of perpendicularly magnetized circular submicron dot arrays", *Appl. Phys. Lett.*, **85**, 443–445 (2004).

[381] Y.D. Kalafati and V.L. Safonov, "Thermodynamic approach in the theory of parametric resonance of magnons", *Sov. Phys. JETP*, **68**, 1162–1167 (1989).

[382] Y.D. Kalafati and V.L. Safonov, "Thermodynamic theory of saturation of the impulse magnon excitation", *J. Phys. France*, **50**, 1157–1161 (1989).

[383] Y.D. Kalafati and V.L. Safonov, "Theory of Bose condensation of magnons excited by noise", *J. Magn. Magn. Mater.*, **123**, 184–186 (1993).

[384] B.A. Kalinikos, N.G. Kovshikov, and A.N. Slavin, "Spin-wave envelope solitons in thin ferromagnetic films", *J. Appl. Phys.*, **67**, 5633–5638 (1990).

[385] B.A. Kalinikos, N.G. Kovshikov, and A.N. Slavin, "Envelope solitons of highly dispersive and low dispersive spin waves in magnetic films", *J. Appl. Phys.*, **69**, 5712–5717 (1991).

[386] L.V. Kantorovich and G.P. Akilov, *Functional Analysis*, Pergamon Press, Oxford, 1982.

[387] J.A. Katine, F.J. Albert, R.A. Buhrman, E.B. Myers, and D.C. Ralph, "Current-driven magnetization reversal and spin-wave excitations in Co/Cu/Co pillars", *Phys. Rev. Lett.*, **84**, 3149–3152 (2000).

[388] H.G. Katzgraber and G.T. Zimanyi, "Hysteretic memory effects in disordered magnets", *Phys. Rev. B*, **74**, 020405(R) (2006).

[389] N. Kazantseva, R. Wieser, and U. Nowak, "Transition to linear domain walls in nanoconstrictions", *Phys. Rev. Lett.*, **94**, 037206 (2005).

[390] D. Kelly, J.E. Wegrowe, T. Truong, X. Hoffer, and J.P. Ansermet, "Spin-polarized current-induced magnetization reversal in single nanowires", *Phys. Rev. B*, **68**, 134425 (2003).

[391] A.D. Kent, U. Ruediger, J. Yu, L. Thomas, and S.S.P. Parkin, "Magnetoresistance. micromagnetism, and domain wall effects in epitaxial Fe and Co structures with stripe domains", *J. Appl. Phys.*, **85**, 5243–5248 (1999).

[392] A.F. Khapikov, "Dynamics of the magnetization reversal of a cylinder in an alternating magnetic field", *JETP Lett.*, **55**, 352–356 (1992).

[393] A.F. Khapikov, S. Wang, B. Xu, and J.W. Harrell, "Zero-field relaxation and exchange interactions in magnetic thin films", *Phys. Rev. B*, **63**, 020401(R) (2000).

[394] R. Kikuchi, "On the minimum of magnetization reversal time", *J. Appl. Phys.*, **27**, 1352–1357 (1956).

[395] J.V. Kim, "Stochastic theory of spin-transfer oscillator linewidths", *Phys. Rev. B*, **73**, 174412 (2006).

[396] J.V. Kim, V. Tiberkevich, and A.N. Slavin, "Generation linewidth of an auto-oscillator with a nonlinear frequency shift: spin-torque nano-oscillator", *Phys. Rev. Lett.*, **100**, 017207 (2008).

[397] M. Kirschner, T. Schrefl, F. Dorfbauer, G. Hrkac, D. Suess, and J. Fidler, "Cell size corrections for nonzero-temperature micromagnetics", *J. Appl. Phys.*, **97**, 10E301 (2005).

[398] S.I. Kiselev, J.C. Sankey, I.N. Krivorotov, N.C. Emley, R.J. Schoelkopf, R.A. Buhrman, and D.C. Ralph, "Microwave oscillations of a nanomagnet driven by a spin-polarized current", *Nature*, **425**, 380–383 (2003).

[399] S.I. Kiselev, J.C. Sankey, I.N. Krivorotov, N.C. Emley, M. Rinkoski, C. Perez, R.A. Buhrman, and D.C. Ralph, "Current-induced nanomagnet dynamics for magnetic fields perpendicular to the sample plane", *Phys. Rev. Lett.*, **93**, 036601 (2004).

[400] S.I. Kiselev, J.C. Sankey, I.N. Krivorotov, N.C. Emley, A.G.F. Garcia, R.A. Buhrman, and D.C. Ralph, "Spin-transfer excitations of permalloy nanopillars for large applied currents", *Phys. Rev. B*, **72**, 064430 (2005).

[401] C. Kittel, "Interpretation of anomalous larmor frequencies in ferromagnetic resonance experiment", *Phys. Rev.*, **71**, 270–271 (1947).

[402] C. Kittel, "On the theory of ferromagnetic resonance absorption", *Phys. Rev.*, **73**, 155–161 (1948).

[403] C. Kittel, "On the gyromagnetic ratio and spectroscopic splitting factor of ferromagnetic substances", *Phys. Rev.*, **76**, 743–748 (1949).

[404] C. Kittel and E. Abrahams, "Relaxation processes in ferromagnetism", *Rev. Mod. Phys.*, **25**, 233–238 (1953).

[405] C. Kittel, "Excitation of spin waves in a ferromagnet by a uniform rf field", *Phys. Rev.*, **110**, 1295–1297 (1958).

[406] M. Klaui, C.A.F. Vaz, J.A.C. Bland, W. Wernsdorfer, G. Faini, E. Cambril, and L.J. Heyderman, "Domain wall motion induced by spin polarized currents in ferromagnetic ring structures", *Appl. Phys. Lett.*, **83**, 105–107 (2003).

[407] M. Klaui, C.A.F. Vaz, J.A.C. Bland, T.L. Monchesky, J. Unguris, E. Bauer, S. Cherifi, S. Heun, A. Locatelli, L.J. Heyderman, and Z. Cui, "Direct observation of spin configurations and classification of switching processes in mesoscopic ferromagnetic rings", *Phys. Rev. B*, **68**, 134426 (2003).

[408] M. Klaui, C.A.F. Vaz, J. Rothman, J.A.C. Bland, W. Wernsdorfer, G. Faini, and E. Cambril, "Domain wall pinning in narrow ferromagnetic ring structures probed by magnetoresistance measurements", *Phys. Rev. Lett.*, **90**, 097202 (2003).

[409] R.H. Koch, G. Grinstein, G.A. Keefe, Y. Lu, P.L. Trouilloud, W.J. Gallagher, and S.S.P. Parkin, "Thermally assisted magnetization reversal in submicron-sized magnetic thin films", *Phys. Rev. Lett.*, **84**, 5419–5422 (2000).

[410] R.H. Koch, J.A. Katine, and J.Z. Sun, "Time-resolved reversal of spin-transfer switching in a nanomagnet", *Phys. Rev. Lett.*, **92**, 088302 (2004).

[411] J. Koetzler, D.A. Garanin, M. Hartl, and L. Jahn, "Evidence for critical fluctuations in Bloch walls near their disordering temperature", *Phys. Rev. Lett.*, **71**, 177–180 (1993).

[412] R.V. Kohn, M.G. Reznikoff, and E. Vanden-Eijnden, "Magnetic elements at finite temperature and large deviation theory", *J. Nonlinear Sci.*, **15**, 223–253 (2005).

[413] A. Konovalenko, V. Korenivski, I.K. Yanson, and Y.G. Naidyuk, "Spin-torque driven excitations and hysteresis in magnetic point contacts", *J. Appl. Phys.*, **99**, 08G503 (2006).

[414] C. Kosaka, K. Nakamura, S. Murugesh, and M. Lakshmanan, "Equatorial and related non-equilibrium states in magnetization dynamics of ferromagnets: generalization of Suhl's spin-wave instabilities", *Physica D*, **203**, 233–248 (2005).

[415] A.A. Kovalev, A. Brataas, and G.E.W. Bauer, "Spin transfer in diffusive ferromagnet normal metal systems with spin-flip scattering", *Phys. Rev. B*, **66**, 224424 (2002).

[416] H.A. Kramers, "Brownian motion in a field of force and the diffusion model of chemical reactions", *Physica*, **7**, 284–304 (1940).

[417] P.S. Krishnaprasad and X. Tan, "Cayley transformations in micromagnetics", *Physica B*, **306**, 195 (2001).

[418] I.N. Krivorotov, N.C. Emley, A.G.F. Garcia, J.C. Sankey, S.I. Kiselev, D.C. Ralph, and R.A. Buhrman, "Temperature dependence of spin-transfer-induced switching of nanomagnets", *Phys. Rev. Lett.*, **93**, 166603 (2004).

[419] I.N. Krivorotov, N.C. Emley, J.C. Sankey, S.I. Kiselev, D.C. Ralph, and R.A. Buhrman, "Time-domain measurements of nanomagnet dynamics driven by spin-transfer torques", *Science*, **307**, 228–231 (2005).

[420] H. Kronmuller and M. Fahnle, *Micromagnetism and the Microstructure of Ferromagnetic Solids*, Cambridge University Press, Cambridge, 2003.

[421] V.V. Kruglyak and A.N. Kuchko, "Effect of the modulation of magnetic viscosity on the damping of spin waves in multilayer magnetic systems", *Phys. Met. Metall.*, **92**, 211–214 (2001).

[422] V.V. Kruglyak and A.N. Kuchko, "Effect of the intralayer inhomogeneity in the distribution of the parameter of magnetic damping on the propagation of spin waves in multilayers", *Phys. Met. Metall.*, **93**, 511–514 (2002).

[423] V.V. Kruglyak and A.N. Kuchko, "Spectrum of spin waves propagating in a periodic magnetic structure", *Physica B*, **339**, 130–133 (2003).

[424] R. Kubo, "The fluctuation-dissipation theorem", *Rep. Progr. Phys.*, **29**, 255–284 (1966).

[425] R. Kubo and N. Hashitsume, "Brownian motion of spins", *Progr. Theor. Phys. Suppl.*, **46**, 210 (1970).

[426] R. Kubo, *Statistical Mechanics*, North-Holland, Amsterdam, 1990.

[427] R. Kubo, M. Toda, and N. Hashitsume, *Statistical Physics II*, Springer, Berlin, 1991.

[428] Y.A. Kuznetsov, *Elements of Applied Bifurcation Theory*, Springer, New York, 1995.

[429] L.D. Landau and E.M. Lifshitz, "On the theory of the dispersion of magnetic permeability in ferromagnetic bodies", *Physik. Zeits. Sowjetunion*, **8**, 153–169 (1935).

[430] L.D. Landau and E.M. Lifshitz, "On the theory of the dispersion of magnetic permeability in ferromagnetic bodies", In *Collected Papers of L. D. Landau*, (D. terHaar, ed.), pp. 101–114, Pergamon Press, Oxford, 1965.

[431] L.D. Landau and E.M. Lifshitz, *Mechanics*, Pergamon Press, Oxford, 1976.

[432] L.D. Landau and E.M. Lifshitz, *Statistical Physics Part 1*, Pergamon Press, Oxford, 1980.

[433] L.D. Landau, E.M. Lifshitz, and L.P. Pitaevskii, *Electrodynamics of Continuous Media*, Pergamon Press, Oxford, 1984.

[434] P.T. Landsberg, "Foundations of thermodynamics", *Rev. Mod. Phys.*, **28**, 363–392 (1956).

[435] A.S. Landsberg and E.J. Friedman, "Dynamical effects of partial orderings in physical systems", *Phys. Rev. E*, **54**, 3135–3141 (1996).

[436] J.S. Langer, "Statistical theory of the decay of metastable states", *Ann. Phys.*, **54**, 258–275 (1969).

[437] A. Lasota and M.C. Mackey, *Chaos, Fractals, and Noise*, Springer, New York, 1995.

[438] T.H. Lee, "Oscillator phase noise: a tutorial", *IEEE J. Solid-State Circuits*, **35**, 326–336 (2000).

[439] S. Lemerle, J. Ferré, C. Chappert, V. Mathet, T. Giamarchi, and P. leDoussal, "Domain wall creep in an ising ultrathin magnetic film", *Phys. Rev. Lett.*, **80**, 849–852 (1998).

[440] H. Leschke and M. Schmutz, "Operator orderings and functional formulations of quantum and stochastic dynamics", *Z. Physik B*, **27**, 85–94 (1977).

[441] P.M. Levy and S. Zhang, "Resistivity due to domain wall scattering", *Phys. Rev. Lett.*, **79**, 5110–5113 (1997).

[442] D. Lewis and N. Nigam, "Geometric integration on spheres and some interesting applications", *J. Comput. Appl. Math.*, **151**, 141 (2003).

[443] Y. Li, K. Baberschke, and M. Farle, "Critical spin fluctuations of Ni monolayers at the Curie temperature: a magnetic resonance study in UHV", *J. Appl. Phys.*, **69**, 4992–4996 (1991).

[444] Z. Li and S. Zhang, "Magnetization dynamics with a spin-transfer torque", *Phys. Rev. B*, **68**, 024404 (2003).

[445] Z. Li and S. Zhang, "Thermally assisted magnetization reversal in the presence of a spin-transfer torque", *Phys. Rev. B*, **69**, 134416 (2004).

[446] Z. Li and S. Zhang, "Domain-wall dynamics driven by adiabatic spin-transfer torques", *Phys. Rev. B*, **70**, 024417 (2004).

[447] Z. Li and S. Zhang, "Domain-wall dynamics and spin-wave excitations with spin-transfer torques", *Phys. Rev. Lett.*, **92**, 207203 (2004).

[448] Z. Li, J. He, and S. Zhang, "Stability of precessional states induced by spin-current", *Phys. Rev. B*, **72**, 212411 (2005).

[449] Z. Li, J. He, and S. Zhang, "Effects of spin current on ferromagnets", *J. Appl. Phys.*, **99**, 08Q702 (2006).

[450] Z. Li, Y.C. Li, and S. Zhang, "Dynamic magnetization states of a spin valve in the presence of dc and ac currents: synchronization, modification, and chaos", *Phys. Rev. B*, **74**, 054417 (2006).

[451] C.S. Liu, "Lie symmetry of the Landau–Lifshitz–Gilbert equation and exact linearization in the Minkowski space", *Z. Angew. Math. Phys.*, **55**, 606–625 (2004).

[452] L. Lopez-Diaz, L. Torres, and E. Moro, "Transition from ferromagnetism to superparamagnetism on the nanosecond time scale", *Phys. Rev. B*, **65**, 224406 (2002).

[453] A. Magni, G. Bertotti, C. Serpico, and I.D. Mayergoyz, "Dynamic generalization of Stoner-Wohlfarth model", *J. Appl. Phys.*, **89**, 7451–7453 (2001).

[454] R.S. Maier and D.L. Stein, "Escape problem for irreversible systems", *Phys. Rev. E*, **48**, 931–940 (1993).

[455] R.S. Maier and D.L. Stein, "Oscillatory behavior of the rate of escape through an unstable limit cycle", *Phys. Rev. Lett.*, **77**, 4860–4863 (1996).

[456] R.S. Maier and D.L. Stein, "Droplet nucleation and domain wall motion in a bounded interval", *Phys. Rev. Lett.*, **87**, 270601 (2001).

[457] J.C. Mallinson, "On damped gyromagnetic precession", *IEEE Trans. Magn.*, **23**, 2003–2004 (1987).

[458] J.C. Mallinson, *Magneto-Resistive Heads*, Academic Press, San Diego, 1995.

[459] J.C. Mallinson, "Damped gyromagnetic switching", *IEEE Trans. Magn.*, **36**, 1976–1981 (2000).

[460] F.B. Mancoff and S.E. Russek, "Spin-current-induced magnetotransport in Co–Cu–Co nanostructures", *IEEE Trans. Magn.*, **38**, 2853–2855 (2002).

[461] F.B. Mancoff, R.W. Dave, N.D. Rizzo, T.C. Eschrich, B.N. Engel, and S. Tehrani, "Angular dependence of spin-transfer switching in a magnetic nanostructure", *Appl. Phys. Lett.*, **83**, 1596–1598 (2003).

[462] F.B. Mancoff, N.D. Rizzo, B.N. Engel, and S. Tehrani, "Phase-locking in double-point-contact spin-transfer devices", *Nature*, **437**, 393–395 (2005).

[463] F.B. Mancoff, N.D. Rizzo, B.N. Engel, and S. Tehrani, "Area dependence of high-frequency spin-transfer resonance in giant magnetoresistance contacts up to 300 nm diameter", *Appl. Phys. Lett.*, **88**, 112507 (2006).

[464] B.B. Mandelbrot and J.W. van Ness, "Fractional Brownian motions, fractional noises and applications", *SIAM Review*, **10**, 422–437 (1968).

[465] S. Mangin, D. Ravelosona, J.A. Katine, M.J. Carey, B.D. Terris, and E.E. Fullerton, "Current-induced magnetization reversal in nanopillars with perpendicular anisotropy", *Nature Mater.*, **5**, 210–215 (2006).

[466] B.B. Maranville, R.D. McMichael, S.A. Kim, W.L. Johnson, C.A. Ross, and J.Y. Cheng, "Characterization of magnetic properties at edges by edge-mode dynamics", *J. Appl. Phys.*, **99**, 08C703 (2006).

[467] J.E. Marsden and T.S. Ratiu, *Introduction to Mechanics and Symmetry*, Springer, New York, 1999.

[468] J.I. Masters, "Instability of magnetic resonance in single crystal spheres of yttrium iron garnet", *J. Appl. Phys.*, **31**, 41S–42S (1960).

[469] D.C. Mattis, *The Theory of Magnetism I*, Springer-Verlag, Berlin, 1981.

[470] D.C. Mattis, *The Theory of Magnetism II*, Springer-Verlag, Berlin, 1985.

[471] J.L. Maurice, D. Imhoff, P. Etienne, O. Durand, S. Dubois, L. Piraux, J.M. George, P. Galtier, and A. Fert, "Microstructure of magnetic metallic superlattices grown by electrodeposition in membrane nanopores", *J. Magn. Magn. Mater.*, **184**, 1–18 (1998).

[472] I.D. Mayergoyz, "Mathematical models of hysteresis", *Phys. Rev. Lett.*, **56**, 1518–1521 (1986).

[473] I.D. Mayergoyz, *Nonlinear Diffusion of Electromagnetic Fields*, Academic Press, Boston, 1998.

[474] I.D. Mayergoyz, G. Bertotti, and C. Serpico, "Rotationally symmetric solutions of the Landau–Lifshitz and diffusion equations", *J. Appl. Phys.*, **87**, 5511–5513 (2000).

[475] I.D. Mayergoyz, C. Serpico, and Y. Shimizu, "Coupling between eddy currents and Landau–Lifshitz dynamics", *J. Appl. Phys.*, **87**, 5529–5531 (2000).

[476] I.D. Mayergoyz, *Mathematical Models of Hysteresis and their Applications*, Elsevier, Amsterdam, 2003.

[477] I.D. Mayergoyz, M. Dimian, G. Bertotti, and C. Serpico, "Inverse problem approach to the design of magnetic field pulses for precessional switching", *J. Appl. Phys.*, **95**, 7004–7006 (2004).

[478] I.D. Mayergoyz, M. Dimian, G. Bertotti, and C. Serpico, "Critical fields and pulse durations for precessional switching of perpendicular media", *J. Appl. Phys.*, **97**, 10E509 (2005).

[479] I.D. Mayergoyz, M. Dimian, G. Bertotti, and C. Serpico, "Inverse problem approach to precessional switching in perpendicular media", *J. Appl. Phys.*, **97**, 10A703 (2005).

[480] I.D. Mayergoyz, C. Serpico, G. Bertotti, R. Bonin, and M. d'Aquino, "Analysis of power spectral density of random Landau–Lifshitz–Slonczewski dynamics by using stochastic processes on graphs", *J. Appl. Phys.*, **103**, 07B120 (2008).

[481] R.D. McMichael and P.E. Wigen, "High-power ferromagnetic resonance without a degenerate spin-wave manifold", *Phys. Rev. Lett.*, **64**, 64–67 (1990).

[482] R.D. McMichael and P.E. Wigen, "Parametric excitation of magnetostatic modes in circular ferromagnetic films", *Phys. Rev. B*, **42**, 6723–6726 (1990).

[483] R.D. McMichael and P.E. Wigen, "Parametric excitation of magnetostatic modes in thin yttrium iron garnet films", *J. Appl. Phys.*, **69**, 5425–5429 (1991).

[484] R.D. McMichael, M.D. Stiles, P.J. Chen, and W.F. Egelhoff, "Ferromagnetic resonance linewidth in thin films coupled to NiO", *J. Appl. Phys.*, **83**, 7037–7039 (1998).

[485] R.D. McMichael, D.J. Twisselmann, J.E. Bonevich, A.P. Chen, and W.F. Egelhoff, "Ferromagnetic resonance mode interactions in periodically perturbed films", *J. Appl. Phys.*, **91**, 8647–8649 (2002).

[486] R.D. McMichael, D.J. Twisselmann, and A. Kunz, "Localized ferromagnetic resonance in inhomogeneous thin films", *Phys. Rev. Lett.*, **90**, 227601 (2003).

[487] R.D. McMichael, "Ferromagnetic resonance linewidth models for perpendicular media", *J. Appl. Phys.*, **95**, 7001–7003 (2004).

[488] R.D. McMichael and M.D. Stiles, "Magnetic normal modes of nanoelements", *J. Appl. Phys.*, **97**, 10J901 (2005).

[489] J.E. Mercereau and R.P. Feynman, "Physical conditions for ferromagnetic resonance", *Phys. Rev.*, **104**, 63 (1956).

[490] D. Mercier, J.C.S. Levy, G. Viau, F. Fievet-Vincent, F. Fievet, P. Toneguzzo, and O. Acher, "Magnetic resonance in spherical Co–Ni and Fe–Co–Ni particles", *Phys. Rev. B*, **62**, 532–544 (2000).

[491] K. Mibu, T. Nagahama, T. Shinjo, and T. Ono, "Magnetoresistance of Bloch-wall-type magnetic structures induced in NiFe/CoSm exchange-spring bilayers", *Phys. Rev. B*, **58**, 6442–6446 (1998).

[492] G.N. Milstein, Y.M. Repin, and M.V. Tretyakov, "Numerical methods for stochastic systems preserving symplectic structure", *SIAM J. Numer. Anal.*, **40**, 1583–1604 (2002).

[493] J. Miltat, G. Albuquerque, A. Thiaville, and C. Vouille, "Spin transfer into an inhomogeneous magnetization distribution", *J. Appl. Phys.*, **89**, 6982–6984 (2001).

[494] Q. Mistral, J.V. Kim, T. Devolder, P. Crozat, C. Chappert, J.A. Katine, M.J. Carey, and K. Itô, "Current-driven microwave oscillations in current perpendicular-to-plane spin-valve nanopillars", *Appl. Phys. Lett.*, **88**, 192507 (2006).

[495] P.B. Monk and O. Vacus, "Error estimates for a numerical scheme for ferromagnetic problems", *SIAM J. Numer. Anal.*, **36**, 696–718 (1998).

[496] P.B. Monk and O. Vacus, "Accurate discretization of a nonlinear micromagnetic problem", *Comput. Methods Appl. Mech. Eng.*, **190**, 5243–5269 (2001).

[497] B. Montigny and J. Miltat, "Micromagnetic simulations of current-induced microwave excitations", *J. Appl. Phys.*, **97**, 10C708 (2005).

[498] A.H. Morrish, *The Physical Principles of Magnetism*, IEEE Press, Piscataway, 2001.

[499] mu mag. group website. http://www.ctcms.nist.gov/rdm/mumag.org.html.

[500] E.B. Myers, D.C. Ralph, J.A. Katine, R.N. Louie, and R.A. Buhrman, "Current-induced switching of domains in magnetic multilayers devices", *Science*, **285**, 867–870 (1999).

[501] E.B. Myers, F.J. Albert, J.C. Sankey, E. Bonet, R.A. Buhrman, and D.C. Ralph, "Thermally activated magnetic reversal induced by a spin-polarized current", *Phys. Rev. Lett.*, **89**, 196801 (2002).

[502] O. Narayan, "Self-similar Barkhausen noise in magnetic domain wall motion", *Phys. Rev. Lett.*, **77**, 3855–3857 (1996).

[503] A.V. Nazarov, H.S. Cho, J. Nowak, S. Stokes, and N. Tabat, "Tunable ferromagnetic resonance peak in tunneling magnetoresistive sensor structures", *Appl. Phys. Lett.*, **81**, 4559–4561 (2002).

[504] T. Needham, *Visual Complex Analysis*, Oxford University Press, Oxford, 1998.

[505] L. Néel, "Théorie du trainage magnétique des ferromagnétiques an grains fins avec application aux terres cuites", *Ann. Geophys.*, **5**, 99–136 (1949).

[506] H.T. Nembach, P. Martin-Pimentel, S.J. Hermsdoerfer, B. Leven, B. Hillebrands, and S.O. Demokritov, "Microwave assisted switching in a Ni81Fe19 ellipsoid", *Appl. Phys. Lett.*, **90**, 062503 (2007).

[507] J.P. Nibarger, R. Lopusnik, and T.J. Silva, "Damping as a function of pulsed field amplitude and bias field in thin film permalloy", *Appl. Phys. Lett.*, **82**, 2112–2114 (2003).

[508] J.P. Nibarger, R. Lopusnik, Z. Celinski, and T.J. Silva, "Variation of magnetization and Landé g factor with thickness in Ni-Fe films", *Appl. Phys. Lett.*, **83**, 1–4 (2003).

[509] G. Nicolis, "Irreversible thermodynamics", *Rep. Progr. Phys.*, **42**, 225–268 (1979).

[510] G. Nicolis, "Dissipative systems", *Rep. Progr. Phys.*, **49**, 873–949 (1986).

[511] V. Novosad, M. Grimsditch, K.Y. Guslienko, P. Vavassori, Y. Otani, and S.D. Bader, "Spin excitations of magnetic vortices in ferromagnetic nanodots", *Phys. Rev. B*, **66**, 052407 (2002).

[512] V. Novosad, K.Y. Guslienko, H. Shima, Y. Otani, S.G. Kim, K. Fukamichi, N. Kikuchi, O. Kitakami, and Y. Shimada, "Effect of interdot magnetostatic interaction of magnetization reversal in circular dot arrays", *Phys. Rev. B*, **65**, 060402(R) (2002).

[513] U. Nowak, R.W. Chantrell, and E.C. Kennedy, "Monte Carlo simulation with time step quantification in terms of Langevin dynamics", *Phys. Rev. Lett.*, **84**, 163–166 (2000).

[514] U. Nowak, O.N. Mryasov, R. Wieser, K. Guslienko, and R.W. Chantrell, "Spin dynamics of magnetic nanoparticles: beyond Brown's theory", *Phys. Rev. B*, **72**, 172410 (2005).

[515] R.C. O'Handley, *Modern Magnetic Materials*, Wiley, New York, 2000.

[516] T. Ono, Y. Ooka, H. Miyajima, and Y. Otani, "$2e^2/h$ to e^2/h switching of quantum conductance associated with a change in nanoscale ferromagnetic domain structure", *Appl. Phys. Lett.*, **75**, 1622–1624 (1999).

[517] L. Onsager, "Reciprocal relations in irreversible processes. I", *Phys. Rev.*, **37**, 405–426 (1931).

[518] L. Onsager, "Reciprocal relations in irreversible processes. II", *Phys. Rev.*, **38**, 2265–2279 (1931).

[519] L. Onsager and S. Machlup, "Fluctuations and irreversible processes", *Phys. Rev.*, **91**, 1505–1512 (1953).

[520] L. Onsager and S. Machlup, "Fluctuations and irreversible processes. II. Systems with kinetic energy", *Phys. Rev.*, **91**, 1512–1515 (1953).

[521] E. Ott, *Chaos in Dynamical Systems*, Cambridge University Press, Cambridge, 1997.

[522] B. Ozyilmaz, A.D. Kent, D. Monsma, J.Z. Sun, M.J. Rooks, and R.H. Koch, "Current-induced magnetization reversal in high magnetic fields in Co/Cu/Co nanopillars", *Phys. Rev. Lett.*, **91**, 067203 (2003).

[523] B. Ozyilmaz, A.D. Kent, J.Z. Sun, M.J. Rooks, and R.H. Koch, "Current-induced excitations in single cobalt ferromagnetic layer nanopillars", *Phys. Rev. Lett.*, **93**, 176604 (2003).

[524] L. Pantelidis, "Nonlinear spin waves for the Heisenberg model and the ferromagnetic-antiferromagnetic bifurcations", *J. Phys. A: Math. Gen.*, **37**, 8835–8852 (2004).

[525] A. Papoulis, *Probability, Random Variables, and Stochastic Processes*, McGraw-Hill, New York, 1991.

[526] M.J. Pechan, C. Yu, D. Owen, J. Katine, L. Folks, and M. Carey, "Vortex magnetodynamics: ferromagnetic resonance in permalloy dot arrays", *J. Appl. Phys.*, **99**, 08C702 (2006).

[527] L.M. Pecora, "Derivation and generalization of the Suhl spin-wave instability relations", *Phys. Rev. B*, **37**, 5473–5477 (1988).

[528] L. Perko, "Bifurcation of limit cycles from centers and separatrix cycles of planar analytic systems", *SIAM Review*, **36**, 341–376 (1994).

[529] L. Perko, *Differential Equations and Dynamical Systems*, Springer, New York, 1996.

[530] J. Persson, Y. Zhou, and J. Akerman, "Phase-locked spin torque oscillators: Impact of device variability and time delay", *J. Appl. Phys.*, **101**, 09A503 (2007).

[531] S. Petit, C. Baraduc, C. Thirion, U. Ebels, Y. Liu, M. Li, P. Wang, and B. Dieny, "Spin-torque influence on the high-frequency magnetization fluctuations in magnetic tunnel junctions", *Phys. Rev. Lett.*, **98**, 077203 (2007).

[532] M.S. Pierce, C.R. Buechler, L.B. Sorensen, J.J. Turner, S.D. Kevan, E.A. Jagla, J.M. Deutsch, T. Mai, O. Narayan, J.E. Davies, K. Liu, J. Hunter-Dunn, K.M. Chesnel, J.B. Kortright, O. Hellwig, and E.E. Fullerton, "Disorder-induced microscopic magnetic memory", *Phys. Rev. Lett.*, **94**, 017202 (2005).

[533] P. Pincus, "Excitation of spin-waves in ferromagnets: eddy current and boundary condition effects", *Phys. Rev.*, **118**, 658–664 (1960).

[534] G. Pisante, "Homogenisation of micromagnetics large bodies", *ESAIM: Control, Optimisation and Calculus of Variations*, **10**, 295 (2004).

[535] W. Platow, A.N. Anisimov, G.L. Dunifer, M. Farle, and K. Baberschke, "Correlations between ferromagnetic-resonance linewidths and sample quality in the study of metallic ultrathin films", *Phys. Rev. B*, **58**, 5611–5621 (1998).

[536] M. Plischke and B. Bergersen, *Equilibrium Statistical Physics*, World Scientific, Singapore, 2006.

[537] J. Podbielski, D. Heitmann, and D. Grundler, "Microwave-assisted switching of microscopic rings: correlation between nonlinear spin dynamics and critical microwave fields", *Phys. Rev. Lett.*, **99**, 207202 (2007).

[538] L. Podio-Guidugli, "On dissipation mechanisms in micromagnetics", *Eur. Phys. J. B*, **19**, 417–424 (2001).

[539] M.L. Polianski and P.W. Brouwer, "Current-induced transverse spin-wave instability in a thin nanomagnet", *Phys. Rev. Lett.*, **92**, 026602 (2004).

[540] D. Polder, "On the quantum theory of ferromagnetic resonance", *Phys. Rev.*, **73**, 1116 (1948).

[541] D.G. Porter, "Analytical determination of the LLG zero-damping critical switching field", *IEEE Trans. Magn.*, **34**, 1663–1665 (1998).

[542] V.S. Pribiag, I.N. Krivorotov, G.D. Fuchs, P.M. Braganca, O. Ozatay, J.C. Sankey, D.C. Ralph, and R.A. Buhrman, "Magnetic vortex oscillator driven by d.c. spin-polarized current", *Nature Physics*, **3**, 498–503 (2007).

[543] A. Prohl, *Computational Micromagnetism*, Teubner, Leipzig, 2001.

[544] M.R. Pufall, W.H. Rippard, and T.J. Silva, "Materials dependence of the spin-momentum transfer efficiency and critical current in ferromagnetic metal/Cu multilayers", *Appl. Phys. Lett.*, **83**, 323–325 (2003).

[545] M.R. Pufall, W.H. Rippard, S. Kaka, S.E. Russek, and T.J. Silva, "Large-angle, gigahertz-rate random telegraph switching induced by spin-momentum transfer", *Phys. Rev. B*, **69**, 214409 (2004).

[546] M.R. Pufall, W.H. Rippard, S. Kaka, T.J. Silva, and S.E. Russek, "Frequency modulation of spin-transfer oscillators", *Appl. Phys. Lett.*, **86**, 082506 (2005).

[547] E. Puppin, "Statistical properties of Barkhausen noise in thin Fe films", *Phys. Rev. Lett.*, **84**, 5415–5418 (2000).

[548] F.J. Rachford, T.L. Carroll, and L.M. Pecora, "Chaos in polished and roughened YIG spheres", *J. de Physique*, **49-C8**, 1595–1596 (1988).

[549] Y.L. Raikher and V.I. Stepanov, "Intrinsic magnetic resonance in superparamagnetic systems", *Phys. Rev. B*, **51**, 16428–16431 (1995).

[550] B. Raquet, R. Mamy, and J.C. Ousset, "Magnetization reversal dynamics in ultrathin magnetic layers", *Phys. Rev. B*, **54**, 4128–4136 (1996).

[551] D. Ravelosona, A. Cebollada, F. Briones, C. Diaz-Paniagua, M.A. Hidalgo, and F. Batallan, "Domain-wall scattering in epitaxial FePd ordered alloy films with perpendicular magnetic anisotropy", *Phys. Rev. B*, **59**, 4322–4326 (1999).

[552] S.M. Rezende, O.F. de Alcantara-Bonfim, and F.M. de Aguiar, "Model for chaotic dynamics of the perpendicular-pumping spin-wave instability", *Phys. Rev. B*, **33**, 5153–5156 (1986).

[553] S.M. Rezende, F.M. de Aguiar, and A. Azevedo, "Spin-wave auto-oscillations still in need of a good model", *J. Appl. Phys.*, **67**, 5624–5626 (1990).

[554] S.M. Rezende, F.M. de Aguiar, and A. Azevedo, "Spin-wave theory for the dynamics induced by direct currents in magnetic multilayers", *Phys. Rev. Lett.*, **94**, 037202 (2005).

[555] S.M. Rezende, F.M. de Aguiar, and A. Azevedo, "Magnon excitation by spin-polarized direct currents in magnetic nanostructures", *Phys. Rev. B*, **73**, 094402 (2006).

[556] S.M. Rezende, F.M. de Aguiar, R.L. Rodriguez-Suarez, and A. Azevedo, "Mode locking of spin waves excited by direct currents in microwave nano-oscillators", *Phys. Rev. Lett.*, **98**, 087202 (2007).

[557] W.H. Rippard, M.R. Pufall, and T.J. Silva, "Quantitative studies of spin-momentum-transfer-induced excitations in Co/Cu multilayer films using point-contact spectroscopy", *Appl. Phys. Lett.*, **82**, 1260–1262 (2003).

[558] W.H. Rippard, M.R. Pufall, S. Kaka, S.E. Russek, and T.J. Silva, "Direct-current induced dynamics in CoFe/NiFe point contacts", *Phys. Rev. Lett.*, **92**, 027201 (2004).

[559] W.H. Rippard, M.R. Pufall, S. Kaka, T.J. Silva, and S.E. Russek, "Current-driven microwave dynamics in magnetic point contacts as a function of applied field angle", *Phys. Rev. B*, **70**, 100406(R) (2004).

[560] W.H. Rippard, M.R. Pufall, S. Kaka, T.J. Silva, S.E. Russek, and J.A. Katine, "Injection locking and phase control of spin transfer nano-oscillators", *Phys. Rev. Lett.*, **95**, 067203 (2005).

[561] H. Risken, *The Fokker–Planck Equation*, Springer, Berlin, 1996.

[562] N.D. Rizzo and T.J. Silva, "Thermal relaxation in the strong-demagnetizing limit", *IEEE Trans. Magn.*, **34**, 1857–1859 (1998).

[563] N.D. Rizzo, T.J. Silva, and A.B. Kos, "Relaxation times for magnetization reversal in a high coercivity magnetic thin film", *Phys. Rev. Lett.*, **83**, 4876–4879 (1999).

[564] N.D. Rizzo, T.J. Silva, and A.B. Kos, "Nanosecond magnetization reversal in high coercivity thin films", *IEEE Trans. Magn.*, **36**, 159–165 (2000).

[565] A. Roethlein, F. Baumann, and M. Pleimling, "Symmetry-based determination of space-time functions in nonequilibrium growth processes", *Phys. Rev. E*, **74**, 061604 (2006).

[566] C.A. Ross, F.J. Castano, D. Morecroft, W. Jung, H.I. Smith, T.A. Moore, T.J. Hayward, J.A.C. Bland, T.J. Bromwich, and A.K. Petford-Long, "Mesoscopic thin-film magnetic rings", *J. Appl. Phys.*, **99**, 08S501 (2006).

[567] J. Rothman, M. Klaui, L. Lopez-Diaz, C.A.F. Vaz, A. Bleloch, J.A.C. Bland, Z. Cui, and R. Speaks, "Observation of a bi-domain state and nucleation free switching in mesoscopic ring magnets", *Phys. Rev. Lett.*, **86**, 1098–1101 (2001).

[568] U. Ruediger, J. Yu, S. Zhang, A.D. Kent, and S.S.P. Parkin, "Negative domain wall contribution to the resistivity of microfabricated Fe wires", *Phys. Rev. Lett.*, **80**, 5639–5642 (1998).

[569] U. Ruediger, J. Yu, L. Thomas, S.S.P. Parkin, and A.D. Kent, "Magnetoresistance, micromagnetism, and domain-wall scattering in epitaxial hcp Co films", *Phys. Rev. B*, **59**, 11914–11918 (1999).

[570] I. Ruiz-Feal, T.A. Moore, L. Lopez-Diaz, and J.A.C. Bland, "Model for reversal dynamics of ultrathin ferromagnetic films", *Phys. Rev. B*, **65**, 054409 (2002).

[571] S.E. Russek, S. Kaka, W.H. Rippard, M.R. Pufall, and T.J. Silva, "Finite-temperature modeling of nanoscale spin-transfer oscillators", *Phys. Rev. B*, **71**, 104425 (2005).

[572] V.L. Safonov, "Thermodynamic description of strongly excited Bose systems", *Physica A*, **188**, 675–686 (1991).

[573] V.L. Safonov and H.N. Bertram, "Magnetization reversal as a nonlinear multimode process", *J. Appl. Phys.*, **85**, 5072–5074 (1999).

[574] V.L. Safonov and H.N. Bertram, "Intrinsic mechanism of nonlinear damping in magnetization reversal", *J. Appl. Phys.*, **87**, 5508–5510 (2000).

[575] V.L. Safonov and H.N. Bertram, "Spin-wave dynamic magnetization reversal in a quasi-single-domain magnetic grain", *Phys. Rev. B*, **63**, 094419 (2001).

[576] V.L. Safonov and H.N. Bertram, "Thermal magnetization noise in a thin film", *Phys. Rev. B*, **65**, 172417 (2002).

[577] V.L. Safonov and H.N. Bertram, "Linear stochastic magnetization dynamics and microscopic relaxation mechanisms", *J. Appl. Phys.*, **94**, 529–538 (2003).

[578] J.C. Sankey, I.N. Krivorotov, S.I. Kiselev, P.M. Braganca, N.C. Emley, R.A. Buhrman, and D.C. Ralph, "Mechanisms limiting the coherence time of spontaneous magnetic oscillations driven by dc spin-polarized currents", *Phys. Rev. B*, **72**, 224427 (2005).

[579] J.C. Sankey, P.M. Braganca, A.G.F. Garcia, I.N. Krivorotov, R.A. Buhrman, and D.C. Ralph, "Spin-transfer-driven ferromagnetic resonance of individual nanomagnets", *Phys. Rev. Lett.*, **96**, 227601 (2006).

[580] R. Sappey, E. Vincent, M. Ocio, and J. Hammann, "Disentangling distribution effects and nature of the dynamics in relaxation measurements: the RMR method", *J. Magn. Magn. Mater.*, **221**, 87–98 (2000).

[581] M. Sasaki, P.E. Jonsson, H. Takayama, and H. Mamiya, "Aging and memory effects in superparamagnets and superspin glasses", *Phys. Rev. B*, **71**, 104405 (2005).

[582] M.E. Schabes and A. Aharoni, "Magnetostatic interaction fields for a three-dimensional array of ferromagnetic cubes", *IEEE Trans. Magn.*, **23**, 3882–3888 (1987).

[583] M.R. Scheinfein and J.L. Blue, "Micromagnetic calculations of 180 surface domain walls", *J. Appl. Phys.*, **69**, 7740–7751 (1991).

[584] E. Schlomann, "Inhomogeneous broadening of ferromagnetic resonance lines", *Phys. Rev.*, **182**, 632–645 (1969).

[585] W. Scholz. (2003). PhD thesis. http://magnet.atp.tuwien.ac.at/scholz/.

[586] N.L. Schryer and L.R. Walker, "The motion of 180 domain walls in uniform dc magnetic fields", *J. Appl. Phys.*, **45**, 5406–5421 (1974).

[587] H. Schumacher, C. Chappert, R. Sousa, P. Freitas, and J. Miltat, "Quasiballistic Magnetization Reversal", *Phys. Rev. Lett.*, **90**, 017204 (2003).

[588] H. Schwerdtfeger, *Geometry of Complex Numbers*, Dover, New York, 2001.

[589] M.M. Scott, C.E. Patton, M.P. Kostylev, and B.A. Kalinikos, "Nonlinear damping of high-power magnetostatic waves in yttrium–iron–garnet films", *J. Appl. Phys.*, **95**, 6294–6301 (2004).

[590] D.J. Seagle, S.H. Charap, and J.O. Artman, "Foldover in YIG.", *J. Appl. Phys.*, **57**, 3706–3708 (1985).

[591] C. Serpico, I.D. Mayergoyz, and G. Bertotti, "Numerical technique for integration of the Landau–Lifshitz equation", *J. Appl. Phys.*, **89**, 6991–6993 (2001).

[592] C. Serpico, I.D. Mayergoyz, and G. Bertotti, "Analysis of eddy currents with Landau–Lifshitz equation as a constitutive relation", *IEEE Trans. Magn.*, **37**, 3546–3549 (2001).

[593] C. Serpico, I.D. Mayergoyz, and G. Bertotti, "Analytical solutions of Landau–Lifshitz equation for precessional switching", *J. Appl. Phys.*, **93**, 6909–6911 (2003).

[594] C. Serpico, M. d'Aquino, G. Bertotti, and I.D. Mayergoyz, "Quasiperiodic magnetization dynamics in uniformly magnetized particles and films", *J. Appl. Phys.*, **95**, 7052–7054 (2004).

[595] C. Serpico, M. d'Aquino, G. Bertotti, and I.D. Mayergoyz, "Analysis of quasiperiodic Landau–Lifshitz–Gilbert dynamics", *J. Magn. Magn. Mater.*, **272–276**, 734–735 (2004).

[596] C. Serpico, M. d'Aquino, G. Bertotti, and I.D. Mayergoyz, "Analytical approach to current-driven self-oscillations in Landau–Lifshitz–Gilbert dynamics", *J. Magn. Magn. Mater.*, **290–291**, 502–505 (2005).

[597] C. Serpico, G. Bertotti, M. d'Aquino, R. Bonin, and I.D. Mayergoyz, "Transient dynamics leading to self-oscillations in nanomagnets driven by spin-polarized currents", *IEEE Trans. Magn.*, **41**, 3100–3102 (2005).

[598] C. Serpico, G. Bertotti, I.D. Mayergoyz, M. d'Aquino, and R. Bonin, "Thermal stability in spin-torque-driven magnetization dynamics", *J. Appl. Phys.*, **99**, 08G505 (2006).

[599] C. Serpico, R. Bonin, G. Bertotti, I.D. Mayergoyz, and M. d'Aquino, "Thermal stability in uniaxial nanomagnets driven by spin-polarized currents", *IEEE Trans. Magn.*, **42**, 2679–2681 (2006).

[600] C. Serpico, G. Bertotti, I.D. Mayergoyz, and M. d'Aquino, "Nonlinear magnetization dynamics in nanomagnets", In *Handbook of Magnetism and Advanced Magnetic Materials. Volume 2*, (H. Kronmuller and S. Parkin, eds), pp. 824–857, Wiley, New York, 2007.

[601] C. Serpico, G. Bertotti, R. Bonin, M. d'Aquino, and I.D. Mayergoyz, "Power spectrum of current-induced magnetization dynamics in uniaxial nanomagnets", *J. Appl. Phys.*, **101**, 09A507 (2007).

[602] C. Serpico, I.D. Mayergoyz, G. Bertotti, M. d'Aquino, and R. Bonin, "Generalized Landau–Lifshitz–Gilbert equation for uniformly magnetized bodies", *Physica B*, **403**, 282–285 (2008).

[603] C.C. Shir, "Computations of the micromagnetic dynamics in domain walls", *J. Appl. Phys.*, **49**, 3413–3421 (1978).

[604] A. Shpiro, P.M. Levy, and S. Zhang, "Self-consistent treatment of nonequilibrium spin torques in magnetic multilayers", *Phys. Rev. B*, **67**, 104430 (2003).

[605] S.W. Sides, P.A. Rikvold, and M.A. Novotny, "Kinetic Ising model in an oscillating field: finite-size scaling at the dynamic phase transition", *Phys. Rev. Lett.*, **81**, 834–837 (1998).

[606] S.W. Sides, P.A. Rikvold, and M.A. Novotny, "Stochastic hysteresis and resonance in a kinetic Ising system", *Phys. Rev. E*, **57**, 6512–6533 (1998).

[607] S.W. Sides, P.A. Rikvold, and M.A. Novotny, "Kinetic Ising model in an oscillating field: Avrami theory for the hysteretic response and finite-size scaling for the dynamic phase transition", *Phys. Rev. E*, **59**, 2710–2729 (1999).

[608] T.J. Silva, C.S. Lee, T.M. Crawford, and C.T. Rogers, "Inductive measurement of ultrafast magnetization dynamics in thin-film Permalloy", *J. Appl. Phys.*, **85**, 7849–7862 (1999).

[609] T.J. Silva, P. Kabos, and M.R. Pufall, "Detection of coherent and incoherent spin dynamics during the magnetic switching process using vector-resolved nonlinear magneto-optics", *Appl. Phys. Lett.*, **81**, 2205–2207 (2002).

[610] T.J. Silva, M.R. Pufall, and P. Kabos, "Nonlinear magneto-optic measurement of flux propagation dynamics in thin Permalloy films", *J. Appl. Phys.*, **91**, 1066–1073 (2002).

[611] G.V. Skrotskii and Y.I. Alimov, "Ferromagnetic resonance in a circularly polarized magnetic field of arbitrary amplitude", *Sov. Phys. JETP*, **35**, 1035–1037 (1959).

[612] G.V. Skrotskii and Y.I. Alimov, "Effect of specimen shape on ferromagnetic resonance in a strong radio-frequency field", *Sov. Phys. JETP*, **36**, 899–901 (1959).

[613] A.N. Slavin and I.V. Rojdestvenski, "Bright and dark spin wave envelope solitons in magnetic films", *IEEE Trans. Magn.*, **30**, 37–45 (1994).

[614] A.N. Slavin and P. Kabos, "Approximate theory of microwave generation in a current-driven magnetic nanocontact magnetized in an arbitrary direction", *IEEE Trans. Magn.*, **41**, 1264–1273 (2005).

[615] A.N. Slavin and V.S. Tiberkevich, "Current-induced bistability and dynamic range of microwave generation in magnetic nanostructures", *Phys. Rev. B*, **72**, 094428 (2005).

[616] A.N. Slavin and V.S. Tiberkevich, "Spin wave mode excited by spin-polarized current in a magnetic nanocontact is a standing self-localized wave bullet", *Phys. Rev. Lett.*, **95**, 237201 (2005).

[617] A.N. Slavin and V.S. Tiberkevich, "Nonlinear self-phase-locking effect in an array of current-driven magnetic nanocontacts", *Phys. Rev. B*, **72**, 092407 (2005).

[618] A.N. Slavin and V.S. Tiberkevich, "Theory of mutual phase locking of spin-torque nanosized oscillators", *Phys. Rev. B*, **74**, 104401 (2006).

[619] M. Slodicka and I. Cimrak, "Numerical study of nonlinear ferromagnetic materials", *Appl. Numer. Math.*, **46**, 95–111 (2003).

[620] M. Slodicka and L. Banas, "A numerical scheme for a Maxwell–Landau–Lifshitz–Gilbert system", *Appl. Math. Comput.*, **158**, 79–99 (2004).

[621] J.C. Slonczewski, "Conductance and exchange coupling of two ferromagnets separated by a tunneling barrier", *Phys. Rev. B*, **39**, 6995–7002 (1989).

[622] J.C. Slonczewski, "Current-driven excitation of magnetic multilayers", *J. Magn. Magn. Mater.*, **159**, L1–L7 (1996).

[623] J.C. Slonczewski, "Excitation of spin waves by an electric current", *J. Magn. Magn. Mater.*, **195**, L261–L268 (1999).

[624] J.C. Slonczewski, "Currents and torques in metallic magnetic multilayers", *J. Magn. Magn. Mater.*, **247**, 324–338 (2002).

[625] V. Smirnov, *Cours de Mathématiques Supérieures*, Mir, Moscow, 1989.

[626] N. Smith, "Modeling and measurement of spin torques in current-perpendicular-to-plane giant magnetoresistive", *J. Appl. Phys.*, **99**, 08Q703 (2006).

[627] A.W. Spargo, P.H.W. Ridley, and G.W. Roberts, "Geometric integration of the Gilbert equation", *J. Appl. Phys.*, **93**, 6805 (2003).

[628] M. Sparks, R. Loudon, and C. Kittel, "Ferromagnetic relaxation. I. Theory of the relaxation of the uniform precession and the degenerate spectrum in insulators at low temperatures", *Phys. Rev.*, **122**, 791–803 (1961).

[629] M. Sparks, "Ferromagnetic resonance in thin films. I. Theory of normal-mode frequencies", *Phys. Rev. B*, **1**, 3831–3856 (1970).

[630] M. Sparks, "Ferromagnetic resonance in thin films. II. Theory of linewidths", *Phys. Rev. B*, **1**, 3856–3869 (1970).

[631] M. Sparks, "Ferromagnetic Resonance in Thin Films. III. Theory of mode intensities", *Phys. Rev. B*, **1**, 3869–3880 (1970).

[632] J.C. Sprott, *Chaos and Time-Series Analysis*, Oxford University Press, Oxford, 2003.

[633] C.D. Stanciu, F. Hansteen, A.V. Kimel, A. Kirilyuk, A. Tsukamoto, A. Itoh, and T. Rasing, "All-optical magnetic recording with circularly polarized light", *Phys. Rev. Lett.*, **99**, 047601 (2007).

[634] H.E. Stanley, *Introduction to Phase Transitions and Critical Phenomena*, Clarendon Press, Oxford, 1971.

[635] M.D. Stiles and A. Zangwill, "Anatomy of spin-transfer torque", *Phys. Rev. B*, **66**, 014407 (2002).

[636] M.D. Stiles and A. Zangwill, "Noncollinear spin transfer in Co/Cu/Co multilayers", *J. Appl. Phys.*, **91**, 6812–6817 (2002).

[637] M.D. Stiles, J. Xiao, and A. Zangwill, "Phenomenological theory of current-induced magnetization precession", *Phys. Rev. B*, **69**, 054408 (2004).

[638] M.D. Stiles, W.M. Saslow, M.J. Donahue, and A. Zangwill, "Adiabatic domain wall motion and Landau–Lifshitz damping", *Phys. Rev. B*, **75**, 214423 (2007).

[639] E.C. Stoner and E.P. Wohlfarth, "A mechanism of magnetic hysteresis in heterogeneous alloys", *Phil. Trans. Roy. Soc. A*, **240**, 599–642 (1948).

[640] R.L. Stratonovich, *Topics in the Theory of Random Noise, Volume I*, Gordon and Breach, New York, 1963.

[641] A.M. Stuart and A.R. Humphries, "Model problems in numerical stability theory for initial value problems", *SIAM Review*, **36**, 226–257 (1994).

[642] A.M. Stuart and A.R. Humphries, *Dynamical Systems and Numerical Analysis*, Cambridge University Press, Cambridge, 1998.

[643] N. Stutzke, S.L. Burkett, and S.E. Russek, "Temperature and field dependence of high-frequency magnetic noise in spin valve devices", *Appl. Phys. Lett.*, **82**, 91–93 (2003).

[644] D. Suess, T. Schrefl, and J. Fidler, "Micromagnetic simulation of high energy density permanent magnets", *IEEE Trans. Magn.*, **36**, 3282–3284 (2000).

[645] H. Suhl, "The nonlinear behavior of ferrites at high microwave signal levels", *Proc. IRE*, **44**, 1270–1284 (1956).

[646] H. Suhl, "The theory of ferromagnetic resonance at high signal powers", *J. Phys. Chem. Solids*, **1**, 209–227 (1957).

[647] H. Suhl and X.Y. Zhang, "Spatial and temporal patterns in high-power ferromagnetic resonance", *Phys. Rev. Lett.*, **57**, 1480–1483 (1986).

[648] H. Suhl, "Theory of the magnetic damping constant", *IEEE Trans. Magn.*, **34**, 1834–1838 (1998).

[649] H. Suhl, *Relaxation Processes in Micromagnetics*, Oxford University Press, Oxford, 2007.

[650] J.Z. Sun, "Current-driven magnetic switching in manganite trilayer junctions", *J. Magn. Magn. Mater.*, **202**, 157–162 (1999).

[651] J.Z. Sun, "Spin-current interaction with a monodomain magnetic body: a model study", *Phys. Rev. B*, **62**, 570–578 (2000).

[652] J.Z. Sun, D.J. Monsma, D.W. Abraham, M.J. Rooks, and R.H. Koch, "Batch-fabricated spin-injection magnetic switches", *Appl. Phys. Lett.*, **81**, 2202–2204 (2002).

[653] Y. Sun, M.B. Salamon, K. Garnier, and R.S. Averback, "Memory effects in an interacting magnetic nanoparticle system", *Phys. Rev. Lett.*, **91**, 167206 (2003).

[654] Z.Z. Sun and X.R. Wang, "Theoretical limit of the minimal magnetization switching field and the optimal field pulse for Stoner particles", *Phys. Rev. Lett.*, **97**, 077205 (2006).

[655] J. Sun and P. Monk, "An adaptive algebraic multigrid algorithm for micromagnetism", *IEEE Trans. Magn.*, **42**, 1643–1647 (2006).

[656] M.R. Swift, H. Bokil, R.D.M. Travasso, and A.J. Bray, "Glassy behavior in a ferromagnetic p-spin model", *Phys. Rev. B*, **62**, 11494–11498 (2000).

[657] Y. Taguchi, Y. Oohara, H. Yoshizawa, N. Nagaosa, and Y. Tokura, "Spin chirality, Berry phase, and anomalous Hall effect in a frustrated ferromagnet", *Science*, **291**, 2573–2576 (2001).

[658] T. Taniguchi and E.G.D. Cohen, "Onsager-Machlup theory of nonequilibrium steady states and fluctuations theorems", *J. Stat. Phys.*, **126**, 1–41 (2007).

[659] T. Taniyama, I. Nakatani, T. Namikawa, and Y. Yamazaki, "Resistivity due to domain walls in Co zigzag wires", *Phys. Rev. Lett.*, **82**, 2780–2783 (1999).

[660] T. Taniyama, I. Nakatani, T. Yakabe, and Y. Yamazaki, "Control of domain structures and magnetotransport properties in patterned ferromagnetic wires", *Appl. Phys. Lett.*, **76**, 613–615 (2000).

[661] G. Tatara and H. Fukuyama, "Resistivity due to a domain wall in ferromagnetic metal", *Phys. Rev. Lett.*, **78**, 3773–3776 (1997).

[662] G. Tatara, Y.W. Zhao, M. Munoz, and N. Garcia, "Domain wall scattering explains 300 percent ballistic magnetoconductance of nanocontacts", *Phys. Rev. Lett.*, **83**, 2030–2033 (1999).

[663] G. Tatara and H. Kohno, "Theory of current-driven domain wall motion: spin transfer versus momentum transfer", *Phys. Rev. Lett.*, **92**, 086601 (2004).

[664] A. Thiaville, "Coherent rotation of magnetization in three dimensions: a geometric approach", *Phys. Rev. B*, **61**, 12221–12232 (2000).

[665] A. Thiaville, J.M. Garcia, R. Dittrich, J. Miltat, and T. Schrefl, "Micromagnetic study of Bloch-point-mediated vortex core reversal", *Phys. Rev. B*, **67**, 094410 (2003).

[666] A. Thiaville, Y. Nakatani, J. Miltat, and N. Vernier, "Domain wall motion by spin-polarized current: a micromagnetic study", *J. Appl. Phys.*, **95**, 7049–7051 (2004).

[667] C. Thirion, W. Wernsdorfer, and D. Mailly, "Switching of magnetization by nonlinear resonance studied in single nanoparticles", *Nat. Mater.*, **2**, 524–527 (2003).

[668] J.M.T. Thompson, "Chaotic phenomena triggering the escape from a potential well", *Proc. Roy. Soc. London A*, **421**, 195–225 (1989).

[669] R.F.M. Thornley, "Pulse response of recording media", *IEEE Trans. Magn.*, **11**, 1197 (1975).

[670] S.M. Thompson, "The discovery, development and future of GMR: The Nobel Prize 2007", *J. Phys. D: Appl. Phys.*, **41**, 093001 (2008).

[671] V.S. Tiberkevich and A.N. Slavin, "Nonlinear phenomenological model of magnetic dissipation for large precession angles: generalization of the Gilbert model", *Phys. Rev. B*, **75**, 014440 (2007).

[672] M. Toda, R. Kubo, and N. Saito, *Statistical Physics I*, Springer, Berlin, 1995.

[673] R.C. Tolman and P.C. Fine, "On the irrevesible production of entropy", *Rev. Mod. Phys.*, **20**, 51–77 (1948).

[674] T. Träxler, W. Just, and H. Sauermann, "Dynamics of homogeneous magnetizations in strong transverse driving fields", *Z. Phys. B*, **99**, 285–295 (1996).

[675] Y. Tserkovnyak, A. Brataas, and G.E.W. Bauer, "Enhanced Gilbert damping in thin ferromagnetic films", *Phys. Rev. Lett.*, **88**, 117601 (2002).

[676] Y. Tserkovnyak, A. Brataas, and G.E.W. Bauer, "Spin pumping and magnetization dynamics in metallic multilayers", *Phys. Rev. B*, **66**, 224403 (2002).

[677] Y. Tserkovnyak, A. Brataas, and G.E.W. Bauer, "Dynamic stiffness of spin valves", *Phys. Rev. B*, **67**, 140404(R) (2003).

[678] V. Tsiantos, W. Scholz, D. Suess, T. Schrefl, and J. Fidler, "The effect of the cell size in Langevin micromagnetic simulations", *J. Magn. Magn. Mater.*, **242–245**, 999–1001 (2002).

[679] M. Tsoi, A.G.M. Jansen, and J. Bass, "Search for point-contact giant magnetoresistance in Co–Cu multilayers", *J. Appl. Phys.*, **81**, 5530–5532 (1997).

[680] M. Tsoi, A.G.M. Jansen, J. Bass, W.C. Chiang, M. Seck, V. Tsoi, and P. Wyder, "Excitation of a magnetic multilayer by an electric current", *Phys. Rev. Lett.*, **80**, 4281–4284 (1998).

[681] M. Tsoi, A.G.M. Jansen, J. Bass, W.C. Chiang, V. Tsoi, and P. Wyder, "Generation and detection of phase-coherent current-driven magnons in magnetic multilayers", *Nature*, **406**, 46–48 (2000).

[682] M. Tsoi, V. Tsoi, J. Bass, A.G.M. Jansen, and P. Wyder, "Current-driven resonances in magnetic multilayers", *Phys. Rev. Lett.*, **89**, 246803 (2002).

[683] M. Tsoi, "Electromagnetic wave radiation by current-driven magnons in magnetic multilayers", *J. Appl. Phys.*, **91**, 6801–6805 (2002).

[684] M. Tsoi, "Phase-coherent current-driven magnons in magnetic multilayers", *J. Magn. Magn. Mater.*, **240**, 103–107 (2002).

[685] M. Tsoi, J.Z. Sun, and S.S.P. Parkin, "Current-driven excitations in symmetric magnetic nanopillars", *Phys. Rev. Lett.*, **93**, 036602 (2004).

[686] M. Tsoi, J.Z. Sun, M.J. Rooks, R.H. Koch, and S.S.P. Parkin, "Current-driven excitations in magnetic multilayer nanopillars from 4.2 K to 300 K", *Phys. Rev. B*, **69**, 100406(R) (2004).

[687] A.A. Tulapurkar, T. Devolder, K. Yagami, P. Crozat, C. Chappert, A. Fukushima, and Y. Suzuki, "Subnanosecond magnetization reversal in magnetic nanopillars by spin angular momentum transfer", *Appl. Phys. Lett.*, **85**, 5358–5360 (2004).

[688] A.A. Tulapurkar, Y. Suzuki, A. Fukushima, H. Kubota, H. Maehara, K. Tsunekawa, D.D. Djayaprawira, N. Watanabe, and S. Yuasa, "Spin-torque diode effect in magnetic tunnel junctions", *Nature*, **438**, 339–342 (2005).

[689] D.J. Twisselmann and R.D. McMichael, "Intrinsic damping and intentional ferromagnetic resonance broadening in thin permalloy films", *J. Appl. Phys.*, **93**, 6903–6905 (2003).

[690] G.E. Uhlenbeck and L.S. Ornstein, "On the theory of the Brownian motion", *Phys. Rev.*, **36**, 823–841 (1930).

[691] S. Urazhdin, N.O. Birge, W.P. Pratt, and J. Bass, "Current-driven magnetic excitations in permalloy-based multilayer nanopillars", *Phys. Rev. Lett.*, **91**, 146803 (2003).

[692] S. Urazhdin, H. Kurt, W.P. Pratt, and J. Bass, "Effect of antiferromagnetic interlayer coupling on current-assisted magnetization switching", *Appl. Phys. Lett.*, **83**, 114–116 (2003).

[693] T. Valet and A. Fert, "Theory of the perpendicular magnetoresistance in magnetic multilayers", *Phys. Rev. B*, **48**, 7099–7113 (1993).

[694] H.A.M. van den Berg, "Self-consistent domain theory in soft-ferromagnetic media II. Basic domain structures in thin films objects", *J. Appl. Phys.*, **60**, 1104–1113 (1986).

[695] H.A.M. van den Berg, "Order in the domain structure in soft-magnetic thin-film elements: a review", *IBM J. Res. Dev.*, **33**, 540 (1989).

[696] E. vande Riet and F. Roozeboom, "Ferromagnetic resonance and eddy currents in high-permeable thin films", *J. Appl. Phys.*, **81**, 350–354 (1997).

[697] R.P. van Gorkom, J. Caro, S.J.C.H. Theeuwen, K.P. Wellock, N.N. Gribov, and S. Radelaar, "Micromagnetics and magnetoresistance of a Permalloy point contact", *Appl. Phys. Lett.*, **74**, 422–424 (1999).

[698] N.G. van Kampen, *Stochastic Processes in Physics and Chemistry*, North-Holland, Amsterdam, 1981.

[699] M. van Kampen, C. Jozsa, J.T. Kohlhepp, P. LeClair, L. Lagae, W.J.M. de Jonge, and B. Koopmans, "All-optical probe of coherent spin waves", *Phys. Rev. Lett.*, **88**, 227201 (2002).

[700] P.C. van Son, H. van Kampen, and P. Wyder, "Boundary resistance of the ferromagnetic–non ferromagnetic metal interface", *Phys. Rev. Lett.*, **58**, 2271–2274 (1987).

[701] J.H. van Vleck, "Concerning the theory of ferromagnetic resonance absorption", *Phys. Rev.*, **78**, 266–274 (1950).

[702] R. van Zon and E.G.D. Cohen, "Extension of the fluctuation theorem", *Phys. Rev. Lett.*, **91**, 110601 (2003).

[703] R. van Zon and E.G.D. Cohen, "Stationary and transient work-fluctuation theorems for a dragged Brownian particle", *Phys. Rev. E*, **67**, 046102 (2003).

[704] R. van Zon, S. Ciliberto, and E.G.D. Cohen, "Power and heat fluctuation theorems for electric circuits", *Phys. Rev. Lett.*, **92**, 130601 (2004).

[705] C.A.F. Vaz, C. Athanasiou, J.A.C. Bland, and G. Rowlands, "Energetics of magnetic ring and disk elements: uniform versus vortex state", *Phys. Rev. B*, **73**, 054411 (2006).

[706] J.J. Versluijs, M.A. Bari, and J.M.D. Coey, "Magnetoresistance of half-metallic oxide nanocontacts", *Phys. Rev. Lett.*, **87**, 026601 (2001).

[707] M. Viret, D. Vignoles, D. Cole, J.M.D. Coey, W. Allen, D.S. Daniel, and J.F. Gregg, "Spin scattering in ferromagnetic thin films", *Phys. Rev. B*, **53**, 8464–8468 (1996).

[708] M. Viret, Y. Samson, P. Warin, A. Marty, F. Ott, E. Sondergard, O. Klein, and C. Fermon, "Anisotropy of domain wall resistance", *Phys. Rev. Lett.*, **85**, 3962–3965 (2000).

[709] A. Visintin, *Differential Models of Hysteresis*, Springer, Berlin, 1994.

[710] P.B. Visscher and D.M. Apalkov, "Fokker-Planck calculation of spin-torque resistance hysteresis and switching currents", *J. Appl. Phys.*, **97**, 10C704 (2005).

[711] P.B. Visscher and D.M. Apalkov, "Non-Boltzmann energy distributions in spin-torque devices", *J. Appl. Phys.*, **99**, 08G513 (2006).

[712] E. Vives and A. Planes, "Hysteresis and avalanches in disordered systems", *J. Magn. Magn. Mater.*, **221**, 164–171 (2000).

[713] M. Vomir, L.H.F. Andrade, L. Guidoni, E. Beaurepaire, and J.Y. Bigot, "Real space trajectory of the ultrafast magnetization dynamics in ferromagnetic metals", *Phys. Rev. Lett.*, **94**, 237601 (2005).

[714] M. Vomir, L.H.F. Andrade, E. Beaurepaire, M. Albrecht, and J.Y. Bigot, "Ultrafast magnetization dynamics investigated in real space", *J. Appl. Phys.*, **99**, 08A501 (2006).

[715] X. Waintal, E.B. Myers, P.W. Brouwer, and D.C. Ralph, "Role of spin-dependent interface scattering in generating current-induced torques in magnetic multilayers", *Phys. Rev. B*, **62**, 12317–12327 (2000).

[716] L.R. Walker, "Magnetostatic modes in ferromagnetic resonance", *Phys. Rev.*, **105**, 390–399 (1957).

[717] L.R. Walker, "Resonant Modes of Ferromagnetic Spheroids", *J. Appl. Phys.*, **29**, 318–323 (1958).

[718] M.C. Wang and G.E. Uhlenbeck, "On the theory of the Brownian motion II", *Rev. Mod. Phys.*, **17**, 323–342 (1945).

[719] S.X. Wang and A.M. Taratorin, *Magnetic Information Storage Technology*, Academic Press, San Diego, 1999.

[720] X. Wang, C.J. Garcia-Cervera, and W. E, "A Gauss-Seidel projection method for micromagnetics simulations", *J. Comput. Phys.*, **171**, 357–372 (2001).

[721] D. Wang, A. Verekin, R. Sobolewski, R. Adam, A. vander Hart, and R. Franchy, "Magnetooptical Kerr effect measurements of ultrafast spin dynamics in cobalt nanodots", *IEEE Trans. Nanotech.*, **4**, 460–464 (2005).

[722] R.K. Wangsness, "Magnetic resonance for arbitrary field strengths", *Phys. Rev.*, **98**, 927–933 (1955).

[723] R.K. Wangsness, "Magnetic resonance and minimum entropy production. Macroscopic equations of motion", *Phys. Rev.*, **104**, 857–866 (1956).

[724] W. Weber, S. Riesen, and H.C. Siegmann, "Magnetization precession by hot spin injection", *Science*, **291**, 1015–1018 (2001).

[725] J.E. Wegrowe, D. Kelly, Y. Jaccard, P. Guittienne, and J.P. Ansermet, "Current-induced magnetization reversal in magnetic nanowires", *Europhys. Lett.*, **45**, 626–632 (1999).

[726] J.E. Wegrowe, A. Comment, Y. Jaccard, J.P. Ansermet, N.M. Dempsey, and J.P. Nozieres, "Spin-dependent scattering of a domain wall of controlled size", *Phys. Rev. B*, **61**, 12216–12220 (2000).

[727] J.E. Wegrowe, "Thermokinetic approach of the generalized Landau–Lifshitz–Gilbert equation with spin-polarized current", *Phys. Rev. B*, **62**, 1067–1074 (2000).

[728] J.E. Wegrowe, D. Kelly, X. Hoffer, P. Guittienne, and J.P. Ansermet, "Tailoring anisotropic magnetoresistance and giant magnetoresistance hysteresis loops with spin-polarized current injection", *J. Appl. Phys.*, **89**, 7127–7129 (2001).

[729] J.E. Wegrowe, D. Kelly, T. Truong, P. Guittienne, and J.P. Ansermet, "Magnetization reversal triggered by spin-polarized current in magnetic nanowires", *Europhys. Lett.*, **56**, 748–754 (2001).

[730] J.E. Wegrowe, A. Fabian, P. Guittienne, X. Hoffer, D. Kelly, J.P. Ansermet, and E. Olive, "Exchange torque and spin transfer between spin polarized current and ferromagnetic layers", *Appl. Phys. Lett.*, **80**, 3775–3777 (2002).

[731] J.E. Wegrowe, X. Hoffer, P. Guittienne, A. Fabian, L. Gravier, T. Wade, and J.P. Ansermet, "Spin-polarized current induced magnetization switch: Is the modulus of the magnetic layer conserved?", *J. Appl. Phys.*, **91**, 6806–6811 (2002).

[732] J.E. Wegrowe, "Magnetization reversal and two-level fluctuations by spin injection in a ferromagnetic metallic layer", *Phys. Rev. B*, **68**, 214414 (2003).

[733] J.E. Wegrowe, M.C. Ciornei, and H.J. Drouhin, "Spin transfer in an open ferromagnetic layer: from negative damping to effective temperature", *J. Phys.: Condens. Matter*, **19**, 165213 (2007).

[734] M.T. Weiss, "Microwave and low-frequency oscillation due to resonance instabilities in ferrites", *Phys. Rev. Lett.*, **1**, 239–241 (1958).

[735] U. Weiss, "Operator ordering schemes and covariant path integrals of quantum and stochastic processes in curved space", *Z. Physik B*, **30**, 429–436 (1978).

[736] U. Weiss, "Decay of unstable states in macroscopic systems", *Phys. Rev. A*, **25**, 2444–2447 (1982).

[737] N. Wellander and G. Kristensson, "Homogenization of the Maxwell equations at fixed frequency", *SIAM J. Appl. Math.*, **64**, 170 (2003).

[738] W. Wernsdorfer, E. Bonet-Orozco, K. Hasselbach, A. Benoit, B. Barbara, N. Demoncy, A. Loiseau, H. Pascard, and D. Mailly, "Experimental evidence of the Néel-Brown model of magnetization reversal", *Phys. Rev. Lett.*, **78**, 1791–1794 (1997).

[739] R.M. White, *Quantum Theory of Magnetism*, Springer-Verlag, New York, 2007.

[740] P.E. Wigen (ed.), *Nonlinear Phenomena and Chaos In Magnetic Materials*, World Scientific Publishing, Singapore, 1994.

[741] S. Wiggins, *Introduction to Applied Nonlinear Dynamical Systems and Chaos*, Springer, New York, 1990.

[742] D.C. Worledge, "Magnetic phase diagram of two identical coupled nanomagnets", *Appl. Phys. Lett.*, **84**, 2847–2849 (2004).

[743] D.C. Worledge, "Spin flop switching for magnetic random access memory", *Appl. Phys. Lett.*, **84**, 4559–4561 (2004).

[744] H. Xi, K.Z. Gao, and Y. Shi, "Microwave generation by a direct current spin-polarized current in nanoscale square magnets", *Appl. Phys. Lett.*, **84**, 4977–4979 (2004).

[745] H. Xi and Z. Lin, "In-plane magnetization dynamics driven by spin-polarized currents in magnetic nanostructures", *Phys. Rev. B*, **70**, 092403 (2004).

[746] K. Xia, P.J. Kelly, G.E.W. Bauer, A. Brataas, and I. Turek, "Effect of antiferromagnetic interlayer coupling on current-assisted magnetization switching", *Phys. Rev. B*, **65**, 220401(R) (2002).

[747] D. Xiao, M. Tsoi, and Q. Niu, "Minimal field requirement in precessional magnetization switching", *J. Appl. Phys.*, **99**, 013903 (2006).

[748] Y.B. Xu, C.A.F. Vaz, A. Hirohata, C.C. Yao, W.Y. Lee, J.A.C. Bland, F. Rousseaux, E. Cambril, and H. Launois, "Domain wall trapping probed by magnetoresistance and magnetic force microscopy in submicron ferromagnetic wire structures", *J. Appl. Phys.*, **85**, 6178–6180 (1999).

[749] A. Yamaguchi, T. Ono, S. Nasu, K. Miyake, K. Mibu, and T. Shinjo, "Real-space observation of current-driven domain wall motion in submicron magnetic wires", *Phys. Rev. Lett.*, **92**, 077205 (2004).

[750] M. Yamanouchi, D. Chiba, F. Matsukura, and H. Ohno, "Current-induced domain-wall switching in a ferromagnetic semiconductor structure", *Nature*, **428**, 539–542 (2004).

[751] A. Yamasaki, W. Wulfhekel, R. Hertel, S. Suga, and J. Kirschner, "Direct observation of the single-domain limit of Fe nanomagnets by spin-polarized scanning tunneling spectroscopy", *Phys. Rev. Lett.*, **91**, 127201 (2003).

[752] Z. Yang, S. Zhang, and Y.C. Li, "Chaotic dynamics of spin-valve oscillator", *Phys. Rev. Lett.*, **99**, 134101 (2007).

[753] Y.G. Yoo, M. Klaui, C.A.F. Vaz, L.J. Heyderman, and J.A.C. Bland, "Switching field phase diagram of Co nanoring magnets", *Appl. Phys. Lett.*, **82**, 2470–2472 (2003).

[754] S.W. Yuan and H.N. Bertram, "Fast adaptive algorithms for micromagnetics", *IEEE Trans. Magn.*, **28**, 2031 (1992).

[755] X.Y. Zhang and H. Suhl, "Theory of auto-oscillations in high-power ferromagnetic resonance", *Phys. Rev. B*, **38**, 4893–4905 (1988).

[756] Z. Zhang, L. Zhou, P.E. Wigen, and K. Ounadjela, "Using ferromagnetic resonance as a sensitive method to study temperature dependence of interlayer exchange coupling", *Phys. Rev. Lett.*, **73**, 336–339 (1994).

[757] S. Zhang, P.M. Levy, A.C. Marley, and S.S.P. Parkin, "Quenching of magnetoresistance by hot electrons in magnetic tunnel junctions", *Phys. Rev. Lett.*, **79**, 3744–3747 (1997).

[758] S. Zhang, P.M. Levy, and A. Fert, "Mechanisms of spin-polarized current-driven magnetization switching", *Phys. Rev. Lett.*, **88**, 236601 (2002).

[759] S. Zhang and Z. Li, "Roles of nonequilibrium conduction electrons on the magnetization dynamics of ferromagnets", *Phys. Rev. Lett.*, **93**, 127204 (2004).

[760] Y. Zhang, Z. Zhang, Y. Liu, B. Ma, and Q.Y. Jin, "Spin-transfer-induced magnetization switching in magnetic tunnel junctions", *J. Appl. Phys.*, **99**, 08G515 (2006).

[761] J.G. Zhu, "Thermal magnetic noise and spectra in spin valve heads", *J. Appl. Phys.*, **91**, 7273–7275 (2002).

[762] J.G. Zhu, X. Zhu, and Y. Tang, "Micorwave assisted magnetic recording", *IEEE Trans. Magn.*, **44**, 125–131 (2008).

[763] I. Zutic, J. Fabian, and S. das Sarma, "Spintronics: fundamentals and applications", *Rev. Mod. Phys.*, **76**, 323–410 (2004).

Index